UNIVERSITY OF SOUTHAMPTON

FACULTY OF ENGINEERING AND THE ENVIRONMENT

Engineering Sciences

Exploring the Use of Tomography for the Quantification of Cementum Growth Patterns Across the Mammal Phylogeny

by

Elis Newham

A thesis submitted in partial fulfillment for the degree of Doctor of Philosophy

Supervisors: **Dr Philipp Schneider**
Dr Neil Gostling, Dr Pamela Gill & Dr Ian Corfe.

1st May, 2018

UNIVERSITY OF SOUTHAMPTON

ABSTRACT

FACULTY OF ENGINEERING AND THE ENVIRONMENT

Doctor of Philosophy

EXPLORING THE USE OF TOMOGRAPHY FOR THE QUANTIFICATION OF CEMENTUM GROWTH PATTERNS ACROSS THE MAMMAL PHYLOGENY

by Elis Newham

This project is focused on the application of state-of-the-art imaging technologies and novel analytical techniques in order to improve understanding of the growth and structure of cementum; the mineralised tissue that connects teeth to the peridontium in mammals. Like all vertebrate hard tissues, the growth of cementum is controlled by a series of natural rhythms that control its pattern and pace. This is recorded in circum-annual increments (similar to tree rings) hypothetically created by dietary differences in the production rate of its two key components; hydroxyapatite matrix and collagen fibres. As cementum is only rarely resorbed, these increments can be counted to provide a direct estimate of chronological age, a technique known as cementochronology. Further, the circum-annual rhythm followed by cementum increments may also allow them to record discrete life history events that create severe strain on body metabolism over the course of several months, such as pregnancy.

However, the exact causation and rhythm of cementum increments is still poorly understood due to a paucity of direct experimental study. The majority of previous studies of cementochronology have been based on thin-section histology, and several caveats of this approach have undermined confidence in the ability to quantitatively analyse cementum increments. Overall, current study of cementum lacks the application of modern technology and analytical methods that have revolutionised interpretation of microstructures and ultrastructures of other hard tissues such as bone, and increased their use as hallmarks of disease or as records of life history.

The application of synchrotron X-ray tomography (SR CT) has here been used to improve understanding of the structure and count of cementum increments in mammals ranging from our oldest ancestors, to some of our closest relatives. The non-destructive nature and high throughput of SR CT has allowed study of large samples of *Morganucodon* and *Kuehneotherium*, two of the oldest known fossil mammals from the early Jurassic (~200 million years ago). The three-dimensional perspective and ultra-high resolutions (<500nm voxel size) of SR CT data provided an unprecedented level of detail to study and more precise counts of increments than previous thin-section-based techniques, which in-turn provided minimum estimates of maximum lifespan for both animals. Further, as the lifespans of modern mammals are inversely related to their basal metabolic rate and post-natal growth rate, these

estimates have been used to improve understanding of the physiology of early mammals and the evolution of the sophisticated endothermic (warm-blooded) physiology of modern mammals.

From this study the potential of SR CT for analyzing cementum growth, and the relationship between cementum growth and life history variables, was made clear. Subsequent SR CT imaging was conducted on a sample of rhesus macaque monkeys (*Macaca mulatta*), raised in laboratory conditions. One sub-sample consisted of breeding females, another of non-breeding females, as well as a juvenile female and a male. This sample was used to study the optimal experimental settings for SR CT imaging of cementum, and generate an image processing and analysis workflow to automatically count cementum increments and study their shape and texture using computer vision. This workflow was then used to study sexual dimorphism in increment structure, and to investigate the potential for pregnancy events to be recorded in SR CT cementum data in both the *M. mulatta* sample and samples of C12th and C19th century archaeological humans of known sex (including three C19th individuals of known age and reproductive history). Significant dimorphism in increment shape and texture was found in both taxa. Female increments were found to be significantly more tortuous than males, with lower contrast and less-well defined boundaries. Further, increments formed during pregnancy were found to be more chaotic in shape and texture than surrounding increments.

Finally, SR CT was used to image the cementum increments of a diverse fauna of fossil mammals from the Middle Jurassic of the UK (Bathonian: ~168-166 million years ago). This fauna can be split into stem mammals (mammaliaforms alongside *Morganucodon* and *Kuehneotherium*), and crown mammals (bracketed evolutionarily by living mammals). Using the automative counting technique developed for counting primate cementum increments, it was found that mammaliaforms lived signficiantly longer maximum lifespans than contemporary crown mammals. This in-turn suggests a proportional disparity in metabolic potential, and that Mid Jurassic crown mammals had developed a similar basal metabolic rate to living mammals of comparable body mass.

In summary, the work presented in this thesis has shown that the application of state-of-the-art analysis techniques has the ability to maximise the potential of cementum as a recording structure of disparate elements of life history among mammals. The workflow for imaging, processing and study developed here can be applied to a wide range of life history variables, for both fossil and extant taxa. The automated nature of the image analysis techniques presented overcomes many of the major caveats highlighted in previous thin-section based studies of cementum and their applicability, robusticity and accuracy can only be improved by their continued development in the wider cementochronology community outside of this project.

Table of Contents

List of figures

quantitative histological measurements of extant mammals, and fossil cyncodonts (**node 3**) have been used to suggest fairly static resting metabolic rates close to those of extant mammals amongst Late Permian-Triassic cynodonts. Evidence of maxillary nasal turbinates, now only seen in extant endotherms, are first seen in derived therocephalians of the Early Triassic. Histological evidence also suggests that these taxa may have had comparably sized red blood cells compared with extant mammals. However, these taxa show a fall in the proportion of fibrolamellar bone through their evolution. Members of the derived Late Triassic cynodont clade Prozostrodontia show the earliest evidence of an ossified intraorbital canal, that house the base of sensory vibrissae (whiskers) in extant mammals. *Morganucodon* is the most basal member of the Mammaliaformes (**node 4**), and shows the earliest evidence of diphyodonty (single replacement of 'milk teeth'), that has been used to suggest maternal feeding of young via a mammary gland. Measurements of the morphology of the dentary bone of *Morganucodon* have also been used to suggest that the majority of growth of this element occurred before the replacement of the deciduous 'milk' tooth, which may be indicative of the origin of the rigid 'determinate' growth strategy experienced by extant mammals. A more derived docodont mammaliaform, *Castorocauda*, is the most basal synapsid with evidence of a full fur pelage covering the body, a prerequisite for mammalian endothermy. *Castorocauda* is also inferred as occupying a semi-aquatic ecology, and forms an early member of a hypothesised adaptive ecological radiation of mammaliaforms and crown mammals (**node 5**) during the Early-mid Jurassic. This included several gliding taxa including *Arboroharamiya* (a euharamiyidan taxon that may be part of Mammaliaformes or crown Mammalia). Finally, a truly parasagittal posture (upright as opposed to sprawling) has not been shown in any taxon until the earliest therian (**node 6**) relatives of metatherian/marsupial and eutherian/placental mammals in the Early Cretaceous. Sketches of synapsids running from left (Early Permian) to right (End Cretaceous): *Dimetrodon* (original by Dmitry Bogdanov), *Sycosaurus* (original by Eduardo Karkemish), *Lystrosaurus* (original by Eduardo Karkemish), *Thrinaxodon* (original by Kana Hebi), *Morganucodon* (original by Martin Chavez), *Castorocauda* (original by April Neander), *Arboroharamiya* (original by Shi Ai-juan), *Vilevolodon* (original by April Neander), *Zhangheotherium* (original by Nix illustrations), *Liaoconodon* (original by Nix illustrations), *Repenomamus* (original by Nix illustrations), *Catopsbaatar* (original by Nix illustrations). Numbered references: **1** –

List of tables

Declaration of Authorship

I, Elis Newham, declare that the thesis entitled *Exploring the use of tomography for the quantification of cementum growth patterns across the mammal phylogeny* and the work presented in the thesis are both my own, and have been generated by me as the result of my own original research. I confirm that:

- This work was done wholly or mainly while in candidature for a research degree at this University;
- Where any part of this thesis has previously been submitted for a degree or any other qualification at this University or any other institution, this has been clearly stated;
- Where I have consulted the published work of others, this is always clearly attributed;
- Where I have quoted from the work of others, the source is always given. With the exception of such quotations, this thesis is entirely my own work;
- I have acknowledged all main sources of help;
- Where the thesis is based on work done by myself jointly with others, I have made clear exactly what was done by others and what I have contributed myself;

Signed _____

Date 01/05/2018

Acknowledgements

First and foremost, I would like to thank Dr Pamela Gill for her supervision, guidance and patience over the last six years of my academic career. Without Dr Gill I would not be writing this passage today and that is no exaggeration. In that vein I also thank my entire supervisory team (in order of appearance): Dr Ian Corfe, Dr Philipp Schneider and Dr Neil Gostling. I emphasize the word team more than anything as working on this project has rarely felt like a hierarchical affair, and each member has finely tuned the balance between professionalism and friendship so that I can happily call them my friends and look back over four years of excitement, laughter and brilliant science. I would also like to thank Prof. Kate Robson Brown for her continued support, access to specimens and enthusiasm, and Prof. Ian Sinclair for his accommodation of the project as an examiner for each major milestone it has reached.

A major factor of this project has been experimentation at various synchrotron X-ray light sources, and anyone who has experience of these experiments knows exactly how intense they are and how vital the nature of the experimental team is. I am thus exceedingly grateful to every member of each experiment. These include; the staff at the μ-VIS imaging centre: Dr Orestis Katsamenis, Dr Sharif Ahmed, Dr Mark Mavrogordato, Dr Neil O'brien and Dr Richard Boardman; several engineering PhD students: Dr Berit Zeller-Plumhoff, Juan A. Núñez and Gregor Borstnar; and a host of palaeontologists and archaeologists: Prof. Thomas Martin, Dr Pip Brewer, Dr Simone Hoffman, Dr Julia Schultz, Dr Jen Bright, Dr Liz Martin-Silverstone, Dr Aubrey Roberts, Dr Jessica Laurence, Christianne Fernee, Elsa Panciroli, and Kai Jäger; and finally our tame physicists: Dr Aki Kallonen and Dr Heikki Haario.

This project was funded by both the Natural Environmental Research Council, and the Engineering and Physical Sciences Research Council, and received multiple grants from the European Union to fund synchrotron experiments.

For Mud.

Chapter 1

Introduction

1.1. Cementum as a recording structure of life history in mammals

The study of life history has been a focal point of biology for centuries. The differing behaviours, lifestyles and growth series (ontogenies) of animals and how they relate to morphology form a cornerstone of Darwin's theory of natural selection. Before Darwin, empirical observation of animal behaviour was used as an important tool in the early classification of Animalia; from Ancient Greece to Carl Linnaeus. The twentieth century saw the advent and development of our understanding of genetics, and with this the mechanisms of how behavioural and physiological traits interplay with evolution. The identification of hallmarks of various life history traits in the morphology and microstructure of mineralised tissues including bone and teeth in extant (living) animals have also offered insight into the life histories of fossils and how they evolved through deep time.

Mammals can be taxonomically defined by several life history traits and variables, the combination of which is not seen in any other extant (living) clade (Kemp, 2007; Luo, 2007). Most of these variables are inherently related to endothermy, the ability to produce and control body temperature and metabolic output. This is maintained by several soft tissue characteristics such as a "breathable" skin and fur that allow efficient transfer or storage of body heat (Kemp, 2006), and brown adipose tissue (body fat) that allows for non-shivering thermogenesis (heat production)(Pond et al., 1984). Endotherms are characterised by elevated juvenile growth rates that reach a rapid asymptote before almost stopping completely during adulthood at the attainment of skeletal and sexual maturity ("determinate growth strategies")(O'Meara and Asher, 2016).

A stable body temperature and elevated metabolic rate may have fostered the evolution of pregnancy, another key mammalian innovation. While not the only living or fossil animals to develop viviparity (internal development and live birth of offspring), the eutherian clade of mammals have developed the most efficient form of nutrient

exchange between mother and foetus; the placenta. Members of each major mammalian clade (eutherians, metatherians and monotremes) nutritionally sustain their infants for a significant period after they are born using secretions from the mammary gland, another unique mammalian innovation.

Pregnancy is one of several key life history variables and events among living mammal populations that are the focus of study in a wide range of biological disciplines. These include maximum lifespan (Sacher, 1975; Smith, 1989; McKee, 1995; Hulbert et al., 2007; Shattuck and williams, 2010), age at sexual maturity (DeMaster, 1984; Oli and Dobson, 1999; Rosing-Asvid et al., 2002; Dutta and Sengupta, 2016), and reproductive rate and success (DeGabriel et al., 2009; Reale et al., 2009; Lukas and Clutton-Brock, 2014; Douhard et al., 2016). During this period of dramatic and global environmental change, habitat restriction and unsustainable agriculture, the monitoring of animal populations under threat is of unprecedented importance for ecology, zoology, and even agricultural science. These variables have been studied using a wide variety of biological structures, the overwhelming majority of research being focussed on osteological and histological indicators. These can be generally classified into two categories: indicators that estimate age based on the accumulation of morphological skeletal/hard tissue characteristics with age (Saunders et al., 1992; Dudar et al., 1993; Ritz-Timme et al., 2000); and incremental structures in the microscopic texture of mineralised tissues (Klevezal and Kleinenberg, 1967; Stout et al., 1992; Klevezal, 1995; Padian, 2013). Several studies have reported substantial discrepancies between 'biological' age estimated by morphological indicators and true chronological age (Morris, 1972; Spinage, 1973; DeMaster, 1984; Lovejoy et al., 1985; Jones, 1988; Hoppa, 2000). These inconsistencies have led to a considerable amount of research into the use of direct records of life history using the ultrastructure of mineralised tissues (Gauthier and Schutkowski, 2013; Kolb, 2015; Naji et al., 2016).

All mammalian mineralised dental tissues comprise a series of growth markers of differing periodicity and causation (Klevezal, 1995; Le Cabec et al., 2015). Cementum is the mineralised tissue surrounding root dentine, serving as an attachment site between the tooth root and the periodontal ligament (PDL) by mineralizing around and incorporating the collagenous Sharpey's fibres of the PDL. The tissue is unique amongst dental hard tissues as it grows continuously throughout life, in a step-wise manner that is widely regarded as following a circum-annual periodocity (Klevezal, 1995; Naji et al.,

2016)(Fig. 1.1). This mode of development is represented by a series of increments of different chemical and physical properties, creating discrete changes in optical luminance when viewed using optical microscopy (Zander, 1958; Lieberman, 1993, 1994; Stock et al., 2017). Cementochronology, the study of these increments, has been frequently used to estimate the chronological lifespan of extant mammals, and as a record of life history events that affect their physiology (Naji et al., 2016).

Cementochronology offers a useful tool for the forensic analysis of the life histories of both living and fossil mammals, including humans. The study of cementum increments has been conducted for decades as a record of chronological lifespan for over 70 species of extant mammals (Naji et al., 2016). The ability to confidently estimate age-at-death to the specific year benefits studies of maximum lifespan in populations of animals (Wall-Scheffler and Foley, 2008), and archaeological human populations (Stutz, 2002). Further, the opportunity afforded by the circum-annual rhythm of cementum increments allows specific events to be pinpointed within the cementum of an individual animal of known life history, in order to investigate potential relationships between such events and cementum growth. This has led to authors highlighting significant effects of various life history variables on cementum growth including the advent of sexual maturity (Klevezal and Stewart, 1994), pregnancy and parturition (von Biela et al., 2008; Medill et al., 2010), and even disease (Kagerer and Grupe, 2001).

However, the reception of cementochronology in the wider biological community has been undermined by repeated findings of poor accuracy between counts of increments and known age, especially in long living animals including humans, and poor precision in counts between workers (Renz and Radlanski, 2006). This is largely due to complexities in the pattern of increments frequently seen in populations of extant mammals (Klevezal, 1995). Cementum is a dynamic, biomechanically responsive tissue and increments can be seen to lense and coalesce in thin-sections. Problems created by these phenomena are compounded by the limitations of current methods used to study cementum increments, and disparities in the interpretation of cementum growth and structure between laboratories and individual researchers (Naji et al., 2016).

1.2. Cementochronology as a tool for assessing physiology in fossil mammaliaforms

In addition to its use in extant biology and recent archaeology, I propose that cementum may provide a novel tool for assessing the evolution of key life history variables among fossil crown mammals and their close stem mammalian relatives, the mammaliaforms (Fig. 1.2). In phylogenetics (the systematic study of interrelationships of organisms), crown groups are defined as the collection of taxa consisting of all of its living representations, and extinct members that are bracketed by living members back to their most recent common ancestor (see Fig. 1.3 for an explanation of stem-crown systematics). Mammaliaforms are stem mammals, and while they share many important mammalian characters including diphyodonty (with a single replacement of non-molariform teeth), heterodonty (the specialization of teeth into certain morphologies) and for at least some taxa, fur. They retain several primitive characteristics including restrictive shoulder and hip morphologies, and the retention of post-dentary bones in the mandible (and so no definitive "mammalian" middle ear detached completely from the mandible). Although a series of indirect and proximal indicators of metabolism have been used to suggest endothermy in mammaliaform taxa (discussed in detail in **Chapter 3**), the metabolic potential of these and early crown mammal taxa remains unclear, relative to extant mammals.

It is widely considered that relative growth and metabolic rates are recorded in the bone microstructure of tetrapods. The rapid juvenile growths of endothermic birds and mammals are reflected in their long-bone histology, producing a chaotic assemblage of woven bone fibres known as "fibrolamellar" bone. This is in contrast to the more orderly, laminar bone texture of ectothermic (cold blooded) animals that exhibit significantly slower growth rates (Ray et al., 2004). Endotherms also possess a series of other skeletal modifications specific to endothermy, including maxillary turbinates within the anterior nasal passage of the skull (Hillenius, 1994). These thin, highly complex structures counteract the dessicating effects on air flowing through the nasal passage associated with high endothermic ventilation rates, and allow endotherms to regulate internal water during aerobic activity. As cold external air is inhaled, it absorbs heat and moisture from the turbinal linings, preventing dessication of the lungs. Conversely, upon exhalation, warm, moist air from the lungs is cooled as it passes over the turbinates, and excess water vapour condenses on to the turbinal

surfaces where it is reclaimed into the body.

Mammals are the living representatives of Synapsida, a major lineage of animals originating in the Late Carboniferous. The evolution of Synapsida is characterised by a long-term phylogenetic trend towards more active lifestyle and endothermy (Kemp, 2006; 2007). This trend is evidenced in the appearance of fibrolamellar bone in intermittent taxa from pelycosaur-grade (basal order of synapsids including the sail-backed *Dimetrodon*) taxa in the Mid-Late Permian (Shelton and Sander, 2017). Evidence of maxillary turbinates has also been reported for several therapsid taxa including therocephalians (Fig. 1.2)(Ray et al., 2004), and more derived cynodont taxa (Olivier et al., 2017)(Fig. 1.2). However, although useful for interpreting aspects of physiology in fossils, the above lines of evidence can only offer a limited window onto the evolution of endothermy amongst synapsids, the wider clade of animals that eventually led to extant (living) mammals (Fig. 1.2). The relationship between bone growth and metabolism is complicated (Kemp, 2006), and the presence of fibrolamellar bone in some extant ectotherms including crocodiles and turtles (Tumarkin-Deratzian, 2007) suggests that it cannot be used as a conclusive indicator of endothermy in fossils. Further, the secondary reduction and loss of turbinates in extant endothermic birds, alongside comparable structures in the nasal pathways of ectothermic crocodilians, suggests that the presence of these turbinates is not a conclusive indicator of endothermy (Owerkowicz et al., 2015).

A series of more recent studies have focussed on indirect indicators of physiology in fossils. These range from inferring the size of red blood cells from bone microvasculature (Huttenlocker and Farmer, 2017), to assessing variation in oxygen isotopes in therapsid fossil bone through time (Rey et al., 2017), to estimating brain size relative to body mass using micro-computed tomographic imaging (μCT)(Rowe et al., 2011; Benoit et al., 2017; Laaß & Kaestner 2017). Each line of evidence enforces the hypothesis of a correlated progression towards higher metabolic potential through the synapsid lineage. However, the differing rates of evolution of various metabolic indicators suggests that this progression was complicated, involving a mosaic pattern of various traits evolving under changing selective pressures through time (Fig. 1.2).

Cementum offers the chance to estimate maximum lifespan in fossil taxa. The maximum lifespan of extant mammals is inversely proportional to their body mass (Hulbert et al., 2007). This relationship is believed to reflect several aspects of

metabolic scaling between mammals that significantly depart from allometry; smaller mammals live faster and die younger than larger mammals. The relationship between metabolism, lifespan and body mass among extant tetrapods can be illustrated by comparing the scaling relationships between body mass and lifespan in ectothermic reptiles versus endothermic mammals. While logarithmic regression slopes are similar for both clades, reptiles are predicted to have significantly higher lifespans than mammals of comparable body mass. Thus, if both lifespan and body mass can be confidently estimated for fossil taxa across the early mammaliaform and mammal phylogeny, their plotted metabolic values and positions relative to living mammal taxa and reptile taxa may provide a new line of evidence for the metabolic potential of fossil mammaliaforms and mammals.

1.3. Aims of this thesis

It is clear that cementum is a tissue of exciting potential for the study of life history in living and fossil mammals. However, for this potential to be fulfilled, current methods for imaging and analysis must be improved in order to improve our understanding of the growth of cementum and its relationship with life history in mammals. This research project primarily aims to explore new avenues for the study of cementum increments and their relationship with life history in mammals. There are three principal objectives:

1. **Critically evaluate the current state-of-the-art in cementum imaging and analysis, taking inspiration from other disciplines to suggest new avenues for study.** The current most commonly used method for imaging and analysis of cementum increments is the microscopic study of histological thin-sections. The caveats to this method will be discussed and, by placing current methodologies in a broader scientific context, lessons learned from studying other biological and man-made microstructures can be applied to cementum. A review will be conducted regarding the wealth of technologies and methodologies commonly applied to other biological structures and their potential for studying cementum discussed.

2. **Explore and optimize the use of one such technology, synchrotron radiation based micro-computed tomography (SR CT), for imaging and analyzing cementum increments.** SR CT offers a non-destructive, high resolution imaging technology for studying cementum increments. As a volumetric imaging modality, SR CT may also overcome several of the key caveats identified for thin-section imaging of complexities in increment patterns. Here, SR CT will be trialed for imaging cementum increments from a sample of female *Macaca mulatta* (Rhesus macaque) cementum. The effects of changing key experimental parameters will be assessed in regards to the image quality of eventual reconstructions, in order to generate an optimum set of parameters for imaging cementum increments. Finally, a suite of novel image processing and analysis techniques will be developed and validated for isolating key morphological and textural parameters of cementum increments.

3. **Use this new imaging and analysis protocol to investigate the potential of cementum as a record of life history.** This objective will be achieved through two principal experiments:

    a. **SR CT investigation of sexual dimorphism in cementum microstructure.** The cementum of female versus male individuals will be compared in a laboratory population of breeding female, non-breeding female and male *M. mulatta* individuals, a C12th century archaeological human population and a C19th century archaeological human population (both sexed using osteoarchaeological metrics) in a quantitative manner using the techniques developed to isolate increment morphology.

    b. **SR CT imaging of cementum increments to estimate lifespan among early mammals.** The non-destructive nature of SR CT has allowed the imaging of cementum increments in Mesozoic fossils for the first time. Initial investigation will focus on two basal mammaliaforms from the Late Triassic (stem mammals) *Morganucodon* and *Kuehneotherium.* The study of population-sized samples will allow an estimate of maximum lifespan for both taxa. Following the series of proportional relationships between lifespan, body mass, basal metabolic rate and post-natal growth rate, comparison between the predicted lifespans and body masses of these basal fossil taxa with those of extant mammals will provide new information on the metabolic potential of

basal mammaliaforms. This work will then be expanded and placed in a broader context by studying a diverse mammaliaform fauna from the Mid Jurassic, comprising both stem mammaliaforms and crown mammals, in order to assess differences in life history strategies amongst contemporaneous taxa occupying different nodes of the mammalian phylogeny.

1.4. Thesis structure

Chapter 2 introduces the biology of cementum and current understanding of the nature and causation of its circum-annual increment patterns. The complexities in studying cementum increments are split into biological uncertainties; focusing on the causation of increments and their complexities and how these have been perceived and addressed in previous studies, and methodological uncertainties; providing a critical review of current thin-sectioning and analysis methods. A summary of suggestions inspired by other age estimation techniques are then presented that may benefit future studies. Finally, a variety of techniques are presented that may offer new insights into the relationship between life history and cementum growth, focusing particularly on micro-computed tomography (μCT) and synchrotron radiation based computed-tomography (SR CT).

Chapter 3 serves as a case study for the use of SR CT for imaging cementum increments in some of the basal-most mammaliaforms, *Morganucodon* and *Kuehneotherium* from the Latest Triassic. The imaging of population-sized samples allowed for minimum estimates of maximum lifespan of nine years for *Khueneotherium* and 14 years for *Morganucodon*, with increments counted using both human and computer vision. Scanning dentulous specimens suggests that counts are robust to potential diagenetic alteration, as the same counts are generated for several teeth and within the dentary bone itself. When these lifespans are projected against body mass estimates for both taxa, and compared to extant mammals and reptiles, it is strongly suggestive that both taxa occupied a lower metabolic grade than living mammals of comparable body mass. This is supported by estimates of basal metabolic rates and post-natal growth rates generated from these lifespan estimates, that in-turn suggest significantly lower growth and metabolic rates than living mammals of similar body mass.

A lower metabolic potential, relative to living mammals, is also suggested for *Morganucodon* from analysis performed in this chapter of the ratio between the area of its nutrient foramen aperture and the volume of its femur. The aperture of the nutrient foramina in the femurs of extant mammals and reptiles is known to direct correlate with the maximum metabolic rate an animal can achieve during sustained aerobic exercise. Its size, relative to the volume of the femur, can be used to estimate an index of blood flow for the animal in question. Mammals have been shown to have significantly higher estimates of blood flow from this ratio than reptiles. However, *Morganucodon* provides an estimate significantly closer to those of reptiles, suggesting that it could not attain the elevated metabolic rates during aerobic exercise characteristic of extant mammals.

Chapter 4 introduces, describes and discusses the results of an experiment designed to pioneer the use of SR CT for imaging cementum increments, and isolate the effects of experimental parameters on the quality of SR CT data of cementum increments in a laboratory-raised sample of rhesus macaque (*Macaca mulatta*) females. Following data acquisition, SR CT datasets are subject to a novel workflow for processing and analyzing increment data. Datasets are processed in order to isolate and straighten the cementum tissue, before maximizing increment contrast using steerable Gaussian filtering. Prior to filtering, the "texture" of images are quantitatively analysed by using micro-textural metrics to characterize greyscale distribution in individual SR CT slices. Results of these analyses can further be compared using principal components analysis in order to generate quantitative "texture space", where the most significant variation between datasets can be isolated. After filtering, contrast is sufficient to algorithmically isolate increments, transplanting them into their own images. This allows quantitative estimates of two-dimensional tortuosity to be generated, based on the ratio between the path-length of individual increments and the shortest possible path-length between its two end-points. Finally, an algorithmic increment counting technique is introduced that can generate accurate counts, compared to counts expected from known age, using solely computer vision. All methods introduced here are first validated in order to test their robusticity, accuracy and relationship with data quality.

Chapter 5 presents a second SR CT experiment designed to generate data that can be applied to the novel image analysis suite presented in **Chapter 4** to

investigate whether sexual dimorphism is present in primate cementum. The female *Macaca mulatta* sample studied in **Chapter 4** consists of females that were allowed to breed, and periods of pregnancy were closely monitored and recorded. A further sub-sample of non-breeding females, a juvenile female and a male specimen from the same population were also studied and analysed here. Two further samples of archaeological human cementum were also studied; the first originating from a C12th excavation from Taunton, Somerset (UK); the second originating from a C19th excavation at St Georges Church, Bristol (UK). Both archaeological human samples consisted of osteologically sexed individuals, and the C19th sample contains three individuals of known life history, including two females with known pregnancy records. The application of quantitative analyses of cementum texture and increment tortuosity suggest that female cementum produces significantly more tortuous increments that follow chaotic paths through the cementum, relative to highly contrasting but relatively straighter male increments. Further, increments formed during pregnancy are noticeably more isotropic and disturbed, compared to surrounding increments. The degree to which female cementum differs from male cementum may be sufficient to predict sex, and potentially individual pregnancy events in individuals of unknown life history.

Chapter 6 extends the SR CT study of fossil cementum into the Middle Jurassic to cover both mammaliaform and early crown mammal taxa. Cementum was studied in a wide range of taxa living coevally from the Bathonian fauna (~166-168 million years ago) of Oxfordshire, UK. From increment counts, maximum lifespans of mammaliaform taxa are similar to those of *Morganucodon* and *Kuehneotherium*, and significantly extend beyond those of extant mammals of comparable body mass. However, no fossil crown taxon provided lifespan estimates beyond those of extant mammals of similar body mass. This disparity in lifespan estimates is in-turn reflected in estimates of basal metabolic rate and post-natal growth rate, suggesting that crown taxa have significantly higher basal metabolic and growth rates than stem taxa living coevally in the same fauna.

The mid-Jurassic is a period of significant diversification in the mammalian fossil record, witnessing a pulse of both taxonomic and ecomorphological diversity. From the results reported here, it is posited that this reflects a proportional increase in metabolic potential among crown mammals to similar levels shown by extant forms.

Finally, **Chapter 7** summarises the progress made during this project in the context of previous imaging techniques, understanding and conclusions regarding cementum study. Future avenues of study are suggested to both test and expand upon conclusions made here regarding the relationship between cementum growth and aspects of life history, and to overcome limitations encountered through this project.

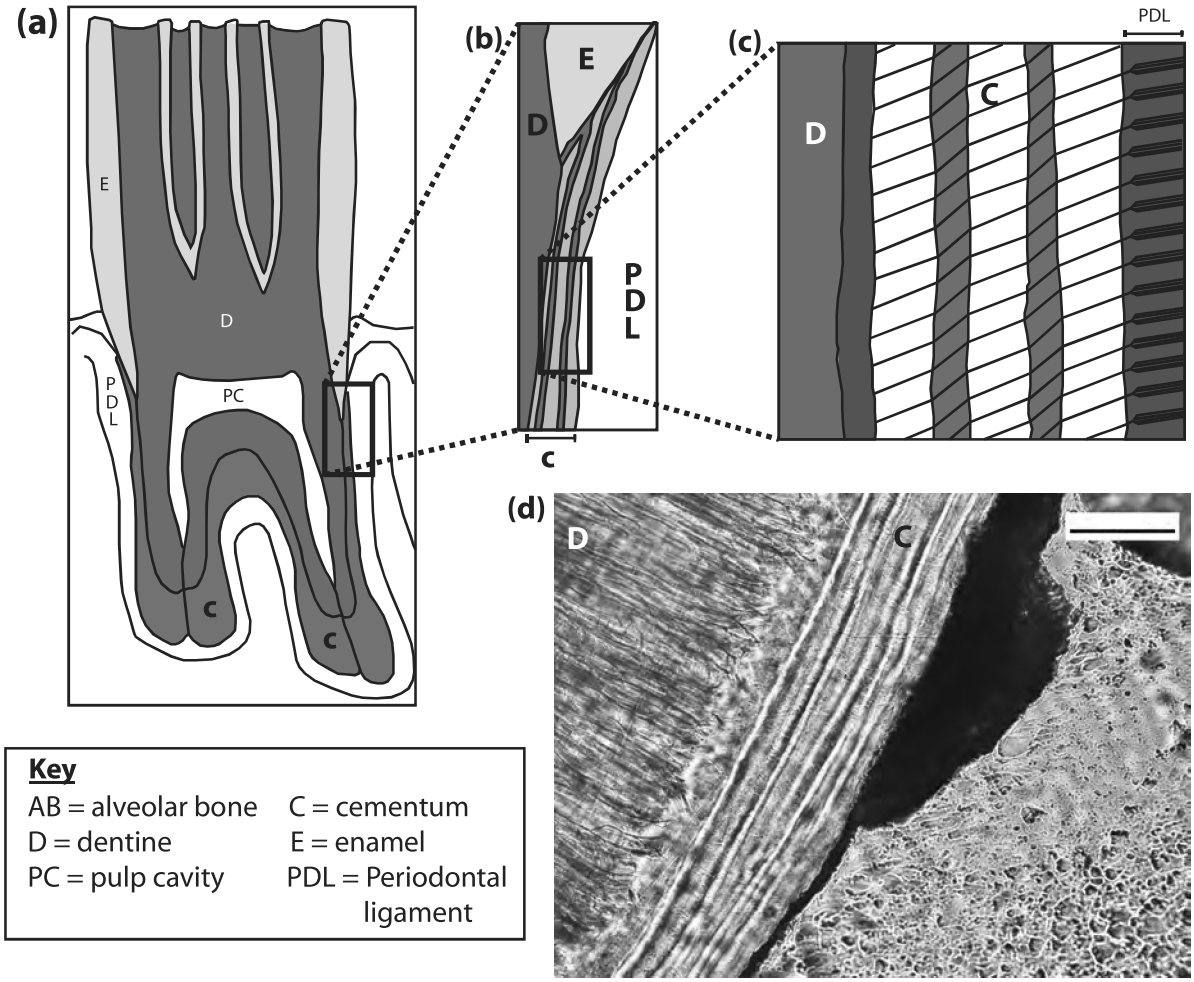

Figure 1.1. Summary of cementum ultrastructure. (**a**) Schematic longitudinal cross section through an adult bovid molar highlighting the extent of cementum deposition (red). (**b**) Schematic cross section of incremental cementum banding. (**c**) Schematic cross section across incremental cementum bands. Obliquely oriented cementoblasts (cementum-forming cells) first form due to the disintegration of Hertwig's sheath as a tooth erupts. Cementoblasts aggregate to form a single layer in contact with the tooths dentine, and deposit collagen fibres onto the dentine surface as the tooth continues to erupt. Fibres become held in place by calcitic material that is deposited within an amorphous substance surrounding them, forming the inorganic component of cementum. As cementum grows it attaches to Sharpey's fibrils, the principal fibres of the periodontal membrane, securely attaching the tooth to the alveolus. This process continually repeats itself through life, and the progressive nature of growth allows the attachment of the tooth root to the alveolus to be altered according to the functionality of the specific tooth. As the mineralisation front migrates through life, the angle of collagen fibril mineralisation will commonly shift in response to seasonal changes in food quality, with narrower layers corresponding to lower dietary quality. All images in (**a-c**) sourced and modified from Stutz (2002). (**d**) Detail from a histological thin section of the cementum of a European hedgehog (*Erinaceus europaeus*) viewed under reflected light, displaying distinct series of cementum increments. Scale bar = 50 μm.

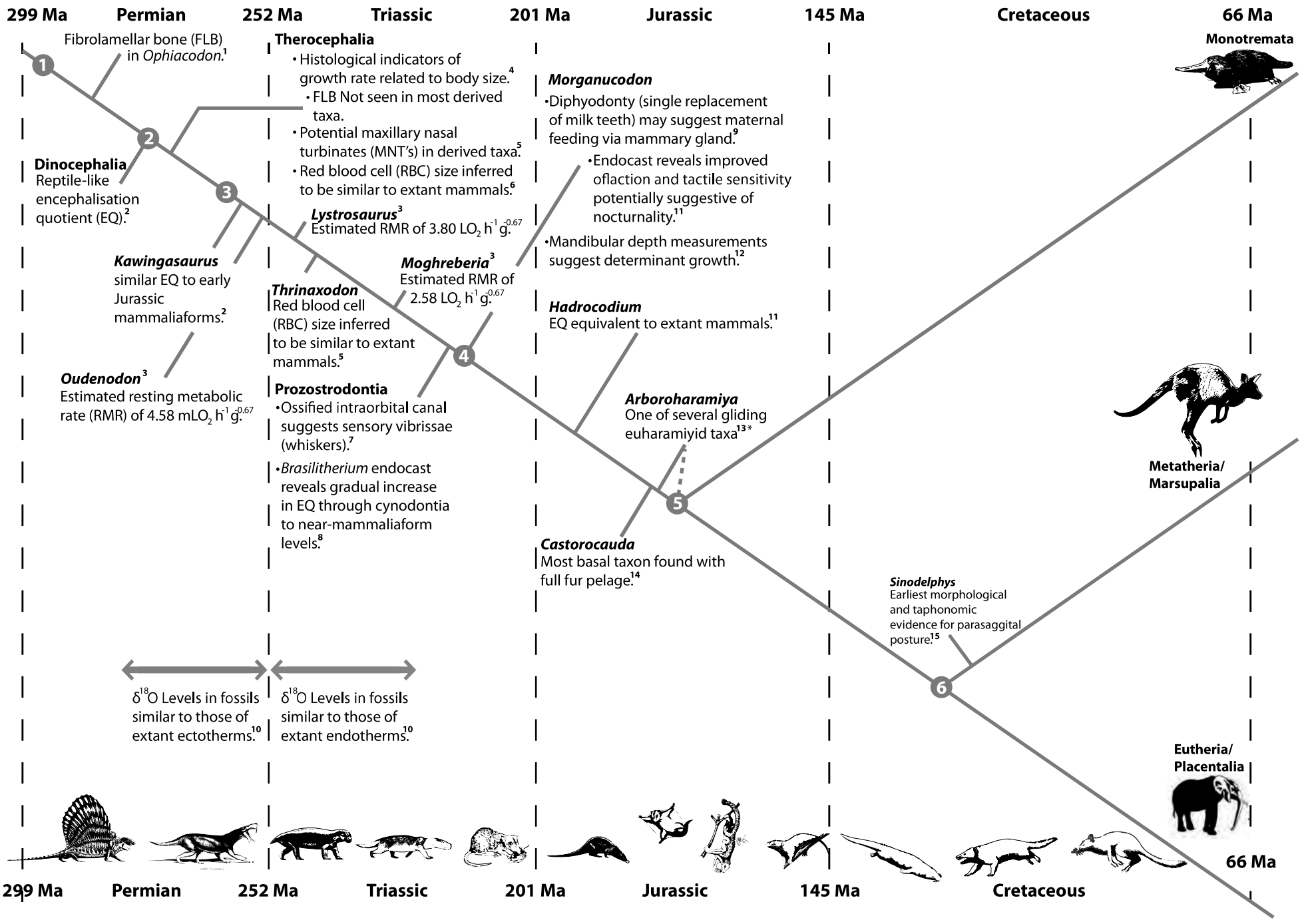
299 Ma
Permian
252 Ma
Triassic
201 Ma
Jurassic
145 Ma
Cretaceous
66 Ma
Fibrolamellar bone (FLB) in Ophiacodon.[1]
1
2
3
4
5
6
Dinocephalia
Reptile-like encephalisation quotient (EQ).[2]
Kawingasaurus
similar EQ to early Jurassic mammaliaforms.[2]
Oudenodon[3]
Estimated resting metabolic rate (RMR) of 4.58 mLO2 h-1 g-0.67
Therocephalia
• Histological indicators of growth rate related to body size.[4]
• FLB Not seen in most derived taxa.
• Potential maxillary nasal turbinates (MNT's) in derived taxa.[5]
• Red blood cell (RBC) size inferred to be similar to extant mammals.[6]
Lystrosaurus[3]
Estimated RMR of 3.80 LO2 h-1 g-0.67
Thrinaxodon
Red blood cell (RBC) size inferred to be similar to extant mammals.[5]
Moghreberia[3]
Estimated RMR of 2.58 LO2 h-1 g-0.67
Prozostrodontia
•Ossified intraorbital canal suggests sensory vibrissae (whiskers).[7]
•Brasilitherium endocast reveals gradual increase in EQ through cynodontia to near-mammaliaform levels.[8]
Morganucodon
•Diphyodonty (single replacement of milk teeth) may suggest maternal feeding via mammary gland.[9]
•Endocast reveals improved oflaction and tactile sensitivity potentially suggestive of nocturnality.[11]
•Mandibular depth measurements suggest determinant growth.[12]
Hadrocodium
EQ equivalent to extant mammals.[11]
Arboroharamiya
One of several gliding euharamiyid taxa[13*]
Castorocauda
Most basal taxon found with full fur pelage.[14]
Sinodelphys
Earliest morphological and taphonomic evidence for parasaggital posture.[15]
Monotremata
Metatheria/ Marsupalia
Eutheria/ Placentalia
δ18O Levels in fossils similar to those of extant ectotherms.[10]
δ18O Levels in fossils similar to those of extant endotherms.[10]

Figure 1.2. Summary of various lines of evidence for physiological evolution amongst synapsids between the Early Permian and End Cretaceous periods (299-66 million years; herein Ma [mega-annum]). Red nodes with white numbers 1-8 highlight the divergence of major lineages. Fibrolamellar bone indicative of fast growth rates found in intermittent taxa from the Early Permian derived pelycosaur (**node 1**) *Ophiacodon.* Micro-computed tomographic scanning has shown that encephalisation quotients (ratio between brain volume and body mass) steadily increased from levels similar to extant reptiles amongst the Mid Permian basal therapsid (**node 2**) clade Dinocephalia, to levels approaching that of extant mammals in the Early Jurassic mammaliaform (**node 4**) taxa *Morganucodon* and *Hadrocodium.* Comparative quantitative histological measurements of extant mammals, and fossil cyncodonts (**node 3**) have been used to suggest fairly static resting metabolic rates close to those of extant mammals amongst Late Permian-Triassic cynodonts. Evidence of maxillary nasal turbinates, now only seen in extant endotherms, are first seen in derived therocephalians of the Early Triassic. Histological evidence also suggests that these taxa may have had comparably sized red blood cells compared with extant mammals. However, these taxa show a fall in the proportion of fibrolamellar bone through their evolution. Members of the derived Late Triassic cynodont clade Prozostrodontia show the earliest evidence of an ossified intraorbital canal, that house the base of sensory vibrissae (whiskers) in extant mammals. *Morganucodon* is the most basal member of Mammaliaformes (**node 4**), and shows the earliest evidence of diphyodonty (single replacement of 'milk teeth'), that has been used to suggest maternal feeding of young via a mammary gland. Measurements of the morphology of the dentary bone of *Morganucodon* have also been used to suggest that the majority of growth of this element occurred before the replacement of the deciduous 'milk' tooth, which may be indicative of the origin of the rigid 'determinate' growth strategy experienced by extant mammals. A more derived docodont mammaliaform, *Castorocauda*, is the most basal synapsid with evidence of a full fur pelage covering the body, a prerequisite for mammalian endothermy. *Castorocauda* is also inferred as occupying a semi-aquatic ecology, and forms an early member of a hypothesised adaptive ecological radiation of mammaliaforms and crown mammals (**node 5**) during the Early-mid Jurassic. This included several gliding taxa including *Arboroharamiya* (a euharamiyidan taxon that may be part of Mammaliaformes or crown Mammalia). Finally, a truly parasagittal posture (upright as

opposed to sprawling) has not been shown in any taxon until the earliest therian (**node 6**) relatives of metatherian/marsupial and eutherian/placental mammals in the Early Cretaceous. Sketches of synapsids running from left (Early Permian) to right (End Cretaceous): *Dimetrodon* (original by Dmitry Bogdanov), *Sycosaurus* (original by Eduardo Karkemish), *Lystrosaurus* (original by Eduardo Karkemish), *Thrinaxodon* (original by Kana Hebi), *Morganucodon* (original by Martin Chavez), *Castorocauda* (original by April Neander), *Arboroharamiya* (original by Shi Ai-juan), *Vilevolodon* (original by April Neander), *Zhangheotherium* (original by Nix illustrations), *Liaoconodon* (original by Nix illustrations), *Repenomamus* (original by Nix illustrations), *Catopsbaatar* (original by Nix illustrations). Numbered references: **1** – Shelton and Sander, 2017; **2** – Benoit et al., 2017; **3** – Olivier et al., 2017; **4** – Huttenlocker and Brink, 2014; **5** – Hillenius, 1994; **6** – Huttenlocker and Farmer, 2017; **7** – Benoit et al., 2016; **8** – Rodrigues et al., 2014; **9** – Luo et al., 2004; **10** – Rey et al., 2017; **11** – Rowe et al., 2011; **12** – O'meara and Asher, 2014; **13** – Meng et al., 2018; **14** – Ji et al., 2006; **15** – Luo et al., 2003.

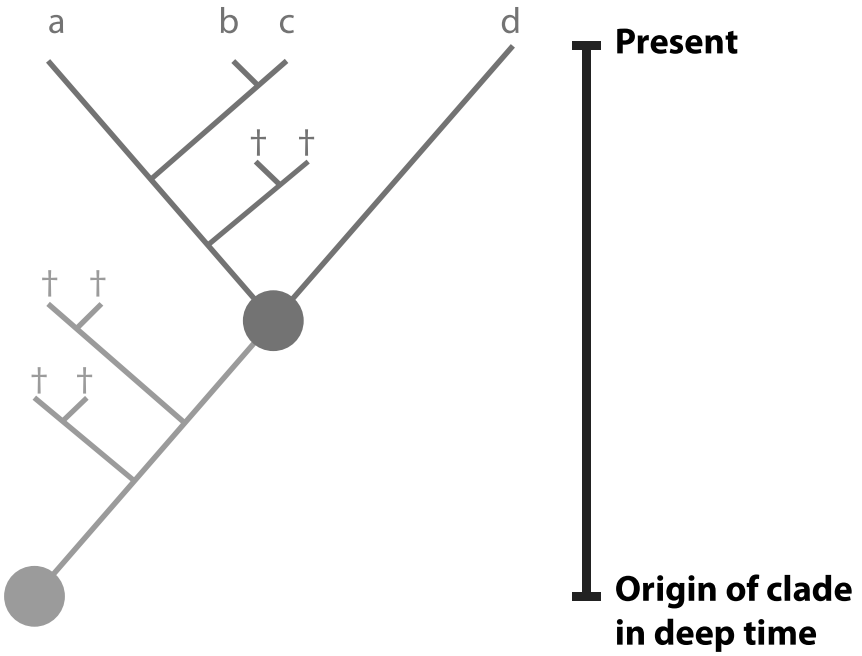

Figure 1.3. Hypothetical cladogram (evolutionary tree) to summarise stem-crown classification. The green node (circle) represents the basal node for this group. The stem members of the group are highlighted in green and are seperated from the crown node (red circle), that represents the last common ancester of all currently living members of the entire group (a-d). † Represents extinct taxa.

Chapter 2

New avenues for the study of cementochronology

Mammalian dental hard tissues follow a series of natural rhythms that control the pattern and pace of their deposition. These rhythms are often recorded by lines of arrested growth and accretional annuli that are produced at a range of periodicities. Such structures are understood to reflect cyclic changes in deposition rates from external environmental cues, internal rhythms, and disruptions to deposition due to important life history events. Cementum, the mineralised tissue that connects teeth to the periodontal ligament in mammal taxa, is made up of appositional increments of frequently noted annual periodicity. Further, as it is only resorbed in cases of severe gingival infection, many workers have attempted to use cementum increment count as a direct chronological age indicator, a technique known as cementochronology.

However, the exact causation and rhythm of cementum increments is still poorly understood due to a paucity of direct experimental study. The majority of previous studies of cementochronology have been based on thin-section histology, and several caveats of this approach have undermined confidence in the ability to quantitatively analyse cementum increments. Overall, current study of cementum lacks the application of modern technology and analytical methods that have revolutionised interpretation of microstructures and ultrastructures of other hard tissues such as bone, and increased their use as hallmarks of disease or as records of life history. This review is intended to highlight novel avenues of cementum study that provide the opportunity to broaden our knowledge of its growth and maximise its potential as a record of the physiology and ecology of, principally, living and fossil mammals.

2.1. INTRODUCTION

Mammals play a pivotal role in a diverse range of global ecosystems, and assessing their life history is a crucial element of many biological disciplines. Several methods have been suggested to estimate unknown elements of the lives of both living and deceased mammals. These can be generally classified into two categories: indicators that estimate age based on the correlation of various characteristics with bodily age (Saunders et al., 1992; Dudar et al., 1993; Ritz-Timme et al., 2000); and direct records of growth represented mainly by the ultrastructure of mineralised tissues (Klevezal and Kleinenberg, 1967; Stout et al., 1992; Klevezal, 1996; Padian, 2013). The first category, correlative age estimation methods, range from simple body mass estimates, to the fusion of epiphyses in long bones. However, several studies have reported substantial discrepancies between 'biological' age estimated by such indicators, and true chronological age (Morris, 1972; Spinage, 1973; DeMaster, 1984; Lovejoy et al., 1985; Jones, 1988; Hoppa, 2000). This inconsistency has led to a considerable amount of research into the second category, direct records of life history, and particularly the ultrastructure of mineralised tissues (Gauthier and Schutkowski, 2013; Kolb, 2015; Naji et al., 2016).

All mammalian mineralised dental tissues comprise a series of growth markers of differing periodicity and causation (Klevezal, 1995; Le Cabec et al., 2015). The two primary dental hard tissues, enamel and dentine, both produce two sets of growth markers of differing periodicity that record the growth of teeth. Cross- striations within enamel prisms, and lines of Von-Ebner within dentine represent diurnal cycles in the precipitation of both tissues. Striae of Retzius in the enamel and Andresen lines in the dentine record more long-term periods in growth rate, and both follow the same weekly-to-monthly periodicity (Klevezal, 1996). Although individual taxa have been shown to have a wide range in their periodicity of growth markers, these markers are well understood and have been studied in a host of extant mammal taxa and also in fossil teeth (von Koenigswald and Mörs, 2001; Castanet et al., 2004; Tafforeau and Smith, 2008). However, their use as a record of life history is generally restricted to the period of tooth growth and formation, which, dependent on species, may be only a small proportion of an animal's lifespan. In contrast, cementum, the mineralised tissue surrounding root dentine, grows continuously throughout life, in a step-wise, appositional manner. This mode of development is represented by a series of

increments of different chemical and physical properties, creating discrete changes in optical luminance (Lieberman, 1993, 1994; Stock et al., 2017; Zander, 1958). Cementochronology, the study of these increments, has been frequently used to estimate the chronological lifespan of extant mammals, and as a record of life history events that affect their physiology (Naji et al., 2016).

However, current understanding of the causation of cementum increments, and the relationship between increment count and age in extant mammals, is incomplete. This is largely due to complexities in the pattern of increments frequently seen in populations of extant mammals (Klevezal, 1995). Problems created by these phenomena are compounded by the limitations of current methods used to study cementum increments, and disparities in the interpretation of cementum growth and structure between laboratories and individual researchers (Naji et al., 2016). The following review aims to both evaluate current approaches to studying cementum increments, and outline new methods applied in other disciplines that may optimise future studies based on cementonchronology. We believe that application of these methods, combined with a solid grounding in cementum biology and standardised approaches of assessing accuracy and precision, should increase understanding of the influence of life history variables on cementum increments. The application of such methods should maximise the potential of cementum as a record of lifespan and life history in both living and fossil mammals.

Additionally, cementum has been found in a series of fossil and extant animals outside of the mammalian phylogeny, including crocodiles (Enax et al., 2013), iguanian squamate reptiles (Luan et al., 2009), ichthyosaurs (Maxwell et al., 2011), mosasaurs (Luan et al., 2009; LeBlanc et al., 2017), non-mammalian synapsids (LeBlanc et al., 2016), dinosaurs (Garcia & Zurriaguz 2015; Dumont et al., 2016; LeBlanc et al., 2017b), and toothed fossil birds (Dumont et al. 2016). It has recently been hypothesized that cementum, alongside alveolar bone, a periodontal ligament, and thecodont tooth implantation, is a plesiomorphic shared feature of amniotes in general due to its presence in stem amniote diadectid fossils that are over 290 million years old (Le Blanc & Reisz 2013; LeBlanc et al., 2017). Under this scenario, secondary loss of cementum and other periodontal features is associated with an increased rate of calcification of the periodontal ligament and timing changes of development and calcification of other dental tissues (LeBlanc et al., 2017). While we concentrate principally on cementum in living and fossil mammals in this review, the application of cementochronology thus

offers the opportunity to open a window on to the lives of a broad range of extant and extinct animals, and development of new techniques will be applicable to all of these.

2.2 Current understanding of cementum biology

Cementum is a mineralised connective tissue composed of collagen fibres encased within a matrix formed of hydroxyapatite, the primary component of bone and teeth. The cementum tissue is common to all animals that display thecodonty (teeth emplaced in specialised sockets) throughout the fossil record, and has been recently hypothesised to be plesiomorphic or primitive among amniotes (LeBlanc and Reisz, 2013). The growth of cementum is initiated and regulated by cells known as cementoblasts, and is triggered by the eruption of a tooth germ through the epithelial sheath of Hertwig (Bosshardt and Selvig, 1997). When fully developed, cementum surrounds the entirety of each root surface (Fig. 1.3). Cementum can also be found in other regions of the tooth in certain taxa, such as the occlusal surface of the crown in some hypsodont (high tooth-crowned) mammals.

Collagenous fibres found within cementum can be divided into intrinsic collagen fibres created within the cementum itself, and extrinsic Sharpey's fibres (Bosshardt and Selvig, 1997). Sharpey's fibres are the extension of periodontal collagen fibres within the cementum, anchored along the axis of major occlusive forces exerted by the surrounding hydroxyapatite matrix (Hiiemae and Crompton, 1985). The primary function of cementum is to attach teeth to the periodontal ligament, the soft tissue that supports teeth against occlusal forces. A secondary function is to combat the erosive effects of wear to the tooth crown, by increasing the height of the tooth within the dental alveolus or tooth socket. The rate of collagen apposition is at least partially dependent on the relative mastication forces acting upon the tooth, with higher shear stresses encouraging faster growth (Klevezal, 1995; Leider and Eugene Garbarino, 1987). Apposition rates of cellular and acellular cementum have been measured using fluorochrome marking in the monkey *Macaca fascicularis*, and at 0.1-0.5μm and 0.1 μm respectively, were shown to be one to two orders of magnitude lower than those of dentine in the same teeth (Bosshardt et al., 1989).

Histological study of cementum using optical microscopy has shown that its growth is recorded by a sequence of repeated sets of light and dark increments of

different optical transparencies (Klevezal and Kleinenberg, 1967). Reflected light microscopy has traditionally been used to partition these series into discrete phases. Under reflected light, each phase comprises a thick increment of high transparency cementum (a 'light' band), followed by a thin, highly opaque increment of dark cementum (a 'dark' band) (Fig. 1.3). For consistency, 'light' increments are defined as light under reflected light microscopy, and 'dark' increments are defined as dark under reflected light microscopy from herein. Scanning electron microscopy (SEM) has been used to suggest that the bands represent changes in the arrangement of Sharpey's fibres and the rate of their production, relative to the precipitation of the surrounding hydroxyapatite matrix (Boyde and Jones, 1968; Lieberman, 1993). Lieberman (1993) hypothesized that in thick light bands the matrix is produced at a sufficient rate to support Sharpey's fibres, resulting in fibrils organised perpendicular to the cemento-dentine junction. Thin dark bands in contrast are proposed to be composed of chaotically arranged fibrils oriented at lower angles relative to the cemento-dentine junction, and matrix that is not produced at a sufficient rate to properly support them (Lieberman, 1993, 1994). As mineralisation rates have been shown to be fairly uniform relative to these changes in matrix precipitation production, the lower rate of precipitation through unfavourable seasons usually leads to hypermineralisation of dark layers (Klevezal, 1995; Lieberman, 1994).

In a recent study, Stock et al. (2017) applied synchrotron X-ray radiation to examine several chemical and structural elements of beluga whale cementum using X-ray fluorescence and X-ray diffraction mapping. With resolutions of ~30μm, mapping highlighted discrete peaks in calcium and zinc content within thick 'light' bands, compared to surrounding thin 'dark' bands. This, along with corresponding peaks in carbonated hydroxyapatite, supports previous interpretation of differing degrees of mineral deposition between bands. However, the equivocal results of their crystallographic diffraction mapping showed no clear evidence of differences in hydroxyapatite between dark and light bands, and do not support previous interpretations of discrete changes in Sharpey's fibre orientation and structure between bands. One possibility is that these results may be specific to marine mammals since they are the opposite of those found in black bears by Smith et al. (1994), who found no differences in calcium and phosphorous between dark and light bands. However, another recent study (Colard et al. 2016) used polarized Raman spectroscopy of human canine teeth and also observed no difference in orientation of mineral crystals and

collagen fibres between dark and light bands, but instead a small increase in orientation variability in light lines. Together, these recent results suggest that our current understanding of the chemical and structural nature of incremental cementum is incomplete, and may be improved using such novel techniques and methodologies.

Cementum is unique in that its radial growth is continuous throughout an individual's entire life, although it is entirely avascular. It is also only rarely resorbed, in periods of severe gingival infection and caries. These phenomena have led many workers to derive chronological age estimates from absolute counts of cementum layers. So far, cementochronology has been used to accurately predict age in more than 70 extant mammal species, spanning 21 families and nine orders (Klevezal, 1995; Naji et al., 2016). Although the annual periodicity of cementum increments has been widely corroborated since the 1960's, there have been several hypotheses proposed to explain the causation of cementum incrementation. Early publications reported a relationship between the pattern of increments and reproductive cycles within several taxa (Low et al., 1963; Mitchell, 1967). However, this interpretation cannot explain increment patterns found in all animals studied. Regular increments can be found in juvenile animals, while castration does not seem to have any effect on the pattern of incrementation (Klevezal, 1995).

The causes of cementum increments are more widely considered to be seasonal differences in the general growth rate of an individual. Several studies have implemented tetracycline staining (both intravenously and orally) of teeth to show that growth of cementum is retarded or stopped altogether during unfavourable seasons (Coy and Garshelis, 1992; Klevezal, 1995; Kvaal and Solheim, 1995). This most often correlates with the formation of thin dark increments. However, the timing of formation of these increments has also been shown to be subject to age and sexual variation. The only direct experimental study of the causation of cementum increments has highlighted a correspondence with changes in the frequency and magnitude of mechanical strain on teeth caused by diet, and differences in the nutritional quality of diet, in domestic goats (*Capra hircus*) (Lieberman, 1994). Variations in the orientation of collagen fibres were found to be due to changes in the 'hardness' of foodstuffs making up an individual's diet (i.e. the proportion of preliminary softening of food before feeding), and the resulting magnitude and frequency of occlusal stresses acting upon the tooth. Variation in the nutritional quality of seasonal diets resulted in changes in the rate of

cementogenesis, creating thin hypermineralised layers during periods of poor nutritional intake.

This evidence suggests that light/dark layers are formed due to seasonal changes in diet quality and mechanical properties. However, this hypothesis can only explain the occurrence of increments in herbivorous mammals that experience seasonal changes in diet quality, whereas cementum increments are found across extant Mammalia regardless of ecology, phylogeny or environment (Appendix 2). Hence, several studies have sought to examine the effects of other environmental pressures including ambient temperature (Klevezal and Kleinenberg, 1967; Cipriano, 2002), ultra-violet radiation, and latitude (Klevezal, 1995; Pike-Tay et al., 1999). The results of these studies, although equivocal, suggest that a combination of external and internal factors occurring over seasonal periodicities exert substantial control on the growth of cementum.

As cementum increments have been suggested to correspond to changes in the rate of formation of its collagen matrix relative to a near-constant rate of hydroxyapatite mineralization (Lieberman, 1993), several authors have also shown that the relative thickness of particular increments can correspond to discrete life history events that significantly affect the metabolism of the tissue. In several animals, including humans, incidents such as storm events (Cipriano, 2002), the attainment of sexual maturity (Klevezal and Stuart, 1994), birth and parturition (Kagarer and Grupe, 2001; Medill et al., 2010), and even occurrences of renal disease (Kagerer and Grupe, 2001) have all been demonstrated to record increments of anomalous morphology. Using phase contrast microscopy, Cipriano (2002) identified significantly broad hypomineralised bands corresponding with winter storm events in the cementum of captive great apes. Klevezal and Stewart (1994) noted a distinct decrease in cementum increment width and an increase in increment organization and contrast with the advent of sexual maturity in female northern elephant seals (*Mirounga angustirostris*). Medill et al. (2010) used a novel indexing system for quantifying cementum increment thickness to show that female polar bears deposit 'light' cementum bands (under reflected light) that are significantly thinner than surrounding light increments during both pregnancy and parturition. The significance of these differences allowed for a 70% success rate in a blind predictive test of the same polar bear material based on relative increm,ent thickness. Finally, Kagarer and Grupe (2001) used phase contrast microscopy to analyse

a large sample of human teeth (80 individuals), and found that a range of life history events were recorded as significantly broad, translucent cementum increments including pregnancy and renal disease.

The expectation of a consistent correlation between increment count and chronological age has led to the use of cementochronology in a wide range of scientific disciplines; from ecology (Coy and Garshelis, 1992; Grue and Jensen, 1979), conservation biology (Spinage, 1973; Goodwin and Ballard, 1985; Christensen-Dalsgaard et al., 2010), to archaeology (Klevezal and Shishlina, 2000; Roksandic et al., 2009) and zooarchaeology (Beasley, 1987; Beasley et al., 1992; Burke, 1992, 1994; Burk and castanet, 1995; Stutz, 2002), palaeoanthropology (Dean 2000), and forensic science including criminology (Wedel et al., 2013; Colard et al., 2015). There are also commercial applications of cementochronology, with a number of businesses dedicated to age estimation of mammals through cementum increment counting, principally associated with the hunting, and wildlife monitoring and management, industries (Hamlin et al. 2000). However, reports of poor accuracy and precision in several validation studies (Renz and Radlanski, 2006; Kasetty et al., 2010) have led to a lack of uptake of cementochronology by some workers from related disciplines such as skeletochronology and palaeohistology.

To put these difficulties into context, it must be noted that cementum is a dynamic, biomechanically responsive tissue, composed of a series of distinct tissue types (e.g. cellular versus acellular cementum) of differing function and structure (Naji et al. 2016; Bosshardt & Selvig 1997). As such cementum does not grow homogeneously, and varies both spatially and temporally in terms of tissue type and increment quality. This results in two principal forms of uncertainty in the process of estimating age from periodic biological features;

(a) Biological uncertainty of the correlation between increment periodicity and chronological age.

(b) Methodological uncertainty due to subjectivity of counting-based age estimation procedures, especially when data can be noisy.

Methodological uncertainty due to subjective procedures originates primarily from the lack of an agreed standardisation of cementum preparation, assessment, evaluation, and interpretation, as well as from a deficiency in understanding of the underlying biology and structure of the cementum tissue between labs and researchers. Both forms

of uncertainty have led to mixed results in the accuracy (i.e. proximity of counts to known/true chronological age) and precision (i.e. repeatability and reproducibility) of estimated ages in previous validation studies of cementochronology. The highest correlations between known age and predicted age based on cementum increment count have reached an accuracy of ± 1 year (Hamlin et al., 2000; Rolandsen et al., 2008; Schrivner et al., 2014). Strong correlations between increment count and chronological age have even been found in humans that lived from 12 to 96 years of age. In a study conducted by Wittwer-Backofen et al. (2004), in a sample of 433 teeth from humans of known age only 2.2% of increment counts deviated from expected counts by more than 5%. Other studies report no significant correlation at all between known and estimated age, and significant errors in the precision of estimates between workers (i.e. low reproducibility) (Kasetty et al., 2010; Renz and Radlanski, 2006). In summary, while most results highlight the potential and general high levels of accuracy of cementochronology as a tool for assessing longevity and life history in mammals (Klevezal, 1995, Naji et al. 2016), it is also clear that the contribution of biological and methodological uncertainty, and the spread of accuracy of results across all studies, require further investigation.

2.3. Biological uncertainty: complexity in incremental growth patterns

It is rare for a complete sample of teeth to provide data that give rise to perfect correlation between cementum increment count and known age. In a meta-analysis of the previous literature, Klevezal (1995) found that 90% of individuals in 65% of previous studies involving animals of known age showed a perfect correlation between increment count and chronological age. The propensity for at least one individual in most populations studied to show a complex pattern of additional dark bands indicates that there is an inherent genetic variety in growth strategies in mammal populations, or plasticity in their response to external environmental signals. Additional dark bands correspond to additional phases of growth retardation during a single year, and such polyphase growth is also frequently recorded in long bone and other dental growth markers (Bowen et al., 1983; Klevezal, 1995; Castanet et al., 2004). Such complex patterns are often referred to as the ‘doubling effect’, and are commonly found in tropical-to-sub-tropical mammals where two dark bands, instead of one dark band, are

formed every year. This phenomenon was first observed in sub-tropical male deer by Low and Cowan (1963), and ascribed to the biomechanical effects of habitual rutting during yearly mating seasons ("rut lines"). However, the presence of the doubling effect in juvenile animals and even spayed captive animals undermines this interpretation (Klevezal, 1995).

Although there are no hard-and-fast rules controlling the proportion of animals experiencing polyphase growth in a population, there exist several general trends. Figure 2.1. presents the results of a meta-analysis of 141 previous cementochronological studies conducted for this review, in order to examine statistical correlations between climate-type and the proportion of individuals displaying complex cementum increments (full dataset in Appendix 2). The populations studied were grouped by their geographic locations into Köppen climate classes; "A" (equatorial/tropical rainy), "B" (arid/dry), "C" (warm temperate/humid mesothermal), and "D" (snow/humid microthermal) (Lohmann et al., 1993; Kottek et al., 2006;). Köppen climate classification allows the climates of geographically disparate regions to be quantitatively compared on a global scale, by combining average annual and monthly temperatures and the seasonality of precipitation. By grouping populations by the Köppen climate category under which they were living, one can attempt to investigate which climates are statistically more likely to encourage complex cementum growth patterns. We note (Fig. 2.1.a) that lower latitude populations (equatorial/tropical rainy climates – climate type 'A', 60% of studies report complex increments; arid/dry climates – climate type 'B', also 60%) show higher proportions of studies with individuals displaying complex increments than higher latitude populations (warm temperate/humid mesothermal climates – climate type 'C', 36%; snow/humid microthermal climates – climate type 'D', 47%). However, non-parametric Kruskal-Wallis testing suggests that this difference is not statistically significant (n=120, p =0.1157). In total, of the 120 studies examined, 61 (50.8%) had one or more individuals that displayed complex increments. The mean percentage of individuals with complex incrementation across all studies was 16.37%.

For the 61 populations containing one or more individuals with complex cementum increments, we used Kruskal-Wallis testing to examine differences in the proportion of individuals displaying complexities between climate types. The mean proportions were (Fig. 2.1.b); equatorial/tropical rainy climates – climate type 'A': **48.3**% of individuals report complex increments; arid/dry climates – climate type 'B':

24.6%; warm temperate/humid mesothermal climates – climate type 'C': **23.1**%; snow/humid microthermal climates – climate type 'D': **41**% (Fig. 1.3). We identified a statistically significant difference in mean ranks between climate types (n = 61 p =0.048). Posthoc individual Tukey-Kramer procedures were then performed between all climate types to determine the specific climate type pairs that show significant differences in the proportions of individuals with complex increment patterns. Tukey-Kramer procuedures found that p values exceeded an honest significant difference (HSD) critical value of 3.79 for comparisons between climate type 'A' populations and climate type 'B' populations (HSD=4.271), climate type 'B' populations and climate type 'D' populations (HSD=4.133), and between climate type 'C' populations and climate type 'D' populations (HSD=4.677). However, comparisons between climate type 'A' populations and climate type 'D' populations (HSD=1.83), and between climate type 'B' and climate type 'C' populations (HSD=0.26), produced non significant HSD values (Table 2).

Our results show that in general, when comparing only populations with some number of individuals having complex incrementation, populations within equatorial/tropical rainy regions (climate type 'A') have the highest proportions of such individuals. In contrast, populations in arid/dry regions (climate type 'B', often bordering equatorial regions) show the lowest proportion of individuals with complex increments. However, following a latitudinal gradient towards the poles, populations in warm temperate/humid mesothermal climates (type C) and then snow/humid microthermal climates (type D) show an increasing proportion of individuals with complex cementum increments, although not to levels observed in equatorial/tropical rainy (type A) regions. This supports a series of general patterns previously qualitatively described by Klevezal (1995). The authors noted that populations of the same species living under different climatic conditions consistently show proportions of individuals with polyphase growth strategies that differ in a predictable way. In general, populations that experience less seasonal climatic change will have a higher proportion of individuals with polyphase growth strategies, indicated by complex cementum patterns. That our data suggests equatorial/tropical rainy regions (climate type 'A') have the highest proportions of complex cementum increments confirms the observations of Klevezal (1995), as this climate type generally displays the lowest seasonality of those analysed. We show here that this variation is resistant to

phylogeny, with disparate clades showing similar patterns (Appendix 2). It has been shown experimentally that both seasonal climate variation and seasonal diet variation act as factors acting against polyphase growth and complex increment patterns, and in favour of annual increments (Klevezal and Kleinenburg, 1967; Klevezal, 1995; Lieberman, 1994). This combination of genetics and ecology must be acknowledged in cementum studies, and potential variation away from annual (two-phase) growth patterns accounted for when using cementum increments in age estimation.

Several studies have also suggested that the periodicity and 'readability' of cementum increments changes predictably between juvenile and adult teeth of certain species. A number of previous validation studies have shown that increment counts in the youngest individuals of a population show a tendency towards over-estimation of known age, whereas counts in the oldest individuals show the opposite and may under-represent known age (Condon et al., 1986; McLaughlin et al., 1990; Renz and Radlanski, 2006; Christensen-Dalsgaard, et al., 2010). In several long-living species, the attainment of sexual maturity is often marked by a decrease in increment complexity (i.e. a change from two dark increments a year to one), and an increase in the 'readability' of increments (Klevezal and Stewart, 1994; Medill et al., 2009). The readability of increments has been developed as an index of several factors that affect their ease of counting (Zhivotovsky, 1982). These include the contrast between light and dark layers, the sinuosity of individual layers (i.e the number and intensity of curves they experience), and the presence/absence of lensing and coalescing of layers. The change in readability of cementum with age has been suggested to represent a change from intense juvenile growth rates to slower adult growth rates, with increments in adults more affected by changing environmental conditions (Klevezal, 1995).

While such an intrinsic flexibility in growth patterns must be expected in mammal populations, the negative effects of the previously described phenomena on the estimation of chronological age using cementochronology can be further compounded by a lack of understanding of the components of cementum tissue as a whole. Cementum can generally be divided into three main types based on structure and function. Acellular extrinsic fibre cementum follows a consistent growth rate and is the predominant attachment surface for Sharpey's fibres originating in the periodontal ligament. In contrast, cellular intrinsic fibre cementum and cellular mixed stratified cementum are both reactive tissues with growth rates that depend on the extent of

occlusal forces that the tooth experiences (Bosshardt and Selvig, 1997; Schroeder, 1993). The differences in causation and growth rates between these three cementum types must be noted as they have been shown to influence the interpretation of increment counts and patterns (Naji et al., 2016; Schroeder, 1986, 1993). Several recent studies have shown that only acellular extrinsic fibre cementum provides a reliable record of chronological age, and cellular intrinsic fibre cementum as well as cellular mixed stratified cementum provide unstable increment counts with common coalescence and lensing of increments (Bosshardt and Schroeder, 1990, 1992; Naji et al., 2014). Acellular extrinsic fibre cementum has also been shown to have considerably lower instances of complex incrementation with fewer additional lines or increments (Klezeval 1996 p. 223). By using only acellular extrinsic fibre cementum therefore, a considerable reduction in the proportions of individuals and studies showing complex cementum incrementation over the figures shown in the meta-analysis above can be achieved. However, the distribution of tissue types is not homogeneous around root surfaces, and is affected by a changing series of external and internal influences through life (Bosshardt and Selvig, 1997).

2.4. Methodological uncertainty: the need for standardisation in preparation and study of cementum increments

Although a series of imaging techniques have been used to study cementum ultrastructure including radiography (Rökert, 1956; Dreyfuss & Frank 1964; Lieberman, 1993; Burke & Castanet 1995), SEM (Boyde & Jones 1968; Lieberman, 1993, 94), optical coherence tomography (OCT) (Liess-Holzinger et al., 2015), Raman spectroscopic imaging (Schulze et al., 2004; Colard et al., 2016), and synchrotron-based X-ray fluorescence mapping (Martin et al., 2004, 2007; Stock et al., 2016), the vast majority of previous studies that have employed cementochronology have been based on optical microscopy of thin sections. A wide variety of protocols have been suggested for the preparation and analysis of thin sections. Regarding choice of teeth, most validation studies have shown that gross increment patterns and counts are generally mirrored between right and left lower teeth at the same position, after accounting for variation in the age of eruption of different tooth types (Wittwer-Backofen et al., 2004; Medill et al., 2009). It has been suggested that for some purposes such as analyses of

parturition timing, data from upper and lower premolar teeth of the same position (e.g. upper and lower first premolars) should not be pooled, as this may bias counts and inferences of increment patterns (Medill et al., 2009). Several methods of tooth extraction have also been implemented, although most studies have boiled mandibles for short periods before manually removing the tooth using dental equipment. Some studies have advocated sectioning the tooth while still surrounded by an amount of alveolar bone to minimize the risk of damage to the outer cementum layers (Lieberman et al 1990; Lieberman 1994; Burke & Castanet 1995). It should be noted that cementum from specimens that have been kept in formalin for significant periods of time (more than 6 months), peels and deteriorates after removal (Driscoll et al., 1985; *pers obs*).

There is no current standard for cementum thin section preparation, and many laboratories professionally produce thin sections of comparable quality using markedly different techniques (Rolandsen et al., 2008; Naji et al., 2016). The only (implicit) important standardisation that currently exists is the experimental need for a low refractive index of the embedding and mounting materials, which should be as close to zero as possible to minimise optical interference when analysing cementum increments (Naji et al., 2016). Several studies have advocated the use of polarising light to study cementum increments (Burke, 1992, 1994; Stutz, 2002). To this end, the birefringent properties of any mounting medium should be as close to zero as possible to minimise their effect on the biogenic birefringence patterns of cementum increments (see Stutz [2002] for a thorough review of polarized light microscopy of cementum increments). The most vocal argument regarding thin section preparation has been between workers who favour or avoid decalcification. Most early studies implemented decalcification in order to chemically stain very thin (4-70 μm) sections. Chemical staining, usually using haematoxylin and eosin (H&E staining), increases the contrast between increments, where dark increments are stained considerably more intensively than light increments (Klevezal, 1995; Kvall and Solheim, 1996). Experimental staining by Foster (2000) may indicate that this reflects a difference in the relative proportion of extracellular collagen fibres between light/dark increments. However, validation studies that have compared decalcified versus undecalcified sections have shown that the difference in increment contrast is not great enough to warrant the added time and cost of decalcification of large samples, and has even been shown to reduce readability in some studies when not using a staining medium by reducing contrast between light and dark increments

(Beasley et al., 1992; Naji et al., 2016).

The correct orientation of thin-sections has also been debated in the literature. The majority of studies have been based on longitudinal sections, which allow the entire vertical profile of increments to be studied. This orientation allows false increments to be most easily distinguished from principal (annual) increments, as false increments can be typically shown to coalesce into neighbouring increments towards both the apex, and cervical neck of the root (Klevezal, 1995; although see Gasaway et al., 1978; Naji et al., 2016). Regardless of orientation, multiple sections should be prepared to represent one tooth. Non-decalcified sections should be polished to ~70-100 μm thickness. Above this threshold, increment thickness can have a pronounced effect on the clarity of increments and hence their readability, as their longitudinal trajectories are commonly shown to change, affecting the contrast between observed increments (Naji et al., 2016). Below this threshold, increments are too vague to confidently interpret.

Thin sections are studied using both transmitted and reflected light microscopy, generally coupled with digital photography. It must be remembered that the optical nature of increments are reversed under each light source; thick hypomineralised bands are darker under transmitted light and lighter under reflected light, and thin hypermineralised bands are lighter under transmitted light and darker under reflected light. Incorrect interpretation of brightness differences, which are dependent on the light imaging modality, has occurred in the past and can lead to erroneous interpretations of relative mineralisation of increments. For example, Cipriano (2002) introduced dark hypermineralised bands as fast growth 'summer' bands, and light hypomineralised bands as slow growth 'winter' bands. Although this definition is erroneous regarding the relative proportions of mineralization between winter and summer, it is not made clear under which imaging modality these definitions refer to and so summer increments may indeed be dark under transmitted light. The area(s) of highest increment readability from one or more thin sections are commonly chosen subjectively and recorded digitally. Various image processing methods have been used to process images of cementum increments to maximise contrast (Fancy, 1980; Lieberman et al., 1990; Wall and Wall, 2007), including digital contrast stretching, noise reduction and binarisation.

Although the relative merits of different thin section preparation methods have been widely discussed (Naji et al., 2016), it is the analysis of thin sections that has

created the most severe uncertainty in the application of cementochronology. Generally, it is the thin layers that appear dark under reflected light that are counted. Age estimates are then based on the total count of dark layers, plus the average age of eruption of the specific tooth, in the animal under study. Cementochronology requires both a fundamental understanding of (a) the underlying biological mechanisms creating incrementation; and (b) a robust methodology for counting increments that must be strictly followed. However, examples of the failure to meet one or both of these prerequisites can be frequently seen in the literature. Many workers lack an appreciation of the complexity of cementum growth, and there is a prevalent notion that increments follow simple, homogenous deposition around an entire root. Hence, several studies, in an attempt to minimise the subjectivity of increment counting, have followed dendrochronology studies by objectively choosing multiple regions along the cementum tissue in which to count increments (Kvaal and Solheim, 1996; Renz and Radlanski, 2006). For instance, Renz and Radlanski (2006) divided thin-sections into buccal, distal, mesial and lingual portions and only counted and compared increments within these pre-defined regions. Counts are generated in each of these fixed regions in several horizontal sections created along the entire vertical length of the root. Several such studies, having found contradictory counts within different regions, questioned the relationship between increment count and chronological age (Obertová and Francken, 2009), and others dismissed cementochronology altogether (Renz and Radlanski, 2006).

However, these approaches ignore the known variation in the deposition of acellular extrinsic fibre cementum versus secondary cementum such as cellular intrinsic fibre cementum and cellular mixed stratified cementum, which may erroneously affect counts in fixed regions of study. Hence, one should expect differences in increment counts based on cementum tissue type, and be able to systematically choose regions of study, which are based on the prevalence of acellular extrinsic fibre cementum.

Such an approach stems from an otherwise to-be-commended common effort to minimise the subjectivity of increment counting in what is often a complex record. Increment counting by eye is an inherently subjective activity, and differences in counts between readers of the same material, and between readings by the same worker can undermine their use as age estimates (Rolandsen, 2008; Frie et al., 2011, 2013). Most validation studies have attempted to quantify the readability of increments, and the accuracy and precision of age estimates of known age material. The popular use of a

standardised index of readability suggested by Zhivostovsky (1982) (developed from an original index by Gasaway et al., 1978) in studies throughout the 1980's and 1990's allowed the readability of different samples from different studies to be quantitatively compared (Klevezal, 1995). These indices were used as a quantitative context for assessing the effects of various factors on increment counts, and the differences between age estimates based on increment counts and known age between separate studies and taxa. However, such a standard of cementum quality evaluation has been little used in the recent literature.

Recent analyses of increment counts have used various methodologies and statistical analyses, both to count increments and to test the accuracy and precision of these counts. Accuracy is widely defined as the deviation of counts from those expected given an animals known age. Precision is the deviation between individual counts of the same cementum specimen. Several recent validation studies have used general linear models (GLMs) to compare the amount of deviation statistically explained by a series of factors (reader, sex of individual studied, readability score) and/or covariates (age of individual studied) that are believed to affect the accuracy of increment counts (Frie et al., 2011, 2013; Rolandsen et al., 2008). Yet methods for testing these GLMs differ widely in their complexity and logic, as well as the nature of factors they analyse, and as such they are heavily dependent on the application and data at hand. On this account, the wide variety of reported causes of inaccuracies of recent studies may not be able to be confidently and directly compared. This minimises the impact and application of the results of these studies for other workers, and has done little to assuage the doubts as to the validity of cementochronology expressed by several authors (McLaughlin et al., 1990; Renz and Radlanski, 2006; Roksandic et al., 2009).

It is evident that cementum is a tissue of important potential as a chronological record, offering the chance to decode important elements of the life histories of living and fossil animals. However, before this potential can be fulfilled, further work is needed to both accurately correlate the relationship between increment count and chronological age, and to quantify the factors that cause and control the growth of cementum and the periodicity of its layers. From this summary, it is clear that the use of cementochronology for life history analysis is dependent on;

(a) the ecology and environment of the population under study;

(b) the methodology used to analyse increments; and

(c) the understanding of the reader about the biology of cementum growth and incrementation (summarised in Figure 2.2.).

Quantification of the effects of external and internal life history variables on cementum growth is needed, using a standardised methodology following protocols developed to study the cementum tissue that best records incremental growth patterns. The remaining review outlines potential ways of following this line of enquiry and improving on our current understanding of cementochronology.

2.5. Towards a standardised methodology for increment counting and analysis

The need to develop a global standard to cementum study was recognized in 2010 through the formation of the "Cementochronology Research Program" by workers in Paris, France. In a recent review (Naji et al. 2016), members of the program propose a single protocol for the production and study of cementum increments in extant animals. The simplicity of this protocol and level of detail of its explanation is sufficient for the novice to begin to study cementum increments, and can be easily implemented to modify on-going research protocols to meet this standard. However, it does not significantly alleviate the key problems of the cementochronology technique; the subjectivity, and inherent dependence on user experience. These are noted as a potential flaw of cementochronology that can only be minimised by user experience according to the Cementochronology Research Program, and a methodological solution other than increased training to gain such experience is not presented by Naji et al. (2016).

The increments of various mineralised structures are routinely studied at an industrial scale for age estimation purposes in agricultural disciplines such as fishery management and deer farming. The high financial and ecological risk associated with error in reading these structures has led to considerable efforts to attain quality control and minimise observer error (Van den Broek, 1983; Beamish and Chilton, 1982; Kahn and Mohead, 2010; Morrongiello et al., 2012). These errors have led to rigorous quality control testing of more intensely used ageing structures such as the otoliths of fish. Quality control is usually focused on the development of a reference catalogue of images covering all known pathologies and inconsistencies that have previously caused

uncertainty and bias in age estimates from the tissue in question. This is one of the most crucial aspects of aging practice in fishery management (Campana, 2001). The repeated referencing of images that highlight negative effects on the correlation between increment count and chronological age maximises the likelihood that such effects are taken account of in further age estimates. The continued reference to such catalogues has thus been shown to significantly improve precision between age estimates of different workers, and to minimise drift in intra-specific worker accuracy through time (Campana et al., 1995; Campana, 2001). The development of such a tool for cementochronology has the potential to improve the accuracy of age estimates based on cementum increments by providing a universally applicable tool to calibrate increment data against. This will ultimately improve understanding of both the biology of cementum, and variability in the periodicity of increments, allowing readers to more confidently distinguish principal increments from accessory increments.

Several cementochronological studies have advocated the use of objective means for counting increments, which place minimal dependence on user experience (Lieberman, 1990; Wall and Wall, 2007; Wall-Scheffler and Foley, 2008). These are primarily based on the quantification of pixel brightness values in digital images of cementum increments. By analysing optical increment patterns as peaks and troughs in pixel values, workers have used statistical methods for counting increments with no need for manual counting by humans. This method was proposed by Lieberman et al. (1990), who first used computer image analysis to measure greyscale values along radial transects through digitized images of cementum. Light increments were interpreted from peaks, and dark increments as troughs, in greyscale values along a luminance profile. Although no further work was performed to diagnose genuine increments from background noise, and manual counting was used in this study, the authors suggested that the difference between the mean pixel value of the cementum and the value at the cemento-dentine boundary be used as a reference for this practice in further studies. Any peak/trough that did not depart from the mean beyond a third of this value should not be counted. Since this study, related methodologies have been further developed by a number of authors, including Wall and Wall (2006), Wall-Scheffler and Foley (2008), Czermak et al. (2006), Klauenberg & Lagona (2007), and Greenfield et al. (2015). The first two of these papers named their method Digital Cementum Luminance Analyses (DCLA). DCLA attempts to improve the original methodology outlined by Lieberman et al. (1990) by adding an absolute cut-off for

discerning between genuine cementum increments and background noise, and automating the counting of increments based on the cut-off. Pixel values are recorded for each peak and trough found along a radial cementum transect, although any peak or trough with a maximum or minimum point within two greyscale values of the last peak or trough (respectively) are not counted as increments. Greenfield et al. (2015) further develop this technique by using automatic peak/trough identification algorithms to further remove the human element from increment counting. Czermak et al., (2006) developed a stand-alone piece of software, 'Auto-TCA', to automatically count cementum increments in selected regions of interest. The software uses Gaussian and direct Fourier filtering to both rearrange the cementum tissue through bicupic interpolation, and increase contrast between increments. This aids interpretation of trough/peak pairs and eases counting as it minimizes the effects of refraction artifacts and linear scratches from preperation. Finally, radial transects are plotted through the cementum for every single pixel of the respective ROI, and their greyscale values recorded. These values are then reversed so that dark increments form peaks in resultant histograms. These peaks are automatically counted to generate increment counts, creating 300-500 individual counts. Final estimates of increment counts are taken as the mean of these individual counts. Klauenberg & Lagona (2007) follow a different strategy, by using hidden Markov random field modeling to estimate average increment width instead of peak/trough counts. Dividing the radial width of the cementum tissue by this estimate then generates increment counts.

Some of the methods described above, including DCLA, rely upon (*a-priori*) assumptions regarding the distribution of pixel values caused by incrementation versus those caused by background noise, defining an absolute threshold value at a certain distance from the mean pixel value, that a peak or trough must pass through to be distinguished as reflecting a 'true' increment. This value is ultimately specific to the data and/or methods in the original study, and so may not be confidently applied to other imaging modalities or techniques, or to taxa that fail to meet the specified cut-off parameter specified in the original study. Thus, the next stage in DCLA development, and indeed in such methods in general, should focus on developing a more flexible strategy for distinguishing cementum increments based on relative instead of absolute greyscale distribution criteria.

These studies provide a clear step towards the methodological reduction of subjectivity in counting. However, such techniques have yet to be implemented on a broader scale in the cementochronology community, and individual methods are seldom

developed beyond the working group in which they are developed. Some of the reasons for this may include accessibility of the papers describing the methods, accessibility of the software for carrying out the analyses, and ease of use of the workflow. Improvements in each of these categories for existing or forthcoming methods should help to increase their uptake and use.

It becomes clear from this discussion that the implementation of a standardized approach is indeed possible for cementochronology. The need for such an approach is recognised within the community (Naji et al. 2016), and although a global standard for production is more easily obtained than for analysis of cementum thin-sections, the two form complementary approaches for increasing the accuracy and precision of cementochronology. Regarding thin section analysis, inspiration from other disciplines may foster crucial steps to help minimise the subjectivity and dependence on user experience suffered by current methodologies. The development of an internet database of taxon-specific and/or pathology-specific reference images may provide an efficient way of storing and transferring invaluable knowledge of cementum growth and structure that would otherwise only be attained through decades of user experience. Further, once users have used this information to confidently choose the most representative digital images of cementum increments, objective DCLA counting methodologies could be applied to minimise subjectivity and maximise accuracy and precision in increment counts. While not entirely eliminating subjectivity in analysis, this methodology should provide a significant step towards a global standard to study cementum increments, with minimal constraint from user experience and subjective increment counting.

2.6. New possibilities: The application of novel techniques for studying cementum growth

The advent and availability of powerful new tools for studying the structural and material properties of biological materials has created significant progression in our understanding of the growth of various hard tissues such as bones, shells or teeth. Here, we select and discuss specific techniques that may benefit our understanding of the growth and nature of cementum increments (Table 3).

2.7. Virtual histology and its potential for cementum study

Thin section image analysis represents the current 'gold standard' for studying cementum histology, and the combination of high-powered microscopes, optional chemical staining and digital imaging allows study of cementum increments in high definition. However, as previously discussed, several potential problems exist when estimating increment counts based on thin sections, primarily due to the restrictive number of samples available per-tooth, and the lack of a three-dimensional (3D) perspective of study. Counts of layers in an individual's cementum that are based on a restricted number of thin sections are essentially subjective, as they cannot be viewed in the context of the entire tooth and because the orientation of the cut surface determines irrevocably the (only) direction in which growth markers can be analysed. In contrast, cementum is a dynamic, biomechanically responsive tissue, and the pattern and number of layers are known to change both temporally and spatially along and perpendicular to the tooth's longitudinal axis in different portions of cementum (Klevezal, 1995; Naji et al., 2016). As this cannot be fully accounted for in histological data, when seen in thin sections, such phenomena undermine confidence in counts and limit our understanding of the relationship between increment count and chronological age.

The study of internal structures of other mineralised tissues has been revolutionised in the last two decades by the development of X-ray micro-computed tomography (microCT or μCT). Conventional (i.e. X-ray absorption-based) CT makes it possible to reconstruct the 3D structure of an object by combining series of two dimensional (2D) radiographic projections, or slices, that spatially encode the intensity of transmitted radiation after X-ray wave-fronts have been partially absorbed through the object at different angles. This allows the study of internal structures of biological tissues at high resolutions in 3D, with no physical damage to the object in question. This overcomes several of the major drawbacks of thin-section histology, by allowing scientists to visualise growth markers in virtual sections that can be aligned in 3D at will, and to map and evaluate their 3D trajectories within fossil and extant enamel and dentine without the need for physically cutting thin-sections (Le Cabec et al., 2015; Smith et al., 2015; Tafforeau et al., 2007; Tafforeau and Smith, 2008). With particular reference to fossil, archaeological, and some forensic samples, taphonomic, diagenetic

remineralisation alters the chemical structure of the specimen to a greater or lesser extent. This can lead to regions where structures such as cementum increments are altered enough that they are no longer detectable (Stutz 2002; Roksandic et al., 2009; Naji et al. 2016). Tomographic data allows an almost infinite number of virtual sections at different orientations through the entire volume of the cementum, such that regions can be identified with sufficiently good cementum increment preservation to obtain accurate increment counts, even in specimens where much of the cementum is greatly altered.

μCT desktop systems were first developed and applied in the field of bone research (Kuhn et al., 1990), along with guidelines for the assessment and quantification of cortical and trabecular bone specimens from animals and humans (e.g. Bouxsein et al., 2010). Such systems have spread in time with increasing development and accessibility, and μCT scanners are now commonly used in in a host of biological disciplines. However, the restricted resolution of conventional laboratory-based μCT systems has so far restricted their use for research to covering quantitative measurements of gross thickness and density of dental tissues (Olejniczak et al., 2007). Although many laboratory-based μCT systems advertise sufficient voxel resolutions for imaging cementum increments (< 1 μm), imaging artifacts such as noise and beam-hardening effects reduce the actual object resolution possible, and generally obstruct cementum increments in μCT reconstructions (Fig. 2.3). The tomographic measurement of dental growth markers has so far been solely based on higher resolution and lower noise synchrotron radiation-based CT (SR CT) (Smith, 2008; Smith and Tafforeau, 2008; Tafforeau and Smith, 2008; Smith et al., 2010; Smith et al., 2015). SR CT based on X-ray absorption is by far the most powerful X-ray method that is regularly used in this context, where an electron accelerator acts as a highly brilliant X-ray source. Compared to X-ray sources in conventional μCT scanners (i.e. X-ray tubes), SR sources have a markedly smaller spot size and provide a very high X-ray flux. This offers a superior signal-to-noise ratio, especially at high spatial resolutions, and sufficient image contrast to visualize growth markers in teeth (Olejniczak et al., 2007). In addition, the energy spectrum of X-rays emitted at SR sources for CT are commonly filtered to provide a quasi-monochromatic X-ray beam, which leads to less reconstruction artifacts (e.g. the so-called 'beam hardening' effect) that can otherwise be pronounced for conventional, polychromatic X-ray tubes that emit over a broad energy spectrum. Finally, quasi-monochromatic SR CT light allows novel phase contrast techniques to be used, which

exploit the local phase shifts of the X-ray beam that are induced by the object under investigation, so that boundaries between materials with similar and/or (very) low X-ray absorption are resolved more clearly (Paganin et al. 2002, Davis et al., 2003). This is of great benefit to dental increment studies, where material properties and density differences between increments can be very small.

The majority of published SR CT studies of incremental dental growth to date have been focused on the contrasting topics of hominid evolution (Smith, 2008; Smith and Tafforeau, 2008; Tafforeau and Smith, 2008; Smith et al., 2010), and evolution of the earliest vertebrate teeth (Gai et al., 2011; Cunningham et al., 2012; Jones et al., 2012; Rucklin et al 2012; Murdock et al. 2013; Chen et al., 2016). The use of phase contrast-enhanced CT imaging has allowed incremental features in tooth enamel and dentine to be identified in tomographic data of both extant and fossil teeth, and the increasingly high spatial resolutions available allow highly precise measurements of their 3D patterns and periodicity (Le Cabec et al., 2015; Smith et al., 2015; Tafforeau et al., 2007; Tafforeau and Smith, 2008). 3D models of enamel and dentine based on SR CT data have revealed features that cannot be readily understood from series of 2D thin sections such as ontogenetic differences and discrete cellular differences between tissues (Sanchez et al., 2012). The non-destructive nature of tomography has also permitted the study of fossils of great importance and fragility including pterosaurs (Martin and Palmer, 2014), non-mammalian therapsids (Fernandez et al., 2015; Benoit et al., 2017), and early tetrapods (Sanchez et al., 2016), and has led to the quantification of evolutionary changes in growth rates in early hominid evolution by comparing fossil and extant hominid growth increments (Le Cabec et al., 2015; Tafforeau et al., 2007).

Cementum layers are typically between one and ten μm in width in terrestrial mammals (Wall-Scheffler and Foley, 2008), but can be as wide as 20μm in cetaceans (Stock et al., 2017). This makes them a prime candidate to be studied using high-resolution CT (Fig. 2.3). However, CT has only so far been applied when studying the structure of the cemento- dentine junction, and cemento-periodontal junction (Grandfield et al., 2014; Ho et al., 2010). Although optical coherence tomography has been recently used to identify cementum increments in a fossil cave bear (*Ursus spelaeus*) molar, the nature of optical coherence tomography only allowed for a single area of cementum to be studied, and the spatial resolution provided by this technique was insufficient to provide accurate increment counts (Leiss-Holzinger et al., 2015). As

a mineralised tissue, cementum is very similar in structure and chemistry to bone (Lieberman, 1993). As bone is likely the most common tissue to be studied using high resolution CT, the parameters suitable for optimizing image acquisition of microstructure and ultrastructure are reasonably well understood, and a host of novel techniques have been developed to analyse bone ultra-structure data using tomographic data (Burghardt et al., 2011; Dalzell et al., 2009; Schneider et al., 2009; Schaff et al., 2015). These techniques may thus be applied to reveal cementum increments in 3D for the first time.

CT imaging of incremental patterns in the ultrastructure of the same tissue (e.g. cementum increments) is ultimately a matter of contrast as much as spatial resolution. Non-polarized thin section histological data observed by light microscopy represents changes in the transmitted luminance and optical properties within materials, based on their composition and 3D ultrastructure. Cementum increments are thus thought to be distinguished in histological data due to changes in the orientation of collagen fibres (Lieberman, 1994) and/or the proportion of mineralised matrix between increments (see Stock et al., [2016] for new evidence supporting differing formation rates and undermining the hypothesis of changing fibre orientation between increments). However, tomographic reconstructions based on X-ray absorption cannot be expected to show changes in luminance due to differential collagen fibre orientation. Instead absorption-based CT reconstructions reflect changes in the absorption of X-rays through an object, based on relative densities, ultrastructure and chemistry of internal materials. Thus, contrasts in x-ray absorption due to incremental change in structure/organisation of the same tissue may be too subtle to be detected to a quantifiable degree using conventional μCT technology. This has long been the case for μCT imaging of soft biological tissues such as muscle (Strandberg et al., 2010; Umetani et al., 2013; Fourmax et al., 2017) and there are two principal methods used for increasing contrast in μCT imaging; (a) phase contrast approaches noted above and most widely available at synchrotron light sources (although phase contrast approaches are being developed and increasingly used in laboratory CT settings; Birnbacher et al., 2016; Krenkel et al., 2016; Marenzana et al., 2013); and (b) the use of contrast enhancing staining or perfusion methods applied prior to scanning. The use of contrast agents are of growing importance in soft tissue tomographic imaging and several agents are commonly used (Metscher, 2009; Gignac et al., 2016; see Pauwels et al., 2013 for a review of frequently used contrast agents and their pros and cons). Further, tomographic contrast agents including gold nanoparticles

and barium sulphate are increasingly being used to successfully improve contrast between layers of bone (Leng et al., 2008; Zhang et al., 2010; Ross and Roeder, 2011). Hence, the application of contrast agents may be a promising avenue of research for the tomographic study of cementum.

In summary, high-resolution CT imaging can allow changes in the pattern of cementum increments to be studied across the tooth, both through an essentially infinite number of arbitrary 2D planes of any orientation and position within the root, as well as fully in 3D across the entire tissue. This will allow principal increments to be discerned from transitory accessory lines, providing a higher level of confidence and accuracy of increment counts. Existing morphometric measures derived from CT data sets of other biological tissues, such as vascular tortuosity in bone (Freilich et al., 1986; Folarin et al., 2010) and root canal geometry in teeth (Peters et al., 2001; Hübscher and Barbakow, 2003), absolute tissue volume of dentine/enamel in teeth (Conroy, 1991; Grine, 1991; Olejniczak and Grine, 2006), or specific surface area of bone (Hara et al., 2002; Grimand et al., 2009) may also be usefully applied when studying cementum increments. These measurements will allow the gross properties of cementum increments to be studied in a quantitative fashion in 3D for the first time. Comparisons between the 3D properties of differing increments may provide new insights into patterns of incrementation and relationships between increment structure and life history variables beyond their 2D structure. Differences in 2D increment thickness, the most predominant form of identifying life history variables in thin-section (Coy and Garshelis, 1992; Gagarer and Grupe, 2001; Medhill et al., 2010), may reflect further differences in 3D properties such as increment volume and tortuosity.

2.8. Studying cementum as a material

X-ray tomography is a powerful tool with exciting potential for cementochronology. However, tomographic data is still predominantly visual, and characteristics of cementum layers in 3D need to be properly defined and quantified (although aspects such as mineral density can be estimated using tomographic data; see Isoda et al., 2012). Cementum is a composite, woven material. Changes in optical properties between increments have been frequently attributed to changes in collagen fibre density and orientation, as well as to the relative mineralisation of the surrounding matrix (Klevezal,

1995; Lieberman, 1993, 1994). As such, optical incrementation should occur hand in hand with changes in material properties and the tissue ultrastructure. Several recent studies have applied methods previously used for studying physical and chemical properties of other composite biological structures to reveal new information on the relationship between the chemistry, structure and incrementation of cementum (Colard et al., 2016; Stock et al., 2016). These will be discussed here, alongside discussion of other methods yet to be used on incremental cementum that have the potential to further our understanding of its growth, chemistry and structure.

Although they do not offer the same extent of 3D visualisation, several microscopy techniques allow considerably higher spatial resolutions than conventional X-ray CT. X-ray CT is usually limited by the diffraction limit of visible light at a few hundred nanometres because X-rays are converted into visible light before actual acquisition of radiographic projections on the detector. Many other imaging techniques are not limited by this factor, and have been used to study changes in ultra-structure at markedly higher spatial resolutions of up to 10 nanometers or less. Scanning electron microscopy (SEM) was the first tool used to determine the collagen structure of cementum (Boyde and Jones, 1968). Since then, SEM has frequently been applied when studying ultrastructure along the boundaries between cementum and dentine (Grandfield, 2014), cementum and the periodontal ligament (Grandfield et al., 2015), and between cementum increments (Lieberman, 1994). The recent development of serial-block-face SEM bridges the gap between the volumetric nature of X-ray CT data and the nanometer-resolution of SEM. Using an ultramicrotome mounted inside the vacuum chamber of an SEM microscope, the surface of a sample is repeatedly imaged and subsequently sectioned in order to generate a volumetric, tomographic dataset (Fig. 2.4.b.). This technique may prove a useful tool for further studying the differences between collagen structure and mineralization between light/dark layers, and identifying hallmarks of life history events in the same specimen (Fig. 1.3).

SEM images have been used to statistically characterize and compare specific patterns in the microscopic wear facets (micro-wear) found on the tooth crowns of several extant animal taxa. Pioneered by Purnell et al. (2012) several recent micro-wear studies have employed three-dimensional surface profiling metrics commonly used in tribology, by modelling the distribution of greyscale values across two-dimensional SEM images as a third dimension. As greyscale values for each pixel directly relate to the distance of the sampled region of a surface to the electron detector, their

distribution provides a height map across the image (Fig. 2.4.c.). This map is then subject to quantitative metrics designed to characterize discrete elements of greyscale distribution. These metrics have been shown to isolate significant differences between the micro-wear of teeth from animals of different feeding ecology (Purnell, 2012; Purnell et al., 2012, 2013; Evans, 2013; DeSantis, 2016).

A series of techniques have been used for the study of cementum in the wake of the initial SEM cementum research. These techniques may offer alternative ways of quantifying changes in structural and material properties between increments. Second harmonic generation (SHG) imaging is of growing interest in the study of bone and dental enamel. The technique is based on the ability to generate second-harmonic light, which differs between materials. When high intensity laser light interacts with materials that possess certain optical properties, namely asymmetric crystal shape (non-centrosymmetry) and high second-order nonlinear coefficient (Camagnola et al., 2003), the original waveform is converted into light at twice the incident frequency. Collagen possesses both of these properties, and has been imaged at nanometre resolutions using SHG imaging in a variety of hard and soft tissues (Fig. 2.4.d.) (Moreaux et al., 2000; Brown et al., 2003a, b; Han et al., 2005; Ambekar et al., 2012). As SHG imaging is particularly sensitive for collagen, relative to the surrounding matrix, SHG imaging provides better contrast between discrete collagen fabrics than SEM or optical microscopy (Ambeker et al., 2012). SHG has been previously used by Aboulfadi and Hulliger (2015) to study the absolute orientation of collagen fibres within cementum. The authors found uniform radial extrinsic fibres and a complex association of bipolar circumferential intrinsic fibres running through the tissue. The study also showed that SHG has sufficient resolution to compare collagen arrangement between increments. This could be used in future studies to tease apart structural differences between increments formed under differing circumstances of life history. A similar technique, third harmonic generation microscopy (THG) has recently been used to distinguish and image dentine tubules in fossil teeth (Chen et al., 2015; Brink et al., 2016). THG is more sensitive than SHG to materials of low contrast in collagen structure and may thus also be useful for studying partially or completely re-mineralised increments in fossil cementum.

Another technique, atomic force microscopy (AFM), has the potential to record several optical and structural phenomena at exceptionally high spatial resolutions, based

on the interaction of the surface topology of a sectioned specimen with the tip of a cantilever governed by Hook's law. AFM has been used to visualise collagen ultrastructure at sub-nanometre resolution in other mineralised tissues such as bone (Fig. 2.4.e.)(Wallace, 2012) and enamel (Poggio, 2014). There are a wide variety of cantilever types available, specialised for measuring an equally wide array of properties. AFM has been previously used by Ho et al. (2004) in order to establish the optimal preparation techniques and experimental settings for studying the biomechanical properties of cementum, while Ho et al. (2007) used AFM (both microscopy and nanoindentation) to hypothesise a newly discovered fibrous joint between dentine and cementum, analogous to that between cementum and alveolar bone. Hurng et al. (2011) used AFM (again both microscopy and nanoindentation) to image and quantify mechanical properties of the structural organization of cementum in human specimens with reduced periodontal ligament regions. Jang et al. (2014) used AFM to investigate age related change to the cemento-dentine boundary layer, discovering that the width of the junction significantly decreased with age.

Following the results of these studies, the use of AFM to analyse the biomechanical properties of cementum increments in ultra-thin sectioned thin sections (300 nanometres thick) appears entirely feasible, and may allow visualization and quantification of the biomechanical and other material properties of dark/light layers, and those that represent discrete life history events. The use of AFM for studying cementum increments may thus provide novel data for testing current hypotheses for their causation. Cementum is widely hypothesised to combat occlusal forces by redistributing pressure from the tooth to the periodontal ligament, and to combat wear by raising the height of the tooth above the alveolus (Mays et al., 1995; Veiberg et al., 2007). These biomechanical functions are put under different pressure regimes due to seasonal differences in dietary quality, as indicated by changes in the growth rate between cementum layers. By allowing both material and structural properties to be studied concomitantly, AFM microscopy would allow the investigation of whether changes in ultra-structural collagen arrangements between increments had any significant correspondence with biomechanical properties indicative of different loading regimes such as elasticity and hardness. A good initial example of this is the study of Grandfield et al. (2015), which while not focused on cementum increments, used a number of methods including microCT, Raman spectroscopy and AFM to examine change in the cementum and alveolar bone of rat molar teeth exposed to artificial mechanical strain, finding a disconnect

between the resulting planes of induced alveolar bone and cementum growth.

Although of high spatial resolution, many optical techniques are unsuitable for quantitatively studying chemical aspects of biological tissues that are of importance for studying cementum, such as the proportion of organic collagen to inorganic mineral content. Raman spectroscopy is one exception. This technique is based on the characteristic inelastic ('Raman') scattering of laser light created by molecules of different origins. Precise measurement of the resulting spectrum of scattered light allows sub-micrometre changes in the ratios of chemical components of a material to be studied (Fig.2.4.f.). Raman spectroscopy has been frequently used to study differences in the mineralisation of biological tissues including bone (Buckley et al., 2012) and dentine (Tsuda et al., 1996; Salehi et al., 2013). Raman spectroscopy has also been used alongside AFM to study chemical changes across the cemento-dentine boundary (Grandfield et al. 2014). Further, Colard et al. (2016) used Raman imaging to study changes in chemical composition and mineral structure within acellular extrinsic fibre cementum (AEFC), and to examine changes in structure between AEFC increments. The study found that 'dark' bands (under transmitted light) correspond to more mineralized layers in the cementum. However, conforming to the results of Stock et al., (2016), the study found no evidence of alternating collagen fibre orientation between 'light' and 'dark' increments.

The Raman spectroscopy technique may be further utilised in cementochronology studies to identify possible chemical fingerprints created by specific life history events within single increments. For instance, reproduction, lactation and infant rearing are energetically expensive processes. Their physiological demands may significantly influence the ratio between mineral matrix and collagen fibres within the cementum, leaving discrete changes in the proportion of organic and mineral phases within corresponding cementum increments. Distinguishing such chemical signals, and comparing them to structural patterns within/between increments may provide a robust test for predictions of life history events based on structural properties. Several authors have also previously attributed additional increments to cycles of sexual activity occurring within each year (Coy and Garshelis, 1992; Medill et al., 2010). This interpretation could be tested using Raman spectroscopy and if supported, this technique may prove a useful tool for distinguishing between additional and principal (annual) increments.

Use of the above techniques, in combination with quantitative morphometry based on 3D image data derived from X-ray tomography, may significantly improve understanding of what controls cementum incrementation, and how discrete events through life leave particular imprints on cementum growth. Comparison between structural patterns and those of collagen ultrastructure and material properties may provide a robust test for hypotheses regarding the typical hallmarks of life history variables. However, all methods described here, excluding tomography, are invasive and involve destructive preparation of samples. This severely limits their potential for the study of fossil cementum, as permission for researchers to destructively analyse internal tissue structures can be difficult to achieve, and likelihood decreases with the rarity of specimens. This reaffirms the need for an accurate method for distinguishing signals of life history events within non-destructive tomographic data.

2.9. Quantifying the relationship between cementum growth, incrementation and life history variables

In order to correctly interpret a series of structural hallmarks of life history events within cementum increments of animals of unknown life history, the same hallmarks must be first validated in animals of known and controlled life history. To date, the overwhelming majority of studies that have described a relationship between environmental/physiological factors and cementum incrementation have been qualitative and anecdotal (Bodkin et al., 1993; Cipriano, 2002; Kagerer and Grupe, 2001). Only recently have workers begun to study these relationships quantitatively (Wall-Scheffler and Foley, 2008). Such studies are however still affected by the caveats of thin section histology (Medill et al., 2009, 2010). Techniques described in this review may elucidate whether such relationships exist, although a robust experimental design must be employed.

Very few experiments have been based on animals living in controlled or closely monitored environments. Such study is necessary in order to isolate the particular effects of single variables from one another on the structure of cementum increments. The only previous studies known to the authors, where the aim was to determine a controlling factor of cementum growth using direct experimentation, have been reported by Lieberman (1993; 1994) and Klevezal (1995). Through controlling the diets of three

sub-samples of domestic goats (*C. aegagrus*), Leiberman successfully isolated the effects of nutrition on cementum structure in 2D, showing that both the nutritional quality and material hardness of diet affected the orientation and rate of production of collagen fibres. However, conclusions were based on qualitative and quantitative examination of 2D SEM images of collagen ultra-structure, as opposed to gross increment morphology. This may limit the implications of this study for the future analysis of cementum incrementation, as such high-resolution changes in ultra-structure are rarely assessed. Among other experiments examining the relationship between cementum increments and various factors such as environmental conditions (Klevezal, 1995), Klevezal (1975) compared wild, hibernating dormice (*Dryomys nitedula*) and hamsters (*Mesocricetus brandti*) with those kept indoors that did not hibernate. The non-hibernating hamster individuals continued to grow through the winter, and no dark resting increment was formed in either cementum or jaw bone; however, the non-hibernating dormice did not grow through the winter, and formed a dark resting increment in jaw bones (cementum was not analysed). This leads to the suggestion that different species respond differently to interruption of physiological events such as hibernation, as does cementum incrementation.

Similar experimental designs to these studies, but additionally employing CT methodologies, may be used to quantitatively distinguish the effects of different environmental and physiological variables on the gross morphology of cementum increments. Further, the study of several disparate taxa will provide evidence on whether the relationship between environmental variables and increment structure are universal across extant Mammalia and beyond, or if particular clades show individual phenotypic responses.

2.10. Conclusions

(**1**) The biology of cementum has been the subject of study for decades. However, since the earliest recognition of correlation between cementum incrementation and chronological age, the development and application of cementochronology has received substantial debate. Much of this stems from a relatively small number of validation studies that brought into question the correlation between increment count and chronological age, and highlighted the inherent subjectivity of increment counting between observers.

(**2**) The perceived accuracy of increment counts as a record of chronological age is affected by the extent of *a priori* knowledge of the biology of cementum, and the external/internal factors affecting the periodicity of cementum increments. Several of the validation studies expected increments to follow a regular pattern. However, our meta-analysis of previous studies of cementochronology in wild-living mammals shows that approximately **48%** of populations of mammals have a proportion of individuals that are genetically predisposed to deposit more complex series of increments. This proportion is less prevalent in climates with stronger seasonal influence. Within studies the number of individuals with complex cementum increments ranges from 0% to **100**%, with a mean of 16.37%. Since many of the studies analysed used cellular cementum, which is known to be more prone to complex incrementation than acellular cementum, we expect with appropriate choice of cementum tissue these numbers will begin to be further reduced in future studies. The biomechanical function of certain types of cementum tissue can also result in complex patterns of increments, regardless of environment. We believe that not accounting for these two phenomena contributed to several studies being unable to determine a strong correlation between cementum increments and absolute age.

(**3**) The problems caused by such biological complexity have also been compounded by methodological inconsistencies between cementochronology studies. We have here discussed a well-established protocol for aging using other mineralised tissues; the development of a globally accessible reference collection of cementum images. The application of this common quality control measure may provide a solution for both the lack of global understanding of biological complexities, and the lack of a universal standard for assessing their effects on cementochronology. The negative effects of low reader experience and prior knowledge of cementum biology might be minimised by developing collections of images displaying both perfect correlation between increment count and chronological age, and a series of examples of common issues affecting increment periodicity. Continuously adding images from new studies and taxa to such a reference collection will help further optimize the accuracy of increment counts. Finally, the use of objective counting methodologies, based on (semi)automated image processing procedures as opposed to human increment counting, should minimise the inter and intra-observer uncertainty of increment counts.

(**4**) The incorporation of analytical techniques commonly used in other disciplines may further aid the study of cementochronology. Computed tomography offers a 3D

perspective at high spatial resolutions, with no physical damage to the specimen under study. This technique thus presents an important tool for the future study of cementochronology, allowing the 3D nature of cementum incrementation to be explored for the first time, through the entirety of the cementum tissue. It will also open up the technique of cementochronology to unique specimens, such as fossils, that are unavailable for destructive thin-section sampling.

(**5**) Other microscopy-based techniques (such as second-harmonic generation imaging and atomic force microscopy), and spectroscopic/chemical techniques (such as Raman spectroscopy), have the potential to allow quantitative examination of the effects of life history variables and events on the structural and material properties of cementum and cementum increments. The isolation of such life history variables, through rearing animals in controlled environments, may allow hallmarks representing their particular impact on cementum structure and material properties to be identified using these and other techniques. If significant differences in whichever aspects of specific increments are measured exist, and they are shown to correspond to known life history events in such controlled experiments, then this variation and the resulting hallmarks can be used to predict similar events in individuals of unknown life histories.

(**6**) In summary, we believe that that by combining improvements in current methodology with new techniques and rigorous experiments, the accuracy, precision, and usefulness of cementochronology will all be greatly improved. The potential of the application of a better understood and validated cementochronology to a wide range of fields (including but not limited to ecology, conservation biology, archaeology, zooarchaeology, anthropology, palaeontology, palaeoanthropology, forensic criminology, and commercial hunting, wildlife monitoring and management), will ensure that it is viewed and used as a powerful technique for investigating a great variety of aspects of individual and population age and life history.

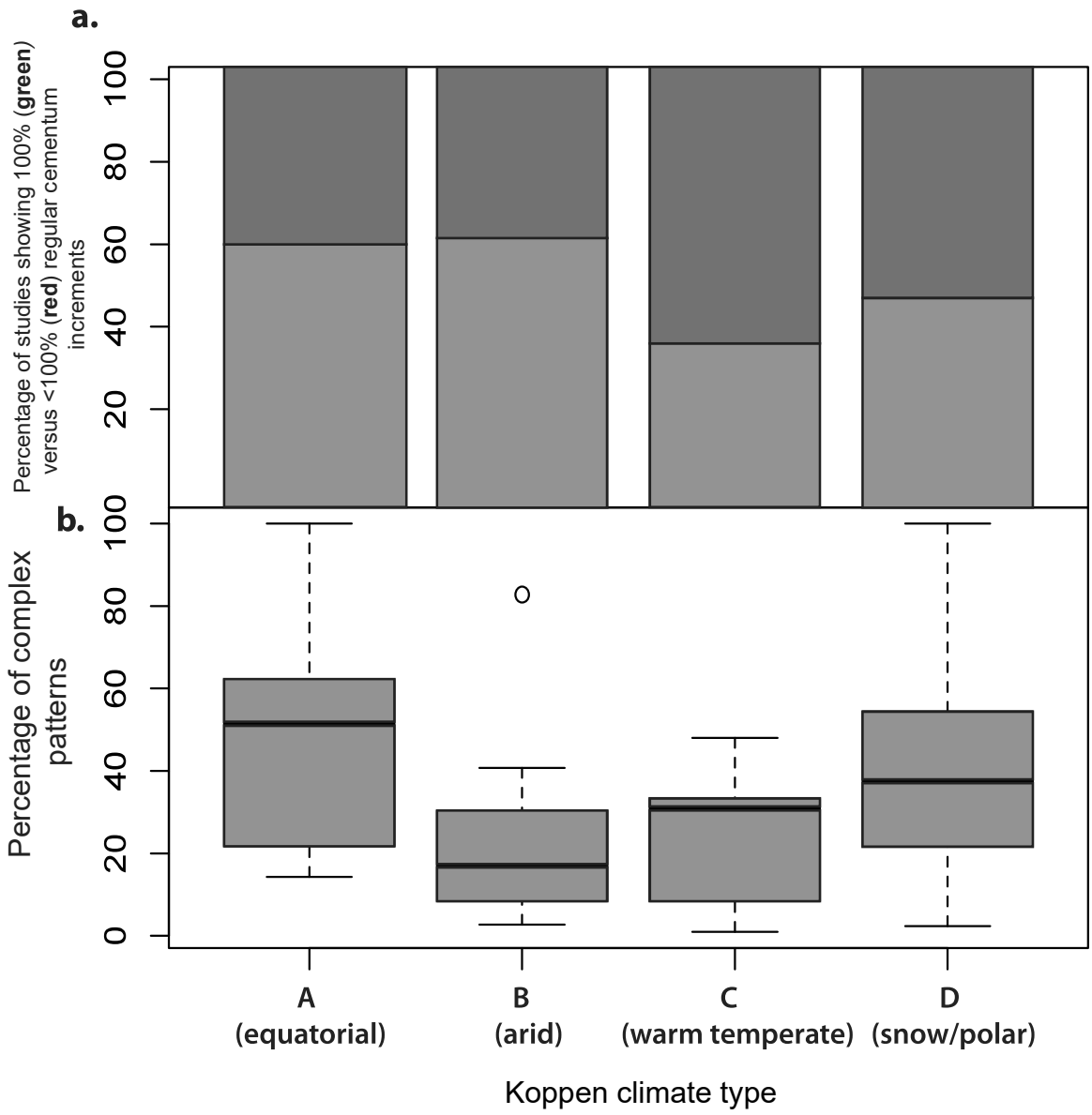

Figure 2.1. (**a**) Proportion of studies with 100% of individuals showing regular increments (green) versus <100% of individuals showing regular increments (red). (**b**) Comparison between the proportions of individuals producing complex cementum increment patterns within populations grouped into major köppen climate types. Thick dark lines represent mean values, bracketed lines represent upper and lower quartiles, single circle represents individual population falling outside of the upper quartile. $n = 61$.

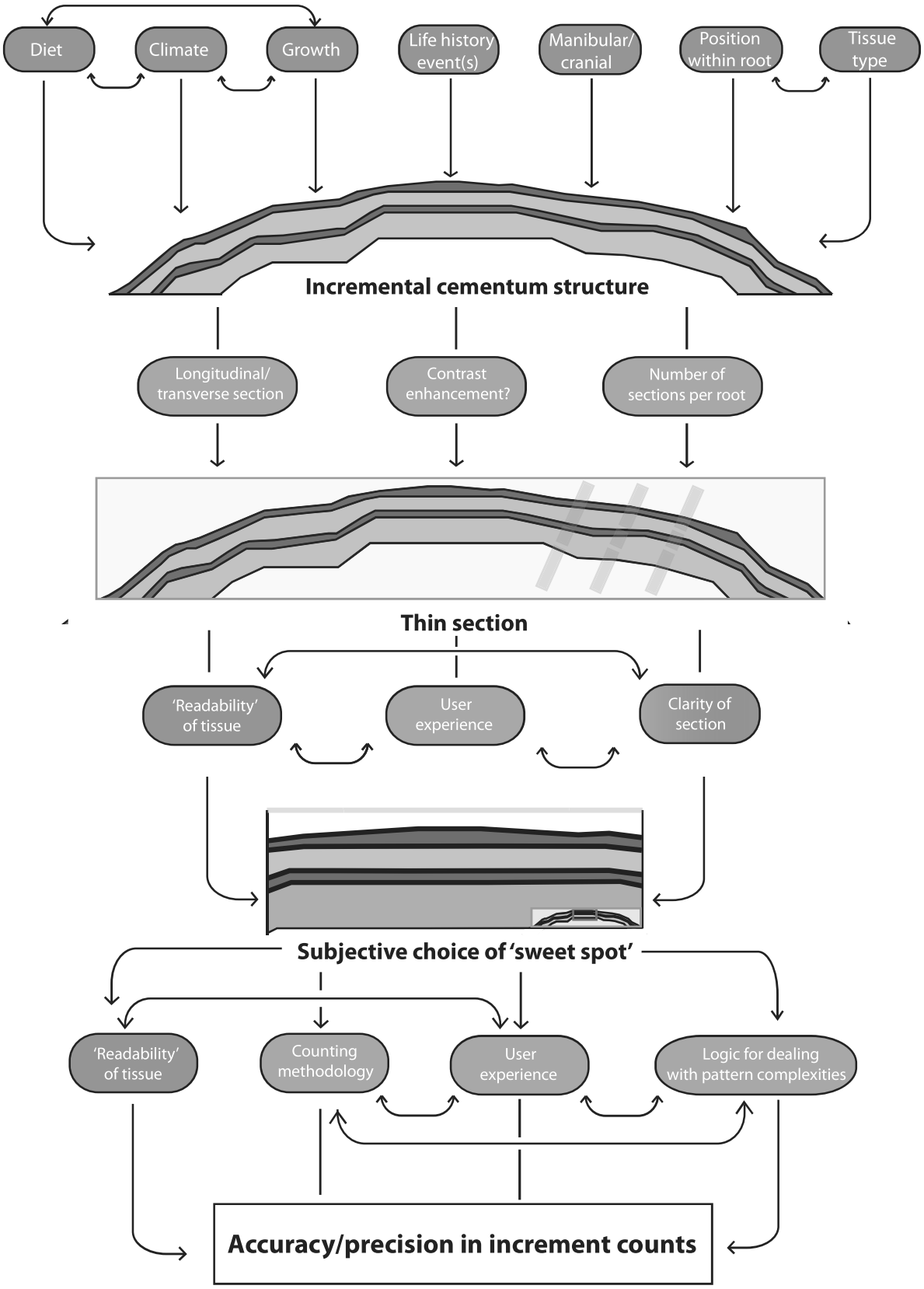

Figure 2.2. Schematic flow chart of the principal factors affecting the accuracy and precision of counts of cementum increments at each major stage of the current cementochronology technique. Green boxes highlight biological factors, orange boxes represent methdological factors.

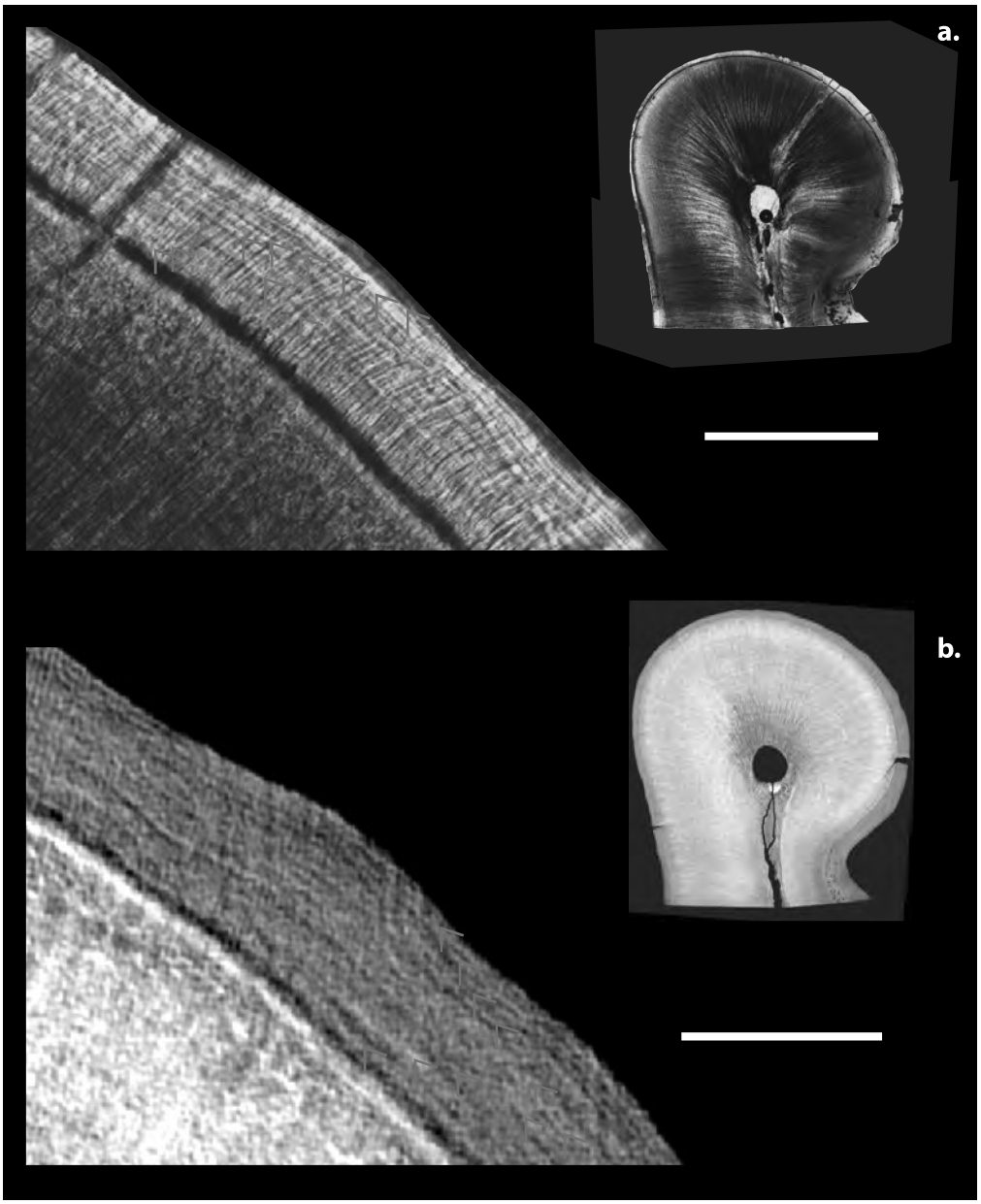

Figure 2.3. Comparison between thin section histological data and synchrotron microcomputed tomographic (SR CT) data of incremental dental cementum. (**a**) thin section histological image of the cementum of a female rhesus macaque (*Macaca mulatta*) cementum displaying 10 increment pairs considerably obstructed by radial Sharpey's fibres. (**b**) Propagation-based phase-contrast reconstuction image of the same region displaying the same 10 increment pairs, and considerably higher increment contrast with substantially less disruption from Sharpey's fibres. SR CT imaging performed at the TOMCAT beamline of the Swiss Light Source Synchrotron using a voxel resolution of 650 nm. Whitescale bars represent 100 μm. See supplementary information for explanation of thin sectioning techniques, and SR CT experimental parameters.

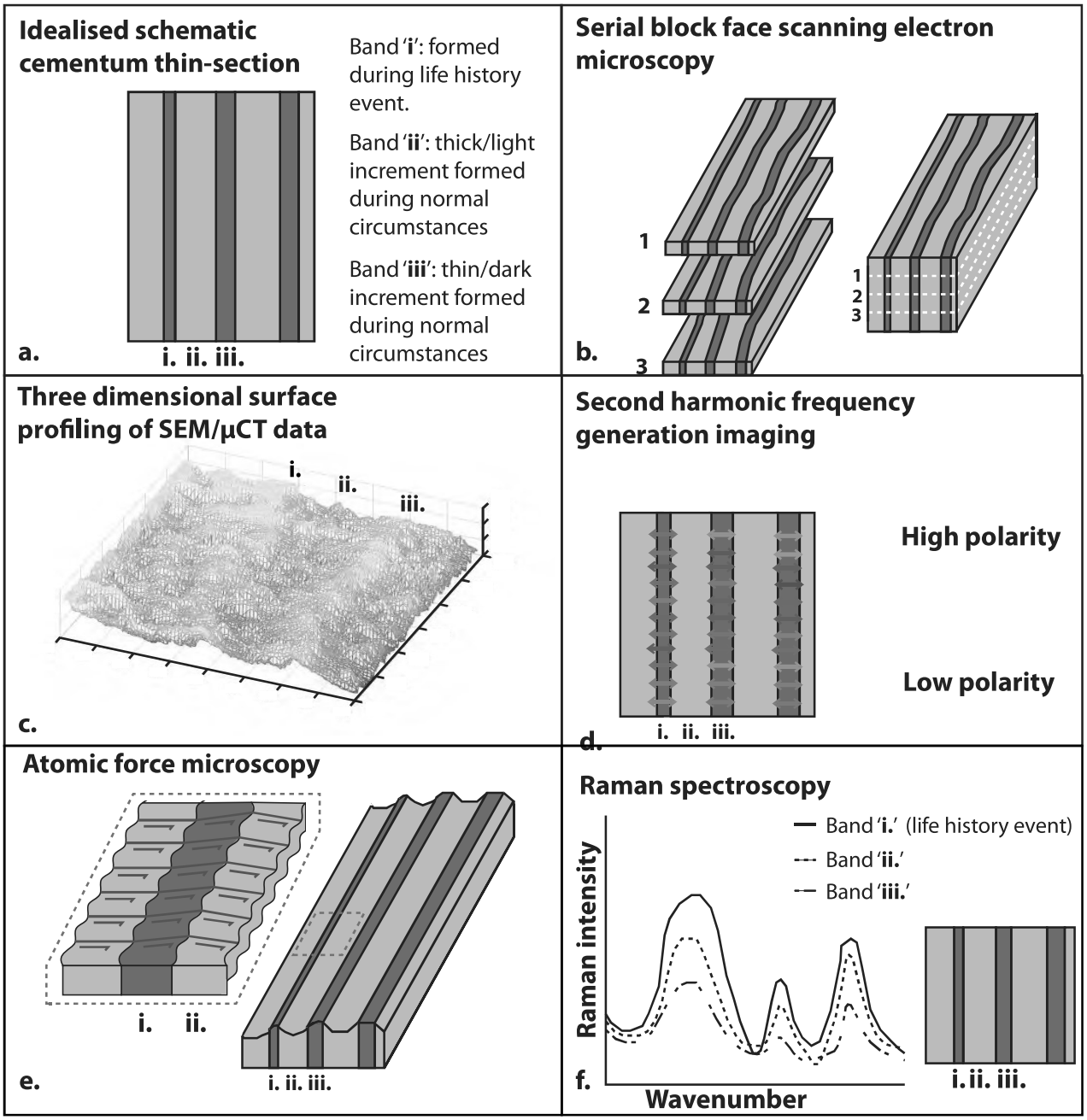

Figure 2.4. (**a**) Schematic diagram of cementum thin section displaying one increment formed during a year where an important life history event likely to affect body metabolism has occurred (e.g. pregnancy, disease, poor winter) (band '**i**'). (**b**) Schematic of serial-block-face scanning electron microscopy for assessing and comparing volumetric changes in increment shape and structure. (**c**) Three dimensional surface mesh based on grey-value distributions of tomographic data. (**d**) Schematic of the application of second harmonic frequency generation imaging for analysing and comparing the polarity of collagen fibres within and between cementum increments. (**e**) Schematic of the application of atomic force microscopy for defining topographic distribution of collagen fibres across and between neighbouring increments formed under different life history circumstances. (**f**) Schematic of the potential use of the raman spectroscopy method for imaging and assessing chemical differences between cementum increments.

Köppen climate type	Populations with >1 individuals with complex cementum increments	Average proportion of individuals per population with complex cementum increments	Variance
A	8	48.299	818.509
B	8	24.636	685.671
C	11	23.107	235.619
D	34	41.031	751.169

Table 2.1. Proportion of individuals with complex increments in populations representing the four Köppen climate types studied here. Climate type A represents equatorial /tropical rainy climates. Climate type B represents arid/dry climates. Climate type C represents warm temperate/humid mesothermal climates. Climate type D represents snow/humid microthermal climates.

Comparison between Köppen climate types	Difference in means	Honest significant difference
A versus B	23.663	**3.682**
A versus C	25.192	**4.271**
A versus D	7.268	1.832
B versus C	1.529	0.259
B versus D	16.395	**4.133**
C versus D	17.924	**4.677**

Table 2.2. Results of Tukey-Kramer procedures for each comparison between Köppen climate types (following Kramer, 1956). Significant values of honest significant difference (HSD) are highlighted in bold text. These are values that exceed the critical HSD value of 3.79 for a series of comparisons of 57 degrees of freedom and four treatments. Climate type A represents equatorial /tropical rainy climates. Climate type B represents arid/dry climates. Climate type C represents warm temperate/humid mesothermal climates. Climate type D represents snow/humid microthermal climates.

Method	Abbreviation/ AKA	Resolution (spatial/optical) (nm)	Previous use	Possible use for cementochronology	Limitations	References
Micro Computed tomography	MicroCT / µCT	500	Material science; bone histology; bone morphometry; dental histology; dental morphometry	Non-invasive analysis; 3D characterisation of increment patterns and morphometry	Limited resolution; difficult to quantify morphometric properties; comparison with histological data yet to be attempted	Ritman 2004; Rowe and Frank, 2011; Sanchez et al., 2012
Synchrotron radiation nano-tomography	SR CT	10	Organic/inorganic chemistry; material science; cell biology	3D characterisation of collagen ultrastructure	Very limited field of view; destructive sampling of most teeth; low contrast	Leis et al., 2009; Midgeley et al., 2007
Scanning electron microscopy	SEM	5	Material science; bone histology; dental histology; cementum histology	Quantitative description of collagen fibre ultra-structure; quantitative comparison of ultra-structure between increments formed during calcium-limiting events and surrounding cementum	Destructive sample preparation (metal coating; limited field of view	Boyde et al., 1985; Lieberman, 1994;

Focused ion beam/serial block face SEM	FIB SEM	10	"3D" cross-sectional analysis of material close to the scanned surface; semi-conductor material science/engineering; soft tissue study; bone ultra-structure characterisation	Characterisation of the 3D architecture of collagen ultra-structure; quantitative comparison of 3D ultrastructure between increments formed during calcium-limiting events and surrounding cementum increments	Destructive sample preparation (metal coating; limited field of view; time consuming	Morrissey and Lich, 2006; Pediie and Collinson, 2014; Morrissey et al., 2005
Second harmonic generation imaging	SHGI	100	High contrast imaging of materials possessing non-centrosymmetry and second-order nonlinear coefficient	3D, high contrast imaging of collagen ultra-structure in different cementum increments	Low depth penetration; destructive sample preparation; expensive	Cox et al., 2003; Gauderon et al., 2000
Atomic force microscopy	AFM		semi-conductor material science/engineering; cell biology; soft tissue histology; bone histology; ligament biomechanics; cementum biomechanics	Quantitative characterisation and comparison of material properties between cementum increments	Expensive; time consuming; destructive sample preparation; very limited field of view	Chen et al., 2-12; Francis et al., 2010; Ho et al., 2007; Thurner, 2009

Raman spectrometry		20-30	Semi-conductor material science; Pharmacology; forensic science; bone chemistry/material; Cementodentine junction chemistry	Quantitative characterisation and comparison of chemical properties between cementum increments; Development of chemical hallmarks of certain life history events within cementum	Destructive sample preparation; Weak Raman signal may make comparison of spectra difficult	Buckley et al., 2012; Carter and Edwards, 2000; Granfield et al., 2014

Table 2.3. Description of state-of-the-art techniques used for ultra-structural study of other biological and artificial materials, and their possible uses for cementochronology.

Chapter 3.

Synchrotron radiation-based computed tomography reveals reptile-like physiology of early mammals

A succession of recent discoveries and analyses have revolutionised our knowledge of the ecological, morphological, and taxonomic diversity of Mesozoic mammals (Luo, 2007; Wilson et al., 2012; Grossnickle and Polly, 2013; Bi et al., 2014; Gill et al., 2014; Krause et al., 2014; Newham et al., 2014; Close et al., 2015; Martin et al., 2015; Meng et al., 2015), and have opened new windows onto aspects of their development (Han et al., 2017), systematics (Bi et al., 2014; Krause et al., 2014; Luo et al., 2015) and macroevolution (Wilson et al., 2012; Close et al., 2015; Grossnickle and Newham 2016). However, details of the physiologies of Mesozoic mammals are more difficult to determine from their fossils, and our knowledge of their physiological evolution remains comparatively poor. Living mammals are endotherms, possessing the ability to control and maintain metabolically produced heat, and have a substantially higher capacity for sustained aerobic activity than ectothermic animals (Bennett and Ruben, 1979; Kemp, 2006; Clarke and Pörtner, 2010). The origin of endothermy is an important event in mammalian evolution, and a number of competing hypotheses have been proposed to explain the selective pressures and adaptive pathways of endothermic evolution. These alternatively suggest that higher maximum metabolic rate (MMR) was originally selected for to provide more sustained rapid activity (Bennett and ruben, 1979; Koteja, 2000), that higher basal metabolic rate (BMR) was initially selected for enhanced thermoregulative control (Crompton et al., 1978; Farmer, 2003), or that both evolved in lockstep with each other (Kemp, 2006; Clarke and Pörtner, 2010). Within these hypotheses, various initial selective pressures have been suggested. For example, increased sustained aerobic activity, whether for its own benefit (Bennett and Ruben,

1979), to allow increased parental care and provisioning (Koteja, 2000) and increased foraging ability (Hopson, 2012). Alternatively, increased metabolic efficiency would allow increased sustained activity (Clarke and Pörtner, 2010) and the benefits of embryonic incubation (Farmer, 2003). Overall, increases in both sustained aerobic capacity and metabolic efficiency would lead to more efficient, integrated animals (Kemp, 2006).

Direct evidence from modern mammals for any hypothesis is equivocal (Kemp, 2006). Several indirect indicators of metabolic physiology in fossil synapsids have been suggested (Fig. 1.2), but provide contradictory evidence for the timing of the origination of endothermy and its evolutionary tempo. These include the presence of fibrolamellar long bone histology (Gross, 1934; Ray et al., 2004), first seen in the early Permian synapsid *Ophiacodon* ~300 Mega Annums (Ma) ago (Shelton and Sander, 2017) and inferred maxillary nasal turbinates in the Late Permian (~255Ma) therapsid *Glanosuchus*, which have been used to suggest that mammalian levels of endothermy had evolved by the Late Triassic (210Ma)(Hillenius, 1994). Other examples are a trend toward increased relative brain size (Hulbert, 1980) initiated in late Triassic non-mammaliaform cynodonts (Benoit et al., 2017) and the mammaliaform (stem mammal *sensu* Rowe [1988]) *Morganucodon* (Rowe et al., 2011); and acquisition of a parasaggital gait, first seen in the Lower Cretaceous (125 Ma) therian mammals *Eomaia* and *Sinodelphys* (Kilena Jaworowska and Hurum, 2006)(Fig. 1.1.). However, the inconsistency of these characters in time and with respect to phylogeny (Kemp, 2006; Ruf et al., 2014; Crompton et al., 2017), along with recent re-assessments of their function in relation to the evolution of endothermy (Hayes and Garland, 1995; Kemp, 2006; Köhler et al., 2012; Owerkowicz et al., 2015), inhibit their use as conclusive indicators of endothermic physiology.

Although potentially indicative of certain facets of physiology in fossil taxa compared to modern endotherms or ectotherms, few of these proxies are directly related to measurable aspects of metabolic rate. Their relationships to metabolism are therefore uncertain. The contradictory nature of these indicators also suggests that the evolution of mammalian endothermy followed a complex path, with different aspects of physiology following separate rates of evolution towards current mammalian levels (Kemp, 2007).

This chapter presents an attempt to improve understanding of physiology at one of the most important nodes along this transition, by estimating lifespan and blood flow rate for two of the earliest known mammaliaforms; *Morganucodon* and *Kuehneotherium*. Lifespan can be used to estimate both BMR and post-natal growth rate (k) in extant mammals, and estimates of blood flow rate (Q_i) are directly proportional to MMR in both extant mammals and ectothermic reptile. These proxies thus offer a more complete window onto the mammalian physiology, and the chance to directly compare their metabolic potential with extant mammals.

3.1. Lifespan: a proxy for mammaliaform physiology

We chose to use maximum lifespan estimates for fossil mammaliaform taxa as a proxy for both basal metabolic rate (BMR)(Hulbert et al., 2007), and postnatal growth rate (k)(De Magalhães et al., 2007). In extant mammals, negative correlations have been shown between both lifespan and mass-specific BMR (Hulbert et al., 2007), and between lifespan and growth rate (De Magalhães et al., 2007;Werner et al., 2016). In general, the longer a mammal species lives, the lower its size adjusted BMR and growth rate. Growth rates have been shown to strongly correlate with metabolic power in extant vertebrates, with endotherms growing an order of magnitude faster than 'cold blooded' ectotherms (Grady et al., 2014; Werner et al., 2016). An accurate assessment of lifespan in fossil mammals could therefore provide a key towards estimating their state of metabolic evolution.

3.2. Cementochronology of mammaliaforms

To estimate lifespan in mammaliaforms we used counts of annual growth increments in tooth root cementum, a well-established technique used to record lifespan in extant mammals (Klevezal, 1995; Naji et al., 2016) (**Chapter 2**). Growth of cementum is continuous throughout life in extant mammals and seasonally appositional in nature, forming a series of increments of differing thickness and opacity under light microscopy. The correlation between increment count and chronological age is well documented, with one thick increment and one thin, opaque increment deposited every year, and it has been shown that the thin, relatively dense, hyper-mineralized opaque

increments record growth rate reduction in unfavourable seasons (Lieberman, 1993; Stock et al., 2017). Growing evidence from the fossil record suggests that cementum, a periodontal ligament and alveolar bone may be ancestrally characteristic of all amniotes, and secondarily lost in taxa lacking these features (LeBlanc and Reisz, 2013; LeBlanc et al., 2017).

Despite this potential, cementochronology has not previously been attempted for fossil mammals older than the Pleistocene (2.6 Ma) (Stutz, 2002). This is principally due to the destructive nature and the restricted sample view (usually just a single image) provided by histological thin-sectioning techniques. We have overcome these issues by using for the first time synchrotron radiation computed tomography (SR CT) to non-destructively image fossilised cementum increments. The three-dimensional (3D) nature of SR CT allows increments to be studied through the entire cementum tissue and so provides improved understanding of their count and structure. This minimises the effects of occasional coalescence and lensing of increments, phenomena that can otherwise create uncertainty in counts based on single or limited numbers of 2D thin sections created per-tooth (Klevezal, 1995). Using 3D tomographic data, increments can be imaged along their entire transverse and longitudinal trajectories, across periods of noise created by lensing and coalescence, allowing us to confidently distinguish principal annual increments from the additional increments that lensing and coalescence occasionally create.

Our chosen taxa, *Morganucodon* and *Kuehneotherium,* are two of the earliest mammaliaforms and are of fundamental phylogenetic importance (Fig. 1.1). Morganucodontids were one of the most successful early mammaliaform groups, with a global distribution (Kielan-Jaworowska et al., 2004). Kuehneotheriids were less widely distributed and, although possessing advanced molars with cusps arranged in an obtuse-triangle pattern, are of uncertain phylogenetic affinities (Kielan-Jaworowska et al., 2004). Both taxa are shrew-sized insectivores (body masses of ~26g following scaling relationships between mandible length and body mass by Foster [2009]), and co-existed on a small landmass present during the Early Jurassic marine transgression (Hettangian-Early Sinemurian, about 200 Myr ago), in what is now Glamorgan, South Wales, UK (Kermack et al., 1973). Large numbers of their bones and teeth were washed into karst fissures that have subsequently been revealed by quarrying. This provides a rare opportunity for analysing population-sized samples of fossil material needed for

confident estimation of maximum lifespan. Importantly, these are the earliest diphyodont taxa, with a single replacement of non-molar teeth and no molar tooth replacement. Therefore, estimates of lifespan are accurate to the time of the measured tooth root formation, plus only the time from birth to that permanent tooth eruption.

3.3. Synchrotron X-ray tomography

Non-destructive SR CT imaging allowed a substantial sample to be analysed and included both isolated teeth and mandibles with multiple teeth or roots *in-situ*. The sample comprised 72 *Morganucodon* specimens (12 dentaries and 60 isolated teeth), and 116 *Kuehneotherium* specimens (2 dentaries and 114 isolated teeth)(Appendix 3.1). Pilot scans of two *Morganucodon* m2 teeth (specimens CEM4 and CEM3) were performed in 2011 on the nanotomography imaging beamline ID22 at the European Synchrotron Radiation Facility (ESRF). The bulk of all other *Morganucodon* scans (*n*=66) were performed during a four-day experiment at the ID19 beamline of the European Synchrotron Radiation Facility (18/04/2014-22/04/2014)(for proposal see Appendix 1.1.). A near-monochromatic beam with 17KeV energy was used with single propagation distance tomography, and voxel resolutions of 280, 350 and 700 nanometres (nm).

All scans of *Kuehneotherium* specimens (*n*=116), and eight *Morganucodon* specimens, were performed during a three-day experiment at the TOMCAT tomographic beamline of the Swiss light Source synchrotron, Switzerland (13/04/2015-16/04/2015)(for proposal see Appendix 1.2.). A near-monochromatic beam with 20KeV energy was used with single propagation distance tomography, at a constant voxel resolution of 330nm.

Reconstructions of tomographic data were generated using both X-ray absorption-based filtered back-projection algorithms, and “Paganin-style” single propagation phase retrieval algorithms (Mokso et al., 2013) developed in-house at each respective beamline. Phase contrast reconstruction techniques are sensitive to the phase-shift introduced to X-rays as they interact with a sample. This signal can be up to three orders of magnitude higher than the absorption coefficient (μ) of a specimen, making phase contrast reconstruction a useful alternative to traditional X-ray absorption-based reconstruction techniques. Single distance phase retrieval algorithms such as the

paganin-style algorithms implemented here are based on detecting Fresnel edge diffraction as different rays of the synchrotron beam are affected by hitting the edges of materials of different material properties. They require a value of β and δ to be inputted, related to the real and imaginary portions of the complex refractive index of the sample under investigation ($n = 1 - \delta + i\beta$). For both experiments β was set at 3.7 10^{-8}, and δ was set at 1.7 10^{-10}, following validation experiments by beamline staff at TOMCAT to determine the optimal values for imaging hard tissues.

The majority of isolated teeth measured were lower second molars (m2), since unlike the m1 of *Morganucodon* where there is uncertainty as to whether it was replaced (Luo et al., 2004), (which would reset the cementum increment clock), no evidence suggests replacement of m2. However i2, c, p3, p4, m1, m3, m4 teeth were also studied in dentulous *Morganucodon* specimens, and p3, p4, m1 m3 and m4 teeth were studied in *Kuehneotherium* specimens (Table 3.1.).

3.4. Increment counting

Increments were counted by-eye by three different observers following digital image processing and enhancement. Observer One (Newham) had considerable experience in counting cementum increments (>100 specimens studied), Observer Two had training in counting cementum increments (30 specimens studied under guidance from Observer One) and experience in studying growth patterns in SR CT data of long-bones. Observer Three had no experience in counting increments or studying growth patterns. Before counting, every SR CT dataset was investigated by Observer One in order to find the region(s) of highest contrast between cementum increments and to ensure that regions of lensing and coalescence were not used for increment counting. The chosen regions were then used to create 'virtual thin-sections' by using the "Z projection" tool in imageJ/Fiji (Schneider et al., 2012) to combine 10 transverse SR CT slices into one image. This is known to considerably increase contrast between cementum increments, and all counts were based on these images (Sanchez et al., 2012).

3.5. Long lifespans and low basal metabolic rates

From the total sample, 34 *Morganucodon,* and 27 *Kuehneotherium* specimens were of sufficient preservational quality for three observers to independently estimate lifespan from cementum increments. The remainder showed physical and/or diagenetic damage that prevented increments from being measured (Fig. 3.1.).

Tomographic data presents a number of features that confirm the presence of cementum in *Morganucodon* and *Kuehneotherium*. Cementum is distinguished from dentine in tomographic data by a distinct boundary layer separating the two mineralized tissues, external to the granular layer of Tomes of the dentine and interpreted as the hyaline layer of Hopewell Smith (Fig. 3.2.), often separated from the cementum by a circumferential crack. Ultra-high resolution imaging (30nm voxel resolution) reveals that individual Sharpey's fibre bundles are preserved in several exceptionally preserved specimens, which can be traced radially through the cementum (Fig. 3.2.). When studied along the transverse axis of tooth roots, the cementum tissue is ~10—70μm in radial thickness, and displays a series of contrasting light and dark circumferential increments representing different material densities (Fig. 3.2.b-f.). Higher density increments (represented by higher greyscale values) are on average 2-3μm in radial thickness, and lower density increments are on average 1-3μm in radial thickness (Fig. 3.2.d.). Individual increments can be followed continuously both longitudinally and transversely through the entire volume of a tooth root (Fig. 3.2.g.). Following cementum increments through the characteristic bulbous portion at the root apex of several *Morganucodon* molar roots reveals that this morphology is due to the increasingly chaotic nature of cementum through these portions, with increments loosing definition and becoming globular (Fig. 3.3) However, it should also be noted that no evidence of cellular cementum, the cementum tissue that creates similar bulbous projections along the roots of extant mammals (Naji et al., 2016), was found in any specimen.

Counts of cementum and dentary increments by each observer provided a minimum estimate of maximum lifespan of **14 years for *Morganucodon***, and **nine years for *Kuehneotherium*** (Fig. 3.4.a-b.). Counts were identical between all three observers for 18 *Morganucodon* specimens (53%) and 16 *Kuehneotherium* specimens (59%). Of the 16 *Morganucodon* specimens that differed in counts between observers, 13 differed by one count. Two specimens differed by two counts, and one differed by

four. All 11 *Kuehneotherium* specimens that differed in counts only differed by one count (Fig. 3.4.a-b. and Table 3.2.). The precision between increment counts by each observer was quantified by generating their coefficients of variation (*CV*; *CV* = (standard deviation/mean)*100) and Pearson's correlation coefficient (*r*), and given context within the wider cementochronology literature by comparing these metrics to those of 10 previous cementochronological studies of extant mammals with similar age ranges (Table 3.3). Mean *CV* values were 9.32 for *Morganucodon* and 4.89 for *Kuehneotherium.* ANOVA comparisons suggest that these values are considerably lower than any extant study ($F = 11.7$; $p<0.01$). Mean *r* values between observers were 0.92 for *Morganucodon* and 0.96 for *Kuehneotherium.* ANOVA comparisons showed no significant difference between these values and those of extant mammals ($F=1.55$; $p=0.241$). Our *r* values correspond with the highest values in the extant sample, with only one extant study providing higher values. Both precision metrics analysed here suggest that SR CT study of fossil cementum increments offers comparable, if not higher, precision for increment counting than traditional histological methods.

The distributions of age estimates for both taxa follow similar patterns, although the skew and kurtosis is more exaggerated within the *Morganucodon* sample (Fig. 3.4.a-b.). Both show a left (young) skew (mean skewness between observers = 2.05 and 0.47 around a mean age of 5) and positive kurtosis (kurtosis = 5.78 and 0.31 for *Morganucodon* and Kuehneotherium, respectively). Age at death distributions of similarly sized extant wild mammals show similar trends to our data; left skew, positive kurtosis, and a distinct paucity of yearling taxa (Castanet et al., 2004; Kryštufek, 2005; Haigh et al., 2014). However, in extant mammals the second youngest age or age category generally has the highest frequency (Kryštufek et al., 2005; Haigh et al., 2014). This is not shown in our samples, and this difference may be due to several factors. As a fissure-suite death assemblage, our sample cannot be classed as a true population sample, and is expected to be time averaged over hundreds of years (Flessa et al.,1993). This may have amplified existing biases in the proportion of individuals of particular age preserved in the fissures including preservational biases against more fragile juvenile material.

Maximum lifespan and body mass were plotted for *Morganucodon* and *Kuehneotherium* and recorded data for large wild samples of extant mammal (n=206; not including gliding or flying taxa) and non-avian reptile (n=190) species (Appendix

3.2.). ANCOVA comparisons suggest significant differences between the relationships of logged body mass to logged lifespan in extant mammals and our fossil taxa (F=15.4; p<0.001), and no significant difference between fossil mammaliaforms and extant reptiles (F=0.39; p=0.53). This is highlighted when logged values are regressed alongside those of extant mammals and reptiles using least squares regression (Fig. 3.4.c.). The regressions between logged body mass and logged lifespan for extant mammals and reptiles are separated for animals below 1kg, and begin to converge in animals above this mass, as mammals provide a steeper regression slope (0.261) than reptiles (0.236), and reptiles provide a lower r^2 value (0.592) than that of mammals (0.726)(Fig. 3.4.c). *Morganucodon* and *Kuehneotherium* are further above the mammal regression mean line than all extant mammals in the sample below 1kg. *Morganucodon* is also the furthest non-reptile taxon above the mammal regression line. This suggests that both fossil taxa have longer maximum lifespans for their body size than any living terrestrial mammal, and are the only synapsid taxa below 1kg studied here to attain lifespans above the regression average of extant non-avian reptiles of comparable body mass. Regression slopes for extant mammals (0.26) and reptiles (0.24) are similar, although significantly separated (p<0.001), with reptiles on average living 3 years longer than mammals of the same body mass.

The only extant mammals in our dataset with relatively extended wild lifespans, and of comparable body mass to *Morganucodon* and *Kuehneotherium*, and are members of the heterothermic Gliridae (dormice) and Geomyidae (gophers) (Fig. 3.4.c.). Heterothermy allows such taxa to control their metabolic expenditure, concentrating activity during favourable conditions and conserving energy during unfavourable periods using hibernation, aestivation and torpor. This considerably extends the potential lifespan of heterotherms compared to homeothermic taxa of comparable body mass (Sibly and Brown, 2007; Giroud et al., 2008)(Fig. 3.4.c.). Comparing mean maximum lifespans of heterothermic and homeothermic mammals of similar body mass with ANCOVA regression slopes, the intercept for heterotherms is significantly higher than homeotherms (p<0.001), whereas the slope is significantly lower (p<0.001) (Fig. 3.5.). This indicates that smaller heterotherms have significantly higher lifespans than smaller homeotherms, although this difference begins to diminish when body mass is over 100g. The presence of heterothermic physiological/ecological strategies in Mesozoic mammals has been previously suggested by analyses of the phylogenetic and

ontogenetic distribution of such strategies within and between extant mammal clades (Grigg et al., 2004; Lovegrove, 2012, 2017).

However, more direct evidence of heterothermy is needed before the relatively long maximum lifespans we estimate for *Morganucodon* and *Kuehneotherium* can be attributed to such a strategy for energy conservation. The inverse relationship between lifespan and post-natal growth rate (*k*) in living mammals (De Magalhães et al., 2007) suggests a markedly lower growth rate in our basal fossil mammals, compared to living mammals of similar size. We used the regression between growth rate and lifespan provided by Magalhães et al. (2007) to estimate an average post-natal growth rate of 0.01*k* for *Morganucodon* and 0.03*k* in *Kuehneotherium* (*k* is a growth rate constant in $days^{-1}$ estimated for extant mammals by gompertz modelling of growth curves by Zullinger et al. [1984]). The value is 0.18*k* for the most profoundly heterothermic living mammal of comparable body mass, the hazel dormouse (*Muscardinus avellanarius*). Similarly, we used the negative relationship between mammalian lifespan and BMR identified by Hulbert et al. (2007) to estimate a BMR of ~150 $kj.kg^{-1}.day^{-1}$ for *Morganucodon*, and 241 $kj.kg^{-1}.day^{-1}$ for *Kuehneotherium.* This is significantly lower than any extant mammal between 2.4-100g ($p<0.001$) (e.g. *Muscardinus avellanarius* provides an estimated BMR of ~1000 $kj.kg^{-1}.day^{-1}$). Instead, this value is closer to that of taxa over four times the predicted body mass for these fossil taxa. For example the coyote, *Canis latrans*, weighs 13kg and has a maximum wild lifespan of 14.5 years.

3.6. Mandible age estimates match cementum results

The accuracy of cementum increment counts for predicting lifespan in our fossils mammals was tested by the additional SR CT imaging of annual lines of arrested growth in the periosteal region of the dentary bone in five *Morganucodon* specimens with teeth *in-situ.* Increments closely matching those seen in histological sections of extant mammals are clearly visible in fossil dentaries (Fig 3.6.a.). Dentary increments were counted by each of the three observers and compared to the count from the tooth cementum in the same specimen. Counts of m1 and m2 cementum increments are identical to dentary increments (Fig. 3.6; Table 3.4.). This agreement between cementum and dentary increments suggests that growth in both teeth and jaws was

following the same, circum-annual rhythm. We consider this strong support for the accuracy of lifespan estimates based on these increment counts.

The study of dentary specimens also allowed us to compare counts of cementum increments in multiple positions along the tooth row of individual *Morganucodon* specimens, providing new information on basal mammaliaform dental development and the evolution of diphyodonty. *Morganucodon* is considered to be the most basal diphyodont synapsid, possessing the modern mammalian condition of replacement of the first set of deciduous teeth with a second, permanent set (Luo et al., 2004). The number of increments was found to be the same in the p4, m1 and m2 teeth. However, in specimen "bd10" the m4 tooth has one less increment pair (eight pairs) than the m1-m3 teeth (nine pairs), and in specimen "bd13" the m3 tooth has one less increment pair (four pairs) than the m1 and m2 teeth (five pairs). Further, the last incisor and canine of specimen NHMUK M95790 comprise one less increment pair (five pairs) than the pm2 and pm3 teeth (six pairs). This pattern supports previous hypotheses that tooth replacement of the non-molariform teeth occurs in *Morganucodon*, while anterior premolars are generally shed but not replaced (Luo et al., 2004). The molars m2-m4 (and m5 when present), are generally thought to have not replaced (although some evidence for replacement of the m1 has been shown previously). The similarity in increment counts between premolar and m1-2 teeth suggests that the premolars weren't lost until *Morganucodon* reached a substantial age. The variability in eruption times for m3 and m4 that we have found here suggests a labile eruption schedule of primary teeth in basal mammaliaforms. While the time gap of as much as a year between eruption times of periosteal molariform teeth indicates an extremely slow eruption schedule in comparison with living mammals of similar body size.

3.7. Femoral blood-flow suggests low maximum metabolic rate

To gain further understanding of the physiology of basal mammaliaforms, we used a second proxy to estimate Maximum metabolic rate (MMR). This reflects locomotory ability and records the highest levels of instantaneous and sustained metabolic activity an animal is able to produce (Seymour et al., 2012). To generate estimates of MMR we used micro CT imaging of the most complete *Morganucodon* femoral diaphyses

available, measuring the minimal cross sectional area of their nutrient foramina (Fig. 3.5.a.), and plotted this against femoral length (mm). A strong, positive relationship between these two properties has been previously shown in extant mammals, reptiles and birds, and the ratio between foramen area and femur length has been used as an index for relative blood flow through the element during metabolically demanding exercise ($Qi=r_f^4/L$; where r_f=foramen radius and L=femur length)(Seymour et al., 2012; Allan et al., 2014), which in-turn scales with MMR. Unfortunately *Kuehneotherium* could not be included in this analysis due to a lack of suitable femoral specimens.

We compared the estimated blood flow index (Q_i) of *Morganucodon* with existing and new data for extant reptiles (n=27), extant mammals (n=44), and seven species of extant varanid lizards that show significantly higher metabolic rates than other reptile taxa (Grady et al., 2014)(Appendix 3.3.). Data for all reptiles and 39 mammals originated from the supplementary material of Seymour et al. (2012). An additional five mammals were studied here, as the dataset of Seymour et al. (2012) did not provide any mammal of comparable body mass to *Morganucodon* (<50g).

The femora of three adult individuals of 11 extant mammal species of comparable body mass to *Morganucodon* were imaged using micro-computed tomography (μCT) at the University of Helsinki using a Skyscan 1272 μCT scanner (Table 3.5.). A 60 kV source was used with a 166 uA current (Appendix 3.4.). For each scan, a total of 1800 angular projections were collected during a 180^0 rotation, with each projection occurring over an exposure time of 1060 ms. The raw projection data were reconstructed using filtered back-projection by the skyscan reconstruction software "NRecon" (Version 1.7.1.0).

Analysis of μCT femora data was conducted using the Avizo image analysis software (Version 9.3.0). Foramina were located using the "Orthoslice" tool, to scroll through transverse CT slices of each femur. Once located, the width of the foramen was calculated by projecting the volume of the femur using the "volume rendering" tool. This allowed the maximum width of the foramen to be assessed, and measured using the "Line Measurement" tool.

Although *Morganucodon* femoral elements are fairly common in the *Hirmeriella* fissure suite, the overwhelming majority are incomplete. We here chose the three most complete femoral specimens known from the Pontalun 3 fauna, the same fauna that the *Morganucodon* teeth imaged using SR CT originated from. Elements

chosen preserve at least half of the femoral shaft. Length was estimated fro the mid-shaft diaphysial width of each element using the scaling relationship between the two measurements established for extant rodents and insectivores by Bou et al. (1987) where:

$$\textbf{Length} = 0.9464 * \textbf{width}^{0.7145}$$

Least squares regression and ANCOVA show that *Morganucodon* had a significantly lower *Qi* than extant mammals (F=6.88 p=0.001), and so could not have achieved the same rates of sustained aerobic exercise. Instead, ANCOVA comparisons suggest that *Morganucodon* falls within the Q_i range of extant reptiles including varanids (F=1.783, p=0.55) (Fig. 3.5.). The intercepts of regression slopes for extant mammals (Q_i =7.37E^{-09}) and reptiles (Q_i =3.63E^{-07}) are significantly different (p=<0.01). The slopes for extant mammals and reptiles are also significantly different (mammals=0.54, reptiles=0.8; p=0.036). Finally, the significant relationship found between Q_i and MMR found by Seymour et al. (2012)(log(MMR) = 7.938(log(Q_i)) + 0.843) allowed us to estimate an MMR of 340 kJ.kg^{-1}.day^{-1} for *Morganucodon*. This value is considerably lower than that predicted for any modern mammal of comparable body size based on Q_i. For instance the Q_i of *Microtus levis* (East European Vole), the mammal with one of the most similar body masses to the maximum body mass predicted for *Morganucodon*, provides an MMR estimate of 1514 kJ.kg^{-1}.day^{-1}.

3.8. Discussion and conclusions

Assessment of three proxies for metabolic rate (growth rate, basal metabolic rate and maximum metabolic rate) suggests that the entire scope of metabolic potential in the most basal mammaliaforms had yet to develop significantly beyond what is seen in modern reptiles. This places previous lines of evidence in a new context, adding quantitative data to our knowledge of physiology at an important point in mammalian evolution. We find *Morganucodon* and *Kuehneotherium* to possess a mosaic of plesiomorphic and derived characters relating to life history and endothermy. Phylogenetic bracketing suggests that both taxa may have exhibited fur (Martin et al., 2015; Benoit et al., 2016) and a muscular diaphragm (Martin et al.,2015); both considered key innovations for mammalian endothermy. *Morganucodon* also potentially

followed a typically 'mammalian' pattern of comparatively rapid juvenile growth followed by truncated adult growth (O'Meara and Asher, 2016). However, our discovery of prolonged lifespan and low aerobic capacity suggests that basal mammaliaforms occupied a lower metabolic grade than modern mammals, and had yet to attain their level of endothermic physiology. A low, reptilian MMR may suggest that the insectivorous *Morganucodon* (Gill et al., 2014) used burst or ambush tactics similar to modern reptilian insectivores, as opposed to more sustained foraging tactics seen in extant mammalian counterparts. Such low-energy feeding strategies fit with the low BMR and growth rates we have estimated from the exceptionally long lifespans found for *Morganucodon* and *Kuehneotherium*, as lower metabolic demand places lower requirements on food consumption.

Our results and interpretation of multiple life history and physiology related traits in *Morganucodon* and *Kuehneotherium* suggest that the use of previous proxies for physiology and endothermy in fossil synapsids based on presence or absence of single morphological and/or histological traits needs to be re-assessed. Evidence in non-mammalian synapsids, including changes in gait (Kemp, 2005), long-bone histology (Huttenlocker and Rega, 2012) and development of secondary osteological features correlated with increased metabolic rate (Benoit et al., 2016; Crompton et al., 2017), indicate an unquestionable change in physiology from pelycosaur to cynodont-grade taxa. However, mammalian metabolic physiology had yet to reach the endothermic levels recorded in modern mammals by the Early Jurassic. This is inconsistent with previous interpretations of 'proto-endothermic' or fully endothermic physiology in non-mammalian synapsids. Such a contradiction may be due to the often-binary nature of previous lines of evidence such as the presence/absence of fibrolamellar bone and/or respiratory nasal turbinates. As these proxies are unable to accurately represent the complex scale of physiological characteristics that range between 'ectothermy' and 'endothermy', our data offers a more direct link to measurable aspects of endothermy such as basal and maximum metabolic rate. The apparently mosaic nature of mammalian endothermy evolution shown here indicates that use of a single proxy or trait is unlikely to be able to explain the timing and rates of all aspects of endothermic evolution.

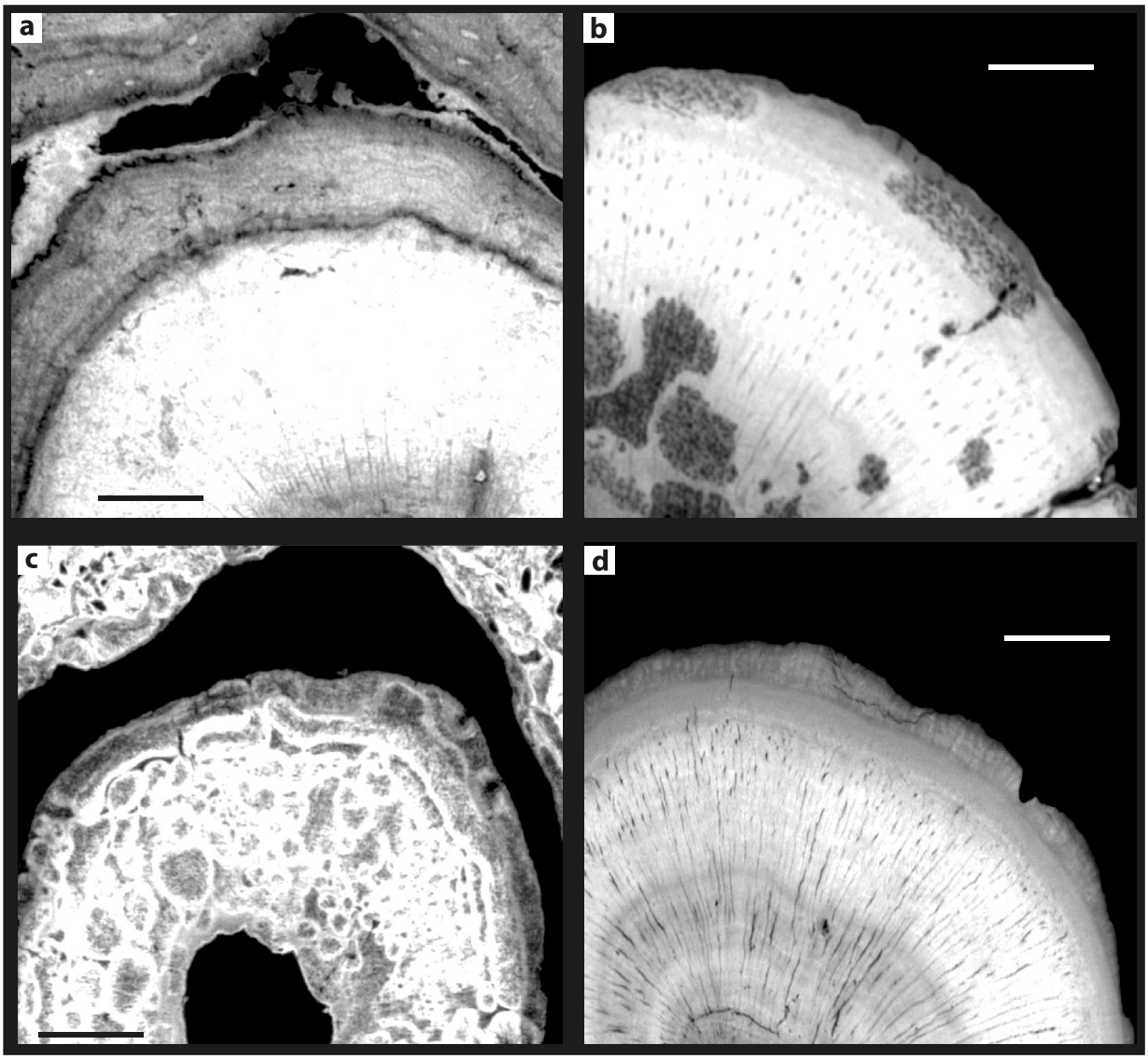

Extended data figure 5 | Common diagenetic fabrics encountered in tomographic data of fossil cementum. (**a**) Substantial variation in the thickness of individual cementum annuli along their trajectories in the anterior root of the m2 of specimen bd10. (**b**) Discrete regions of diagenetic alteration within the root of m96086, a specimen of otherwise excellent preservation. (**c**) Globular diagenetic fabrics have adulterated all ultrastruture in the anterior root of the m1 of specimen m95809. (**d**) physical damage to the cementum layer has removed outer annuli in discrete regions of the cementum of the anterior root of m96273. White/black lines = 50μm.

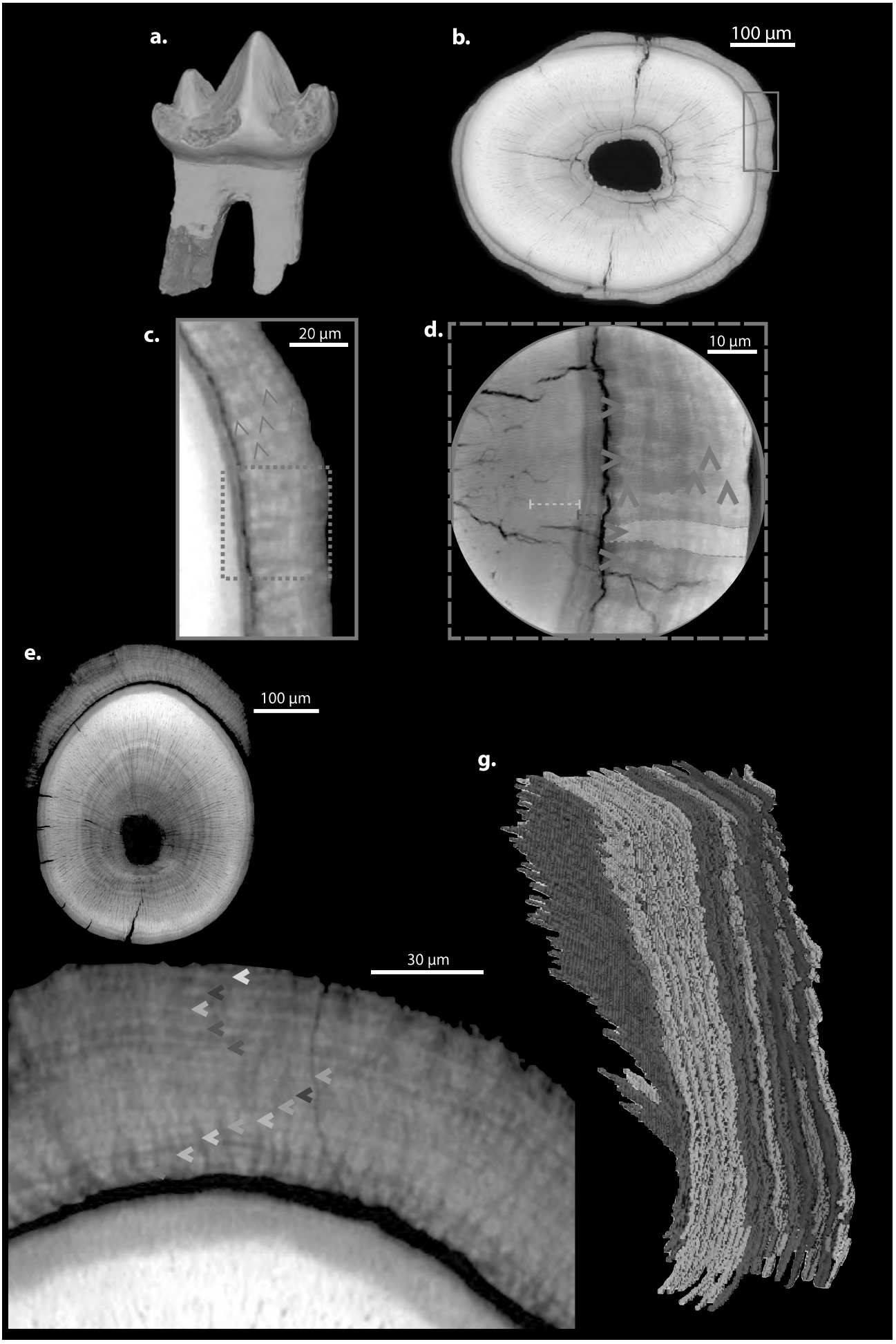
a.
b.
100 µm
c.
20 µm
d.
10 µm
e.
100 µm
g.
30 µm

Figure 3.2. (**a**) Micro-computed tomographic reconstruction of *Morganucodon* tooth en105. Green highlights cementum layer. (**b**) Transverse slice of a synchrotron radiation-based computed tomographic (SR CT) single distance phase contrast reconstruction of the root of en105. Cementum is the darker tissue surrounding the dentine. (**c**) Detail of cementum highlighted by red box in (**b**). Circumferential increments highlighted using red arrows. (**d**) Ultra-high resolution SR CT slice of the region highlighted by dashed red box in (**c**) (not exactly equivalent as the region highlighted in **c** was not imaged using ultra-high resolution SR CT). Circumferential increments highlighted using red arrows; radial bands of preserved Sharpey's fibres highlighted using blue arrows; Granular layer of Tomes highlighted using yellow dashed line; hyaline layer of Hopewell-Smith highlighted using green dashed line. (**e**) Transverse slice of a SR CT single distance phase contrast reconstruction of the root of *Morganucodon* specimen BD12 showing considerably thick layer of cementum around the root dentine. (**f**) Detail of the cementum of BD12. Cementum increments highlighted by 14 multi-coloured arrows. (**g**) Three-dimensional reconstruction of the cementum increments of BD12. The colour of each increment conforms to the colours of each arrow in (**f**).

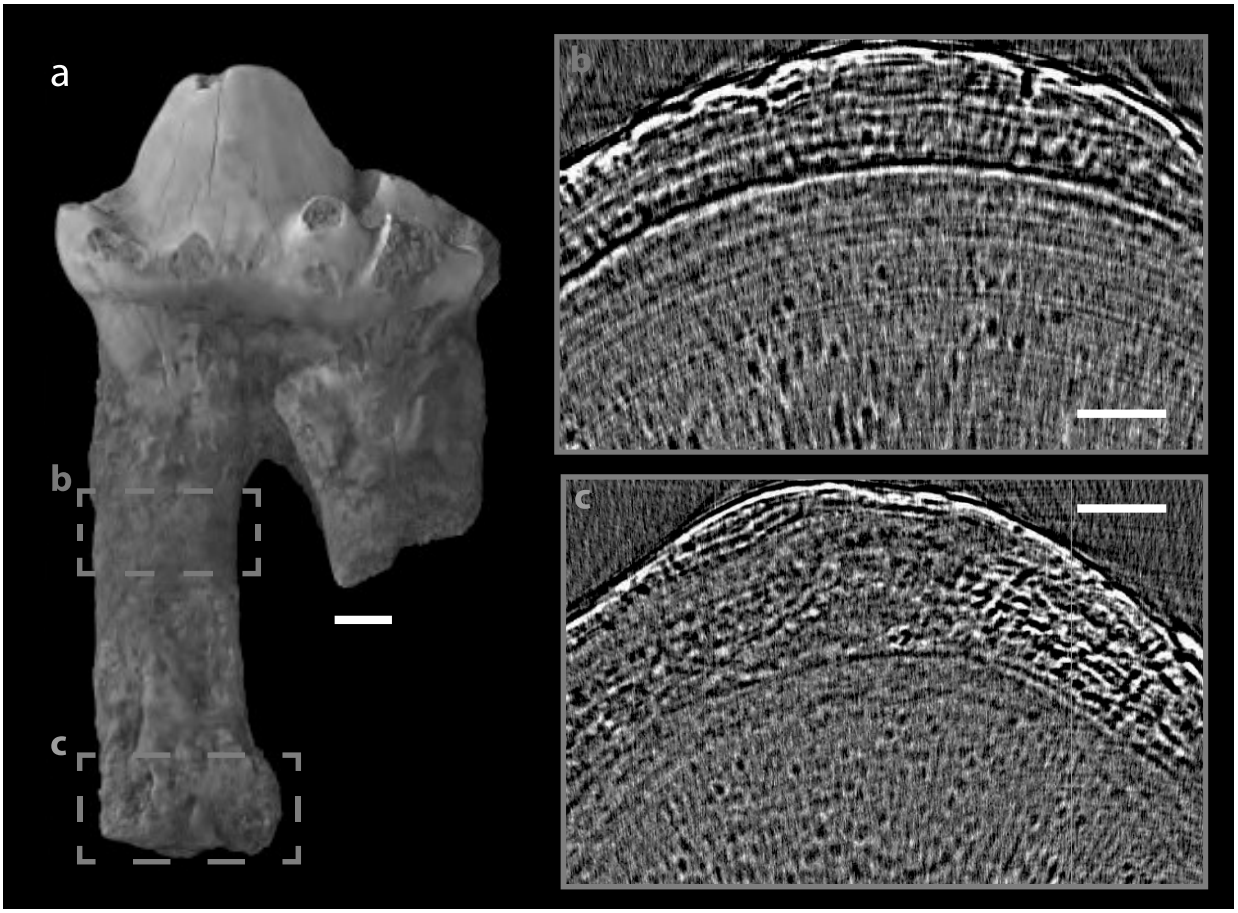

Figure 3.3. Comparison of cementum increment quality between areas of the root. (**a**) Tomographic reconstruction of an example *Morganucodon* m2 tooth, showing the bulbous base that characterises these teeth, sourced from Rowe and Frank (2011). Red and green boxes highlight the same areas shown in (**b**) and (**c**) (respectively), although these are from a different specimen; CEM4. (**b**) Tomographic slice from the middle third of the distal root of the CEM4 specimen, showing well-structured regular increments. (**c**) Tomographic slice from the base of the same root, showing chaotic plexiform structure. All white scale bars represent 30 μm.

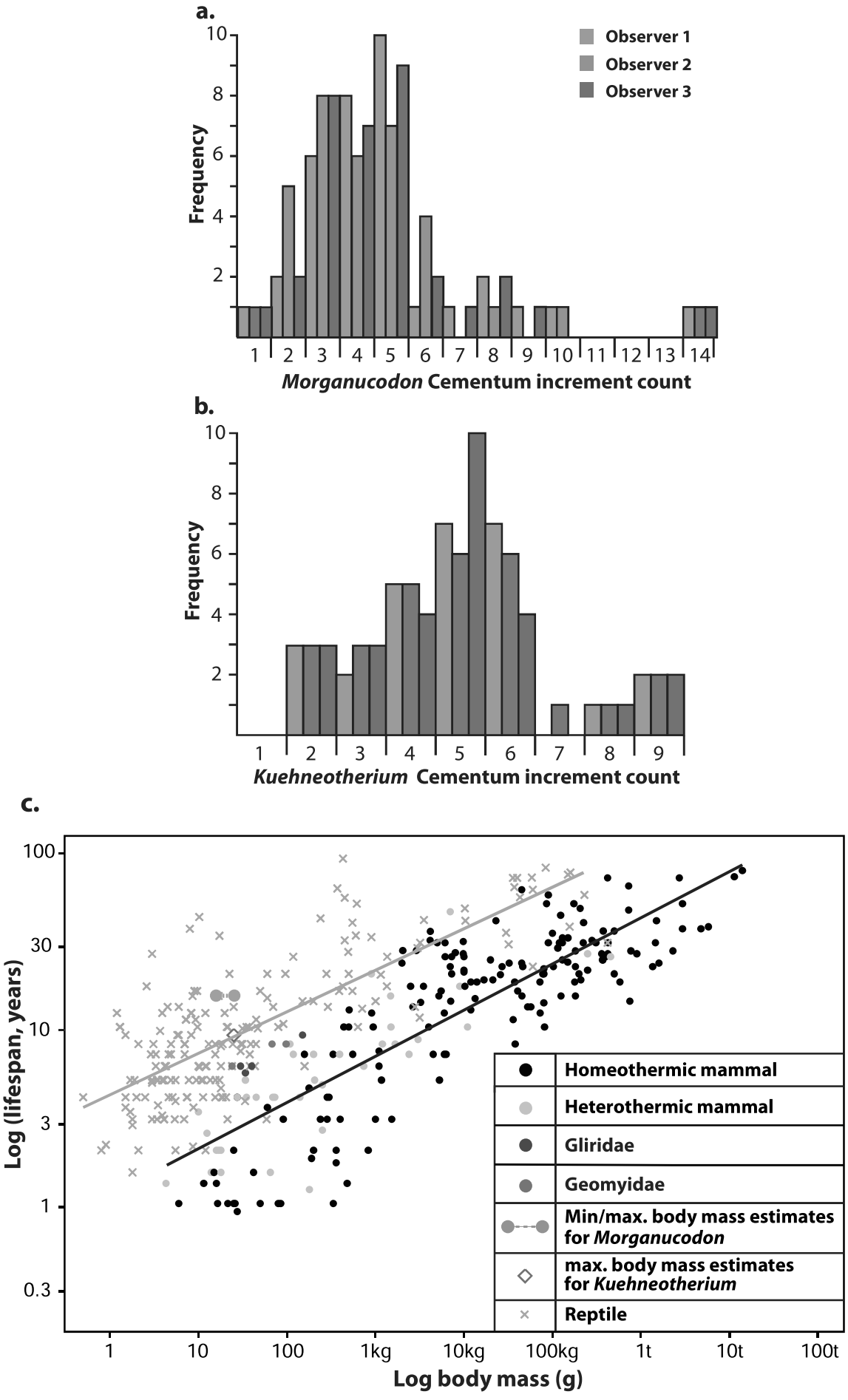
a.
Observer 1
Observer 2
Observer 3
Frequency
10
8
6
4
2
1 2 3 4 5 6 7 8 9 10 11 12 13 14
Morganucodon Cementum increment count
b.
Frequency
10
8
6
4
2
1 2 3 4 5 6 7 8 9
Kuehneotherium Cementum increment count
c.
Log (lifespan, years)
100
30
10
3
1
0.3
1 10 100 1kg 10kg 100kg 1t 10t 100t
Log body mass (g)
Homeothermic mammal
Heterothermic mammal
Gliridae
Geomyidae
Min/max. body mass estimates for Morganucodon
max. body mass estimates for Kuehneotherium
Reptile

Figure 3.4. (**a**) Histogram of *Morganucodon* cementum increment counts provided by each of the three observers. (**b**) Histogram of *Kuehneotherium* cementum increment counts provided by each of the three observers. (**c**) Linear regressions between logged body mass and logged maximum lifespan for extant mammals (circles), extant non-avian ectothermic reptiles (blue crosses), *Morganucodon* (green circles) and *Kuehneotherium* (red diamonds). Minimum body mass estimate for *Morganucodon* following Luo et al. (2004), maximum body mass estimate following Foster (2009).

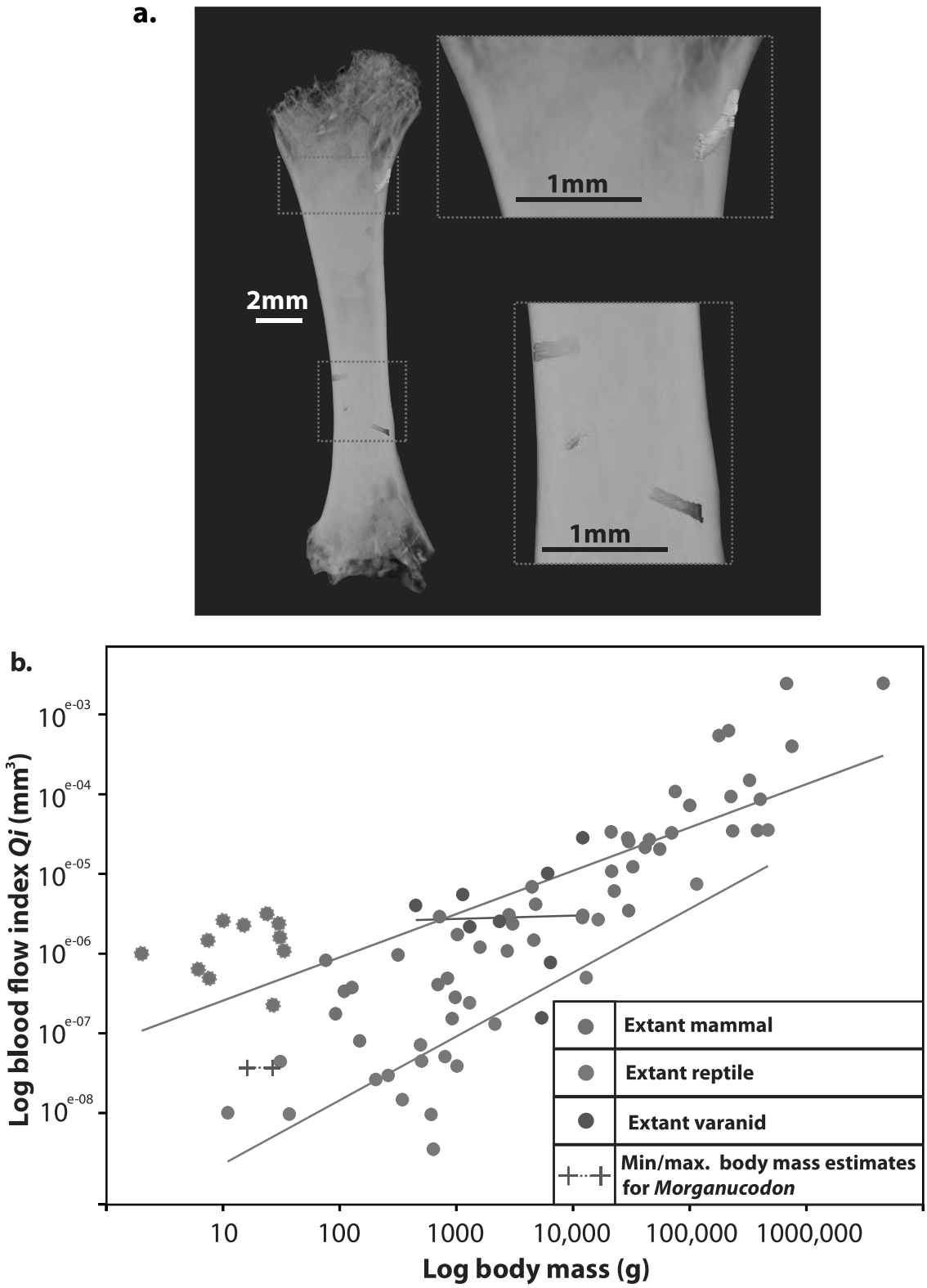

Figure 3.5. Studies of nutrient foramina in the femora of *Morganucodon* and comparison with extant mammals and reptiles. (**a**) Volume rendering of a *Morganucodon* femur, with foramina highlighted red, green, gold and blue. (**b**) Linear regression between logged body mass (g), and logged estimated blood flow index (*Qi*) for extant reptiles (green circles), extant mammals (red circles from Seymour et al., 2011; red circles with dotted margins from this study), extant varanid lizards (purple circles), and *Morganucodon* (blue crosses).

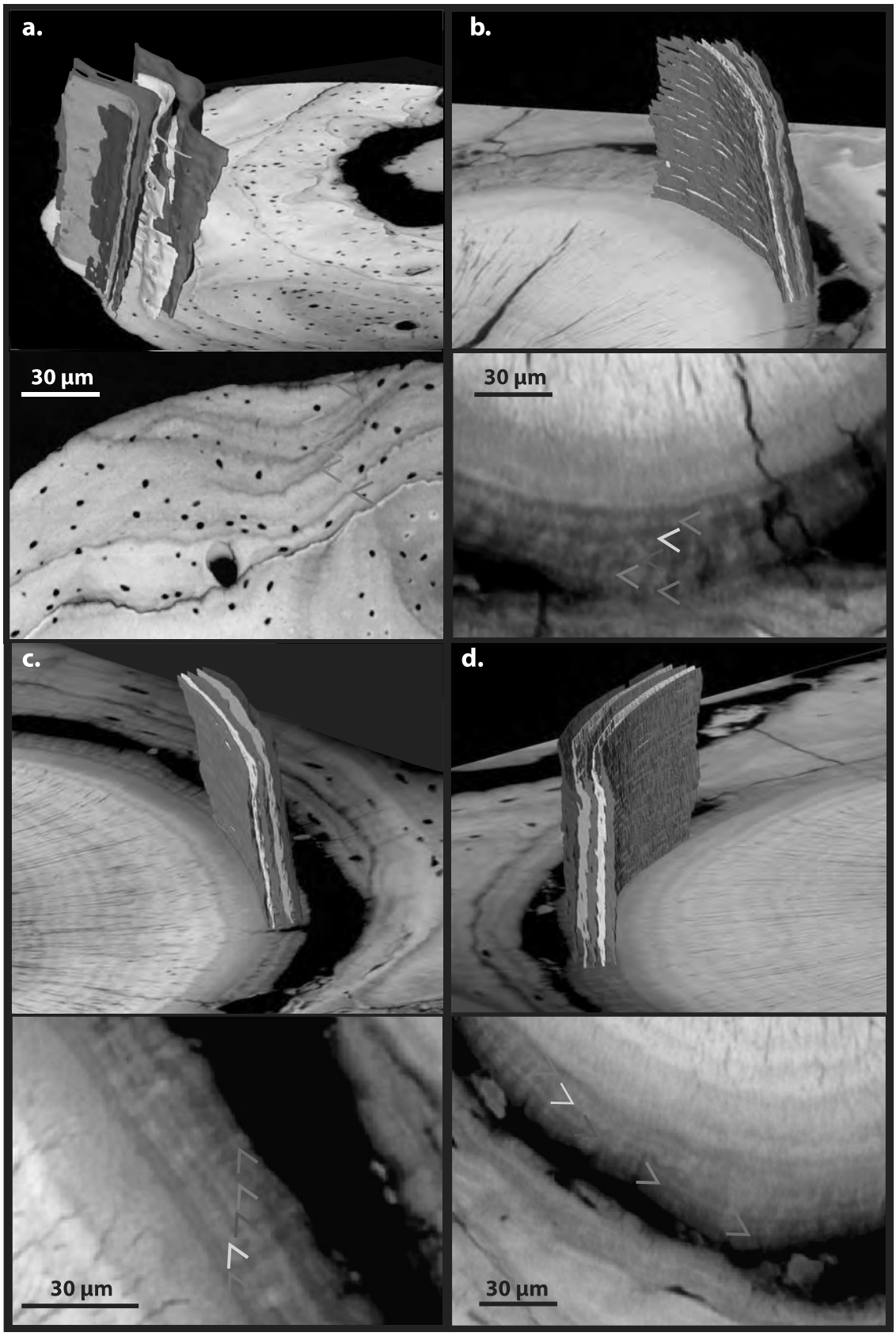

Figure 3.6. Shared increment patterns between roots of the same tooth, the root of another tooth, and the dentary of specimen m96413. (a) Four clear increments within the periosteal region of the dentary, and a fifth incipient increment, marked by multi-coloured three-dimensional bands, and correspondingly coloured arrows in the accompanying transverse tomographic slice. (b) This pattern is mirrored in the anterior root of the m1 tooth; (c) the posterior root of the same tooth; and (d) the anterior root of the m2 tooth.

Taxon	Element	Number of specimens scanned	Number of specimens w. readable cementum increments
Morganucodon	dentary	4	2
	i4	1	1
	canine	1	1
	p1	1	1
	p2	2	2
	p3	3	3
	p4	5	2
	m1	17	12
	m2	70	30
Kuehneotherium	p1	1	0
	p3	1	0
	p5	1	0
	p6	1	1
	m1	4	2
	m2	180	26

Table 3.1. All elements imaged using synchrotron radiation-based computed tomography.

Specimen	Taxon	Observer 1 increment count	Observer 2 increment count	Observer 3 increment count
en138	*Morganucodon*	2	2	2
m9463	*Morganucodon*	2	2	2
m92528	*Morganucodon*	3	2	3
m95809	*Morganucodon*	3	2	3
m96085	*Morganucodon*	3	2	3
en024	*Morganucodon*	3	3	3
m96490	*Morganucodon*	3	3	3
m96444	*Morganucodon*	3	3	3
cem3	*Morganucodon*	4	3	3
cem5	*Morganucodon*	4	3	4
m96086	*Morganucodon*	4	3	4
en105	*Morganucodon*	4	4	4
m46463	*Morganucodon*	4	4	4
m96380	*Morganucodon*	4	4	4
m96396	*Morganucodon*	4	4	4
m96474	*Morganucodon*	4	4	5
m96141	*Morganucodon*	5	5	3
en147	*Morganucodon*	5	3	4
bd13	*Morganucodon*	5	5	5
m96441	*Morganucodon*	5	3	5
bd6	*Morganucodon*	5	5	5
en123	*Morganucodon*	5	5	5
m96413	*Morganucodon*	5	5	5
m96476	*Morganucodon*	5	5	5
bd1	*Morganucodon*	5	6	5
m95810	*Morganucodon*	5	6	5
m96463	*Morganucodon*	6	6	6
m96418	*Morganucodon*	7	6	7
m95805	*Morganucodon*	8	4	8
m96075	*Morganucodon*	8	8	8
bd10	*Morganucodon*	9	5	6
l3 003	*Morganucodon*	10	10	9
bd2	*Morganucodon*	14	14	14
juve	*Morganucodon*	1	1	1
m21081	*Kuehneotherium*	2	2	2
m27301	*Kuehneotherium*	2	2	2
m27305	*Kuehneotherium*	2	2	2
m20990	*Kuehneotherium*	3	3	3
m27816	*Kuehneotherium*	3	3	3
sy121	*Kuehneotherium*	4	4	3

m27257	*Kuehneotherium*	4	3	4
m27436	*Kuehneotherium*	4	4	4
m27443	*Kuehneotherium*	4	4	4
m21080	*Kuehneotherium*	5	5	4
m27273	*Kuehneotherium*	5	4	5
m27628	*Kuehneotherium*	5	4	5
m27550	*Kuehneotherium*	4	5	5
m27520	*Kuehneotherium*	5	5	5
m27529	*Kuehneotherium*	5	5	5
m27537	*Kuehneotherium*	5	5	5
m27344	*Kuehneotherium*	6	5	5
m20982	*Kuehneotherium*	5	6	5
m27308	*Kuehneotherium*	6	6	5
m27505	*Kuehneotherium*	6	6	5
m21069	*Kuehneotherium*	6	6	6
m27538	*Kuehneotherium*	6	6	6
m27545	*Kuehneotherium*	6	6	6
m27745	*Kuehneotherium*	6	7	6
sy106	*Kuehneotherium*	8	8	8
m27653	*Kuehneotherium*	9	9	9
sy141	*Kuehneotherium*	9	9	9

Table 3.2. Estimated increment counts by each of three observers for all *Morganucodon* and *Kuehneotherium* specimens that produced readable cementum increments in synchrotron radiation-based micro-computed tomographic images

Study	Taxon	*n*	Maximum age (years)	Mean *CV*	Mean *r*
Thesis Chapter 3	*Morganucodon*	34	14	9.32	0.92
Thesis Chapter 3	*Kuehneotherium*	27	9	4.89	0.96
Gasawey et al. 1978	*Alces Alces*	72	9	14.2	0.4
Christensen-Dalsgaard et al. 2010	*Ursus maritimus*	32	15	15.2	0.86
Perez-Barberia et al. 2014	*Cervus elaphus*	490	17	16.22	0.96
Pasda, 2014	*Rangifer tarandus*	63	16	19.4	0.64
Klevezal and Pucek 1987	*Bison bonasus*	45	21	20.57	0.86
Grau et al. 1970	*Procyon lotor*	54	9	20.6	0.92
Landon et al., 1998	*Canis lupus*	12	6.8	25.92	0.78
Bodkin et al., 1998	*Enhydra lutris*	14	14	26.24	0.88
Kay and Cant, 1988	*Macaca mulatta*	65	24	29.34	0.79
Cederlund et al. 1991	*Capreolus capreolus*	74	9	30.5	0.86

Table 3.3. Results of quantitative analyses of precision for the fossil mammals studied here, *Morganucodon* and *Kuehneotherium*, and those of previous studies of extant mammals. *CV* – coefficient of variation; *r* – Pearson's correlation coefficient.

Specimen	Element	Count
m96441	m1	5
m96441	m2	5
m96413	m1	5
m96413	m2	5
m96413	p4	5
m96396	m1	4
m96396	m2	4
m96396	dentary	4
m96396	m3	3
m96396	p4	4
m95809	m1	3
m95809	m2	3
bd13	m1	5
bd13	m2	5
bd13	m3	4
bd10	m1	9
bd10	m2	9
bd10	m3	9
bd10	m4	?
bd6	m1	4
bd6	m2	4
scan 1	i4	6
scan 2	canine	6
scan 3	p1	6
scan 4	p2	7
scan 5	p3	6

Table 3.4. Cementum increment counts for each element in dentulous *Morganucodon* specimens.

Taxon	Mean *Qi*	Mean femur length (cm)
Apodemus flavicolis	3.144E-05	2.15
Micromys minutus	1.468E-05	1.1
Microtus levis	2.255E-05	1.43
Mus musculus	2.38E-05	1.51
Peromyscus truei	1.098E-05	1.75
Sorex minimutissimus	1.002E-05	0.48
Sicista betulina	2.59E-05	1.04
Sorex araneus	4.89E-06	0.83
Sorex minutus	6.37E-06	0.56
Myodes rutilis	1.609E-5	1.17
Neomys fodiens	2.28E-05	1.04
Morganucodon watsoni	3.829E-06	1.25

Table 3.5. Blood flow index (Q_i) and mean femur length for the 11 extant mammals studied here and *Morganucodon.*

Chapter 4.

Optimizing synchrotron radiation-based computed tomographic imaging and computer vision approaches for studying cementum

Following the use of synchrotron radiation-based computed tomography (SR CT) for studying fossilised cementum increments, this chapter focuses on developing methods for imaging and analysing cementum increments in 'fresh' (unfossilised) cementum. An optimal experimental protocol will be discussed and developed, followed by the presentation of a series of algorithms designed to analyse the count, shape and texture of cementum increments using computer vision. SR CT has been performed for a sample of rhesus macaque (*Macaca mulatta*) lower first molars from a laboratory population of known age and controlled life history. The novel method for automatic increment counting has been integrated in a purpose-built software package in Matlab for studying cementum increments. Comparison with histological data has confirmed that SR CT imaging did reliably record cementum increments. The microscopic spatial resolutions offered by SR CT at excellent signal-to-noise ratio levels has allowed for quantitative comparisons of increment morphology and texture between individuals, using the purpose-built software package for dental cementum analysis. First results suggest that our novel framework for studying dental cementum in 3D, combining SR CT imaging and user-independent approaches for cementum analysis, may provide a powerful tool for identifying the effects of discrete life history variables on cementum growth and incrementation. In summary, the use of semi-automated computer vision approaches to analysing volumetric SR CT images have the potential to significantly improve understanding of cementum increments and their development through the lifecourse.

4.1. Introduction

4.1.1. Synchrotron radiation computed tomography and computer vision for counting cementum increments

In **Chapter 2** the principal caveats of the current gold-standard techniques for imaging and analysing cementum increments were discussed. The overwhelming majority of previous cementochronological studies have relied on thin-sectioning to image cementum increments using light microscopy (Naji et al., 2016). This allows cementum increments to be viewed at high spatial resolutions, and offers a range of optical manipulation techniques that filter and highlight increments to varying degrees, including wave plates for polarised light microscopy (Stutz, 2002) or digital image enhancement (Lieberman et al., 1990; Wall-Scheffler and Foley, 2008). However, the destructive nature of thin-sectioning and the restrictive two-dimensional (2D) perspective offered by histological sections both limit the understanding of the complex nature of cementum and its increments (Renz and Radlanski, 2006).

Cementum is a dynamic, biomechanically responsive tissue comprised of three discrete tissue-types; acellular extrinsic fibre cementum (AEFC), cellular intrinsic fibre cementum (CIFC), and cellular mixed stratified cementum. AECF grows continuously throughout life, depositing increments with a predominantly uniform, circum-annual rhythm. CIFC is deposited during periods of substantial occlusal stresses including damage to the periodontal ligament (Levy and Mailland, 1980; Bosshardt and Schroeder, 1990, 1992; Lisgarten et al., 1991), and can produce complex patterns of increments with a poorly constrained increment periodicity and low correspondence with the animal's age in years (Naji et al., 2016). Equatorial animals also produce complex patterns of cementum increments, often experiencing an annual doubling of dark increments that represent bi-seasonal precipitation patterns rather than circum-annual weather patterns (Spinage, 1973). Problems created by such phenomena, in terms of counting increments and understanding their development, are often compounded by the restricted window onto the tissue itself offered by 2D imaging of thin sections (Obertová and Francken, 2009). Complex patterns of additional increments cannot easily be distinguished from prevailing increment patterns using a restricted number of 2D images. One example for such complex increments patterns is lensing of individual increments and coalescence between increments. This has often led to a lack

of accuracy between expected and observed increment counts, and a low precision between increment counts from different observers of the same material, as shown in several recent validation studies using populations of known chronological age (Lipsinic et al., 1986; Renz and Radlanski, 2006; Obertová and Francken, 2009).

The use of synchrotron radiation-based computed tomography (SR CT) for imaging fossilised cementum in **Chapter 3** has shown how 3D imaging can overcome these limitations. The volumetric nature of tomographic data allowed the inspection of cementum increments through their entire trajectory through the tissue in both transverse and longitudinal aspects. This directly overcame one of the major issues highlighted in this and previous studies of thin section imaging of cementum; the restricted view of increments, their count and patterns offered by thin section imaging. By following increments through the cementum, the regions of highest increment contrast were located. Although the accuracy of increment counts estimated in these regions could not be quantified for fossil mammals, the identification of these regions and subsequent image processing (creation of virtual thin sections) had a significant positive impact on the precision of estimated increment counts between three independent observers, evidenced by the significantly lower coefficients of variation for these observers compared to previous studies of similarly aged extant taxa using thin section histology.

However, the technique used for increment counting in **Chapter 3** did not overcome the second principal caveat of previous histological studies of cementum increments; the inherent subjectivity involved in estimating increment counts by eye. This subjectivity is reflected in several findings of a correlation between the accuracy of increment counts and the experience of the observer, with more experienced observers providing significantly more accurate counts (Rolandsen, 2008; Frie et al., 2011, 2013). Numerous attempts have been made in the past to develop objective means of analysing cementum images. These include quantifying and indexing the ‘readability’ of cementum images, in order to provide a robust framework for distinguishing the aspects of cementum images affecting their quality for increment counting. Individual images can then be graded in terms of specific aspects of increment quality including contrast between increments, level of complexity in their pattern and presence of imaging or technical artefacts from the thin sectioning process. The grade of a particular image can

then be used in order to distinguish the amount of confidence an observer can have in counts estimated from this image, relative to other images of differing grades within a sample (Gasaway et al., 1978; Zhivotovsky, 1982).

Several studies have attempted to use computer vision both to aid human counting of cementum increments, and even to overcome the need for human counting itself (Czermak et al., 2006; Klauenberg & Lagona, 2007). For instance, by examining cementum increments in digital images from light microscopy of serial sections, peaks and troughs in cementum opacity or greyscale 'luminance' can be extracted using image processing program such as 'ImageJ' (Schneider et al., 2012), and studied by using a method called 'Digital Cementum Luminance Analysis' (DCLA) (Wall and Wall, 2006). DCLA methods typically plot luminance values along radial transects of cementum (Fig. 4.1.a.). Along these transects, thick translucent increments are represented by distinct peaks in luminance values, and thin opaque increments by distinct troughs in luminance values (Fig. 4.1.b.). These patterns can then be interpreted either by eye, counting peaks and/or troughs, or through computer vision using peak/trough detection algorithms now common to several software packages (e.g. "findpeaks" in Matlab [MATLAB and Statistics Toolbox release 2015b, the MathWorks Inc., Natick, Massachusetts, US], and "find peaks" in ImageJ/Fiji). DCLA offers a less subjective mean of counting increments by eye, compared to directly reading thin-section images. The often-complex patterns followed by increments through thin sections can be difficult to interpret by observers (Renz and Radlanski, 2006), as the contrast between neighbouring increments is variable at the sub-millimetre scale and so individual increments can be hard to follow through the entire section (Fig. 4.2.). The use of radial transects through the cementum minimises the effects of these complexities for increment counting, as increments can be simplified to peaks and troughs in luminance values over one dimension (Fig. 4.1.b.). Further, the use of numerical greyscale values to distinguish neighbouring light and dark increments (light increments providing high greyscale values versus dark increments providing low values) allows quantitative thresholds to be developed for distinguishing between genuine increments and background noise in greyscale values (Fig. 4.1.c.). These thresholds are often a specific value in greyscale that peaks/troughs representing light/dark increments must differ from either the last respective peak or trough, or the

mean value of greyscale for the transect under study, in order to be distinguished as a 'true' increment (as opposed to noise in greyscale). For instance, the method proposed by Wall-Scheffler and Foley (2008) states that each peak/trough must differ from the greyscale value of the last respective peak/trough by a minimum of two values in order to be distinguished as a true increment (Fig. 4.1.c.). DCLA approaches have thus offered a step forward in the objective counting and analysis of increments, as increments are given an objective definition along each transect, unaffected by human interpretation of thin sections. However, DCLA techniques have so far relied upon (*a priori*) assumptions regarding the contrast in greyscale values caused by incrementation versus those caused by background noise. The chosen threshold value for distinguishing increments from noise in each DCLA technique is specific to the image data and/or analysis methods in the original study, and so may not be confidently applied to other imaging modalities or techniques, or to taxa that fail to meet the specified threshold specified in the original study. For instance, it is understood that the cementum of animals in populations living under different climates provides different levels of increment contrast and 'readability', with higher levels of seasonal change producing higher contrast increments. So, an absolute threshold value that increments must differ by that is appropriate for distinguishing highly contrasting increments from noise in the cementum of populations living under highly seasonal climates (e.g. high latitude temporal climates) may be too severe for distinguishing increments in the cementum of populations living under less seasonal climates (e.g. equatorial and low latitude climates) (Fig. 4.1.c.). Thus, the next stage in DCLA development should focus on developing a more flexible strategy for distinguishing cementum increments based on relative instead of absolute greyscale distribution criteria.

4.1.2. The nature of cementum increments and life history events

Although seasonal change in dietary quality is the predominant hypothesis for circum-annual cementum incrementation, it cannot be the sole factor affecting cementum growth (Klevezal, 1995). Circum-annual increments are found in human cementum in modern populations that have no significant dietary change throughout the year (Kagerer and Grupe, 2001). Several studies have found close correlation and even exact

matches between increment count and chronological age in populations of modern humans (Condon et al., 1986; Wittwer-Backofen, 2012, Wittwer Backofen et al., 2004). Further work has shown discrete differences in the structure and opacity of increments formed during life history events that significantly affect body metabolism, including sustained weather events (Cipriano, 2002), the attainment of sexual maturity (Klevezal and Stuart, 1994), birth and parturition (Bodkin et al., 1993; Medill et al., 2010), and even occurrences of renal disease (Kagerer and Grupe, 2001).

The effect of pregnancy on cementum growth and incrementation has received particular attention. Several studies have shown that the radial thickness of increments formed during pregnancy is significantly more heterogeneous than surrounding increments (von Beila et al., 2008; Medill et al., 2010). This creates noticeably more chaotic increments with higher tortuosity (circumferential path length versus minimum possible path length) than surrounding increments (von Beila et al., 2008). Increments formed during pregnancy have also been found to be significantly less thick than other increments in several taxa including black bears (*Ursus americanus*) by Coy and Garshelis (1992) and Carrel (1994), polar bears (*Ursus maritimus*) by Medill et al., (2010), humans (Kagarer and Grupe, 2001) and sea otters (*Enhydra lutris*) (von Beila et al., 2008).

Other aspects of cementum structure have yet to be studied with the same level of quantitative rigour in relation to life history. Several studies attempted to use increment thickness to assess the relationship between cementum growth and climate, finding no significant correlation between certain climate metrics (e.g. rainfall or mean air temperature) and increment thickness (Klevezal, 1995; Wall-Scheffler and Foley, 2008). However, this single variable (increment thickness) may not be sufficiently characterising cementum growth and structure.

Following the use of greyscale values as a third dimension for the detailed characterisation of cementum increments by Lieberman et al. (1990), the distribution of greyscale values across an image of cementum may be interpreted as a third dimension or ‘surface’ (Fig. 4.1.b; Fig. 4.3.d). Considering this surface, inspiration may be taken from the characterisation procedures of other dental surfaces that are now routinely investigated in terms of their relationship with life history such as the micro-texture of enamel crowns (Dong et al., 1993; Stout and Blunt, 2000; Purnell et al., 2012, 2013).

Several recent studies of dental micro-texture have employed a range of 3D surface characterisation metrics commonly used in tribological studies of man-made surfaces. This was pioneered by Purnell et al. (2012), who applied a suite of 3D surface characterisation metrics to isolate and statistically compare aspects of micro-texture between the teeth of cichlid fish of varying diet. The authors found significant differences in several metrics between sub samples of separate diets, and these differences were pronounced enough to provide predictive power for diet using principal components analysis (PCA). This methodology may also provide a more detailed technique for characterising texture in images of cementum, in order to pinpoint differences in particular aspects of texture that may relate to life history variables including climate.

4.1.3. Summary and study objectives

Cementum is a tissue of great potential as a record of chronological age and life history events in mammals. However, in order to fulfil this potential and capture this data with confidence, it is evident that improvements must be made to cementochronological imaging and analysis in order to overcome both the effects of biological complexities (lensing and coalescanece) and thin section preparation artefacts on increment counts, and subjectivity in counting incremental features. The combination of high-resolution and 3D imaging offered by SR CT has allowed cementum increments to be followed through their entire longitudinal and transverse trajectories, overcoming the limitations of 2D thin-section-based imaging. However, the technique for counting increments must still be improved to further remove the inherent subjectivity of human vision.

The first objective of this chapter is thus to improve and develop current computer vision approaches for objectively counting increments in tomographic data. This will focus on investigating the optimum imaging parameters for SR CT imaging of cementum increments. A second objective aims to provide a validated and automated computer vision-based analysis method for user-independent counting of cementum increments from SR CT data. The final objective of this chapter will be to characterise and quantify cementum increments and their shape and texture, by further exploring the potential of combining SR CT data with computer vision-based image analysis of cementum increments.

4.2. Materials and Methods

This study is based on SR CT data of the cementum of the lower first molars (m1) of a laboratory population of female rhesus macaques (*Macaca mulatta*). All images have been taken at the TOMCAT beamline of the Swiss Light Source (Villigen, Switzerland). A series of algorithms have been developed and tested that isolate several aspects of cementum increment shape and texture as well as estimates of increment count. A novel image processing workflow has been devised and will be introduced here to isolate and straighten the cementum in SR CT slices, allowing directional filtering to enhance increment image contrast.

The peak-trough method for increment counting along radial transects through the cementum called 'Digital Cementum Luminance Analysis' (DCLA) and described earlier will be developed upon here, by using relative values that increments must exceed from the mean greyscale value of the transect in question to discriminate increments from noise, as these correspond with the unique distribution of greyscale values of each radial transect through the cementum instead of absolute values based on *a-priori* assumptions of their distribution (Fig. 4.4). This method will be incorporated into an algorithm that will allow increment counting using solely computer vision and used to count increments in SR CT cementum data of the known-age Rhesus macaques individuals.

The same cementum data will further be used to develop algorithmic, computer-vision based approaches to quantitatively study aspects of cementum increment morphometry that may relate to life history. We have developed and will present here an automated algorithm for the isolation of individual increments in SR CT slices in order to study their 2D tortuosity. A final algorithm has been developed to quantitatively characterise aspects of greyscale 'texture' in isolated SR CT cementum data, taking inspiration from tribological surface profiling techniques (Dong et al., 1993; Stout, 2000).

4.2.1. Experimental sample

This study is focused on the analysis of the right lower first molars (m1) from a sample of 10 female Rhesus macaques (*Macaca mulatta*), raised under laboratory conditions and bred for biomedical research at the Primate Breeding Facility of Public Health

England, Salisbury (UK) (Table 4.1). The unit was managed by the Defence Science and Technology Laboratory (DSTL) prior to 1st October 2009. The *M. mulatta* colony has been closed and self-contained since 1982, from animals originally imported from India between 1978 and 1982. All animals used here were routinely monitored and checked for primate-born diseases of risk to humans (included hepatitis B, herpes B, and tuberculosis), and were humanely killed using an overdose of pentobarbital, under Home Office establishment licence 70-1707, due to being unfit for breeding or whole-animal scientific procedural use. No animal was killed for the specific purpose of this experiment. Once the animals were killed, their lower jaws were mechanically dislocated and removed by Public Health England. Lower jaws were then freeze-stored at -20°C prior to further tissue preparation.

To prepare specimens from m1, lower jaws were first mechanically cleaned of soft tissue using surgical tools (scalpel, scissors and tweezers). The coronoid and angular processes were then removed using a handsaw. Once prepared, specimens were then bathed in tap water in a sealed plastic container, which was stored in a fume cupboard for three weeks (21 days). This procedure was adopted to rot away the periodontal ligament and alveolar soft tissue that could not be mechanically removed, in a controlled manner. After three weeks, teeth were sufficiently loose within the jaw to be easily removed using surgical pliers, following further cleaning and removal of necrotic soft tissue. Although the majority of teeth were removed without damage, the anterior root of the left m1 was damaged in one specimen (l100). All teeth were removed for all animals, labelled and freeze-stored at -20°C. The left and right m1 teeth of all animals were fixed in 10% paraformaldehyde (PFA) solution for 10 days to minimise risk of infection.

Finally, the crowns of all teeth were removed using a Buehler IsoMet® slow-speed diamond blade saw (Buehler Ltd, Lake Bluff, IL, U.S.). Using the same saw, the anterior and posterior roots of each m1 tooth were mechanically separated and the anterior root cut in half along its longitudinal axis. This was in order to minimise the proportion of dense dentine to cementum to ensure that (SR) CT provides high image quality data, which can be detrimentally affected if the signal-to-noise ratio is low due to tissues or materials with relative high X-ray absorptions such as dentine. Processed tooth roots were then placed on top of 'Ripmax' 2 mm-thick carbon fibre rods (CR200600; Ripmax Ltd, Enfield, UK) cut into 1.5 cm lengths, using Loctite® super

glue (Liquid ethyl cyanoacrylate super glue, Loctite® brand; Henkel Corporation, Westlake, OH, U.S.). Carbon fibre rods are very rigid, yield a low X-ray absorption and do not create any significant X-ray scatter as opposed to metallic sample holders.

4.2.2. X-ray imaging of cementum increments

Dentine, the primary hard tissue of tooth roots, has a substantially higher mineral content compared to bone tissue (Inoue et al., 2013) and cementum. All three mineralised dental tissues consist mainly of a combination of inorganic material (mineralised phase made up primarily of hydroxyapatite), organic material (made up primarily of collagen) and water. The mineralised phase exhibits a (much) higher X-ray absorption compared to the organic phase in the regime relevant for (hard) X-ray imaging. When X-ray imaging tooth material and cementum *in situ*, together with dentine and/or bone tissue, the different mineral content levels of these tissues must be taken into account and can be helpful to distinguish between cementum and the enveloping dentine, based on different contrast levels in the CT data.

For most terrestrial mammals, cementum increments have a (radial) thickness between three and 15 μm (Klevezal, 1995), although they can be as thick as 20 μm in cetaceans (dolphins and whales; Stock, 2017). For CT, at least a few voxels should represent a single feature for reliable identification (and segmentation). When detecting incremental features using CT, feature boundaries between increments can become blurred significantly if imaged at insufficient spatial resolutions due to partial volume effects (Wellington and Vinegar, 1987). Previous studies suggest that neighbouring incremental features should occupy at least six pixels each in transverse cementum sections, with a pixel size of at least 1 μm^2 allowing a series of pixels to accurately represent their border (Lieberman et al., 1990; Wall and Wall, 2007). Hence, the maximum voxel size to identify cementum increments is about 1.5 μm for cementum increments of 10-15 μm radial thickness, and about 0.5 μm for increments between three and nine μm radial thickness.

In addition to high spatial resolutions in the micrometre range, the X-ray CT image contrast between consecutive cementum increments must be sufficient for counting and optimally segmenting them individually. It has been reported that cementum exhibits significant differences in mineral content and chemical composition between light and dark increments, based on X-ray fluorescence data (Stock, 2017).

Preliminary investigation of tomographic imaging using conventional laboratory-based μCT systems suggests that this technique is unsuitable for imaging cementum increments (for discussion and presentation of preliminary μCT cementum data see Appendix 4.1.). Although sub-micron resolutions are achievable in these systems, imaging artefacts including beam hardening and phase artefacts can obstruct boundaries between increments. The substantial scanning times necessary to achieve sufficient transmittance of X-rays through the dense mineralised tissues also creates scan times of over six hours for each individual specimen, which makes μCT imaging of the population-sized samples needed for cementochronology impractical both monetarily and financially. However, the study conducted in **Chapter 3** suggests that the differences in material properties provide sufficient X-ray contrast in SR CT data to differentiate between individual increments. Conventional X-ray absorption-based SR CT alone may offer insufficient image contrast to identify individual cementum increments, and so (free space propagation-based) phase contrast CT imaging approaches should be be explored to enhance image contrast, in addition to the image contrast provided by X-ray absorption only. In phase contrast imaging, the coherent nature of the X-ray source (here the SR source) is utilised. The sample under investigation induces phase shifts of the coherent X-ray waves, which result in intensity changes particularly around feature boundaries (edge enhancement), which can be recorded on a detector, and is added to the intensity changes due to X-ray absorption only. Phase retrieval algorithms (Paganin et al., 2002, Mayo et al., 2003) aim to retrieve local phase shifts, while standard X-ray imaging makes use of X-ray absorption and retrieves local linear X-ray attenuation coefficients of the sample. Hence, phase contrast imaging provides (additional) image contrast between structures yielding similar X-ray absorptions.

4.2.3. Synchrotron radiation micro-computed tomography (SR CT)

SR CT was performed at the TOMCAT beamline of the Swiss Light Source (SLS). Synchrotron sources are large cyclic accelerators in which electrons are accelerated close to the speed of light, to emit X-rays in magnets, so-called ‘insertion devices’, around the storage ring, which can be used for different experiments, including X-ray-based CT. The high brilliance of X-rays generated by SR sources allow achieving high

quality CT data at micrometre resolutions and below for typical scanning times of a few minutes, in terms of signal-to-noise ratio, contrast-to-noise ratio and also image sharpness.

After a preliminary study that was focused on optimising image quality for a range of experimental settings for phase contrast-based SR CT, an X-ray energy of 20 keV and a sample-to-detector distance of 14 mm was chosen. This provided sufficient contrast between increments (as shown later), while retaining a sufficiently short total scan time (6.5 minutes) in order to image the complete sample. For each scan, the integration time was set to 150 ms, where 1501 projections have been taken. Propagation-based phase contrast reconstruction was applied to reconstruct SR CT datasets using a Paganin-style non-iterative phase retrieval algorithm (Paganin et al., 2002). This algorithm retrieves the phase information for each projection, and requires estimation of the complex refractive index $n = 1 - \delta + i\beta$ of the specimen, namely the ratio between δ and β that is assumed to be constant. Here we used values experimentally determined by beamline scientists at TOMCAT, optimal for biological hard tissues: $\beta = 3.7 \cdot 10^{-8}$ and $\delta = 1.7 \cdot 10^{-10}$ at the chosen X-ray energy.

4.2.4. SR CT imaging and optimisation

Cementum increments must be imaged with sufficient image contrast to distinguish thick 'light' and thin 'dark' increments, and at a sufficiently high spatial resolution to identify individual increments within the cementum tissue. Using SR CT this is feasible for cementum tissue, yet experimental settings must be optimised.

The effects of various experimental settings for SR CT on cementum increment imaging were investigated in a quantitative manner. In a preliminary experiment, the coronal third of the cementum tissue of specimen t56 (12 years old; expected increment count between nine and ten following an eruption time of 12-18 months for captive *Macaca mulatta* individuals) was imaged using SR CT for a range of different experimental settings. Four key settings (X-ray energy, exposure time, number of projections, and sample-to-detector distance) were individually varied according to Table 4.2, while all other experimental settings were fixed at an X-ray energy of 20 keV and an exposure time of 150 ms for 1501 projections at a sample-to-detector distance of 14 mm. The effects of changing experimental settings on image quality of cementum

increments were characterised using the image quality metrics signal-to-noise ratio (SNR) and contrast-to-noise ratio (CNR). SNR was calculated following Verdun et al., (2015), and CNR was calculated following Mohammadi et al. (2014). SNR quantifies the level of image signal in an image relative to the background noise. CNR is a useful measure for assessing image contrast between distinct structures, such as dark/light cementum increments.

Image quality metrics for each experimental setting were calculated for 10 SR CT slices representing the same regions of the tooth root of t56 in each scan (Fig. 4.2). SNR was calculated as the ratio between the mean greyscale value for a 150 pixel ´ 150 pixel region of interest (ROI) of cementum (S) and the standard deviation of a 150 pixel ´ 150 pixel sample of background in each slice (σ_1):

$$\boldsymbol{SNR = \frac{S}{\sigma_1}}$$

CNR was calculated using the method described by Muhamaddi et al. (2014), where the ratio of the mean greyscale values of the same ROI's of cementum (g_1) and air (g_2) used for SNR analysis is divided by the square root of the halved sum of their squared standard deviations (σ_1 and σ_2 for cementum and air, respectively):

$$\boldsymbol{CNR = \frac{g_1 - g_2}{\left[(1/2) - \left(\sigma_1^2 + \sigma_2^2\right)\right]^{1/2}}}$$

Mean values of SNR and CNR were calculated from the values for these 10 slices and compared between all experimental settings (Fig. 4.5 and Table 4.2).

4.2.5. Thin-section preparation and histological imaging of cementum

For comparison with SR CT data, the current gold standard of cementum imaging, thin-section histology, was applied to all scanned tooth roots. All roots were embedded in 'EPOTHIN' epoxy resin (Buehler Ltd., Lake Bluff, IL, USA) prior to thin-section preparation. In order to accurately orientate samples, the resin was left to cure for three hours until semi-viscous before embedding. The apical apex of each root was then placed within individual beads of resin within a cylindrical plastic mould of 1cm radius.

Samples were vertically oriented using a fine brush, in order to orient them as close to perpendicular to the mould base as possible. The resin was then left to completely cure for 12 hours. Following this, more 'EPOTHIN' was poured over each specimen until it was entirely coated. Moulds were then placed in a vacuum oven for approximately 20 minutes in order to maximise infiltration of resin within each specimen.

Embedded specimens were ground vertically through the cross-section of roots to the apical third of the root height using a Buehler Beta grinder/polisher with 800p grit sandpaper. Once this region was exposed it was polished using 1200p and 2500p sandpaper, and 6μm and 1μm Beuhler 'MetaDi' diamond suspension paste. Specimens were thoroughly rinsed with tap water and methylated spirit between each polishing grade. The polished face of each specimen was then mounted to frosted glass slides using more EPOTHIN resin. Mounted specimens were ground and polished using the same method until 70μm thick[33].

Thin sections were studied using a Nikon Eclipse Lv100 microscope equipped with a Nikon DS-Fi2 digital viewfinder at 20x, 50x and 100x objectives under polarising and non-polarising light. The Nikon DS-FI2 offered a resolution of 2560/1920 pixels for each objective.

4.2.6. Computer vision and cementum analysis

Computer vision methodologies are now commonly used in the study of biological materials. CT imaging itself can be seen as one first step of computer vision, and tomographic data can be further processed and analysed in an objective, statistical and automated fashion using robust computer vision techniques. This was an important element of our study, especially considering the exceptionally large, volumetric datasets (>200 GB/scan) created by (phase contrast-based) SR CT imaging, which adds a degree of complexity to cementum data in both a spatial (3D versus 2D) and data-handling aspect. The quantitative assessment of increment count, structure and texture is not a simple task. Further, the exceptionally large size of individual SR CT datasets places considerable demand on computing power for quantitative analyses. It is therefore key to optimise the efficiency of image processing and analysis in order to study this data in an effective manner. Automated image processing and analysis provides a means to extract and quantify objects and patterns in digital image data in an objective manner. In terms of cementochronology, it may offer two key advantages over previous methods

based on human vision. Firstly, a reduction in bias and subjectivity in increment counts. Human vision is often prone to bias due to pre-conceived notions of patterns in objects and structures. As a result, studies based on human vision (especially cementochronology studies) often cite low repeatability and precision between human observers (Renz and Radlanski, 2006). Computer vision and automated analysis does not suffer from these problems if analyses are robust and correctly applied. Secondly, a concise, thoroughly planned and sensitive analysis routine can be applied to a large number of samples, and samples of a varied nature. The rapid speeds permitted by modern computer systems can allow an unprecedented amount of cementum data to be analysed using a wealth of techniques in a fraction of the time that would otherwise be required for manual analysis.

4.2.7. Image processing: straightening and filtering

Processing of original data and feature extraction is often needed before digital image analysis. This can involve a wide range of techniques, the vast majority of which are based on the manipulation of two-dimensional (2D) pixels and/or 3D voxels using mathematical operations (Nixon and Aguado, 2012). Here, we applied two principal processing techniques to individual SR CT slices: straightening and isolation of cementum, and directional filtering of increments (discussed later).

For circumferential structures such as cementum increments, it is often difficult to apply core processing tools and analyses without distorting results due to complexities in their patterns and boundaries. Hence, 2D straightening algorithms are often applied in order to further analyse the data. We chose to use the 'Straighten' tool developed for the open source ImageJ/Fiji image analysis software (Schneider et al., 2012). This tool applies cubic-spline interpolation across a segmented midline set by the user. Straightening is then performed using a series of non-linear cubic splines for an arbitrary number of pixels on either side of the midline that can also be determined by the user. We here assigned this number on an individual basis for each dataset, based on the radial thickness of cementum being imaged.

For each dataset, a segmented midline was plotted circumferentially by hand and through the middle of the cementum of the first 16-bit SR CT slice, then the number of pixels occupied by this line was manually adjusted until all the cementum was included, and the "straighten" tool applied (Fig. 4.3). This both isolated cementum data from

bordering dentine, and straightened the cemento-dentine boundary so that potential differences in increment patterns and shape could be analysed orthogonal to this layer. The use of the "macro recorder" tool in imageJ/Fiji then allowed this method to be repeated using a simple macro for all other slices in the dataset, by recording the Cartesian coordinates of each line segment of the midline and number of pixels occupied by the midline. These values could then be copied into the macro and applied for all other slices. However, it should be noted that the spatial distribution of cementum tissue often deviated from this midline as slices progressed vertically through the cementum and the morphology of the root changed. In these instances, a new midline had to be applied from the position along the image stack where the deviation first took place, in order to accurately capture the entire cementum tissue and effectively straighten the cemento-dentine boundary. Following straightening, all resultant images were saved in 16-bit format.

The isolation and straightening of the cementum layer is the only portion of the workflow performed and described here that requires a subjective human input. The plotting of the midline through the cementum to guide straightening may thus have an effect on final measurements of cementum increment shape and texture (see sections 4.12-4.13). The effects of variability in midline plotting are assessed in section 4.14.

Once straightened and isolated, the cementum data could then be further processed using directional filters in order to enhance contrast between increments. Filtering is commonly used to suppress the contribution of unwanted signals, while preserving and enhancing the useful signal for the analysis in question. A wealth of filters can be found in the literature and are commonly available in image processing and analysis software. Several can be tuned and tweaked for data-specific purposes, including oriented filters such as the steerable Gaussian filter.

Oriented filters are a class of filters in which a filter of arbitrary orientation is synthesised as a linear combination of a set of 'basis filters'. Let's assume the following Gaussian function (G) for a set of coordinates x and y that is circularly symmetric:

$$\boldsymbol{G(x,y) = e^{-(x^2+y^2)}}$$

The directional derivative operator (G_i) of this function is steerable. This can be described using a rotation operator $(\ldots)^{\theta}$. This operator can be applied to any function $f(x,y)$ so that $f^{\theta}(x,y)$ represents $f(x,y)$ rotated through an angle θ about the origin. Hence, the first derivative of a Gaussian ($G_1^{0^0}$) is given by:

$$\boldsymbol{G_1^{0^0}} = \frac{\boldsymbol{\delta}}{\boldsymbol{\delta x}} \boldsymbol{e^{-(x^2+y^2)}} = \boldsymbol{-2xe^{-(x^2+y^2)}}$$

The same function rotated by 90^0 is given by:

$$\boldsymbol{G_1^{90^0}} = \frac{\boldsymbol{\delta}}{\boldsymbol{\delta y}} \boldsymbol{e^{-(x^2+y^2)}} = \boldsymbol{-2ye^{-(x^2+y^2)}}$$

On this account, the filter G_1 at an arbitrary orientation θ can be formulated by taking the linear combination of $G_1^{0^0}$ and $G_1^{90^0}$:

$$\boldsymbol{G_1^{\theta^0} = \cos(\theta)\, G_1^{0^0} + \sin(\theta)\, G_1^{90^0}}, \text{ where}$$

$G_1^{0^0}$ and $G_1^{90^0}$ form the basis filters for any rotation of G ($G_1^{\theta^0}$). The cos(θ) and sin(θ) terms are the corresponding interpolation functions of these basis filters.

Straightening of increments allows a single orientation to be used when filtering (e.g. $G_1^{90^0}$ for horizontal increments or $G_1^{0^0}$ for vertical increments), and steerable Gaussian filtering has been shown here to substantially enhance contrast between straightened cementum increments (Fig. 4.3.e.). Implementing a steerable Gaussian filter designed in the Matlab environment (Lanman [2006] following Freeman and Adelson [1991]), with a 90^0 orientation and a directional derivative of 1 creates the first derivative of a cementum image; a separate 8-bit image where light increments are given greyscale values of 255, and dark increments of zero (**Fig. 4.6.b, e.).** The addition of this mask onto the original image thus provides a filtered image that can considerably increase the contrast of cementum increments (**Fig. 4.6.c**). However, the addition of a 'raw' first derivative with the original image can lead to the loss of information due to the saturation of the resultant image, and original textures and contrast within

increments can be significantly reduced (**Fig. 4.6.e.**). This problem can be mediated by dividing the greyscale values of the mask by a certain integer so that its light increment greyscale values are lower and its effects on the original image upon addition are lessened. As it is essential that a filter preserves the fidelity of imaged structures (e.g. greyscale texture, **Fig. 4.6.f.**) for subsequent analyses, this was here performed by dividing all greyscale values within the mask by integers of between two and 10. The effects of these calculations on the eventual filter were analysed and compared in order to optimise the parameters of steerable Gaussian filtering in eventual image processing procedure.

The effects of filter parameters on image contrast and texture were analysed by measuring and comparing greyscale distributions along 10 transects through the cementum of the l14 specimen (**Fig. 4.6.d.**). Distributions were measured along the same transects after applying first derivative masks that had been divided incrementally by integers from two to 10. These filtered datasets are here assigned to a naming convention following "Filter 2" – "Filter 10", with the number describing the integer to which the original first derivative mask was divided by (Table 4.3). The modulation transfer function (MTF) of cementum increments in each transect was used to provide a quantitative estimate of contrast, and how this changed due to filtering strength. The effects of filtering on discrete aspects of greyscale distribution in each transect were also compared to account for potential loss of texture detail.

MTF is a measure of the transfer of contrast ("modulation") from the original object to the image, providing quantitative data of how faithfully the image reproduces detail within the original object. The MTF can be described by the hypothetical greyscale imaging of a square wave function composed of light and dark increments. The maximum greyscale intensity possible will originate from the light increments, and the minimum intensity from the dark increments. The modulation of the original function can be defined as:

$$\mathbf{M_O} = \frac{(\boldsymbol{L}_{\mathbf{max}} - \boldsymbol{L}_{\mathbf{min}})}{(\boldsymbol{L}_{\mathbf{max}} + \boldsymbol{L}_{\mathbf{min}})}$$

where L_{max} describes the maximum greyscale ("luminance") value of the light increments, and L_{min} describes the minimum greyscale value of the dark increments. If

the frequency (v) and the 'modulation' (contrast) of the original function is known, then the modulation of the subsequent image (M_i) can be measured, and the MTF of the image can be calculated as the ratio between the image modulation and the original modulation:

$$\mathbf{MTF}(v) = \frac{\mathbf{M}}{\mathbf{M_o}}$$

For this study, as opposed to comparing the biological contrast of the cementum increments with the contrast of increments imaged using CT, the MTF was used to provide quantitative information of the amount of contrast added by using steerable Gaussian filters of increasing strength. For each filter, modulation functions were calculated for each increment pair along the same 10 transects as unfiltered data, and MTFs subsequently calculated and compared using ANOVA.

The potential loss of signal from filtering was assessed through comparing the greyscale distribution of each transect when imaged under each filter strength. After primary increment pairs had been identified along each transect during MTF analysis, the number of secondary peaks in greyscale was recorded within each increment pair, along with their greyscale value and position (**Fig. 4.6.f.**). ANOVA comparisons were performed between the number of peaks imaged using each filter and the number imaged with no filter, as well as the ratio of their value with that of the corresponding primary peak. This was in order to identify whether certain filter strengths created a significant loss in detail of the texture of increments, which may limit future analyses and comparisons between increments.

ANOVA comparisons of MTF values suggest that dividing the first derivative of an image by between six and 10 provides filters that do not significantly improve contrast relative to unfiltered values (Table 4.3). Dividing by smaller values steadily improve contrast until M_i values of cementum increments become an order of magnitude larger than unfiltered values when the first derivative is divided by between two and four (**Fig. 4.6.f**). This suggests that a minimum division of six, and an optimum division of < four should be used for steerable Gaussian filtering of straightened cementum increments.

Following MTF measurements, ANOVA comparisons suggest that the strength of filtering has no significant effect on the number of secondary peaks within primary

cementum increments. Although filtering affects the absolute relationships between primary peaks and secondary peaks in greyscale (**Fig. 4.6.f.**), their values are changed proportionally, thus preserving their relationships even using the strongest filters. Finally, in visual analysis of transects, the strongest filter ("Filter 2") provided the most clear increment pairs, shown by discrete peaks and troughs in absolute greyscale values directly corresponding to principal light and dark increments, respectively (**Fig. 4.6.f.**). In filters where the mask was divided by larger integers these patterns become masked by secondary peaks and troughs, and become harder to distinguish. This is reflected when using the automated increment counting algorithm to count increment pairs: The strongest filter ("Filter 2") provides the most consistent counts for every measured transect (Table 4.4).

Results of filter comparisons thus suggest that a steerable Gaussian filter should divide the first derivative of an image by half before being employed, in order to both optimise contrast between cementum increments, and preserve texture within increments. As a Matlab function this can be incorporated into an automated image-processing framework, to act consecutively after straightening of increments (E-Appendix 4.2.; for html link to E-Appendices see Appendix 4.2.). This combination of straightening and filtering has been shown here to significantly enhance image quality of cementum increments, and to provide data that can be readily examined in subsequent analyses.

4.2.8. Automated increment counting

The first image analysis algorithm developed here was designed to count increments in an objective, automated fashion using solely computer vision. Based on the 'Digital Cementum Luminance Analysis' technique (DCLA) (Wall and Wall, 2007), this algorithm employs population statistics (mean and standard deviation of greyscale values) to count increments and distinguish 'real' increments from greyscale noise. DCLA was designed to minimise the reliance on human vision for increment counting, by counting increments as peaks and troughs in 8-bit pixel values that extend beyond a pre-determined cut-off. Radial transects are plotted through the cementum, and their greyscale 'luminance' profiles plotted. Increments that are within two greyscale values of the last increment of the same type (light/peak versus dark/trough) are not counted as a principal increment. However, this technique was found to be insufficient for

discriminating increments in SR CT data. An absolute cut-off value could not account for differences in cementum texture and the luminosity of increments between individual scans.

Before the increment counting algorithm presented here was developed, the DCLA method for increment counting was applied to SR CT cementum data following Wall-Scheffler and Foley (2008). Here, the 30 radial transects through the cementum that were later used for the method of automated increment counting of cementum regions identified by human vision ("method two" outlined below), were assessed using the methodology outlined in Wall-Scheffler and Foley (2008). Peaks and troughs were identified in each transect using the "findpeaks" function in Matlab. Peaks were found using "findpeaks" of unadjusted transects, while troughs were found using inversed transects (created using the "flipb" function). From the resultant databases of peaks and troughs, values that differed by less than three greyscale values from the previous value were deleted, and the resultant count of peaks and troughs calculated. If peak count differed from trough count, then increment count was interpreted as their median value.

Mean increment counts estimated using the DCLA method were consistently and significantly higher than the minimum and maximum expected counts for all *Macaca mulatta* individuals (Table 4.5 and Fig. 4.7). The lower 25% quartile matches the maximum estimated age for three specimens (k91, t56 and t59). The maximum difference between the mean estimated count and maximum expected count was eight (l10), while the minimum difference in counts was one (k91 and t59).

The consistent over-estimation of increment counts using DCLA is due to the rigid and arbitrary threshold of two greyscale values that peaks/troughs must differ from the immediately preceding peak/trough (respectively) to be included in counts. For our data this threshold was too small to distinguish between increments and accessory peaks/troughs in greyscale created by noise. Hence, a more flexible approach is needed.

We have here developed a method that distinguishes between increments and noise in luminance values based on the unique distribution of values within each individual SR CT slice. As in DCLA, this method is based on the study of the distribution of greyscale values along transects through cementum. Following convention used in tribological surface profiling (Gadelmawla et al., 2002; Esfahani et al, 2018), individual transects are separated into five sections of equal length. The standard deviation of greyscale values in each cut-off length is then calculated and light-dark

increment pairs are distinguished as peak-trough systems that depart from the mean luminance value beyond the local standard deviation. This simple method can be applied to a broad range of data types, as it makes no *a priori* assumptions about the data itself, other than the assumption of an incremental system.

Most importantly, this new method can be operated algorithmically in an automated fashion using solely computer vision, following an algorithm developed here in the Matlab statistical environment (E-Appendix 4.2.). In Matlab, each individual straightened and filtered SR CT cementum image is investigated along a series of 1000 transects through the cementum (Fig. 4.4.a.). Each transect is divided into five sections of equal length, and a smoothing spline is fitted to the greyscale pattern captured within each section, in order to minimise noise in greyscale values. For these smoothed datasets, the mean greyscale value, its standard deviation and resultant upper and lower 'cut-off' values (mean greyscale value plus or minus the standard deviation, respectively) are calculated. Two new datasets are then created for each section, the first comprised of only greyscale values above the mean, and the other of values below the mean (Fig. 4.4.c-d). The dataset comprised of higher greyscale values thus consists solely of peaks in greyscale, while the dataset comprised of lower greyscale values consists solely of troughs in greyscale. Inversion of the trough dataset produces a series of peaks (inverted troughs) that, alongside those of the peaks dataset, can be identified in terms of their distance from the mean, and location along the section using the "findpeaks" tool. This allows peaks and troughs that extend beyond the top and bottom cut-off values (respectively) for each transect to be identified, providing the first stage of estimating increment counts (Fig. 4.4.c-d). Further measures are taken to ensure that 'piggy-back' features caused by noise along the limbs of an incremental feature do not bias counts (Fig. 4.4.d.). No peaks/troughs are counted that immediately proceed from the last feature of the same type; so only one peak is counted for every trough. No peak/trough system where each feature is separated by less than two pixels are counted to ensure that potential imaging artefacts such as edge effects or phase do not bias counts (Fig. 4.4). A final measure is taken to account for increments that are only partly captured inside each of a neighbouring set of sections along one transect (Fig. 4.4.c-d.). As it is known whether each section starts and ends with either a peak or a trough, the greyscale value of the final pixel of each section will indicate whether the section ends halfway

through a further peak or trough. If the last recorded feature of a section using 'findpeaks' is a trough, then a final greyscale value above the sections upper standard deviation is defined as the ascending limb of a peak and an additional 0.5 is added to both the original increment count of the section in question (Fig. 4.4.c.), and to the increment count of the proceeding section (Fig, 4,d). Whereas if the section ends with a peak, then a final value below the lower standard deviation is defined as indicative of the descending limb of a trough and an additional 0.5 is added to both the original increment count of the section in question and the proceeding section. Once increment counts are estimated for the entire 1000 transects through an image, their mean and standard deviation are calculated, providing a final estimate of increment count and information on the precision of estimates for the image.

Following the development of this algorithm, its robusticity was tested by applying it to a series of digital sine wave patterns of known increment count between five and 30. Random noise of increasing severity was applied to these patterns in a controlled manner by increasing their standard deviation. Noise was increased incrementally by signal-to-noise ratio (SNR) levels of 0.1; starting from a SNR of 0.9, and ending in an SNR of 0.1. For each SNR level, increments were counted for 30 random sine wave patterns for each count between five and 30. Algorithmic estimates were deemed to be robust for each count until the standard deviation for the 30 counted sine wave patterns became erroneous by >2.

Finally, this algorithm was used to generate estimates of increment counts for 30 random straightened and filtered SR CT slices oriented transversely through the tooth roots of each of the 10 *M. mulatta* individuals following two methods. The first method used solely computer vision, generating counts for 1000 10-pixel-thick radial transects through the cementum and saved. The count for each slice was then determined as the mean count for each of its 1000 transects. The second method employed human vision to identify slices displaying the highest increment contrast for each specimen (following **Chapter 3**). Increment counts were generated for 30 radial transects through the cementum for these slices. Counts generated by both methods were then compared statistically using correlation coefficients (Spearman's r and Kendall's τ) with expected counts based on the known chronological age for each individual.

4.2.9. Image analysis: cementum texture

The 16-bit greyscale nature of SR CT volumes offers a rich source of comparative data in terms of grey-scale 'texture'. Texture is here defined as the spatial organisation of greyscale distribution within cementum SR CT data. By studying greyscale as a 'third dimension', several metrics commonly used in surface profiling studies can be applied to SR CT cementum data (Fig. 4.3.d.). 3D surface profiling is now a commonly used technique in both tribology and biology, with metrics and parameters established for tribology being increasingly applied to studies of dental micro-wear (Dong et al., 1993; Stout and Blunt, 2000; Purnell et al., 2012, 2013). These comprise height parameters (the distribution of greyscale values above and below the mean), spatial parameters (the direction and spatial periodicity of greyscale values across the *x*- and *y*-axis), hybrid parameters (combining information present in both the *x*- and *y*-axis with the '*z*-axis' provided by greyscale values) and functional parameters that characterise volumetric information based on the material ratio of the surface in question. 21 metrics were used here and are described in Table 4.6. Metrics were applied in an automated fashion using a custom function in Matlab (E-Appendix 4.2.).

The applicability of automated texture characterization metrics designed here and their discriminatory power for measuring greyscale distributions were tested by performing them for a sample of model images of controlled greyscale distributions. A series of images were created that comprised of incremental greyscale surfaces designed with differing degrees of increment contrast and a range of increment counts (Fig. 4.8) (based on uni-directional Gaussian distributions – see below for script). Metrics were then performed on each image, and their results were compared using both ANOVA comparisons and Principal Component Analyses (PCAs). Results were also compared to the results of metrics performed for five images composed of randomly generated greyscale values between 0 and 255, in order to provide a more robust context for comparisons between surface model images.

The performance of each metric was assessed through comparison between actual results and the results predicted for each surface model based on their contrast and increment count. It was predicted that, (a) models of increasing increment contrast will provide larger values for relative height parameters (e.g. maximum peak height, maximum valley depth), as there will be increasing differences between the average greyscale values of light (high grey value) versus dark (low grey value) increments. (b)

Models of increasing increment count will also provide larger values for relative height parameters as there will be a higher proportion of pixels occupying the highest/lowest greyscale values. (c) Increment count will have a more pronounced effect on functional parameters relative to increment contrast, as higher counts within the same pixel area will create thinner increments and so more fundamentally change the material ratio of the respective surface. (d) Increment count will also have the greatest control on hybrid and spatial values, as higher increment counts will have a greater effect on the directionality of a surface. Finally, (e) increment models will all produce substantially different values for all parameters compared to random greyscale models.

Both PCA and ANOVA comparisons between measured and predicted values for each parameter suggest that the metrics designed here faithfully interpret discrete aspects of surface texture. All ANOVA comparisons between incremental models produced significant results (Table 4.7). Results of metrics are also broadly comparable with those predicted for each model. Values of all height parameters apart from surface skew and kurtosis are considerably higher in both high-contrast and high-increment count models, and high-contrast models have significantly higher values than low-contrast models of equal increment count. Although ANOVA comparisons suggest significant differences between values of skew and kurtosis for each increment model, there is no clear correlation between either parameter and increment count and/or contrast. Increment count has the most pronounced effect on the majority of functional parameters, and only core depth and mean valley depth are less affected by increment count than by increment contrast. Core depth has no clear relationship with either increment contrast or count, and while mean valley depth is significantly correlated with increment count, high-contrast models have significantly higher values than low-contrast models of equal increment count. Increment contrast has the most pronounced effect on hybrid parameters. Values of all hybrid parameters increase with increased increment count. Although contrast does significantly affect the values of hybrid parameters, its effects are considerably smaller than that of increment count. Finally, the most significant differences in all comparisons are between increment models and random greyscale models.

PCA of greyscale models reflect the results of ANOVA comparisons. Figure 4.9. highlights significant separation along principal component 1 (84.8% of total variance) between all increment models and random greyscale models. Models of varying

increment contrast and count are significantly separated along principal component 2 (9% of all variance) in a predictable manner, with a negative, linear correlation between component 2 value and increment count and contrast. These results suggest that the majority of metrics designed here produce meaningful values that discern 'real' patterns in greyscale, and can thus be applied to cementum data.

After validation, a total of 21 metrics were applied to 30 randomly selected slices for each *Macaca mulatta* dataset. These slices were straightened, but not filtered in order to conserve original 16-bit patterns in greyscale. Following straightening and isolation of cementum, slices were saved in RGB format and the central third of the cementum region was isolated (in order to minimise bias produced by phase artifacts at the cemento-dentine junction and outer cementum edge). The algorithm then applied texture metrics to this region sequentially and saved the results in a new dataset. Once each slice had been analysed, their results were compared using ANOVA to reveal which metrics produced the most informative description of cementum texture and differences between teeth. Finally, the results for metrics with significant differences between datasets were investigated using principal components analysis in order to define the principal variation exhibited in cementum texture between datasets.

4.2.10. Image analysis: increment isolation and tortuosity

A principal record of cementum growth is the structure and shape of its constituent increments (Medill et al., 2009, 2010). Several discrete life history variables have previously been traced in the relative shape and thickness of cementum increments in mammal taxa (Klevezal, 1995). We here use computer vision to isolate individual cementum increments in straightened, filtered data, and analyse their geometric 2D tortuosity. 2D tortuosity can be defined by the ratio between the actual length followed by a path, versus the geometric distance between its endpoints (Fig. 4.3.f). Within these straightened datasets, the cemento-dentine boundary provides a straight line upon which transects of increments vary, effectively normalizing their trajectories to this boundary. As the boundary will be the site of initial radiation of cementum, this is believed to provide an accurate means of estimating the true tortuosity of increments relative to each other.

The straightened and filtered cementum slices used for increment counting were subjected to a novel algorithm designed in Matlab, where increments were individually

isolated in a step-wise fashion from the outer-most increment (Appendix 4.4.). Isolation of increments was attempted along radial transects across the x-axis of each slice (Fig. 4.4). For every pixel along the x-axis, y-axis vectors were produced. In filtered data, only 'light' increments will produce grey values above the local standard deviation. Hence, the first and last pixel of each increment should be able to be easily identified using double differentiation along each y-axis vector (Fig. 4.4). These values were recorded for each vector, along with their distance in pixels, in a new dataset providing information on the location, shape and thickness of each individual increment in the slice.

Once increments had been isolated, their path-lengths were measured using the 'Arclength' tool in Matlab (d'Errico, 2012; E-Appendix 4.2). This function computes the arc length of a function or 2D curve using linear chordal approximation. Shortest possible path-lengths were calculated between the two end-points of the increments as the hypotenuse between their x-axis and y-axis coordinates (Fig. 4.3.f.). Finally, tortuosity was calculated as the ratio between these two values.

Before 'real' cementum data was analysed using this algorithm, its accuracy for isolating increments, and precision with human vision were validated. First, a series of 10 binary (black and white) digital images were created in ImageJ/Fiji. These consisted of one-pixel thick white lines, drawn across a black background in increasingly complex wave patterns using the "Freehand" tool (Appendix 4.3). The lengths of these lines was calculated using the "Measure" tool and the minimum length between their end points were measured using the "Analyze skeleton" tool to calculate their Euclidian distance. Tortuosity calculated for each image as the ratio between these values. These images were then subjected to our tortuosity calculation algorithm. The accuracy of our algorithm could thus be measured as the difference between the two calculated tortuosity values for each phantom. Finally, as a test for precision with human vision, 10 increments previously isolated and analysed using the tortuosity algorithm were isolated by-hand using a Wacom mobileStudio Pro 16 interactive computer, in the Avizo 3D analysis software (version 9.3.). The tortuosity of these isolated increments were then compared to those generated solely by the tortuosity algorithm.

Following validation, the tortuosity algorithm was applied to the outer-most five increments in the same 30 straightened and filtered SR CT slices previously analysed for cementum increment count and texture for each scan. Tortuosity results

were saved for each scan in a separate dataset and statistically compared using ANOVA.

4.2.11. Final methodological validation

As a final test for the robustness of the above methodologies, the effects of the only element based on subjective human vision, increment straightening, were assessed. Increment straightening is dependent on human vision as it is required for the user to independently denote the midline for cubic spline interpolation. As a result, repeatability may be compromised due to differences in the co-ordinates of the midline. The effects of these differences were assessed here by independently straightening cementum three times in five different SR CT slices. The resultant straightened images were then processed using the above methodology and their results compared using ANCOVA.

4.3. Results

4.3.1. SR CT imaging of cementum

Cementum is clearly visible in each SR CT dataset as an incremental tissue wrapping around the dentine of tooth roots (Fig. 4.2; Fig. 4.10). The cementum is distinguished from the dentine due to its significantly lower mean grey-values, and the cemento-dentine boundary is marked by the characteristic tissues of the granular layer of tomes and the high-density hyaline layer of Hopewell smith (Fig. 4.10). Individual increments are clearly visible within the cementum and can be followed through the entirety of each dataset both transversely and longitudinally (Fig. 4.11). Increments become more complex through portions of cellular cementum, identified by cellular voids.

Comparison between SR CT slices and histological thin-sections of the same regions of cementum suggests that both modalities represent the same cementum increments, and so that optical differences between increments in histological data are reflected as density differences in SR CT data. Thick light increments in histological data correspond to thick light increments in SR CT data, and so are comparatively dense relative to thin dark increments. The same count of increments can be seen following the same patterns in both imaging modalities (Fig. 4.10). SR CT data can further be

used to help elucidate primary increments from accessory increments in several specimens. This is illustrated in Figure 4.10.(g-h), where the blur created by phase contrast reconstruction serves to minimize the lensing of several increments observed in the corresponding thin-section of the same region.

Quantitative study of signal-to-noise ratios (SNRs) and contrast-to-noise ratios (CNR) of SR CT data acquired using different experimental settings revealed several distinct patterns. When X-ray energy was changed in isolation, SNR became consistently lower with increasing X-ray energy, whereas CNR peaked at 20 keV, before steadily falling with increasing X-ray energy beyond this point (Fig. 4.5.a-b). SNR and CNR steadily improved with increasing exposure time (Fig. 4.5.c-d). SNR and CNR also improved with increased number of projections, although the relative increase in CNR was insignificant between 3001 and 4501 projections (Fig. 4.5.e-f). SNR steadily increases with increased sample-to-detector distance until 60mm distance (Fig. 4.5.g). Whereas CNR steadily rises from 14mm distance to a peak at 28mm distance, before steadily falling between 28mm and 100mm propagation distance (Fig. 4.5.h).

The positive relationship seen here between both SNR and CNR with increasing exposure time and number of projections has been expected. The opposite relationship seen between SNR and X-ray energy can be explained by a diminished X-ray absorption with increased X-ray energy due to an exponentially decreased probability of photoelectric interactions between X-rays and the tissue. CNR has a more complex relationship with each experimental setting, with an optimum setting at a different level compared to SNR for each setting. For instance, we identified the optimal energy at TOMCAT for cementum increments in terms of CNR at around 20-21 keV, while SNR has been generally improved for lower X-ray energies.

The steady increase in SNR with increasing propagation distance between sample and detector is in agreement with the results of Kitchen et al. (2017), but in contrast to the results of Plumhoff et al. (2017). Instead, Plumhoff et al. (2017) found that SNR of single distance propagation-based phase contrast reconstructions of muscle tissue steadily decreased when propagation distance increased between 30mm and 60mm at the same TOMCAT beamline of the Swiss Light Source synchrotron. The main factors producing the increase in SNR with propagation distance in our study are the contrasting patterns between the change in standard deviation (σ_1) of the image background (air) and the mean greyscale value of the cementum (S) with increasing

propagation distance (Fig. 4.12). σ_1 steadily decreases with increasing propagation distance, whereas *S* peaks at 28mm propagation distance, before falling until 100mm distance. The Paganin phase retrieval algorithm acts as a low pass filter, reducing the image noise in resultant reconstructions (Plumhoff et al., 2017). This filtering has been enhanced here with increased propagation distance, as shown by Kitchen et al. (2017). The reason for the different patterns encountered in SNR between the results of Kitchen et al. (2017), and those of Plumhoff et al. (2017) were attributed by Plumhoff et al. (2017) to be due to different objectives when considering the optimal ratio of δ/β values for the phase retrieval algorithm. The objective of Kitchen et al. (2017), and of this study, was primarily to enhance contrast within SR CT data, whereas Plumhoff et al. (2017) also considered the sharpness of boundaries between materials when optimising this ratio. Also, the material properties of our mineralised tissue of study, cementum, are considerably different to the soft tissues studied by both Kitchen et al. (2017)(lung tissue) and Plumhoff et al. (2017)(muscle tissue). The resultant difference in the chosen ratios has in-turn resulted in a different balance between contrast and spatial resolution in the phase-retrieved reconstructions in each study. In order to maximise image sharpness, the ratio used by Plumhoff et al. for reconstructing their SR CT data is significantly larger than either our study or that of Kitchen et al. (2017), and so resultant reconstructions retain a higher proportion of attenuation data and background noise. Our data is more strongly filtered by the paganin phase retrieval algorithm (that acts as a low pass filter), which increases with decreasing Fresnel number and so increasing propagation distance.

The opposing pattern of falling CNR with increasing propagation distance, from a peak at 28mm to a minimum value at 100mm, is principally driven by a fall in mean greyscale values of the cementum ROIs sampled with increasing propagation distance (Fig. 4.12). This pattern conforms to that of Plumhoff et al. (2017), who also found a steady fall in CNR for increasing propagation distances between 30mm and 60mm. Visual inspection of the datasets acquired at different propagation distances suggests that the steady fall in mean greyscale value with increasing distance is due to a decrease in the greyscale contrast between cementum increments due to image blur. The image quality of the dataset imaged at 28mm propagation distance represents an optimum in the trade-off between spatial resolution and contrast, where the blurring inherent in the paganin phase retrieval algorithm smooths increment boundaries and reduces greyscale

noise, while greyscale differences are sufficiently retained between light and dark increments to provide high contrast (Fig. 4.2.c.). For distances below this dataset (14mm-20mm), high greyscale contrast is provided between increments, but their boundaries are noisy and less well defined (Fig. 4.2.b.). For distances above this, the increasing amounts of blur reduce differences in greyscale between light and dark increments such that by 100mm propagation distance they are difficult to distinguish by eye (Fig. 4.2.d.). This can also be shown quantitatively by plotting greyscale values along transects through the same region of cementum in each dataset acquired at different propagation distances. Examining these plots, it is evident that the highest contrasts in greyscale values are provided by the 16mm and 20mm datasets, while the highest overall greyscale values are provided by the 28mm dataset. The lowest contrast and mean greyscale values are provided by the 100mm dataset (Fig. 4.2.e.).
Following these optimisation studies, an X-ray energy of 20 keV and a sample-to-detector distance of 14 mm have been chosen for imaging cementum increments using propagation-based phase contrast SR CT, at a sub-optimal exposure time of 150 ms and 1501 number of projections due to limited SR time available. These settings provided sufficient image quality required to identify cementum increments and allowed for accurate algorithmic increment counts.

4.3.2. Automated increment counting

Robustness tests for our automated increment counting algorithm suggest that it is theoretically resistant to signal-to-noise ratios (SNRs) of up to 0.2 (Fig. 4.13). Average automated counts of increments in sine-wave patterns of known increment count are identical to all known increment counts for SNRs between 0.5-0.9, and standard deviations of automated counts do not exceed beyond these values (Fig. 4.13). Between SNR values of 0.2-0.5, average automated counts occasionally differ from actual counts by a value of one, but actual counts are consistently within the standard deviation of automated counts (Fig. 4.13). SNRs 0f 0.1 produce more consistent errors of between one and two values, but actual increment counts are consistently within the standard deviation of automated counts (Fig. 4.13).

Fully automated increment counts generated using the first method using solely computer vision were compared to counts expected for each *Macaca mulatta* individual

based on the average age of replacement of lower m1 teeth for captive populations of *M. mulatta* (approx. 12-18 months; Bowen and Koch, 1970). A potential variation of six months for m1 replacement necessitated the use of a minimum expected increment count, and a maximum expected increment count for each individual (one increment higher than the minimum expected count).

A spearman's *r* of 0.80 and Kendall's τ of 0.76 suggest significant correlation between automated counts and expected counts of cementum increments. Each mean automated count also met either the minimum expected count or maximum expected count for each individual. Both minimum and maximum expected counts were also within the standard deviation of automated counts for each specimen (Table 4.1)(Fig. 4.14.a).

When employing the alternative method of selecting by-eye regions of highest increment contrast, a series of advantages of SR CT imaging became apparent over thin-sections. Complexities in increment patterns were witnessed intermittently in every specimen (Figs. 4.10-11), with individual increments lensing and coalescing creating apparent accessory increments (Fig. 4.11.a.). However, these complexities can be traced through their entire transverse and longitudinal extent (Fig. 4.11.b), and primary increments distinguished from transitory accessory increments. Cellular cementum could also be distinguished from acellular cementum by the presence of cellular voids, and so could be avoided when identifying high contrast regions. These two factors, along with the entire coronal third of the cementum tissue being imaged, let to the confident interpretation of the most highly contrasting region of only principal cementum increments for each specimen (Fig. 4.11).

Alternate counts provide higher correlations with expected counts than using computer vision alone, with a Spearman's *r* of 0.97 and a Kendall's τ of 0.82. Mean alternate counts either meet the minimum or maximum expected count for each specimen, or fall between the two (Fig. 4.15.b). As for the completely automated counts, both minimum and maximum expected counts are within the standard deviation of alternate counts for each specimen. However, ANOVA analysis suggests that standard deviations are significantly smaller in alternative counts than fully automated counts (Table 4.1)(Fig. 4.14)($P<0.001$).

In summary, although using a more traditional methodology of pinpointing regions of highest increment contrast offers a higher degree of precision when using our

automated increment counting algorithm, a completely automated approach offers comparable accuracy for estimating increment counts. Both techniques offer estimates of counts that either match the minimum or maximum expected count for each specimen, or fall in between the two.

4.3.3. Image analysis: cementum texture

Validation studies of digital phantoms suggest that all 21 texture metrics have the ability to reflect significant differences in cementum texture using ANOVA comparisons (p<0.001) (Table 4.2). Results of metrics are also broadly comparable with those predicted for each digital phantom (Table 4.7.).

Application of texture metrics to cementum data suggests that each metric identifies significant differences in greyscale distribution between cementum datasets using ANOVA (p<0.01)(Table 4.6). Principal components analysis (PCA) separates individual datasets along both the first principal component (33% of variation), and the second principal component (22% of variation). The first principal component reflects differences in the organization of increments, with negative values suggesting poor organization and poor increment structure. The second principal component reflects differences in increment contrast (Fig. 4.15). Positive values suggest low contrast, and negative values suggest high contrast between light and dark increments. Although most datasets occupy their own portion of 'texture space', several overlap substantially (e.g. k16 and k23; Fig. 4.15), indicating fundamental similarities in cementum structure. In summary, validation and application to real SR CT cementum data suggests that the automated application of surface profiling metrics can be used to objectively study differences in cementum structure.

4.3.4. Increment filtering, isolation and tortuosity

Comparison between three algorithmically isolated increments and manually isolated increments suggests that computer vision offers an accurate and precise method for isolating cementum increments in SR CT data. For each dataset, apart from the third increment of slice three, mean distances between algorithmically and manually isolated increments are less than four pixels (~2.65μm), with a maximum difference of 12 pixels (~7.92 μm) (Fig. 4.16). This is well below the 20-pixel threshold assigned for these comparisons, and provides sufficient evidence for confidence in automated, computer-

vision based increment isolation.

Calculations for digital phantoms of known properties also suggest that tortuosity calculations are accurate, as tortuosity estimates are within 0.05 of known values for each phantom (Table 4.8). Finally, tortuosity results reflect real differences in increment shape and structure between scanned cementum tissues. The majority of datasets show regular tortuosity values between individual increments and slices, with low standard deviation (Fig. 4.15.b.). However, others show a significant range in values (examples). These are the same datasets that show the highest variation within 'texture space', and further inspection highlights a proliferation of globular, cellular cementum in these datasets.

4.3.5. Final methodological validation

The final methodological validation performed here was based on comparison between three datasets created from independent straightening of the same series of tomographic slices of the specimen k49. ANOVA comparison of tortuosity values of each dataset produced no significant differences ($P>0.05$) (Table 4.10). This suggests that the impact of human variation in cementum straightening has no significant impact on eventual calculations of increment tortuosity. PCA also suggests that texture metrics are not significantly affected by this variation. Texture metrics for all three datasets cluster together within the texture space occupied by the original k49 dataset (Fig. 4.15.a.), with no significant outliers. Finally, each dataset produces identical automated increment counts, and are also identical to the original k49 dataset. These results allow confidence that the only subjective portion of this methodology is robust to variation that may otherwise bias analyses of cementum texture, increment shape and increment count.

4.4. Discussion

It is evident from this study that SR CT provides a novel imaging modality for cementum study with several advantages over traditional histological methods. The sub-micron resolution and phase contrast reconstruction offered by SR CT imaging performed here provides comparable increment resolution and higher contrast between

increments compared to traditional thin-section histological methods. The volumetric nature of SR CT imaging has further allowed the cementum tissue to be navigated in a way not possible using thin-sections. Cellular cementum can also be easily distinguished from acellular cementum. This is of particular importance for counting cementum increments, as cellular cementum is known to provide less accurate increment counts than acellular cementum (Naji et al., 2016). However, as cellular cementum is an important reactive tissue, deposited during periods of increased occlusal stress (Geppert and Muller, 1951; Bosshardt and Schroeder, 1990, 1992; d'Incau, 2012), the accurate mapping of cellular cementum throughout an entire tooth root may provide evidence for temporal and spatial patterns of occlusal stress during life history. This may in-turn provide a new line of enquiry for assessing dietary trends over macro-evolutionary scales, by comparing the proportion and location of cellular versus acellular cementum between individuals along important evolutionary trajectories (Kaifu et al., 2003; Lozano et al., 2008; von Cramon-Taubadel, 2011).

Although SR CT is generally classed as non-physically destructive, it became apparent during scanning that cellular voids were damaged at the microscopic level. Multiple voids were shown in reconstructions to have burst, creating movement artifacts and eventually micrometer-scale cracks within the cementum tissue. Although this damage could not be seen by eye, it may indicate that further preparation of teeth including dehydration may be necessary before SR CT scanning of cementum (Morse, 1945). Sub-micron imaging resolutions have also been recently shown to damage DNA in cementum during SR CT scanning, although only within the field of view of the scan itself (Immel et al., 2016).

A further advantage of SR CT data is its information-rich, 16-bit greyscale format. Using optimal imaging settings, greyscale values can be expected to directly correspond to physical properties that determine the interaction between cementum increments and X-rays and, as no physical preparation of the tissue is involved, images are not effected by preparation artifacts such as surface scratches and topography (Czermak et al. (2006); Naji et al., 2016). Finally, SR CT data overcomes the common predicament of thin-section thickness. Variability in thickness has been repeatedly shown to effect precision in counts between thin sections of differing thickness, as this property both controls the amount of light that passes through the section and the amount of blur within and between cementum increments (Naji et al., 2016). This

property makes SR CT cementum data ideal for study using computer vision. A minimum slice thickness of 0.65 μm, along with the ability to create 'virtual thin-sections' of any thickness divisible by 0.65 μm allows investigation of the effects of section thickness to be investigated, and overcomes the effect of thin-section thickness on interpretation of cementum increments. Computer vision has thus been here shown to be an effective tool for minimizing the subjectivity of cementum study, and maximizing the information available of cementum growth and structure.

Computer vision may offer a new approach for developing a truly global standard of cementum study. The algorithms introduced here have the potential to minimize the effects of two key factors undermining current analyses: the potential subjectivity of human vision, and reliance of user experience (Naji et al., 2016). These issues have been widely discussed within modern cementum literature in terms of increment counting (Kasetty et al., 2010; Frie et al., 2011, 2012; Rolandsen et al., 2008). Several studies have found significant inconsistencies in increment counts both between individual researchers, and between calculated counts and expected counts for known age individuals (Renz and Radlanski, 2006). Further, the proportion of these errors often correlates with the experience of the observer, with more experienced observers producing significantly more accurate results than inexperienced observers (Rolandsen, 2008; Frie et al., 2011, 2012). The increment counting algorithm developed here offers the potential of avoiding this issue completely, as samples of randomly drawn transverse slices have been shown to produce average counts that accurately reflect those expected for each individual in our sample, with no human vision required. Increment counts for these samples will be identical, no matter how many times they are repeated, and no matter who is using the algorithm. An automated approach means that any observer can confidently generate increment counts with no dependency on experience. This effectively levels the playing field for cementochronology, ensuring that any study following this procedure can operate at the same standard of accuracy and precision.

Information of increment shape and structure and cementum texture in tomographic data may also provide a new quantitative window onto cementum growth and its relationship with life history. The ability to non-invasively study these variables may allow for analysis of the effects of life history on the cementum of individuals previously unavailable for thin-section study, including fossil taxa. Of the various life

history variables previously suggested to have a traceable effect on cementum growth, pregnancy has received the most attention. Several studies have identified increments deposited during pregnancy as relatively thin and ultra-mineralized compared to surrounding increments (Coy and Garshelis, 1992; Kagerer and Grupe 2001; Medill et al., 2010). The imaging methodology and algorithms developed here have both the potential to explore patterns previously interpreted as indicative of pregnancy, and to potentially isolate new tomographic patterns in cementum structure and texture previously unrecognized in histological thin-sections.

Finally, the suite of algorithms developed here are intended to be made freely available online and it is encouraged that interested workers investigate them in order to further develop them and introduce new analyses to the package. This is intended to foster an international effort to develop robust computer vision-based protocols for cementum study that can be applied to a wide range of taxa and data types. In a recent literature review, Naji et al. (2016) identify a lack of a universally subscribed protocol as a major factor undermining current cementum research. Additional to their suggested protocol for thin-section preparation and study, our suite of analyses may form the basis of a new global standard for cementum study.

4.5. Conclusions

We have here provided the first experimental study of non-fossilised incremental dental cementum using synchrotron radiation microcomputed tomography (SR CT). SR CT data provides comparable resolution and contrast of cementum increments to traditional histological thin-sections, and the volumetric nature of SR CT datasets offers several benefits to study over traditional histological methods. These are chiefly the non-invasive imaging of internal tissue, a volumetric perspective over the entire cementum tissue, and the lack of topographic artifacts that can obscure thin-section images. Finally, a suite of algorithmic analyses has been developed to study SR CT cementum data in a novel, automated manner. These have the potential to both remove subjectivity and reliance on user experience when counting cementum increments, and provide a new model for studying increment growth and its relationship with life history.

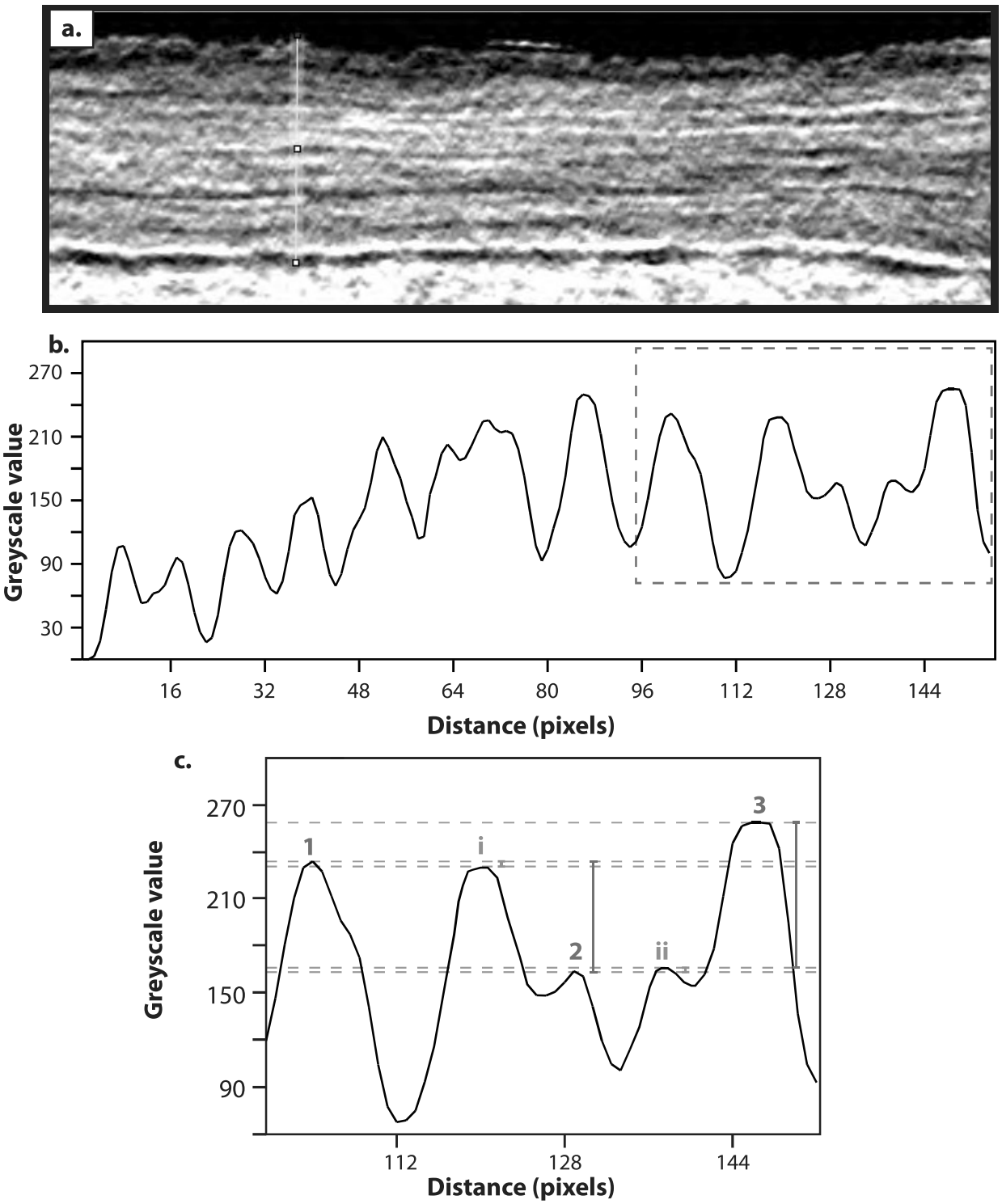

Figure 4.1. Example of Digital cementum luminance analysis for counting cementum increments. (**a**) One straightened, filtered tomographic slice of Macaca mulatta specimen l59. (**b**) Plot of greyscale values along transect highlighted by the yellow line in (**a**). Light increments are represented as significant peaks in greyscale values. Dark increments are represented as significant troughs in greyscale values. Additional 'piggy-back' peaks occur on the ascending and descending limbs of several peaks (**i** - **iii**) caused by imaging noise. (**c**) Detail of plot in (**b**) marked by dashed red box. The DCLA methodology for distinguishing between increments and noise is displayed here. The method uses a threshold value of 2 greyscale values that a peak must differ from the preceding peak to be counted. The peaks counted as light increments are thus labeled **1**-**3** in red, while those that are not counted are labeled **i**-**ii** in blue. It is shown here that this arbitrary absolute threshold value has little relation to the observed pattern of incrementation, as a significant peak representing a light increment (**peak i**) has not been included in counts, whereas a piggy-back peak along its descending limb is counted instead.

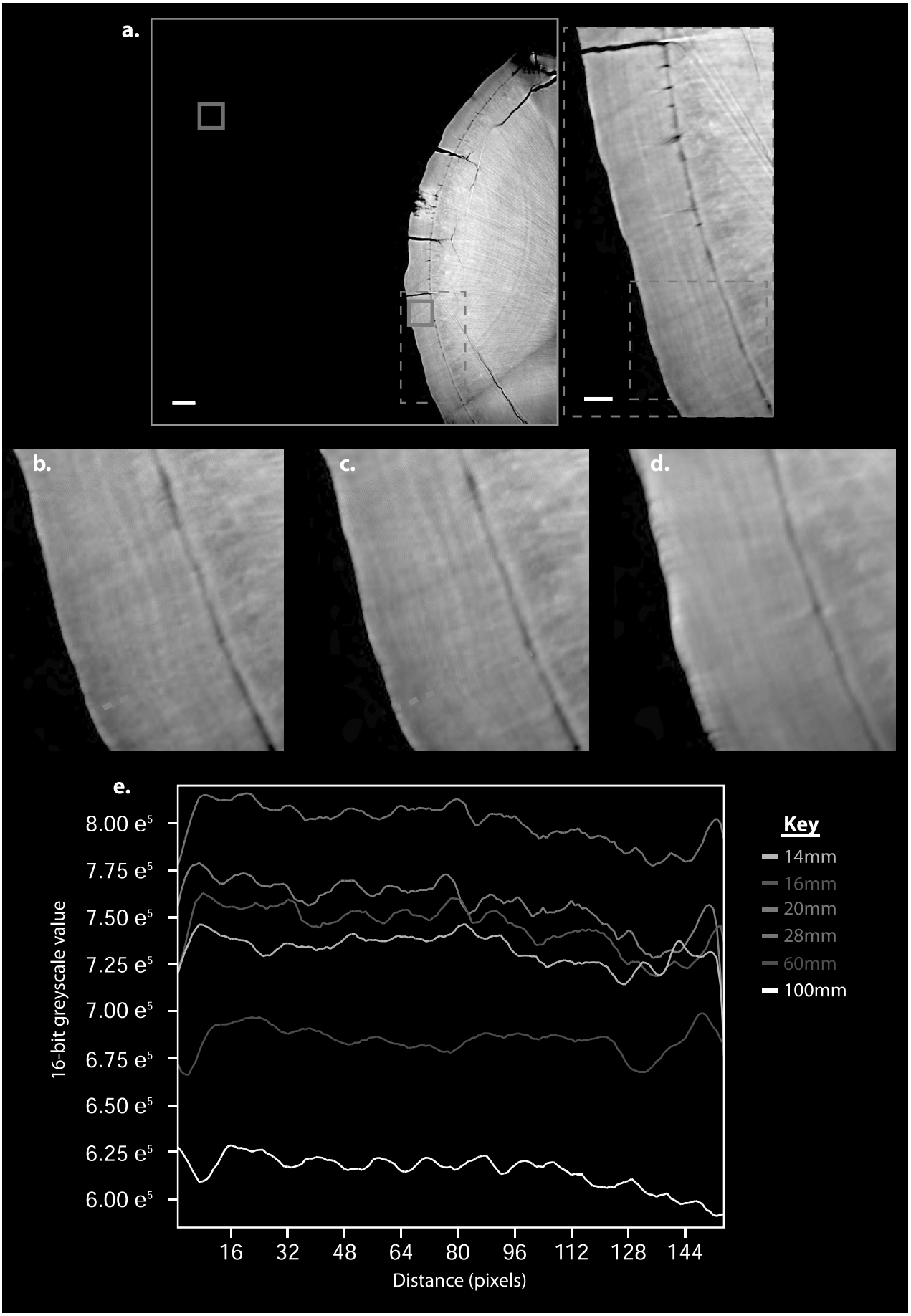
a.
b.
c.
d.
e.
8.00 e5
7.75 e5
7.50 e5
7.25 e5
7.00 e5
6.75 e5
6.50 e5
6.25 e5
6.00 e5
16-bit greyscale value
16
32
48
64
80
96
112
128
144
Distance (pixels)
Key
14mm
16mm
20mm
28mm
60mm
100mm

Figure 4.2. SR CT scan of a tooth root and regions for signal-to-noise ratio (SNR) and contrast-to-noise ratio (CNR) calculations. (**a**) One SR CT slice of the tooth root of *Macaca mulatta* individual t56. Blue box highlights region of interest for evaluation of background signal from which the standard deviation of greyscale values (σ_1) is generated for SNR calculations. Green box highlights sampling area for cementum signal from which the mean greyscale value (*S*) is generated for SNR and CNR calculations. Dashed red boxes indicate regions highlighted for increasing detail. (**b**) Detail from region indicated by dashed red boxes in (**a**) from the dataset acquired at 16mm propagation distance. (**c**) Detail from the same region from the dataset acquired at 28mm propagation distance. (**d**) Detail from the same region from the dataset acquired at 100mm propagation distance. (**e**) Plots of greyscale values along transect indicated by dashed red lines in (**b-d**) in each dataset acquired at differing propagation distances. White scale bars in (**a**) represent 100μm in full slice image, and 30μm in detail highlighted by red dashed box.

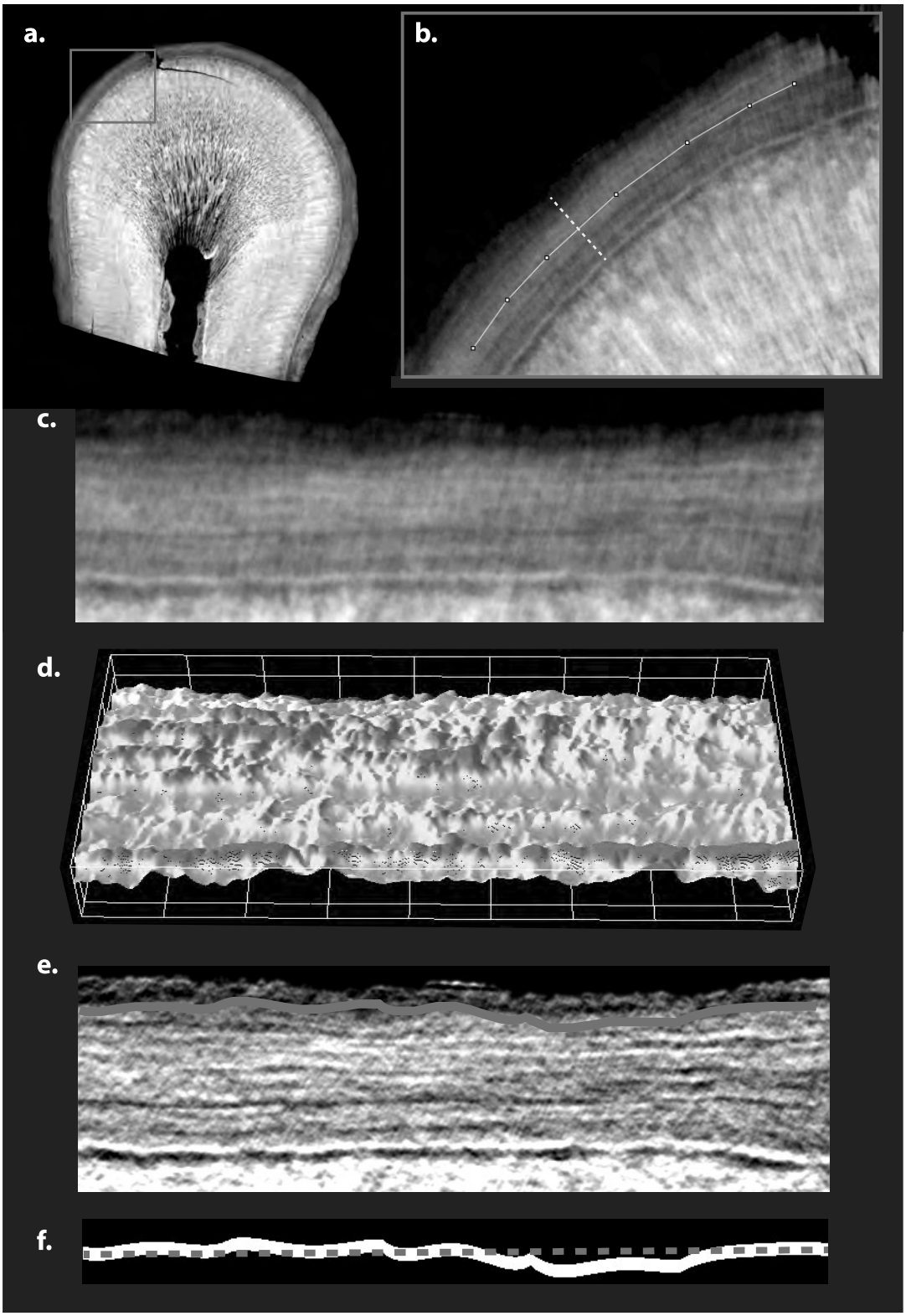

Figure 4.3. Tomographic imaging and analysis of rhesus macaque (*Macaca mulatta*) cementum. (**a**) Single tomographic slice of the specimen 159. (**b**) Detail of tomographic slice highlighting circumferencial cementum increments. (**c**) Striaghtened cementum section following midline highlighted by yellow dashed line in (**b**). (**d**) Three dimensional surface plot of (**c**), heat map indicates greyscale value; red is the highest value (255), blue is the lowest value (0). (**e**) Filtered image of (**d**) using steerable gaussian filter. Red line indicates increment displayed in (**f**). (**f**) Algorithmically isolated increment, red dashed line represents shortest possible path between two end-points, used in tortuosity calculations.

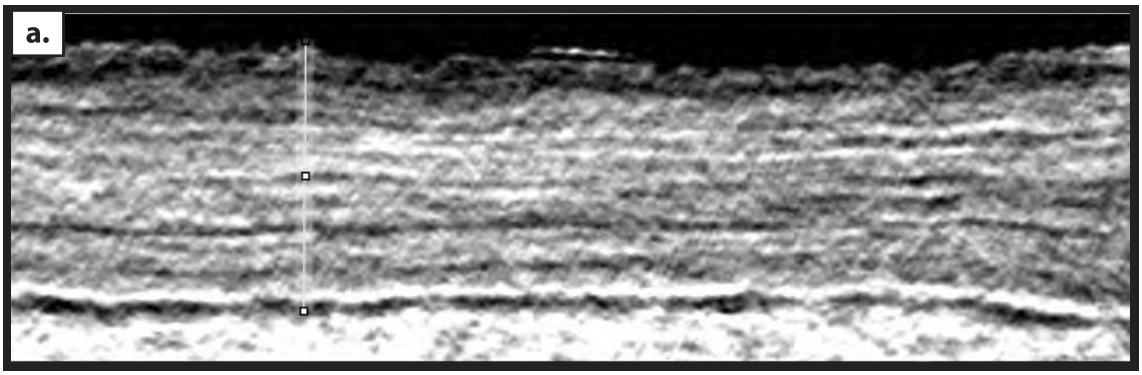

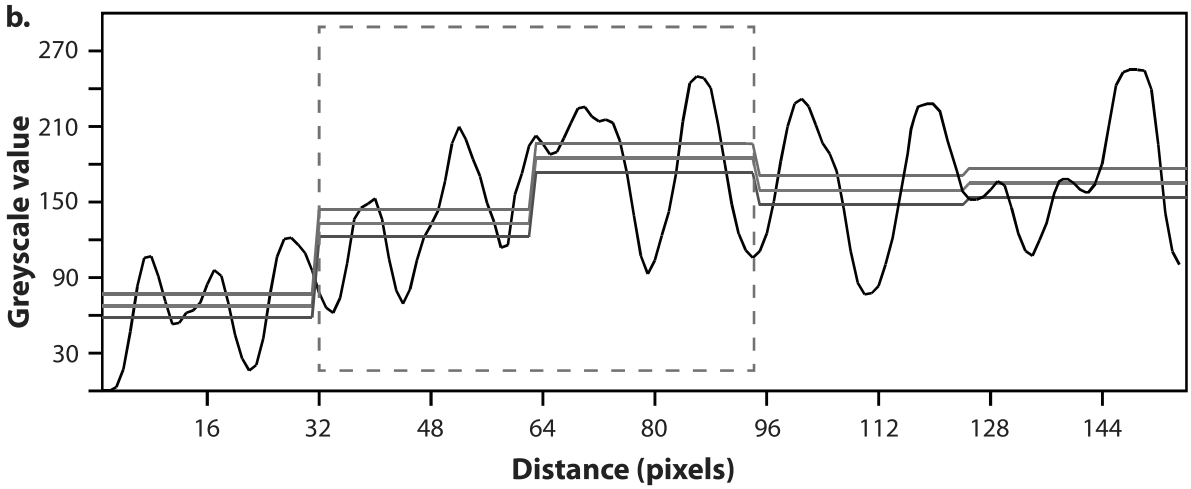

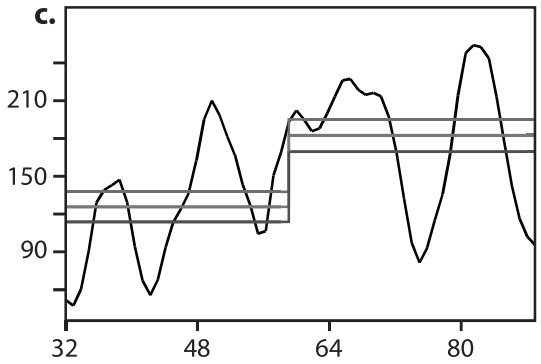

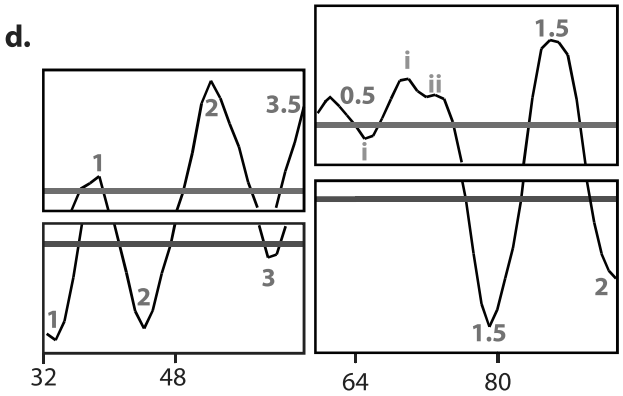

e.

Section	Increment count
1	2.5
2	3.5
3	2
4	2
5	1
Total	11

Figure 4.4. Tomographic cementum increment counting.

(**a**) Straightened, filtered cementum image. (**b**) Plot of greyscale values along transect highlighted by the yellow line in (**a**). Transects are split into five sections or "cut-offs". Light/dark increment pairs are distinguished as peak/trough systems in greyscale values where both the peak and trough depart from the mean greyscale value of that cut-off (red line), beyond the upper (green line) and lower (blue line) standard deviation, respectively. (**c**) Detail of the second and third cut-off denoted by red box in (**b**). (**d**) Cutoffs split into their upper and lower datasets comprising of peaks and troughs in greyscale that exceed beyond the upper and lower standard deviation (respectively). Here, trough-peak pairs are counted, denoted with red numbers. Troughs and peaks that are not counted are denoted in blue numerals, as they either do not exceed the relevant standard deviation, or are less than three pixels in distance from the last respective peak/trough. (**e**) Subsequent counts for each cut-off in (**b**).

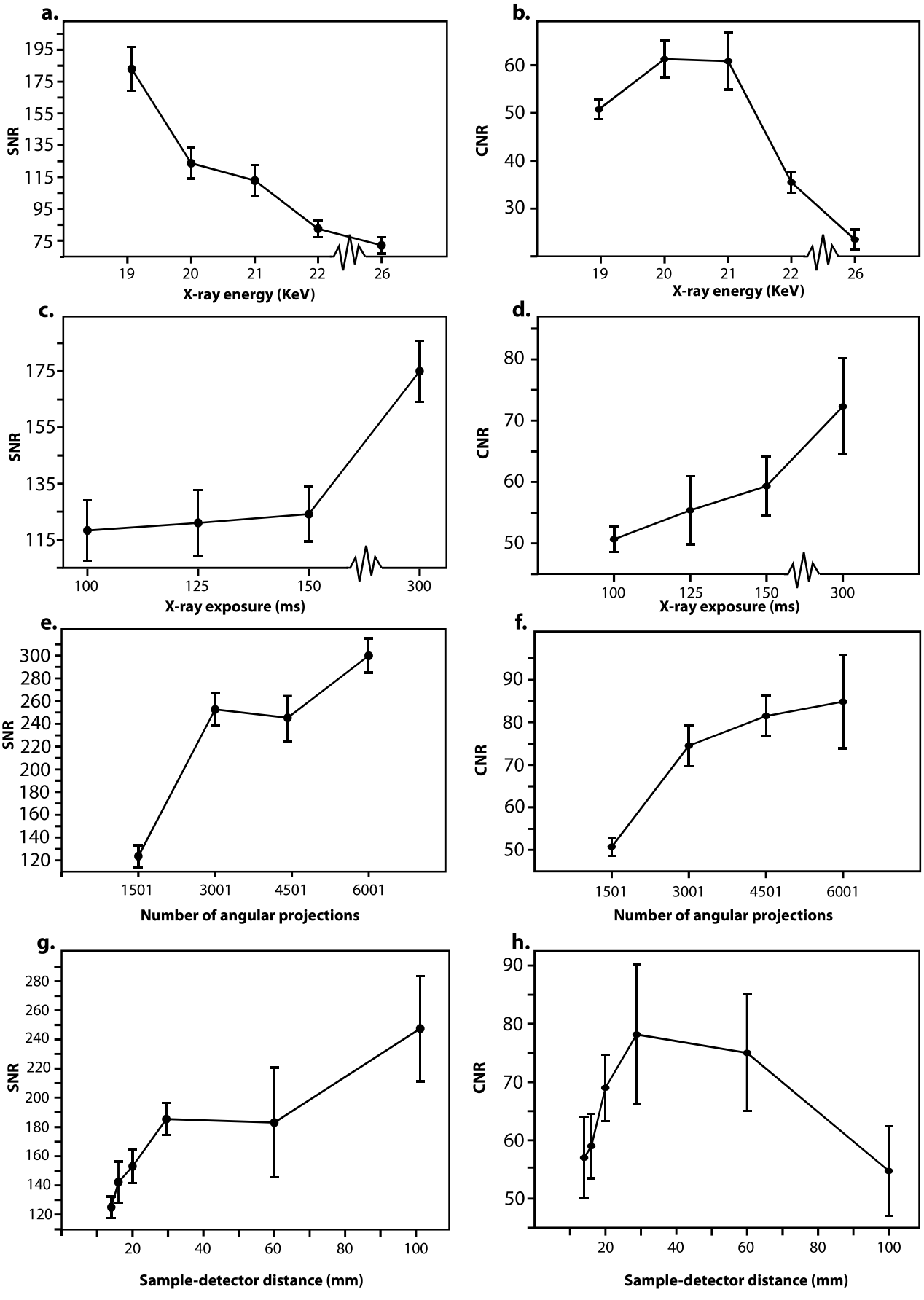
a.
SNR
195
175
155
135
115
95
75
19
20
21
22
26
X-ray energy (KeV)
b.
CNR
60
50
40
30
19
20
21
22
26
X-ray energy (KeV)
c.
SNR
175
155
135
115
100
125
150
300
X-ray exposure (ms)
d.
CNR
80
70
60
50
100
125
150
300
X-ray exposure (ms)
e.
SNR
300
280
260
240
220
200
180
160
140
120
1501
3001
4501
6001
Number of angular projections
f.
CNR
90
80
70
60
50
1501
3001
4501
6001
Number of angular projections
g.
SNR
280
260
240
220
200
180
160
140
120
20
40
60
80
100
Sample-detector distance (mm)
h.
CNR
90
80
70
60
50
20
40
60
80
100
Sample-detector distance (mm)

Figure 4.5. Results of parameter sweep for signal-to-noise ratio (SNR) and contrast-to-noise ratio (CNR) of phase contrast SR CT data of the same region within specimen l56. (**a**) SNR values for different X-ray energies. (**b**) CNR values for different X-ray energies. (**c**) SNR values for different exposure times. (**d**) CNR values for different exposure times. (**e**) SNR values for different numbers of projections. (**f**) CNR values for different numbers of projections. (**g**) SNR values for different sample-to-detector distances. (**h**) CNR values for different sample-to-detector distances.

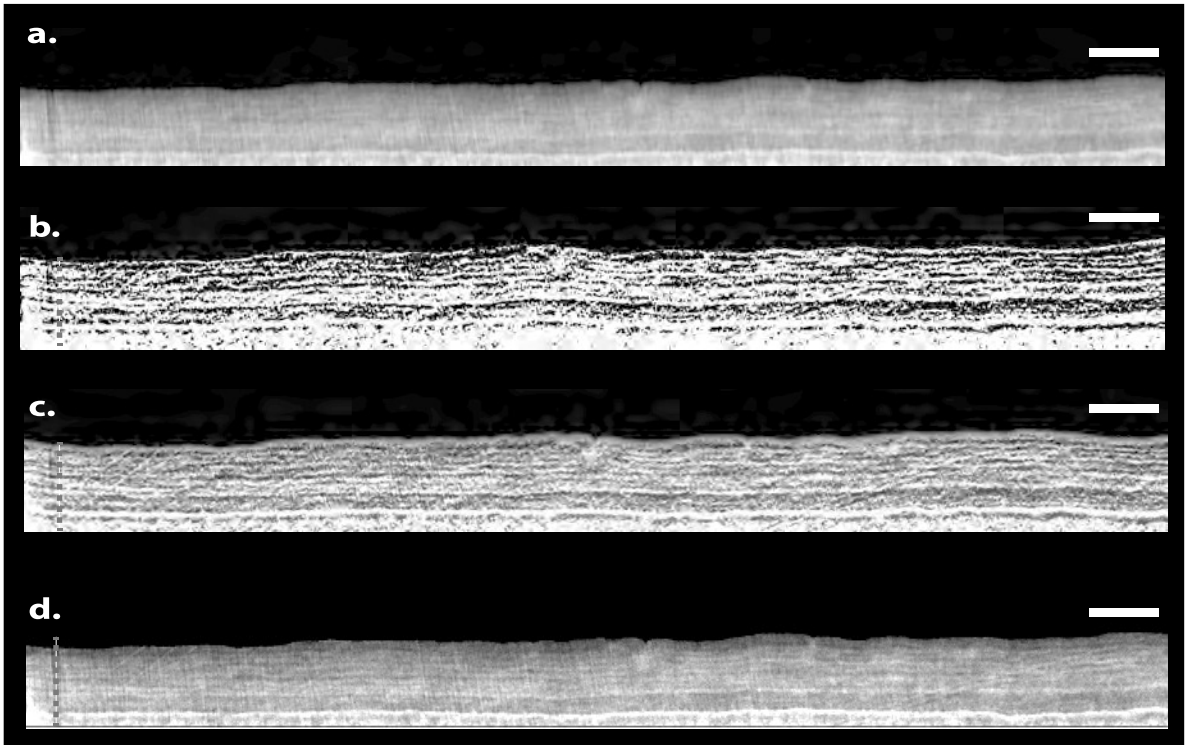
a.
b.
c.
d.

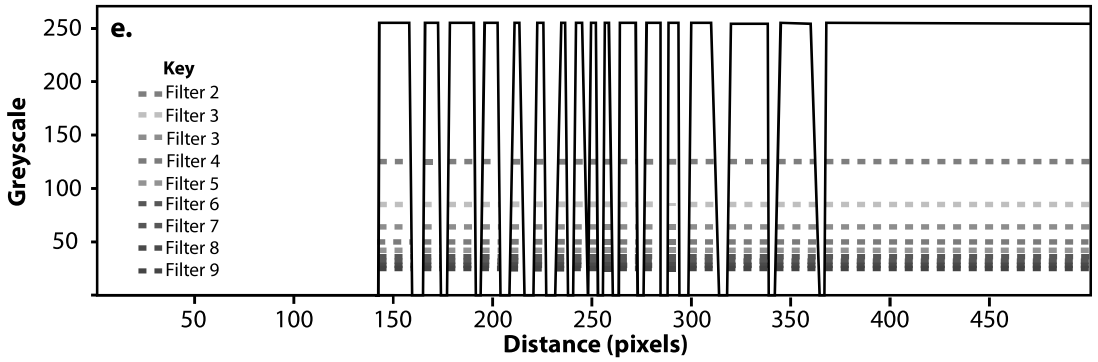
e.
Key
Filter 2
Filter 3
Filter 3
Filter 4
Filter 5
Filter 6
Filter 7
Filter 8
Filter 9
Greyscale
250
200
150
100
50
50
100
150
200
250
300
350
400
450
Distance (pixels)

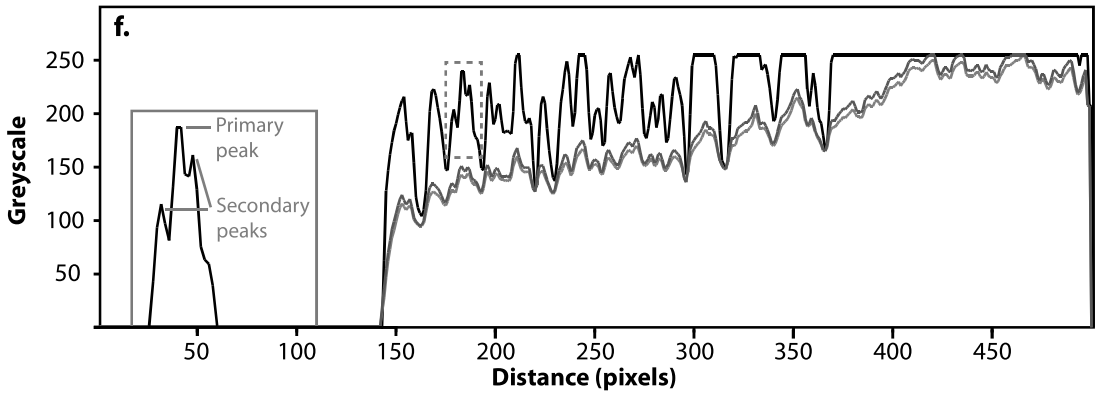
f.
Primary peak
Secondary peaks
Greyscale
250
200
150
100
50
50
100
150
200
250
300
350
400
450
Distance (pixels)

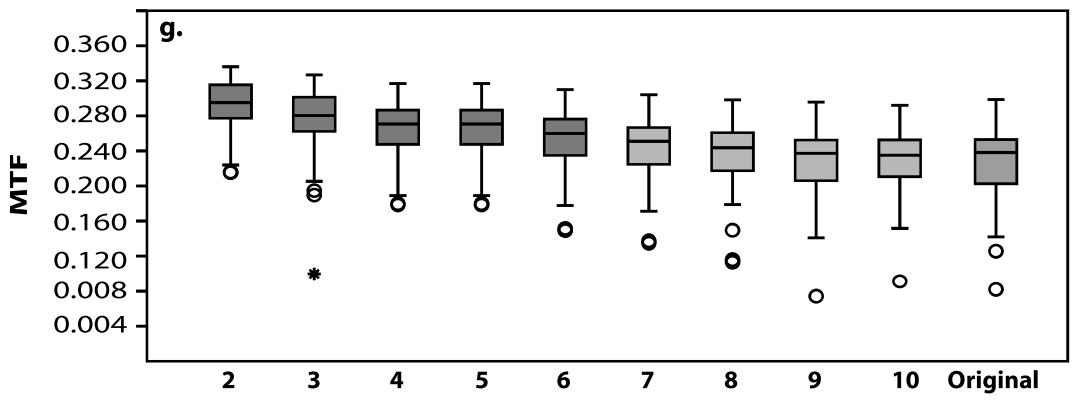
g.
MTF
0.360
0.320
0.280
0.240
0.200
0.160
0.120
0.008
0.004
2
3
4
5
6
7
8
9
10
Original

Figure 4.6. Assessment of the effects of steerable filtering on cementum images. (**a**) Original straightened 8-bit image of the cementum of the *Macaca mulatta* individual l14. (**b**) 8-bit Image in (a) after Gaussian filtration with a 90^0 orientation and a directional derivative of 1, consisting of only greyscale values of 255 (light increments) and zero (dark increments). (**c**) Filtered image produced by addition of (**b**) to the original image, after division of greyscale values in (**b**) by two ("Filter 2"). (**d**) Filtered image produced by addition of (**b**) to the original image, after division of greyscale values in (**b**) by eight ("Filter 8"). (**e**) Greyscale values along transect marked with dashed red line in (**b**). Coloured lines indicate the greyscale values that those of the original mask are reduced to by dividing them by integers between two and 10. (**f**) Comparison between greyscale distributions of Filter 2 (black), Filter 8 (blue) and the original image (red). Red box highlights the distinction between primary peaks and secondary peaks in greyscale used when assessing the potential loss of information due to filtering. (**g**) Comparison of modulation transfer functions of cementum increments between filters. Red boxes indicate filters with significant differences in modulation compared to the original image (green box), whereas blue boxes indicate filters without significant differences to the original (following ANOVA). All scale bars are 75 μm.

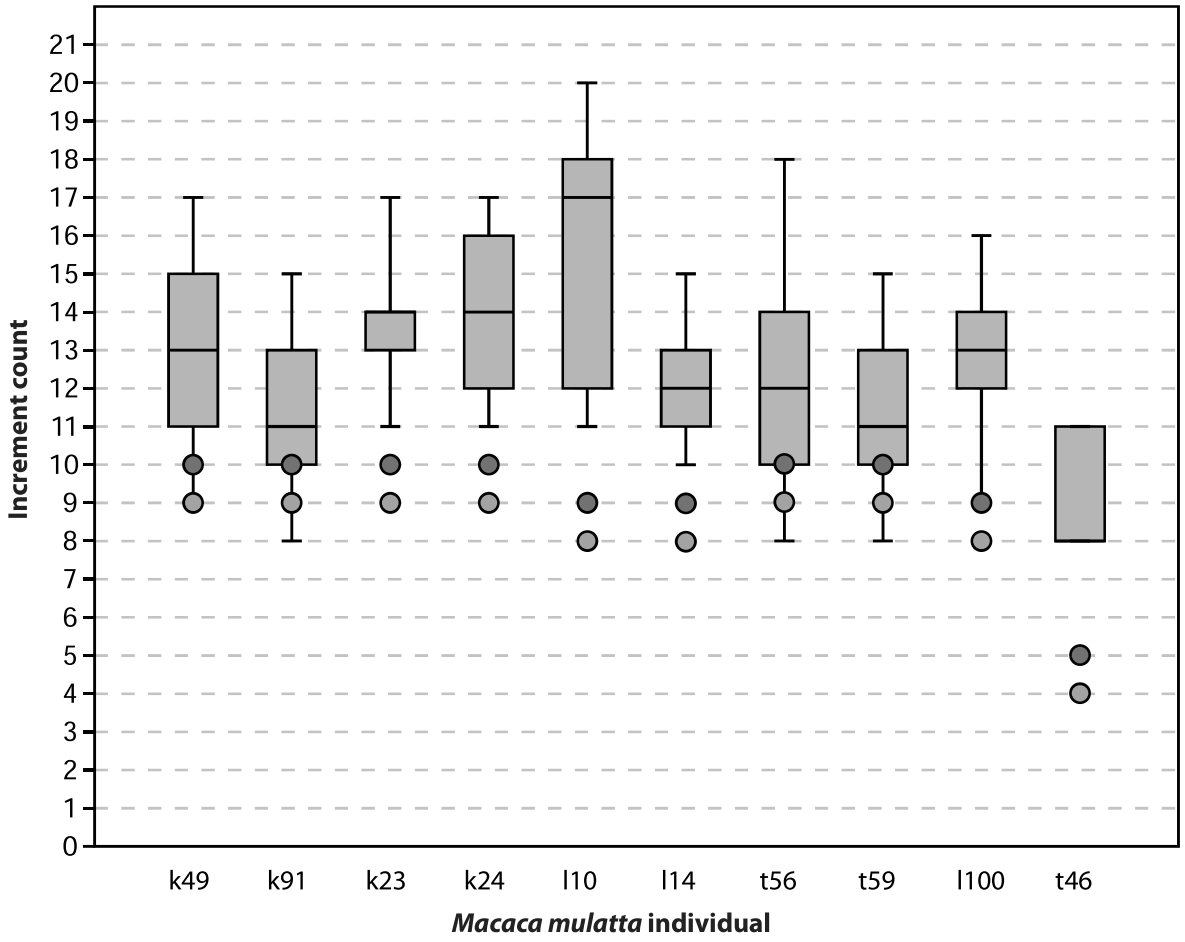

Figure 4.7. Comparison between expected increment counts and those estimated using digital cementum luminance analysis for each *Macaca mulatta* individual. Blue boxes indicate the interquartile range around the mean estimated increment count, indicated by the thick black line. Whiskers represent the extreme lower and upper estimated counts. Red circles indicate the maximum expected increment count. Green circles represent the minimum expected increment count.

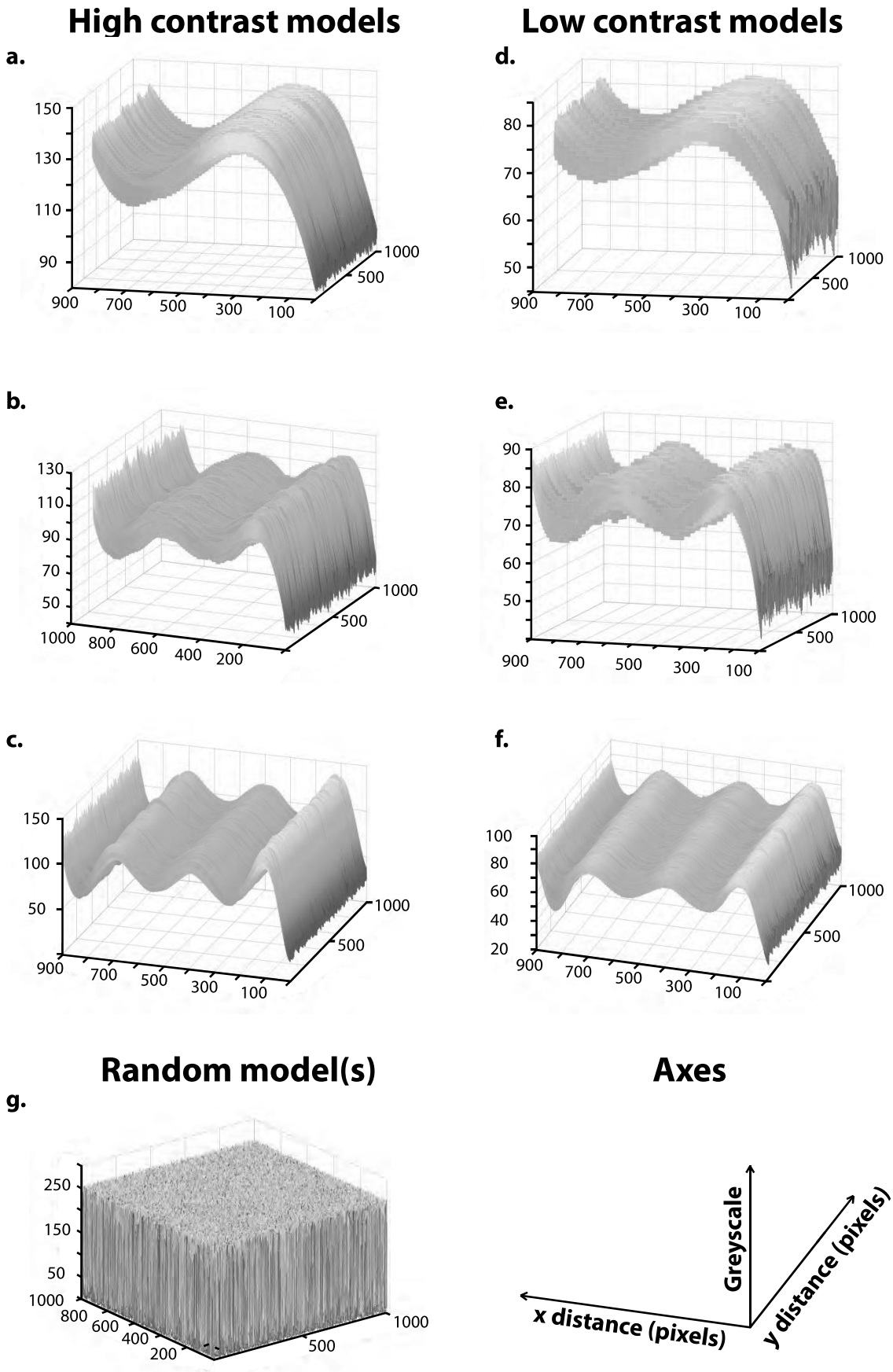

Figure 4.8. Incremental models used to test the sensitivity of automated texture metrics. (**a**-**c**) High contrast models of increasing increment count. (**d**-**f**) low contrast models of increasing increment count. (**g**) Random model of greyscale noise.

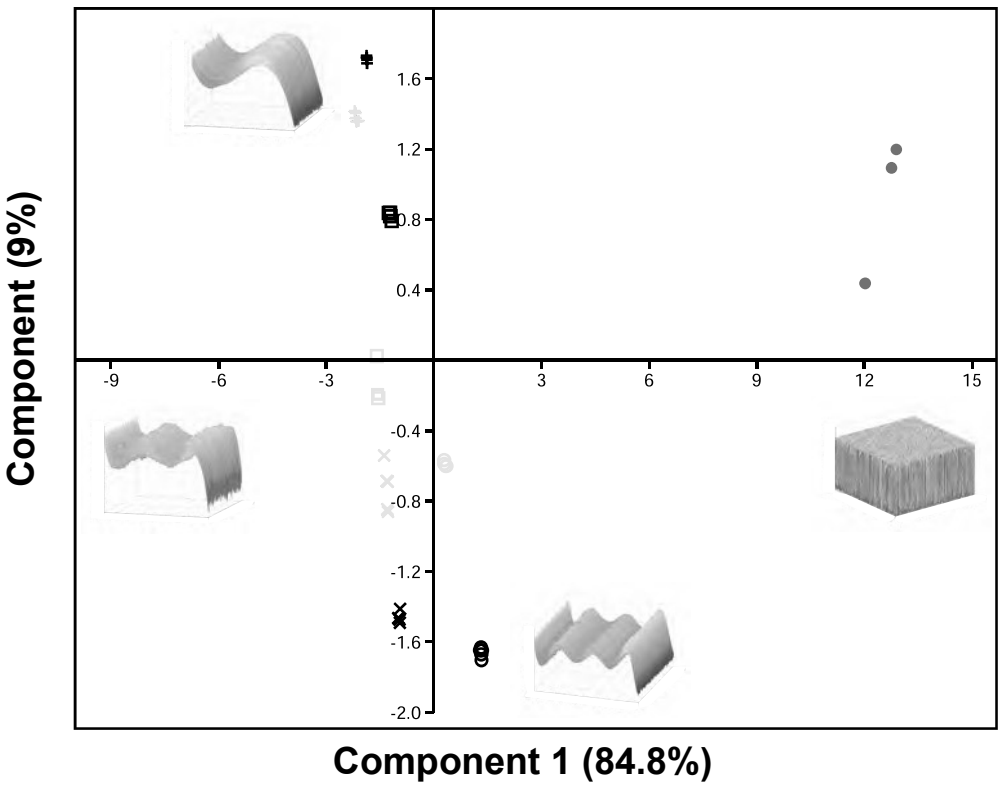

Key:

+	Low contrast; 1 increment
□	Low contrast; 2 increments
×	Low contrast; 3 increments
○	Low contrast; 4 increments
+	High contrast; 1 increment
□	High contrast; 2 increments
×	High contrast; 3 increments
○	High contrast; 4 increments
●	Random greyscale distribution

Figure 4.9. Results of principal components analysis of increment models. Component 1 represents surface roughness (texture spacing, amplitude and directionality). Component 2 represents increment contrast (distance of peaks/valleys from core, proportion of surface comprised by core).

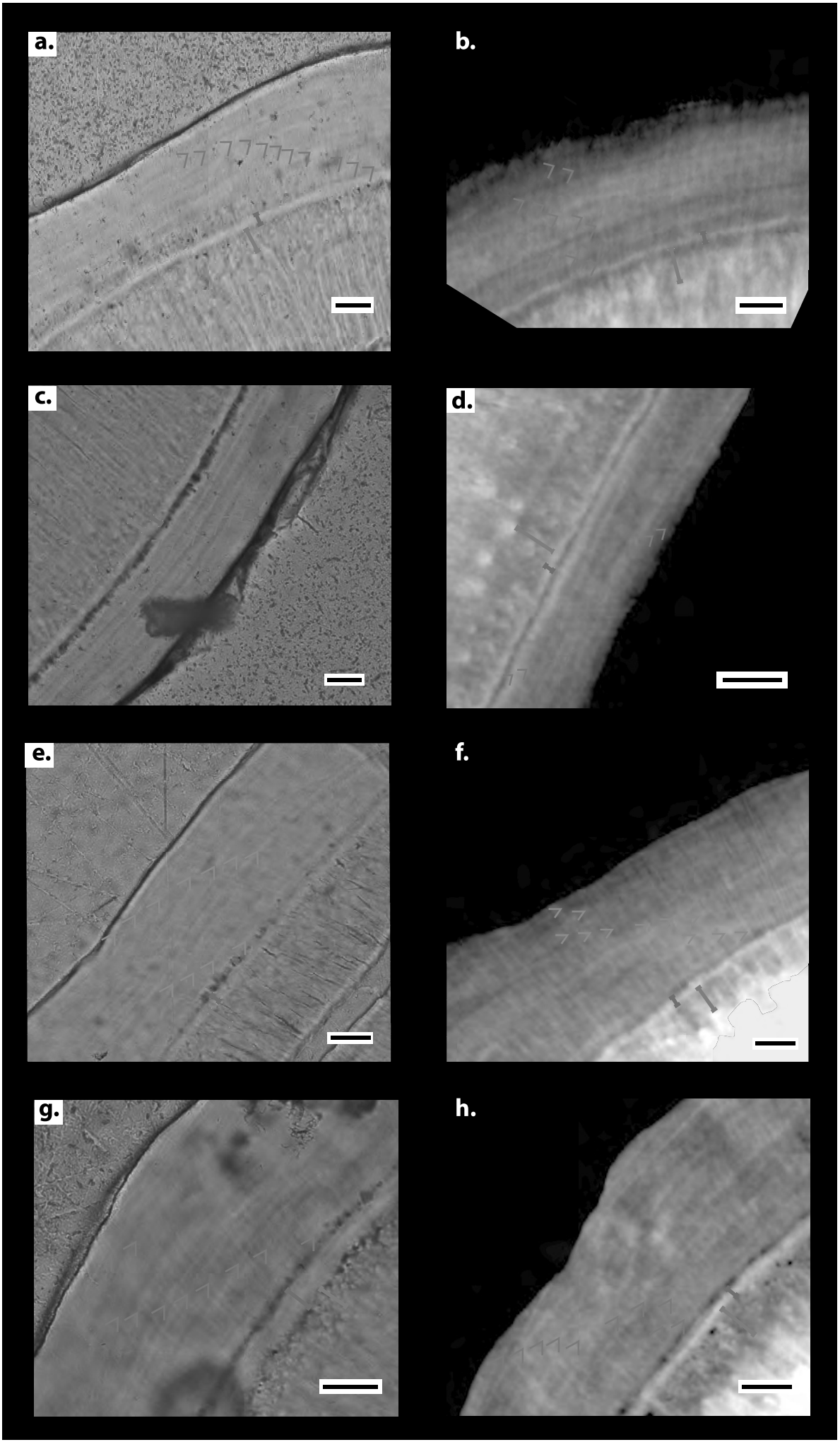
a.
b.
c.
d.
e.
f.
g.
h.

Figure 4.10 (last page overleaf). Comparison between histological and tomographic data. (**a**) Detail of histological thin-section of the k49 specimen displaying 11 light increments indicated by red arrows. (**b**) Detail of phase-contrast reconstruction of the same region as (**a**) displaying 10 increments. (**c**) Detail of histological thin-section of the t46 specimen displaying eight light increments. (**d**) Detail of phase-contrast reconstruction of the same region as (**c**) displaying eight increments. (**e**) Detail of histological thin-section of the l59 specimen displaying 11 light increments. (**f**) Detail of phase-contrast reconstruction of the same region as (**e**) displaying 11 increments. (**g**) Detail of histological thin-section of the t56 specimen displaying 10 light increments. (**h**) Detail of phase-contrast reconstruction of the same region as (**g**) displaying 10 increments. Black scale bars represent 30 μm. Green whiskers highlight the granular layer of Tomes. Blue whiskers highlight the hyaline layer of Hopewell Smith.

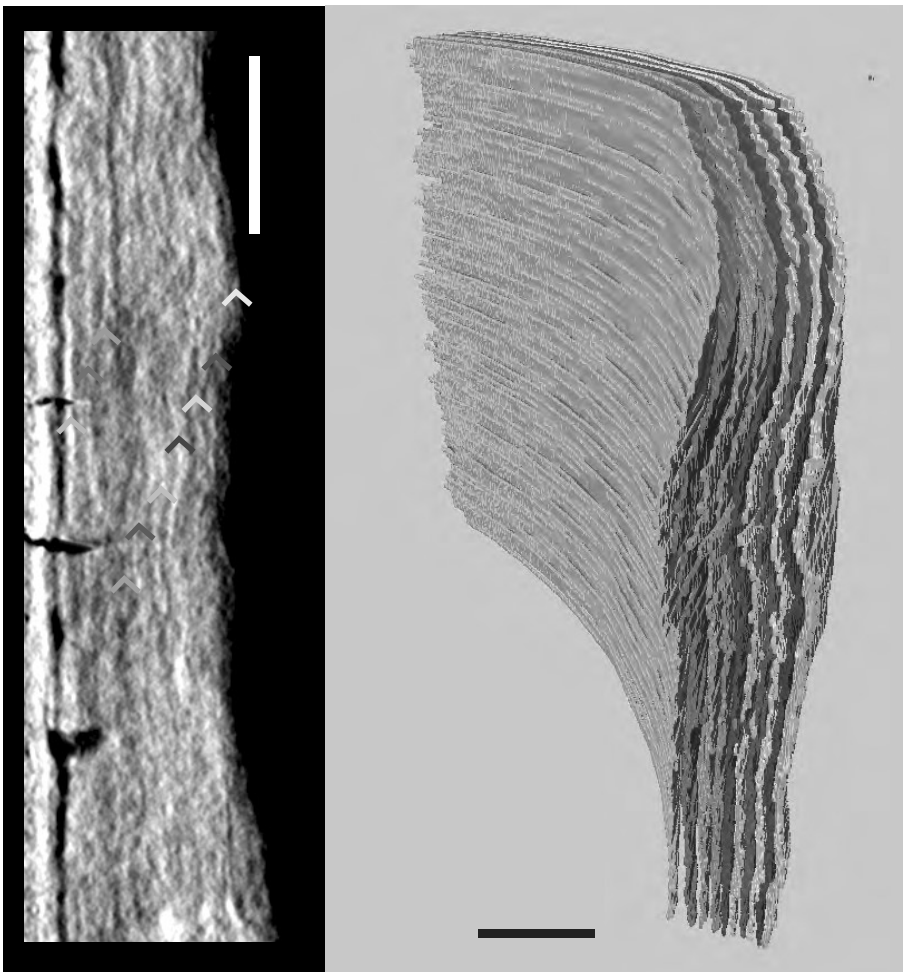

Figure 4.11. Example of 3D tomographic modelling of cementum increments in the male specimen k49. (**a**) Single tomographic slice displaying 10 increment pairs, highlighted with coloured arrows. (**b**) 3D model of increment patterns plotted through the majority of the scanned root**.** White scale bar in (**a**) and black scale bar in (**b**) equal 100μm.

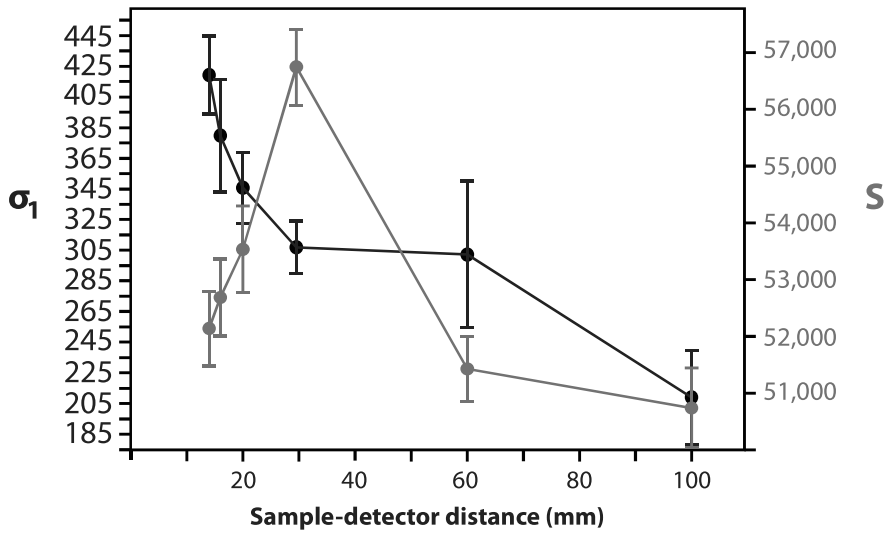

Figure 4.12. The relationship between the standard deviation of 16-bit greyscale values of background signal (σ1), and mean cementum 16 bit greyscale values (S) with increasing sample-to-detector propagation distance.

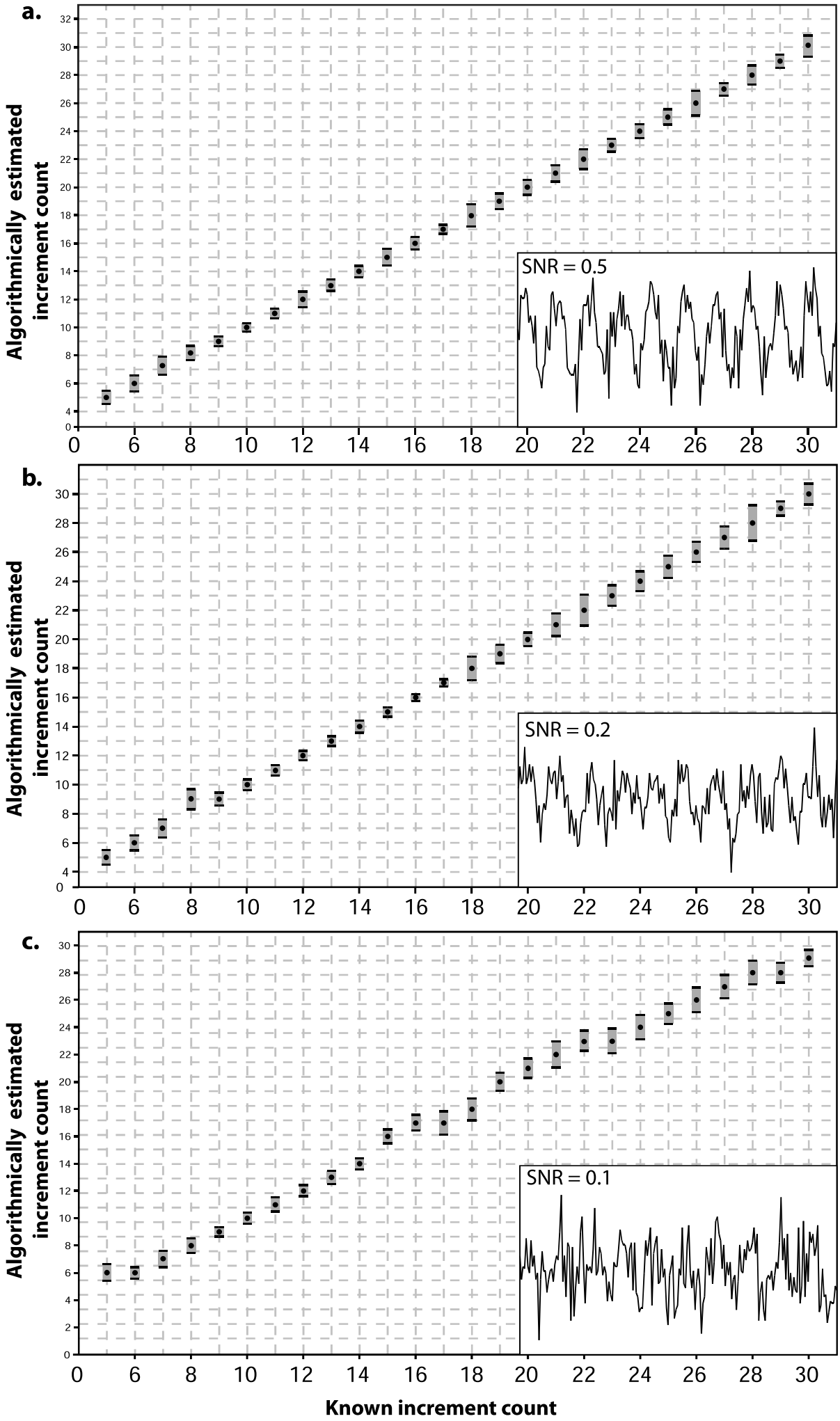
a.
b.
c.
Algorithmically estimated increment count
SNR = 0.5
SNR = 0.2
SNR = 0.1
Known increment count

Figure 4.13 (last page overleaf). Results of robusticity tests for algorithmic increment counts. (**a**) Counts (black circles) and their standard deviations (green boxes) for incremental sine wave patterns of between 5 and 30 increments with signal-to-noise ratios (SNRs) of 0.1-0.5. Inset; box displaying an example of a 10-increment pattern with an SNR of 0.5. (**b**) Counts and their standard deviations for incremental sine wave patterns of between 5 and 30 with SNRs of 0.6-0.8. Inset; box displaying an example of a 10-increment pattern with an SNR of 0.8. (**c**) Counts and their standard deviations for incremental sine wave patterns of between 5 and 30 with an SNR of 0.9. Inset: box displaying an example of a 10-increment pattern with an SNR of 0.9.

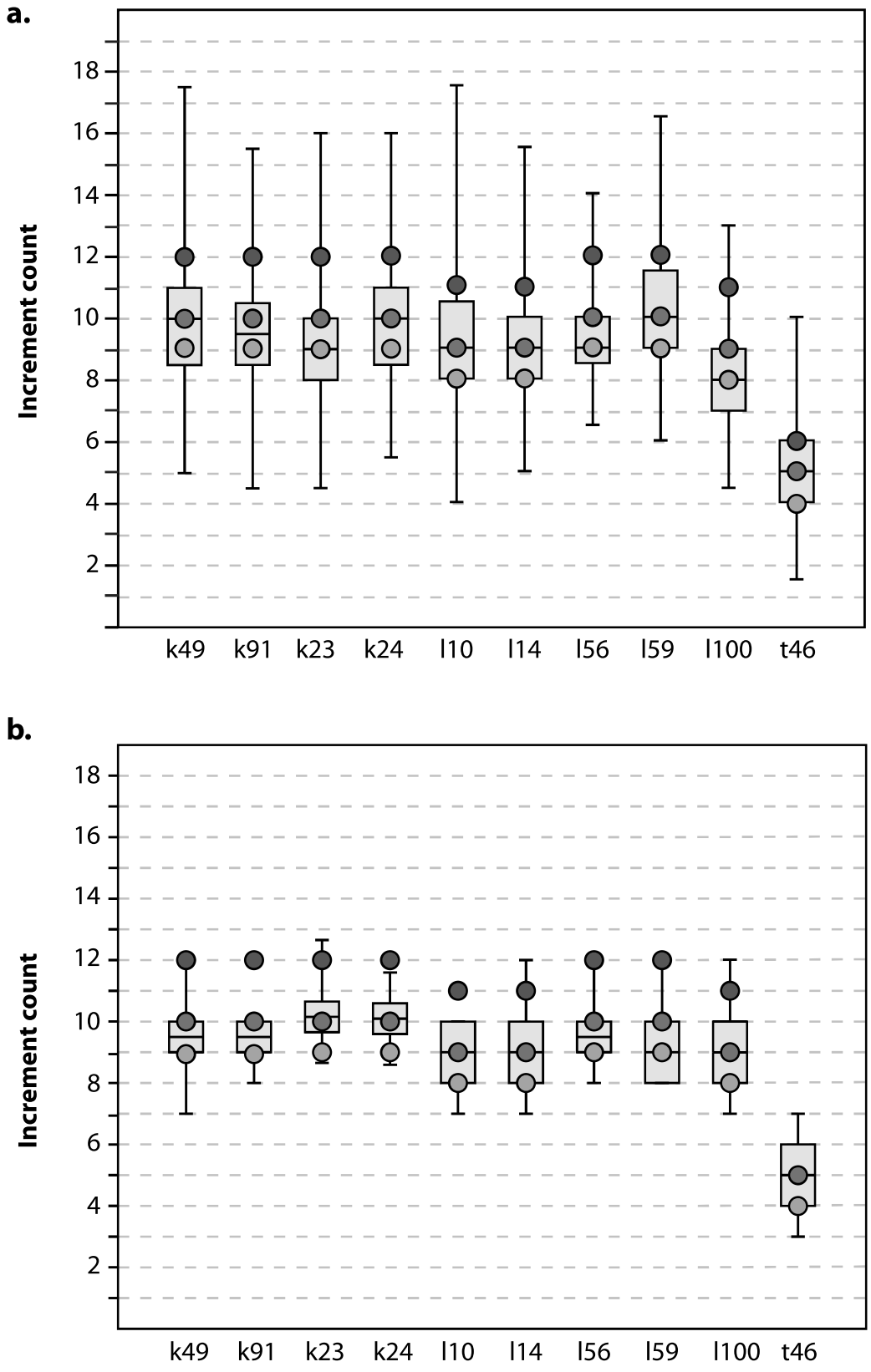

Figure 4.14. Results of two methods of increment counting. (**a**) Results of fully automated increment counts for each specimen. (**b**) Results of semi-automated increment counts for each specimen. Blue boxes represent the standard deviations of counts around the mean count (black line) for each specimen. green circles represent minimum expected counts. Red circles represent maximum expected counts. Purple circles represent known age of each specimen.

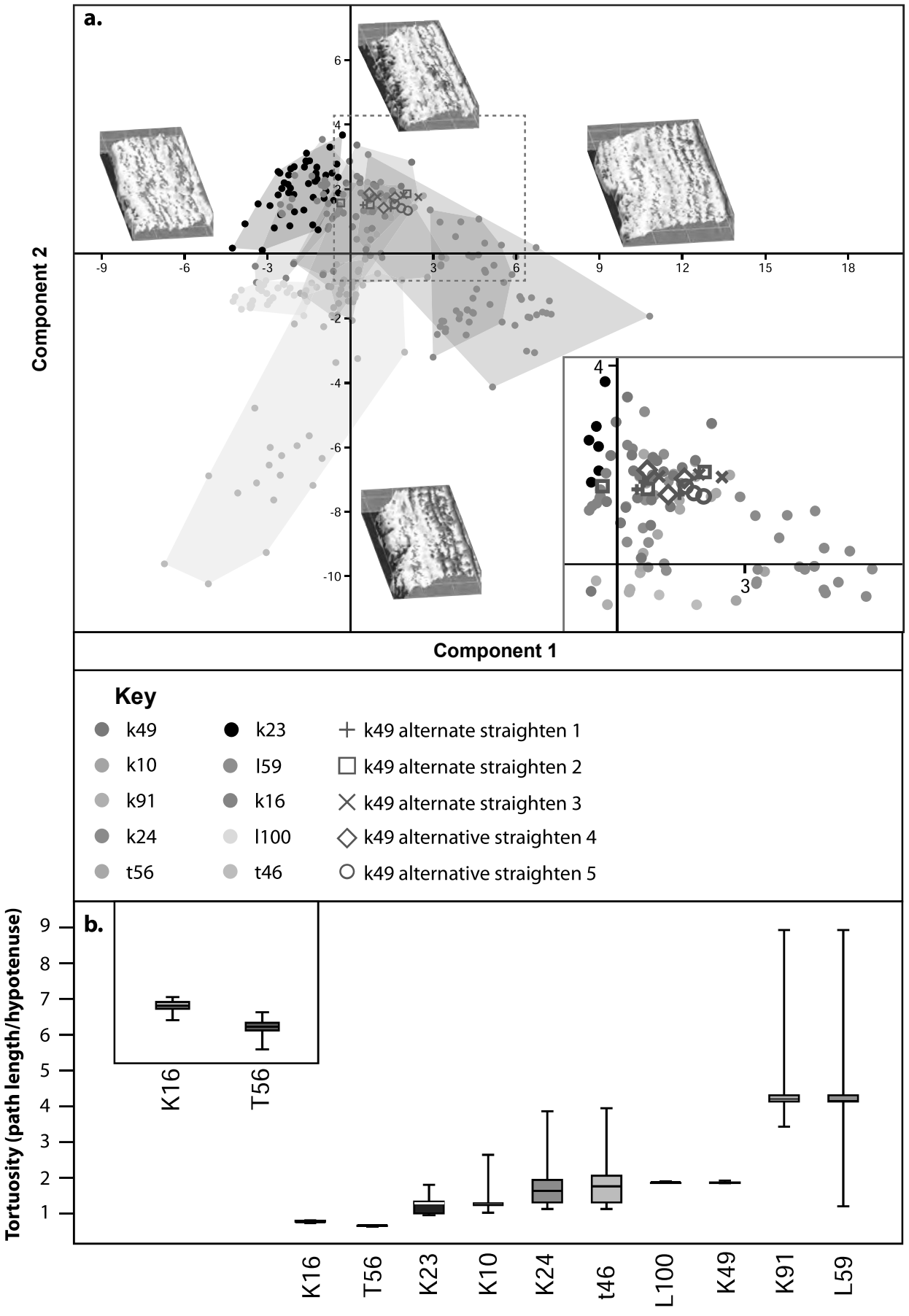
a.
Component 2
Component 1
Key
k49
k23
k49 alternate straighten 1
k10
l59
k49 alternate straighten 2
k91
k16
k49 alternate straighten 3
k24
l100
k49 alternative straighten 4
t56
t46
k49 alternative straighten 5
b.
Tortuosity (path length/hypotenuse)
K16
T56
K23
K10
K24
t46
L100
K49
K91
L59

Figure 4.15. Application of texture and tortuosity analyses to cementum data. (**a**) Results of principal components analysis of 21 texture metrics outlined in **Table 2.** Component 1 represents 33% of variation. Component 2 represents 22% of variation. Three-dimensional surface plots represent endpoints of each component. Inset red box highlights the position of alternate results for the k49 specimen based on different straightening attempts of the same region. (**b**) Results of tortuosity analyses. Coloured boxes represent standard deviations around the mean tortuosity value (black line within boxes) for each specimen. Whiskers represent highest/lowest values for each specimen.

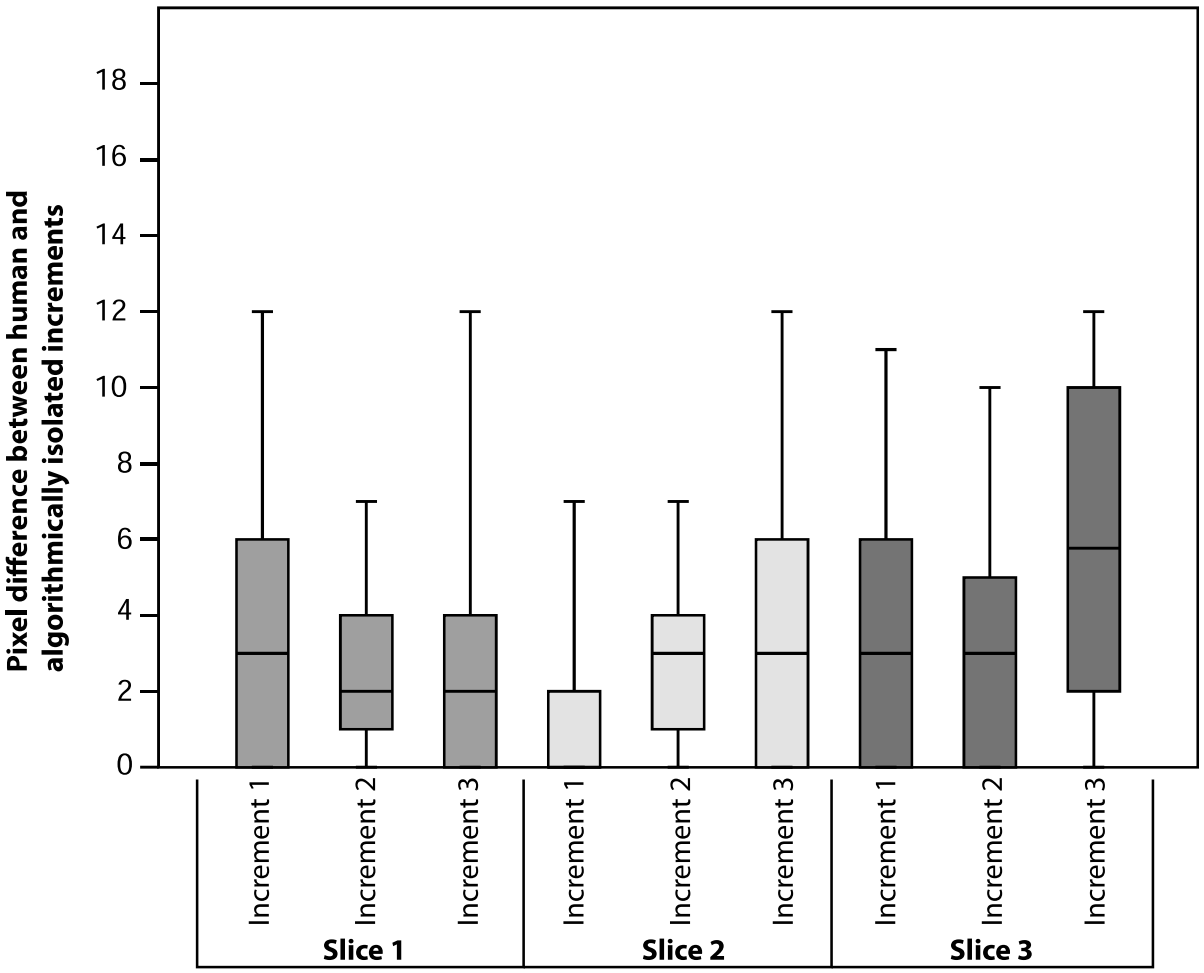

Figure 4.16. Comparison between manually isolated and algorithmically isolated cementum increments. Boxes represent the standard deviations around the mean (black line) difference in pixels between algorithmically isolated and manually isolated versions of the same increment in two-dimensional space. Whiskers represent the highest differences for each increment.

Specimen	Age	DOB	DOD	Expected increment count		Estimated increment count using solely computer vision		Estimated increment count using human and computer vision	
				Minimum	Maximum	Mean	Standard deviation	Mean	Standard deviation
l10	11	20.02.04	08.04.15	8	9	9	1.45	9	0.94
K91	12	06.10.03	10.04.15	10	9	9.5	0.97	9.5	0.5
t56	11	14.04.04	10.04.15	9	10	9	0.96	9.5	0.47
K24	12	12.03.03	08.04.15	9	10	10	1.45	10	0.47
K23	12	09.03.03	09.04.15	9	10	9	0.97	10	0.47
K49	12	09.04.03	08.04.15	9	10	10	1.46	9.5	0.5
l14	12	26.02.03	10.04.15	8	9	9	0.98	9	0.94
L59	11	17.04.04	09.04.15	9	10	10	1.46	9	0.94
L100	11	16.09.04	09.03.15	8	9	8	0.97	9	0.94
T46	5	11.04.10	07.07.15	4	5	5	0.97	5	0.94

Table 4.1. Age, expected and estimated cementum increment counts for the 10 female rhesus macaque (*Macaca mulatta*) individuals studied here.

Scan name	Energy (KeV)	Exposure time (ms)	Number of projections	Distance (mm)	Mean SNR	Mean CNR
SO20	19	150	1501	14	187.9	50.7
SO21	20	150	1501	14	123.8	56.9
SO22	21	150	1501	14	112.9	60.8
SO23	22	150	1501	14	82.6	35.5
SO24	26	150	1501	14	72	24.5
SO25	20	100	1501	14	118.3	50.7
SO26	20	125	1501	14	124	55.4
SO27	20	300	1501	14	177.8	72.3
SO28	20	150	3001	14	24 5.4	74.5
SO29	20	150	4501	14	25 2.7	81.5
SO30	20	150	6001	14	300.5	84.9
SO31	20	150	1501	16	14 2.2	59
SO32	20	150	1501	20	15 2.9	68.9
SO33	20	150	1501	28	18 5.6	75.2
SO34	20	150	1501	60	17 9.6	77.8
SO35	20	150	1501	1 00	247.4	54.9

Table 4.2. Image quality assessments of single distance phase-contrast reconstructions using differing tomographic experimental parameters. SNR; signal-to-noise ratio following Verdun et al. (2015). CNR; contrast-to-noise ratios following mohammadi et al. (2014).

Filter	*F* value	*p* value
Filter 2	167.2	<0.01
Filter 3	81.62	<0.01
Filter 4	59.7	<0.01
Filter 5	31.59	<0.01
Filter 6	15.67	<0.01
Filter 7	5.642	0.2
Filter 8	1.38	0.24
Filter 9	1.05	0.27
Filter 10	0.9	0.36

Table 4.3. Results of ANOVA comparisons of the modulation transfer functions of steerable Gaussian filters of increasing strength, with those of the original image of the cementum of male specimen t56.

	Increment count		
Transect	**Filter 2**	**Filter 3**	**Filter 4**
1	10	12	10
2	10	10	13
3	10	9	9
4	9	9	10
5	10	11	10
6	10	10	9
7	10	9	10
8	10	10	10
9	9	8	9
10	10	11	11

Table 4.4. Algorithmically generated counts of cementum increments along 10 transects in filtered images of individual t56.

Specimen	Age	DOB	DOD	Expected increment count		Estimated count using DCLA	
				Minimum	Maximum	Mean	Standard deviation
l10	11	20.02.04	08.04.15	8	9	15.1	3.414
K91	12	06.10.03	10.04.15	10	9	11.48	2.003
t56	11	14.04.04	10.04.15	9	10	12.32	2.968
K24	12	12.03.03	08.04.15	9	10	14	1.871
K23	12	09.03.03	09.04.15	9	10	13.577	1.58
K49	12	09.04.03	08.04.15	9	10	12.96	2.131
l14	12	26.02.03	10.04.15	8	9	11.963	1.315
L59	11	17.04.04	09.04.15	9	10	11.609	1.725
L100	11	16.09.04	09.03.15	8	9	13.08	1.73
T46	5	11.04.10	07.07.15	4	5	9	1.732

!

Table 4.5. Life history data, expected increment counts and estimated increment counts using digital cementum luminance analysis (DCLA) for each *Macaca mulatta* specimen studied.
DOB = date of birth; DOD = date of death

Parameter	Category	Description	*F* Value	*p* Value
Absolute average height of surface	hieght	average greyscale value	82	<0.001
relative average height of surface	height	average difference between greyscale values above the mean greyscale value and the mean greyscale value	35	<0.001
root mean square height of surface	height	root mean square greyscale value	40	<0.001
maximum peak height of surface	height	value of maximum greyscale peak above average	45	<0.001
average maximum peak height	height	average value of 10 highest greyscale peaks above average	50	<0.001
ten point average maximum peak height	height	10 point moving average value of 10 highest greyscale peaks above average	81	<0.001
minimum valley depth	height	value of lowest greyscale trough below average	87	<0.001
average minimum valley depth	height	average value of 10 lowest greyscale troughs above average	70	<0.001
ten point average mainimum valley depth	height	10 point moving average value of 10 highest greyscale peaks above average	26	<0.001
maximum skew	hybrid	The degree of symmetry of the surface heights about the mean plane	91	<0.001
summit density	hybrid	number of greyscale peaks per unit area	9	<0.001
maximum kurtosis	hybrid	The prominance of inordinantely high peaks and/or deep valleys	30	<0.001
root mean squared gradient of surface	hybrid	root mean square of greyscale slopes, evaluated over all directions	183	<0.001
developed interficial area ratio	hybrid	percentage of additional surface area contributed by the texture as compared to an ideal plane the size of the measurements region	37	<0.001
surface area ratio	functional	ratio between absolute surface area and pixel number	83	<0.001
core roughness depth	functional	proportion of material occupied by the core	79	<0.001
average peak height above core	functional	average difference in greyscale between peaks above the maximum core greyscale value, and the maximum core greyscale value	16	<0.001
average valley depth below core	functional	average difference in greyscale between toughs beolw the minumum core greyscale value, and the minimum core greyscale value	41	<0.001

surface bearing area ratio	functional	proportion of the surface that consists of peaks above the core material	93	<0.001
Autocorrelation length	spatial	horizontal distance of the autocorrelation function (ACF) which has the fastest decay to the value 0.2. **Large value**: surface dominated by low frequencies; **low value**: surface dominated by high frequencies	108	<0.001
texture aspect ratio	spatial	ratio from the distance with the fastest to the distance with the slowest decay of the ACF to the value 0.2-0.3.	17	<0.001

Table 4.6. Texture metrics, their explanation, and results of ANOVA comparisons between their results between *Macaca mulatta* specimens.

Parameter	*F*	*p*	Correlation with increment count			Correlation with increment contrast		
			r^2	*p*	Positive/negative	r^2	*p*	Positive/negative
mean height	>100	<0.001	0.5	<0.001	positive	0.98	<0.001	positive
root mean squared height	>100	<0.001	0.54	<0.001	positive	0.99	<0.001	positive
maximum peak height	>100	<0.001	0.67	<0.001	positive	0.44	0.001	positive
average maximum peak height	>100	<0.001	0.63	<0.001	positive	0.52	<0.001	positive
minimum valley depth	>100	<0.001	0.95	<0.001	positive	0.3	0.01	positive
average minimum valley depth	>100	<0.001	0.96	<0.001	positive	0.4	0.06	positive
ten point average maximum height	>100	<0.001	0.89	<0.001	positive	0.51	0.001	positive
summit density	>100	<0.001	0.95	<0.001	positive	0.15	0.08	negative
root mean squared gradient	>100	<0.001	0.99	<0.001	positive	0.03	0.47	negative
surface area ratio	>100	<0.001	0.94	<0.001	positive	0.02	0.52	-
developed interficial ratio	>100	<0.001	0.99	<0.001	positive	0.02	0.5	-
core roughness depth	>100	<0.001	0.03	0.46	-	0.29	0.02	negative
mean peak height above core	>100	<0.001	0.42	0.003	positive	0.4	0.003	positive
mean valley depth below core	>100	<0.001	0.36	0.008	positive	0.007	0.73	-
surface bearing area ratio	>100	<0.001	0.91	<0.001	positive	0.03	0.49	positive
gradient direction	>100	<0.001	0.74	<0.001	negative	0.37	0.005	-

!

Table 4.7. Results of ANOVA comparisons between increment models for each texture parameter, and least squares regression between parameter value and increment count, and contrast.

Image	Length (pixels)	Euclidian distance (pixels)	Tortuosity	Algorithmically calculated tortuosity	Difference between tortuosity values
1	1355.675	882.11	1.53	1.52	0.01
2	1633.565	932.695	1.75	1.7	0.05
3	2834.685	930	3.048	3.02	0.03
4	2383.204	906.02	2.63	2.66	0.03
5	2982.082	948.675	3.14	3.07	0.07
6	1025.169	927.573	1.11	1.11	0
7	1083.921	944.765	1.15	1.15	0
8	1031	862	1.196	1.19	0.01
9	1235	920	1.342	1.32	0.02
10	1345	912	1.475	1.44	0.03

!

Table 4.8. Comparisons between algebraically calculated and algorithmically calculated tortuosity values for digital phantoms of known length.

Slice	*F* Value	*p* Value
1	0.33	0.72
2	0.83	0.46
3	0.24	0.79
4	0.43	0.66
5	0.84	0.45

Table 4.9. Results of ANOVA comparisons between three different straightened datasets of five tomographic slices sampled randomly from the k49 dataset.

Chapter 5.

Exploring the relationship between life history and cementum growth

This chapter outlines a series of experiments designed to test the hypothesis that differences in physiology between male and female mammals influence cementum growth and structure to a significant degree. The biological reasoning for this hypothesis is discussed, before introducing the experimental samples and design. Here, the novel methodologies for studying cementum outlined and tested in **chapter 4** are used for the first time to test for sexual dimorphism in cementum structure and increment shape in both rhesus macaques (*Macaca mulatta*), and archaeological human populations from two different time periods. Our results, although preliminary, suggest that quantitative analysis of cementum structure and texture may be used to identify sex in primates of unknown life history. Pregnancy events have also been distinguished by a unique suite of increment morphologies that may also be used in the future to predict pregnancies in females of unknown life history. We suggest that the refinement of these techniques and validation using large samples will pave the way for their use in a range of disciplines from anthropology to forensic criminology. An example of such application is given through the pilot study of a single Neanderthal lower first molar (m1) tooth, potentially sexed as a female using our techniques.

5.1. Introduction

5.1.1. Exploring the relationship between sexual physiology and cementum growth

As the only mineralized dental tissue to continue growth throughout life, cementum growth is likely to be directly and/or indirectly effected by several aspects of oral health. Further, as the majority of collagen fibres within cementum originate from the periodontal ligament (Sharpey's fibres), its growth is also directly affected by periodontal health and disease. It is widely accepted in both anthropological and clinical literature that female humans encounter a higher rate of periodontal and dental disease than males, and this pattern is ubiquitous both temporally and geographically (Haugejordan, 1996; Hillson, 2001; Lukacs and Largaespada, 2006). The preferred explanation of this pattern in the anthropological literature is sexual partitioning of labour, with females having more access to food supplies and snacking during food preparation (in traditional societies) (Walker and Hewlett, 1990; Cohen and Bennett, 1993; Larsen, 1995). However, this cannot explain the continued sexual differences in oral health exhibited in more developed societies and even in sub-adults (Mansbridge, 1959; Lukacs and Largaespada, 2006). A steady stream of clinical research has highlighted several key physiological differences between female and male oral environments that may help to explain these differences without the need for invoking such complex behavioral hypotheses (Muhler and Shafer, 1955; Percival et al., 1994; Leimola-Vitranen et al., 2000; Friedlander, 2002; Dodds et al., 2005; Russell and Mayberry, 2008).

A growing body of studies has begun to link fluctuations in certain hormones to oral health in mammals. Several studies on populations of laboratory animals have revealed that instances of dental disease increase proportionally with increasing levels of estrogen and progesterone, the series of gonadal steroid hormones responsible for promoting secondary female sexual characteristics (Fig. 5.1) (Muhler and Shafer, 1955, 1955; Delman, 1955; Laine et al., 1988; Liu and Lin, 1973; Person et al., 1998). Conversely, increases in androgen levels, the gonadal hormones responsible for promoting male secondary sexual characteristics, had no significant effect on oral health (Shafer, 1954; Delman, 1955; Laine et al., 1988; Liu and Lin, 1973; Legler and Menaker, 1980).

The root cause of this relationship between estrogen and dental health was believed to have been identified by Muhler and Shafer (1955), who found that increased

levels of estrogen led to decreased thyroid activity and a reduction in saliva flow rate. Saliva plays several important roles in promoting oral health, including physically protecting tooth crowns, buffering pH levels and so neutralizing bacterial acids (Lenander-Lumikari and Loimaranta, 2000), and hosting antimicrobial agents that break down pathogenic organisms (Marsh, 1999). Further, clinical studies on both animals and humans have revealed sexual differences in the composition and flow rate of saliva (Percival et al., 1994; Dodds et al., 2005). Females are consistently found to have lower rates of saliva production than males, and this is resistant to other factors known to effect saliva production including disease, medical procedures and medications. Reduction of saliva flow has been shown to have a significant detrimental impact on oral health, with increased rates of caries (Lukacs, 2011), and gingivitis (Bergdahl, 2000).

The negative impacts of estrogen on oral health have been shown to rapidly accelerate during puberty and pregnancy, and fluctuate through the menstrual cycle (Lukacs and Largaespada, 2006). These effects extend to the periodontium as well as caries in teeth (Gajendra and Kumar, 2004, Silk et al., 2008). The dramatic rise in production of estrogen and progesterone during puberty is accompanied among females by a proportional increase in gingival inflammation and bleeding. Several studies have also shown a concomitant increase in subgingival bacteria during puberty in females (Hefti et al., 1981; Mombelli et al., 1989; Mealey and Moritz, 2003). Such microbial changes have been suggested to be due to preferential enhancement of these bacteria by female sex hormones (Mealey and Moritz, 2003). Further, significant and observable gingival inflammatory changes have been documented in association with the menstrual cycle. Bleeding and swollen gingiva, and increased tooth mobility have all been reported during ovulation. For example, Hugoson (1971) described an increase in gingival disease of at least 20% during ovulation in more than 75% of a sample of 26 women. The extracellular matrix, gingival vessels and periodontal fibroblasts are all affected by hormonal change. Interaction with various growth hormones and steroids causes activation of proteolytic enzymes from fibroblasts and epithelial cells, which breakdown connective tissue extracellular components of the gingiva including primary collagen. Increased concentrations of estrogen and progesterone have also been shown to stimulate several signaling proteins (cytokines) involved in gingival inflammation, and so may exacerbate symptoms of gingivitis. Finally, the conversion of estrone to estradiol (two of the primary forms of estrogen) has been shown to increase in inflamed

gingiva, and estradiol is known to negatively impact collagen metabolism (Silk et al., 2008).

Fluctuations in female sexual hormone levels are thus expressed directly and indirectly as damage to the gingiva, periodontium and tooth crowns (Fig. 5.1). As these effects include the disruption of growth and breakdown of both periodontal and cementum cells, this damage has the potential to extend to the cementum. As yet there have been relatively few studies exploring possible sexual dimorphism in cementum structure. Kolb (1978) identified significant differences in the timing of formation and proportion of dark 'slow growth' bands in the cementum of male and female foxes (*Vulpes* vulpes). Males showed a consistently thicker slow growth band that was initiated earlier in the year than females. This was also shown in the cementum of European lynxes (*Lynx lynx*) by Kvam (1984).

The techniques introduced and validated in **Chapter 4** have the power to distinguish a wide range of variation in cementum structure and increment shape between samples. Their application for comparison between known female and male individuals may highlight previously unknown sexual dimorphism in dental cementum in primates created via sexual differences in hormonal regimes.

5.1.2. Effects of pregnancy on oral health and dental cementum

Pregnancy is an intensive life history event, and creates substantial pressure on a mother's metabolism. This pressure is known to manifest itself in various hormonal changes (Boggess, 2008), increased nutritional demand on the mother (Bucher et al., 1996), and the harvesting of various minerals from calcified hard tissues (Surarit et al., 2016). These factors have been hypothesised to influence the growth of cementum through the pregnancy term (Coy and Garshelis, 1992; Medill et al., 2010). The periodicity of cementum deposition allows for the entire term of pregnancy to be recorded in most mammals; either during a single increment for animals with gestation periods of <6 months, or during an incremental pair (one light increment followed by one dark increment) for animals with 6-12 month gestation periods. Correspondence between increment width and opacity with pregnancy have been found in the Atlantic walrus (*Odobenus rosmarus* rosmarus; Klevezal, 1995), black bears (*Ursus* americanus; Coy and Garshelis, 1992), ringed seals (*Phoca hispida*; Stewart at al., 1996), humans (Kagerer and Grupe, 2001), northern sea otters (*Enhydra* lutris; Biela et al., 2008), and

most recently polar bears (*Ursus maritimus*; Medill et al., 2010). However, the cause of this phenomenon during pregnancy is rarely discussed beyond increased metabolic demand (Medhill, 2010).

Hormonal changes in the blood, and changes to oral bacterial flora in the saliva are known to cause adverse effects on dental and oral health during pregnancy. Silk et al. (2008) outline the three most common pathologies that affect the gingiva, teeth and periodontal tissue in pregnant women. Gingivitis is the most common oral disease in pregnancy (60-75% prevalence found in Silk et al., [2008]). During pregnancy, inflammation of the superficial gum tissue is aggravated by fluctuations in estrogen and progesterone levels (key hormones involved in maintenance of pregnancy), as well as changes in oral bacterial flora and suppressed immune response. These factors have also been attributed to increased levels of periodontitis during pregnancy, the destructive inflammation of the periodontium. This process involves bacterial infiltration of the periodontium, producing toxins that stimulate a chronic inflammatory response. The periodontium is eventually broken down and destroyed and teeth loosen. Tooth loosening is the third common pathology known during pregnancy, and can occur without prominent levels of gingivitis or periodontitis. This phenomenon has frequently been attributed to increases in estrogen and progesterone during pregnancy, although the mechanisms for increased movement in the absence of gum disease is poorly understood.

The most significant hormonal change during pregnancy is increased production of the steroid hormones estrogen and progesterone. This is mainly due to the development of the placenta, which becomes the main source of both hormones from the second trimester in humans. Estrogen and progesterone serve important roles during pregnancy; increasing basal metabolic rate, modulating the immune system and effecting the vascular system. Concurrent damage to the gingiva and oral tissue is proportional to this significant influx of hormones. Damage and inflammation to gingival tissue also releases macrophages. These are important immune-cells that play a significant part in tissue remodeling by inhibiting tissue breakdown through proteolysis. Pregnant women with clinical gingivitis have been shown to have low concentrations of plasminogen activator inhibitor type-2 (PAI-2), the proteolysis-inhibitor produced by macrophages, relative to non-pregnant women. This reduces the protection of periodontal connective tissue in pregnant women (Kinnby et al., 1996).

In addition to progesterone and estrogen, prolactin is an important hormone

during pregnancy, to ensure adequate calcium supply for fetal development and production of breast milk. As such, prolactin has been shown to be a prominent calciotropic hormone, responsible for resorption of bone and donation of calcium to the fetus. It has been recently shown for the first time that prolactin may have a similar function in the periodontal ligament (PDL). In an *in-vitro* study by Surarit et al. (2016), prolactin receptors were found within the PDL. Further, when the PDL is exposed to concentrations of prolactin similar to those experienced during pregnancy, the stemness potential of PDL cells (that can usually proliferate into a wide range of cells including cementoblasts, osteoblasts and fibroblasts), is heavily reduced and the formation of osteoblasts heavily selected for, as opposed to other tissues including cementoblasts.

It is clear that the substantial changes to hormone levels during pregnancy considerably alter a mother's gingival biology. In particular the destruction, suppression of growth and resorption of periodontal connective tissue may significantly affect the cementum. Growth of acellular cementum is triggered and sustained by fibroblasts and cementoblasts originating in the PDL. So damage to these cells and a reduction of their proliferation from periodontal stem cells during pregnancy is highly likely to have a direct impact on the growth of cementum and quality of cementum matrix. Further, a primary component of the acellular extrinsic fibre cementum is collagenous Sharpey's fibres. As these originate from within the PDL, the joint effects of proteolytic enzymes and estradiol on periodontal collagen formation may add to the negative effects of pregnancy on cementum growth.

The effects of pregnancy can thus be expected to extend to cementum growth. A correspondence between pregnancy events and cementum structure and texture has been inferred several times in previous studies (Kagerer and Grupe, 2001; Medill et al., 2010), and all previous studies suggest a similar effect of pregnancy on observed increment structure. However, previous studies on animals have been field-based, and human studies have relied on long-period data of life histories based on direct questioning of patients. These techniques lack sufficient control of samples and rely on anecdotal and indirect evidence of pregnancy events. This is reflected in their limited power for prediction and estimation of pregnancy events in animals of unknown life history.

The only study known to use cementum measurements to generate a predictive model for pregnancy events was by Medill et al. (2010). Analysis of cementum

increments was here performed on a large sample (>300) of individual polar bears, from a monitored population in the Western Hudson Bay, Canada. Pregnancy events and subsequent periods of parturition were recorded in the field using evidence of females with cubs that appeared less than one year old. The differences between the "growth layer group" (GLGs; one thick light increment and its corresponding thin dark increment) formed during pregnancy and the previous GLG was measured, along with the difference between the two previous GLGs (when applicable). These measurements were then inputted into a logistic regression model. The GLG width difference estimated to provided even (1:1) odds between 'cub' (pregnant) and 'non-cub' (non-pregnant) was then used as a threshold in a predictive model subsequently used to estimate other pregnancy events in a blind test. This model predicted known pregnancy events with 71% accuracy in females with recorded life histories. However, when the model was applied to male polar bears, 40.6% had similar reductions in GLG growth as those seen during pregnancy. This identifies a substantial shortfall in this model, as it is not yet refined enough to determine sex in a population of unknown demographic. The fact that similar results can be generated in both male and breeding female individuals also suggests that further refinement of this methodology is needed, before pregnancy can be confidently estimated in populations and samples of unknown life history and demographic.

The primary elements of experimentation that need to be improved beyond those of previous studies are the level of control of the sample under study, and the sensitivity/robusticity of the techniques used to compare increments formed during pregnancy and all other increments. These techniques must be able to distinguish females that have undergone pregnancy from females that have not undergone pregnancy, and males in order to be used to confidently estimate pregnancy events in samples of unknown sex and age demographic. These in-turn need to be based on comparison between increments formed under no otherwise extenuating circumstances except for the advent and continuation of pregnancy, with increments formed under identical (or as close to identical as possible) external and nutritional conditions. Through the study of laboratory animals with controlled life histories, and monitored reproductive activity, this research project has attempted to meet these parameters for the first time.

5.2. Experimental design

In addition to the 10 female rhesus macaque (*Macaca mulatta*) specimens studied in **chapter 4**, the m1 teeth of two breeding females, one juvenile female, and one male *M. mulatta* specimen were also studied at the TOMCAT beamline of the Swiss Light Source synchrotron facility (SLS) from 04/03/2016 – 07/03/2016. A sample of archaeological human m1 teeth was also studied during this experiment, originating from a C12th population from Taunton, UK. A second three-day experiment was conducted at the TOMCAT beamline from 07/03/2017-10/03/2017, focused on a second sample of archaeological human teeth from C19th Bristol (UK). Both archaeological samples were composed of individuals of known sex. The C12th sample also contained two individuals that could not be sexed using osteoarchaeological metrics. The C19th sample contained three individuals of known age and life history (Table 5.1).

The *M. mulatta* sample was closely monitored through life. Members of the population were allowed to breed at will, and pregnancy events were closely monitored and recorded (Table 5.1). All other aspects of life history (e.g. diet, climate) were identical between individuals. As pregnancy was the only variable allowed to change during the individuals' life histories, the nature of this sample has offered an unprecedented level of control for comparisons between increments formed during pregnancy and those formed otherwise. This, alongside previous validation of the precision and accuracy of SR CT imaging for identifying individual cementum increments (**Chapter 4**), allowed for confident assessment of the effects of pregnancy on cementum growth and structure.

The C12th archaeological human sample originates from the 2005 excavation of the medieval church and cemetery of St Peter and St Paul, Taunton (South Western UK). The cemetery is believed to have been in use from at least AD 1342 (the date of completion of the church; Bush, 1984), until its dissolution in AD 1549. The site was split into five discrete areas during excavation. Two sites were located within the church and priory (sites two and five), and the other three were located within the cemetery. All specimens studied here originate from the cemetery, apart from one male individual (SK5010), that originates from site five within the priory. only teeth from individuals that had been sexed using osteoarchaeological parameters were chosen (sexed by Kate Robson Brown following: Brothwell, 1981; Buikstra and Ubelaker, 1994; Schwartz, 1995; Mays, 1998). The sample studied here consists of three male individuals (sk2011,

sk2072 and sk2203), two females (sk1404 and sk5010) and two individuals of unknown sex (sk1634 and sk2201).

The C19th archaeological human sample originates from a 2007-2008 excavation of the former Roman Catholic convent and chapel of St Catherine of Sienna (later the Bristol Steiner Waldorf School), and a 2016 excavation of a section of the cemetery of St Georges Church, Bristol. Both sites originate from burial activity between 1820-1885. The subsample of four individuals (sk62, sk39, sk11 and sk36) originating from the convent of St Catherine of Sienna have all been sexed using osteoarchaeological parameters and are all designated as female. The three individuals studied from the St Georges church cemetery are associated with coffin plates, and so could be investigated in further detail for aspects of life history including age in years, sex and potential recorded pregnancy/birth events. Harriet Packer (sk53) died at 46 years of age, after having one child at 28 years of age. Harriet Rogers (sk334) died at 51 years of age, after having seven children between the ages of 28 and 44. Finally, Richard Baily (sk228) died at 61 years of age.

The experimental parameters for synchrotron radiation computed tomographic (SR CT) imaging were kept consistent, following those used in **Chapter 4** for each experiment. All *M. mulatta* specimens and C12th archaeological specimens were prepared following **Chapter 4 section 4.4**. Within the C19th sample, teeth from the three named specimens with recorded life histories remained complete, while all other specimens were prepared following **Chapter 4 section 4.4**. The considerably larger size of the un-processed teeth required different experimental parameters to overcome the problem of dentine density (see **Chapter 4 section 4.5.**). Thus, following a quantitative comparison of a range of scanning parameters (Appendix 5.2.), these specimens were scanned using 24 KeV X-ray energy, 275 ms X-ray exposure, 4501 angular projections and 74mm sample-to-detector distance. All phase contrast reconstructions of SR CT data of mechanically processed teeth used the same δ and β values used in **Chapter 4 section 4.2.5**. However, the three unprocessed teeth required a δ value of 9.00 e^{-9} and a β value of 5.00 e^{-5}.

The level of control offered by the *M. mulatta* sample for studying the effects of pregnancy and sexual physiology on cementum growth provides an ideal test for the robusticity of the methods outlined in **Chapter 4** for identifying discrete biological differences in cementum structure and increment shape. Finding such differences between the cementum of breeding female, non-breeding female and male *M. mulatta*

specimens would suggest that these methods may be used to identify sex, and potentially pregnancy events, in primates of unknown life history. Finally, their application to the cementum of both archaeological samples will serve as a further test of their predictive power, and whether they are robust to other factors that may affect archaeological cementum, including taphonomy and diagenesis.

5.3. Results

5.3.1. Sexual dimorphism in *Macaca mulatta* cementum

Qualitative comparison between the cementum increments of male and female *M. mulatta* individuals suggests several discrete differences between their structure and shape. Male cementum increments follow relatively uniform (low tortuosity) transects both transversely and longitudinally through the tissue, and are of roughly equal thickness (Fig. 5.2). Female increments are considerably more chaotic and follow conflicting, tortuous transects through the cementum that produce complex patterns as well as lensing and coalescence (Fig. 5.2). The effects of this tortuosity are compounded through the cementum, often resulting in severe tortuosity in the outermost increment. Female increments also show considerably lower contrast than male increments, and are more poorly organized with lower directionality and higher isotropy than male increments (Fig. 5.2).

Following cementum isolation, straightening and filtering, the quantitative analysis of two-dimensional increment tortuosity supports qualitative inference of higher tortuosity within female cementum increments. Every sample of isolated female increments produces significantly higher tortuosity values when compared to the male sample when compared using ANOVA (Table 5.2, Fig. 5.3.a.).

Quantitative analysis of cementum ‘texture’ (greyscale distribution) also indicates significant differences between female and male cementum. Of the 21 available texture metrics defined in our algorithm, all but three (“ten point average maximum peak height”, “average maximum height” and “core height”) produced significant differences between male and female cementum using ANOVA comparisons (Table 5.3). When the results of these 18 metrics are combined into a principal components analysis, male cementum and female cementum occupy clearly separated regions of ‘texture space’. Principal component one (41% of variance) represents

strength of increment organization, with higher scores reflecting higher isotropy, weaker increment organization and more chaotically arranged increments. Principal component two (33% of variance) represents increment contrast, with higher scores reflecting higher contrast between increments. Juvenile female cementum also occupies its own region of 'texture space', away from both mature female and male cementum. However, there is substantial overlap between non-breeding and breeding female cementum (Fig. 5.4), and the texture of four juvenile slices overlaps into breeding female texture space.

5.3.2. Pinpointing episodes of pregnancy in *Macaca mulatta* cementum

Although they are subtle, a series of hallmarks can be noted that distinguish increments formed during pregnancy events and surrounding increments in the breeding female *M. mulatta* subsample. Increments formed during sexual immaturity consistently provide the highest grey values for each female specimen. Following the advent of sexual maturity (after the third cementum increment, following an average attainment of sexual maturity at four years old in *M. mulatta* females), increments become considerably less well defined and produce lower grey values (Fig. 5.5). The only increments that present comparable grey values to immature increments are formed during pregnancy. These increments are also considerably less well defined than other increments. The first episode of pregnancy is usually the most clearly delineated, as the hypomineralised band formed that year is the thickest and most highly contrasting of any band formed during adulthood (Fig. 5.5). This band is also the site of the most common coalescence of cementum increments, with both the earlier and later light increment merging with it throughout its radial length.

Although they are less obvious than the first pregnancy event, thick hypomineralised bands and complex increment patterns also mark other pregnancy events. Hypomineralised bands formed during pregnancy often truncate, split and coalesce with the accompanying hypermineralised band. The hypomineralised band immediately following increments formed during pregnancy commonly cuts into and coalesces with this increment, in a manner rarely seen in increments formed under 'regular' circumstances. These complexities are not exhibited in male cementum and only rarely in non-breeding female cementum (Fig. 5.f-i.).

Blind sampling of random SR CT slices from each breeding female specimen tested the predictive power of these hallmarks of pregnancy on cementum increment

structure. Slices were inspected for hypomineralised bands of anomalous thickness and contrast formed after the third increment from the cemento-dentine junction, and regions of significant lensing and coalescence of increments. For each slice, the position of the increments where these phenomena were observed was noted within the cementum. The position of these anomalous increments was then compared to the expected incremental position for each pregnancy event.

All pregnancy events coincided with an increment possessing either a hypomineralised band of anomalous greyscale, common and significant coalescence with the immediately following light band, or both (Appendix Table 5.1.). However, in several specimens, there were additional increments that displayed these features that did not directly correspond to individual pregnancy events. These were individuals that underwent pregnancy events every year for several years, with one year between them without pregnancy (e.g. l72, Fig. 5.e.). The majority of non-pregnant increments exhibiting hallmarks of pregnancy occurred during these years sandwiched between multiple pregnancy events.

The results of these blind tests suggest that pregnancy events are recorded in the cementum by disrupting cementum growth in a characteristic fashion. This disruption is significant, and distinct enough to provide predictive power. However, the precision of predictions is so far restricted, as the effects of repeated pregnancy events may extend into the year immediately after the last pregnancy event, with the increment formed this year mimicking those deposited during pregnancy.

5.3.3. Sexual dimorphism in archaeological human cementum

Female cementum differs from male cementum in the same way in the *M. mulatta* and both archaeological human samples. Increments of female cementum in the C12th sample are more tortuous and less defined in female cementum. This has also been shown quantitatively by comparing tortuosity and texture. In both samples female cementum increments are consistently more tortuous than male increments (Fig. 5.3.b-c) (Table 5.4).

Female and male cementum SR CT slices also occupy distinct regions of ‘texture space’ within each archaeological sample (Fig. 5.6). For the C12th sample, principal component one represents 44.4% of variance, and reflects the strength of contrast between increments and strength of incrementation, with higher values

providing more contrast between increments than lower values. Principal component two represents 25.2% of variance reflecting the level of organization of increments, with higher values providing lower isotropy and stronger orientation of increments. Although the majority of male and female slices occupy their own respective region of texture space, there is overlap between them in the C12th sample, with 1 male slice overlapping into female texture space (Fig. 5.6). When the two specimens of unknown sex are included in PCA analysis, specimen SK2201 occupies female texture space, while specimen SK1634 occupies its own texture space, separated from all other specimens by the most significant degree in the entire sample (Fig. 5.6).

The C19th sample also exhibits distinct female and male regions of texture space for each tooth type studied. When PCA is used to compare the m1 teeth of female versus male cementum from the C19th century sample, female slices are significantly separated from males along principal component one. This represents 44.2% of variance, reflecting the degree of organization of cementum increments, with male increments being significantly less isotropic. However, the male specimen SK228 overlaps with female specimen SK53 along principal component two. This represents 34.6% of variance and reflects the level of contrast between cementum increments (Fig. 5.7.a.). For lm2 teeth, female and male cementum slices are separated along principal component two, accounting for 28.7% of all variance. However, there is no clear separation between the sexes along principal component one, accounting for 41.3% of all variance, as male cementum plots between both female specimens (Fig. 5.7.b.).

Finally, although both samples individually show sexual dimorphism in cementum texture and increment tortuosity, this is less pronounced when the samples are merged (Fig. 5.8). Principal component 1 (51% of variance) represents increment organization, with higher scores reflecting more isotropy and lower organizational strength. Principal component one still separates female from male cementum slices in both samples. However, C19th male texture space substantially overlaps C12th female texture space. The C12th data is reversed along principal component one. Although the original shapes of both female and male texture spaces are retained, there is considerably more overlap between them and male cementum slices now produce lower scores along this component than female. Principal component two (21% of variance) reflects differences in the strength of contrast, with higher values reflecting higher contrast between light and dark increments. Trends in the C19th sample originally seen along principal component two are instead reflected along principal component one,

although again there is considerable overlap between female and male texture spaces in the combined texture space. In summary, although there is still a sexual signal within combined PCA texture space, this is weakened. The primary source of variation instead can be interpreted as site-specific.

5.3.4. Pinpointing episodes of pregnancy in archaeological human cementum

Known pregnancy episodes are more difficult to distinguish in the cementum of two human females with known pregnancy events, in comparison with *Macaca mulatta* cementum. This is chiefly due to the density of cementum increments in human cementum. For instance, the m1 root of sk53 has 39 increments within 130 μm radial thickness, with individual increments ranging from ~1.3 μm to 11 μm in thickness (Fig. 5.9.a.). This has made it difficult to determine individual increments by eye and follow their trajectories. However, although the qualitative effects of pregnancy determined in *M. mulatta* cementum are difficult to identify in humans, there are significant differences between increments formed during pregnancy and other increments.

Sk53 (Harriet Packer) had a single child at age 28. The cementum of the m1 root of sk53 provides 38 increments using our algorithmic counting method (Fig. 5.9.a.), the number expected given human replacement of the m1 at between six and seven years of age. Therefore, the increment deposited during this pregnancy could be accurately located. The hypermineralised band of this increment has the greatest radial thickness, and provided the single highest greyscale value through the entire cementum tissue. However, its thickness and morphology were not significantly different than other increments (Fig. 5.9.a.).

Sk334 (Harriot Rogers) exhibited hypercementosis in all teeth studied. This condition creates characteristic and excessive build-up of cementum and is caused by a range of factors including occlusal trauma and stress. Its effects on increment deposition have yet to be studied. However, although the cementum was too thick to fit into an entire field of view at the resolutions used here, distinct increments were found through the entire coronal third of the cementum of the UM1 tooth (Fig. 5.9.b.). These could be counted using both human vision and our automated algorithmic counting method, and the increments mapped that formed between ages 28 and 44 (the period during which Harriot Rogers had seven successful pregnancy events). The increment formed during the first pregnancy event during the 28th year of life is marked by a series of distinct

cellular voids running along its circumferential length (Fig. 5.9.b.). These voids are significantly smaller and more concentrated than other voids and serve to stretch the hypomineralised portion of this increment, making it the thickest increment of the cementum tissue. A similar concentration of these voids creates a comparable, although less pronounced morphology within the increment recorded during the 44th year of life; the last year of pregnancy. Although these voids are not seen in any other increment between the 28th and 44th years, this period is marked by lower increment contrast than the surrounding cementum (Fig. 5.9.b.).

In summary, cementum from both individual archaeological females of known reproductive history shows a morphological reaction to pregnancy. However, the morphologies of increments formed during these periods are not comparable. The increased density recorded in sk53 in reaction to pregnancy is contradictory to the decreased contrast of increments recorded in sk344.

5.4. Discussion

5.4.1. A new method for sexing individuals of unknown life history?

Application of automated quantitative analyses for assessing cementum structure and increment shape have highlighted sexual dimorphism amongst primate and human dental cementum for the first time. Female increments follow more chaotic transects and are less well defined than male increments. Further, episodes of pregnancy, most notably the first episode of pregnancy, are represented in the cementum of female rhesus macaque (*Macaca mulatta*) individuals by exceptionally thick hypermineralised circum-annual bands, which are the sight of common coalescence with the immediately following hypomineralised circum-annual band.

The strength of differences between female and male cementum identified here has the potential to confidently estimate sex from SR CT cementum data of individuals of unknown life history. The consistent difference in 'texture space' occupation by male and female SR CT cementum data in each sample suggests a predictive power to this analysis for sexing cementum data. This can be evidenced when adding data from individuals of unknown sex to the C12th Principal components analysis (PCA). The clustering of SK2201 cementum data within known female texture space may be used to suggest that this specimen was indeed female (Fig. 5.6.b.). The cementum increments of

this specimen also have significantly higher mean tortuosity values than any C12th male individual.

However, the addition of specimens of unknown life history to the C12th sample, and the results of combining both archaeological samples, also suggests that there may be a significant taphonomic signal represented in PCAs of cementum texture metrics. Specimen SK1634 occupies its own distinct region of texture space within the C12th sample. Inspection of the SR CT cementum data of this specimen indicates that it has undergone more severe taphonomic damage than any other specimen. Hence, taphonomy has the potential to bias comparisons between sexed individuals and must be accounted for when estimating the sex of unknown individuals using this technique.

The distortion of originally significant differences in texture space occupation between males and females in individual archaeological samples when they are analysed together may also imply a taphonomic signal in texture data. The samples have been buried in significantly different taphonomic environments. The C12th sample was waterlogged, and the area prone to flooding. Further, there was no clear evidence of coffins being used for the areas where our sample originated. The C19th excavation sites were well drained and each individual was recovered from a coffin. This (and the 700 year time gap) lead to significantly better preservation among the C19th individuals compared that of the C12th sample. The loss of original sexual signal in the resultant combined PCA result indicates that caution should be taken when combining samples.

Our results offer a promising new method for identifying sex in samples of primates of unknown life history, as well as a series of caveats for this method for future studies. However, the low n numbers of individuals of known sex stipulates that our findings can only be preliminary. Future studies with more substantial samples of known individuals (>30 of each sex) should follow in order to more conclusively test whether the key differences in cementum properties between the sexes are retained at a population level and are robust to other life history variables. If these differences are retained, then our methods can be applied to a wide range of applications varying from evolutionary anthropology, zoology, ecology and even forensic criminology. The ability to confidently estimate both age, sex and timing of pregnancy events in women from a single tooth would have significant implications for a range of forensic practices, from criminology to identifying un-named victims of combat ("john/jane does"). Application to archaeological populations will open a new window onto specific population-level

demographics and allow for more accurate assessment of population dynamics, possibly even allowing future workers to draw more accurate conclusions regarding the causes of death assemblages and histories of populations of singular historical significance.

5.4.2. Exploring cementum structure through the early hominin fossil record

One such application will be the use of SR CT for the imaging and analysis of Neanderthal cementum. We performed a pilot study on the cementum of a single Neanderthal m1 tooth (Fig. 5.10.a.) at the SLS TOMCAT beamline using the same experimental settings outlined in **Chapter 4 section 4.2.5**. Subsequent analyses of increment tortuosity and cementum texture were performed on 30 random slices from this scan (that were first checked for cracking and/or diagenetic alteration; any slices that showed either of these features was replaced by another random slice), and the results compared with the macaque, C12th and C19th archaeological human samples.

ANOVA comparisons between tortuosity values of Neanderthal and macaque cementum increments found a statistical difference between male macaque increments (n=45) and Neanderthal increments (n=45)(F=554.7, p<0.001). However, comparisons between female macaque cementum increments (n=585) and Neanderthal increments did not produce statistically significant differences (F=4.86, p=0.054).

ANOVA comparisons between C12th archaeological human cementum increments and Neanderthal increments show that the Neanderthal increments are significantly more tortuous than the increments of any C12th human individual studied here. Comparisons between both male (n=90) and female (n=135) C12th human increments and Neanderthal increments produced highly significant differences in tortuosity values (male comparisons - F=211.1, p<0.001; female comparisons – F=50.81, p<0.001).

Finally, ANOVA comparisons between C19th archaeological human and Neanderthal cementum increments conform to those performed between macaque and Neanderthal cementum. Comparisons between C^{19th} male (n=45) and Neanderthal cementum increments produced highly significant differences in tortuosity (F=284.5, p<0.001). Comparisons between female (n=90) and Neanderthal cementum increments did not produce statistically significant differences in tortuosity values (F=2.44, p=0.123).

When comparing Neanderthal and macaque cementum texture, Neanderthal slices overlap the ‘texture space’ of several female macaque individuals, and do not

overlap with either male or non-breeding juvenile female individuals (Fig. 5.10.b.). Addition of Neanderthal data overturns the macaque PCA along principal component 2, and reduces the distance between male and female texture spaces.

Addition of Neanderthal texture data to the C12th archaeological human sample does not significantly change the distribution of the human sample in texture space. The Neanderthal data again overlaps with female human texture space, clustering most significantly with the sk2201 specimen of unknown sex (Fig. 5.10.c.). However, when Neanderthal data is added to the C19th texture data it instead occupies its own region of texture space, with one data point overlapping into male texture space.

Finally, when Neanderthal texture data is added to the C19th archaeological human sample of m1 teeth, Neanderthal slices occupy their own discrete region of texture space, falling between female and male cementum slices along PC1, and providing the lowest datapoints of PC2 (Fig. 5.10.d.). Addition of Neanderthal data to the lm2 dataset also creates a discrete Neanderthal texture space. But this space correlates with female slices and is the most geometrically opposed to male slices (Fig. 5.10.e.).

The results of pilot imaging and comparison between the increment tortuosity and cementum texture of Neanderthal and extant primate cementum data offers a tempting view onto the potential of these methods for sexing fossilized hominins. The tortuosity of cementum increments of the Neanderthal specimen are significantly higher than any male increment from any extant sample. Further, although the Neanderthals increments are still significantly more tortuous than female human increments form the C12th human sample, they conform to the tortuosity values of females in the macaque sample and C19th human sample. These results, along with correlation between Neanderthal texture data and female texture data in both the macaque sample and the C12th archaeological human sample may be tentatively used to suggest that this individual was female.

The prospect of sexing non-human hominids and early humans using the techniques pioneered here has the potential to open up a new line of enquiry for several aspects of evolutionary anthropology. A wealth of material has been of limited use to previous demographic studies of early hominins as it consists solely of isolated teeth. The ability to conduct demographic studies on the distributions of age, sex and even age at first birth in these populations will greatly increase our knowledge of population

structure and life history among and between hominin species. Further, several hominin collections in various museums throughout the world have come under question as to whether they represent adult and juvenile material of the same species, or two separate species distinguished by body size. We have here shown that SR CT imaging of cementum offers a non-destructive method for ageing primates using increment counts. The removal of teeth and study of the cementum of such specimens with this method may well offer conclusive evidence as to whether they represent individuals of significantly different age, or individuals of similar age but significantly different body size (i.e. potentially different species).

5.4.3. Potential physiological causes for sexual dimorphism in cementum structure and texture

The series of detrimental effects on gingival health described in **section 5.1** may well explain the significant sexual dimorphism identified here in cementum structure and texture. The finding of a consistent difference in cementum texture between female and male individuals, regardless of the occurrence of known pregnancy events, suggests that hormonal differences have a significant effect on cementum growth. As this is found in both laboratory-raised *Macaca mulatta* (rhesus macaque) populations living under controlled life history variables, and archaeological human populations, it may also suggest that this hormonal difference is not overwhelmed by other potential life history variables including diet and climate. This is supported by the finding that increments deposited during pregnancy (especially the first pregnancy event), the most rapid amplification of sexual hormonal differences experienced through life, display the most significant departures in morphology.

For the *M. mulatta* population, the only life history variable which differed amongst individuals was the advent of pregnancy. The effects on cementum of these events have been shown here to be a marked decrease in the definition between an individual's slow growth/fast growth bands, with thicker 'slow growth' bands and a break-down of 'fast growth' bands. This is often met with lensing and coalescence of the proceeding fast growth band. A considerably thicker slow growth band may well correlate with a reduction in growth rate through the last two trimesters of pregnancy, which at approximately seven months is longer than most winter periods posited to correlate with other slow growth bands. This is also the period where females experience a considerable increase in estrogen and progesterone, the major steroid

hormones previously shown to restrict cementum growth (von Beila et al., 2008; Medill et al., 2010), and detrimentally act upon gingival tissues including cementum and the periodontal ligament (PDL). A combination of restricted growth, and damage to the periodontal ligament may also explain the poorly defined, and isotropic nature of the boundary between the thick slow growth band formed during pregnancy and the proceeding fast growth band. The primary collagen fibre constituent of acellular external fibre cementum (AEFC) is contributed directly by the Sharpey's fibres of the PDL. A previous study by Lieberman (1994) has shown that disturbances in the production and quality of Sharpey's fibres may be reflected in the morphology of cementum increments. It has also been shown that damage to the PDL is expressed in the cementum through resorption of the outermost layer of cementum. This is not a homogeneous process, and resorption is characterized by a range of expressions at both the global scale of the root (more intense in labial/lingual surfaces than proximal surfaces – Andreason, 1980a,b,c), and even at the cellular level (Andreason, 1980c). The isotropic surface and poorly defined boundary of this pregnant slow growth layer may thus be a direct expression of this damage caused to the propagating boundary of this layer, along with damage and disturbance in the growth of Sharpey's fibres originating from the PDL. The frequently seen infilling, lensing and coalescence at this boundary may also be the result of the following fast growth layer inheriting a disturbed, homogenous surface, infilling resorbed regions.

Although there is a consistent morphological reaction in the growth of cementum to pregnancy in our *M. mulatta* population, this is not reflected in the cementum of the two C19th human females of known reproductive history. Instead, sk53 shows a prominent, well-defined hypomineralised band rather than a prominent hypermineralised band during pregnancy. This was also found to be the case in humans studied by Kagarer and Grupe (2001), where hypomineralised lines were found to represent a series of life history events including pregnancy. This difference may be tentatively explained by the difference in increment thickness, and spatial separation between long-living humans and *M. mulatta* individuals. Increments are known to become increasingly densely populated in long living modern humans, making them difficult to count in thin section (Wittwer-Backofen, 2011; Naji et al., 2016). This may restrict observed morphological variation within and between increments, serving to 'flatten' their patterns, while preserving or even amplifying density differences between

increments in transverse SR CT slices.

The other C19th individual of known life history (sk334) exhibits a unique series of morphological markers relating to pregnancy. This individual suffered from hypercementosis; an idiopathic condition characterized by the excessive buildup of cementum throughout the tooth root (Souza et al., 2004). As in *M. mulatta* females, the first pregnancy is the most marked, however, this event is marked by series of cellular voids significantly smaller than surrounding cementocytes (an average diameter of 2.52 μm for 10 measured voids, versus an average of 9.46 μm for 10 measured cementocytes) (Fig. 5.9.b.). These voids are not seen in any other region of this scan, and are not seen in any other specimen. The only structures of similar size and distribution found in the literature are epithelial rest cells (Xiong et al., 2013). These cells are believed to be the remnants of Hertwig's Epithelial Sheath that survive in the PDL into adulthood. Although problems in isolating these cells from mesenchymal cells of the PDL have limited our understanding of their function (Bosshardt and Nanci, 2004), several lines of evidence have been brought forward to suggest a function of epithelial rest cells in PDL maintenance, repair and regeneration (Rincon et al., 2006; Bosshardt, 2008; Xiong et al., 2013). The chief line of evidence for this is the consistent finding of these cells along the boundary between resorbing cementum and functionally active PDL during periods of PDL damage, and even in replanted teeth. These periods of regeneration of the PDL are marked by an increased proliferation of epithelial rest cells along the boundary (Xiong et al., 2013). Although research on either subject is still in development within the cementochronological community, the fact that these cells are only seen in increments deposited during pregnancy may be tentatively explained by a combination of rapid cementogenesis caused by hypercementosis, and the proliferation of epithelial cells due to damage of the PDL from an unprecedented surge in androgenous steroid hormones during pregnancy. This may also explain why these cells are only seen in cementum that suffers from hypercementosis, as the growth rate of non-pathogenic cementum may not be sufficient for the tissue to capture these cells during mineralisation.

The particularly pronounced morphology of the first episode of pregnancy may be explained by a series of factors that distinguish this event from later events. It has been shown that levels of estradiol, the estrogen species known to negatively impact collagen metabolism, are significantly higher during the first pregnancy than all other terms (Bernstein et al., 1986). Prolactin levels have also been found to be significantly

higher in first-term pregnancies than later terms (Musey et al., 1987). These may both serve to extend the 'poor growth' period of the cementum increment formed during pregnancy, creating the pronounced dark band seen in each first pregnancy event in our samples.

Pregnancy provides the most pronounced difference in hormonal regime between the sexes within our studied samples. However, the consistent dimorphism between all male and female cementum slices including non-breeding *Macaca mulatta* individuals, and Christian nuns from the $C19^{th}$ sample suggest that background hormonal regimes may also be sufficient to impose significantly different growth regimes in cementum between the sexes. Repeated findings by previous studies of a positive relationship between increased presence of the female sex hormones androgen, estrogen and progesterone hormones and cases of gingival disease/damage may explain the higher isotropy and lower increment contrast found in female relative to male cementum. The menstrual cycle may provide sufficient, regular peaks in these hormones to affect the propagating cementum boundary. Indeed, several studies have found that even in periodontally healthy women, cases of gingival discomfort and periodontal damage increase before or during menses (Machtei et al., 2004). Studies of specific bone resorption markers have also shown that women commonly go through increased bone resorption through menses (Chui et al., 1999). Although no such study has been performed on tooth roots in relation to menses, the effects of periodontal damage can be expected to extend to the cementum in a similar fashion as during pregnancy, which may indeed lead to root resorption along the outermost cementum layer and disturbed production and orientation of Sharpey's Fibres. This consistent monthly disturbance to periodontal health throughout the life of a female is here hypothesized as the primary factor contributing to the sexual dimorphism of cementum structure seen in our primate samples.

5.5. Conclusions and future work

We have here used a suite of novel methods developed and validated in **chapter 4** to explore differences in the structure and texture of male and female cementum in a range of primate species raised under both controlled and natural conditions. These methods and samples have allowed us to isolate for the first time significant sexual dimorphism

in several aspects of both cementum structure; with females showing significantly more tortuous increments, and texture; with female cementum showing significantly less increment contrast and more isotropy. The degree to which the sexes differ in these aspects has been shown to be enough to potentially sex individuals of unknown life history by comparing them to individuals of known sex in the same population. Further, we have shown that episodes of pregnancy are reflected in the cementum through increments of unique morphology.

We hypothesise that such pronounced dimorphism is linked to intrinsic differences in hormonal regimes between the sexes, as female sexual hormones are known to have a damaging effect on the periodontium and encourage root resorption. This may further explain why pregnancy events produce such a significant effect on the cementum, as pregnancy creates an unprecedented increase in female sex hormones.

However, it must be noted that the hypotheses proposed here linking oral health, hormone balance and cementum growth need rigorous testing in future studies. Firstly, as previously stated, the results presented here can only be deemed preliminary due to low sample size. It may indeed be possible to test our hypothesized impact of hormonal regime on cementum health by monitoring or even inducing hormonal regimes in large populations of model organisms. This would provide a further element of control for isolating the effects of hormonal stimuli on cementum growth. Further, the use of large samples would permit a higher temporal resolution for studying cementum growth. Removing teeth on a monthly basis as individuals experience different hormonal regimes may allow the mechanisms through which androgens, oral health, and cementum growth interact. Finally, as our preliminary results agree with conclusions of previous research suggesting heterogeneous effects of pregnancy between taxa, the isolation of hormonal effects on the cementum of a range of taxa, raised under identical conditions, may help to elucidate the specificities of these differences and possible causes.

The application of our methodology to larger populations of primates of known sex and reproductive history will allow for more confident conclusions to be drawn regarding their predictive power within a number of disciplines. There is the potential for sexing and investigating reproductive histories of primates of unknown life history, including a wide range of hominin species. The avenues for research using this validated methodology are discussed here and range from anthropology to forensic criminology.

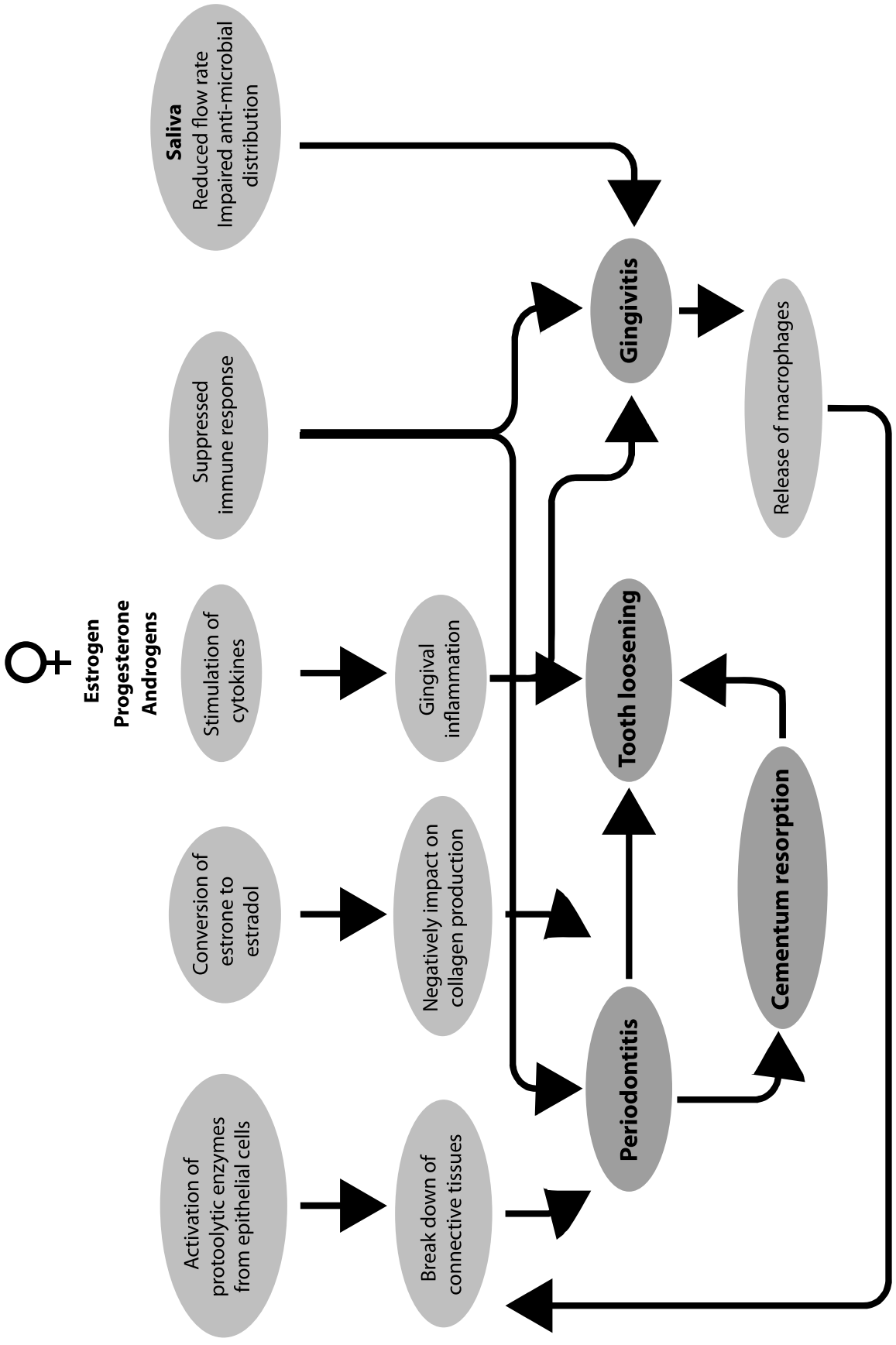

Figure 5.1. Flow chart describing the pathological effects of female sexual hormones on gingival and periodontal health. Orange boxes denote causes; green boxes denote major symptoms on gingival and/or periodontal health.

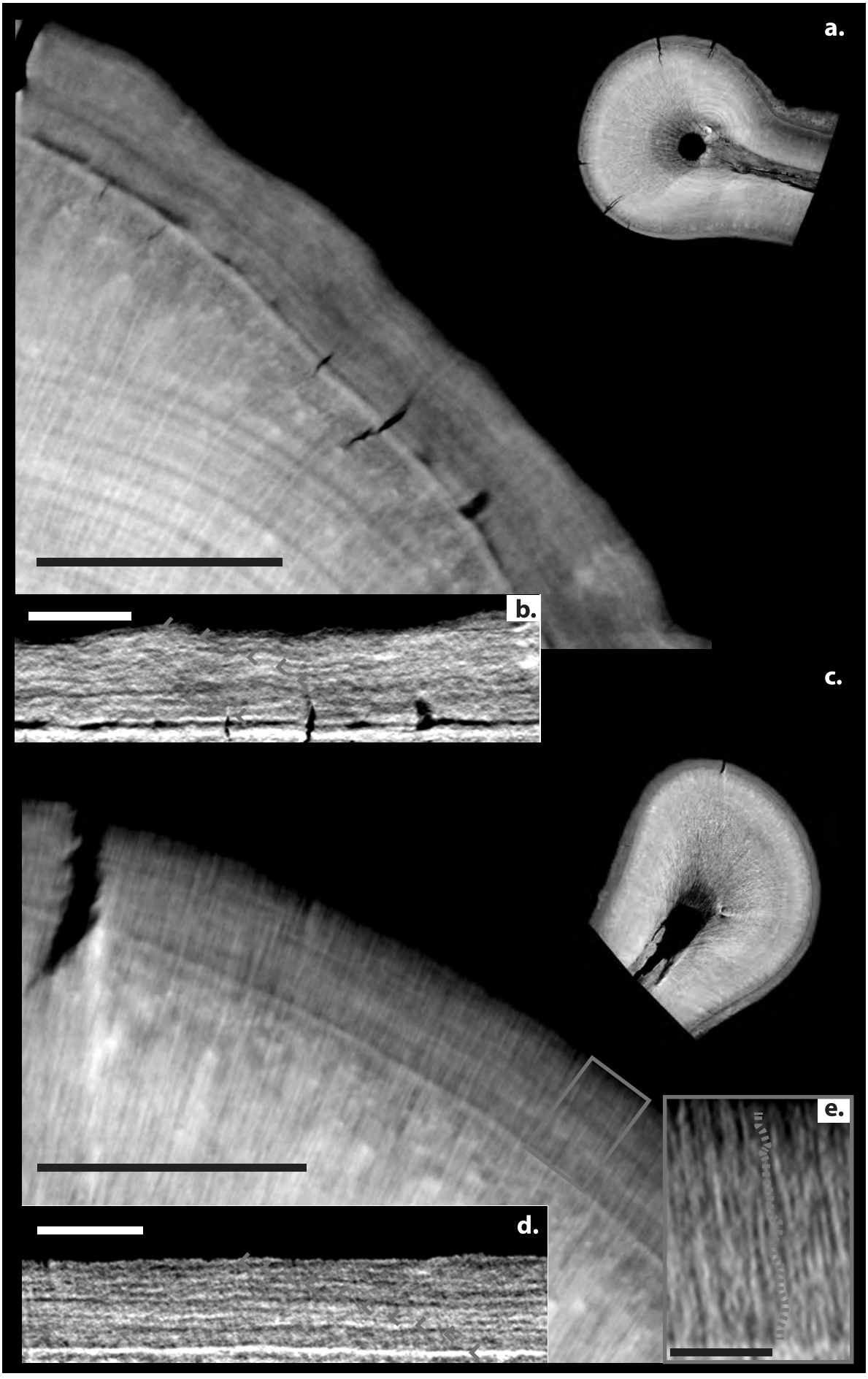
a.
b.
c.
d.
e.

Figure 5.2. Qualitative comparison between increments in breeding female versus male cementum. (**a**) Cementum of breeding female specimen t56. (**b**) Straightened and filtered modification of image (**a**) following image processing methods outlined in **Section 4.2**. Although 10 increments can be counted, they are diffuse and difficult to read through portions of the cementum and follow chaotic, tortuous transects when compared to those of male cementum. (**c**) Cementum of male specimen k39. (**d**) Straightened and filtered modification of (**c**) following image processing methods outlined in section 5.5. 10 increments can be plotted throughout the entire cementum tissue and follow uniform transects and regular thickness. (**e**) Detail highlighted by red box in (**c**) showing series of Sharpey's fibres. Fibres change orientation as they progress through each increment; trending more obliquely to the cemento-dentine junction through thick light increments (as highlighted by dashed green line). Black lines in (**a**) and (**c**) equal 150μm. White lines in (**b**) and (**d**) equal 75 μm. Black line in (**e**) equals 30 μm.

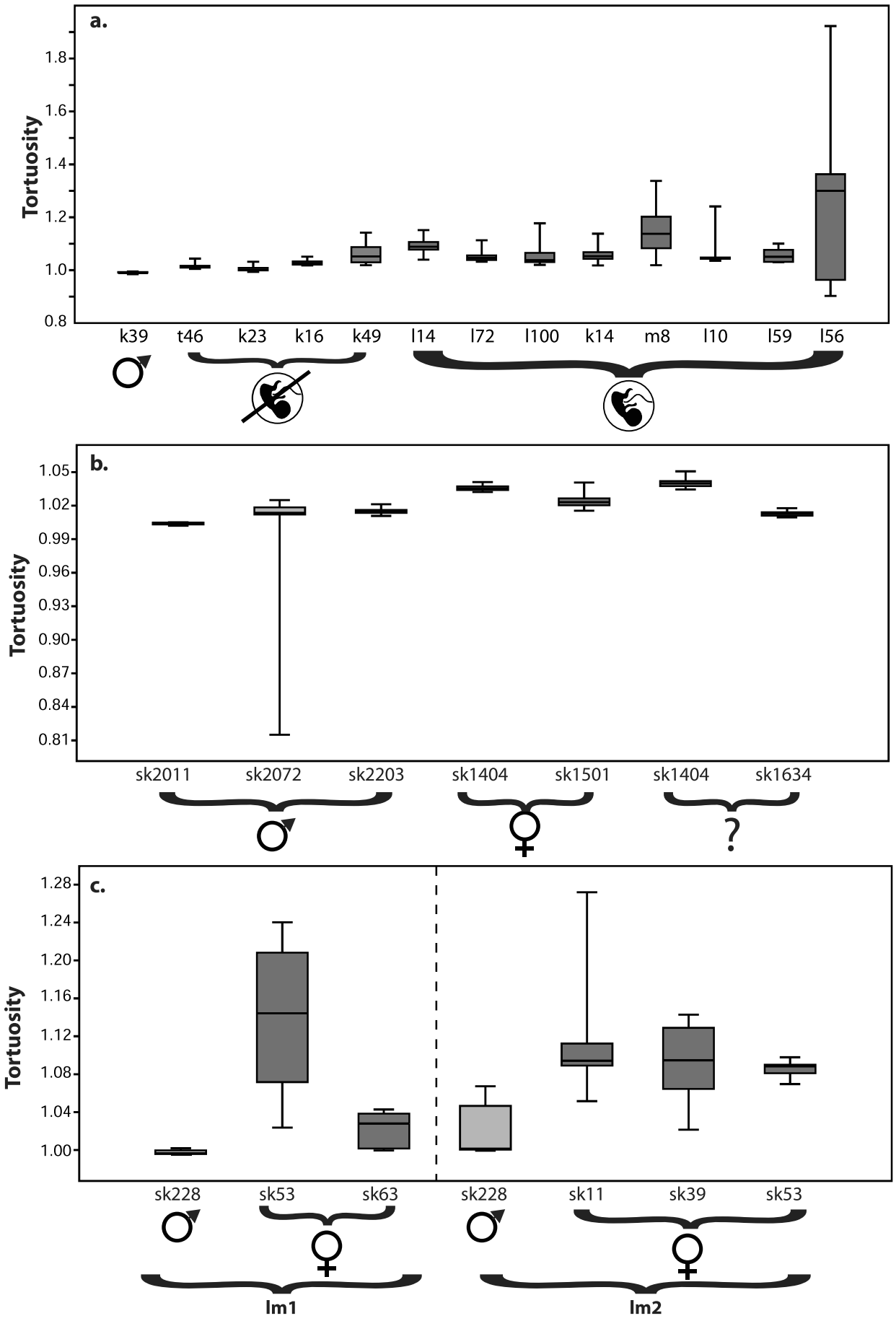
a.
Tortuosity
1.8
1.6
1.4
1.2
1.0
0.8
k39
t46
k23
k16
k49
l14
l72
l100
k14
m8
l10
l59
l56
b.
Tortuosity
1.05
1.02
0.99
0.96
0.93
0.90
0.87
0.84
0.81
sk2011
sk2072
sk2203
sk1404
sk1501
sk1404
sk1634
?
c.
Tortuosity
1.28
1.24
1.20
1.16
1.12
1.08
1.04
1.00
sk228
sk53
sk63
sk228
sk11
sk39
sk53
lm1
lm2

Figure 3. Box-whisker plots displaying the results of tortuosity analyses of isolated cementum increments. (**a**) Results of *Macaca mulatta* tortuosity analyses. (**b**) Results of C12th archaeological human tortuosity analyses. (**d**) Results of C19th tortuosity analyses. Coloured boxes represent standard deviations around the mean value (inset black line) for each specimen. Upper and lower whiskers represent highest and lowest values respectively.

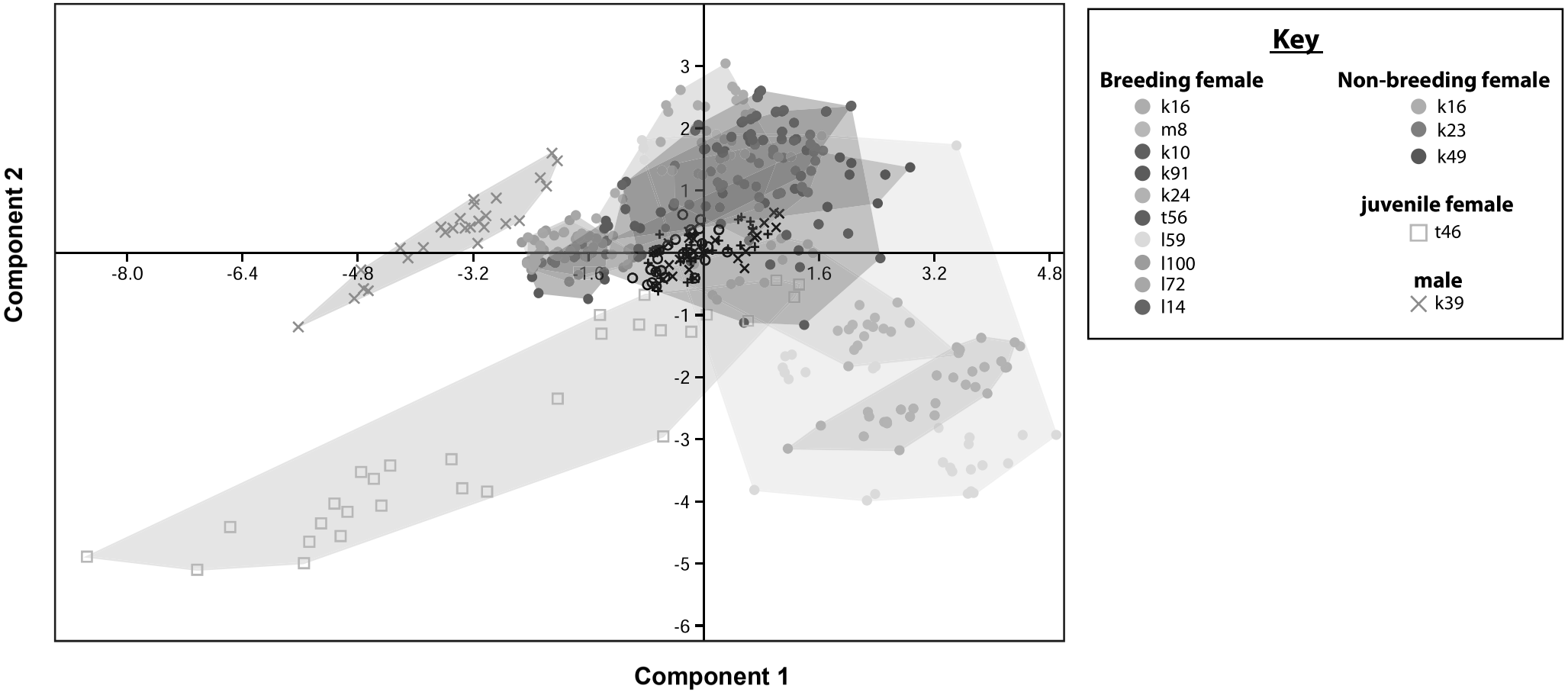

Figure 5.4. Results of principal components analysis of the 18 surface texture metrics applied to the cementum of 30 random slices from synchrotron radiation Computed tomographic reconstructions of each *Macaca mulatta* specimen. Component 1 represents 41% of variance. Component 2 represents 33% of variance.

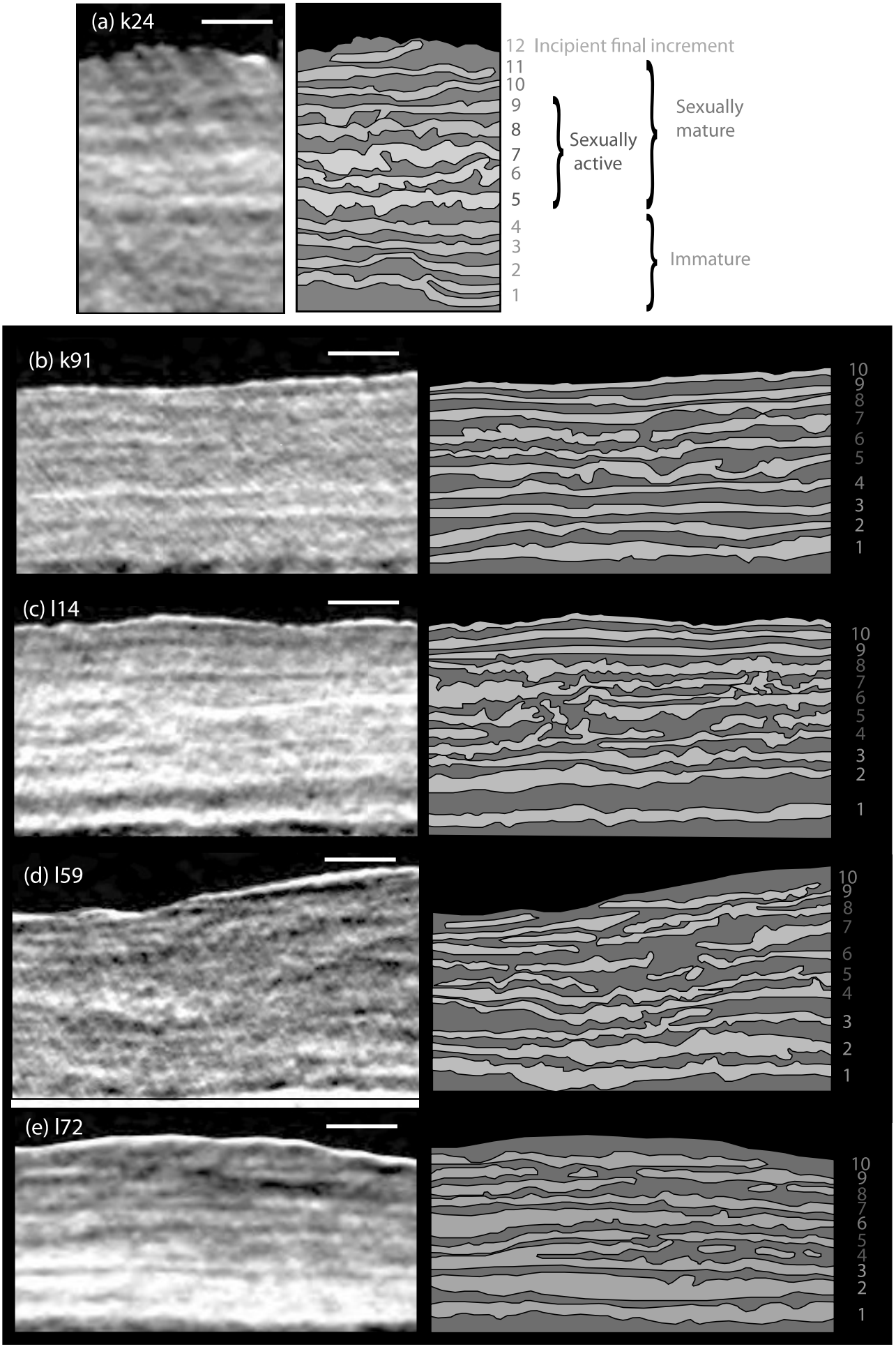
(a) k24
12 Incipient final increment
11
10
9
8
7
6
5
4
3
2
1
Sexually active
Sexually mature
Immature
(b) k91
(c) l14
(d) l59
(e) l72

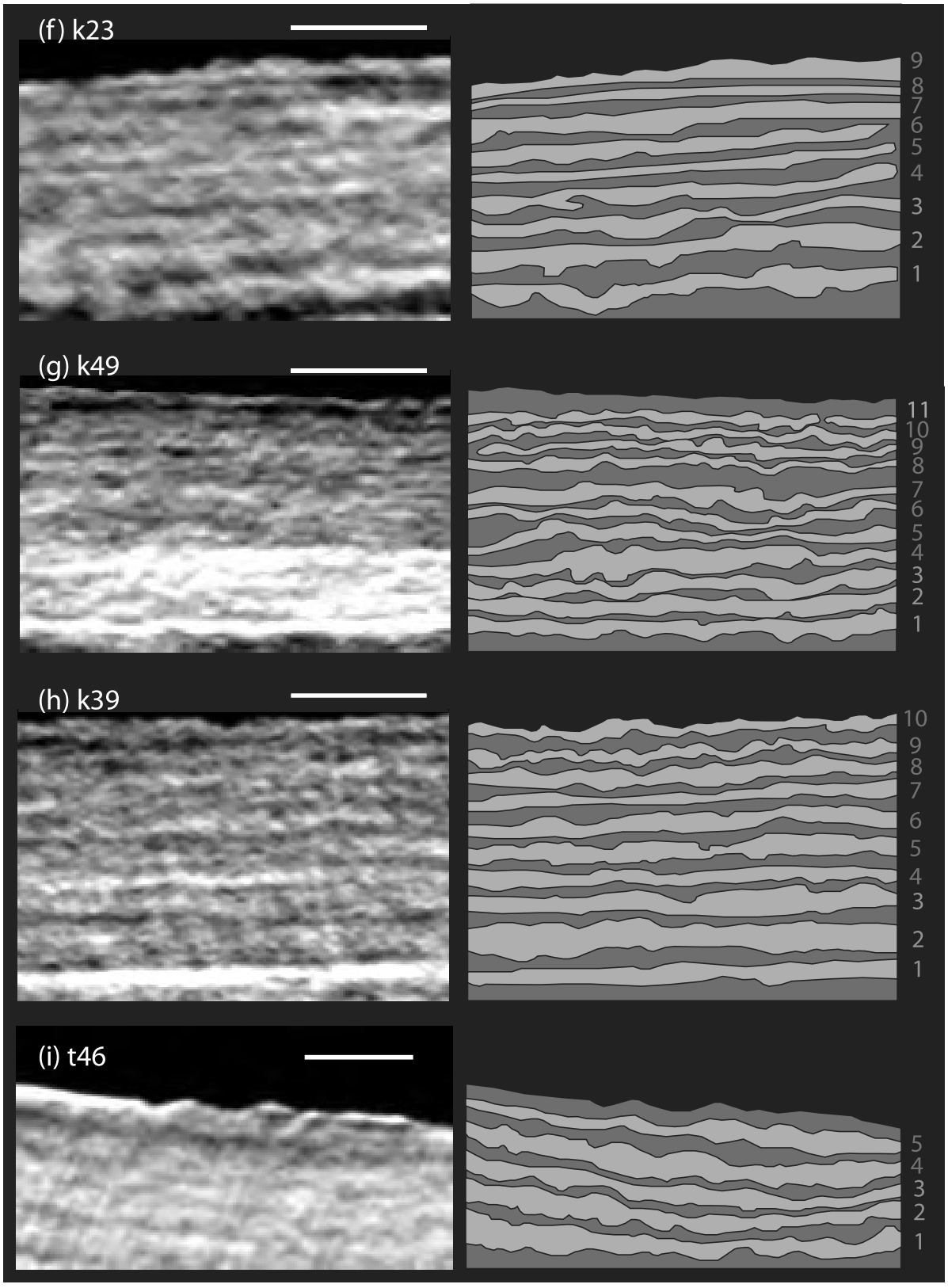
(f) k23
9
8
7
6
5
4
3
2
1
(g) k49
11
10
9
8
7
6
5
4
3
2
1
(h) k39
10
9
8
7
6
5
4
3
2
1
(i) t46
5
4
3
2
1

Figure 5.5. Examples of characteristic morphologies of cementum increments formed during pregnancy in female *Macaca mulatta* individuals, versus non-breeding females, a male and a juvenile. In all adult female specimens (**a-g**), increments formed before sexual maturity produce significantly higher greyscale values than those formed during adulthood (see juvenile specimen in **i)**. For females that undergo pregnancy events (**a-e**), increments formed during pregnancy are the most poorly organised, frequently being disrupted, as well as coalescing with the immediately proceeding increment. This is not seen in non-breeding females (**f-g**), whose adult increments are more regular, although still prone to lensing (**g**). Male cementum increments (**h**) are significantly less chaotic than female increments and do not lense or coalesce. All white scale bars represent 30 μm.

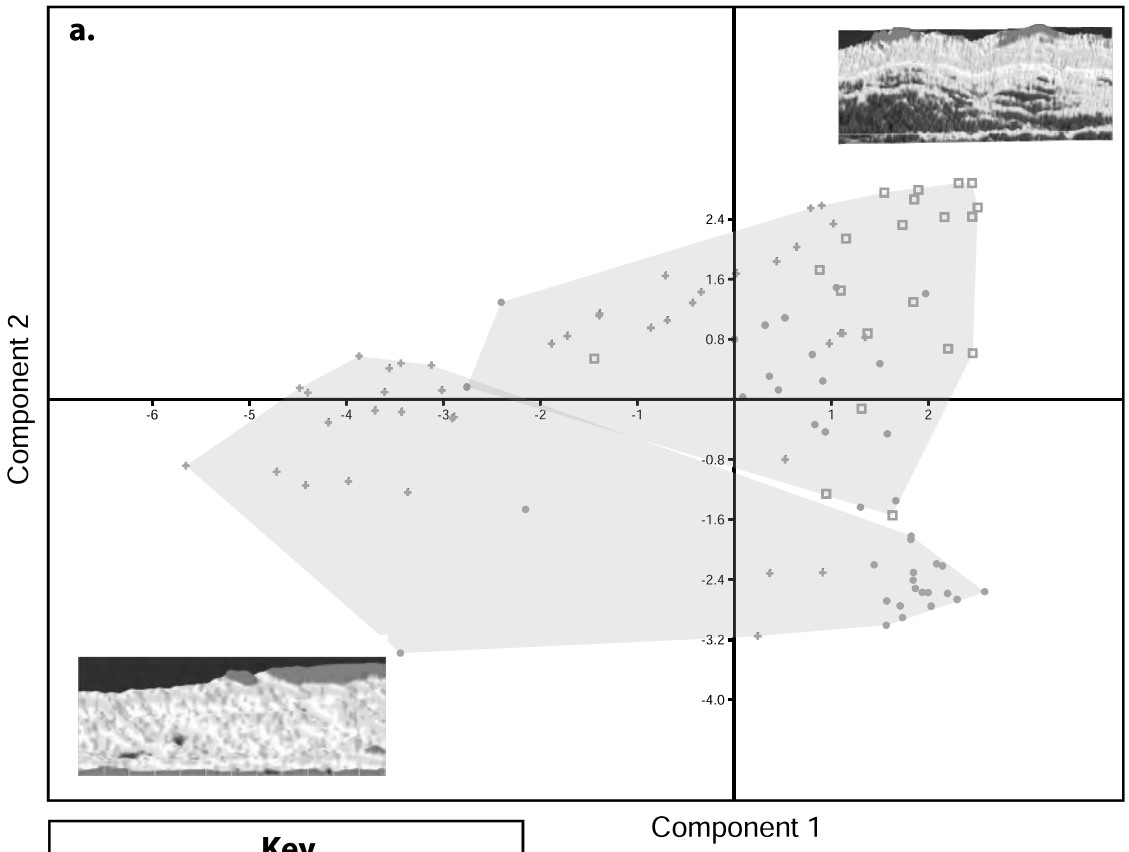

Key

Known female
- sk5010
- sk1404

Sex unknown
- sk1634
- sk2201

Known male
- sk2072
- sk2203
- sk2011

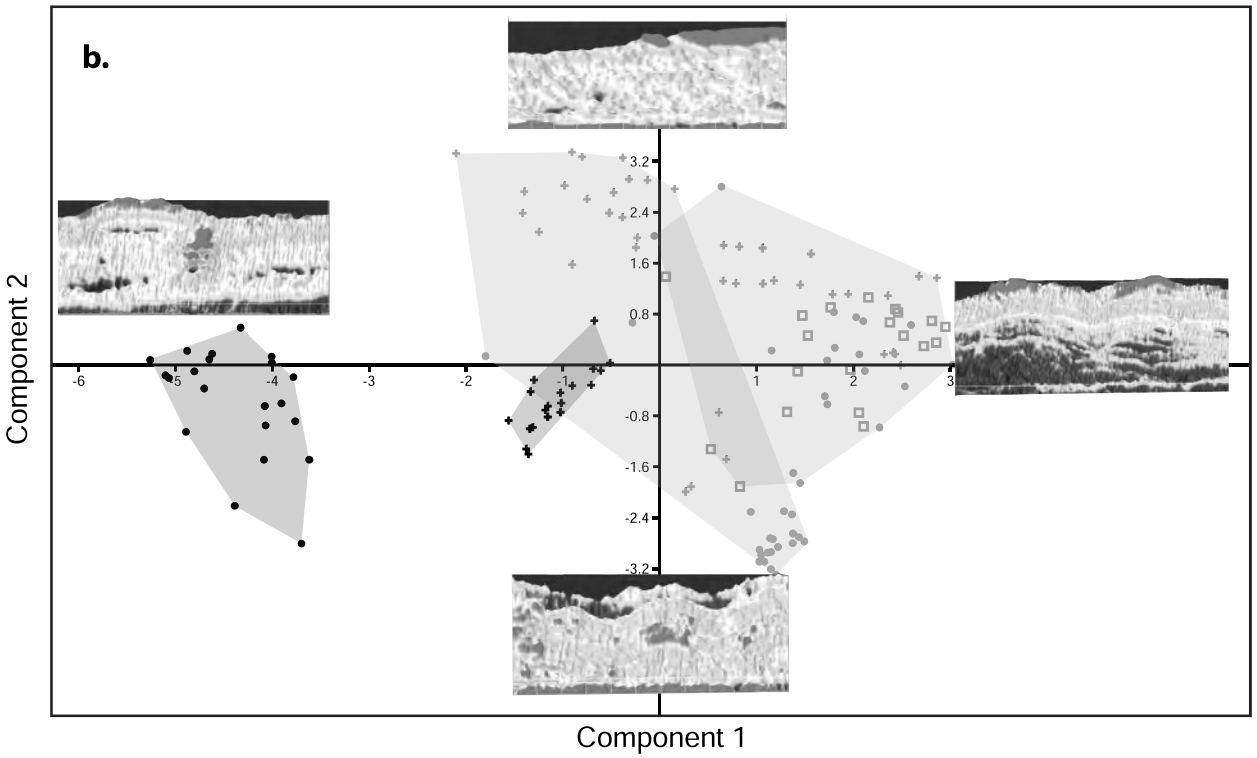

Figure 6. Results of principal components analysis (PCA) of the 11 surface texture metrics applied to the cementum of 30 random slices from synchrotron radiation computed tomographic reconstructions of each C12th archaeological human specimen. (**a**) PCA plot summarising variance between specimens of known sex. Component 1 represents 44.4% of variance. Component 2 represents 25.2% of variance. (**b**) PCA plot summarising variance between all specimens. Component 1 represents 44.28% of variance. Component 2 represents 25.36% of variance.

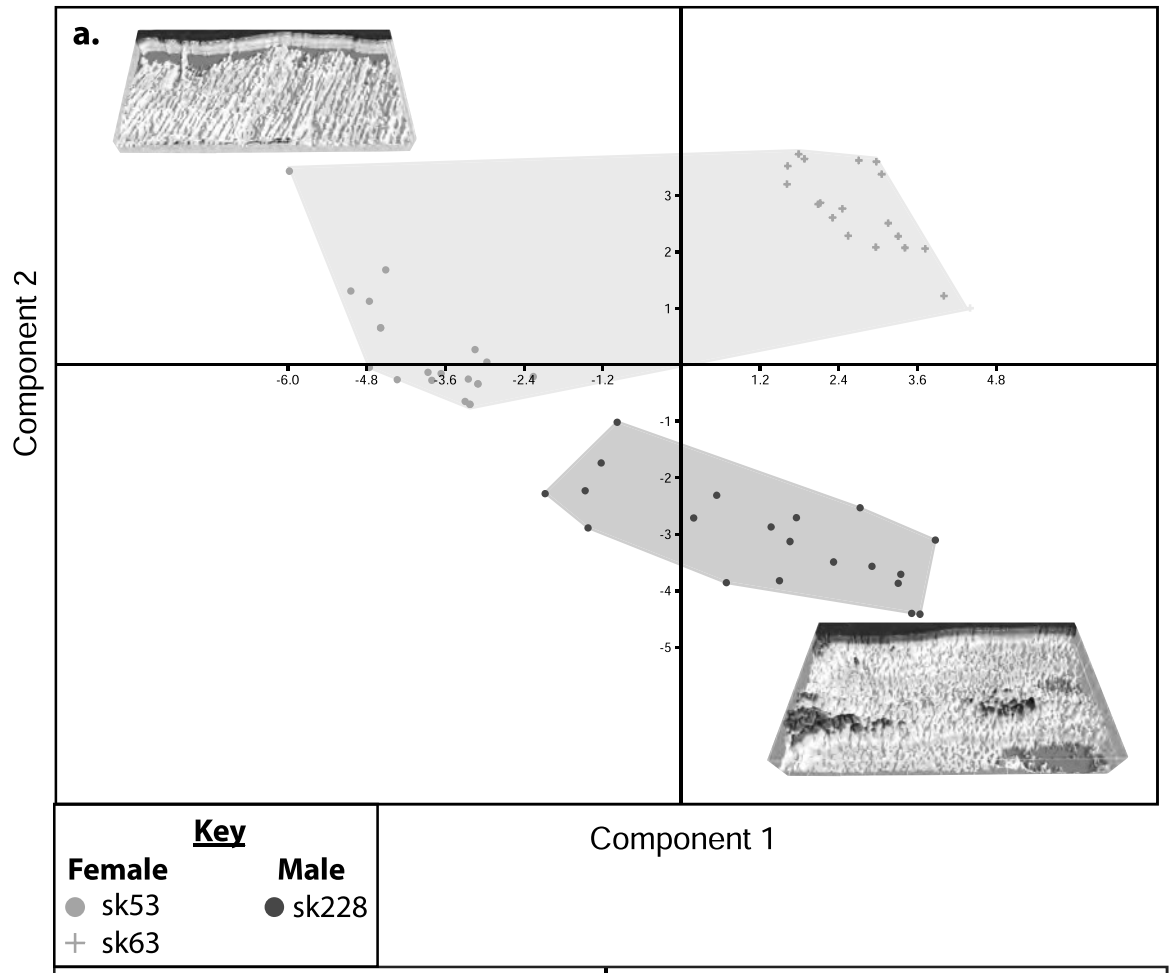
a.
Component 2
Component 1
Key
Female
sk53
sk63
Male
sk228

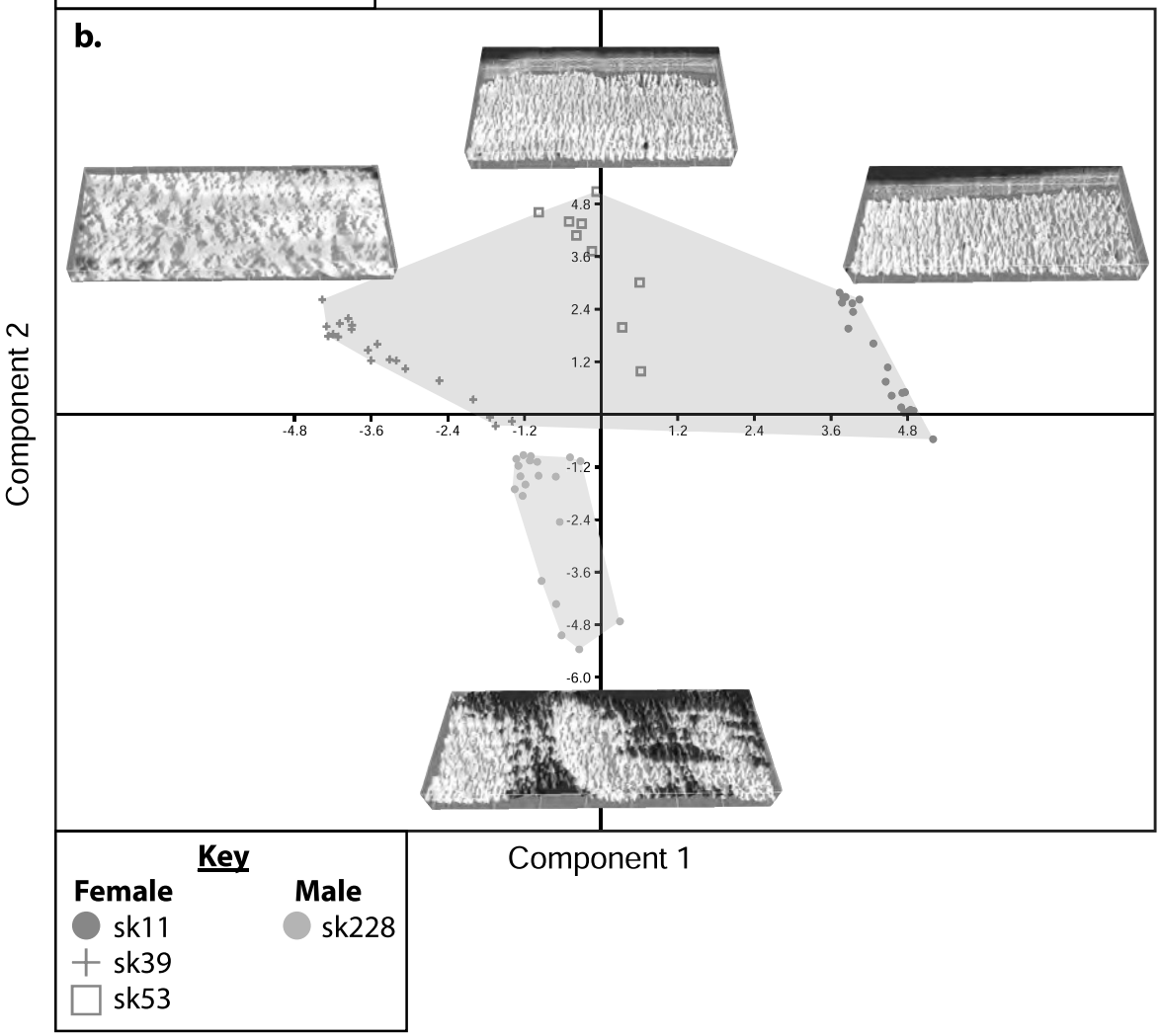
b.
Component 2
Component 1
Key
Female
sk11
sk39
sk53
Male
sk228

Figure 7. Results of principal components analysis (PCA) of the 18 surface texture metrics applied to the cementum of 30 random slices from synchrotron radiation computed tomographic reconstructions of each C19th archaeological human specimen. (**a**) PCA plot summarising variance in texture between lm1 teeth. Component 1 represents 44.2% of variance. Component 2 represents 34.6% of variance. (**b**) PCA plot summarising variance in texture between lm2 teeth. Component 1 represents 41.3& of variance. Component 2 represents 28.7% of variance.

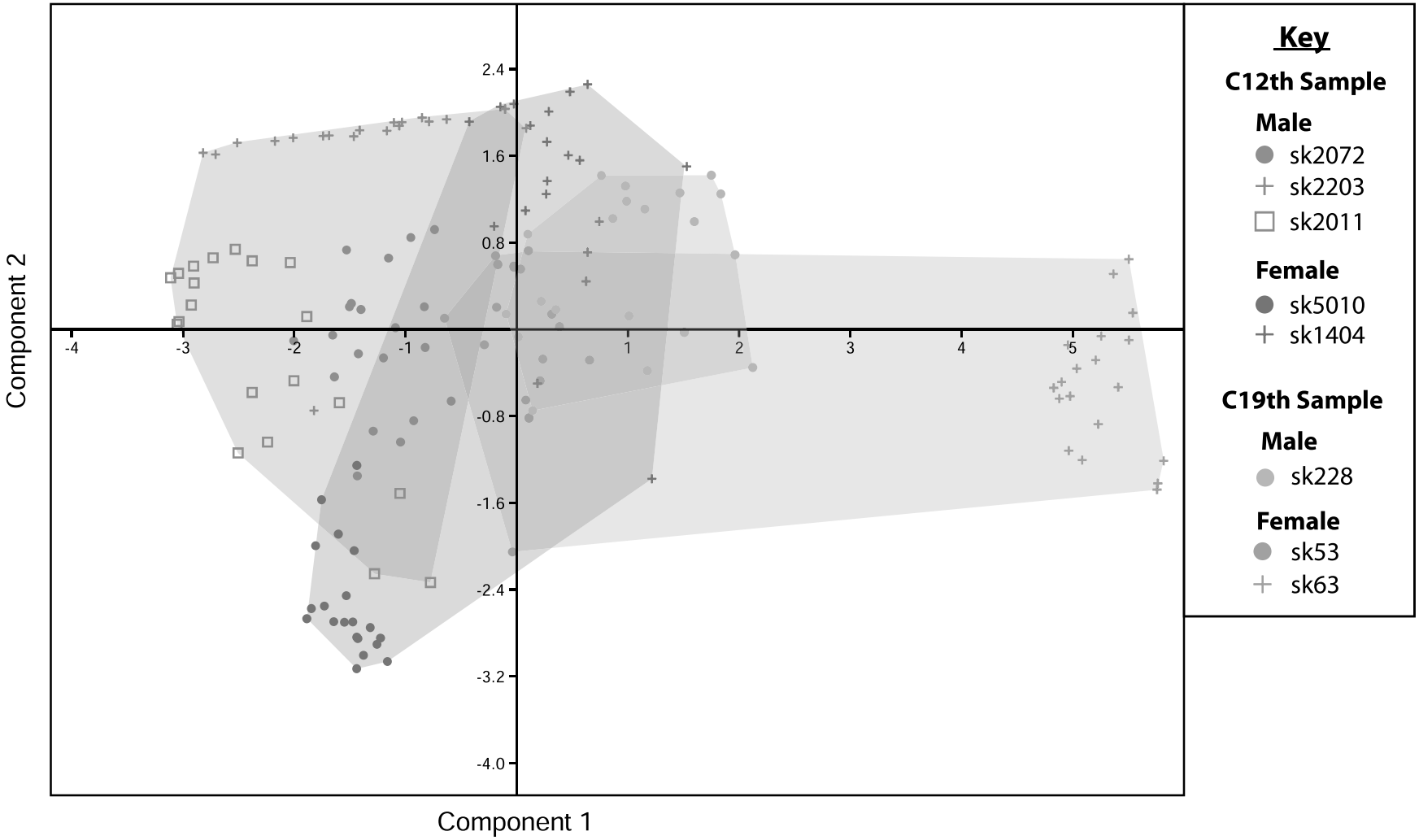

Figure 5.8. Results of principal components analysis (PCA) of the 18 surface texture metrics applied to the cementum of 30 random slices from synchrotron radiation computed tomographic reconstructions of eacharchaeological human specimen from both C12 and C19 samples. Component 1 represents 51% of variance. Component 2 represents 21% of variance.

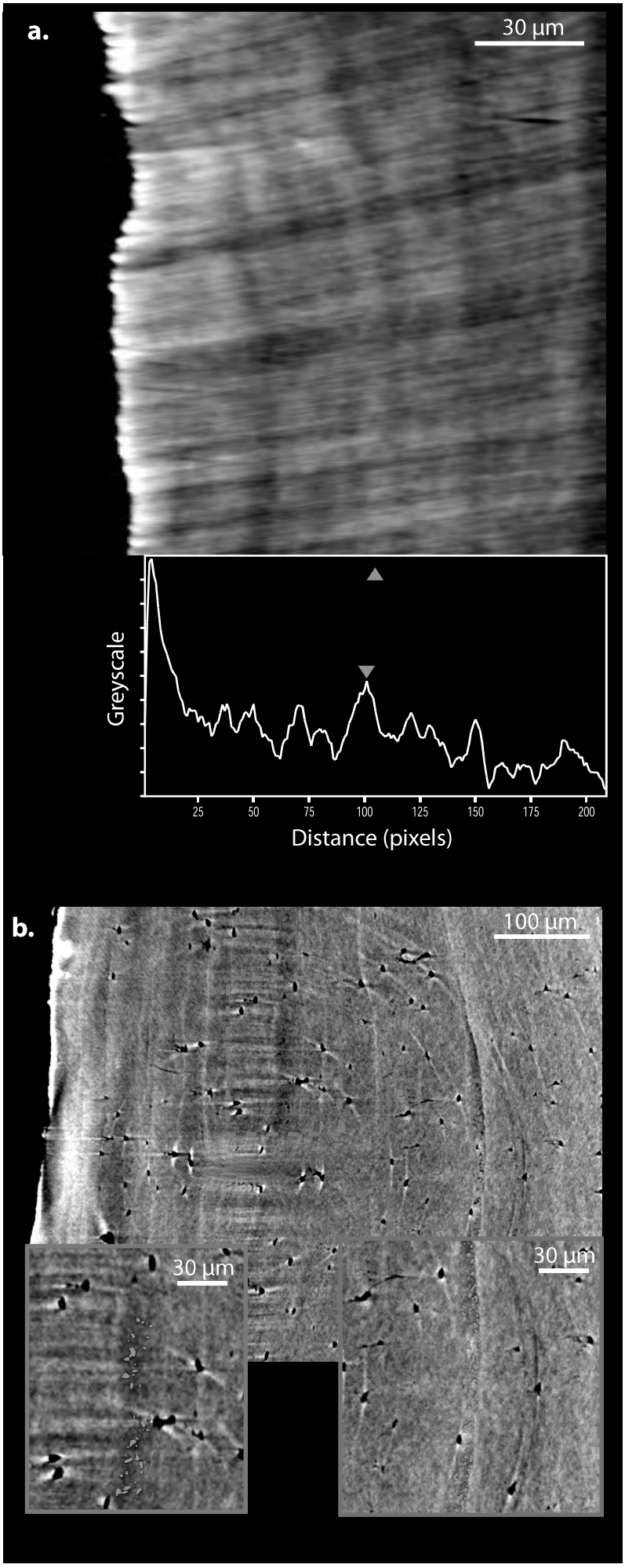
a.
30 µm
Greyscale
25
50
75
100
125
150
175
200
Distance (pixels)
b.
100 µm
30 µm
30 µm

Figure 9 (last page overleaf). Distinguishing pregnancy events in human cementum. (**a**) Single known pregnancy event identified in the cementum of SK53, as the thickest hypomineralised increment of highest greyscale value in the radial trajectory plotted through the cementum, indicated by blue arrows. It must be noted that the higher greyscales at the edge of the cementum are most likely due to edge enhancement along the cementum/air interface captured in the phase contrast reconstruction algorithm. (**b**) First and last pregnancy events identified in the cementum of sk334, who suffered from hypercementosis. These events are marked by series of cellular voids, significantly smaller than surrounding cementocyte voids. These series are highlighted using blue in-fills in the inset red and green boxes.

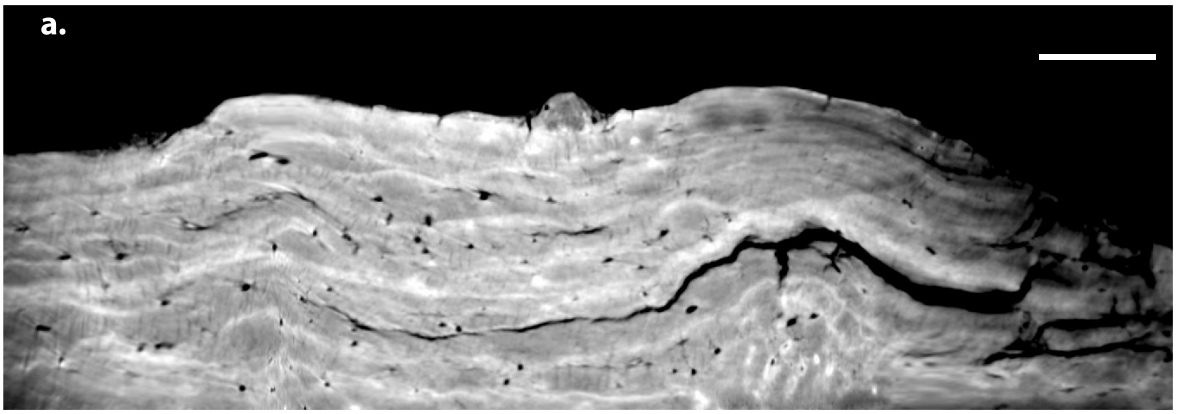
a.

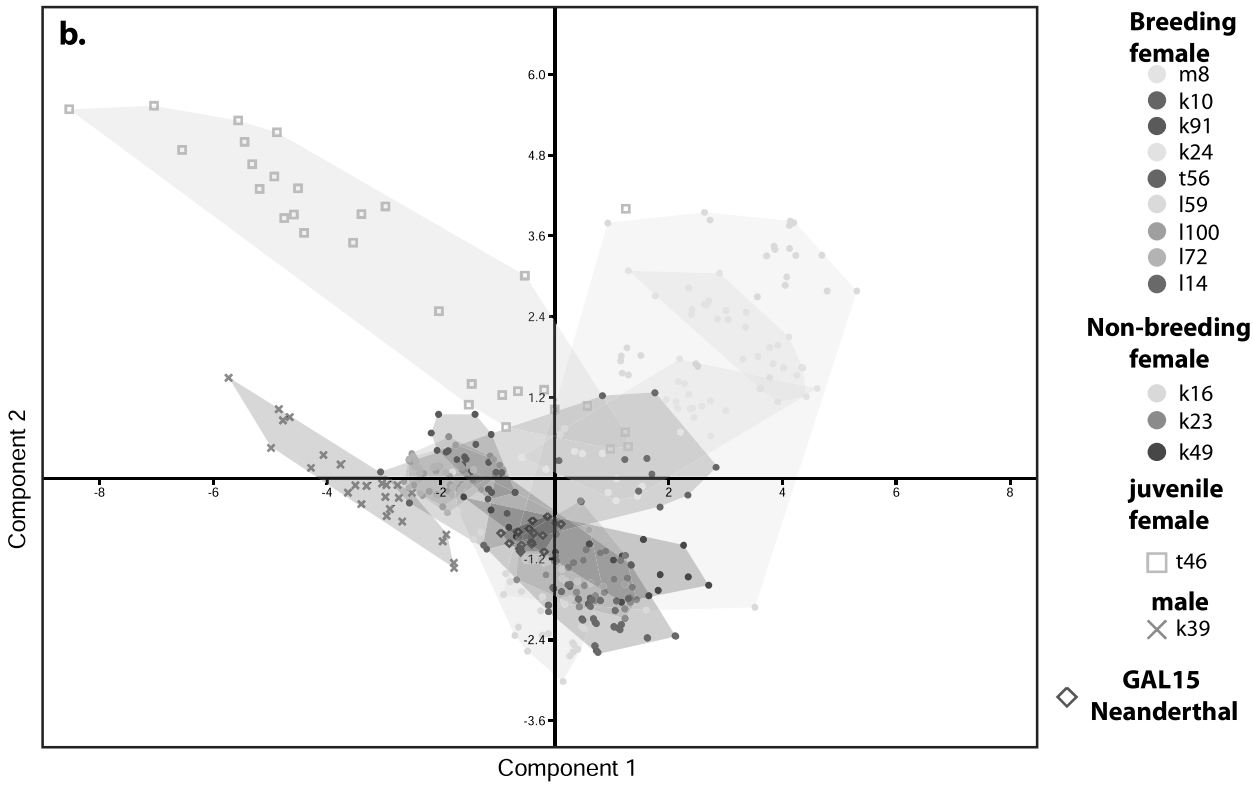
b.
Component 2
Component 1
Breeding female
m8
k10
k91
k24
t56
l59
l100
l72
l14
Non-breeding female
k16
k23
k49
juvenile female
t46
male
k39
GAL15 Neanderthal

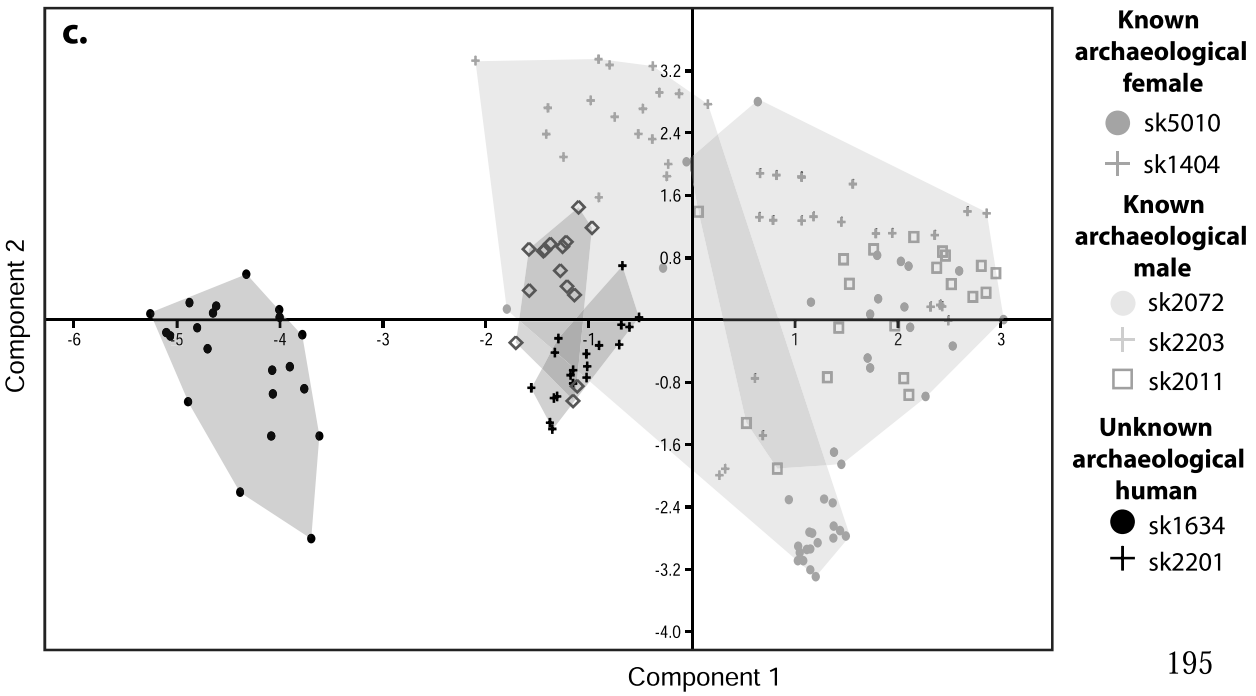
c.
Component 2
Component 1
Known archaeological female
sk5010
sk1404
Known archaeological male
sk2072
sk2203
sk2011
Unknown archaeological human
sk1634
sk2201

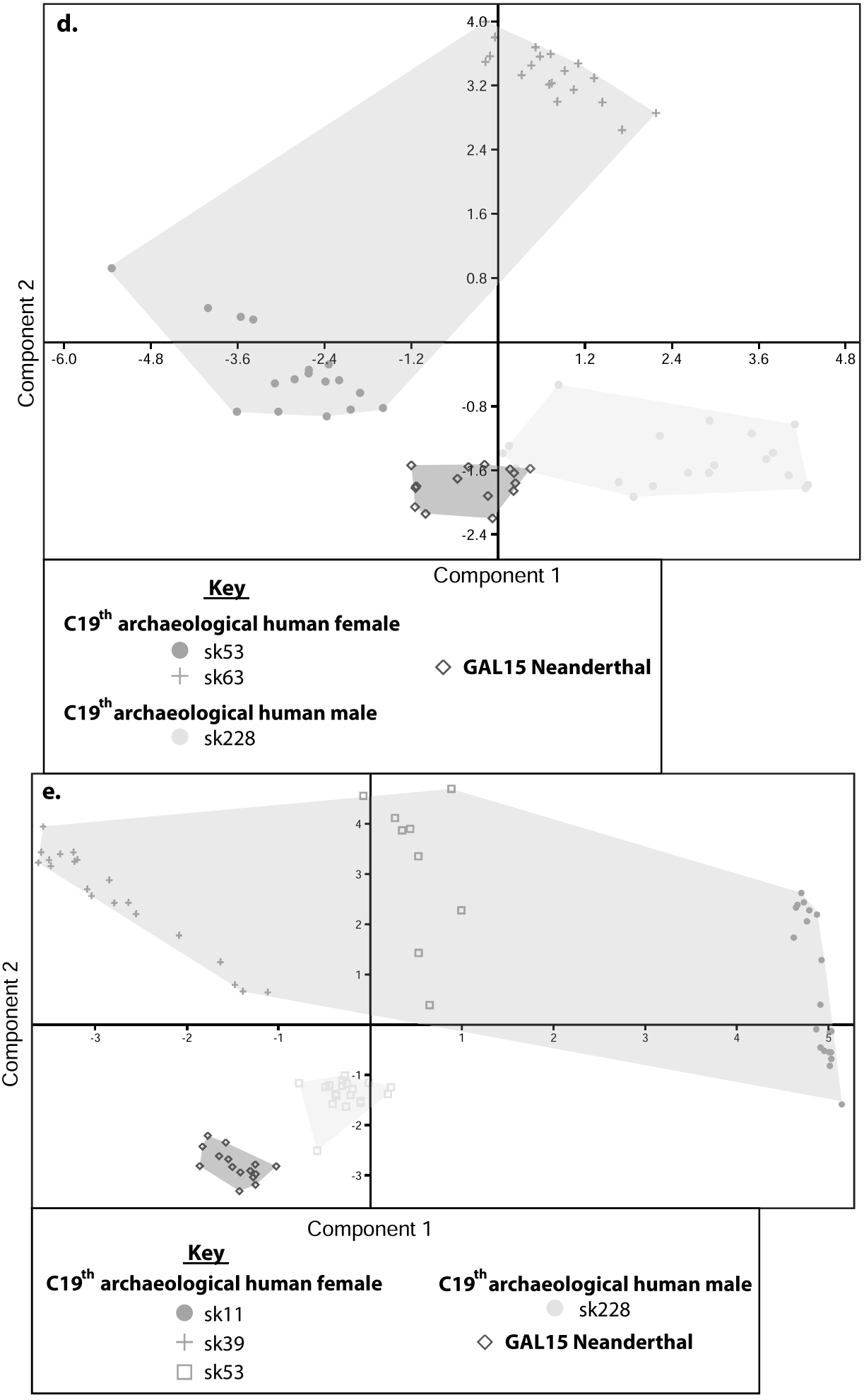
d.
Component 2
Component 1
4.0
3.2
2.4
1.6
0.8
-0.8
-1.6
-2.4
-6.0
-4.8
-3.6
-2.4
-1.2
1.2
2.4
3.6
4.8
Key
C19th archaeological human female
sk53
sk63
C19th archaeological human male
sk228
GAL15 Neanderthal
e.
Component 2
Component 1
4
3
2
1
-1
-2
-3
-3
-2
-1
1
2
3
4
5
Key
C19th archaeological human female
sk11
sk39
sk53
C19th archaeological human male
sk228
GAL15 Neanderthal

Figure 10. Results of principal components analysis (PCA) of the 18 surface texture metrics applied to the cementum of 30 random slices from synchrotron radiation computed tomographic (SR CT) reconstruction of the GAL15 Neanderthal pilot specimen and each extant primate sample. (**a**) Straightened SR CT slice of Neanderthal cementum. Scale bar represents 100 μm. (**b**) PCA plot summarising variation between the texture of *Macaca mulatta* and Neanderthal cementum. (**c**) PCA plot summarising variation between the texture of C12th human and Neanderthal cementum. (**d**) PCA plot summarising variation between the texture of lm1 C19th human and Neanderthal cementum. (**e**) PCA plot summarising variation between the texture of lm2 C19th human and Neanderthal cementum.

Specimen	Age of sample	Taxon	sex	Known age	Age in years at known birth events						
					1st	2nd	3rd	4th	5th	6th	7th
L10	2015	*Macaca mulatta*	female	11	4	6	7	-	-	-	-
T46	2015	*Macaca mulatta*	female	5	-	-	-	-	-	-	-
L100	2015	*Macaca mulatta*	female	11	10	-	-	-	-	-	-
L59	2015	*Macaca mulatta*	female	11	3	5	6	7	8	10	-
L72	2015	*Macaca mulatta*	female	11	3	4	6	7	-	-	-
K91	2015	*Macaca mulatta*	female	12	5	6	7	8	10	-	-
L56	2015	*Macaca mulatta*	female	11	4	6	7	-	-	-	-
M8	2015	*Macaca mulatta*	female	9	3	-	-	-	-	-	-
K39	2015	*Macaca mulatta*	male	12	-	-	-	-	-	-	-
L14	2015	*Macaca mulatta*	female	11	3	4	5	6	7	-	-
K24	2015	*Macaca mulatta*	female	12	5	7	8	-	-	-	-
K23	2015	*Macaca mulatta*	female	12	-	-	-	-	-	-	-
K49	2015	*Macaca mulatta*	female	12	-	-	-	-	-	-	-
K16	2015	*Macaca mulatta*	female	12	-	-	-	-	-	-	-
sk2072	C12th	*Homo sapiens*	male	?	-	-	-	-	-	-	-
sk2203	C12th	*Homo sapiens*	male	?	-	-	-	-	-	-	-
sk2011	C12th	*Homo sapiens*	male	?	-	-	-	-	-	-	-
sk1404	C12th	*Homo sapiens*	female	?	?	?	?	?	?	?	?
sk5010	C12th	*Homo sapiens*	female	?	?	?	?	?	?	?	?
sk1634	C12th	*Homo sapiens*	?	?	?	?	?	?	?	?	?
sk2201	C12th	*Homo sapiens*	?	?	?	?	?	?	?	?	?
sk11	C19th	*Homo sapiens*	female	?	?	?	?	?	?	?	?
sk228	C19th	*Homo sapiens*	male	61	-	-	-	-	-	-	-
sk334	C19th	*Homo sapiens*	female	51	28	-	-	-	-	-	44
sk36	C19th	*Homo sapiens*	female	?	-	-	-	-	-	-	-
sk39	C19th	*Homo sapiens*	female	?	-	-	-	-	-	-	-
sk53	C19th	*Homo sapiens*	female	46	28	-	-	-	-	-	-
sk62	C19th	*Homo sapiens*	female	?	-	-	-	-	-	-	-
sk63	C19th	*Homo sapiens*	female	?	-	-	-	-	-	-	-
n11	40,000 BC	*Homo neanderthalensis*	?	?	?	?	?	?	?	?	?

Table 5.1. Life history information for each sample studied.

Specimen	*F* value	*p* value
k49	168.8	<0.001
l59	369.8	<0.001
k14	429.9	<0.001
l10	247.3	<0.001
l14	682.4	<0.001
l72	164.3	<0.001
l100	333	<0.001
k16	159.6	<0.001
m8	686.4	<0.001
k23	51.45	<0.001
l56	812.3	<0.001
t46	72.5	<0.001

Table 5.2. Results of ANOVA comparisons between the results of tortuosity analyses of the cementum increments of female *Macaca mulatta* individuals and the male individual k39.

Comparison	*F*	*p*
Mean absolute height of surface	15	<0.01
mean relative height of surface	107	<0.01
Root mean square relative height of surface	133	<0.01
Maximum peak height	57	<0.01
Average maximum peak height	127	<0.01
Minimum valley depth	16	<0.01
Average minimum valley depth	20	<0.01
Average maximum peak height	2	0.2
Tenpoint average peak height	2	0.2
Maximum skew	10	<0.01
Summit density	89	<0.01
Maximum kurtosis	15	<0.01
Root mean square gradient	38	<0.01
Surface area	70	<0.01
Developed interfacial area ratio	37	<0.01
Height	47	<0.01
Depth	39	<0.01
Core	1	0.33
Mean peak height above core	42	<0.01
Mean valley depth below core	15.5	<0.01
Surface bearing area ratio	25	<0.01

Table 5.3. Results of ANOVA comparisons between the results of individual texture metric analyses between the cementum of female and male *Macaca mulatta* individuals.

Sample	Female versus male tortuosity ANOVA comparison				
	Tooth position	**Number of female individuals**	**Number of male individuals**	***F* value**	***p* value**
C12th	lm1	2	3	4.5	0.03
C19th	lm1	2	1	34.1	<0.001
C19th	lm2	3	1	54.9	<0.001

Table 5.4. Results of ANOVA comparisons between the results of tortuosity analyses of the cementum increments of female versus male archaeological human specimens.

Chapter 6.

Life history partitioning follows phylogeny among Middle-Jurassic mammaliaforms

Our understanding of the early radiation of Mammaliaformes during the late Triassic-to-Middle Jurassic has rapidly developed over the last decade thanks to a suite of exceptionally preserved fossils, and the application of state-of-the-art methodologies to explore their phylogenetic and ecological evolution. We now have examples of Jurassic mammaliaform taxa occupying an increasingly wide range of highly specialised ecological niches including volant, semi-aquatic, arboreal and fossiliferous forms. Recent studies including these new taxa have suggested that they represent part of a significant adaptive radiation in taxonomic and ecomorphological diversity during the Middle Jurassic, represented by a Mesozoic-wide peak in rates of morphological change during this period. We have here studied the fossilised cementum of a large sample of Middle Jurassic taxa from the Bathonian (168-166 million years ago) of the UK, in order to assess and compare aspects of life history among Middle Jurassic mammaliaform groups. This fauna represents major Jurassic clades, and is divided between mammaliaform (stem mammal) lineages such as the Docodonta, and crown mammalian clades including Eutriconodonta and Trechnotheria. The opportunity afforded by fossilised cementum to study lifespan in fossil taxa has allowed us to assess maximum lifespan for these groups, and we find a significant disparity between short-living crown mammals and long-living mammaliaforms. Further, as lifespan has been shown to correlate robustly with basal metabolic rate and post-natal growth rate in extant mammals, the disparity found in these lifespan estimates suggest a dramatic change in metabolic potential between mammaliaform and crown mammal clades. Mammaliaforms retain a metabolically slow life history, with lifespans akin to the more basal taxa *Morganucodon* and *Kuehneotherium*, and extant reptiles of similar body mass. Crown mammal lineages in contrast show life histories with significantly lower

lifespans, more similarly to extant mammals. We suggest that this increase in metabolic potential potentially fostered the rapid rates of evolutionary change found among crown mammals during this period, and so may be a major factor in the Early-to-Middle Jurassic adaptive radiation of crown mammals.

6.1. Introduction

Since the publication of complex, molariform teeth from Triassic deposits by Owen in 1871, the original radiation of Mammaliaformes (*sensu* Rowe, 1988; see Figures 1.2. and 1.3.) has been firmly placed between the late Triassic and Early Jurassic (Kielan-Jaworowska et al., 2004). However, several elements of this radiation have been under intense debate ever since. These include the phylogenetic patterns of the mammaliaform clade and the placement and origin of crown Mammalia within it (Rowe, 1988; Luo et al., 2004; Zhou et al., 2013; Zheng et al., 2013; Han et al., 2017), the tempo and pattern of taxonomic and ecomorphological diversity through this period (Luo, 2007; Newham et al., 2014; Close et al., 2015), and the evolution of endothermy within Mammaliaformes and the therapsid order that they arise from (Hayes and Garland, 1995; Farmer, 2003; Kemp, 2006; Lovegrove et al., 2017; **Chapter 3**). Much of the initial debate surrounding early mammaliaform evolution was framed by a lack of post-cranial fossils for the overwhelming majority of taxa (Rowe, 1988). However, over the last two decades a steady stream of remarkably preserved fossils from the Early-Mid Jurassic of China (Luo et al., 2001; Ji et al., 2006; Meng et al., 2006; Han et al., 2017)(and a handful from other locations – Dashzeveg et al., 1995; Ruf et al., 2009; Vullo et al., 2010; Martin et al., 2015) has considerably improved our understanding of mammaliaform taxonomy and ecomorphological diversity. Novel methodologies and technologies have also provided a series of new ways to assess aspects of mammaliaform evolution and provided new windows onto the lives of mammaliaform taxa (Rowe et al., 2011; Gill et al., 2014; Grossnickle and Newham, 2016). Several of these studies have highlighted a significant 'burst' in diversity during the mid-Jurassic, coeval with the appearance of the first definitive crown mammal taxa (Luo, 2007; Newham et al., 2014; Close et al., 2015). This radiation has also been postulated to correlate with an increase in metabolic potential, indicated by several changes in morphology between stem and crown mammals indicative of higher metabolic demand

(Kemp, 2006), and a significant increase in encephalization quotient (brain volume versus body mass) between Early Jurassic stem mammals and Middle Jurassic crown mammals (Rowe et al., 2011).

One such emergent technology, synchrotron radiation-based micro-computed tomography (SR CT), has allowed the imaging of dental cementum increments for the first time in fossil mammaliaform taxa (**Chapter 3**). Cementum is a collagenous tissue common to all mammaliaforms, found wrapping around the roots of teeth and serving as an attachment site for the collagenous Sharpey's fibres of the periodontal ligament (Klevezal, 1995). Cementum increments have been shown to record a circum-annual periodicity, with thin-section histological imaging displaying one thick translucent increment and one thin opaque increment deposited every year (Lieberman, 1993; Klevezal, 1995). These increments thus serve as a direct record of lifespan (Naji et al., 2016). Further, a robust inverse correlation between lifespan and both post-natal growth rate and basal metabolic rate (BMR) have allowed lifespan to be used in this thesis (**Chapter 3**) as a proxy for metabolic potential in early mammaliaforms.

We have here repeated the methodology developed **in Chapters 3 and 4** of this thesis for population size samples of fossils from the Middle Jurassic (Bathonian) fauna of Oxfordshire (UK). This site provides a diverse assemblage of fossil teeth representing several key mammaliaform and crown mammal lineages. The application of SR CT provides minimum estimates of maximum lifespan for a substantial number of specimens for each clade. Comparisons of these lifespans have allowed us to infer differences in metabolic potential among mammaliaform lineages, and to test whether these correlate with their phylogenetic placements for the first time.

6.2. Materials and methods

6.2.1. The Bathonian Oxforshire mammaliaform fauna

Disused since 1929, the Kirtlington quarry has provided a highly fossiliferous exposure of white limestone that has been subject to several studies of Middle Jurassic geology and palaeontology. Stratigraphic study by McKerrow et al. (1969), and informal palaeoecological comparisons with middle Bathonian mammal faunas on the Isle of Skye (Waldman and Savage, 1972) by Freeman (1979) suggest a middle-to-upper Bathonian age for the Kirtlington mammal fauna (approx. 167-168 mega annums;

herein Ma). However, later studies suggest an upper Bathonian age (Metcalf and Walker, 1994; Evans and Milner, 1994; Butler and Sigogneau Russell, 2016). The fauna was found within an unconsolidated marl lens and removed using sediment processing techniques outlined in Freeman (1979). Batches of marl sediment were slurried with water, before being sieved using a 2.1mm coarse sieve. Portions of sediment under 2.1mm grain size were then treated using a 15% by volume aqueous acetic acid. This left a residue consisting almost entirely of limonite particles and vertebrate micro-fossils, which were hand-picked by eye. The frequent "hollowing out" of fossil teeth and enlargement of the pulp cavity have led to the hypothesis that the origin of the Kirtlington mammal fauna is likely "coprocoenosis", the accumulation of fossils by predatory action and digestion.

The exploration of an additional site of contemporaneous material in Oxfordshire, Woodeaton quarry (Freeman, 1976), has since added to the taxonomic range of the Bathonian mammaliaform fauna of Oxfordshire. The fauna now includes the holotypes of several taxa (with additional specimens found more recently in other UK localities). These include the docodonts *Cyrtlatherium,* and *Krusatodon,*, the dryolestoid *Palaeoxonodon*, and the Morganucodontids *Wareolestes* and *Cherwellia.* Other taxa with global distributions also found in the fauna can be assigned to crown Mammalia, including eutriconodonts such as *Gobiconodon* (the holotype of species *Gobiconodon bathoniensis* was found in Kirtlington), *Eotriconodon* and other amphitheriids and gobiconodontans that could not be assigned to the genus level, Trechnotherians including the dryolestoid genus *Amphitherium* (and other dryolestids that could not be assigned to the genus level). More enigmatic taxa also found in the Kirtlington fauna include *Shuotherium*, which due to its unique, reversed molar crown pattern (a "pseudotalonid" formed anterior to the trigonid and an underdeveloped talonid) has been difficult to place phylogenetically, most recently placed in the Yinnotheria alongside *Pseudotribos* and Australosphenida. Haramiyidans including *Eleutherodon*, and multituberculates including *Kermackodon, Millsodon* and *Kirtlingtonia* (and other specimens that could not be assigned to the genus level) are also present. The placement of these taxa in relation to each other has been of particularly intense recent debate (Cifelli, 2013; Zheng, 2013; Zhou, 2013). Both clades were traditionally grouped into the "Allotheria" clade due to affinities of their unique molar morphologies, consisting of two longitudinal rows of cusps. However, increasing

amounts of post-cranial remains have led to a reassessment of Allotheria and several authors have dismantled the clade, placing multituberculates among crown mammals and haramiyidans among mammaliaforms. This interpretation has in-turn been questioned most recently, chiefly due to an interpreted lack of a post-dentary trough in several newly discovered exceptionally preserved haramiyidan specimens in several phylogenetic analyses (Zheng et al., 2013; Bi et al., 2014). This hollow in the posterior of the dentary bone is only found in mammaliaform taxa, and housed the delicate post-dentary bones involved in hearing, which were subsequently removed from the dentary in crown mammals (Kielan-Jaworowska et al., 2004). This interpretation places haramiyidans among the mammal crown and resurrects the Allotheria clade. Here, Allotheria is retained due to low numbers of individual multituberculate and haramiyid specimens, in order to provide a more even comparison with other clades represented by higher numbers of specimens. A complete summary of all taxa studied here is presented in Table 6.1. Docodonts are uniformly reconstructed as a mammaliaform clade, appearing along the stem lineage to crown mammals. The only other non-mammalian mammaliaforms from Kirtlington, the morganucodontans including *Wareolestes* (Panciroli and Benson, 2017), are known from limited specimens and neither of the two imaged in this study produced readable cementum increments. All other taxa in our sample are considered to be members of crown group Mammalia.

6.2.2. Synchrotron tomographic imaging of fossil cementum

The cementum of a total of 177 fossil teeth was imaged using synchrotron radiation-based micro-computed tomography (SR CT) during two separate experiments (Appendix 6.1). 109 fossil mammal teeth were imaged during a three-day SR CT experiment at the TOMCAT beamline of the Swiss Light Source synchrotron (Villigen, Aargau, Switzerland) from 18.11.2016–20.11.2016 (for proposal see Appendix 1.5.). Specimens were imaged using a near-monochromatic X-ray beam of 20 KeV X-ray energy, with an exposure time of 150 ms over 1501 angular projections. Propagation-based phase contrast reconstruction techniques were used to reconstruct tomographic data. For these techniques, sample-to-detector distance was kept at 14mm. A β value of $3.7e^{-8}$ and a δ value of $1.7e^{-10}$ were used for phase contrast reconstructions.

The cementum of a second sample of 68 fossil teeth was imaged using SR CT during a three-day experiment conducted at the European Synchrotron Radiation

Facility (Grenoble, France) between 01.02.17–03.02.14 (for proposal see Appendix 1.6.). Here, a near-monochromatic X-ray beam was used at 19 KeV X-ray energy, with an exposure time of 25 ms and 2999 angular projections. Propagation distance was kept at 14mm and a β value of $3.7e^{-8}$ and a δ value of $1.7e^{-10}$ were used for phase contrast reconstructions.

6.2.3. Manual and algorithmic increment counting

The increment counting algorithm explained and validated in **Chapter 4**, designed to count cementum increments using solely computer vision, was used here in conjunction with counting increments by eye. The algorithm is based on distinguishing 'true' increments from background noise in SR CT data without introducing subjectivity inherent in human vision. Radial transects are plotted through the cementum of individual SR CT slices oriented transversely through the tooth root (**Chapter 4**), and the greyscale value of each pixel encountered stored in a database. These transects are then split into five regions of equal length. Within each region, the mean greyscale value and standard deviation are calculated. Incremental pairs are distinguished as peaks (representing light increments) and troughs (dark increments) in greyscale that depart from the mean beyond the upper and lower standard deviation (respectively) (**Chapter 4**).

Increments were also counted by eye in a random sub-sample of 34 cementum images by three observers with previous experience counting cementum increments in SR CT data of fossil cementum (the same observers that previously counted increments in **Chapter 3 Table 3.2**). As in **Chapter 3,** Observer one (Newham) utilised the volumetric nature of SR CT datasets to follow cementum increments through their entire longitudinal and transverse trajectories through the tissue. This allowed the identification of regions of lensing and coalescence between primary cementum increments, and regions of highest increment contrast that did not suffer from these phenomena. Such high contrast regions were selected by the observer, and used to create "virtual thin-sections", whereby 10 transverse SR CT slices were combined using the "z projection" tool in ImageJ/Fiji (Schneider et al., 2012). This considerably improved the contrast between cementum increments in resulting images that were studied by all three observers and used for algorithmic increment counting (Fig. 6.1).

The precision between algorithmic counts and the counts of each observer was quantified by calculating the coefficient of variation (*CV*) between all four estimated counts for each specimen (three human counts and one algorithmic count)(*CV* = [mean count/standard variation]*100), and the Pearson's correlation coefficient (*r*):

$$\mathbf{1.}\ r = \frac{N\Sigma xy - (\Sigma x)(\Sigma y)}{\sqrt{[N\Sigma x^2 - (\Sigma x)^2][N\Sigma y^2 - (\Sigma y)^2]}}$$

where N equals the number of pairs of scores, Σxy equals the sum of the products of paired socres, Σx equals the sum of x scores, Σy the sum of y scores, Σx^2 the sum of squared x scores and Σy^2 the sum of squared y scores.

The resultant values of *CV* and *r* for our counts were given a context within the wider cementum literature by statistically comparing them to values from 10 recent cementochronological studies, including the study described in **chapter 3** (Table 3.4), using ANOVA (analysis of variation).

6.2.4. Estimating body mass in fossil mammaliaforms

Both extant mammals and reptiles exhibit a significant linear relationship between lifespan and body mass when both factors are log transformed (Fig. 3.4.). Comparison of their relationships highlights the significantly longer lifespans experienced by ectothermic reptiles in comparison to endothermic mammals of similar body mass. Comparing the relationship between body mass and lifespan in fossil mammaliaforms with that of extant taxa will thus allow inference of their metabolic grade or potential, in comparison with known ectotherms and endotherms of similar body mass.

Several attempts have been previously made to estimate body mass in fossil mammals and mammaliaforms, based on scaling factors between various skeletal and dental elements with known body mass in extant mammal taxa. These include estimating mass from skull length (Gingerich and Smith, 1984; Millien and Bovy, 2010; Bi et al., 2014; 3), dentary length (Foster, 2009), humerus length (Campione and Evans, 2012) and femoral length (Luo et al., 2017). However, the Mid-Late Bathonian fauna of the UK are represented by a scarcity of long bones and cranial remains, especially those attributable to known mammal taxa. The scaling relationship between dentray length and body mass from Foster (2009) was thus employed here. This study used a robust

scaling relationship between the natural logs (ln) of dentary length and body mass in 41 extant marsupial taxa to estimate body mass from the dentaries of 21 fossil mammaliaform taxa from the Morrison Formation (Late Jurassic; approx. 156.3-146.8 Ma), and an additional six mammaliaforms from the Early Jurassic to Early Cretaceous of the UK and China, where:

2. Ln(body mass; g) = (2.9677*Ln[dentary length; mm]) – 5.6712

The taxa represented in the Kirtlington fauna are only known from isolated teeth and dentulous fragments, and so dentary length could not be directly measured. Instead, dentary length was estimated by developing a series of scaling relationships between (antero-posterior) m1 length and dentary length for fossil taxa of differing molar counts. m1 and dentary lengths were taken directly from Foster (2009) for the 16 non-multituberculate taxa studied (multituberculates and other "allotherian" taxa were excluded as their dentary morphology is highly derived in comparison with other non-therian mammaliaforms), and for an additional 23 taxa from the wider literature (Appendix 6.2). For the additional taxa, lengths were measured directly from accompanying figures, using the scale bars provided. Finally, expected molar counts were generated for each taxon either from direct counts or estimates from the literature, or by expected counts based on their phylogenetic affinities.

A series of scaling factors were then generated by using linear least squares regression to compare m1 length to dentary length, in increasingly broad sub-samples of molar counts. The r^2 values and *n* values were recorded for each subsample (Table 6.2). The broadest subsample (highest *n* value) that included the relevant molar count for each taxon represented in the kirtlington fauna, while providing the highest r^2 value of 0.84 was comprised of 29 specimens of known dentary length and molar counts between 3-5. The regression equation between m1 length and dentary length in this sub sample followed:

3. dentary length (mm) = [m1 length(mm)*10.184] + 8.026

The resultant dentary length estimates based on m1 length for our taxa were then used to estimate body mass in grams (g) using **formula (1).**

For allotherian taxa, body mass was calculated using the scaling formula between m1 area and body mass presented in Wilson et al. (2012):

4. Ln(body mass) = 1.827*Ln(m1 area) + 1.81

6.2.5. Estimating basal metabolic rate and post-natal growth rate in fossil mammaliaforms

Hulbert et al. (2007) used linear regression to find a significant relationship between the logged maximum wild lifespan and the logged mass-specific basal metabolic rate calculated for 267 extant mammal species:

4. Maximum lifespan (years) = 270*basal metabolic rate ($kj.kg^{-1}.day^{-1}$)$^{-0.61}$

This was used to estimate BMR in fossil taxa based on their estimated maximum lifespan.

de Magalhães et al. (2007) alternatively used linear regression to compare the natural logs of lifespan to average post-natal growth rate (*k*), to find a significant negative relationship between the two factors following:

5. Ln(maximum lifespan, years) = [0.475*Ln(*k* ,$days^{-1}$)] – 5.36

This was in-turn used to estimate *k* in fossil taxa based on their maximum lifespan.

6.3. Results and discussion

Of the 177 specimens scanned, 89 produced readable cementum increments. 33 of these specimens were docodonts, nine were eutriconodonts, 19 were Trechnotherians, two were yinotherians (i.e. Shuotherium) six were 'allotherians' (multituberculates and haramiyids), and the remaining 19 could not be assigned taxonomically beyond 'Mammalia *indet*.' (*indet*; *indeterminate*). The other 88 specimens had either lost the cementum tissue, or it had been diagenetically altered beyond the point of increment preservation (Figs. 6.1-2).

Synchrotron radiation-based micro-computed tomography (SR CT) reveals the same histological features in tooth roots of several Mid-Jurassic taxa as found in *Morganucodon* and *Kuehneotherium*. A granular layer of Tomes can be interpreted in

most specimens that provided readable cementum increments (Fig. 6.2.), and a Hyaline layer of Hopewell Smith is also detectable in several specimens (Fig. 6.2.h.). Cementum increments can be followed through the entire tooth root, along both their entire transverse and longitudinal trajectories. There are clear differences in the thickness of cementum between taxa, with docodontans of high increment counts (>6) displaying significantly thicker cementum than fossil crown mammals in transverse SR CT slices (Fig. 6.1.). Both docodontans and crown mammals also display regions of prominent cellular cementum, evidenced by preserved cellular voids within the cementum (Fig. 6.1.). The presence of cellular cementum in the early synapsid *Dimetrodon* (LeBlanc et al., 2016) suggests cellular cementum is pleisiomorphic for mammaliaforms. However, evidence of cellular voids has not been found in either *Morganucodon* or *Kuehneotherium* (**Chapter 3**). The disparity in the presence of cellular cementum between mammaliaform taxa may relate to differences in ecology. Cellular cementum is known to form as a reactive tissue to accommodate significantly high occlusal forces acting upon a tooth root (Klevezal, 1995). However, the crown morphology of the molars of docodonts, eutriconodonts and Trechnotherians suggests an insectivorous ecology similar to that of *Morganucodon* and *Kuehneotherium* (although *Repenomamus* has been suggested to be an active carnivore). A build up of cellular cementum over time may be also explained given the extended lifespans of docodonts. However these are also comparable to those of *Morganucodon* and *Kuehneotherium*.

The cause behind the lack of cellular cementum in *Morganucodon* and *Kuehneotherium* thus remains unclear. *Morganucodon* is regarded as the first mammaliaform to exhibit diphyodont replacement of teeth (single replacement of non-molar teeth). The mechanism behind this transition from continual replacement in the closest non-mammaliaform synapsid (*Sinoconodon*) is unknown. It may be that the relationship between cementum and the periodontium had to fundamentally change in order to achieve this initial evolutionary change, with collagen fibres only being received from the periodontal ligament (and thus only forming acellular cementum). However, this postulation can only remain as such due to the lack of clinical evidence for these fossil taxa.

Increment counts for the sub-sample of SR CT cementum data of 34 random specimens suggest high precision both between increment counts estimated by eye by three independent observers, and between counts estimated by eye and automated

counts generated using computer vision (Fig. 6.3.a.)(Table 6.3.). The mean coefficient of variation (*CV*) between all four counts (three human and one automated count) for all 30 specimens is 6.64. This value is lower than the values for *Morganucodon* (*CV* = 9.32), and higher than those of *Kuehneotherium* (*CV* = 4.89), calculated in **Chapter 3**, and significantly lower than the *CV* value of any of the 10 previous studies of extant mammals cited in **Chapter 3** (Table 6.4). The highest Pearson's correlation coefficient (*r*) value (*r*=0.99) was between automated increment counts and estimated increment counts by Observer 1. This value is higher than that of both *Morganucodon* (*r*=0.92) and *Kuehneotherium* (*r*=0.96)(Table 6.4). However the lowest *r* value, between automated counts and estimated counts by Observer 2 (*r*=0.93), is lower than that of *Kuehneotherium*. These values support the validity of the presented estimates of maximum lifespan presented here, based on estimated increment counts, and the future use of the automated increment counting method pioneered in this thesis.

The Docodonta provide the highest increment counts of any of the fossil clades in this study. Several specimens have increment counts of between eight and 12 (Figs. 6.2a-b, 6.3.b). The highest count of any crown group specimen is six (Table 6.5)(Figs. 6.2.i., 6.3.b). The distribution of age estimates for each higher order taxon studied here (Docodonta, *n*=33; Eutriconodonta, *n*=9; Trechnotheria, *n*=19; Yinotheria, *n*=2; "Allotheria", *n*=6)(Table 6.5) follow a range of patterns in their skew and kurtosis. Docodonta and Eutriconodonta show low kurtosis (0.928 and 0.91 respectively), similar to that of *Kuehneotherium* (kurtosis of 0.31), whereas Trechnotheria and "Allotheria" provide negative kurtosis values (-1.419 and -1.005 respectively). All clades show left (young) skew, with Docodonta providing a considerably higher skew (1.323) than any other Mid Jurassic clade (0.603 for Eutriconodonta, 0.223 for Trechnotheria and 0.47 for "Allotheria"), and the Early Jurassic *Kuehneotherium* (0.47). However, no Mid Jurassic taxon provides a comparably high skew compared to *Morganucodon* (skew = 2.05).

When all fossil lifespan estimates are compiled for broader samples of mammaliaforms (comprising lifespan estimates of docodonts, *Morganucodon* and *Kuehneotherium*, *n*=93) and crown mammals (comprising eutriconodonts, Trechnotherians and allotherians, *n*=36), kurtosis remains higher for mammaliaforms compared to crown mammals (1.779 and -0.91 respectively), as does skew (1.184 and 0.469 respectively). The distribution of the crown mammal sample conforms to the age

distributions of extant mammals of similar body mass (<150g) and maximum lifespan, with an overrepresentation of the youngest age classes resulting in left (positive) skew and low kurtosis around a mean age of three years (Kryštufek et al., 2005; Haigh et al., 2014). The mammaliaform sample instead conforms to the age distributions of reptiles of similar lifespan, with a distinct lack of yearling taxa and kurtosis levels that conform closer to a normal distribution around a mean of 4.6 years (Zug et al., 1987).

Using increment counts as a minimum estimate of maximum lifespan, they were logged, and plotted against logged estimates of body mass for each taxon using least squares linear regression, and compared to data for extant mammals and reptiles (Fig. 6.4). These comparisons show that all docodont taxa straddle the reptile regression line, and are the only non-reptile taxa to do so below 1000g. This suggests that their lifespans significantly extend beyond any extant mammal (or fossil crown mammal) of comparable body mass. Instead they conform to extant reptiles of similar body mass, homoeothermic mammals with body masses two orders of magnitude or more larger (e.g. *Vulpes vulpes*, *Hyaena brunnea*), and heterothermic mammals between one and two orders of magnitude larger (e.g. *Scirius variegatoides*, *Spermophilus parryii*). The lifespans of crown Mammalia fossil taxa instead conform to those of extant mammals of equivalent body size (Fig. 6.4). The maximum lifespan estimated for the Trechnotherian *Palaeoxonodon* correlates with heterothermic taxa of comparable body size (e.g. *Glirulus japonicas, Muscardinus avellanarius*). Whereas the maximum lifespan estimated for the eutriconodont *Phascolotherium* correlates with lies close to (but under) the regression line between body mass and maximum lifespan for extant mammals, alongside *Scalopus aquaticus.*

The differences in lifespans between Mid Jurassic stem and crown fossil taxa of comparable body mass corroborate our previous interpretation of cementum increments in the basal mammaliaform taxa *Morganucodon* and *Kuehneotherium* (Fig. 6.4). Both taxa produced lifespan estimates similar to those of docodonts recorded here (a minimum estimate of maximum lifespan of 14 years for *Morganucodon*, and nine years for *Kuehneotherium*), and significantly longer than extant mammals and fossil crown mammals of comparable body mass. Incorporating the lifespans of these two taxa into our dataset, the lifespans of all stem mammaliforms are shown to be significantly higher than any fossil or extant crown mammal of comparable body mass (Fig. 6.4). Following the inversely proportional relationship between lifespan, basal metabolic rate (BMR),

and post-natal growth rate, this was interpreted as evidence for a lower metabolic potential in mammaliaforms, relative to extant mammals. Our new results add further support to this interpretation, and pinpoint a major change in metabolic potential between stem and crown clades living coevally during the Mid Jurassic.

Estimates of lifespan were in-turn used to quantitatively estimate both the BMR and post-natal growth rate of fossil mammals using the negative logarithmic scaling relationships presented by Hulbert et al., (2007) and de Magalhães et al. (2007)(respectively)(Table 6.6). ANOVA comparisons suggest that BMR is significantly higher amongst Mid Jurassic crown mammal genera (n=2, maximum of 1069 kj.kg.day^{-1} provided by *Phascolotherium*), compared with those of Early-Mid Jurassic mammaliaform genera (n=5, maximum of 241 kj.kg.$^{day-1}$ provided by *Kuehneotherium*)(F=16.29; p=0.01). ANOVA comparisons also suggest that growth rate estimates (k, measured in days^{-1}) are significantly higher in crown taxa (eutriconodonts and Trechnotherians; n=2) compared to mammaliaforms (*Morganucodon*, *Kuehneotherium* and docodonts; n=5)(F=7.95; p=0.031). Although the crown mammal *Palaexonodon* provides one of the smallest body mass estimates in our sample (16.53g), the other crown taxon *Phascolotherium* provides one of the highest estimates (70.76g). Hence, a difference in body mass cannot solely explain the different estimates of physiological properties between mammaliaforms and crown mammals during the Early-Middle Jurassic.

A significant increase in metabolic potential from stem to crown mammals may help explain the well documented 'burst' of crown mammalian diversity identified within the mid-Jurassic (Luo, 2007; Newham et al., 2014; Close et al. 2015). Close et al. (2015) suggest that this burst is associated with the exploration of ecospace in novel adaptive zones, and it is during this period that mammals begin to explore a wide range of ecological niches and behaviours (Luo, 2007). However, until now the causes of this burst have remained open to conjecture. We suggest that the development, among early crown mammalian clades, of metabolic potential to levels similar to extant mammals may be a key driver for this pattern.

Traditionally depicted as obligate terrestrial insectivores with some possible adaptations for digging, recently discovered docodont species including the semi-aquatic *Castorocauda* (one of the largest known mammaliaform taxa at ~500g)(Ji et al., 2006), and the arboreal *Agilodocodon* (Meng et al., 2015) considerably increase their

known ecological diversity. Unfortunately, of these disparate taxa only *Castorocauda* and *Haldanodon* are included in the analysis of Close et al. (2015). The analysis of Close et al. (2015) suggests slow rates of morphological change along the external node separating the Docodonta from other mammaliaforms. Comparably slow rates are also suggested for the Eutriconodonta. However, the nodes separating the Multituberculata, and the Dryolestidae from other crown mammals are represented by some of the fasted rates of morphological change in the analysis of Close et al. (2015), only exceeded during the therian diversification. This is reflected in time series data presented by Close et al. (2015; Fig. 1.b), where the Early-Mid Jurassic is represented by a concentration of data points representing significantly high rates of phenotypic evolution, and no evidence of slow rates of phenotypic evolution. Differences in the rates of behavioural and ecological change, ontogenetic differences at individual levels and responses to environmental change are all strongly influenced by metabolism in tetrapods (Gittleman and Stevens, 2012). Increased metabolic rate has been shown to encourage higher mutation rates caused by free radicals and metabolic by-products (Rand 1994). Ectotherms also show much slower rates of molecular evolution for their size compared to endotherms (Martin, 1995). Hence, the substantial increase in taxonomic and morphological diversity occurring through the Early-Mid Jurassic (Newham et al., 2014; Close et al., 2015), represented by the radiation of major crown mammal clades including eutriconodonts, multituberculates and stem "cladotherians" including dryolestids, may have been fostered by a significant increase in their metabolic potential relative to more primitive taxa including docodonts and morganucodontans.

The evolution of endothermy amongst synapsids has been suggested to follow one of three patterns, differing in the proposed initial selective pressure. These alternatively suggest that (1) higher maximum metabolic rate (MMR) was originally selected for to provide more sustained rapid aerobic activity (the "aerobic scope" hypothesis)(Bennett and Ruben, 1979; Koteja, 2000), (2) that higher basal metabolic rate (BMR) was initially selected for enhanced thermoregulative control (the "thermoregulation-first" hypothesis)(Crompton et al., 1978; Farmer, 2003), or (3) that both evolved in lockstep with each other (the "correlated progression" hypothesis)(Kemp, 2003; Clarke and Pörtner, 2010). Within these hypotheses, various initial selective pressures have been suggested. For example, increased sustained

aerobic activity has been suggested for its own benefit (Bennett and Ruben, 1979), to allow increased parental care and provisioning (Koteja, 2000), or for increased foraging ability (Hopson, 2012). Alternatively increased metabolic efficiency (higher BMR) would allow increased sustained activity (Clarke and Pörtner, 2010) and the benefits of embryonic incubation (Farmer, 2003). Overall, increases in both sustained aerobic capacity and metabolic efficiency would lead to more efficient, integrated animals (Kemp, 2006).

The significant increase found here in estimates of BMR and post-natal growth rate between mammaliaforms and crown mammals among Early-Middle Jurassic fauna suggests that at least one of these selective pressures was already acting upon endothermic evolution during this period. However, the lack of evidence for MMR in the crown mammal taxa studied here means that this result is equally applicable to each of the three hypothesised initial selective pressures. The most subscribed-to hypothesis currently regarding metabolic evolution among synapsids is the 'aerobic capacity model' (Hayes and Garland, 1995). This states that the initial selective driver for endothermic evolution among synapsids was an increase in maximum metabolic rate (MMR), and so increases in BMR occurred concomitantly after increases in MMR. This is possible given our results of significant evolution in BMR between mammaliaforms and crown mammals, although requires evidence of a previous increase in MMR between non-mammalian cynodont taxa and mammaliaforms, unaccompanied by an increase in BMR (Fig. 6.5.a.). The study of fossilised nutrient foramina and their relation to blood flow through the femur of *Morganucodon* in **Chapter 3** suggested that basal mammaliaforms had yet to achieve an MMR beyond that of extant reptiles by the Early Jurassic. However, in lieu of directly comparable proxy evidence for MMR in either more basal non-mammaliaform cynodonts, or more derived Mid-Jurassic crown mammals, the connotation of this finding for the hypothesised pattern of endothermic evolution amongst synapsids remains equivocal. When presented together, these results may either be used to support: (a) an increase in mammaliaform MMR from cynodonts, followed by an increase in crown mammal BMR (the "aerobic scope" hypothesis)(Fig. 6.5.a.), (b) a stasis in MMR but evolutionary increase in BMR between cynodonts, mammaliaforms and crown mammals (the "thermoregulation first" hypothesis)(Fig. 6.5.b.), or (c) both properties evolved in lock-step, from low levels amongs non-mammalian cynodonts, to levels seen in extant ectothermic reptiles amongst

mammaliaforms, to equivalent levels seen in extant mammals in Mid Jurassic crown mammals (Fig. 6.5.c.).

Finally, our data provides further support for the interpretation of a mosaic nature of physiological evolution among mammaliaforms. While exhibiting fur, whiskers, complex life history strategies and potentially a muscular diaphragm, Middle Jurassic docodont-grade mammaliaforms had yet to develop a basal metabolic potential significantly beyond that of ectothermic extant reptiles. This reinforces the need to re-evaluate the use of singular lines of evidence and their presence/absence for evaluating the complex process of endothermic evolution among synapsids. It is clear that various physiological, osteological and morphological traits evolved at different tempos and at different phylogenetic levels during the evolution from ectothermic pelycosaur-grade therapsids to endothermic crown mammals. The development of our dataset to cover mammaliaforms from the Early- to Middle-Jurassic extends the fledgling use of quantifiable measurements of metabolic properties among fossil mammaliforms, offering an evolutionary context to results presented for *Morganucodon* and *Kuehneotherium*, and highlights their use for providing a robust framework for interpreting other lines of evidence for mammaliaform physiology.

6.4. Conclusions

Through the non-destructive sampling of fossilised cementum using synchrotron radiation computed tomography (SR CT), we have estimated maximum lifespan for a variety of mammaliform taxa from the Mid Jurassic of the United Kingdom. This fauna represents several key clades of crown mammals (Eutriconodonta, Trechnotheria and Multituberculata), and the mammaliaform clade Docodonta. A significant disparity in maximum lifespan exists between mammaliaforms and crown mammals; with docodonts living up to 12 years of age and no individual crown mammal living beyond six years. Following body mass estimation using a novel scaling factor between m1 length and dentary length for non-therian taxa, comparisons could be made between estimated body mass and lifespan for these fossil taxa and those of extant mammals and reptiles. These comparisons show that while crown fossil taxa correlate with extant mammals, docodonts significantly outlive any extant mammal of comparable body mass and instead correlate with comparably sized reptile taxa and mammals one–to-two

orders of magnitude larger. The series of inverse proportional relationships between these factors and basal metabolic rate suggests that mammaliaforms occupied a more reptilian metabolic grade compared to both fossil and extant members of crown group Mammalia. This inference is supported by estimates of post-natal growth rate and basal metabolic rate from the maximum lifespans of stem and crown mammal fossil taxa, both of which are significantly higher among the crown mammalian taxa studied here.

The finding of a significant difference in metabolic potential between stem and crown mammals living coevally in the Bathonian of the Middle Jurassic conforms with previous identification of a significant burst of taxonomic and ecomorphological diversity amongst crown mammals during this period. Given the well-known positive relationship between metabolic potential and rate of evolution, we postulate that the attainment of higher metabolic rates among early crown mammals fostered the rapid cladogenesis and elevated rate of morphological change found.

Our findings highlight the exciting potential of tomographic cementochronology for studying the lifespans of Mesozoic mammals. This technique offers the opportunity to test our hypothesis that a significant increase in metabolic potential occurred coevally with the evolution of the mammal crown group, and aided the rapid expansion of crown mammals into novel ecomorphological niches. By studying fossil cementum in taxa representing key clades across the Mesozoic from the Mid Jurassic to the Late Cretaceous, future work may plot trends in metabolic evolution through the crown mammal phylogeny for the first time during this period, with a temporal and quantitative resolution not available using other, binary indicators of physiology in fossils. Comparison of lifespans between taxa from different periods of the Mesozoic will allow us to discriminate whether trends in BMR follow those seen in ecomorphological diversity and rates of morphological change. If lifespan estimates remain static throughout the Mesozoic for crown taxa of particular body mass, proceeding from our Mid Jurassic taxa, this would corroborate the slow rates of morphological change seen in previous studies and support our inference that the attainment of the current mammalian metabolic potential occurred during the Mid Jurassic and drove an adaptive radiation of crown group mammals.

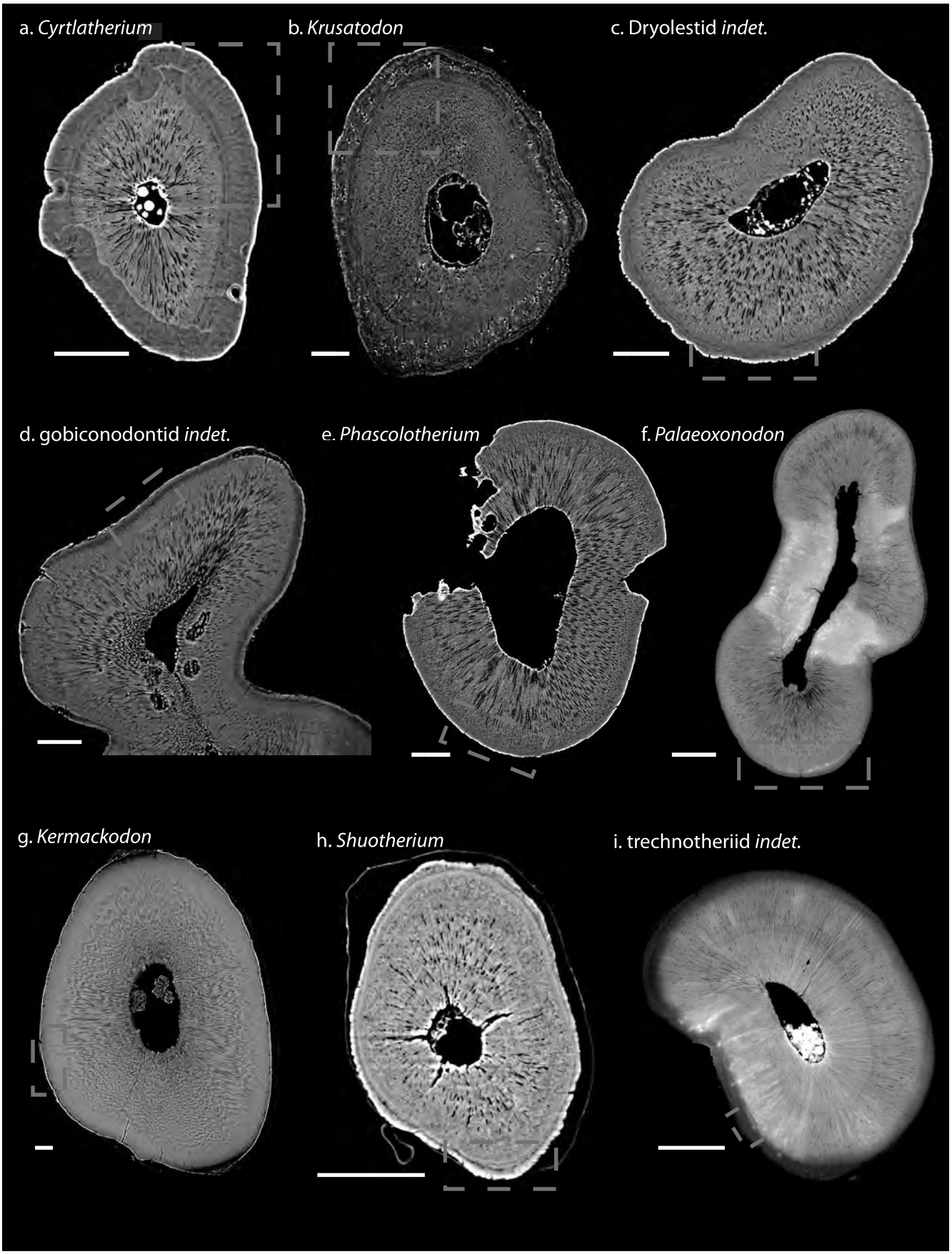
a. *Cyrtlatherium*
b. *Krusatodon*
c. Dryolestid *indet.*
d. gobiconodontid *indet.*
e. *Phascolotherium*
f. *Palaeoxonodon*
g. *Kermackodon*
h. *Shuotherium*
i. trechnotheriid *indet.*

Figure 6.1. Overview of single distance phase contrast reconstruction data from synchrotron radiation computed tomographic imaging of Mid Jurassic (Bathonian, ~168-166 Ma) mammaliaform molar roots from the Kirtlington fauna. (**a**) The Docodont genus *Cyrtlatherium.* (**b**) The docodont genus *Krusatodon.* (**c**) A dryolestoid specimen that could not be identified to generic level. (**d**) A eutriconodontid that could not be identified beyond the family gobiconodonta. (**e**) The eutriconodontid genus *Phascolotherium.* (**f**) The dyrolestoid genus *Palaeoxonodon.* (**g**) The multituberculate genus *Kermackodon.* (**h**) The enigmatic genus *Shuotherium.* (**i**) A trechnotheriid specimen that could not be identified to generic level. All white scale bars represent 100μm. Dashed red boxes indicate regions of interest presented in greater detail in Figure 2.

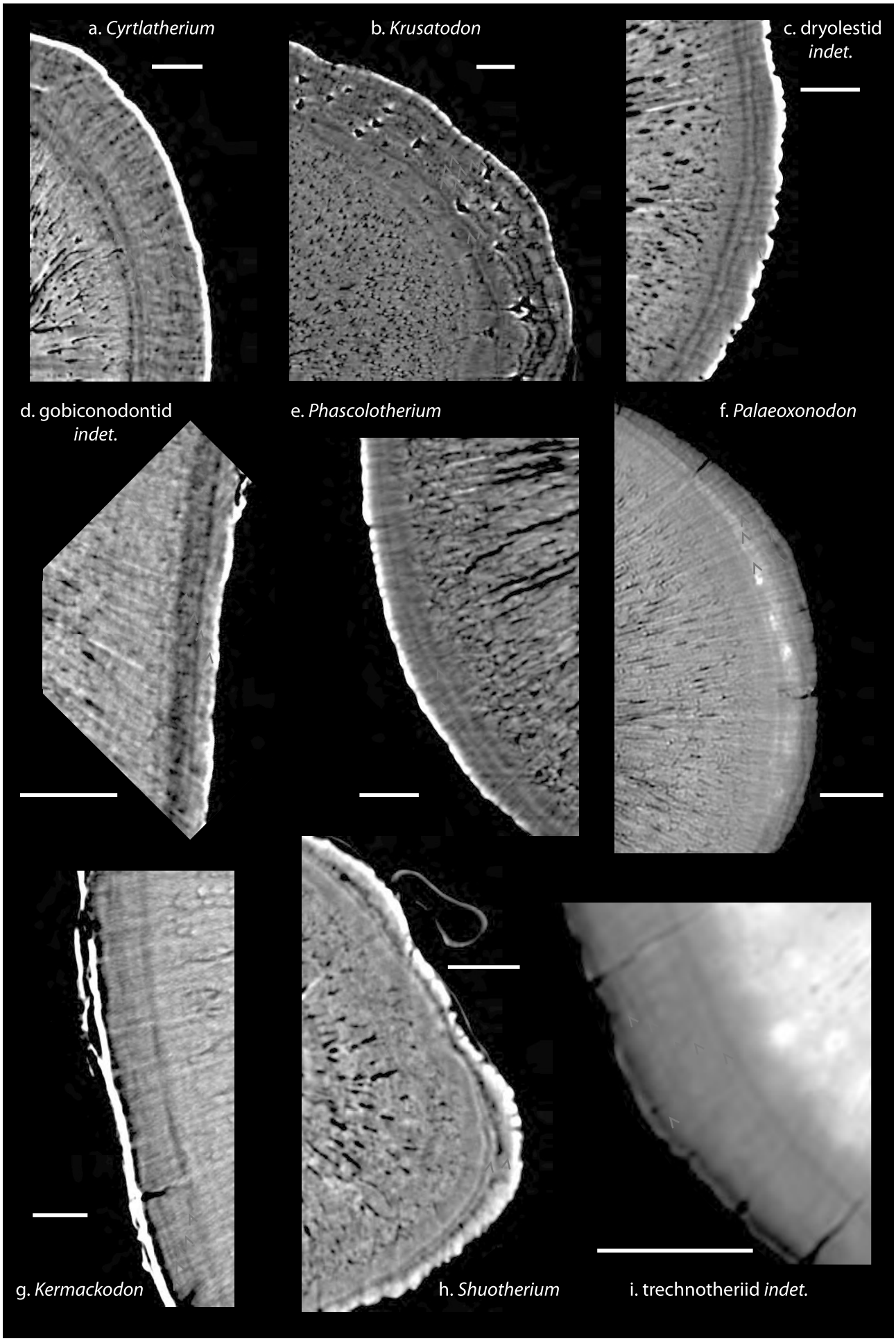
a. *Cyrtlatherium*
b. *Krusatodon*
c. dryolestid *indet.*
d. gobiconodontid *indet.*
e. *Phascolotherium*
f. *Palaeoxonodon*
g. *Kermackodon*
h. *Shuotherium*
i. trechnotheriid *indet.*

Figure 2. Details of the increment cementum in images presented in figure 1. (**a**) The Docodont genus *Cyrtlatherium*, displaying 10 incremental pairs (**b**) The docodont genus *Krusatodon,* displaying eight incremental pairs (**c**) A dryolestoid specimen that could not be identified to generic level, displaying three incremental pairs (**d**) A eutriconodontid that could not be identified beyond the family gobiconodonta, displaying four incremental pairs (**e**) The eutriconodontid genus *Phascolotherium*, two incremental pairs (**f**) The dyrolestoid genus *Palaeoxonodon*, displaying five incremental pairs (**g**) The multituberculate genus *Kermackodon*, displaying five incremental pairs (**h**) The enigmatic genus *Shuotherium,* displaying two incremental pairs. (**i**) A trechnotheriid specimen that could not be identified to generic level, displaying six incremental pairs. All white scale bars represent 30μm. Red arrows highlight the light increment in each incremental pair.

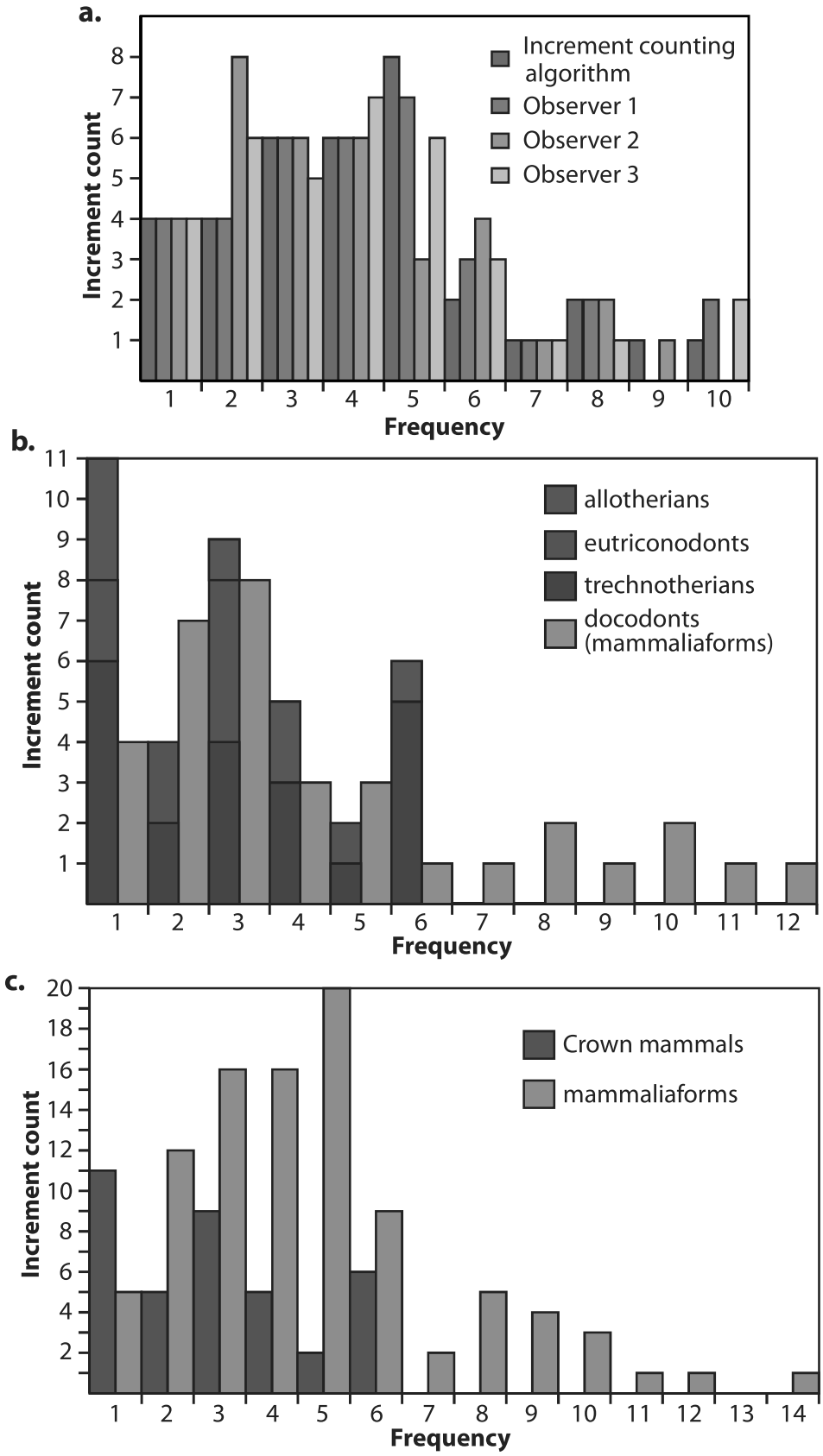

Figure 6.3. Histograms displaying the frequency distributions of cementum increment counts. (**a**) Distributions of counts estimated by eye by three human observers, and automated counts estimated using the algorithm developed in **Chapter 4**. (**b**) Distribution of counts for higher order taxa estimated by Observer one. (**c**) Distributions of counts for all crown mammals studied here versus the combined stem Mammaliaform samples from this study and **Chapter 3**.

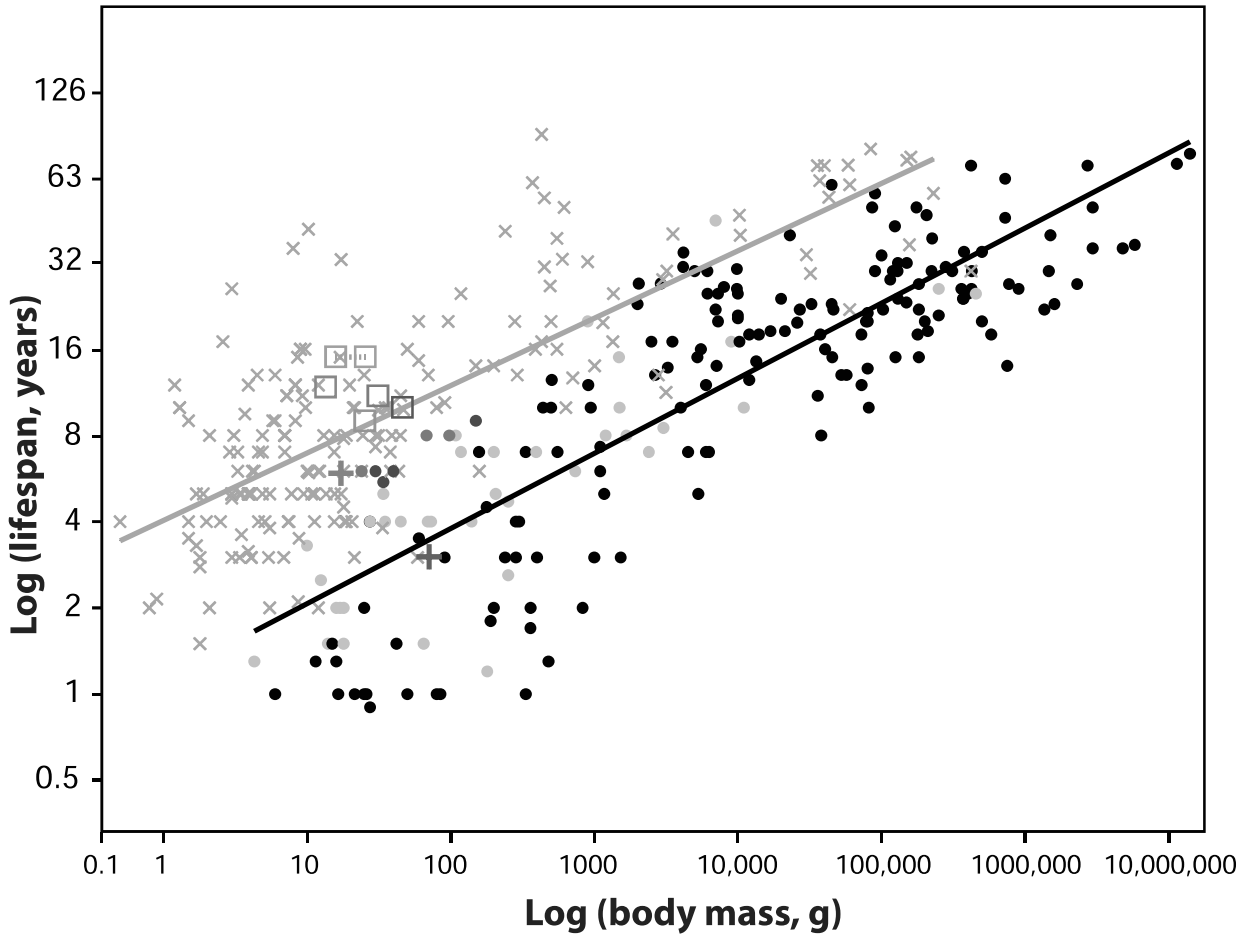

●	Extant homeothermic mammal	×	Extant reptile
●	Extant Heterothermic mammal	□	*Cyrtlatherium*
●	Extant gliridae	□	*Borealestes*
●	Extant geomyidae	□	*Krusatodon*
□□	Min/max. body mass estimates for *Morganucodon*	+	*Phascolotherium*
□	*Kuehneotherium*	+	*Palaeoxonodon*

Figure 6.4. Logged body mass versus logged lifespan for fossil mammaliaforms (green circles), fossil crown mammals (coloured crosses), extant reptiles (blue x's) and extant mammals (coloured circles).

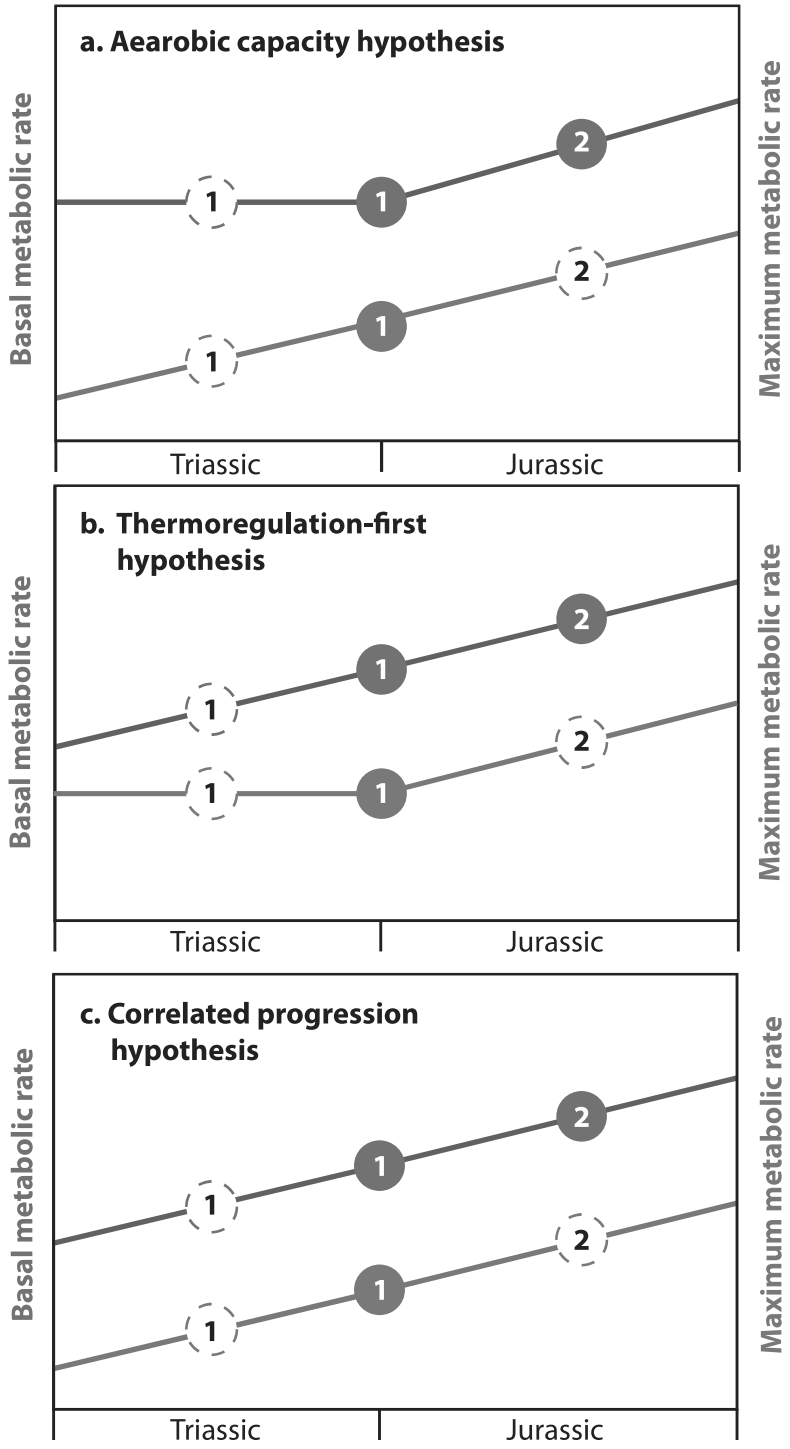

Figure 6.5. Schematic illustrations of the three principal hypothesised patterns for endothermic evolution amongst synapsids. (**a**) The aerobic capacity hypothesis, whereby increase in maximum metabolic rate (MMR) is initially selected for, followed by a concomitant increase in basal metabolic rate (BMR). (**b**) The thermoregulation-first hypothesis, whereby increase in BMR is initially selected for, followed by an increase in MMR. (**c**) The correlated progression hypothesis, where increase in both BMR and MMR follow the same temporal pattern. Solid red circles **1** and **2** Highlight the periods through time where BMR has been confidently estimated among mammaliaforms. Solid green circle **1** highlights the Late Triassic-Early Jurassic interval where MMR has been estimated for *Morganucodon.* Dashed circles indicate where evidence of comparable measurements of BMR and/or MMR are needed to further assess their temporal patterns.

Taxon	Higher level taxon	Specimens imaged	Specimens with readable increments
amphilestid	Eutriconodonta	6	1
Amphitherium	Trechnotheria	2	2
***Borealestes* indet.**	**Docodonta**	13	11
Borealestes serendipitus	**Docodonta**	4	2
***Cyrtlatherium* indet.**	**Docodonta**	11	5
Cyrtlatherium canei	**Docodonta**	1	1
docodont	**Docodonta**	16	6
dryolestid	Trechnotheria	5	2
Eleutherodon	"Allotheria"	6	1
eutriconodont	Eutriconodonta	4	0
gobiconodont	Eutriconodonta	4	2
haramiyid	"Allotheria"	2	1
Kermackodon	"Allotheria"	1	1
Kirtlingtonia	"Allotheria"	1	0
Krusatodon kirtlingtonensis	**Docodonta**	10	7
morganucodontid	**Morganucodonta**	1	0
multituberculate	"Allotheria"	5	4
Palaeoxonodon ooliticus	Trechnotheria	30	15
Peraiocynodon	**Docodonta**	1	1
Phascolotherium	Eutriconodonta	10	5
Shuotherium	Yinotheria	3	1
Shuotherium dongi	Yinotheria	1	1
symmetrodont	Trechnotheria	1	0
Wareolestes	**Morganucodonta**	1	0
mammal indet.	Mammaliaformes	38	19

Table 6.1. Numbers of scans, and numbers of scans that produced readable cementum increments, for each clade studied in both synchrotron experiments.

Subsample	Scale	*r*^2	*n*
3-4 molars	y=(x*10.167)+7.135	0.88	17
3-5 molars	y=(x*10.184)+8.026	0.84	29
3-6 molars	y=(x*10.187)+8.5941	0.78	32
full dataset	y=(x*9.265)+11.214	0.65	38
4-5 molars	y=(x*11.573)+6.58	0.82	22
4-6 molars	y=(x*11.834)+6.766	0.75	25
4-9 molars	y=(x*10.299)+10.421	0.57	31
5-6 molars	y=(x*12.22)+7.004	0.74	15
5-9 molars	y=(x*10.448)+11.363	0.55	21
6-9 molars	y=(x*11.956)+12.638	0.67	9

Table 6.2. Scaling factors between m1 length and dentary length for increasingly broad subsamples of Mesozoic fossil mammals (data presented in Appendix 6.2), separated by number of molars within the molar row.

Taxon	Algorithm count	Observer one count	Observer two count	Observer three count	*CV*
Phascolotherium	3	3	2	3	18.182
Phascolotherium	3	3	2	2	23.094
dryolestid	5	5	2	5	35.294
Borealestes	3	3	3	3	0
Krusatodon	3	3	2	2	23.094
haramiyid	1	1	1	1	0
Mammal *indet.*	8	8	7	7	7.698
Borealestes	4	4	4	4	0
docodont	6	6	6	6	0
Krusatodon	2	2	2	2	0
docodont	2	2	2	2	0
gobiconodont	5	5	5	4	10.526
dryolestid	4	4	3	3	16.496
docodont	4	4	4	4	0
Cyrtlatherium	9	10	9	10	6.077
docodont	8	8	8	8	0
Borealestes	5	5	4	5	10.526
Palaeoxonodon freemani	4	4	4	4	0
Palaeoxonodon freemani	4	4	4	4	0
Shuotherium	3	3	3	3	0
Palaeoxonodon freemani	1	1	1	1	0
Krusatodon kirtlingtonensis	1	1	1	1	0
Palaeoxonodon ooliticus	4	4	4	4	0
Palaeoxonodon ooliticus	5	6	6	6	8.696
Palaeoxonodon ooliticus	6	6	6	5	8.696
Krusatodon	10	10	8	10	10.526
Palaeoxonodon ooliticus	5	5	3	5	2.222
Krusatodon kirtlingtonensis	7	7	6	6	8.882
docodont	5	5	5	5	0
Kermackodon	5	5	5	5	0
Palaeoxonodon ooliticus	1	1	1	1	0
Palaeoxonodon ooliticus	3	3	3	3	0
Shuotherium dongi	2	2	2	2	0
Cyrtlatherium	2	2	2	2	0

Table 6.3. Comparisons between increment counts estimated by three observers, and those generated by the algorithm presented in **Chapter 4**. *CV*; coefficient of variation.

Study	Taxon	*n*	Maximum age (years)	Mean *CV*	Mean *r*
Kirtlington fauna subsample	-	30	10	6.64	0.96
Thesis Chapter 3	*Morganucodon*	34	14	9.32	0.92
Thesis Chapter 3	*Kuehneotherium*	27	9	4.89	0.96
Gasawey et al. 1978	*Alces Alces*	72	9	14.2	0.4
christensen-dalsgaard et al. 2010	*Ursus maritimus*	32	15	15.2	0.86
Perez-Barberia et al. 2014	*Cervus elaphus*	490	17	16.22	0.96
Pasda, 2014	*Rangifer tarandus*	63	16	19.4	0.64
Klevezal and Pucek 1987	*Bison bonasus*	45	21	20.57	0.86
Grau et al. 1970	*Procyon lotor*	54	9	20.6	0.92
Landon et al., 1998	*Canis lupus*	12	6.8	25.92	0.78
Bodkin et al., 1998	*Enhydra lutris*	14	14	26.24	0.88
Kay and Cant, 1988	*Macaca mulatta*	65	24	29.34	0.79
Cederlund et al. 1991	*Capreolus capreolus*	74	9	30.5	0.86

Table 6.4. Comparisons between precision metrics for synchrotron radiation computed tomography data of fossil mammaliforms and previous thin section data of extant mammals. *CV*; coefficient of variation; *r*; Pearson's correlation coefficient.

Specimen	Increment count	Higher level taxon	Taxon
m46212a	1	Docodonta	Peraiocynodon
m100120	3	Eutriconodonta	amphilestidae
CB07a 360 2	4	Trechnotheria	Amphitheriidae
m36516a	1	Trechnotheria	*Amphitherium*
J79453	3	Docodonta	*Borealestes*
j79498	4	Docodonta	*Borealestes*
m100060	8	Docodonta	*Borealestes*
m46001	2	Docodonta	*Borealestes*
m46058	3	Docodonta	*Borealestes*
m46399	2	Docodonta	*Borealestes*
m46404	1	Docodonta	*Borealestes*
m46580	3	Docodonta	*Borealestes*
m46809	11	Docodonta	*Borealestes*
m46847	4	Docodonta	*Borealestes*
m46632	3	Docodonta	*Borealestes serepdipitus*
m46728	3	Docodonta	*Borealestes serepdipitus*
m36524	5	Docodonta	*Borealestes*
m36527	12	Docodonta	*Cyrtlatherium*
m46778	2	Docodonta	*Cyrtlatherium canei*
j79522	6	Docodonta	docodonta
j79536	2	Docodonta	docodonta
m100059	3	Docodonta	docodonta
m36505	4	Docodonta	docodonta
m36541	9	Docodonta	docodonta
m46577	5	Docodonta	docodonta
j79445	6	Trechnotheria	dryolestidae
m100063	3	Trechnotheria	dryolestidae
m100097	4	"Allotheria"	*Eleutherodon*
m100056	2	Eutriconodonta	Gobiconodontidae
m100057	5	Eutriconodonta	Gobiconodontidae
j79472	1	"Allotheria"	haramiyidae
m46430	6	Trechnotheria	*Kennetherium leesi*
m46684	6	"Allotheria"	*Kermackodon*
CB04	5	Docodonta	*Krusatodon*
j79454	3	Docodonta	*Krusatodon*
j79523	2	Docodonta	*Krusatodon*
m46222	1	Docodonta	*Krusatodon*
m46442	10	Docodonta	*Krusatodon*
m46333	1	Docodonta	*Krusatodon kirtlingtonensis*
m46531	7	Docodonta	*krusatodon kirtlingtonensis*
m27628	6	Mammaliaformes	mammal indet.
CB526	4	Mammaliaformes	mammal indet.
j79452	4	Mammaliaformes	mammal indet.
m100061	3	Mammaliaformes	mammal indet.
m100062	2	Mammaliaformes	mammal indet.

m100072	5	Mammaliaformes	mammal indet.
m100083	8	Mammaliaformes	mammal indet.
m100119	4	Mammaliaformes	mammal indet.
m20990	3	Mammaliaformes	mammal indet.
m27537	5	Mammaliaformes	mammal indet.
m46037	2	Mammaliaformes	mammal indet.
m46441	2	Mammaliaformes	mammal indet.
m46542	3	Mammaliaformes	mammal indet.
m46584	5	Mammaliaformes	mammal indet.
m46614	3	Mammaliaformes	mammal indet.
m46623	4	Mammaliaformes	mammal indet.
m46704	1	Mammaliaformes	mammal indet.
m46741	10	Mammaliaformes	mammal indet.
m46764	6	Mammaliaformes	mammal indet.
m100093	4	"Allotheria"	multituberculata
m46234a	1	"Allotheria"	multituberculata
m46289	1	"Allotheria"	multituberculata
pg06	3	"Allotheria"	multituberculata
m46417	3	Trechnotheria	*Palaeoxonodon*
m46197	4	Trechnotheria	*Palaeoxonodon freemani*
m46213	4	Trechnotheria	*Palaeoxonodon freemani*
m46290	1	Trechnotheria	*Palaeoxonodon freemani*
m46388	5	Trechnotheria	*Palaeoxonodon freemani*
m46701	1	Trechnotheria	*Palaeoxonodon freemani*
m46702	3	Trechnotheria	*Palaeoxonodon freemani*
m46429	6	Trechnotheria	*Palaeoxonodon ooliticus*
m46524	6	Trechnotheria	*Palaeoxonodon ooliticus*
m46618	1	Trechnotheria	*Palaeoxonodon ooliticus*
m46657	2	Trechnotheria	*Palaeoxonodon ooliticus*
m46698	1	Trechnotheria	*Palaeoxonodon ooliticus*
m46786	6	Trechnotheria	*Palaeoxonodon ooliticus*
m46792	1	Trechnotheria	*Palaeoxonodon ooliticus*
m46503	2	Eutriconodonta	*Phascolotherium*
CB508	3	Eutriconodonta	*Phascolotherium*
CB522	3	Eutriconodonta	*Phascolotherium*
m100092	3	Eutriconodonta	*Phascolotherium*
m46781	1	Eutriconodonta	*Phascolotherium*
m46226	3	Trechnotheria	*Shuotherium*
m46768	2	Trechnotheria	*Shuotherium dongi*
m46570	1	Docodonta	*Simpsonodon*
m46761	2	Docodonta	*Simpsonodon*
m46785	3	Docodonta	*Simpsonodon oxfordensis*
m46798	2	Docodonta	*Simpsonodon oxfordensis*
m36518	1	Eutriconodonta	Eutriconodonta

Table 6.5. Increment count estimated using the increment counting algorithm developed by Newham et al. 2018b for each specimen that produced readable cementum increments in synchrotron radiation computed tomography data.

Taxon	Lifespan (years)	est. BMR (kj.kg.day-1)	est. Growth rate *k* (days-1)
Borealestes	11	200	0.021
Cyrtlatherium	12	184	0.017
Krusatodon	10	230	0.026
Phascolotherium	3	1069	0.323
Shuotherium	3	1069	0.323
Palaeoxonodon	6	522	0.075
Morganucodon	14	150.72	0.02
Kuehneotherium	9	241	0.02
Kermackodon	6	522	0.075

Table 6.6. Estimates of physiological metrics for the Mid Jurassic fossil mammaliaform taxa of the Oxfordshire Bathonian fauna. BMR; basal metabolic rate.

Chapter 7.

Discussion and conclusions

This research project has attempted to characterise the potential of incremental dental cementum as a record of life history among living and fossil mammals, isolate the current caveats limiting the fulfilment of this potential, and develop methodologies for overcoming these caveats. Cementum increments are believed to represent seasonal changes in growth rates of the individual and the cementum. The circum-annual rhythm and continuous growth throughout life of cementum increments (both unique among mineralised dental tissues), provide an absolute estimate of chronological lifespan (Klevezal, 1995). Lifespan in extant mammals is a crucial element of study for a range of scientific disciplines (Kaplan et al., 2003; Hulbert et al., 2007; Wall-Scheffler, 2007), and cementochronology (the study of cementum increment counts) is now routinely used in ecology and wildlife management (Naji et al., 2016). Lifespan offers an indirect proxy for metabolic potential among fossil mammals in relation to estimates of their body masses (Hulbert et al., 2007; de Magalhães et al. 2007). The circum-annual rhythm of cementum deposition also provides this tissue with the potential for recording significant perturbations to cementum growth beyond those of typical seasonal change (Coy and Garshelis, 1992; Klevezal and Stewart, 1994; Kagarer and Grupe, 2001; Cipriano, 2002; von Beila et al., 2008; Medill et al., 2010). Pregnancy is one such event that has received particular interest in the literature; with several previous studies suggesting that pregnancy events are recorded in increment morphology to a predictable degree (Coy and Garshelis, 1992; Kagarer and Grupe, 2001; von Beila et al., 2008; Medill et al., 2010). The significant increase in flux of the female secondary sexual hormones estrogen and progesterone during pregnancy are understood to negatively impact oral and periodontal health and growth (Bixler et al., 1955; Percival et al., 1994; Leimola-Vitranen et al., 2000; Friedlander, 2002; Dodds et al., 2005; Russell and Mayberry, 2008) and this can be expected to extend to the cementum tissue.

However, the potential of cementum for recording life history is undermined by a series of caveats, both biological and methodological. Cementum is a dynamic, biomechanically responsive tissue and increments have been frequently found to follow

complex trajectories, both lensing and coalescing with neighbouring increments (Spinage, 1973; Klevezal, 1995; Renz and Radlanski, 2006). The meta-analysis conducted in **chapter 2** has suggested that these complexities negatively correlate with the strength of climatic forcing experienced by an individual, with populations in equatorial regions showing the highest rate of complex increment patterns (Spinage, 1973). This problem can be compounded when studying cementum if the heterogeneity of cementum tissue-types is not accounted for. Cementum can be chiefly divided into two tissues; acellular extrinsic fibre cementum (AEFC) and cellular intrinsic fibre cementum (CIFC). AEFC receives collagen fibres (Sharpey's fibres) from the periodontal ligament (PDL). Growth is continuous, and reflective of bodily growth, making this tissue-type the most reliable for estimating age and life history. CIFC creates collagen fibres internally, and grows primarily in response to periods of anomalously high occlusal stress upon the tooth root (Naji et al., 2016).

Beyond biology, the primary limiting factor in previous studies of cementum increments has been the reliance on histological thin-sections for imaging and analysing increments (Renz and Radlanski, 2006; Naji et al., 2016). We have sought to overcome the problems created by this reliance on a restricted, two-dimensional (2D) window onto increments and their complications, by pioneering micro-computed tomographic (μCT) techniques for imaging and analysing cementum. Although we have shown here that current X-ray sources for conventional laboratory-based μCT systems do not provide the image quality at sub-micron resolutions to accurately image cementum increments, tomographic imaging using synchrotron radiation sources has been shown to faithfully image increments at comparable resolution and contrast to histological thin-sections. However, it must be noted that this image quality is only obtained using propagation-based phase contrast reconstruction techniques, and image quality is heavily dependent on choice of experimental settings (**Chapter 4; Section 4.3.1.**). We have here directly experimented on the effects of individual settings on eventual image quality, in order to develop an optimal suite of settings for imaging cementum increments.

7.1. Synchrotron radiation computed tomography and computer vision

Synchrotron radiation computed tomography (SR CT) produces data that allows cementum increments to be studied in a new way, overcoming the primary issues that

have undermined thin-section based studies. The non-destructive nature of SR CT imaging means that the entire cementum tissue can be studied (although here only the coronal third was studied), and so increments can be followed along their entire trajectories through the scanned portion of the tissue. This reveals complications in increment patterns in a more complete context. False increments created by lensing, and coalescence of two increments can be traced and distinguished from 'true' increments. This benefits counting of increments using human vision in two primary ways. First, regions of complexities can be identified and isolated from traditional analyses of single 'virtual thin-sections'. Secondly, increments can be followed volumetrically through an entire scan dataset, producing 3D models of their patterns for the first time.

SR CT data also offers the opportunity to quantitatively study aspects of cementum structure without distortion of features from preparatory artefacts known to effect studies of cementum structure using thin-section images (Naji et al., 2016). This project has developed a novel protocol for processing and analysing SR CT cementum data using a series of both available and custom algorithms designed to isolate, straighten and filter cementum in SRCT data, before estimating the count, shape and texture of its increments. This workflow is summarised in Figure 7.1. and accompanying Table 7.1., and has allowed the quantitative study of certain aspects of life history recorded in the ultra-structure of cementum for the first time.

The increment counting algorithm developed here allows increments to be counted using solely computer vision. This overcomes the major caveats highlighted in previous studies seeking to validate the use of increment counting as an estimate of lifespan in extant mammals. The predominant reliance on human vision for counting increments places an inherent subjectivity upon counts, with individual observers estimating sometimes significantly different counts for the same specimen. This problem can be compounded by repeated findings of a significant correlation between both accuracy and precision of increment counts and experience of the observer. This project has developed a workflow whereby the application of an algorithm, robust to significant levels of background image noise, to multiple transects through the cementum of SRCT slices provides accurate counts of increments to those expected for individuals of known age, with no application of human vision. Thus, although selecting regions of high increment contrast by-eye can improve precision between counts among individual transects of the same image, these results suggest that future cementochronological studies may not need to apply human vision for counting

increments in tomographic data. The issue of precision between observers, and the correlation between accuracy, precision and observer experience would thus be minimised, as repeated analysis of the same image will always generate the same counts.

An obvious next step for the development of this algorithm is testing its robusticity and accuracy for estimating age in long-living organisms with lifespans and increment counts above the 30 tested for here, namely humans. This development must consider and account for a series of factors that have been encountered during the imaging and analysis of human cementum performed here. The validation of cementochronology for ageing humans has been a focal point of study for the last two decades, and the majority of studies have found that the accuracy and precision of increment counts performed using human vision inversely correlates with age (Charles et al., 1986; Condon et al., 1986; Kvaal and Solheim, 1995; Wittwer Backofen et al., 2004, 2012). As humans age, increments become increasingly densely spaced and so more difficult to count by eye (Kagarer and Grupe, 2001; Wittwer-Backofen et al., 2012). The increment counting algorithm developed here has provided accurate estimates of increment counts for one human with a known age of 46. Although this is a promising preliminary result regarding the use of both the scanning parameters and algorithm developed during this project, further experimentation is needed to more conclusively validate their efficiency for counting long-living human cementum increments. The SRCT data acquired for several human individuals suffered from blur between increments created by partial volume effects through significant portions of the scanned tissue, where there were insufficient pixels to accurately represent their boundaries (Fig. 7.2.). This may suggest that the voxel resolution (0.66 μm^3) used may not be sufficient for accurately imaging the cementum of longer living humans. The use of higher resolutions (e.g. 0.33 μm^3) should thus be investigated for studying the cementum of humans living longer lifespans than 60 years. However, higher resolutions provide smaller fields-of-view for SRCT imaging, and so less of the cementum tissue would be represented in each scan. This undermines one of the key benefits interpreted from the results of this project: the ability to study increments along their complete transects through significant portions of the cementum tissue. A trade-off between obtaining sufficient resolution to capture individual increments and imaging sufficient portions of the cementum tissue to overcome the problems of coalescence and lensing represents a common problem in tomographic imaging that must be considered in future

studies. The potential problems for distinguishing primary cementum increments from complexities between them, through the reduced field of view offered at higher resolutions, may be minimised by preliminary investigation using lower resolutions. Regions of acellular extrinsic fibre cementum with high increment contrast can then be identified at these lower resolutions, and then targeted for high resolution scanning.

7.2. Cementochronology of fossil mammaliaforms and crown mammals

The validation of the precision and accuracy of the increment counting algorithm has allowed it to be used here to count cementum increments in Mesozoic fossil mammal specimens for the first time. This has in-turn provided a novel method of estimating metabolic potential among fossil mammals, whereby measurable aspects of metabolism among extant taxa (basal metabolic rate and post-natal growth rate) can be estimated in fossils. The finding of a considerable disparity between the exceptionally long lifespans estimated for Late Triassic-Mid Jurassic stem mammaliaform taxa and crown mammals (both fossil and extant) of comparable body mass suggests that mammaliaforms had yet to develop the elevated endothermic metabolism of extant mammals. Instead, our results suggest that the levels of metabolism indicative of extant taxa evolved among the earliest members of the crown mammal clade during the Mid Jurassic. This corresponds in time to a frequently observed 'burst' of taxonomic (Newham et al., 2014) and ecomorphological (Luo, 2007) diversity that occurred among the earliest crown mammals during the Mid Jurassic (Close et al., 2015). It is proposed here that, following the correlation between metabolic rate and several aspects of evolutionary rate, this burst in diversity can be directly attributed to the development of metabolic potential in early crown mammals to levels seen among extant taxa.

Study of lifespan among, and comparison between, key taxa representing other fossil mammal faunas through time may offer a window onto their physiological reaction to extreme climatic events and major mass extinctions, and give context to previous interpretations of their macroevolutionary patterns (Dineen et al., 2014; Grossnickle and Newham, 2016; Brocklehurst et al., 2017; Liu et al., 2017; Bennett et al, 2018). Faunal reactions to major extinction events are crucial for understanding and modelling ecological dynamics and several discrete patterns in ecomorphological and

taxonomic diversity have been isolated in response to mass extinctions (Pearson, 2001; Twitchett, 2007; Quental and Marshall, 2013). Recent studies have indicated that these may represent changes to key life history variables such as changes in growth patterns and age at sexual maturity, and the ability of a lineage to modify such life history variables in response to environmental change may be key to their survival (Courtillot, 2002; Botha-brink et al., 2016). For example, skeletal histology has been studied in a wide range of synapsid taxa across the End Permian mass extinction event (~251.88 Ma) to assess changes in growth rate and potential age at sexual maturity in relation to the 'Lilliput effect' of reduced body size among surviving taxa (Botha-Brink et al., 2010; Huttenlocker et al., 2013, 2014). Botha-Brink et al. (2016) used the count and spacing of lines of arrested growth (LAGs) within transverse sections of the long bones of therapsids to compare growth rates between End Permain and Earliest Triassic taxa. The study found that reduction in body size in Triassic therapsids was accompanied by a significant increase in growth rate, represented by a reduction in the count and spacing between LAGs. This was interpreted as evidence of shorter life expectancies and younger age-of-reproductive-maturity among early Triassic taxa, relative to their End Permian relatives. The lack of histological indicators of skeletal maturity amongst Triassic individuals was also used to suggest that comparatively fewer therapsids were surviving through to adulthood.

Although cementum cannot offer a complete record of life history in non-mammalian synapsids, including End Permian-Early Triassic therapsids (as these taxa continually replaced their teeth), the level of detail offered by skeletal histology may be both bolstered and 'ground-truthed' by studying cementum in mammal populations experiencing comparable environmental and climatic events during other mass extinctions. The End-Cretaceous mass extinction event (~66 Ma) is marked by a decoupling between patterns in global taxonomic and ecomorphologicval diversity among mammals (Grossnickle and Newham, 2016). This phenomenon was chiefly due to the selective extinction of ecological specialists and proliferation of generalists. The ability to use lifespan estimation from cementochronology in conjunction with histological evidence may provide more information regarding this phenomenon, offering a physiological context as to why certain taxa were selected for over others. The ability offered by cementum to estimate absolute age in individual fossil animals may add a quantitative rigour to studies of their long bone histology, allowing estimation of the year of life that individual LAGs were deposited. This will, in turn,

offer the opportunity to provide quantitative estimates of growth rate through life, as the relationship between LAG count and chronological age can be determined. The ability to estimate the chronological year-of-life that each LAG represents may also allow the estimation of absolute chronological age at sexual maturity attained by each individual, by assessing the year-in-life that osteological correlates of maturity originate. Comparisons between morphological and textural correlates of cementum increments with sexual maturity and activity found in this study, with osteological correlates of sexual maturity in long bones interpreted in previous studies (Klevezal, 1995; Botha-Brink et al, 2016) may also cross-validate their individual accuracy for predicting these life history events in fossil taxa. Finally, assessing the physiological differences between surviving and non-surviving taxa in previous events may suggest which extant mammals are under greater threat from current climate change (Martínez-Meyer et al. 2004; Blois et al., 2013). The addition of this physiological information to statistically robust analyses of patterns in global climate and diversity metrics across previous mass extinction events may add a further level of complexity to models predicting the effects of future events, including the present threat of anthropogenic climate change.

7.3. The relationship between cementum increment morphology and life history in fossil hominins

The development of algorithms designed to isolate and measure aspects of increment shape and texture offers a new approach to studying the relationship between life history and cementum growth. This thesis serves as a case study for such investigation, having developed and tested a thoroughly researched hypothesis for the effects of gender-specific life history variation upon measureable aspects of dimorphic cementum growth. The findings of significant quantitative differences in cementum increment shape and texture between male and female primates suggest that cementum growth is sexually dimorphic among primates. It is posited that these findings reflect clinical evidence that the elevated levels of estrogen and progesterone within the female oral environment negatively impact oral health, and provide a less stable environment for cementum growth (Muhler and Shafer, 1955; Delman, 1955; Laine et al., 1988; Liu and Lin, 1973; Person et al., 1998). These effects are known to amplify with the considerable increase in estrogen and progesterone production during pregnancy events (Gajendra and Kumar, 2004; Lukacs and Largaespada, 2006; Silk et al., 2008). The

development of our increment counting algorithm has allowed the effects of individual pregnancy events on female cementum growth to be analysed and we have found qualitative differences between the properties of individual increments formed during pregnancy and surrounding increments.

The opportunity afforded by the suite of algorithms developed here to quantitatively isolate discrete elements of cementum structure, and statistically compare them between individuals and sub-samples may also allow the effects of other elements of life history upon cementum growth to be studied with the same quantitative rigour. Several variables have been suggested to affect the growth of cementum and nature of incrementation (Klevezal, 1995; Kagarer and grupe, 2001; Cipriano, 2002; Wall-Scheffler and Foley, 2008). Using the methods developed here, these effects can now be characterised in terms of specific aspects of increment shape and/or cementum texture, in order to better elucidate the relationship of these variables with cementum growth. For instance, comparisons of cementum texture (across the entire cementum tissue) of individuals raised under different climates may offer a method for quantitatively studying the effects of climate on cementum growth (Wall-Scheffler and Foley, 2008). The proportion of individuals with complex increments has been shown here to correspond with various climate types. The 21 available texture metrics developed for cementum texture analysis may provide a new level of detail to these comparisons, and new information on the effects of quantifiable aspects of climate such as strength of seasonality and rainfall on the growth of cementum and quality of incrementation.

Ultimately, future studies seeking to further explore the relationships between the aspects of cementum increment structure identified here with pregnancy must utilise larger samples than those provided here. Both the *Macaca mulatta* sample and the archaeological human sample(s) were undermined by an imbalance between breeding females of known life history, and males. The *M. mulatta* sample only consisted of one male individual. Although comparisons of increment shape and texture provided significant differences between this individual and all females in the sample, there were also significant differences between aspects of increment texture between individual breeding females. Further, with only one male individual, the extent of male 'texture-space' occupation is unclear. Hence, more male individuals from this population are needed to conclusively investigate the potential sexual dimorphism preliminarily suggested in this study. Conversely, the archaeological sample studied only comprised two individual females of known reproductive history, and one of these individuals

suffered from a cementum pathology (hypercementosis). While evidence was found for difference in the properties of increments formed during pregnancy and surrounding increments for both individuals, they are not directly comparable and so do not offer mutual support for any one particular hallmark of pregnancy in the SR CT data of cementum increments in modern humans.

If upheld in future studies using more complete samples, the findings of characteristic differences between the structure of individual increments formed during pregnancy and surrounding increments, and between male and female members of the same population, in both recent and archaeological specimens in SRCT data, highlight the potential of the methodology developed here for studying archaeological and fossil specimens with a forensic level of accuracy. Cementum has recently been used as a forensic tool for identifying a single "Jane Doe" (unidentified female body in a criminological context) (Wedel et al., 2015). The chronological age from cementum was used alongside a suite of osteological metrics to assess the most likely individual that the body belonged to in the relevant region of discovery. The majority of fossil and archaeological hominid specimens are fragmented and disarticulated, with teeth being the most common elements. The use of cementum to study populations of disarticulated remains offers the chance to both distinguish between individuals, and study their remains in a new way. If further developed to accurately age long-living hominid individuals, the increment-counting algorithm may be used to distinguish individuals based on their age, and the shape of increments and texture of cementum characterised and statistically compared to reveal potential life history differences.

Further, hominin populations can be compared through time and across the globe to study macroevolutionary patterns in important demographic metrics. The concept of niche construction has gained particular recent attention amongst evolutionary anthropologists studying early human evolution (Fuentes et al, 2010; Kendal et al, 2011; Dean et al, 2012; O'Brien and Laland, 2012; Fuentes, 2015). Niche construction describes the building and reshaping of ecological niches by organisms and thus the changing of the evolutionary pressures, and in human populations can emerge from, and feedback to, wider ecological systems, genetic processes, physiological and life history variables, developmental schedules and cultural processes (Laland et al., 2007). Antón and Snodgrass (2012) proposed that early hominin evolution was characterised by a niche construction whereby increases in dietary quality, cognition, and cooperation resulted in lowered mortality risk and fostered changes in brain size,

life history parameters and behavioural/social complexity. This complex system of interconnecting parameters and group interactions reflects a drive to include elements of the new evolutionary synthesis and modern anthropogenic theory when studying ancient hominin populations (Kendal, 2012; Fuentes, 2015). However, the majority of these studies are based on modelling of modern populations and lack robust evidence of demographic parameters for early hominin communities and populations. The potential demographic data available from SR CT studies of the cementum of hominid communities, ranging from proportion of genders, age structure, fertility and age at first reproduction, offer the chance to model aspects of the complex multidimensional group interactions involved in human niche construction based on direct evidence in the fossil and archaeological records.

7.4. Summary

The development and validation of SR CT imaging and computer vision approaches to studying cementum increments pioneered in this project have been attempted to bring this discipline up-to-date with the techniques and methodologies used to study other more commonly studied hard tissues and materials. The volumetric nature and sub-micron resolution of SR CT imaging has overcome the principal caveats of previous studies based on a limited number of two-dimensional thin sections used to represent individual specimens. SR CT data has also provided a source for developing a suite of image analysis algorithms that may benefit future studies of both counts of cementum increments, and the relationship between their properties and various life history variables. The increment counting algorithm developed here has been shown to be both robust to low theoretical signal-to-noise ratios and accurate for ageing primates. The opportunity afforded by this algorithm to count increments using solely computer vision overcomes another principal caveat of previous studies, the subjective nature of human vision. The final two algorithms developed here are based on characterising aspects of increment morphology and texture in SR CT slices that are potentially indicative of heterogeneities in their growth relating to life history parameters.

The relationship between cementum increment properties and life history has been explored along two different lines of enquiry; firstly analysing physiological evolution amongst our earliest ancestors, and secondly studying potential sexual dimorphism in our most recent relatives. The discovery of preserved increments within

fossil cementum in the late Triassic/Early Jurassic mammaliaforms *Morganucodon* and *Kuehneotherium*, and subsequent scanning of these and the increments of later mammaliform taxa and contemporaneous crown mammals from the Mid Jurassic revealed a significant disparity between long-living mammaliaforms and short-living crown mammals. The subsequent use of these lifespans for estimating basal metabolic rate and post-natal growth rate amongst fossil taxa revealed a comparable disparity between mammaliaforms and crown mammals, suggesting a significant increase in metabolic potential amongst the earliest crown mammals.

The application of quantitative analyses of increment shape and texture have been applied to preliminary samples of primates, a rhesus macaque sample and two separate archaeological human samples, in order to investigate potential sexual differences between male and female cementum increments. In all samples, male increments were found to differ significantly from females in both increment shape and texture. Although small sample size means that the results presented can only be considered as preliminary and caveats were found, namely that two separate archaeological samples from different periods and preservational contexts should be combined with caution, these preliminary findings suggest that cementum increment morphology may be used in future studies to estimate gender in individuals of unknown life history. The finding of further qualitative differences between increments formed during known pregnancy events and surrounding increments in females also highlights the potential of using increment parameters to estimate discrete life history events using the cementum of individuals of unknown life history.

These two studies of disparate elements of both mammal phylogeny and life history highlight the potential of cementum as a life record. This potential can be maximised with the continued use of non-destructive imaging and quantitative analysis of robust samples of controlled life history, building upon the preliminary samples case-studied in this project.

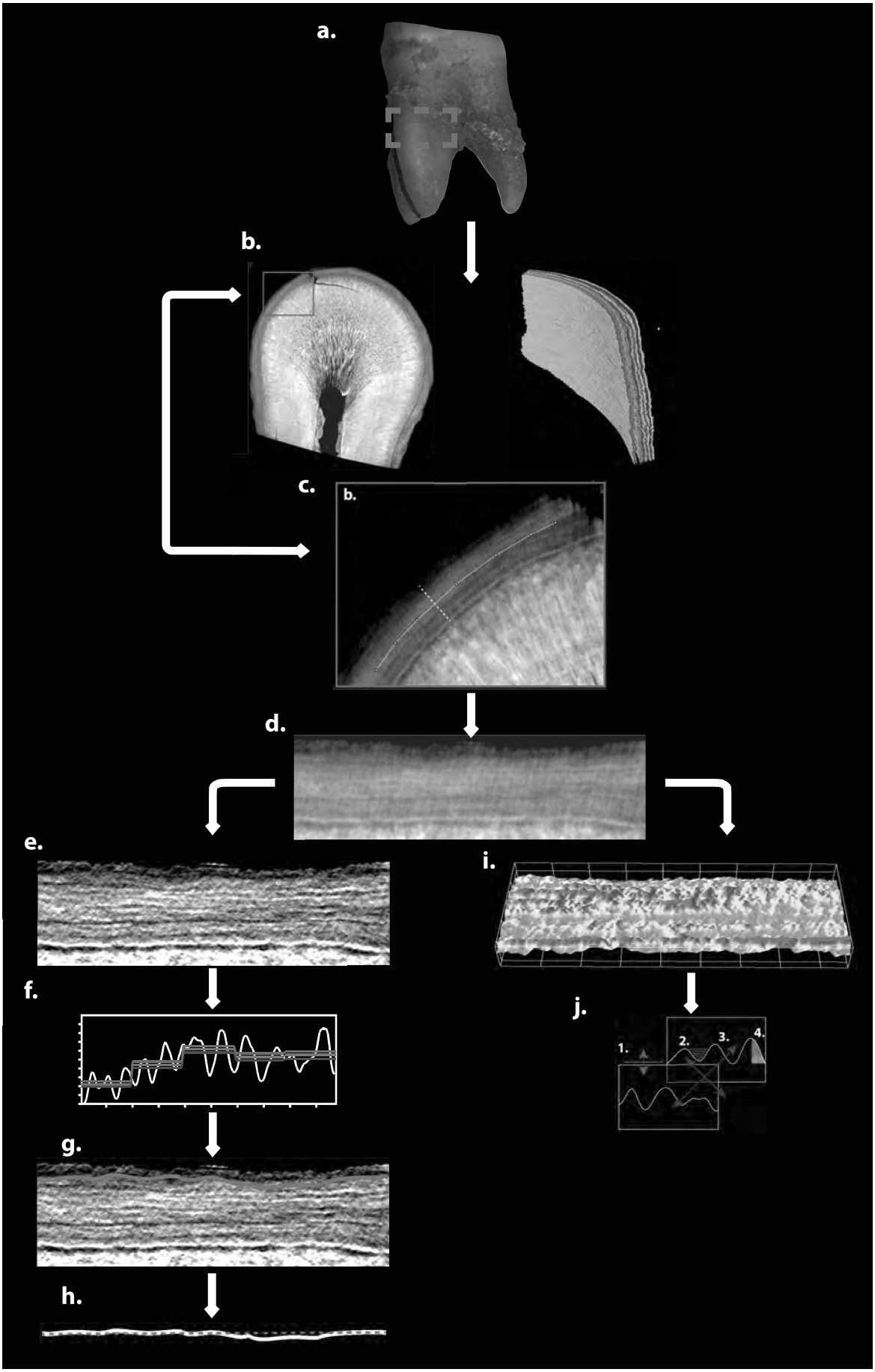

Figure 7.1. Summary of workflow developed for this project. Each stage is described and explaind in accompanying **Table 7.1.**

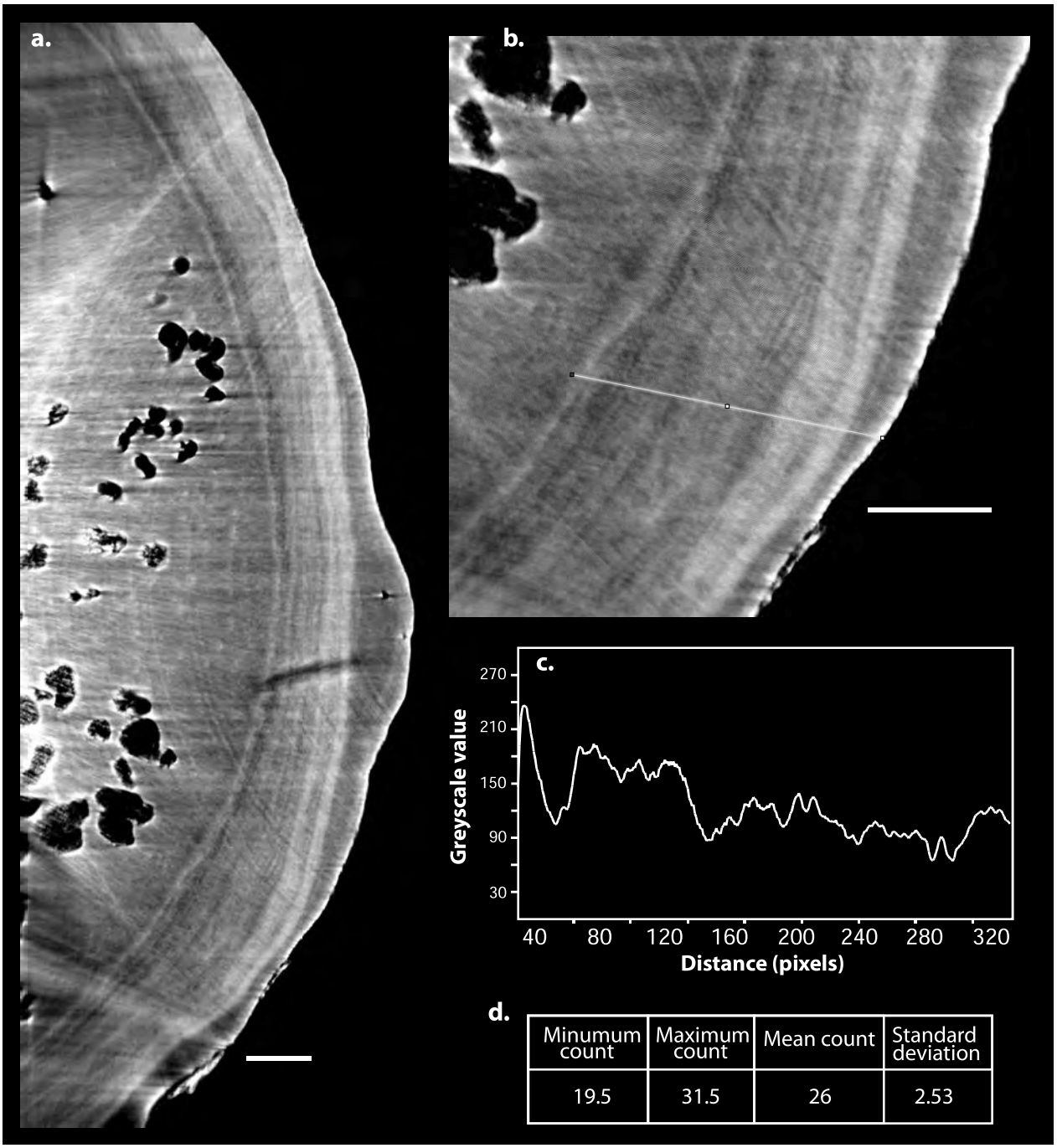

Figure 7.2. Illustration of the partial volume effect on densely spaced cementum increments within adult human cementum. (**a**) transverse SR CT slice through the cementum of C19 individual sk11, showing densely spaced increments that become even more tightly spaced through the central portion of cementum where it is grown over by non-incremental cellular cementum. (**b**) Detail of cementum marked by dashed box in (**a**), showing partial volume effects along portions of several increments, where they cannot be easily distinguished from neighbouring increments by eye. (**c**) Greyscale values across radial transect marked by yellow line in (**b**), highlighting low contrast between increments. (**d**) Summary statistics of automated increment counts for 1000 transects plotted through the isolated, straightened cementum within (**a**). Scale bars in (**a**) and (**b**) represent 100 μm.

Stage	Optional or Core process?	Description	Input	Output	Software
a	core	SR CT imaging of coronal third of the cementum tissue.	Either entire tooth or root section	Propagation-based phase contrast reconstruction. A volumetric dataset comprised of a stack of ~2000 16 bit Tiff images	In-house synchrotron software
b	optional	Human-vision analysis of increments and their count. Shown to increase precision of automated increment counts	16 bit propagation-based SR CT reconstruction	1. "Virtual thin sections" comprised of a summation of greyscale values of particular regions of cementum 2. Increment counts generated by-eye following increments through their entire trajectory	1. ImageJ/Fiji 2. Avizo
c	core	Selection of 30 random SR CT slices	16 bit propagation-based SR CT reconstruction	16 bit propagation-based SR CT reconstruction	ImageJ/fiji
d	core	Isolation and straightening of cementum in transverse SR CT slices using the "Straighten" tool in imageJ/fiji	16 bit propagation-based SR CT reconstruction	Isolated, straight 8-bit image of cementum	ImageJ/fiji
e	core	Filtering of 8-bit cementum image using steerable Gaussian filter oriented at 90^0	Isolated, straight 8-bit image of cementum	Contrast-enhanced 8-bit image of cementum	Matlab
f	core	Analysis of radial transects through contrast-enhanced cementum images to distinguish peaks/troughs representing light/dark increments in order to count them and isolate them using computer-vision	Contrast-enhanced 8-bit image of cementum	1. Database of locations of light/dark increments for 1000 transects through the cementum 2. Estimate of increment counts based on mean count for 1000 transects through the cementum	Matlab
g	core	Isolation of individual cementum increments based on data of their positions along 1000 radial transects through the image	1. Contrast-enhanced 8-bit image of cementum 2. Database of locations of light/dark increments for 1000 transects through the cementum	Individual images consisting of single isolated increments	Matlab
h	core	Analysis of tortuosity of individual cementum increments	Individual images consisting of single isolated increments	Database of tortuosity estimates for each individual scanned specimen	Matlab
i	core	Model the greyscale distribution of un-filtered SR CT cementum image	Isolated, straight 8-bit image of cementum	Texture-map of greyscale distribution	Matlab
j	core	Apply 21 3D surface texture metrics to study greyscale texture map	Texture-map of greyscale distribution	Database of values for 21 texture metrics	Matlab

Table 7.1. Accompanying explanation of each stage of **Figure 7.1.**

Appendices

EUROPEAN SYNCHROTRON RADIATION FACILITY
ESRF User Office
BP 220, F-38043 GRENOBLE CEDEX, France
Delivery address: 6 rue Jules Horowitz, 38043 GRENOBLE, France
Tel: +33 (0)4 7688 2552; fax: +33 (0)4 7688 2020; email: useroff@esrf.fr; web: http://www.esrf.fr

Application for beam time at ESRF – Experimental Method

Proposal Summary (should state the aims and scientific basis of the proposal): We propose a high-resolution (~40nm-1um) x-ray micro-/nano-tomography comparative study of the molar teeth of the 200 million year old fossil early mammal *Morganucodon watsoni* plus a range of modern insectivorous mammals. The purpose is non-destructive identification, mapping and quantification of growth increments (hereafter referred to as lines of arrested growth, LAGs) in order to reconstruct life history variables in the earliest mammals. There is considerable interest in determining the physiology of early mammals [1] but basic life history variables such as lifespan and growth rate are unknown or poorly understood. All three principal mineralised tissues of the teeth, cementum, dentine and enamel, are known to record LAGs, from which life history and developmental patterns can be measured and reconstructed using synchrotron tomography [2]. Using existing and improved methodologies, this study will provide a clearer understanding of life history at the earliest stages of mammalian evolution.

Scientific background: During the process of mineralisation, dental tissues such as cementum, dentine and enamel record periodic incremental features, LAGS, which represent a chronological record of development. If unmodified by diagenetic processes during fossilisation, these form a permanent record of the growth of the tooth. Such LAGs have been known for centuries but only recently have non-destructive synchrotron tomographic methods allowed their visualisation and use for determination of life history parameters in rare or unique fossils [2]. Thus far, only dentine and enamel LAGs visualised through synchrotron tomography have been utilised; we aim to combine these with new methods based around cementum LAG visualisation and quantification to increase understanding of early mammalian evolution.

Relative to the hominids for which life history variables have been determined using synchrotron methods, early mammals likely had shorter lifespans and much shorter tooth development times, as do extant analogues including small insectivores such as shrews and hedgehogs. We therefore propose to use existing methods for analysis using enamel and especially dentine LAGs [2] alongside the development of synchrotron data based methods designed to overcome many of the shortfalls of current destructive sectioning for cementum LAG acquisition. Cementum is a collagenous mineralised tissue that connects tooth roots to the periodontal ligament, supporting dentition within the alveolus against forces applied through mastication. Cementum LAGs have been shown to reflect seasonal changes, creating alternating bands within the tissue [3]. As cementum grows continuously through life, these bands offer an absolute record of annual seasonal change, and hence an estimate of annular age and season of death. Cementum lines obtained through destructive thin sectioning have been used for aging a range of taxa, including humans, and for archaeological, zoological, palaeontological and forensic purposes including conservation and identification of crime victims. However, limitations of the method have been identified, prinicipally due to difficulties in objectively quantifying LAG numbers from single histological thin sections of variable location and quality. We feel that this can be improved through the use of tomographic acquisition of cementum LAGS, which will allow more accurate quantification of LAG numbers due to the availability of whole root LAG data acquisition, instead of single tooth root thin sections per specimen.

The abundance of well preserved fossil teeth of *M. watsoni* (fig 1A) presents a unique opportunity for a quantifiable, population-level sample for non-destructive study of the dental histology and therefore life history of one of the earliest mammals. Data on the basal condition within mammals is critical for understanding the evolution of life history in the group as a whole. The large sample includes sufficient specimens to scan animals of different ontogenetic ages (based on tooth wear and replacement), different tooth loci etc. Comparison with data from extant insectivore teeth will allow both validation of the use of cementum LAGS, and allow comparison with the modern condition in small mammals. Pilot data from *M. watsoni* tooth roots scanned on ESRF beamline ID22 show cementum LAGS throughout the root (fig 1B)> These have been validated with histological thin sections of the same tooth roots, also showing the LAGS (Fig 1C), and trial segmentation of cementum LAG lines from this data was successful (Fig 1D). Synchrotron scanning will allow sample sizes that cannot be obtained from destructive methods.

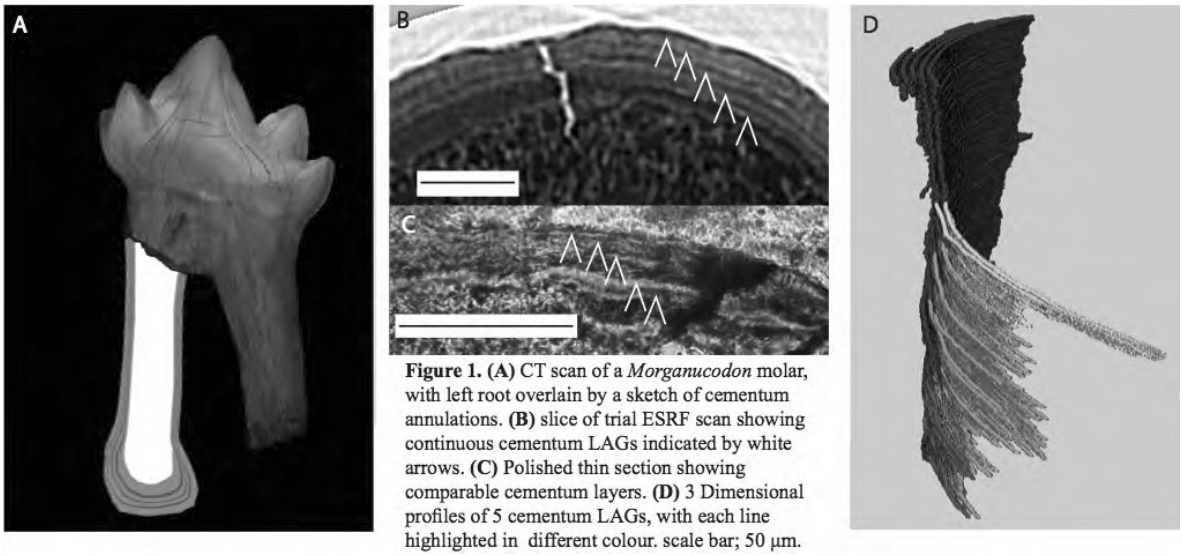

Figure 1. (A) CT scan of a *Morganucodon* molar, with left root overlain by a sketch of cementum annulations. **(B)** slice of trial ESRF scan showing continuous cementum LAGs indicated by white arrows. **(C)** Polished thin section showing comparable cementum layers. **(D)** 3 Dimensional profiles of 5 cementum LAGs, with each line highlighted in different colour. scale bar; 50 µm.

With this data, we will test the following questions/hypotheses: 1) *Do modern insectivorous mammals show a direct correlation between ontogenetic age and cementum LAG count? 2) Does the LAG count of Morganucodon watsoni differ significantly from modern insectivorous mammals?*

The proposed experiments will form an integral part of continuing large-scale developmental and evolutionary biology collaboration, focused on teeth, between the Department of Physics and the Institute of Biotechnology at the University of Helsinki [3], and additionally incorporate the early mammal palaeontological expertise of colleaues at the Department of Earth Sciences, University of Bristol. The resolution offered at the ESRF facility is crucial to this study due to the size of the *M. watsoni* specimens; roots are ~0.2-1mm in length and LAGs can be less than 1µm thick. Non-synchrotron microCT scanning attempts to resolve these features have been unsuccessful.

Experimental technique(s), required set-up(s), measurement strategy, sample details (quantity..etc) :
The proposed experiments will be carried out at ID19 (pink beam, 19keV) using single propagation distance phase-contrast micro-tomography at 0.25-1um voxel size resolutions, and at ID16A (17/34keV) using magnified holotomography (multi-propagation distance phase contrast nano-tomography) at 40nm voxel size. Samples will be prepared at the home laboratory. The sample series will consist of molar teeth and jaws of fossil and recent mammals, to be measured separately at different resolutions and in different parts of the tooth/jaw. The samples do not require any special sample environment. The reconstructed data will be analysed in Helsinki with dedicated software (Avizo, Amira, VolumeGraphics, Matlab etc.).

Beamline(s) and beam time requested with justification : Our team has previously achieved excellent results examining tooth microstructure with tomography on beamlines ID19 and ID22 (see reports). The principal request for beamtime is for ID19, where Paul Tafforeau and team are world leaders in tomographic visualization of tooth incremental structures. Additional nanoscale resolution beamtime on ID16A will enable validation of results from ID19 but is not essential; the project is viable using ID19 only. ID19 measurements will take approx. 30 minutes each allowing a maximum of 48 per day; including pre-measurement setup and optimization, we require four full days (12 x eight hour shifts) to scan suitable samples sizes of *M. watsoni* and extant species. The ID16A sample will be more modest and each measurement approx. 2.5 hours; we require two full days (six 8 hour shifts) of beamtime including setup.

Results expected and their significance in the respective field of research: We aim to validate a direct correlation between annular ontogenetic age and cementum LAG count in insectivourous mammals, thereby obtaining an average estimated ontogenetic age for the early mammal *Morganucodon*. Such results will allow important inferences into various aspects of the ecology and life history of early mammals, and will provide mehodological improvements in zoological, archaeological paleo and forensic sciences.

References [1] T. Rowe *et al.*, *Science* **332**, 955-957 (2011) [2] T. Smith *et al. P.N.A.S* **107**, 20923-20928 (2010) [3] D. Lieberman, *Science*, **261**, 1162-1164 (1993) [4] E. Harjunmaa *et al.*, *Nature*, **483**, 324-327 (2012)

Proposal 20141278

Title
Reconstructing the life history of the first mammals - using dental increments to make leaps in understanding

Abstract
The earliest mammal fossils, 200 milliion years old, are pedominantly tiny teeth and jaws, and too valuable to be subjected to destructive sampling in large numbers. We propose a novel combined palaeontological and engineering approach which uses high resolution synchrotron-based CT (SR microCT) imaging of dental increments from tooth root cementum across a population sized sample. This will reveal whether their life history and physiology, at the root of the mammalian tree, differs from that of living mammals.

Proposer / Spokesperson	
Dr. Pamela G Gill	Dept. of Earth Sciences, Univ. of Bristol pam.gill@bristol.ac.uk

Principal investigator	
Dr. Pamela G Gill	Dept. of Earth Sciences, Univ. of Bristol

Co-Proposer	
Dr. Philipp Schneider	Faculty of Engineering and the Environment, Univ. of Southampton
Dr. Ian J Corfe	Inst. of Biotechnology, Univ. of Helsinki
Mr. Elis Newham	Faculty of Engineering and the Environment, Univ. of Southampton
Dr. Philippa Brewer	Dep.of Palaeontology, Natural History Museum

Experiment Category	
Experiment Type	Normal
Research Area	Environmental and Earth Science

Experiment Requirements	
Eligible for EU Support	Yes
Number of Shifts Required	12
Schedule Preferences	none
Beamline/Station	TOMCAT

Description
A) Goal of the experiment We propose a high-resolution X-ray computed tomography (CT) study of the teeth of the 200 million-year-old fossil early mammal Kuehneotherium. The purpose is non-destructive identification, mapping and quantification of growth increments (lines of arrested growth, LAGs) in order to reconstruct life history variables in the earliest mammals. There is considerable interest in determining the biology and physiology of early mammals [1,2] but basic life history variables such as lifespan and growth rate are unknown or poorly understood. We focus on one of the mineralised tissues of the teeth, cementum, which is known to record LAGs and, unlike bone, is not remodelled during life. Life history and developmental patterns will be measured and reconstructed using synchrotron-based CT (SR microCT) [3]. Using existing and improved methodologies, this study will provide a clearer understanding of life history at the earliest stages of mammalian evolution. B) Background During the process of mineralisation, dental tissues such as cementum, dentine and enamel record periodic incremental features, LAGs, which represent a chronological record of development. If unmodified by diagenetic processes during fossilisation, these form a permanent record of the growth of the tooth. Such LAGs have been known for centuries but only recently have non-destructive synchrotron tomographic methods allowed their visualisation and use for determination of life history parameters in rare or unique fossils [3]. Cementum is a collagenous mineralised tissue that connects tooth roots to the periodontal ligament, supporting dentition within the alveolus against forces applied through mastication. Cementum LAGs have been shown to reflect seasonal changes, creating alternating bands within the tissue [4]. As cementum grows continuously through life, these bands offer an absolute record of annual seasonal change, and hence an estimate of annular age and season of death. Cementum lines obtained through destructive thin sectioning have been used for ageing a range of taxa, including humans, and for archaeological, zoological, palaeontological and forensic purposes. However, limitations of the method have been identified, principally due to difficulties in objectively quantifying LAG numbers in 2D from single histological thin sections of variable location and quality. The use of tomographic acquisition of cementum LAGs will allow more accurate quantification of LAG numbers and morphology, due to the availability of whole root LAG data acquisition in 3D instead of single tooth root thin sections per specimen. Recent pilot scans demonstrated the feasibility of visualizing tooth cementum LAG microstructures using 3D high-resolution SR CT on the tooth roots of Morganucodon, a tiny (~30 grams) early mammal, which co-existed with Kuehneotherium during the Early Jurassic (Fig. 1A). A sample of Morganucodon teeth (Fig. 1B) was scanned at the European Synchrotron Radiation Facility (ESRF) ID19 beamline. Image post-processing (Fig. 2A; 2B) and morphometry allowed quantitative characterisation of the cementum LAGs, which were compared with histological thin sections of some of the same tooth roots (Fig. 2C). This cross-comparison between conventional histology and SR CT demonstrated that the same LAGs could be found with both methods. Initial results of high LAG numbers and thus high lifespans for such a small animal are suggestive of a very different life history and physiology to extant mammals: similar sized living shrews typically display very limited LAG numbers, and have lifespans of a maximum of 18 months and correspondingly high metabolic rate physiologies. We therefore propose to test quantitatively the hypothesis that early mammals shared this different life history and physiology, and that this represents the basal condition from which modern mammals have evolved. Deposits from Glamorgan, UK, have yielded a unique collection of thousands of fossil teeth and bones from both Morganucodon and the distantly related early mammal Kuehneotherium [1]. The abundance of well-preserved teeth of Kuehneotherium (Fig. 3) presents an unprecedented opportunity for a comparative study of the lifespan and physiology of early mammals. Data on the basal condition within mammals is critical for understanding the evolution of life history in the class Mammalia as a whole. The large sample of Kuehneotherium teeth includes sufficient specimens to examine animals of different ontogenetic ages (based on tooth wear and replacement), allowing a population-level age distribution to be determined, including a maximum sampled lifespan. High-resolution SR CT scanning will allow assessment of microscopic LAGs of early mammals in 3D non-destructively, which cannot be achieved by destructive histological thin section methods in 2D. The high isotropic spatial resolution offered at TOMCAT is crucial to this study due to the small size of the Kuehneotherium specimens; roots are ~0.3-0.6 mm in diameter and LAGs can be less than 1μm thick. Non-synchrotron CT scanning attempts to resolve these features in Morganucodon have been unsuccessful to date. With the tomographic data generated at TOMCAT we will test the following questions:

Description
Does the population LAG distribution, maximum LAG count and resulting maximum estimated lifespan of Kuehneotherium differ from: 1) modern mammals of similar body size? 2) the co-existing early mammal Morganucodon? The proposed experiments will form a collaboration drawing on the unique combination of early mammal palaeontological expertise at the University of Bristol, bioengineering and imaging expertise at the University of Southampton, developmental and evolutionary biology expertise focused on teeth at the University of Helsinki, and the early mammal collections and expertise of the Natural History Museum London. C) Experimental method; specific requirements Samples will be prepared at the home laboratory in Bristol or the Natural History Museum. The sample series will consist of fossil teeth of Kuehneotherium, and the samples do not require any special sample environment. The proposed experiments will be carried out at TOMCAT at very high resolutions using 40x and 20x objectives and fields of view of 0.35 and 0.7 mm respectively, at energies around 18 keV. The region of interest is a single tooth root, from just below the neck to just above the root apex (Fig. 3). The reconstructed data will be analysed and evaluated using commercial software (Avizo, Amira) and in-house software routines available to and developed by the applicants, respectively. Quantitative morphometry for LAGs will include measures such as number, thickness, separation and their respective variations. D) Results expected Quantitative morphometry measures characterising the cementum LAGs will provide an estimated ontogenetic age for the early mammal Kuehneotherium, in comparison to Morganucodon (ESRF data). Such results will allow important inferences into various aspects of the ecology and life history of early mammals, and will provide methodological improvements in zoological, archaeological, palaeontological and forensic sciences. E) Estimate and justification of the beamtime Our team has previously achieved excellent pilot results examining Morganucodon tooth microstructure with SR CT at ESRF beamline ID19. The preservation of many teeth was exquisite, but some had suffered diagenetic alteration to the internal fabric, which could not be detected pre-scanning. The sample size allows for this contingency. This request for beamtime is for TOMCAT, where Marco Stampanoni and team are world leaders in tomographic visualisation of dental microstructure and incremental features [5]. We estimate that TOMCAT measurements will take 20 minutes at 18 keV allowing a maximum of 48 samples per day. Including pre-measurement setup and optimisation, we require four full days (12 x eight-hour shifts) to scan a suitable sample size (approximately 180) of Kuehneotherium tooth roots. F) References relevant to the experiment description [1] P. Gill et al., Nature 512, 303-305 (2014) [2] T. Rowe et al., Science 332, 955-957 (2011) [3] T. Smith et al. P.N.A.S 107, 20923-20928 (2010) [4] D. Lieberman, Science, 261, 1162-1164 (1993) [5] M. Ruecklin et al., Nature 491, 748-751 (2012)

SLS related publications of the proposers (within the last 18 months)
Gill P G, Purnell M A, Crumpton N, Robson Brown K, Gostling N J, Stampanoni M, Rayfield E JDietary specializations and diversity in feeding ecology of the earliest stem mammals. NATURE 512 303 (2014)Beamline: TOMCAT
Carriero A., Doube M., Vogt M., Busse B., Zustin J., Levchuk A., Schneider P., Mueller R., Shefelbine S. J.Altered lacunar and vascular porosity in osteogenesis imperfecta mouse bone as revealed by synchrotron tomography contributes to bone fragilityBONE 61 116-124 (2014)Beamline: TOMCAT
Webster Duncan J., Schneider Philipp, Dallas Sarah L., Mueller RalphStudying osteocytes within their environmentBONE 54 285-295 (2013)Beamlines: cSAXS,cSAXS,cSAXS
Mader Kevin Scott, Schneider Philipp, Mueller Ralph, Stampanoni MarcoA quantitative framework for the 3D characterization of the osteocyte lacunar systemBONE 57 142-154 (2013)Beamlines: TOMCAT,TOMCAT,TOMCAT,TOMCAT
Schneider Philipp, Voide Romain, Stampanoni Marco, Donahue Leah Rae, Mueller RalphThe importance of the intracortical canal network for murine bone mechanicsBONE 53 120-128 (2013)Beamline: TOMCAT
Schneider P, Ruffoni D, Larsson D, Chiapparini I, Mueller RImage-based finite element models for the investigation of osteocyte mechanotransductionJOURNAL OF BIOMECHANICS 45(S1) S436 (2012)Beamlines: cSAXS,cSAXS,cSAXS

Figure 1. A) The Early Jurassic fossil mammals from the Glamorgan fissure fills; *Morganucodon* (foreground) and *Kuehneotherium* in their island environment. (Painting by John Sibbick). B) *Morganucodon* molar, with root overlain by a sketch of cementum annulations.

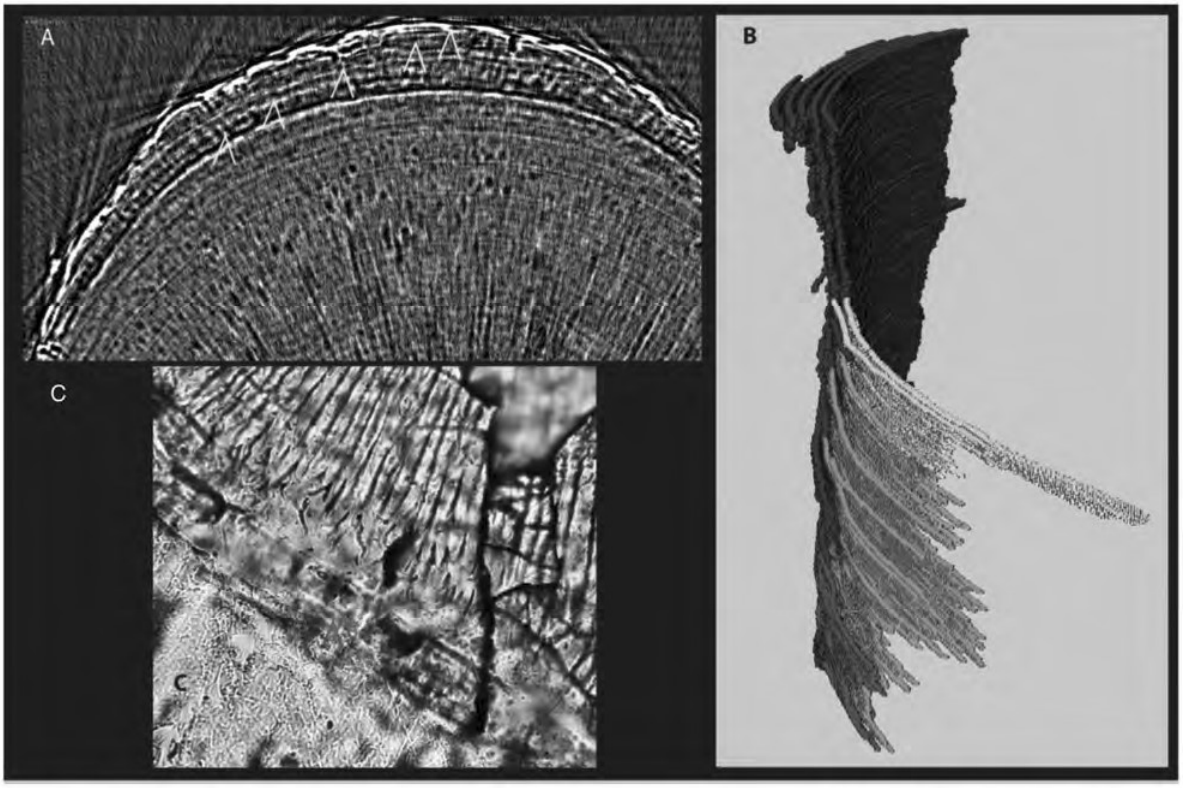

Figure 2. A) Tomographic slice of the root of a *Morganucodon* molar (ESRF data), highlighting five distinct annuli in the cementum. B) 3D tomographic model of cementum annuli showing the extent of the same five annuli. C) Thin section histological slice of the same area as the tomographic image.

Title
Novel 3D assessment of growth increments in dental tissue for studying discrete life history events.

Abstract
We propose a novel 3D approach for assessment of pregnancy markers in dental tissue growth increments using high resolution synchrotron-based CT. This will be the most quantitatively rigorous study of its kind to date, studying the molar teeth of a group of female macaque in comparison to a group of non-breeding females and males, all otherwise raised under the same controlled conditions. It is expected that results will form a predictive model, which will then be used to estimate pregnancy events in a group of mediaeval humans.

Proposer / Spokesperson	
Dr. Pamela G Gill	Dept. of Earth Sciences, Univ. of Bristol pam.gill@bristol.ac.uk

Principal investigator	
Dr. Pamela G Gill	Dept. of Earth Sciences, Univ. of Bristol

Co-Proposer	
Mr. Elis Newham	Faculty of Engineering and the Environment, Univ. of Southampton
Dr. Ian J Corfe	Inst. of Biotechnology, Univ. of Helsinki
Dr. Kate A Robson Brown	Dept. of Archaeology and Anthropology, Univ. of Bristol
Dr. Philippa Brewer	Dep.of Palaeontology, Natural History Museum
Dr. Philipp Schneider	Faculty of Engineering and the Environment, Univ. of Southampton

Experiment Category	
Experiment Type	Normal
Research Area	Life and Medical Sciences (excluding Crystallography)

Experiment Requirements	
Eligible for EU Support	Yes
Number of Shifts Required	12
Schedule Preferences	Earlier if possible
Beamline/Station	TOMCAT

Links to related proposals of relevance to the current proposal			
Proposal	Title/Proposer/Infos given by the proposer about the relation		Report
20141278	Title: Proposer:	Reconstructing the life history of the first mammals - using dental increments to make leaps in understanding Dr. Pamela G Gill	Available

Description
A) Goal of the experiment: We propose a high-resolution X-ray computed tomography (CT) study to test whether episodes of pregnancy can be predicted from patterns of growth increments in the cementum of dental tissue. By using a sample of primates raised under controlled conditions and known life histories we aim to generate a predictive model for detecting pregnancy events by mapping the three dimensional (3D) structure of increments to identify patterns in increment structure. This model will then be used to infer pregnancy events from the cementum of an archaeological human population of known sex. We suggest that synchrotron-based radiation tomography (SR CT) will allow us to assess the potential of cementum as a record of pregnancy in a robust fashion, by allowing us to quantify the relationship between pregnancy events and 3D cementum growth for the first time. The non-destructive nature of tomographic measurement will also allow us to develop a method for predicting pregnancy in specimens that cannot be analysed using traditional destructive histological techniques including rare or unique fossil material. B) Background: The monitoring and interpretation of life history in both living and fossil mammals is of crucial importance for a range of biological disciplines, and the structure of cementum increments has been previously suggested to correspond to both an individual age, and important events such as pregnancy that affect the animal's physiology and growth. The growth and development of mineralised dental tissue, (cementum, dentine and enamel) is recorded by a series of incremental features of differing periodicity and causation. Cementum, the connective tissue that anchors mammalian teeth within the alveolar socket, is unique among these tissues as its growth is continuous throughout life, and annual in rhythm. This rhythm is recorded by a series of circumannual increments of contrasting opacity when viewed under light microscopy, with relatively dense hyper-mineralized opaque increments recording a reduction of growth rates during unfavourable seasons [1] (Fig. 1). Cementum increments have been the subject of histological study for decades and their counts have successfully been used as an absolute estimate of chronological age in over 70 species of extant mammals [2]. Further, several recent studies have indicated that certain life history events, which significantly affect the physiology of mammals, may be recorded in cementum. However, these studies have relied on anecdotal and observed field evidence (e. g. presence of cubs) for pregnancy events, and thin section histology for studying their effects [3]. The reliance on thin-section based histological analysis has placed limits on current understanding of the nature of the structure and causation of cementum increments. Cementum is a dynamic, biomechanically responsive tissue and increments can be seen to lense and coalesce in apparently random areas of their vertical and horizontal trajectory. The 2D perspective of study over a limited number of thin sections available per tooth (often only one), means that such discrepancies in increment patterns cannot be accounted for in the context of the entire cementum tissue. This creates uncertainty in counts and makes it difficult to discern patterns in increment structure from transitory noise created by lensing and coalescence [2]. We aim to use the sub-micron resolution at high signal-to-noise ration and within a 3D context offered by SR CT as an improved imaging method for studying cementum increments, allowing us to more confidently study increment structure in relation to pregnancy events. Recent pilot measurements conducted at the TOMCAT beamline of the Swiss Light Source Synchrotron demonstrated the feasibility of imaging tooth cementum increments in both extant and fossil mammals using SR CT (Fig. 2; Figures 1.b. and 3 in experimental report of proposal 20141278). Pilot measurements of the teeth of the extant European hedgehog, Erinaceus europaeus, during our recent project (Proposal 20141278) reveal increments in sufficient contrast and resolution to allow characterisation of their vertical and horizontal trajectories through the majority of the cementum, as well as quantitative analysis of relative increment thickness, a necessity for determination of pregnancy events. Comparisons between reconstructions and histological thin-sections of the same teeth further demonstrated that tomographic increments reflected optical changes in cementum structure (Fig. 2). Based on these promising data, we propose a comparative study of the cementum increments of a sample of female macaque monkeys (Macaca mulatta) that have undergone recorded biennial insemination and pregnancy events, versus a control sample consisting of the increments of females that were never inseminated and males. All individuals (12) in this sample were otherwise raised under the same controlled conditions. This will allow us to test previously hypothesised relationships between pregnancy and cementum growth with an unprecedented quantitative rigour, in order to establish whether pregnancy events can be estimated using the cementum of animals of unknown life history. The analysis of

Description
tomographic data will allow us to generate a predictive model to study the cementum of specimens that would otherwise be unavailable for destructive histological analysis. Our second sample consists of a population of archaeological humans from the late mediaeval (AD 1086-1539) Priory of St. Peter and Paul, Somerset (UK). The identification of pregnancy events in this sample will provide important information on aspects of population structure including absolute pregnancy numbers per individual. Additionally, existing burial information will be used to assess similarities and differences in relative numbers of pregnancies, and average age of first pregnancy, in women of known differing status [4]. The proposed experiment will form a collaboration of a combination of expertise in mammal dental development at the University of Helsinki, mammalian evolution and palaeoanthropology at the University of Bristol, and bioengineering and X-ray imaging at the University of Southampton. Developing a new, non-destructive record of pregnancy, an important aspect of life history in mammals will be of benefit to a wide range of disciplines including ecology [1], archaeozoology [5], paleoanthropology [6] and even forensic criminology [7]. C) Experimental method; specific requirements: Macaque samples will consist of molariform teeth removed from animals culled prior-to this project, then buffered and dehydrated at the university of Southampton. No animals were culled specifically for this project, and all samples have been screened for pathologies and are certified not to carry any disease of danger to humans. The project has full ethical approval from the University of Southampton and the respective funding bodies to conduct this experiment. Proposed experiments will take place at the TOMCAT beamline using 40x and 20x objectives at 0.33 and 0.65 micrometer voxel dimensions (respectively), at energy levels of 20 keV. Reconstructions will use conventional X-ray absorption based ("grid rec") algorithms, and exploratory phase-contrast enhancement ("Paganin-style") algorithms as these have produced the most precise measurements to date (Fig. 2). Reconstructed data will be analysed using commercial software (Avizo, Fiji) in order to process increment data. Two roots from each macaque tooth will be scanned and separated into two subsamples. Quantitative morphometric techniques will be applied to one subsample to assess variation in relative widths between increments formed during pregnancy and surrounding increments. If significant differences are found, they will form the basis of a predictive model, the power of which will be assessed using a randomised blind analysis of the second subsample, and a blind study of archaeological teeth from humans of known sex. D) Results expected: We expect that the effects of pregnancy on the body will extend to the cementum tissue in a predictable way, and that we will be able to identify this effect in tomographic data. Pregnancy is known to reduce the growth and effect the composition of bone tissue. As cementum is composed of the same principal components as bone (collagen and hydroxyapatite) in similar proportions, and is also continuously growing throughout life, it is logical that its growth will be similarly affected. We thus hypothesise that the increment formed during pregnancy should have a distinctly different structure compared to surrounding increments of the same type. E) Estimate and justification of the beamtime: Our experiment will involve studying both roots of the lower left m1 tooth of 12 individual macaques and single roots of single teeth for five male and at least 25 female archaeological humans. The requested voxel resolutions will ultimately limit the field of view per-scan to approx. 0.8x0.7mm for 0.35 micrometer voxel resolution, and 1.7x1.4mm for 0.65 micrometer voxel resolution. A region of interest (ROI) has been chosen within the cervical third of the root (Fig. 1a), as this region is frequently noted as providing the most reliable increment patterns for aging1. We aim to conduct three measurements along the length of each root within this ROI, in order to sample a sufficient extent of the cementum tissue. Based on previous experiments, measurements will take approx. 30 minutes each, allowing a maximum of 48 per day. 12 macaque samples x 2 roots x 3 measurements = 72 measurements; 30 human samples x 3 measurements = 90 measurements, for a total of 162 measurements (81 hours, 10.125 shifts). We thus request four full days of beamtime (12* 8 hour shifts), including pre-measurement setup and optimization. F) References [1] Klevezal, G. A. & Mina, M. V. (1995). Recording structures of mammals. CRC Press. [2] Naji, S., et al. (2014). International Journal of Paleopathology. doi:10.1016/j.ijpp.2014.05.003 [3] Medhill, S., et al. (2010). Polar Biology 33, 115-124. [4] Dawson, H and Robson Brown, K. (2013). American Journal of Physical Anthropology 150:433-441. [5] Dean, C. (2000). Journal of Anatomy. [6] Jones, J. R. (2012). Quaternary International 252, 195- 201. [7] Colard, T., et al. (2015). International Journal of Legal Medicine 1-8.

SLS related publications of the proposers (within the last 18 months)
Gill P G, Purnell M A, Crumpton N, Robson Brown K, Gostling N J, Stampanoni M, Rayfield E JDietary specializations and diversity in feeding ecology of the earliest stem mammals. NATURE 512 303 (2014)Beamline: TOMCAT
Georgiadis Marios, Guizar-Sicairos Manuel, Zwahlen Alexander, Trussel Andreas J., Bunk Oliver, Muller Ralph, Schneider Philipp3D scanning SAXS: A novel method for the assessment of bone ultrastructure orientationBONE 71 42-52 (2015)Beamlines: cSAXS, cSAXS
Carriero A., Doube M., Vogt M., Busse B., Zustin J., Levchuk A., Schneider P., Mueller R., Shefelbine S. J.Altered lacunar and vascular porosity in osteogenesis imperfecta mouse bone as revealed by synchrotron tomography contributes to bone fragilityBONE 61 116-124 (2014)Beamline: TOMCAT
Mader Kevin Scott, Schneider Philipp, Mueller Ralph, Stampanoni MarcoA quantitative framework for the 3D characterization of the osteocyte lacunar systemBONE 57 142-154 (2013)Beamlines: TOMCAT,TOMCAT,TOMCAT,TOMCAT
Schneider Philipp, Voide Romain, Stampanoni Marco, Donahue Leah Rae, Mueller RalphThe importance of the intracortical canal network for murine bone mechanicsBONE 53 120-128 (2013)Beamline: TOMCAT
Thimm BW, Hofmann S, Schneider P, Carretta R, Mueller RImaging of Cellular Spread on a Three-Dimensional Scaffold by Means of a Novel Cell-Labeling Technique for High-Resolution Computed TomographyTISSUE ENGINEERING PART C-METHODS 18 167-175 (2012)Beamlines: TOMCAT,TOMCAT
Dierolf M, Menzel A, Thibault P, Schneider P, Kewish CM, Wepf R, Bunk O, Pfeiffer FPtychographic X-ray computed tomography at the nanoscaleNATURE 467 436 (2010) Beamlines: cSAXS,cSAXS,cSAXS,cSAXS
Bergomi M, Cugnoni J, Wiskott HWA, Schneider P, Stampanoni M, Botsis J, Belser UCThree-dimensional morphometry of strained bovine periodontal ligament using synchrotron radiation-based tomographyJOURNAL OF ANATOMY 217 126 (2010)Beamline: TOMCAT
Schneider P, Stauber M, Voide R, Stampanoni M, Donahue LR, Muller RUltrastructural properties in cortical bone vary greatly in two inbred strains of mice as assessed by synchrotron light based micro- and Nano-CTJOURNAL OF BONE AND MINERAL RESEARCH 22 1557 (2007)Beamlines: TOMCAT,MS-Tomo,MS-Tomo,MS-Tomo,MS-Tomo

Other publications of the proposers (within the last 18 months)
Acquaah, F., Robson Brown, K.A., Ahmed, F., Jeffery, N. and Abel, R. 2015. Early trabecular development: overproduction, constructive regression and refinement. Frontiers in Endocrinology – Bone Research 6:67doi: 10.3389/fendo.2015.00067.
Dawson, H., and Robson Brown, K. 2013. Exploring the relationship between dental wear and status in late medieval subadults from England. American Journal of Physical Anthropology 150:433-441.
Robson Brown, K., Tarsuslugil, S., Wijayathungam V.N., Wilcox, R.K. 2014. Comparative finite element analysis: a single computational modeling method can estimate the mechanical properties of porcine and human vertebrae. Royal Society Interface. 11 95 20140186; doi:10.1098/rsif.2014.0.0186. 1742-5662.
Bayle, P., L Luyer, M. and Robson Brown, K. 2016. The Dental Remains: Enamel Thickness, and Tissue Proportions. Chapter 9 of The People of Palomas: The Neandertals from the Sima de las Palomas del Cabezo Gordo, Southeastern Spain. Eds E Trinkaus and M Walker. Accepted and in press with Texas A & M University Press.
Harjunmaa, E., Seidel, K., Häkkinen, T., Renvoise, E., Corfe, I.J., Kallonen, A., Evans, A.R., Zhang, Z.-Q., Mikkola, M.L., Salazar-Ciudad, I., Klein, O.D. & Jernvall, J. (2014). Replaying evolutionary transitions from the fossil record. Nature, 512, 44-48.
Newham, E., Benson, R., Upchurch, P., & Goswami, A. 2014. Mesozoic mammaliaform diversity: The effect of sampling corrections on reconstructions of evolutionary dynamics. Palaeogeography, Palaeoclimatology, Palaeoecology, 412, 32-44. doi:10.1016/j. palaeo.2014.07.017.

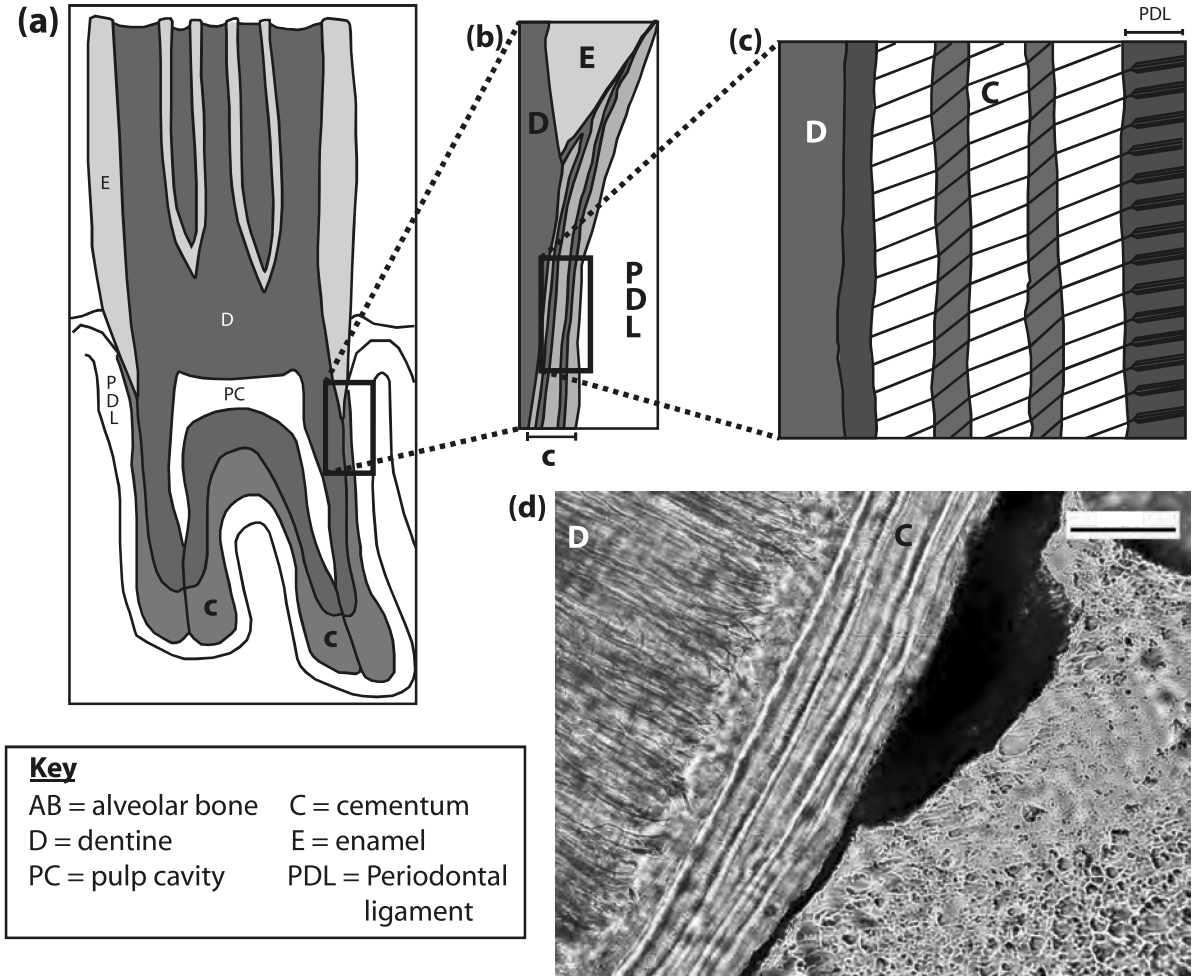

Figure 1. Summary of cementum ultrastructure. (**a**) Schematic longitudinal cross section through an adult bovid molar highlighting the extent of cementum deposition (red). (**b**) Schematic cross section of incremental cementum banding. (**c**) Schematic cross section across incremental cementum bands. Obliquely oriented cementoblasts (cementum-forming cells) first form due to the disintegration of Hertwig's sheath as a tooth erupts. Cementoblasts aggregate to form a single layer in contact with the tooths dentine, and deposit collagen fibres onto the dentine surface as the tooth continues to erupt. Fibres become held in place by calcitic material that is deposited within an amorphous substance surrounding them, forming the inorganic component of cementum. As cementum grows it attaches to Sharpey's fibrils, the principal fibres of the periodontal membrane, securely attaching the tooth to the alveolus. This process continually repeats itself through life, and the progressive nature of growth allows the attachment of the tooth root to the alveolus to be altered according to the functionality of the specific tooth. As the mineralisation front migrates through life, the angle of collagen fibril mineralisation will commonly shift in response to seasonal changes in food quality, with narrower layers corresponding to lower dietary quality. All images in (**a**-**c**) sourced and modified from Stutz (2002). (**d**) Detail from a histological thin section of the cementum of a European hedgehog (*Erinaceus europaeus*) viewed under reflected light, displaying distinct series of cementum increments. Scale bar = 50 μm.

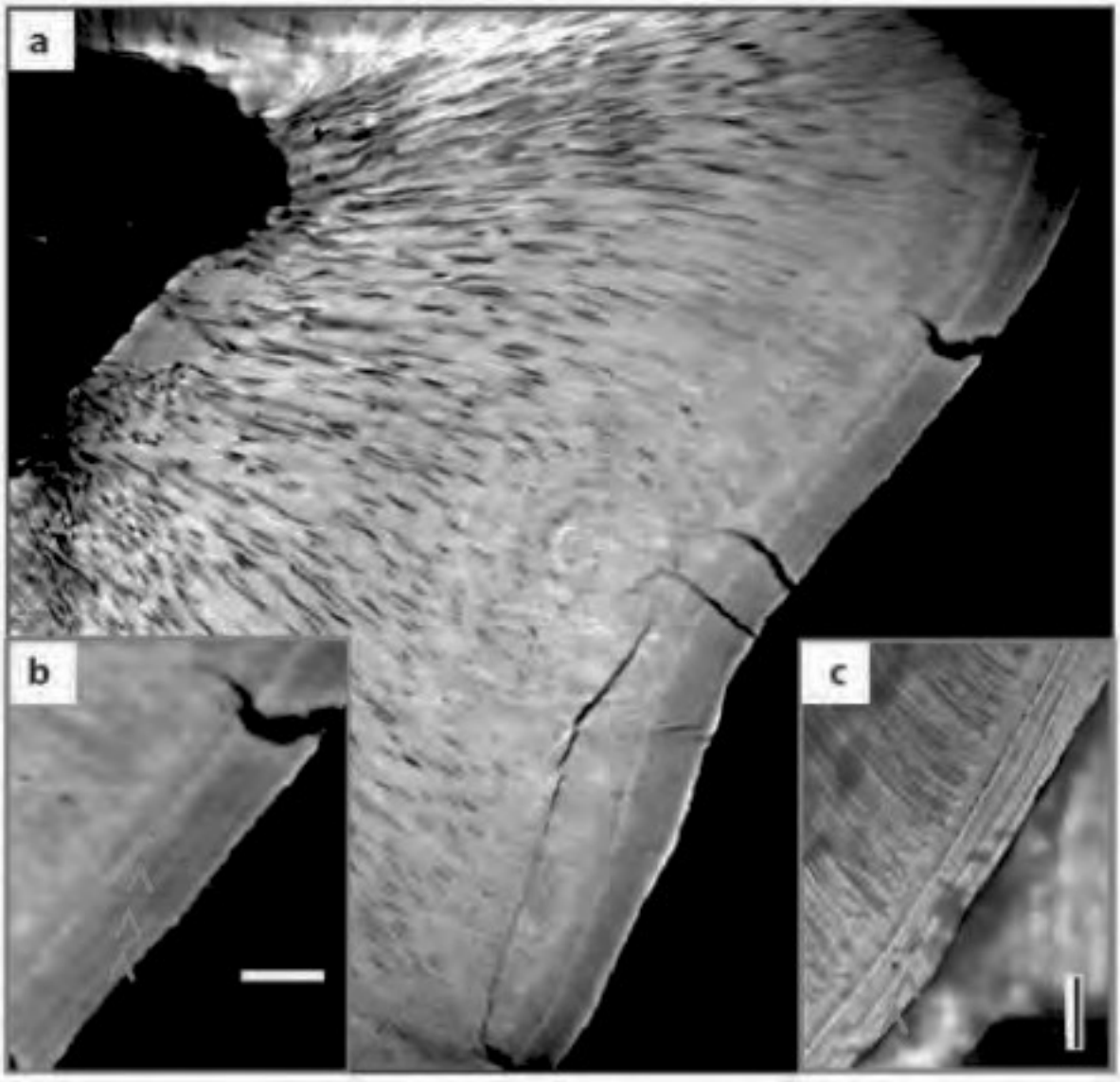

Figure 2. (a) Transverse orthoslice of a section of Erinaceus europaeus molar root displaying circumferencial increments within the cementum layer, which is distinguished from the dentine by a bright circumferencial boundary between the two tissues. (b) Detail of the same orthoslice, highlighting three clear increments marked by red arrows. (c) Detail of a histological thin-section of the same area of the same root, displaying the same three increments. White line in (b), and black line in (c) each represent 50µm.

This is a continuation request	
Original proposal	20151391 [Type=Normal] Click here to download.
Original title	Novel 3D assessment of growth increments in dental tissue for studying discrete life history events.
Report for 20151391	Available, last update: Thu, 15 Sep 2016 23:31:37 +0200

Justification for continuation
Proposal 20151391 was a successful experiment, with high quality data gathered in general. However, due to the random nature of preservation of the archaeological human samples, a number of measurements produced poor quality data because of diagenetic sample alteration. This can be determined only once initial measurements on these samples are carried out. This meant that the resulting sample of high quality data from archaeological human samples, by chance, was biased heavily towards male specimens instead of being at parity with or less than female sample numbers. In order to address this, tomographic data from additional female samples are required in order to construct statistically robust sample sizes for statistical testing of separation in morphospace of cementum increments between male and female samples. In addition, because of the relatively high number of poorly preserved archaeological samples, meaning numerous initial scans resulted in poor quality data, not all tests for intra-tooth, intra-root and intra-tooth position variation of increments were carried out for the archaeological samples. Additionally, and for the same reason, no entire macaque tooth root sample was assessed for whole volume cementum increment variation as required. We therefore request an additional 9 shifts in order to produce a publishable dataset.

Proposer / Spokesperson	
Dr. Pamela G Gill	Dept. of Earth Sciences, Univ. of Bristol pam.gill@bristol.ac.uk

Experiment Requirements	
Number of Shifts Required	9
Schedule Preferences	Earlier if possible
Beamline/Station	TOMCAT

Experimental report	
Proposal ID	20151391
Last modified	15.Sep.2016 23:31:37

A) Overview

In this TOMCAT experiment we used single distance phase contrast x-ray microtomography to test whether episodes of pregnancy can be predicted from patterns of growth increments in the cementum of dental tissue. By using a sample of primates raised under controlled conditions and with known life histories we are beginning to generate a predictive model for detecting pregnancy events by mapping the three dimensional (3D) structure of increments to identify patterns in increment structure. This model will then be used to infer pregnancy events from the cementum of an archaeological human population of known sex. Synchrotron-based radiation tomography (SR CT) has let us assess the potential of cementum as a record of pregnancy in a robust fashion, by allowing us to quantify the relationship between pregnancy events and 3D cementum growth for the first time. The non-destructive nature of the tomographic measurements will also allow us to develop a method for predicting pregnancy in specimens that cannot be analysed using traditional destructive histological techniques, including rare or unique fossil material.

The monitoring and interpretation of life history in both living and fossil mammals is of crucial importance for a range of biological disciplines, and the structure of cementum increments has been previously suggested to correspond to both an individual age, and important events such as pregnancy that affect the animal's physiology and growth. The growth and development of mineralised dental tissue, (cementum, dentine and enamel) is recorded by a series of incremental features of differing periodicity and causation. Cementum, the connective tissue that anchors mammalian teeth within the alveolar socket, is unique among these tissues as its growth is continuous throughout life, and annual in rhythm. This rhythm is recorded by a series of circumannual increments of contrasting opacity when viewed under light microscopy, with relatively dense hyper-mineralized opaque increments recording a reduction of growth rates during unfavourable seasons. Cementum increments have been the subject of histological study for decades and their counts have successfully been used as an absolute estimate of chronological age in over 70 species of extant mammals. Further, several recent studies have indicated that certain life history events, which significantly affect the physiology of mammals, may be recorded in cementum. However, these studies have relied on anecdotal and observed field evidence (e. g. presence of cubs) for pregnancy events, and thin section histology for studying their effects. The reliance on thin-section based histological analysis has placed limits on current understanding of the nature of the structure and causation of cementum increments. Cementum is a dynamic, biomechanically responsive tissue and increments can be seen to lense and coalesce in apparently random areas of their vertical and horizontal trajectory. The 2D perspective of study over a limited number of thin sections available per tooth (often only one), means that such discrepancies in increment patterns cannot be accounted for in the context of the entire cementum tissue. This creates uncertainty in counts and makes it difficult to discern patterns in increment structure from transitory noise created by lensing and coalescence. Our 3D SRCT analyses and animals of known life history allow these issues to be overcome.

B) Quality of measurement/data

Almost 200 non-setup measurements were completed during the 9 shifts. The entire sample of 14 macaque monkeys was scanned, with multiple tooth row positions, anterior and/or posterior tooth roots, and regions of interest within roots imaged. A total of 138 measurements were made on this sample. 10 specimens of the archaeological human sample were scanned, though with only 17 measurements of these, recording a similar range of toothrow/root/within root locations as for the macaques was not accomplished. An additional 11 measurements of other hominid specimens as pilot data for future SLS applications were also made.

A pink beam with 21 KeV energy was used, with 150ms exposure times over 1501 angular projections. This secured a minimum of 25% transmission through the tooth root and resulted in total scan times of three minutes. Generally, 10x magnification, voxel sizes of 0.65μ m, and used 'half-acquisition mode' to double the lateral field of view to enable the entire lateral width of the tooth roots to be imaged in a single measurement. Both X-ray absorption-based (Fourier grid) reconstruction algorithms and phase contrast-based algorithms

Experimental report
(Paganin) were used to reconstruct SR CT data during the experiment, which allowed some specimens to be discontinued from additional scans due to preservational issues. Paganin reconstruction algorithms require the input of # and $ values for phase retrieval of CT data. These were chosen following an iterative analysis of image contrast, to be #=3.7 e-8 and $=1.7 e-10. Phase-contrast based reconstructions proved to provide substantially more detail and less noise than absorption based data, and so were used for subsequent analyses. Data quality was generally excellent, with low noise images and few movement artefacts.   C) Status and progress of evaluation The initial results have been used for an 18 month MSc-to-PhD report, with the student successfully progressing to the full PhD, and have just been submitted in abstract form to an invited symposium presentation to a high profile international conference in 2017. The data is currently being fully analysed, and it is expected that it will be submitted for publication in early 2017. The initial analyses of the data have concentrated on identifying sex of specimens, and discriminating between breeding and non-breeding females using the 3D microstructure of the cementum and cementum increments. To date, all 14 macaque specimens and 8 of 10 archaeoogical specimens have been analysed for discrimination of sex by cementum microstructure. The next steps are to assess individual increments in the cementum of the macaques, and compare against known life history records of individuals to see whether morphometric features of the increments correlate with pregnancy events. This can then be used to attempt to identify pregnancy events in the archaeological sample without known life histories.   D) Results Principal Component Analysis (PCA) of all 14 macaque specimens shows that the 3D microtexture of cementum increments visualized with SRCT (Fig 1a,b) clearly separates males from females, and mostly separates breeding females from non/breeding females (Fig 2a). Similarly, male and female specimens are fully separated in a PCA of 8 of the 10 archaeological specimens (Fig 2b). These results show the potential of our methods as a tool for sexing fragmented remains in forensic, anthropological and archaeological contexts, as well as sexing in fossil species.

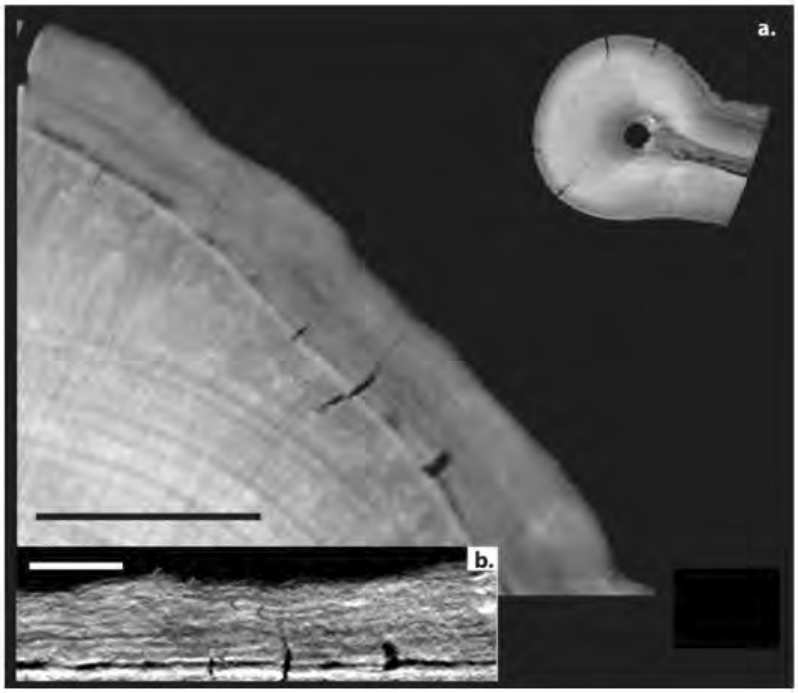

Fig 1 – Cementum increments in breeding macaque female. **a)** whole scan inset, zoomed region main picture. **b)** straightened and filtered cementum increments, red arrows indicate pairs. Scale – black line in a = 150um, white line in b = 75um.

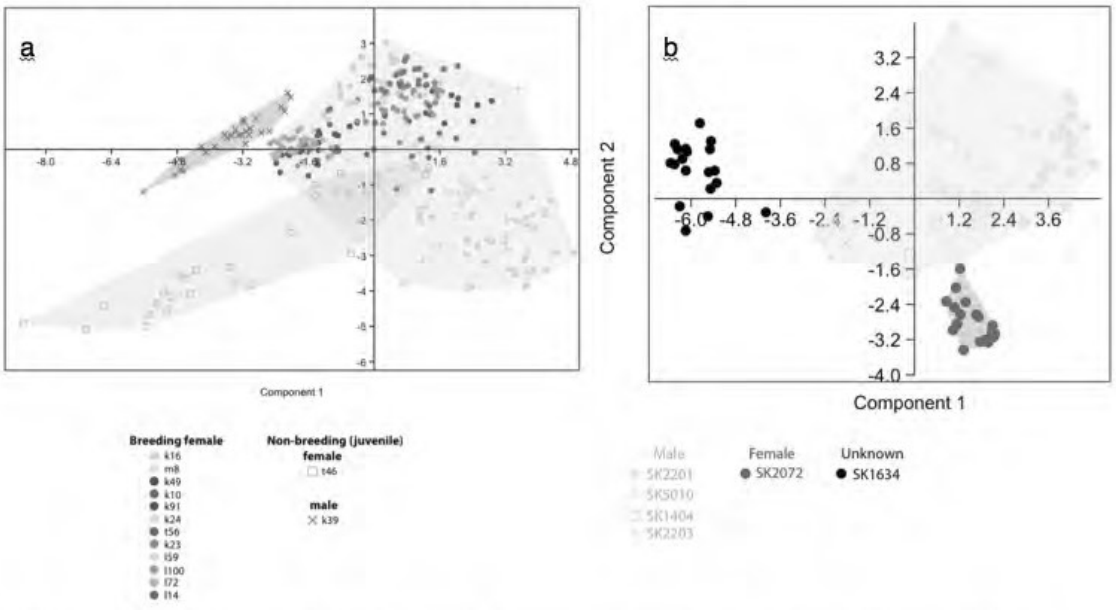

Fig 2 – PCA morphospace plots of female vs male cementum 3D microtexture showing clear separation of sexes in morphospace. **a)** Macaque monkeys, **b)** archaeological humans

Cementum increments and PCA morphospace analyses

Title
Life and Death in the Middle Jurassic - Metabolic Rates and Lifespans of Mesozoic Mammals Determined Through Phase Contrast Imaging of Tooth Cementum Increments

Abstract
We propose phase contrast imaging of the teeth of a diverse range of early mammals from the Mid-Jurassic; a critical period in mammalian evolution. Synchrotron-based CT will allow us to non-destructively measure tooth cementum growth increments in several key lineages of Mesozoic mammals, in order to estimate individual ages at death and maximum lifespans for each species. Using maximum lifespan as a proxy for metabolic rates, this will allow us to reconstruct their physiological evolution for the first time.

Proposer / Spokesperson	
Dr. Pamela G Gill	Dept. of Earth Sciences, Univ. of Bristol pam.gill@bristol.ac.uk

Principal investigator	
Dr. Pamela G Gill	Dept. of Earth Sciences, Univ. of Bristol

Co-Proposer	
Dr. Ian J Corfe	Inst. of Biotechnology, Univ. of Helsinki
Dr. Philipp Schneider	Faculty of Engineering and the Environment, Univ. of Southampton
Mr. Elis Newham	Faculty of Engineering and the Environment, Univ. of Southampton
Dr. Philippa Brewer	Dep.of Palaeontology, Natural History Museum
Dr. Neil J Gostling	Centre for Biological Sciences, Univ. of Southampton

Experiment Category	
Experiment Type	Normal
Research Area	Environmental and Earth Science

Experiment Requirements	
Eligible for EU Support	Yes
Number of Shifts Required	12
Schedule Preferences	None
Beamline/Station	TOMCAT

Links to related proposals of relevance to the current proposal			
Proposal	Title/Proposer/Infos given by the proposer about the relation		Report
20141278	Title: Proposer: Infos:	Reconstructing the life history of the first mammals - using dental increments to make leaps in understanding Dr. Pamela G Gill This earlier proposal demonstrated the feasibility of using phase contrast imaging to visualise tooth cementum increments in small early mammal tooth roots, and establish lifespans. The surprisingly long lifespans suggested that the earliest mammals had not attained the highly developed endothermic regulation of modern taxa. Having established this baseline, we now propose a further study of a later critical time in Mesozoic mammal evolution.	Available

Description (1 / 3)

A) Goal of the experiment. We propose a high-resolution X-ray computed tomography (CT) study of the teeth of a diverse range of early mammals from the Mid-Jurassic (~174-163 million years ago, herein Ma) (Fig.1); a critical period in mammalian evolution. The purpose is non-destructive identification, mapping and quantification of tooth cementum growth increments (lines of arrested growth, LAGs), in order to estimate lifespan and reconstruct the evolution of physiology in the earliest mammals. There is great interest in determining the biology, ecology and physiology of early mammals[1-4] but basic life history variables such as lifespan and growth rate, and physiological characters like metabolic rate and grade, remain unknown. We focus on one of the mineralised tissues of the teeth, cementum, which is known to record LAGs and, unlike bone, is not remodelled during life. Synchrotron-based CT (SR CT) will allow us to non-destructively measure these structures in the representatives of several key lineages of early mammals, in order to estimate their lifespan, and reconstruct their physiological evolution for the first time.

B) Background. During the process of mineralisation, dental tissues such as cementum, dentine and enamel record periodic incremental features, LAGs, which represent a chronological record of animal development. If unmodified by diagenetic processes during fossilisation, these form a permanent record of the growth of the tooth. Such LAGs have been known for centuries but only recently have non-destructive SR CT methods allowed their visualisation and use for determination of life history parameters in rare or unique fossils[5]. Cementum is a collagenous mineralised tissue that connects tooth roots to the periodontal ligament, supporting dentition within the alveolus against forces applied through mastication. Cementum LAGs have been shown to reflect annual seasonal changes, creating alternating bands within the tissue[6]. As cementum grows continuously through life, counts of these bands provide an estimate of annular age and season of death.

Cementum lines obtained through destructive thin sectioning have been used for ageing a range of taxa for archaeological, zoological, palaeontological and forensic purposes[6]. However, limitations of the method have been identified, principally due to difficulties in objectively quantifying LAG numbers in 2D from single histological thin sections of variable location and quality. The use of SR CT for studying cementum LAGs will allow more accurate quantification of LAG numbers and morphology, due to the ability to study entire roots in 3D, instead of a restricted number of 2D thin sections per specimen.

In recent experiments (Report 20141278) we demonstrated the feasibility and necessity of 3D high-resolution SR CT for visualizing tooth cementum LAG microstructures in the tooth roots of *Morganucodon* and *Kuehneotherium*. These are examples of the earliest mammals, and were tiny (~30 grams) animals that co-existed during the Early Jurassic (~200 Ma) (Fig. 1). Samples of teeth (Fig. 2a) were scanned at the TOMCAT beamline at the Swiss Light Source (SLS) using voxel sizes of 325 nm. Image post-processing and morphometry allowed quantitative characterisation and counting of cementum LAGs in both taxa (Figs 2b,d). The large sample size permitted by rapid, non-destructive third-generation SR CT also allowed statistically robust, population-level specimen counts (ca. 150 specimens scanned for each taxon). Large sample sizes are vital for providing accurate minimum estimates of maximum lifespan for fossil animal groups, equivalent to the statistically robust population sampling used to estimate maximum lifespan in living animals.

The lifespans of living mammals are inversely correlated with their basal metabolic rate (BMR), and growth rate[7,8]. The maximum age estimates resulting from our SR CT analyses of the earliest mammals can therefore be used to provide a rare insight into their physiology. Surprisingly high lifespans were estimated for both *Morganucodon* and *Kuehneotherium* relative to their body mass, and are within the range of living reptiles rather than living mammals. Resulting low estimates for growth rate and BMR suggest a

Description (2 / 3)

substantially different physiology than similar sized modern mammals such as shrews, dormice and desert mice, more akin to those of modern reptiles. This has important implications for understanding of the evolution of the highly sophisticated endothermic ("warm-blooded") mammalian physiology.

Having established the physiology of the earliest mammals as a baseline (*Morganucodon* and *Kuehneotherium*; Report 20141278 and Newham *et al*. in prep.), we therefore propose further studies of the cementum increments and lifespans of fossil mammals that fall between the earliest mammals and modern groups, both phylogenetically and temporally. Since large sample sizes are needed to statistically robustly estimate maximum lifespan for species, exceptional fossil faunas are required.

Following the appearance of the earliest mammals, the next important interval for mammalian evolution is the Mid-Jurassic (~174-164 Ma)[9]. This period records the origination of major new groups, and a peak in rates of morphological and taxonomic diversification[10]. Bathonian stage (168-166 Ma) sites in the UK have yielded most of the known mammal fossil record for this period. Localities such as Kirtlington, Oxfordshire, have produced over 1000 well-preserved isolated mammal teeth, with species often represented by 20-80 fossils. Other sites (e.g. Stonesfield, Oxfordshire and the Isle of Skye, Scotland) have fewer specimens but preserve whole jaws of species known from isolated teeth in Kirtlington and elsewhere, allowing analyses of multiple teeth representing individual animals.

These collections form a diverse assemblage, representing key mammal groups[3,9,10] (Fig. 1) For example, docodonts (e.g. *Borealestes*; ~40 teeth available) are the first major clade of mammals to evolve and diversify following the basal mammals such as *Morganucodon.* Eutriconodonts (e.g. *Amphilestes*; ~80 teeth available) are one of the most diverse Mesozoic mammalian lineages, and are one of the earliest known crown mammal groups (phylogenetically bracketed by living groups). Cladotherians (e.g. *Palaeoxonodon*; >50 teeth available: *Amphitherium*; ~40 teeth available), are more derived crown mammals, closer to modern mammals than any other group known during this period.

Cementum studies of these robust samples will thus provide life history and physiological data for important mammal groups during a key period of evolution. Pilot data from Mid-Jurassic teeth from Kirtlington (Fig. 2c) suggests that the very high resolution (325 nm voxel size), high signal-to-noise ratio, and high throughput available (<30 minute scans) at SLS TOMCAT are crucial for analysing the ultrastructure of fossil teeth in sufficient sample sizes, and these requirements cannot be met using current lab-based CT techniques. SR CT data of fossil mammal cementum LAGs acquired at TOMCAT will therefore allow us to test the following questions for the first time:

1) Do the lifespans of different fossil mammal groups differ significantly?
2) Are these lifespans significantly different to extant mammals of comparable size?
3) Is there a distinct temporal and/or phylogenetic trend in the distribution of lifespans?

The answers to these questions will provide an unprecedented level of detail for our understanding of physiological evolution in the oldest mammals.

C) Experimental method; specific requirements. Appropriate initial permissions have been obtained so that samples will be loaned from relevant institutions and prepared prior to experimentation at the Universities of Bristol and Southampton. The non-destructive nature and exciting results of previous SR CT studies have ensured approval from the institutions housing these collections. Samples will consist of isolated fossil teeth, and teeth within jaw bones, and do not require specialised sample environments. Proposed SR CT experiments at TOMCAT will require mainly

Description (3 / 3)

20x objective to obtain 325 nm voxel sizes (and possibly some 10x objective, 650 nm voxel size), at an X-ray energy of 20 keV. For tomographic reconstructions, we will use a conventional X-ray absorption-based ("grid rec") and an exploratory phase retrieval ("Paganin-style") approach, as comparisons between these two different reconstruction methods have allowed for more confident LAG counts in our previous studies. Resulting reconstructed 3D data will be studied using customised in-house image post-processing tools. Quantitative morphometry for LAGs will include number, thickness, separation, and their respective variations.

D) Results expected. Quantitative morphometric measurements of cementum LAGs imaged using SR CT will provide estimates of age-at-death for statistically robust samples of a diverse range of Mid-Jurassic Mesozoic mammals. These will form the basis of minimum estimates of maximum lifespan that can be compared with our previous SR CT results for the Early Jurassic basal mammals *Morganucodon* and *Kuehneotherium*, (Report 20141278) and with lifespan data for living mammals. Information about BMR and growth rates of several groups of early Mesozoic mammals, will provide previously unobtainable insights into the rate of evolution of early mammalian physiology and the development of endothermy.

E) Estimate and justification of beamtime. Our team has previously scanned both isolated and in-jaw fossil mammal teeth at SLS TOMCAT, at an average of 20 and 30 minutes per specimen respectively (including sample change, orienting and scanning). We intend to scan approximately 135 isolated teeth (45 hours) and 90 scans of teeth in jaws (45 hours). This is to produce a robust sample size of minimum 40 specimens for each of the three representative groups of Mid-Jurassic mammals in this proposal. With an additional experimental setup time of 6 hours we thus request a total beamtime of 4 days/96 hours or 12 shifts.

F) References relevant to the experiment description (proposers in bold). [1] **Gill**, Purnell, Crumpton, Robson-Brown, **Gostling**, Stampanoni and Rayfield, *Nature* **512**, 303-305 (2014) [2] Rowe *et al.*, *Science* **332**, 955-957 (2011). [3] Close et al., *Current Biology*, **25**, 2137-2142. [4**]** Wilson, Evans, **Corfe** *et al.*, *Nature*, 483, 457-460 (2014) [5] Smith *et al. P.N.A.S* **107**, 20923-20928 (2010) [6] Lieberman, *Science*, **261**, 1162-1164 (1993). [7] Magalhaes et al., *J Gerontol A Biol Sci Med* Sci, 62, 149-160. **[**8**]** Hulbert *et al.*, *Physiol. Rev*. 87, 1175-1213 (2007) [9] Kielan-Jaworowska *et al.*, *Mammals from the age of dinosaurs.* (2004) [10] **Newham** *et al.*, *Palaeogeography, Palaeoclimatology & Palaeocology* **412**, 32-44 (2014).

SLS related publications of the proposers (within the last 18 months)
Liebi M, Georgiadis M, Menzel A, Schneider P, Kohlbrecher J, Bunk O, Guizar-Sicairos MNanostructure surveys of macroscopic specimens by small-angle scattering tensor tomographyNATURE 527 349 (2015)Beamline: cSAXS
Georgiadis Marios, Guizar-Sicairos Manuel, Zwahlen Alexander, Trussel Andreas J., Bunk Oliver, Muller Ralph, Schneider Philipp3D scanning SAXS: A novel method for the assessment of bone ultrastructure orientationBONE 71 42-52 (2015)Beamlines: cSAXS, cSAXS
Zwahlen Alexander, Christen David, Ruffoni Davide, Schneider Philipp, Schmoelz Werner, Mueller RalphInverse Finite Element Modeling for Characterization of Local Elastic Properties in Image-Guided Failure Assessment of Human Trabecular BoneJOURNAL OF BIOMECHANICAL ENGINEERING-TRANSACTIONS OF THE ASME 137 011012 (2015) Beamline: TOMCAT
Fessel G, Li Y, Diederich V, Guizar-Sicairos M, Schneider P, Sell DR, Monnier VM, Snedeker JGAdvanced Glycation End-Products Reduce Collagen Molecular Sliding to Affect Collagen Fibril Damage Mechanisms but Not StiffnessPLOS ONE 9 e110948 (2014)Beamline: cSAXS
Carriero A., Doube M., Vogt M., Busse B., Zustin J., Levchuk A., Schneider P., Mueller R., Shefelbine S. J.Altered lacunar and vascular porosity in osteogenesis imperfecta mouse bone as revealed by synchrotron tomography contributes to bone fragilityBONE 61 116-124 (2014)Beamline: TOMCAT
Gill P G, Purnell M A, Crumpton N, Robson Brown K, Gostling N J, Stampanoni M, Rayfield E JDietary specializations and diversity in feeding ecology of the earliest stem mammals. NATURE 512 303 (2014)Beamline: TOMCAT

Other publications of the proposers (within the last 18 months)
Whiteside, D.I., Duffin, C.J., Gill, P.G., Marshall, J.E.A., and Benton, M.J. 2016. (In press) The Late Triassic and Early Jurassic fissure faunas from Bristol and South Wales: Stratigraphy and setting. Palaeontologia Polonica 67.
Newham, E., Benson, R., Upchurch, P., Goswami, A. (2014). Mesozoic mammaliaform diversity: The effect of sampling corrections on reconstructions of evolutionary dynamics. Palaeogeography, Palaeoclimatology, Palaeoecology, 412 32-44.

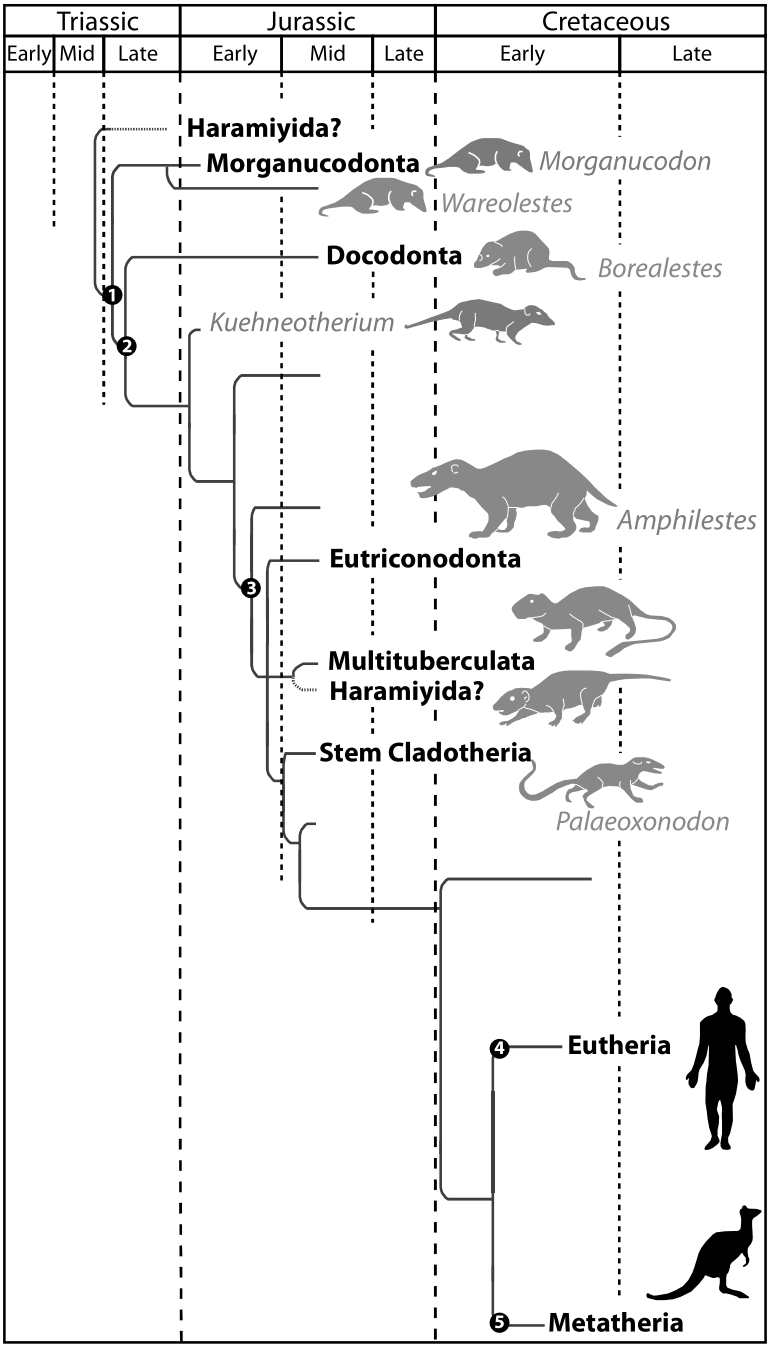

Early Jurassic assemblages
Pontalun Quarry (South Wales, UK)
Pant Quarry (South Wales, UK)

Mid Jurassic assemblages
Kirtlington Quarry (Oxfordshire, UK)
Hornsleaslow Quarry (Gloucestershire, UK)
Isle of Skye (Inner Hebrides, UK)

Figure 1. Schematic cladogram highlighting the phylogenetic diversity of Early Jurassic (red) and Mid Jurassic (green) mammal assemblages of the UK. Nodes 1-5 represent; (**1**) The Early Jurassic radiation of Mammaliaformes; (**2**) The Mid-Jurassic diversification of docodont mammals and other novel groups; (**3**) The radiation of crown mammals; (**4**) The radiation of eutherian mammals (stem placentals); (**5**) The radiation of metatherian mammals (stem marsupials). Sourced and modified from Luo (2007). Note timings of branch endings indicate originations and not extinctions of major groups.

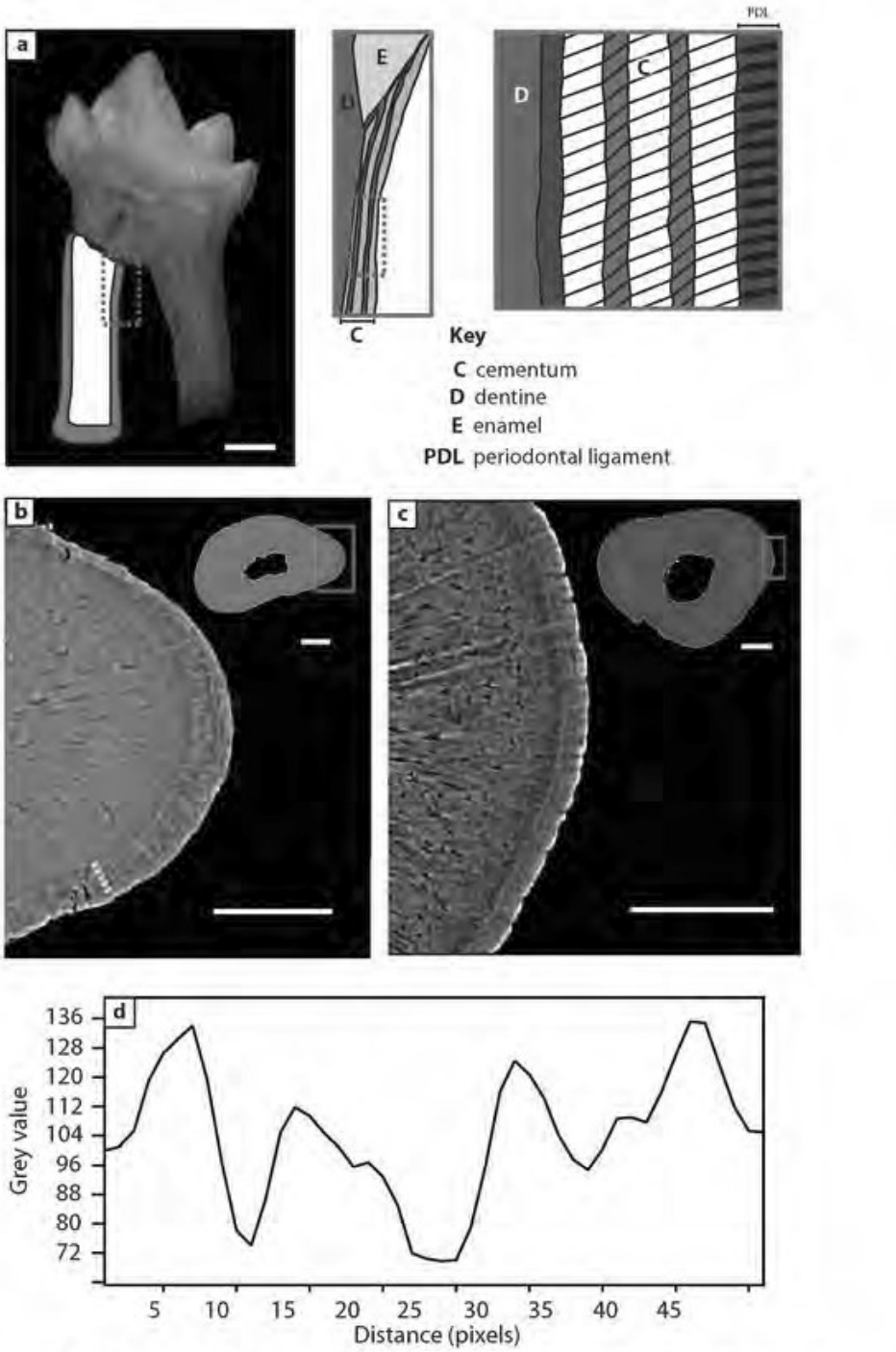

Figure 2. (a) *Morganucodon* tooth with cementum layer highlighted in red, and green boxes showing increasing detail of idealised morphology and incrementation. **(b)** Orthoslice of *Kuehneotherium* root with detail of cementum showing clear increments, scanned during experiment 20141278 . **(c)** Pilot data of Bathonian age docodont root from the Kirtlington fauna, showing comparable cementum increments. **(d)** Greyscale distributions of pixels along yellow transect in **(b)** showing clear peaks and troughs corresponding to respective light and dark increments. White scales bar in **(a)** = 500μm. White bars in all other images = 50μm.

Figure 2: Cementum increments

EUROPEAN SYNCHROTRON RADIATION FACILITY
ESRF User Office
CS 40220, F-38043 GRENOBLE Cedex 9, France
Delivery address: 71 avenue des Martyrs, 38000 GRENOBLE, France
Tel: +33 (0)4 7688 2552; fax: +33 (0)4 7688 2020; email: useroff@esrf.fr; web: http://www.esrf.fr

Application for beam time at ESRF – Experimental Method

Proposal Summary (should state the aims and scientific basis of the proposal): We propose a high-resolution X-ray computed tomography (CT) study of the teeth of a diverse range of early mammals from the Mid-Jurassic; a critical period in mammalian evolution. The purpose is non-destructive identification, mapping and quantification of tooth cementum growth increments (lines of arrested growth, LAGs), in order to estimate lifespan and reconstruct the evolution of physiology in Mesozoic mammals. There is great interest in determining the biology, ecology, physiology and evolution of early mammals[1,2,3,4] but basic life history variables such as lifespan and growth rate, and physiological characters like metabolic rate and grade, remain unknown. Synchrotron-based CT (SRCT) measurements of cementum LAGs in representatives of several key lineages of early mammals will allow us to estimate lifespans, and building on our prior ESRF data from the earliest mammals, reconstruct their physiological evolution, including evolution of the mammalian endothermic metabolic grade ('warm-bloodedness').

Scientific background: During tooth mineralisation, the dental tissues cementum, dentine and enamel record periodic incremental features, LAGs, which represent a chronological record of development. If unmodified by diagenetic fossilisation processes, these form permanent records of tooth growth. Such LAGs have been known for centuries but only recently have non-destructive SRCT methods allowed their visualisation and use for determination of life history parameters in rare or unique fossils[5]. Cementum LAGs reflect annular seasonal changes throughout life, creating alternating bands which record an estimate of annular age and season of death[6]. Destructive thin sectioning to visualise cementum has been used with many species for archaeological, zoological, palaeontological and forensic purposes[6]. In recent experiments [ES152a (ID19) & ES152b (ID16A)] we demonstrate that 3D tomographic cementum LAG imaging allows more accurate quantification of LAG numbers and morphology than single destructive histological thin sections of variable location/quality. We visualised 3D tooth cementum LAG microstructures in roots of two of the earliest basal mammals[1], *Morganucodon* and *Kuehneotherium*, tiny (~30 grams) animals that co-existed in the UK during the Late Triassic and Early Jurassic (~200Ma) **Fig 1a.** Image post-processing and morphometry allowed quantitative characterisation and counting of cementum LAGs in both species **(Fig. 1b,d).** The large sample size permitted by rapid, non-destructive SRCT allowed maximum lifespan estimation from these methods in statistically robust population-level samples. Living mammal lifespans are inversely correlated with their basal metabolic rate (BMR) and growth rate[7,8]. Maximum age estimates from SRCT analysis of early mammals can thus be used to provide insight into their physiology. Surprisingly high lifespans were identified for *Morganucodon* and *Kuehneotherium* relative to their body mass, and resulting low estimates for growth rate and BMR suggest a substantially different physiology and metabolism, more akin to those of modern reptiles than similar sized modern mammals such as shrews and dormice.

Having established the physiology of the earliest mammals as a baseline (Newham *et al.* in prep), we therefore propose further studies of the cementum increments and lifespans of fossil mammals that fall between the earliest mammals (*Morganucodon* and *Kuehneotherium*) and modern mammals, both phylogenetically and temporally. Since large sample sizes are needed to statistically robustly estimate maximum lifespan for species, exceptional fossil faunas are required. Following the appearance of the earliest mammals, the next important interval for mammalian evolution is the Mid-Jurassic (~174-164 Ma), which records the origination of major new groups and a peak in rates of morphological and taxonomic diversification[3,4,9]. Bathonian stage (168-166Ma) sites in the UK have yielded most of the known mammal fossil record for this period[9]. Localities such as Kirtlington, Oxfordshire, have produced over 1000 well-preserved isolated mammal teeth, with species often represented by 20-80 fossils. Important groups include multituberculates, haramiyids, docodonts, pseudotribosphenids, morganucodontids, eutriconodonts, and cladotherians (the group leading to living mammals). Other sites (e.g. Stonesfield, Oxfordshire and the Isle of Skye, Scotland) have fewer specimens but preserve whole jaws of species known from isolated teeth in Kirtlington and elsewhere, allowing analyses of

multiple teeth representing individual animals.

Pilot SRCT data from a Kirtlington specimen **fig 1c** suggests that the sub-micron resolution, high signal to noise ratio, and phase-contrast based reconstruction available at ESRF ID19 are crucial for imaging the ultra-structure of small fossil teeth. Lab based CT has proven insufficient, despite measurements of relevant specimens showing excellent general preservation. We propose that SRCT ID19 cementum studies of these samples will provide life history and physiological data during a key period of mammalian evolution and allow us to test the following: **1)** Do estimated lifespans, growth rates and BMR of Mesozoic mammals differ significantly between groups? **2)** Are these characteristics significantly different to those of extant mammals? **3)** Are there temporal /phylogenetic trends in the distribution and evolution of these characters? Answers to these questions will provide evidence for testing current hypotheses of the evolution of the highly sophisticated endothermic physiology of modern mammals.

The proposed experiments form part of continuing large-scale developmental and evolutionary biology collaboration, focused on teeth, between the Department of Physics and Institute of Biotechnology at University of Helsinki, and incorporate expertise in mammalian evolution at University of Bristol and the Natural History Museum, London, and bioengineering/X-ray imaging at University of Southampton.

Experimental technique(s), required set-up(s), measurement strategy, sample details (quantity...etc):! Appropriate permissions have been obtained for samples to be loaned from relevant institutions and prepared prior to experimentation at the Universities of Bristol and Southampton. Samples will consist of 145 isolated fossil teeth, and 90 teeth within jaw bones. Proposed experiments are for ID19 beamline, pink beam, 26 keV, 10x and 20x objectives at 0.70µm & 0.35um voxel dimensions. Absorption & phase contrast reconstructed data will be analysed with commercial software (Avizo). Resulting increment data will be studied using custom tools in Matlab statistical analysis environment. Quantitative morphometry for LAGs will include number, thickness, separation, and their variations.

Beamline(s) and beam time requested with justification: The request for beamtime is for ID19, where Paul Tafforeau and team are world leaders in tomographic visualisation of tooth incremental structures. Our team has previously (reports ES152a,b) measured isolated & in-jaw fossil mammal teeth on beamline ID19, at an average of 20 and 30 minutes per-specimen respectively (including sample change & orienting; acquisitions ≈ 12 minutes). We intend to measure approximately 135 isolated teeth (45 hours, 5.625 shifts) plus 90 measurements of teeth in jaws (45 hours, 5.625 shifts); we thus request a total beamtime of 4 days/96 hours (12*8 hour shifts) including experimental setup time of 6 hours (45+45+6 hours = 96).

Results expected and their significance in the respective field of research: We aim to determine maximum lifespan in a range of Middle Jurassic mammals, and infer aspects of their physiology and its evolution at a critical stage of the mammal fossil record. Improvements in cementum increment ageing methodologies will also benefit many disciplines including ecology[1], archaeology /archaeozoology[6], palaeontology (project ES152), palaeoanthropology[5] and forensic criminology.

References (proposers in bold): **[1]Gill** *et al.*, *Nature* 512, 303-305 (2014) **[2]**Rowe *et al.*, *Science* 332, 955-957 (2011) **[3]**Close *et al.*, *Current Biology*, 25, 2137-2142 (2015)) **[4]**Wilson, Evans, **Corfe** *et al.*, *Nature*, 483, 457-460 (2014) **[5]**Smith *et al. P.N.A.S* 107, 20923-20928 (2010) **[6]**Lieberman, *Science*, 261, 1162-1164 (1993) **[7]** Hulbert *et al.*, *Physiol. Rev.* 87, 1175-1213 (2007) **[8]** De Magalhães *et al.*, *J. Gerontol. A. Biol. Sci.* 62, 149-160 (2007) **[9]Newham** *et al.*, *Palaeogeography, Palaeoclimatology & Palaeocology* 412, 32-44 (2015).

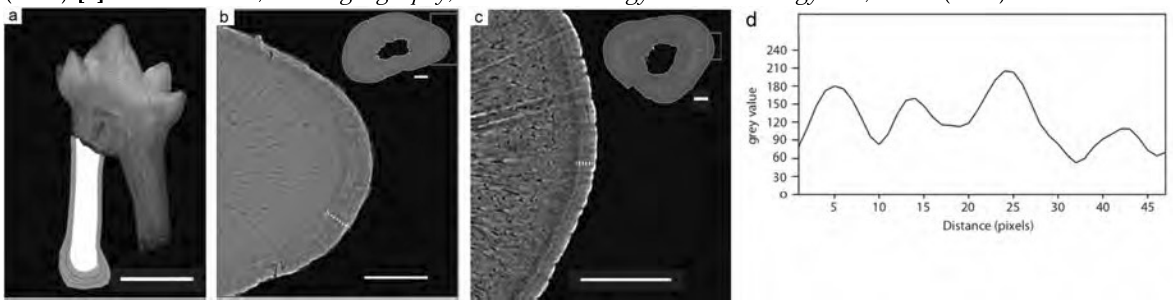

Figure 1. a) *Morganucodon* tooth with cementum lines overlain on left root. b) *Kuhneotherium* ES152 data virtual root slices, whole slice inset, zoomed portion showing increments. c) Kirtlington Bathonian docodont pilot data showing comparable increments. d) Transect showing lumiance/density across yellow transect in 1b, with 4 peaks. Scale = 1mm in a, 50um elsewhere.

Order	Family	Genus	Species	Aka	Study			Ecology			Readability				species/ population/ experiment specific notes	Summary notes
								Country			Accessory lines					
					Population	n	Reference	Region	Latitude midpoint	Koppen Climate	Non-perfect	Complex Ratio	Contrast	Combined (mean) readability score		
Carnivora	Mustelidae	Mustela	*Mustela vison*	American mink	captive	26	Pascal and delattre, 1981	France	47	maritime temperate climate	8	0			annual cementum increments	
Carnivora	Mustelidae	Mustela	*Mustela vison*	American mink	captive	20	Klevezal (book)	European region of Russia	54	warm summer continental	5	0			annual cementum increments	
Carnivora	Mustelidae	Mustela	*Mustela vison*	American mink	?	19	Klevezal (book)	Far East of Russia	67.5	continental subarctic/tundra				4		
Carnivora	Mustelidae	Mustela	*Mustela sibirica*	siberian weasel	?	21	Klevezal (book)	Kamchatka Peninsula, Russia	55	subarctic polar		0		4.5		
Carnivora	Mustelidae	Mustela	*Mustela erminea*	stoat	?	65	Klevezal (book)	Siberia	63.5	continental subarctic/tundra		0		4.2		
Carnivora	Mustelidae	Martes	*Martes martes*	European pine martin		307	Klevezal (book)		0			0			incremental line formed earlier in older animals. No sexual dimoprphism	
Carnivora	Mustelidae	Martes	*Martes martes*	European pine martin	?	86	Klevezal (book)	the Ural Mountains, Russia	62.5	continental subarctic				3.7		
Carnivora	Mustelidae	Martes	*Martes pennati*	fisher	captive	8	Strickland et al., 1982; lifespan estimate from Powell, 1993	USA - New York, Ontario	47.5	warm summer continental/continental subarctic	0	0			annual cementum increments	
Carnivora	Mustelidae	Martes	*Martes pennati*	fisher	wild	14	Arthur et al., 1992	USA - Maine	44.5	warm summer continental	50	14			annual cementum increments in half the population	

Carnivora	Mustelidae	Martes	*Martes zibellina*	sable	?	73	Klevezal (book); lifespan estimate from Tarasov, 1975	Siberia	63.5	continental subarctic/tundra		0		3.5		
Carnivora	Mustelidae	Martes	*Martes zibellina*	sable	?	24	Klevezal (book); lifespan estimate from Tarasov, 1975	Far East of Russia	67.5	continental subarctic/tundra				3.6		
Carnivora	Canidae	Apolex	*Alopex lagopus*	Arctic fox	wild	1	Klevezal (book); lifespan estimate from Angerbjorn et al., 2004	Komandorski e islands, Russia	55	continental subarctic		0			Same animal - no change in readability due to captivity	
Carnivora	Canidae	Apolex	*Alopex lagopus*	Arctic fox	Captive	1	Klevezal (book); lifespan estimate from Angerbjorn et al., 2004	Moscow, Russia	55	warm summer continental		0				
Carnivora	Canidae	Apolex	*Alopex lagopus*	Arctic fox			Bradley et al. (1981); lifespan estimate from Angerbjorn et al., 2004	Canada	0			0			incremental line formed earlier in older animals	
Carnivora	Canidae	Apolex	*Alopex lagopus*	Arctic fox	captive	20	Grue and Jensen, 1976; lifespan estimate from Angerbjorn et al., 2004	Denmark	55.5	maritime temperate climate	0	0			annual cementum increments	
Carnivora	Canidae	Apolex	*Alopex lagopus*	Arctic fox	captive	6	Shilyaeva et al., 1972; lifespan estimate from Angerbjorn et al., 2004	European region of Russia	54	warm summer continental	0	0			annual cementum increments	

Carnivora	Canidae	Apolex	*Alopex lagopus*	Arctic fox	captive	14	Shilyaeva and Krivoshein, 1984; lifespan estimate from Angerbjorn et al., 2004	European region of Russia	54	warm summer continental	0	0			annual cementum increments	
Carnivora	Canidae	Apolex	*Alopex lagopus*	Arctic fox	captive	30	Klevezal and Kleinenberg, 1967; lifespan estimate from Angerbjorn et al., 2004	European region of Russia	54	warm summer continental	0	0			annual cementum increments	
Carnivora	Canidae	Apolex	*Alopex lagopus*	Arctic fox	wild	19	Klevezal and Mina, 1973; lifespan estimate from Angerbjorn et al., 2004	New Siberian Islands of Russia	75	continental subarctic climate with extremely cold winters/tundra	21	0			annual cementum increments	
Carnivora	Canidae	Apolex	*Alopex lagopus*	Arctic fox	?	12 1	Klevezal (book); lifespan estimate from Angerbjorn et al., 2004	Siberia	63.5	continental subarctic/tundra				4.4		
Carnivora	Canidae	Canis	*Canis lupus*	grey wolf	wild	10	Klevezal (book)	Russia (different regions)	0		60	0			No sexual dimorphism, annual layers in less than half of sample	Different to conclude regional differences as sample from each region is small
Carnivora	Canidae	Canis	*Canis lupus*	grey wolf	captive	2	Goodwin and Ballard, 1985	USA - Washington	47	dry summer (aka meditteranean)	0	0			annual cementum increments	
Carnivora	Canidae	Canis	*Canis lupus*	grey wolf	?	32	Klevezal (book)	Poland	51.75	maritime temperate climate/warm summer continental				4.3		

Carnivora	Canidae	Canis	*Canis lupus*	grey wolf	?	7	Klevezal (book)	Siberia	63.5	continental subarctic/tundra				4.7		
Carnivora	Canidae	Canis	*Canis lupus*	grey wolf	?	9	Klevezal (book)	The Caucasus, Russia	42	warm summer continental/maritime temperate/continental subarctic				3.5		
Carnivora	Canidae	Canis	*Canis lupus*	grey wolf	?	5	Klevezal (book)	Kamchatka Peninsula, Russia	56	continental subarctic/tundra				3.4		
Carnivora	Canidae	Canis	*canis latrans*	coyote	captive	52	Schrivner et al., 2014	USA - California	35		5	5			annual cementum increments	
Carnivora	Canidae	Canis	*canis latrans*	coyote	wild/captive	8	Allen and Kohn, 1976	USA - North Dakota	47.5	warm summer continental	0	0			annual cementum increments	
Carnivora	Canidae	Canis	*canis latrans*	coyote	wild/captive	30	linhart and Knowlton, 1967	USA (all)	0		0	0			annual cementum increments	
Carnivora	Canidae	Canis	*canis latrans*	coyote	wild	7	Bowen, 1982	Jasper national park; Edmonton, Canada	53	continental subarctic/tundra	0	0			annual cementum increments	
Carnivora	Canidae	Canis	*canis latrans*	coyote	wild/captive	7	Nellis et al., 1978	Rochester, Canada	54	continental subarctic/tundra	0	0			annual cementum increments	
Artiodactyla	Cervidae	Rangifer	*Rangifer tarandus*	Reindeer	wild	63	Pasda, 2014	Gnuuk, Greenland	64	tundra	92	38			poor correlation between increment count and age	
Artiodactyla	Cervidae	Rangifer	*Rangifer tarandus*	Reindeer		115	Klevezal (book)		0						No sexual dimorphism	
Artiodactyla	Cervidae	Rangifer	*Rangifer tarandus*	Reindeer	wild/captive	85	Reimers and Nordby, 1968	Ottadalen, Norway	62	continental subarctic/tundra	2	0			annual cementum increments	NO double lines in the poorer population. This population also had clearer lines - MORE ENVI.

															PRESSURE?
Artiodactyla	Cervidae	Rangifer	*Rangifer tarandus*	Reindeer	wild	24	Matson, 1991	USA	0		0	0			annual cementum increments in half the population	
Artiodactyla	Cervidae	Rangifer	*Rangifer tarandus*	Reindeer	wild	72	Leader-Williams, 1979	South Georgia Island	-54.5	semi arid/tundra	38	0			annual cementum increments in half the population	Females had less readable layers than males - often UNDEREST IMATED. But comparing month-scale eruption estimates with annual cemenutm pattersn isn't roubust
Artiodactyla	Cervidae	Rangifer	*Rangifer tarandus*	Reindeer	?	27	Klevezal (book)	Siberia	63.5	continental subarctic/tundra				4		
Carnivora	Felidae	Felis	*Felis lynx*	lynx	wild	3	Kvam (1983); body mass from nowell and Jackson, 1996	Sweden	62	maritime temperate climate/warm summer continental/continental subarctic	33	0			. Annual cementum increments. Sexual dimorphism - males form incremental line earlier than females	
Carnivora	Felidae	Felis	*Felis lynx*	lynx		37	Klevezal (book)	the Ural Mountains, Russia	62.5	continental subarctic				4.6		
Carnivora	Canidae	Vulpes	*Vulpes vulpes*	red fox			Kolb (1978)		0						Sexual dimorphism - males form incremental line earlier than females	
Carnivora	Canidae	Vulpes	*Vulpes vulpes*	red fox	wild	135	Grue and Jensen, 1976	Denmark	55.5	maritime temperate climate	0	0			annual cementum increments	

Carnivora	Canidae	Vulpes	*Vulpes vulpes*	red fox	captive	2	Maekawa et al., 1980	Japan	38	humid subtropical/warm summer continental	0	0			annual cementum increments - small sample	
Carnivora	Canidae	Vulpes	*Vulpes vulpes*	red fox	?	29	Klevezal (book)	Poland	51.75	maritime temperate climate/warm summer continental		0		4.2		
Carnivora	Canidae	Vulpes	*Vulpes vulpes*	red fox	?	20	Klevezal (book)	the Ural Mountains, Russia	62.5	continental subarctic		0		4.4		
Carnivora	Canidae	Vulpes	*Vulpes vulpes*	red fox	?	5	Klevezal (book)	Kamchatka Peninsula, Russia	56	continental subarctic/tundra				3.4		
Carnivora	Canidae	Vulpes	*Vulpes fulva*	American red fox	captive	50	Monson et al., 1973	USA - New York	42.5	warm summer continental	0	0			annual cementum increments	
Carnivora	Canidae	Vulpes	*Vulpes fulva*	American red fox	wild	95	Allen, 1974	USA - North Dakota	47.5	warm summer continental	0	0			annual cementum increments	
Rodentia	Muridae	Apodemus	*Apodemus agrarius*	striped field mouse	wild - kept in vivarium	6	Klevezal (book); lifespan estimate from Balciauskiene, 2007	vivarium	0		0	0			Single study - shows how lack of environmental pressure can effect subsequent generations of populations with initial high proportions of individuals with high readability	
Rodentia	Muridae	Apodemus	*Apodemus agrarius*	striped field mouse	1st generation vivarium	9	Klevezal (book); lifespan estimate from Balciauskiene, 2007	vivarium	0		0	0				
Rodentia	Muridae	Apodemus	*Apodemus agrarius*	striped field mouse	2nd generation vivarium	11	Klevezal (book); lifespan estimate from Balciauskiene, 2007	vivarium	0		55	0				

Rodentia	Muridae	Apodemus	*Apodemus agrarius*	striped field mouse	wild	7	Klevezal (book); lifespan estimate from Balciauskiene, 2007	Baltic, Russia	58	warm summer continental	42	0			Single study - shows how increased environemtnal pressure can increase the proportion of individuals with high readability in subsequent generations from an orginal population of low readability	
Rodentia	Muridae	Apodemus	*Apodemus agrarius*	striped field mouse	1st generation captive in Moscow	13	Klevezal (book); lifespan estimate from Balciauskiene, 2007	Moscow, Russia	55	warm summer continental	24	0				
Rodentia	Muridae	Apodemus	*Apodemus agrarius*	striped field mouse	2nd generation catpive in Moscow	13	Klevezal (book); lifespan estimate from Balciauskiene, 2007	Moscow, Russia	55	warm summer continental	7	0				
Rodentia	Muridae	Apodemus	*Apodemus agrarius*	striped field mouse	wild	28	Klevezal (book); lifespan estimate from Balciauskiene, 2007	Moscow, Russia	55	warm summer continental						
Rodentia	Muridae	Apodemus	*Apodemus flavicollis*	yellow necked mouse	wild		Klevezal (book); lifespan estimate from Bobek, 1969	Moscow, Russia	55	warm summer continental	4	0				
Rodentia	Muridae	Apodemus	*Apodemus agrarius*	striped field mouse	captive	31	Klevezal (book)	European region of russia	54	warm summer continental		0			No growth recorded by tetracycline injection despite continuing wear - **principal elements record a caessation in**	Principal elements record a cessation in overall growth triggered by light/diet cues, not just a change in physical
Rodentia	Muridae	Apodemus	*Apodemus sylvaticus*	wood mouse			Klevezal (book)		0			0				

															growth triggered by light/diet cues	forcing from diet
Rodentia	Gliridae	Dryomys	*Dryomys nitedula*	forest dormouse	wild		Klevezal, 1975		0						incremental line developed in cementum over winter hibernation	Experiment implies that increments are only deposited when overall growth stops, and so don't form if growth continues through winter
Rodentia	Gliridae	Dryomys	*Dryomys nitedula*	forest dormouse	lab	4	Klevezal, 1975		0						did not hibernate, no change in diet regime. BUT no weight increase or growth during winter (October-January) and an incremental line still deposited	
Rodentia	Cricetidae	Mesocricetus	*Mesocricetus brandti*	turkish hamster	wild		Klevezal, 1975		0						incremental line developed in cementum over winter hibernation	
Rodentia	Cricetidae	Mesocricetus	*Mesocricetus brandti*	turkish hamster	lab	6	Klevezal, 1975		0						Did not hibernate, no change in diet regime. steady weight increase over winter and no incremental line formed	
Erinaceomorpha	Erinaceidae	Erinaceus	*Erinaceus europaeus*	European hedgehog	captive	12	Morris, 1972		0						Did not hibernate, growth during winter - no incremental line formed	
Carnivora	Ursidae	Ursus	*Ursus americanus*	American black bear	wild	10	Marks and Erickson, 1966	USA - Michigan	44	warm summer continental	0	0			annual cementum increments	

Carnivora	Ursidae	Ursus	*Ursus americanus*	American black bear	wild	6	Sauer et al., 1966	USA - New York	42.5	warm summer continental	0	0			annual cementum increments	
Carnivora	Ursidae	Ursus	*Ursus americanus*	American black bear	wild	185	McLaughlin et al., 1990	USA - Maine	44.5	warm summer continental	0	0			annual cementum increments in half the population	
Carnivora	Ursidae	Ursus	*Ursus americanus*	American black bear	captive	1	Free and Sauer, 1966	Canada	61.5	continental subarctic/tundra	0	0			annual cementum increments	
Carnivora	Ursidae	Ursus	*Ursus americanus*	American black bear	wild	3	Stoneberg and Jonkel, 1966	USA - Montana	47	semi-arid/continental subarctic	0	0			annual cementum increments	
Carnivora	Ursidae	Ursus	*Ursus americanus*	American black bear	wild	27	Matson, 1991	USA	0		0	0			annual cementum increments	
Carnivora	Ursidae	Ursus	*Ursus arctos*	brown bear	captive	1	Rausch, 1969		0						Did not hibernate, growth during winter - no incremental line formed	
Carnivora	Ursidae	Ursus	*Ursus arctos*	brown bear	captive	8	Inukai and Kadosaki, 1972	Japan	38	humid subtropical/warm summer continental	0	0			annual cementum increments	
Carnivora	Ursidae	Ursus	*Ursus arctos*	brown bear	wild	12	Craighead et al., 1970	USA - Wyoming	43	semi arid/desert	0	0			annual cementum increments	
Carnivora	Ursidae	Ursus	*Ursus arctos*	brown bear	wild	76	Matson, 1991	USA	0		0	0			annual cementum increments	
Carnivora	Ursidae	Ursus	*Ursus maritimus*	polar bear	wild	57	Hensel and Sorensen, 1980	USA -Alaska	65	continental subarctic/tundra	54	54			annual cementum increments in half the population	
Carnivora	Ursidae	Ursus	*Ursus maritimus*	polar bear	wild	207	Calvert and Ramsay, 1988	Canada - Manitoba			62	14				
Carnivora	Ursidae	Ursus	*Ursus maritimus*	polar bear	wild	618	Calvert and Ramsay, 1995	USA -Alaska	65	continental subarctic/tundra	31	31			annual cementum increments	

Carnivora	Ursidae	Ursus	*Ursus maritimus*	polar bear	wild	32	Christensen-Dalsgaard et al., 2009	Norway	64.5	continental subarctic/tundra	75	22				
Rodentia	Sciuridae	Citellus	*Citellus undulatus*	Long tailed ground squirrel	wild		Klevezal, 1978; lifespan estimate from Morton, 1984		0			0			winter cessation is progressively earlier in the year as individuals age	
Rodentia	Sciuridae	Citellus	*Citellus pygmaeus*	Little ground squirrel	wild	33	Klevezal (book)		0			0			Cementum increment forms bfore dentine and bone increments in majority of animals	
Rodentia	Sciuridae	Citellus	*Citellus pygmaeus*	Little ground squirrel	captive	6	Klevezal (book)	European region of Russia	54	warm summer continental	0	0			annual cementum increments in half the population	
Rodentia	Sciuridae	Citellus	*Citellus pygmaeus*	Little ground squirrel	wild	5	Klevezal (book)	Volgograd oblast, Russia	49.5	hot summer continental climates/continental subarctic	0	0			annual cementum increments	possible sexual differences in layer complexity
Rodentia	Sciuridae	Citellus	*Citellus pygmaeus*	Little ground squirrel	wild	14	Klevezal (book)	Volgograd oblast, Russia	49.5	hot summer continental climates/continental subarctic	64	64			more complex than males	
Diprotodontia	Phalangeridae	Trichosurus	*Trichosurus vulpecula*	common brushtail possum	wild	11	Clout, 1982	New Zealand	-41	warm temperate/maritime temperate	0	0			annual cementum increments	
Diprotodontia	Phalangeridae	Trichosurus	*Trichosurus vulpecula*	common brushtail possum	captive	11	Pekelharing, 1970	Australia	-25	!	0	0			annual cementum increments	
Diprotodontia	Macropodidae	Macropus	*Macropus eugenii*	Tammar wallaby	wild	8	Inns, 1982	Australia	-25	!	0	0			annual cementum increments in half the population	

Erinaceomorpha	Erinaceidae	Hemiechinus	*Hemiechinus auritus*	long eared hedgehog	captive	3	Isakov, 1984	Tadzhikistan	38.5	tundra/continental subarctic/warm summer continental/mediterranean/semi-arad	0	0			annual cementum increments	
Primates	Primates	Macaca	*Macaca fuscata*	Japanese Macaque	captive	4	Ohtaishi et al., 1976	Japan	38	humid subtropical/warm summer continental	0	0			annual cementum increments	
Rodentia	Sciuridae	Sciurus	*Sciurus vulgaris*	red squirrel	wild/captive	58	Bogodjazh, 1984	European region of Russia	54	warm summer continental	0	0			annual cementum increments	
Rodentia	Sciuridae	Sciurus	*Sciurus vulgaris*	red squirrel	captive	39	Lemnell, 1974	Sweden	62	maritime temperate climate/warm summer continental/continental subarctic	0	0			annual cementum increments	
Rodentia	Sciuridae	Sciurus	*Sciurus carolinensis*	eastern gray squirrel	wild	59	Fogl and Mosby, 1978	USA - virginia	38	humid subtropical/oceanic	0	0			annual cementum increments	
Rodentia	Sciuridae	Spermophilus	*Spermophilus beecheyi*	California ground squirrel	captive	22	Adams and Watkins, 1967	USA - California	37.25	dry summer mediterranean/semi-arid	9	9			annual cementum increments	
Rodentia	Sciuridae	Urocitellus	*Urocitellus armatus*	uinta ground squirrel	wild	?	Montgomery et al., 1971	USA - Utah	39.5	semi-arid/desert		0				
Rodentia	Sciuridae	Marmota	*Marmota menzbieri*	Menzbier's marmot	wild	5	Maschkin, 1979; body mass from Armitage and Blumstein, 2002	Uzbekistan	41.75	semi-arid/desert	0	0			annual cementum increments	

Rodentia	Sciuridae	Marmota	*Marmota baibacina*	grey marmot	?	23	Klevezal (book); body mass from Armitage and Blumstein, 2002	European region of Russia	54	warm summer continental	83	0			
Rodentia	Castoridae	Castor	*Castor canadensis*	North American beaver	wild	42	van Nostrand and Stephenson, 1964	Canada	61.5	continental subarctic/tundra	0	0			annual cementum increments	Beavers have wide cementum bands that often have obviously less contrasting additional increments within them
Rodentia	Erethizontidae	Erethizon	*Erethizon dorsatum*	North American porcupine	captive	2	Earle and Kramm, 1980	USA - Michigan	44	warm summer continental	0	0			annual cementum increments - small sample	
Rodentia	Echimyidae	Myocastor	*Myocastor coypus*	coypu	captive	10	Klevezal (book)	European region of Russia	54	warm summer continental	40	40			annual cementum increments in half the population	
Carnivora	Canidae	Urocyon	*Urocyon cinereoargenteus*	gray fox	wild	5	Nicholson and Hill, 1980	USA - Alabama, Georgia	32.75	warm temperate	0	0			annual cementum increments	
Carnivora	Procyonidae	Procyon	*Procyon lotor*	raccoon	captive	54	Grau et al., 1970	USA - Illinoise	39.75	warm-hot summer contintnental climate	23	9			annual cementum increments	
Carnivora	Procyonidae	Procyon	*Procyon lotor*	raccoon	?	19	Matson, 1993	USA	0		0	0			annual cementum increments	
Carnivora	Mustelidae	Mustela	*Mustela erminea*	stoat	wild	20	Grue and King, 1984	New Zealand	-41	warm temperate/maritime temperate	0	0			annual cementum increments	
Carnivora	Mustelidae	Meles	*Meles meles*	European badger	captive	4	Klevezal (book)	FAR EAST of Russia	67.5	continental subarctic/tundra	0	0			annual cementum increments - small sample	
Carnivora	Mustelidae	Lutra	*Lutra canadensis*	North American river otter	captive	4	Stephenson, 1977	Canada	61.5	continental subarctic/tundra	0	0			annual cementum increments - small sample	

Carnivora	Mustelidae	Enhydra	*Enhydra lutris*	sea otter	captive	1	Schneider, 1973	USA - Alaska	65	continental subarctic/tundra	0	0			annual cementum increments - small sample	
Carnivora	Mustelidae	Enhydra	*Enhydra lutris*	sea otter	wild	10	Pietz et al., 1988	USA - Alaska	37.25	dry summer mediterranean/semi-arid	0	0			annual cementum increments	
Carnivora	Mustelidae	Enhydra	*Enhydra lutris*	sea otter	wild	17	Matson, 1993	USA	0		0	0			annual cementum increments in half the population	
Carnivora	Felidae	Enchydra	*Lynx lynx*	Lynx	wild	3	Kvam, 1984	Sweden	0		0	0			annual cementum increments - small sample	
Carnivora	Phocidae	Phoca	*Phoca vitulina*	harbour seal	wild	6	Norgaard and Larsen, 1991	Denmark	62	maritime temperate climate/warm summer continental/continental subarctic	0	0			annual cementum increments	
Carnivora	Phocidae	Phoca	*Phoca vitulina*	harbour seal	wild	7	Dietz et al., 1991	Denmark	55.5	maritime temperate climate	0	0			annual cementum increments	
Carnivora	Phocidae	Halichoerus	*Halichoerus grypus*	grey seal	wild	82	Mansfield, 1991	Canada	61.5	continental subarctic/tundra	0	0			annual cementum increments	
Carnivora	Miroungi	Mirounga	*Mirounga angustirostris*	Northern elephant seals	wild	4	Klevezal and Stewart, 1994	USA - California	37.25	dry summer mediterranean/semi-arid	100	0			annual cementum increments	
Carnivora	Otariidae	Arctocephalus	*Arctocephalus pusillus*	brown fur seal	wild	40	Fletemeyer, 1978	South Africa	-28.75	marine	0	0			annual cementum increments	
Artiodactyla	Suidae	Sus	*Sus scrofa*	wild boar	wild	3	Klevezal (book)	Poland	51.75	maritime temperate climate/warm summer continental	33	0			annual cementum increments - small sample	
Artiodactyla	Cervidae	Capreolus	*Capreolus capreolus*	roe deer	wild	9	Aitken, 1975	Norfolk, England	37	maritime temperate climate	0	0			annual cementum increments	

Artiodactyla	Cervidae	Capreolus	*Capreolus capreolus*	roe deer	wild	10	Blazhis, 1971	Latvia	57	warm summer continental	0	0			annual cementum increments	
Artiodactyla	Cervidae	Capreolus	*Capreolus capreolus*	roe deer	captive	8	Klevezal (book)	Latvia	57	warm summer continental	38	38			annual cementum increments	
Artiodactyla	Cervidae	Capreolus	*Capreolus capreolus*	roe deer	?	39	Klevezal (book)	Baltic Region, Russia	58	warm summer continental	96	4		2.6		
Artiodactyla	Cervidae	Capreolus	*Capreolus capreolus*	roe deer	?	64	Klevezal (book)	Altai and Kazakhstan	48.5	semi-arid/desert		0		3.4		
Artiodactyla	Cervidae	Capreolus	*Capreolus capreolus*	roe deer	wild	74	Cederland et al., 1991	Grimso and Oster Malma research areas, Central Sweden			75	29				
Artiodactyla	Cervidae	Odocoileus	*Odocoileus hemionus*	Mule deer	wild	994	Asmus and Wreckerly, 2011	USA - California	37.25	dry summer mediterranean/semi-arid	31	0			annual cementum increments	
Artiodactyla	Cervidae	Odocoileus	*Odocoileus hemionus*	Mule deer	wild/captive	16	Erickson and Seliger, 1969	USA - Colorado	39	semi-arid	0	0			annual cementum increments	
Artiodactyla	Cervidae	Odocoileus	*Odocoileus hemionus*	Mule deer	captive	40	Low and Cowan, 1963	Canada	61.5	continental subarctic/tundra	43	0			annual cementum increments	
Artiodactyla	Cervidae	Odocoileus	*Odocoileus hemionus*	Mule deer	wild/captive	37	Thomas and Bandy, 1973	Canada	61.5	continental subarctic/tundra	0	0			annual cementum increments	
Artiodactyla	Cervidae	Odocoileus	*Odocoileus hemionus*	Mule deer	wild	5	Connoly et al., 1969	USA - California	37.25	dry summer mediterranean/semi-arid	100	100			poor correlation between increment count and age	
Artiodactyla	Cervidae	Odocoileus	*Odocoileus virginianus*	white-tailed deer	wild/captive	10	Gilbert, 1966	USA - Michigan	44	warm summer continental	0	0			annual cementum increments	
Artiodactyla	Cervidae	Odocoileus	*Odocoileus virginianus*	white-tailed deer	wild/captive	366	Lockhard, 1972	USA - Ohio	0		52	26			annual cementum incrementsin majority	69 out of 175 females had double annuli; 27 out of 97 males had double annuli; definite increase in

																readability with seasonality.
Artiodactyla	Cervidae	Odocoileus	*Odocoileus virginianus*	white-tailed deer	wild/captive	16	Ransom, 1966	USA - Michigan, Minnesota	44	warm summer continental	0	0			annual cementum increments	
Artiodactyla	Cervidae	Odocoileus	*Odocoileus virginianus*	white-tailed deer	wild	524	Rice, 1980	USA - South Dacota	44.5	warm summer continental	30	0			annual cementum increments	
Artiodactyla	Cervidae	Odocoileus	*Odocoileus virginianus*	white-tailed deer	wild	3	Sohn, 1967	USA - Michigan	44	warm summer continental	0	0			annual cementum increments	
Artiodactyla	Cervidae	Odocoileus	*Odocoileus virginianus*	white-tailed deer	?	44	Matson, 1991	USA	0		0	0			annual cementum increments	
Artiodactyla	Cervidae	Odocoileus	*Odocoileus virginianus*	white-tailed deer	wild	20	DeYoung, 1989	USA - Texas	27.5	semi-arid	0	0			annual cementum increments in half the population	
Artiodactyla	Cervidae	Alces	*Alces alces*	moose	wild	51	Rolandsen et al., 2008	Norway	64.5	continental subarctic/tundra	10	2			annual cementum increments	
Artiodactyla	Cervidae	Alces	*Alces alces*	moose	wild	71	Gasaway et al., 1978	Matanuska and Tana Valleys, Alaska	65	continental subarctic/tundra	35	7			annual cementum increments in half the population	
Artiodactyla	Cervidae	Alces	*Alces alces*	moose	?	1	Sergeant and Pimlott, 1959	Canada	61.5	continental subarctic/tundra	0	0			annual cementum increments - small sample	
Artiodactyla	Cervidae	Alces	*Alces alces*	moose	?	19	Matson, 1991	USA	0		0	0			annual cementum increments	
Artiodactyla	Cervidae	Alces	*Alces alces*	moose	wild	10	Klevezal (book)	Russia (unknown)	0		50	0			annual cementum increments in half the population	
Artiodactyla	Cervidae	Alces	*Alces alces*	moose	?	17	Klevezal (book)	Siberia	63.5	continental subarctic/tundra				4.3		
Artiodactyla	Cervidae	Cervus	*Cervus elephus*	red deer	wild	3	Almasan and Rieck, 1970; body mass from ADW	Romania	46	maritime/warm temperate/warm summer continental	0	0			annual cementum increments	

Artiodactyla	Cervidae	Cervus	*Cervus elephus*	red deer	wild	34	Lowe, 1967; body mass from ADW	Scotland	56.5	maritime temperate climate	0	0			annual cementum increments in half the population	
Artiodactyla	Cervidae	Cervus	*Cervus elephus*	red deer	wild	22	Mitchell, 1967; body mass from ADW	Scotland	56.5	maritime temperate climate		0			annual cementum increments	
Artiodactyla	Cervidae	Cervus	*Cervus elephus*	red deer	?	3	Querre and Pascal, 1967; body mass from ADW	France	47		0	0			annual cementum increments	
Artiodactyla	Cervidae	Cervus	*Cervus nippon*	sika deer	captive	100	Prisyazhnyuk, 1968	FAR EAST of Russia	67.5	continental subarctic/tundra	0	0			annual cementum increments	
Artiodactyla	Cervidae	Cervus	*Cervus canadensis*	elk	wild	18	Keiss, 1966	USA - Wyoming	43	semi arid/desert	0	0			annual cementum increments	
Artiodactyla	Cervidae	Cervus	*Cervus canadensis*	elk	?	16	Matson, 1991	USA	0		0	0			annual cementum increments in half the population	
Artiodactyla	Antilocapridae	Antilocapra	*Antilocapra americana*	pronghorn	?	10	McCutchen, 1969	USA - Montana, Wyoming	45	semi-arid/continental subarctic/desert	20	0			annual cementum increments	
Artiodactyla	Bovidae	Capricornis	*Capricornis crispus*	Japanese serow	wild/captive	18	Miura, 1985; body mass from Miura and Maruyama, 1986	Japan	38	humid subtropical/warm summer continental	0	0			annual cementum increments	
Artiodactyla	Bovidae	Ovibos	*Ovibos moschatus*	muskox	wild/captive	16	Gronquist and Dinneford, 1984	USA - Alaska	65	continental subarctic/tundra	0	0			poor correlation between increment count and age	
Artiodactyla	Bovidae	Ovis	*Ovis canadensis*	Bighorn sheep	wild/captive	11	Turner, 1977	USA	0		0	0			annual cementum increments	

Artiodactyla	Bovidae	Bison	*Bison bonasus*	european bison	wild	19	Klevezal and Pucek, 1987	Poland	51.75	maritime temperate climate/warm summer continental	53	53			annual cementum increments in half the population	
Artiodactyla	Bovidae	Bison	*Bison bonasus*	european bison	captive	20	Klevezal et al., 1991	European region of Russia	54	warm summer continental	0	0			poor correlation between increment count and age	
Artiodactyla	Bovidae	Bison	*Bison bonasus*	european bison	?	30	Klevezal (book)	Poland	51.75	maritime temperate climate/warm summer continental				3.1		
Soricomorpha	Soricidae	Sorex	*Sorex araneus*	common shrew	?	?	Klevezal (book)	?	0			0				
Soricomorpha	Talpidae	Talpa	*Talpa europaea*	European mole	?	?	Klevezal (book)	?	0			0				
Rodentia	Castoridae	Castor	*Castor fiber*	Eurasian beaver			Klevezal (book)	?	0			0				
Artiodactyla	Bovidae	Nemorhaedus	*Nemorhaedus goral*	Goral	?	?	Klevezal (book)	?	0			20				
Chiroptera	Phyllostomidae	Desmodus	*Desmodus rotundus*	South American vampire bat	wild	97	Linhart, 1973	Mexico	0		10	10			annual cementum increments	
Chiroptera	Phyllostomidae	Desmodus	*Desmodus rotundus*	South American vampire bat	wild	2	Linhart, 1973	Argentina	0		0	0			annual cementum increments - small sample	
Primates	Primates	Saguinus	*Saguinus fuscicollis*	brown-mantled tamarin		7	Yoneda, 1982	Bolivia	-14	tropical rainforest monsoon/savannah	14	14			annual cementum increments	
Primates	Primates	Saguinus	*Saguinus labiatus*	white-lipped tamarin		5	Yoneda, 1983	Bolivia	-14	tropical rainforest monsoon/savannah	0	0			annual cementum increments	

Primates	Primates	Saguinus	*Saguinus mystax*	moustached tamarin		2	Yoneda, 1984	Peru	-14	tropical rainforest monsoon/savanna h	0	0			annual cementum increments	
Primates	Primates	Macaca	*macaca mulatta*	rhesus macaque	captive	8	Kay et al., 1984	India	15	savannah	25	0			annual cementum increments	
Artiodactyla	Bovidae	Kobus	*Kobus ellipsiprymnus*	waterbuck	wild	?	Spinage, 1967	Uganda	2.25	tropical rainforest/savanna h		0				
Artiodactyla	Bovidae	Gazelle	*Nanger granti*	Grant's gazelle	wild	?	Spinage, 1976; body mass from Skirka et al., 1971	Tanzania	-7	savannah		0				
Artiodactyla	Bovidae	Gazelle	*Eudorcas thomsoni*	Thompson's gazelle	wild	?	Spinage, 1976; body mass from Skirka et al., 1971	Tanzania	-7	savannah		0				
Artiodactyla	Bovidae	Tragelaphus	*Tragelaphus strepsiceros*	greater kudu	wild	?	Simpson and Elder, 1969	Zimbabwe	-19	warm temperate/semi-arid		0				
Artiodactyla	Bovidae	Tragelaphus	*Tragelaphus scriptus*	bushbuck	wild	?	Simpson, 1973; body mass from Estes, 1993 and Skinner and Smithers, 1990	Zimbabwe	-19	warm temperate/semi-arid		0				
Artiodactyla	Suidae	Hylochoerus	*Hylochoerus meinertzhageni*	giant forest hog	wild	10	d'Huart, 1980	Democratic republic of Congo	-7.5	savannah	70	50				
Artiodactyla	Bovidae	Hippotragus	*Hippotragus niger*	sable antelope	wild	30	Grobler, 1980	Zimbabwe	-19	warm temperate/semi-arid	41	33				
Artiodactyla	Bovidae	Syncerus	*Syncerus caffer*	African buffalo		17	Spinage, 1976	Tanzania	-7	savannah	53	24				
Perissodactyla	Rhinocerotidae	Diceros	*Diceros bicornis*	black rhino	wild	1	Spinage, 1976	Kenya	-2.5	savannah/matitme temperate	100	0				
Carnivora	Felidae	Panthera	*Panthera leo*	African lion	captive	1	Spinage, 1976	Kenya	-2.5	savannah/matitme temperate	100	100				

Artiodactyla	Giraffidae	Giraffa	*Giraffa camelopardalis*	giraffe	captive	1	Spinage, 1976	London	51.5	maritime temperate climate	100	0				
Artiodactyla	Bovidae	Bubalus	*Bubalus bubalis*	water buffalo	wild	?	Ashby, 1985	Sri Lanka	7.75	tropical rainforest/savannah		0				
Artiodactyla	Cervidae	Cervus	*cervus unicolor*	sambar deer	?	?	Ashby, 1985	Sri Lanka	7.75	tropical rainforest/savannah		0				
Artiodactyla	Cervidae	Axis	*Axis axis*	Chital	?	?	Ashby, 1985	Sri Lanka	7.75	tropical rainforest/savannah		0				
Artiodactyla	Bovidae	Damaliscus	*Damaliscus pygargus*	blesbok	captive	22	Oliver and Greyling, 1990; body mass from Kingdom, 1997	Hedielburg Province (Western Cape), South Africa	-26.5	Temperate highland tropical climate with dry winters	0	0				
Artiodactyla	Giraffidae	Giraffa	*Giraffa camelopardalis*	Giraffe	wild	63	Hall-Martin, 1976	Eastern Transvaal Lowveld, South Africa	-25.5	Temperate highland tropical climate with dry winters/semi-arid	33	6			Double lines found only in sexually mature animals	
Artiodactyla	Equidae	Equus	*Equus zebra zebra*	Cape mountain zebra	wild	17	Plenzhorn,1982	Cape mountain, South Africa	-34	meditteranean	0	0				
Perissodactyla	Felidae	Panthera	*Panthera leo*	African lion	wild/captive	120	smuts et al., 1978	Kruger national park, northeast South Africa	-23.5	semi-arid		0				
Artiodactyla	Hystricidae	Hystrix	*Hystrix africaeaustralis*	Cape porcupine	captive	29	Van Aarde, 1985	Pretoria, South Africa	-26	semi-arid	83	17	5			
Artiodactyla	Suidae	Phacochoerus	*Phacochoerus africanus*	warthog	wild	181	Mason, 1984	hluhluwe game reserve	-28	warm/maritime temperate	100	26	60			
Artiodactyla	Cervidae	Odocoileus	*Odocoileus virginianus*	whit-tailed deer	wild	682	Gilbert and Stolt, 1970	USA - Maine	44.5	warm summer continental	100	0				

Carnivora	Procyonidae	Procyon	*Procyon lotor*	raccoon	wild	54	Grau et al., 1970	USA, Illinoise	39.75	warm-hot summer contintnental climate	100	50	27			
Carnivora	Felidae	Prionailurus	*Prionailurus bengalensis iriomotensis*	iriomote cat	wild	12	Nakanishi et al., 2009	Japan	38	humid subtropical/warm summer continental	55	0			annual cementum increments	
Carnivora	Felidae	Prionailurus	*Prionailurus bengalensis iriomotensis*	iriomote cat	captive	2	Nakanishi et al., 2009	Japan	38	humid subtropical/warm summer continental	50	0				
Artiodactyla	Delphinidae	Tursiops	*tursiops truncatus*	bottlenose dolphin	wild	23	Hohn et al., 1989	USA -Florida			33	19				
Artiodactyla	Cervidae	Cervus	*Cervus elaphus*	Rocky mountain Elk	wild	111	Hamlin et al., 2000	USA - Montana			3					
Artiodactyla	Cervidae	Odocoileus	*Odocoileus hemionus*	Mule deer	wild	108	Hamlin et al., 2000	USA - Montana			6					
Artiodactyla	Cervidae	Odocoileus	*Odocoileus virginianus*	whit-tailed deer	wild	74	Hamlin et al., 2000	USA - Montana			15					
Artiodactyla	Cervidae	Dama	*Dama dama*	fallow deer	wild	50	Moore et al., 1995	Dublin, Ireland			52					
Artiodactyla	Bovidae	Ovis	*Ovis aries*	domestic sheep	captive	26	Rudge, 1976	North island, New Zealand			33					
Carnivora	Canidae	Canis	*Canis lupus*	grey wolf	wild	12	Landon et al., 1998	USA - Michigan			25					
Carnivora	Canidae	Vulpes	*Vulpes vulpes*	red fox	wild	32	Goddard and Reynolds, 1993	Southern England			19					
Artiodactyla	Bovidae	Bison	*Bison bison*	bison	wild	37	Moffitt, 1998	USA - North Dakota			22					
Carnivora	Ursidae	Ursus	*Ursus americanus*	American black bear	wild	26	Costello et al., 2004	USA - New Mexico			19					
Carnivora	Ursidae	Ursus	*Ursus americanus*	American black bear	wild	527	Harshyne, 1998	USA - Pennsylvania			8					
Artiodactyla	Cervidae	Odocoileus	*Odocoileus virginianus*	whit-tailed deer	wild	38	Brokx, 1972	Venezuela			18					

Appendix 2. Dataset for meta-analysis of previous cementochronology studies

Specimen	Element	Taxon
4906	m1	*Morganucodon*
BD1	m2	*Morganucodon*
BD10	m2	*Morganucodon*
BD10	m3	*Morganucodon*
BD10	m4	*Morganucodon*
BD10	m3	*Morganucodon*
BD10	m1	*Morganucodon*
BD13	m3	*Morganucodon*
BD13	m2	*Morganucodon*
BD13	m3	*Morganucodon*
BD2	m2	*Morganucodon*
BD2	m1	*Morganucodon*
BD2	p3	*Morganucodon*
BD6	m2	*Morganucodon*
BD6	m1	*Morganucodon*
CEM2	m2	*Morganucodon*
cem3	m2	*Morganucodon*
CEM5	m2	*Morganucodon*
en023	m2	*Morganucodon*
en024	m2	*Morganucodon*
en038	m2	*Morganucodon*
en070	m2	*Morganucodon*
en076	m2	*Morganucodon*
en083	m2	*Morganucodon*
en088	m2	*Morganucodon*
EN089	m2	*Morganucodon*
en094	m2	*Morganucodon*
en099	m2	*Morganucodon*
en105	m2	*Morganucodon*
en107	m2	*Morganucodon*
en123	m2	*Morganucodon*
en132	m2	*Morganucodon*
en134	m2	*Morganucodon*
en138	m2	*Morganucodon*
en147	m2	*Morganucodon*
L3_003	m2	*Morganucodon*
L3_005	m2	*Morganucodon*
L3_086	m2	*Morganucodon*
L3_087	m2	*Morganucodon*
L3_087	dentary	*Morganucodon*
M46463	m2	*Morganucodon*
M92528	m2	*Morganucodon*
M92530	m2	*Morganucodon*

M92533	m2	*Morganucodon*
M95805	m2	*Morganucodon*
M95808	m2	*Morganucodon*
M95809	m2	*Morganucodon*
M95809	m1	*Morganucodon*
M95810	m2	*Morganucodon*
M95810	m1	*Morganucodon*
M95810	dentary	*Morganucodon*
M96072	m2	*Morganucodon*
m96075	m2	*Morganucodon*
m96085	m2	*Morganucodon*
M96086	m2	*Morganucodon*
M96090	m2	*Morganucodon*
m96109	m2	*Morganucodon*
M96117	m2	*Morganucodon*
M96118	m2	*Morganucodon*
M96137	m2	*Morganucodon*
M96141	m2	*Morganucodon*
M96144	m2	*Morganucodon*
M96379	m2	*Morganucodon*
M96380	m1	*Morganucodon*
M96389	m1	*Morganucodon*
M96396	m3	*Morganucodon*
M96396	m2	*Morganucodon*
M96396	m1	*Morganucodon*
M96396	p4	*Morganucodon*
M96396	dentary	*Morganucodon*
M96413	m2	*Morganucodon*
M96413	m1	*Morganucodon*
M96418	m1	*Morganucodon*
M96441	m1	*Morganucodon*
M96441	m2	*Morganucodon*
M96444	m2	*Morganucodon*
M96447	m2	*Morganucodon*
M96454	m2	*Morganucodon*
M96455	m2	*Morganucodon*
M96463	m2	*Morganucodon*
M96467	m2	*Morganucodon*
M96474	m2	*Morganucodon*
M96475	m2	*Morganucodon*
m96476	m2	*Morganucodon*
m96483	m2	*Morganucodon*
m96487	m2	*Morganucodon*
m96488	m2	*Morganucodon*

m96489	m2	*Morganucodon*
M96490	m2	*Morganucodon*
ElisMD1	m1	*Morganucodon*
Felix Dentary 3	m3	*Morganucodon*
M95788	m1	*Morganucodon*
M95788	m1	*Morganucodon*
M95788	p4	*Morganucodon*
M95789	m2	*Morganucodon*
M95789	m2	*Morganucodon*
M95789	m1	*Morganucodon*
M95789	m1	*Morganucodon*
M95789	p4	*Morganucodon*
M95790	i4	*Morganucodon*
M95790	canine	*Morganucodon*
M95790	p1	*Morganucodon*
M95790	p2	*Morganucodon*
M95790	p3	*Morganucodon*
M95791	p4	*Morganucodon*
M95791	m1	*Morganucodon*
M95791	m1	*Morganucodon*
M95791	m2	*Morganucodon*
M95802	m3	*Morganucodon*
M95802	m3	*Morganucodon*
M95802	m3	*Morganucodon*
M95802	m4	*Morganucodon*
M95802	m4	*Morganucodon*
M95802	dentary	*Morganucodon*
M95803	m2	*Morganucodon*
M95806	m2	*Morganucodon*
M96398	m1	*Morganucodon*
M96398	p2	*Morganucodon*
M96398	m1	*Morganucodon*
M96398	m1	*Morganucodon*
M96398	m1	*Morganucodon*
M96398	p4	*Morganucodon*
M96398	p4	*Morganucodon*
M96398	p4	*Morganucodon*
M96398	p3	*Morganucodon*
M96398	p3	*Morganucodon*
M96398	p3	*Morganucodon*
M20982	m2	*Kuehneotherium*
M27273	m1	*Kuehneotherium*
M19138	m2	*Kuehneotherium*
M20772	m2	*Kuehneotherium*

M20775	m2	*Kuehneotherium*
M20785	m2	*Kuehneotherium*
M20797	m2	*Kuehneotherium*
M20801	m2	*Kuehneotherium*
M20797	m2	*Kuehneotherium*
M20804	m2	*Kuehneotherium*
M20813	m2	*Kuehneotherium*
M20822	m2	*Kuehneotherium*
M20850	m2	*Kuehneotherium*
M20852	m2	*Kuehneotherium*
M20856	m2	*Kuehneotherium*
M20858	m2	*Kuehneotherium*
M20859	m2	*Kuehneotherium*
M20873	m2	*Kuehneotherium*
M20882	m2	*Kuehneotherium*
M20887	m2	*Kuehneotherium*
M20888	m2	*Kuehneotherium*
M20890	m2	*Kuehneotherium*
M20893	m2	*Kuehneotherium*
M20895	m2	*Kuehneotherium*
M20897	m2	*Kuehneotherium*
M20901	m2	*Kuehneotherium*
M20931	m2	*Kuehneotherium*
M20934	m2	*Kuehneotherium*
M20942	m2	*Kuehneotherium*
M20949	m2	*Kuehneotherium*
M20956	m2	*Kuehneotherium*
M20959	m2	*Kuehneotherium*
M20968	m2	*Kuehneotherium*
M20973	m2	*Kuehneotherium*
M20980	m2	*Kuehneotherium*
M20981	m2	*Kuehneotherium*
M20982	m2	*Kuehneotherium*
M20984	m2	*Kuehneotherium*
M20990	m2	*Kuehneotherium*
M20990	m2	*Kuehneotherium*
M20996	m2	*Kuehneotherium*
M21011	m2	*Kuehneotherium*
M21014	m2	*Kuehneotherium*
M21021	m2	*Kuehneotherium*
M21040	m2	*Kuehneotherium*
M21066	m2	*Kuehneotherium*
M21069	m2	*Kuehneotherium*
M21080	m2	*Kuehneotherium*

M21081	m2	*Kuehneotherium*
M21086	m2	*Kuehneotherium*
M21091	m2	*Kuehneotherium*
M21094	m2	*Kuehneotherium*
M21095	m2	*Kuehneotherium*
M21097	m2	*Kuehneotherium*
M21111	m2	*Kuehneotherium*
M21120	m2	*Kuehneotherium*
M24849	m1	*Kuehneotherium*
M24868	m2	*Kuehneotherium*
M24868	m2	*Kuehneotherium*
M24868	m1	*Kuehneotherium*
M27257	m2	*Kuehneotherium*
M27273	m1	*Kuehneotherium*
M27273	p6	*Kuehneotherium*
M27273	p6	*Kuehneotherium*
M27273	p6	*Kuehneotherium*
M27273	p6	*Kuehneotherium*
M27273	m2	*Kuehneotherium*
M27295	m2	*Kuehneotherium*
M27301	m2	*Kuehneotherium*
M27305	m2	*Kuehneotherium*
M27308	m2	*Kuehneotherium*
M27311	m2	*Kuehneotherium*
M27317	m2	*Kuehneotherium*
M27320	m2	*Kuehneotherium*
M27322	m2	*Kuehneotherium*
M27328	m2	*Kuehneotherium*
M27344	m2	*Kuehneotherium*
M27436	m2	*Kuehneotherium*
M27443	m2	*Kuehneotherium*
M27444	m2	*Kuehneotherium*
M27447	m2	*Kuehneotherium*
M27448	m2	*Kuehneotherium*
M27450	m2	*Kuehneotherium*
M27472	m2	*Kuehneotherium*
M27489	m2	*Kuehneotherium*
M27495	m2	*Kuehneotherium*
M27505	m2	*Kuehneotherium*
M27512	m2	*Kuehneotherium*
M27513	m2	*Kuehneotherium*
M27520	m2	*Kuehneotherium*
M27523	m2	*Kuehneotherium*
M27524	m2	*Kuehneotherium*

M27529	m2	*Kuehneotherium*
M27534	m2	*Kuehneotherium*
M27537	m2	*Kuehneotherium*
M27538	m2	*Kuehneotherium*
M27541	m2	*Kuehneotherium*
M27542	m2	*Kuehneotherium*
M27545	m2	*Kuehneotherium*
M27548	m2	*Kuehneotherium*
M27550	m2	*Kuehneotherium*
M27593	m2	*Kuehneotherium*
M27608	m2	*Kuehneotherium*
M27628	m2	*Kuehneotherium*
M27639	m2	*Kuehneotherium*
M27651	m2	*Kuehneotherium*
M27652	m2	*Kuehneotherium*
M27653	m2	*Kuehneotherium*
M27663	m2	*Kuehneotherium*
M27666	m2	*Kuehneotherium*
M27674	m2	*Kuehneotherium*
M27675	m2	*Kuehneotherium*
M27745	m2	*Kuehneotherium*
M27816	m2	*Kuehneotherium*
M45265	p5	*Kuehneotherium*
M45265	p5	*Kuehneotherium*
M45265	p5	*Kuehneotherium*
M45265	p3	*Kuehneotherium*
M45265	p1	*Kuehneotherium*
M92774	m2	*Kuehneotherium*
SY104	m2	*Kuehneotherium*
SY106	m2	*Kuehneotherium*
SY124	m2	*Kuehneotherium*
SY133	m2	*Kuehneotherium*
SY141	m2	*Kuehneotherium*
SY2	m2	*Kuehneotherium*
SY49	m2	*Kuehneotherium*
SY50	m2	*Kuehneotherium*
SY61	m2	*Kuehneotherium*
SY92	m2	*Kuehneotherium*

Appendix 3.1. Full list of all *Morganucodon* and *Kuehneotherium* specimens scanned.

Class	Species	Body Mass (g)	Wild lifespan (years)
Mammalia	*Vulpes vulpes*	6000	12
Mammalia	*Tamiasciurus hudsonicus*	333	7
Mammalia	*Bison spp.*	500,000	20
Mammalia	*Ursus (= Euarchtos) americanus*	250,000	26
Mammalia	*Rangifer tarandus*	182,034	15
Mammalia	*Lagenorhynchus acutus*	182,000	27
Mammalia	*Lagenorhynchus acutus*	182,000	22
Mammalia	*Balaena mysticetus*	100000000	40
Mammalia	*Mustela vison*	945	10
Mammalia	*Scalopus aquaticus*	91	3
Mammalia	*Echinops telfairi*	180	1.2
Mammalia	*Hydrurga leptonyx*	360000	26
Mammalia	*Macropus robustus*	21262.5	18.5
Mammalia	*Leptonychotes weddelli*	400000	25
Mammalia	*Mustela lutreola*	440	10
Mammalia	*Martes pennanti*	4000	10
Mammalia	*Potorous tridactyles*	1100	7.3
Mammalia	*Alouatta palliata*	7274.9	25
Mammalia	*Eulemur macaco*	2040	27.1
Mammalia	*Eutamias (= Tamias) ruficaudus*	68	8
Mammalia	*Cercocebus albigena*	10000	21
Mammalia	*Cercocebus atys*	14000	18
Mammalia	*Cercocebus torquatus*	10000	20.5
Mammalia	*Cercopithecus (= Chlorocebus) aethiops*	4155	31
Mammalia	*Cercopithecus diana*	4175	34.8
Mammalia	*Colobus polykomos*	9834.9	26
Mammalia	*Macaca arctoides*	5000	30
Mammalia	*Lemur catta*	2900	27.1
Mammalia	*Mirounga leonina*	1600000	23
Mammalia	*Procavia capensis*	3030	8.5
Mammalia	*Marmosa spp.*	26	1
Mammalia	*Dugong dugon*	420000	70
Mammalia	*Canis latrans*	13406.3	14.5
Mammalia	*Sicista spp.*	10	3.3
Mammalia	*Aepyceros melampus*	57000	13
Mammalia	*Hyperoodon ampullatus*	5800000	37
Mammalia	*Phocoenoides dalli*	102500	22
Mammalia	*Damaliscus dorcas*	80000	21.4
Mammalia	*Syncerus caffer*	580002.7	18
Mammalia	*Mellivora capensis*	8000	26.4

Mammalia	*Taxidea taxus*	7107.6	14
Mammalia	*Procyon lotor*	5525	16
Mammalia	*Dasyuroides byrnei*	140	4
Mammalia	*Phascolarctos cinereus*	10250	17
Mammalia	*Mirounga angustirostris*	750000	14
Mammalia	*Pan troglodytes*	44999.7	60
Mammalia	*Proechimys semispinosus*	360.5	2
Mammalia	*Apodemus sylvaticus*	21.5	1
Mammalia	*Sciurus carolinensis*	506.5	12.5
Mammalia	*Trichosurus vulpecula*	2650	13
Mammalia	*Elaphurus davidianus*	149000	23.3
Mammalia	*Platanista gangetica*	115000	28
Mammalia	*Neophocaena phocaenoides*	32500	23
Mammalia	*Globicephala sieboldii (= macrorhynchus)*	726000	63
Mammalia	*Globicephala sieboldii (= macrorhynchus)*	726000	46
Mammalia	*Monachus schauinslandi*	223000	30
Mammalia	*Phoca caspica*	86000	50
Mammalia	*Lobodon carcinophagus*	225000	39
Mammalia	*Eumetopias jubatus*	310000	30
Mammalia	*Ommatophoca rossi*	250000	21
Mammalia	*Phoca groenlandica*	120000	30
Mammalia	*Phoca sibirica*	90000	56
Mammalia	*Arctocephalus pusillus*	178500	18
Mammalia	*Elephas maximus*	2720000	70
Mammalia	*Tragelaphus spekei*	77999.2	20
Mammalia	*Macropus giganteus*	25875	19.8
Mammalia	*Macropus parma*	4500	7
Mammalia	*Macropus rufogriseus*	16850	18.5
Mammalia	*Macropus rufus*	46250	22
Mammalia	*Galea musteloides*	480	1.3
Mammalia	*Delphinus delphis*	80000	20
Mammalia	*Tragelaphus imberbis*	81575.5	10
Mammalia	*Litocranius walleri*	37999.7	8
Mammalia	*Physeter catodon*	14025000	77
Mammalia	*Alcelaphus buselaphus*	200000	20
Mammalia	*Phoca largha*	150000	32
Mammalia	*Ochotona princeps*	157.6	7
Mammalia	*Antechinus stuartii*	27.5	0.9
Mammalia	*Panthera tigris*	423000	26
Mammalia	*Berardius bairdii*	11380000	71
Mammalia	*Mesoplodon densirostris*	2300000	27
Mammalia	*Ziphius cavirostris*	4775000	36

Mammalia	*Mustela putorius*	1100	6
Mammalia	*Canis lupus*	80000	13.7
Mammalia	*Sundamys muelleri*	334	0.5
Mammalia	*Chiropodomys gliroides*	25	2
Mammalia	*Priodontes maximus*	45359.7	15
Mammalia	*Tolypeutes spp.*	1487	15
Mammalia	*Gorilla gorilla*	175000	50
Mammalia	*Hyaena brunnea*	72600	12
Mammalia	*Tursiops aduncus (= truncatus)*	500000	35
Mammalia	*Sminthopsis crassicaudata*	15	1.5
Mammalia	*Sminthopsis crassicaudata*	16	1.3
Mammalia	*Rhombomys opimus*	285	4
Mammalia	*Rhombomys opimus*	285	3
Mammalia	*Chinchilla spp.*	500	10
Mammalia	*Cystophora cristata*	375000	35
Mammalia	*Phoca vitulina*	100000	34
Mammalia	*Equus zebra*	372000	24
Mammalia	*Steno bredanensis*	130000	32
Mammalia	*Pseudorca crassidens*	1360000	22
Mammalia	*Alces alces*	771000	27
Mammalia	*Delphinapterus leucas*	1460000	30
Mammalia	*Antilope cervicapra*	37500	18
Mammalia	*Galemys pyrenaicus*	60.2	3.5
Mammalia	*Alouatta seniculus*	6145.5	25
Mammalia	*Aotus trivirgatus*	900	20
Mammalia	*Colobus polykomos*	9834.9	30.5
Mammalia	*Macaca sinica*	6120	30
Mammalia	*Macaca sylvanus*	7000	22
Mammalia	*Papio cynocephalus*	23000	40
Mammalia	*Enhydra lutris*	45000	23
Mammalia	*Nannospalax spp.*	178	4.5
Mammalia	*Sylvilagus floridanus*	1172.8	5
Mammalia	*Setonix brachyurus*	3250	13.8
Mammalia	*Setonix brachyurus*	3250	13.8
Mammalia	*Castor fiber*	20,000	24
Mammalia	*Gymnobelideus leadbeateri*	127	9
Mammalia	*Cratogeomys castanops*	251.8	2.6
Mammalia	*Cratogeomys castanops*	251.8	4.7
Mammalia	*Kobus ellipsiprymnus*	210000.3	18.5
Mammalia	*Inia geoffrensis*	129250	30
Mammalia	*Pontoporia blainvillei*	40500	16
Mammalia	*Trichosurus caninus*	3500	17

Mammalia	*Georychus capensis*	239.3	3
Mammalia	*Peponocephala electra*	206000	47
Mammalia	*Erignathus barbatus*	280000	31
Mammalia	*Phoca fasciata*	90000	30
Mammalia	*Alouatta palliata*	7274.9	20
Mammalia	*Ovibos moschatus*	368502.1	24
Mammalia	*Hylobates syndactylus*	10000	25
Mammalia	*Arctocephalus galapagoensis*	27000	22
Mammalia	*Didelphis virginia*	1000	3
Mammalia	*Erinaceus europaeus*	1200	8
Mammalia	*Muscardinus avellanarius*	27.5	4
Mammalia	*Ursus arctos*	454000	25
Mammalia	*Giraffa camelopardalis*	899994.8	26
Mammalia	*Ursus (= Thalarctos) maritimus*	425000	30
Mammalia	*Madoqua (= Rhynchotragus) kirki*	5300.1	5
Mammalia	*Erethizon dorsatum*	12000	18
Mammalia	*Proechimys semispinosus*	360	1.7
Mammalia	*Odobenus rosmarus*	1500000	40
Mammalia	*Reithrodontomys spp.*	18	1.5
Mammalia	*Liomys adspersus*	65	1.5
Mammalia	*Lycaon pictus*	36000	11
Mammalia	*Phoca hispida*	124000	43
Mammalia	*Phocoena phocoena*	52500	13
Mammalia	*Ovis aries*	200000	20
Mammalia	*Ovis aries*	130000	24
Mammalia	*Cephalorhynchus commersonii*	72400	18
Mammalia	*Ceratotherium simum*	2949986.3	36
Mammalia	*Ceratotherium simum*	2949986.3	50
Mammalia	*Ctenomys talarum*	190	1.8
Mammalia	*Jaculus jaculus*	73	4
Mammalia	*Graphiurus surdus*	34	5
Mammalia	*Muscardinus avellanarius*	30	6
Mammalia	*Microcavia australis*	300	4
Mammalia	*reitherodontomys megalotis*	17	2
Mammalia	*Rattus exulans*	80	1
Mammalia	*Glirulus japonicus*	40	6
Mammalia	*Glis glis*	150	9
Mammalia	*graphiurus murinus*	34	5.5
Mammalia	*Cuniculus paca*	12000	12.5
Mammalia	*Napaeozapus insignis*	35	4

Mammalia	*Marmota flaviventris*	5220	15
Mammalia	*Spermophilus beecheyi*	738	6
Mammalia	*Zapus princeps*	24	6
Mammalia	*Ochotona collaris*	200	7
Mammalia	*tenrec ecaudatus*	2400	7
Mammalia	*Tamias palmeri*	69.4	4
Mammalia	*Tachyglossus aculeatus*	7000	45
Mammalia	*Ornithorhynchus anatinus*	2500	17
Mammalia	*Tamias senex*	108.5	8
Mammalia	*Tamias townsendii*	118	7
Mammalia	*spermophilus lateralis*	394	7
Mammalia	*meles anakuma*	11000	10
Mammalia	*perognathus fasciatus*	14	1.5
Mammalia	*microtus longicaudus*	85	1
Mammalia	*salpingotus pallidus*	12.5	2.5
Mammalia	*marmota himalayana*	9000	17
Mammalia	*Micromys minutus*	6	1
Mammalia	*ochotona curzoniae*	200	2
Mammalia	*ochotona rutila*	400	3
Mammalia	*cynomys ludovicianus*	1675	8
Mammalia	*Chaetodipus nelsoni*	16.5	1
Mammalia	*sciurus variegatoides*	909	12
Mammalia	*Memphitis*	6300	7
Mammalia	*Sorex alpinus*	11.5	1.3
Mammalia	*ailuropoda melanoleceuca*	125000	15
Mammalia	*sylvilagus floridanus*	1530	3
Mammalia	*myodes gapperi*	42	1.5
Mammalia	*peromyscus leucopus*	25	1
Mammalia	*orthogeomys grandis*	830	2
Mammalia	*synaptomys cooperi*	50	1
Mammalia	*Chaetodipus villosus*	2000	23
Mammalia	*Spermophilus parryii*	1500	10
Mammalia	*Burramys parvus*	45	4
Mammalia	*Microcebus rufus*	98	8
Mammalia	*Planigale ingrami*	4.3	1.3
Mammalia	*tarsipes rostratus*	18	2
Mammalia	*Perognathus flavescens*	16	2
Mammalia	*Pseudochirulus mayeri*	206	5
Mammalia	*Atelerix frontalis*	555	7
Mammalia	*Zapus trinotatus*	27.45	4
Mammalia	*Crocidura russula*	14	1.5
Reptilia	*Acanthodactylus boskianus*	8.3	9.0
Reptilia	*Acanthodactylus*	7.4	4.0

	pardalis		
Reptilia	*Alsophylax pipiens*	1.5	3.5
Reptilia	*Amalosia lesueurii*	3.7	9.5
Reptilia	*Amblyrhynchus cristatus*	3000.0	28.0
Reptilia	*Amphibolurus muricatus*	46.8	4.0
Reptilia	*Amphibolurus norrisi*	38.0	7.0
Reptilia	*Anolis carolinensis*	7.0	7.0
Reptilia	*Anolis cupreus*	1.8	1.5
Reptilia	*Anolis gemmosus*	4.1	3.0
Reptilia	*Anolis gundlachi*	6.9	3.0
Reptilia	*Anolis humilis*	1.8	3.0
Reptilia	*Anolis intermedius*	2.1	2.0
Reptilia	*Anolis tropidolepis*	3.0	3.0
Reptilia	*Aspidoscelis laredoensis*	21.4	3.0
Reptilia	*Aspidoscelis neomexicana*	18.6	4.0
Reptilia	*Aspidoscelis rodecki*	12.0	2.0
Reptilia	*Aspidoscelis scalaris*	58.9	3.0
Reptilia	*Aspidoscelis tesselata*	15.6	5.0
Reptilia	*Aspidoscelis tigris*	15.5	8.0
Reptilia	*Callisaurus draconoides*	10.3	5.9
Reptilia	*Chalcides chalcides*	18.8	4.0
Reptilia	*Cnemidophorus murinus*	33.5	5.0
Reptilia	*Cophosaurus texanus*	10.2	6.0
Reptilia	*Coronella girondica*	50.0	16.0
Reptilia	*Crotaphytus collaris*	37.1	10.0
Reptilia	*Ctenophorus fordi*	4.1	3.0
Reptilia	*Ctenophorus maculosus*	8.8	3.5
Reptilia	*Ctenosaura hemilopha*	2800.0	13.0
Reptilia	*Ctenotus atlas*	2.5	4.0
Reptilia	*Ctenotus lancelini*	3.3	6.0
Reptilia	*Ctenotus leonhardii*	4.9	7.0
Reptilia	*Ctenotus regius*	5.1	4.0
Reptilia	*Ctenotus schomburgkii*	1.7	5.0
Reptilia	*Cyclura carinata*	1005.0	14.0
Reptilia	*Cyclura cychlura*	10380.0	40.0
Reptilia	*Darevskia armeniaca*	2.1	8.0
Reptilia	*Darevskia brauneri*	4.5	13.0
Reptilia	*Darevskia unisexualis*	4.6	7.0
Reptilia	*Dinarolacerta mosorensis*	5.8	9.0
Reptilia	*Diplodactylus conspicillatus*	3.9	3.2
Reptilia	*Draco volans*	5.4	3.0
Reptilia	*Egernia kingii*	291.0	13.0
Reptilia	*Elgaria coerulea*	31.5	8.0

Reptilia	*Eremias argus*	7.2	11.0
Reptilia	*Eremias strauchi*	3.3	7.0
Reptilia	*Eulamprus leuraensis*	10.0	6.0
Reptilia	*Eulamprus tympanum*	17.0	15.0
Reptilia	*Eutropis multifasciata*	24.5	8.0
Reptilia	*Gallotia bravoana*	158.5	6.0
Reptilia	*Gallotia intermedia*	91.2	10.4
Reptilia	*Gambelia wislizenii*	47.0	9.8
Reptilia	*Gehyra variegata*	3.0	26.0
Reptilia	*Hemidactylus brookii*	2.0	4.0
Reptilia	*Hesperoedura reticulata*	7.2	11.0
Reptilia	*Holbrookia maculata*	4.9	5.0
Reptilia	*Hoplodactylus duvaucelii*	118.0	25.0
Reptilia	*Iberolacerta aurelioi*	2.6	17.0
Reptilia	*Iberolacerta monticola*	8.6	15.0
Reptilia	*Lacerta agilis*	8.3	12.0
Reptilia	*Lacerta schreiberi*	21.0	10.0
Reptilia	*Lacerta strigata*	20.6	4.0
Reptilia	*Leposoma guianense*	0.8	2.0
Reptilia	*Liopholis modesta*	5.5	5.0
Reptilia	*Lygodactylus capensis*	0.9	2.1
Reptilia	*Malpolon monspessulanus*	500.0	20.0
Reptilia	*Mesalina olivieri*	1.9	5.0
Reptilia	*Nephrurus stellatus*	13.1	8.0
Reptilia	*Niveoscincus ocellatus*	12.0	12.0
Reptilia	*Notechis scutatus*	1349.0	17.0
Reptilia	*Oligosoma alani*	60.0	20.0
Reptilia	*Oligosoma chloronoton*	44.7	8.0
Reptilia	*Oligosoma lineoocellatum*	30.2	8.0
Reptilia	*Oligosoma suteri*	19.8	12.0
Reptilia	*Oligosoma whitakeri*	22.4	20.0
Reptilia	*Ophisops elegans*	3.0	5.0
Reptilia	*Papuascincus stanleyanus*	4.2	6.0
Reptilia	*Paralaudakia caucasia*	70.0	13.0
Reptilia	*Paralaudakia stoliczkana*	80.0	10.0
Reptilia	*Parvilacerta parva*	3.1	8.0
Reptilia	*Phrynocephalus guttatus*	4.1	5.0
Reptilia	*Phrynocephalus persicus*	7.8	5.0
Reptilia	*Phrynosoma platyrhinos*	18.8	8.0
Reptilia	*Plestiodon reynoldsi*	1.3	10.0
Reptilia	*Plestiodon skiltonianus*	4.9	8.0

Reptilia	*Podarcis bocagei*	4.6	4.0
Reptilia	*Podarcis erhardii*	9.5	5.0
Reptilia	*Podarcis gaigeae*	10.8	5.0
Reptilia	*Pristidactylus achalensis*	45.0	11.0
Reptilia	*Ptyas mucosa*	3162.3	11.3
Reptilia	*Rhinechis scalaris*	389.0	16.0
Reptilia	*Rhynchoedura ornata*	1.8	2.8
Reptilia	*Sauromalus ater*	550.0	39.0
Reptilia	*Scelarcis perspicillata*	3.4	5.0
Reptilia	*Sceloporus cowlesi*	11.3	5.0
Reptilia	*Sceloporus graciosus*	7.0	8.0
Reptilia	*Sceloporus magister*	43.6	6.0
Reptilia	*Sceloporus occidentalis*	13.6	5.0
Reptilia	*Sceloporus olivaceus*	33.6	3.8
Reptilia	*Sceloporus undulatus*	11.3	4.0
Reptilia	*Sceloporus variabilis*	11.0	1.5
Reptilia	*Scincella lateralis*	1.5	4.0
Reptilia	*Sitana ponticeriana*	12.3	6.0
Reptilia	*Sphaerodactylus vincenti*	0.5	4.0
Reptilia	*Teira dugesii*	9.0	16.0
Reptilia	*Teratoscincus roborowskii*	12.0	6.0
Reptilia	*Toropuku stephensi*	9.7	16.0
Reptilia	*Trioceros hoehnelii*	18.0	4.5
Reptilia	*Uma inornata*	17.3	5.0
Reptilia	*Uromastyx aegyptia*	600.0	33.0
Reptilia	*Urosaurus graciosus*	3.5	5
Reptilia	*Urosaurus ornatus*	3.4	3.0
Reptilia	*Uta stansburiana*	3.0	4.8
Reptilia	*Varanus komodoensis*	37140.0	62.0
Reptilia	*Vipera latastei*	199.5	14.0
Reptilia	*Woodworthia brunneus*	10.2	42.0
Reptilia	*Xantusia riversiana*	17.3	32.9
Reptilia	*Zootoca vivipara*	3.9	5.0
Reptilia	*Acanthodactylus erythrurus*	8.7	2.1
Reptilia	*Alligator sinensis*	35800	70
Reptilia	*Anatololacerta anatolica*	9.8	10.0
Reptilia	*apodus*	450	54
Reptilia	*Aspidoscelis dixoni*	18.3	4.0
Reptilia	*Aspidoscelis exsanguis*	15.5	4.0
Reptilia	*Aspidoscelis uniparens*	7.5	4.0
Reptilia	*Bassiana duperreyi*	2.9	7.0
Reptilia	*Caimen latirostris*	60000	22
Reptilia	*Callisaurus dracoides*	18	6

Reptilia	*caretta*	156500	37
Reptilia	*Carlia rostralis*	5.5	3.8
Reptilia	*Carlia rubrigularis*	3.5	3.6
Reptilia	*Carlia storri*	1.7	3.3
Reptilia	*constrictor*	3532	40.4
Reptilia	*coriacea*	420000	30
Reptilia	*crocodylus siamensis*	60000	60
Reptilia	*Ctenophorus isolepis*	5.5	2.0
Reptilia	*Darevskia*	6	13
Reptilia	*Dinarolacerta mosorensis*	6	9
Reptilia	*dorsalis*	60	14.6
Reptilia	*durissus*	1150	19.8
Reptilia	*Ergenia whitii*	25	13
Reptilia	*exanthematicus*	709	12.7
Reptilia	*Gallotia simonyi*	280	20
Reptilia	*Gambelia sila*	38.2	6.0
Reptilia	*guttata*	900	32.3
Reptilia	*Hoplodactylus maculatus*	8	17
Reptilia	*Hydrosaurus ambionensis*	1360	25
Reptilia	*kingi*	635	10
Reptilia	*Lacerta agilis*	8.3	12
Reptilia	*Lacerta viridis*	39	8
Reptilia	*Lacerta vivipara*	3.9	12
Reptilia	*Lampropholis delicata*	1.2	12
Reptilia	*Mecistops cataphractus*	230000	56
Reptilia	*mississippiensis*	150000	73.1
Reptilia	*molurus*	30000	34.2
Reptilia	*moreletii*	84000	80
Reptilia	*multicarinata*	31.5	9.8
Reptilia	*mydas*	160000	75
Reptilia	*natrix*	96.25	20
Reptilia	*Plestiodon reynoldski*	1.3	10
Reptilia	*Plestiodon obsoletus*	30	7.3
Reptilia	*Ophisops elegans*	3	5
Reptilia	*picta*	371.8	61
Reptilia	*Plestiodon septentrionalis*	15.5	7
Reptilia	*Pristidactylus achalensis*	35	10
Reptilia	*Pseudemys scritpa*	3200	30
Reptilia	*Ptyodactylus hasselquisti*	9.3	11
Reptilia	*punctatus*	430	90
Reptilia	*reticulatus*	32000	29.4
Reptilia	*Sauromalus ater*	550	16
Reptilia	*Sceloporus graciosus*	7	8

Reptilia	*Sceloporus graciosus gracilis*	7	8
Reptilia	*Sceloporus Jarrovi*	24	6
Reptilia	*Sceloporus merriami*	4.3	6.0
Reptilia	*Sceloporus scalaris*	4	5
Reptilia	*scincoides*	493	26.6
Reptilia	*scripta*	240	41.3
Reptilia	*serpentina*	10250	47
Reptilia	*sirtalis*	150	14
Reptilia	*sulcata*	43000	54.3
Reptilia	*Teira dugesii*	9	16
Reptilia	*temminckii*	58500	70.3
Reptilia	*tetraspis*	40000	70
Reptilia	*tigris*	18	7.8
Reptilia	*Tiliqua rugosa*	617	50
Reptilia	*trivirgata*	450	31
Reptilia	*varanus griseus*	430	17
Reptilia	*viridis*	21.5	10
Reptilia	*Xantusia vigilis*	1.5	9
Reptilia	*Zootoca vivipara*	3.9	5

Appendix 3.2. List of all extant taxa used in linear regressions between logged body mass and logged lifespan.

Class	Species	Body mass (g)	Femur length (mm)	Foreman diameter (mm)	Qi
Mammaliaformes	*Morganucodon watsoni*	16.000	12.500	0.476	3.829 e-7
Mammaliaformes	*Morganucodon watsoni*	26.400	12.500	0.476	3.829 e-7
Mammalia	*Aepyprymnus rufescens*	2820.000	103.961	0.599	3.068 e-5
Mammalia	*Alces alces*	325000.000	429.500	1.789	1.498 e-3
Mammalia	*Apodemus flavicolis*	23.900	21.500	1.213	3.144 e-5
Mammalia	*Arctocephalus pusillus doriferus*	75000.000	128.413	1.024	1.081 e-3
Mammalia	*Bettongia penicillata*	1018.000	79.610	0.406	1.733 e-5
Mammalia	*Bos taurus*	225000.000	390.000	1.554	9.346 e-4
Mammalia	*Camelus dromedarius*	402000.000	456.250	1.564	8.637 e-4
Mammalia	*Capra hircus*	45000.000	196.000	0.959	2.702 e-4
Mammalia	*Dama dama*	70000.000	249.500	1.060	3.271 e-4
Mammalia	*Dasyuroides byrnei*	92.000	33.693	0.157	1.756 e-6
Mammalia	*Elephas maximus*	4545400.000	1010.000	4.359	2.466 e-2
Mammalia	*Equus asinus*	177500.000	356.500	2.320	5.430 e-3
Mammalia	*Equus caballus*	675000.000	463.750	3.558	2.447 e-2
Mammalia	*felis catus*	4600.000	109.100	0.378	1.475 e-5
Mammalia	*Gazella dorcos*	21370.000	154.000	0.718	1.080 e-4
Mammalia	*Giraffa camelopardalis*	750000.000	435.000	2.295	3.995 e-3
Mammalia	*Hydrurga leptonyx*	380000.000	139.250	0.940	3.5 e-4
Mammalia	*Isoodon obesulus*	717.000	62.035	0.370	2.913 e-5
Mammalia	*Lama glama*	100000.000	290.000	1.310	7.234 e-4
Mammalia	*Lasiorhinus latifrons*	29917.000	132.550	0.522	3.463 e-5
Mammalia	*Leporillus conditor*	315.000	41.503	0.395	9.644 e-6
Mammalia	*Lepus capensis*	3030.000	119.500	0.461	2.365 e-5
Mammalia	*Lobodon carcinophagus*	215000.000	111.720	1.809	6.276 e-3
Mammalia	*macroderma gigas*	148.000	43.470	0.153	8.033 e-7
Mammalia	*Macropus agilis*	12000.000	184.500	0.512	2.812 e-5
Mammalia	*Macropus parryi*	12000.000	195.500	0.556	3.060 e-5
Mammalia	*Macropus robustus*	29300.000	193.500	0.952	2.812 e-4
Mammalia	*Macropus rufus*	32490.000	250.750	0.805	1.232 e-4

Mammalia	*Micromys minutus*	7.400	11.000	0.613	1.468 e-5
Mammalia	*Microtus levis*	26.800	14.325	0.710	2.255 e-6
Mammalia	*Mucropus fuliginosus*	30000.000	267.125	1.013	2.552 e-4
Mammalia	*Mus musculus*	30.000	15.100	0.719	2 e-5
Mammalia	*myodes rutilis*	30.620	11.700	0.655	1.609 e-5
Mammalia	*Neomys fodiens*	15.000	10.500	0.677	2.564 e-5
Mammalia	*Ornithorhyncus anatinus*	693.000	43.220	0.230	4.088 e-6
Mammalia	*Oryctolagus cuniculus*	1590.000	84.292	0.341	1.203 e-5
Mammalia	*Ovis aries*	21150.000	196.500	1.013	3.367 e-4
Mammalia	*panthera pardus*	41400.000	244.000	0.956	2.155 e-4
Mammalia	*perameles gunnii*	837.000	41.800	0.295	4.904 e-6
Mammalia	*Peromyscus truei*	33.200	17.950	0.638	1.099 e-5
Mammalia	*Petaurus breviceps*	127.000	40.756	0.213	3.704 e-6
Mammalia	*Phascolarctos cinereus*	4765.000	155.000	0.597	4.158 e-5
Mammalia	*potorous tridactylus*	976.000	79.028	0.244	2.823 e-6
Mammalia	*Pseudocheirus peregrinus*	916.000	59.038	0.233	1.531 e-6
Mammalia	*Rattus fuscipes greyii*	76.000	27.108	0.172	8.241 e-6
Mammalia	*Rattus lutreolus*	109.000	28.955	0.199	3.365 e-6
Mammalia	*Sicista betulina*	10.000	10.400	0.708	2.590 e-5
Mammalia	*Sorex araneus*	7.600	8.300	0.438	7.159 e-6
Mammalia	*Sorex minimutissimus*	2.000	4.800	0.398	1 e-5
Mammalia	*Sus scrofa*	55300.000	225.500	0.925	2.045 e-4
Mammalia	*Tachyglossus aculeatus*	2725.000	59.295	0.266	1.081 e-5
Mammalia	*Ursus arctos*	233000.000	356.500	1.185	3.462 e-4
Mammalia	*Vombatus ursinus*	22500.000	148.413	1.005	6.094 e-5
Mammalia	*Vulpes vulpes*	4440.000	127.775	0.604	6.877 e-5
Reptilia	*Brachylophus vitiensis*	345.000	47.270	0.100	1.471 e-7
Reptilia	*Caretta caretta*	13000.000	158.000	0.307	5.003 e-6
Reptilia	*Chelodina mydas*	115000.000	47.628	0.478	7.452 e-5
Reptilia	*Chelodina rugosa*	2146.000	49.657	0.167	1.311 e-6
Reptilia	*Chlamydosaurus kingii*	635.000	67.175	0.121	3.521 e-8
Reptilia	*Corucia zebrata*	1014.000	30.390	0.115	3.887 e-7

Reptilia	*Crocodylus johnsoni*	16385.000	115.875	0.414	2.674 e-5
Reptilia	*Crocodylus porosus*	470000.000	249.000	0.922	3.554 e-4
Reptilia	*Ctenophorus nuchalis*	37.000	17.770	0.071	9.706 e-8
Reptilia	*Egernia cunninghami*	261.000	25.687	0.101	2.970 e-7
Reptilia	*Emydura krefftii*	1300.000	39.090	0.194	2.419 e-6
Reptilia	*Moloch horridus*	31.000	23.295	0.113	4.391 e-7
Reptilia	*Nephrurus levis*	11.000	26.075	0.080	1.009 e-7
Reptilia	*Physignathus lesueurii*	504.000	51.108	0.128	4.496 e-7
Reptilia	*Tiliqua multifasciata*	204.000	22.450	0.097	2.639 e-7
Reptilia	*Tiliqua nigrolutea*	800.000	28.690	0.120	5.099 e-7
Reptilia	*Tiliqua rugosa*	609.000	28.840	0.079	9.599 e-8
Reptilia	*Tliqua scincoides*	493.000	21.192	0.122	7.177 e-7
Reptilia	*Varanus giganteus*	5333.000	94.315	0.343	1.55427 e-6
Reptilia	*Varanus gouldii*	443.000	64.208	0.615	3.994 e-5
Reptilia	*Varanus indicus*	1287.000	54.400	0.461	2.167 e-5
Reptilia	*Varanus komodoensis*	12000.000	105.500	0.956	2.816 e-4
Reptilia	*Varanus mertensi*	1121.000	61.575	0.574	5.479 e-5
Reptilia	*Varanus panoptes*	2317.000	81.500	0.523	2.522 e-5
Reptilia	*Varanus spenceri*	6000.000	98.500	0.828	1.007 e-4
Reptilia	*Varanus varius*	6343.000	78.563	0.329	7.683 e-6

Appendix 3.3. List of all taxa used for Q_i and MMR calculations

Taxon	Qi	Femur length (cm)
Apodemus flavicolis	3.144 E-5	2.15
Micromys minutus	1.468 E-5	1.1
Microtus levis	2.255 E-5	1.43
Mus musculus	2.38 E-5	1.51
Peromyscus truei	1.098 E-5	1.75
Sorex minimutissimus	1.002 E-5	0.48
Sicista betulina	2.590 E-5	1.04
Sorex araneus	4.89 E-6	0.83
Sorex minutus	6.37 E-6	0.56
Myodes rutilis	1.609 E-5	1.17
Neomys fodiens	2.28 E-5	1.04
Morganucodon watsoni	3.829 E-6	1.25

Appendix 3.4. List of all femur specimens imaged using micro-computed tomography. Qi: blood flow index.

Appendix 4.1. Preliminary micro-computed tomographic investigation of cementum increments

Preliminary tomographic measurements of *Macaca mulatta* cementum were performed using laboratory based μCT equipment in order to gain first approximations of the parameters needed for imaging 'fresh' (i.e. non-fossil) dental cementum. Initial μCT scanning of the anterior and posterior roots of the m1 tooth of the k23 specimen was performed using a Zeiss/Xradia Versa 510 system on 09/10/2015 at the University of Southampton. The specimen was 12 years old when the m1 tooth was removed. Voxel size was set at 3μm, as this is the smallest voxel size that still allowed the entire root to fit within the field of view. X-ray energy was 45KeV, the minimum energy that ensured sufficient X-ray transmittance through the specimen per projection (25% transmission), at a voltage of 4.5W. However this transmittance was only attained at exposure times of 12 seconds. The source-to-sample distance was minimized (13mm) in order to optimize flux without adjusting X-ray energy. Two 6:30 hour scans were performed for each root (four total scans), leading to a total scan time of 26 hours. Scans were centered on the tip of each root, with the first and third scans including the tip apex of the anterior and posterior root (respectively). The second and fourth scans were centered at a height 6mm below that of scans 1 and 3 (respectively), Providing an overlap of ~480 μm between scan 1 and 2 (anterior root), and scan 3 and 4 (posterior root).

Cementum is readily distinguished from dentine in μCT tomographic data as a darker tissue along the circumference of the root. Both tissues are clearly delineated by a dark layer along their boundary (**Fig. 5.3.a**) for the entire vertical length of the root. The dentine appears as a homogeneous tissue with little internal features (**Fig. 5.3.a**). No incremental structures (striae of Retzius or lines of Von Ebner) can be detected. Radial patterns can be distinguished within the dentine that may represent dentine tubules. These are only apparent in higher contrasting regions towards the root tip.

Cellular cementum can be distinguished from acellular cementum throughout both roots by cellular voids that are shown to cluster in irregular regions (**Fig. 5.3.a**). This allowed volumetric mapping of cellular cementum for the first time (**Fig. 5.4**). Mapping indicates that although the overall pattern of cellular cementum is chaotic, it becomes increasingly more prevalent towards the root apex. Contrast-to-noise ratios of μCT data did not permit automatic segmentation of cellular voids and so quantitative

analysis of their distribution concentration could not be performed.

Four thick light increments can be seen intermittently within the acellular cementum of the anterior root, separated by three dark increments and proceeded by a fourth dark increment forming the border between the cementum and dentine tissues (**Fig. 5.3**). Only the inner-most and outer-most increment pairs are visible for the entire length of the root. Increments become increasingly highly contrasting apically through the cementum, and all four increments can only be seen in the apical-most 2mm of the root.

The identification of four highly contrasting increment pairs in data generated using laboratory-based μCT X-ray sources suggests that this may well be a viable technique for cementochronology. However, consideration of the quantitative measurements of image quality, the accuracy of μCT data for representing true biological structure, and the practical and technical aspects of these preliminary studies must be assessed in order to further optimise the experimental parameters used in these preliminary studies.

Comparison between histological data and preliminary μCT data of the same region of the k23 specimen suggests that preliminary scanning settings provide sub-optimal image quality for unfossilised cementum increments (**Fig. 5.5**). The k23 specimen was 12 years old when the lm1 tooth was removed. *Macaca mulatta* are understood to replace their lower first molars during their second year of life (Bowen and Koch, 1970). This should allow for 10 increment pairs to be deposited within the cementum. 10 increment pairs are revealed by thin-section histology of the specimen's cementum (**Fig. 5.5).** However, as only four increment pairs were found the tomographic dataset of either root, this represents a substantial error in the preliminary use of μCT for cementochronological purposes in unfossilised teeth. Further, the substantial scanning times required to ensure sufficient X-ray transmittance through the specimen at the voxel resolutions required for studying cementum increments (<1 μm) mean that the technique is probably not suitable for imaging the large, population-level samples required for most comentochronological studies.

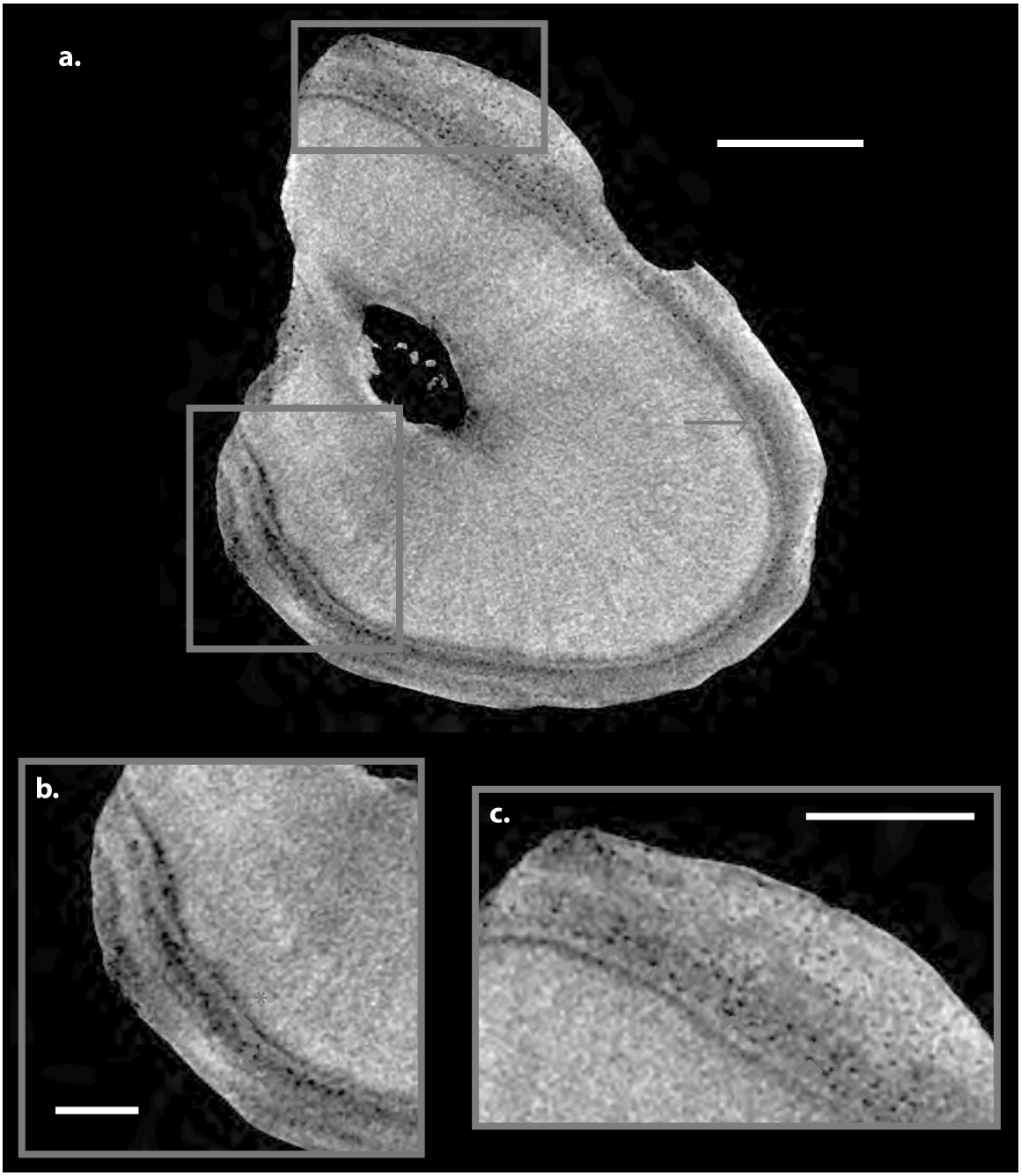

Appendix 4.1. Figure 1. Laboratory-based µCT data of *Macaca mulatta* dental root tissues imaged using the Zeiss/Xradia versa 510 system. (**a**) Transverse orthoslice of the entire root; cemento-dentine boundary distinguished by a highly contrasting circumferential dark/light incremental feature (red arrow). Radial texture can be interpretted within the dentine, although contrast and/or resolution is insufficient to identify radial dentine tubules. No incremental features can be identified in the dentine. Acellular cementum (red box) can be distinguished from cellular cementum (green box) due to the cellular voids imaged in the latter. (**b**) Detail of cellular cementum highlighted in the red box of (**a**). Four light increments can be plotted (red arrow), although the middle two increments coalesce and are not present through the entire tissue. Top arrow (highlighted with *) indicates increment pair used in step response function, and contrast-to-noise ratio calculations. (**c**) Cellular cementum comprising multiple cellular voids, with four such voids identified using green arrows. White scale bar in (**a**) equals 350 µm; in (**b**) equals 150 µm; and in (**c**) equals 250 µm.

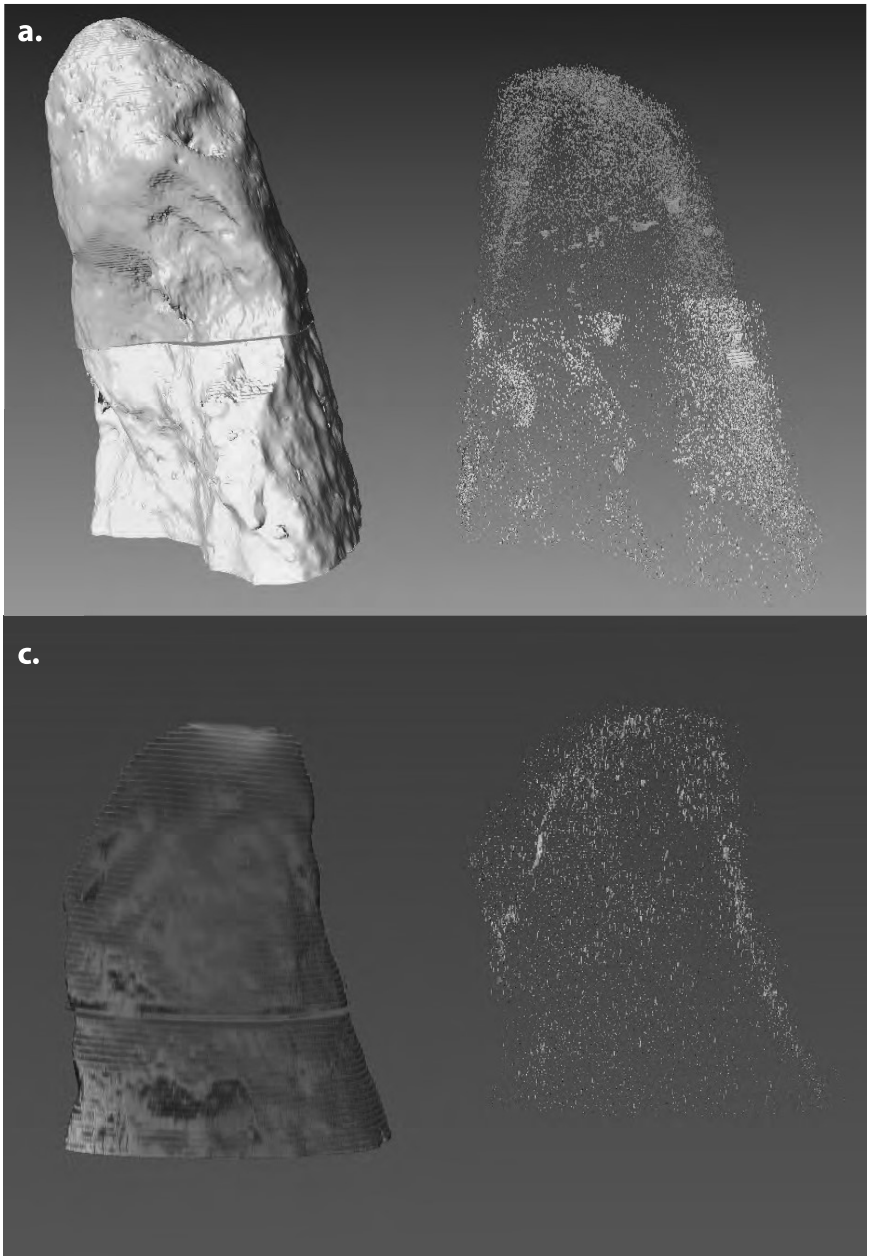

Appendix 4.1. Figure 2. Analysis of cellular voids in cementum. (**a**) Pore counts in the cementum of the anterior root of the k23 specimen. The proportion of pore counts increases with proximity to the root tip through the lower scan (yellow) and the upper scan (orange), and clusters of pores correlate with discrete nodular morphologies in the cementum surface. (**b**) This is reflected in heat maps that reflect correlation between pore count and distance from the centroid of each orthoslice. Blue represents strong correlation, yellow represents weak correlation in the posterior root of the k23 specimen.

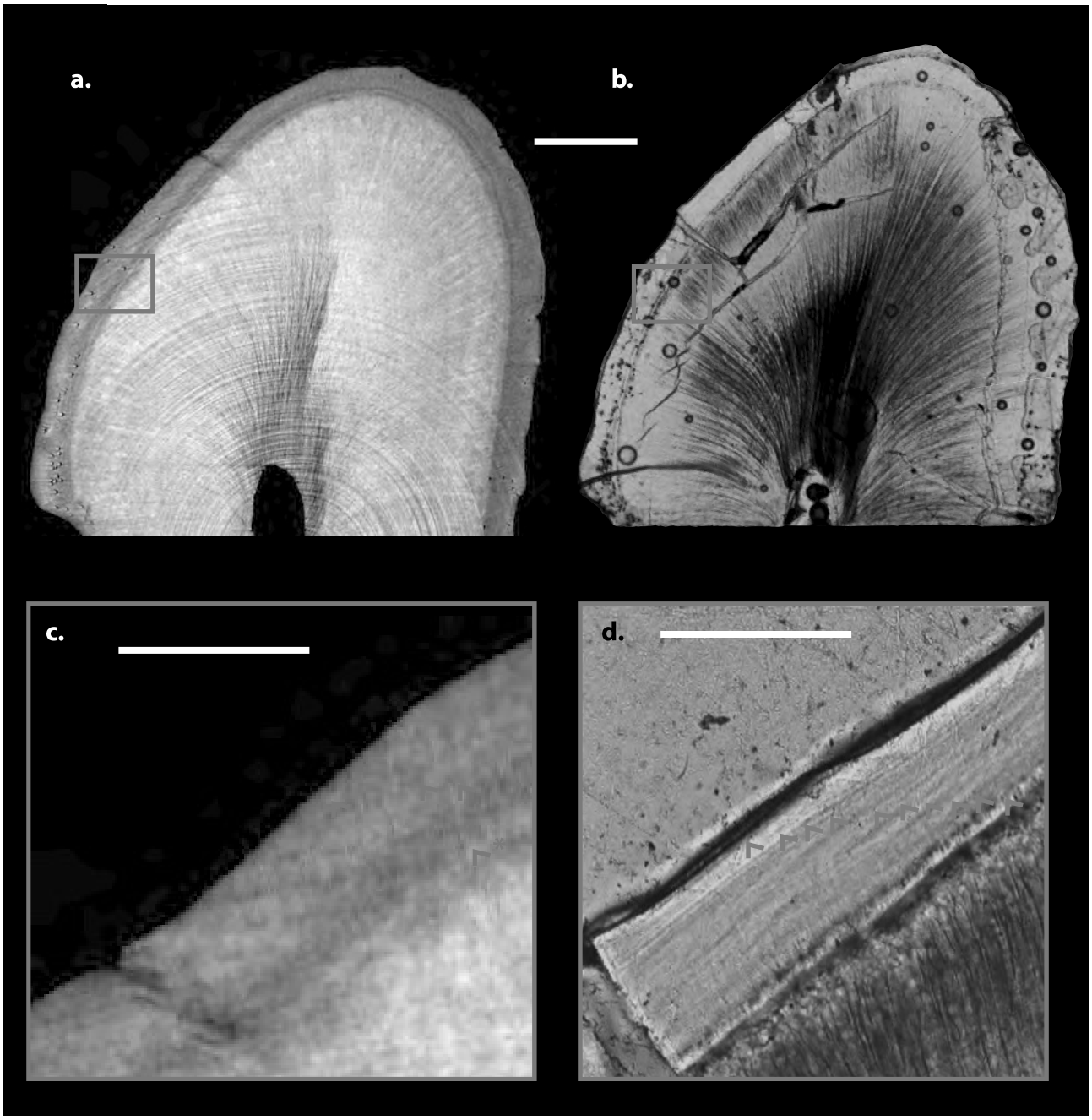

Appendix 4.1. Figure 3. Comparison between µCT data and thin-section histological data of *Macaca mulatta* cementum. (**a**) Transverse orthoslice of the dental root of specimen k23. (**b**) Transverse histological thin-section of the same region imaged in (**a**). (**c**) Detail of SR CT cementum data. (**d**) Histological data of the same region as (**c**), highlighting a series of 10 increment pairs (green arrows), only four of which are captured in (**c**) (red arrows). White scalebar shared between (**a**) and (**b**) equals 150 µm, and in (**c**) and (**d**) equals 100 µm.

https://www.dropbox.com/home/Elis%20Newham%20PhD%20e-appendices

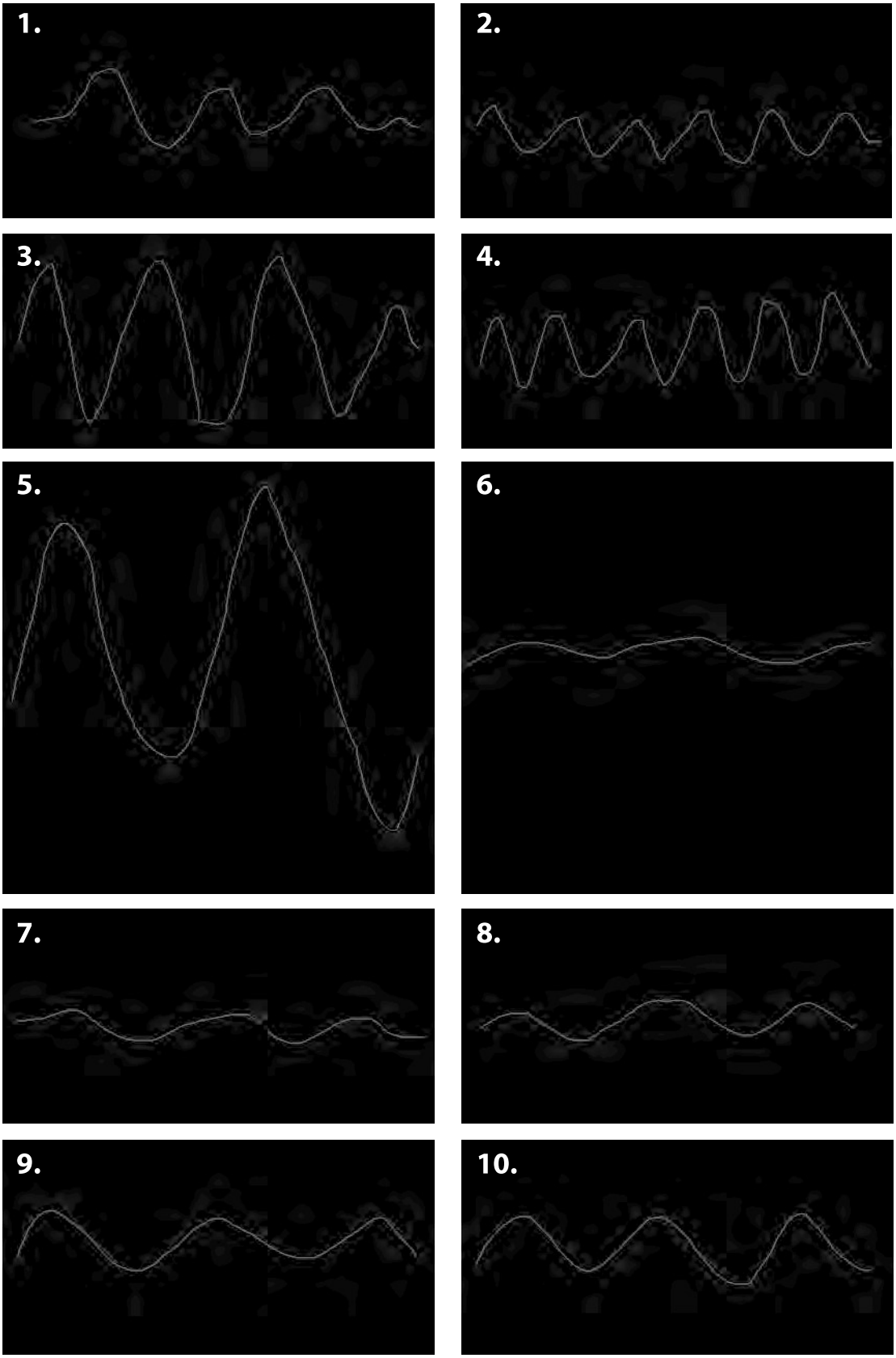

Appendix 4.3. Digital phantoms of known length designed to test the accuracy of the cementum increment tortuosity algorithm. The number of each image corresponds with the numbers used in **Table 4.8.** (Copy of this table overleaf on page 319).

Image	Length (pixels)	Euclidian distance (pixels)	Tortuosity	Algorithmically calculated tortuosity	Difference between tortuosity values
1	1355.675	882.11	1.53	1.52	0.01
2	1633.565	932.695	1.75	1.7	0.05
3	2834.685	930	3.048	3.02	0.03
4	2383.204	906.02	2.63	2.66	0.03
5	2982.082	948.675	3.14	3.07	0.07
6	1025.169	927.573	1.11	1.11	0
7	1083.921	944.765	1.15	1.15	0
8	1031	862	1.196	1.19	0.01
9	1235	920	1.342	1.32	0.02
10	1345	912	1.475	1.44	0.03

Copy of Table 4.8. Comparisons between algebraically calculated and algorithmically calculated tortuosity values for digital phantoms of known length

Specimen	D.O.B.	D.O.D.	Birth events	Notes on increment morphology	Correspondence with life history
l59	17.04.04	09.04.15	6	doubling of increment 1	year of eruption of tooth
				increment 3 blurred and poorly defined	corresponds with first pregnanc
				twinning of increments 5 and 6?	corresponds with second pregnancy
				increment 7 poorly defined	corresponds with third pregnancy
				potential doubling of increment 9	corresponds with fourth pregnancy
				lines 10 and 11 poorly VERY defined from each other	corresponds with fifth pregnancy
l72	29.04.04	08.04.15	4	increments 4 and 5 bleed into each other	corresponds with 1st birth
				increments 6, 7 and 8 bleed into each other	-
				increments 7/8 poorly defined from each other	corresponds with 3rd birth
				increments 9/10 poorly defined from each other	corresponds with birth event 4
l56	14.04.04	10.04.15	3	increment 4 bleeds into increment 3	corresponds with birth event 1
				potential doubling of increment 4 and poor definition between increments 4 and 5	
				doubling of increment 7	corresponds with birth event 2
				increment 8 poorly defined	
				increments 10 and 11 coalesce with each other	corresponds with birth event 3
l14	27.02.04	08.04.15	5	increments 4 and 5 bleed into each other	
				increment 4 poorly defined and thin	Correspond to first two birth events
				increments 7 and 8 poorly defined from each other]	correspond to third event?
				increments 8 and 9 well defined from each other	
				increments 10 and 11coalesce	correspond to fourth birth event

l14				increment 11 thin and ill defined	potentially corresponds to fifth birth event, but also incipient and not fully formed
				thick dark increment between 8 and 9	
k24	12.03.03	08.04.15	3	thick dark increment between 4 and 5	
				increment 7 poorly defined	corresponds with birth event 2
				increment 9 bleeds into increment 8	corresponds with birth event 3
m8	01.02.08	18.06.15	1	Thick dark increment during only pregnancy that coalesces with proceeding light increment	corresponds with birth event
l100	16.09.04	09.03.15	1	thick dark increment between increment 2 and 3	-
				coalescence between increments 6 and 7	corresponds with only birth event
l10	20.02.04	08.04.15	5	third and fourth increment poorly defined fropm each other and coalesce	corresponds with first and second birth events
				fifth to seventh increments least well defined in entire series. Lots of coalesce and lensing	corresponds to third-fifth birth events
k91	06.10.03	10.04.15	5	increments 5-7 very poorly defined and coalaesce with each other.	corresponds with first three birth events
				increment 8 comparatively well-defined but coalascsese with increment 7. importantly well defined from increment 9 with no coalescense	corresponds with fourth birth event

Appendix 5.1. Notes on the correspondence between cementum increment morphology and life history in the sub-sample of breeding Rhesus macaque (*Macaca mulatta*) females.

Specimen	Energy (KeV)	Exposure (ms)	Projections
sk334	26	800	3001
sk334	26	400	1501
sk334	26	200	1501
sk334	34	275	1501
sk334	34	275	3001
sk334	34	275	4501
sk228	24	275	4501
sk228	26	275	4501

Appendix 5.2. List of experimental parameters investigated for imaging entire human tooth roots.

Specimen	Taxon
CB04	*Krusatodon*
CB07	Amphetheriid
CB113	*Shuotherium*
CB19	*Cyrtlatherium*
CB500	*Phascolotherium*
CB506	docodont
CB508	*Phascolotherium*
CB509	docodont
CB515	multituberculate
CB519	mammal indet.
CB522	*Phascolotherium*
CB526	mammal indet.
J79445	docodont
J79452	mammal indet.
J79453	*Borealestes*
J79454	*Krusatodon*
J79462	*Palaeoxonodon*
J79472	haramiyid
J79474	*Borealestes*
J79475	*Borealestes*
J79476	*Krusatodon*
J79481	multituberculate
J79496	multituberculate
J79498	*Borealestes*
J79502	amphilestid
J79511	dryolestid
J79522	docodont
J79523	*Krusatodon*
J79536	docodont
M100056	gobiconodontid
M100057	gobiconodontid
M100059	docodont
M100060	eutriconodont
M100061	mammal indet.
M100062	mammal indet.
M100063	dryolestid
M100067	dryolestid
M100068	mammal indet.
M100070	mammal indet.
M100072	mammal indet.
M100073	docodont
M100074	mammal indet.
M100076	mammal indet.

M100083	mammal indet.
M100086	haramiyid
M100092	*Phascolotherium*
M100093	multituberculate
M100097	*Eleutherodon*
M100099	mammal indet.
M100114	amphilestid
M100116	amphilestid
M100117	*Phascolotherium*
M100119	mammal indet.
M100120	amphilestid
M100121	amphilestid
M100123	eutriconodont
M36501	docodont
M36505	docodont
M36512	*Palaeoxonodon*
M36513	docodont
M36516	*Amphitherium*
M36518	eutriconodont
M36524	*Borealestes*
M36527	*Cyrtlatherium*
M36530	*Palaeoxonodon*
M36531	"pantothere"
M36538	*Cyrtlatherium*
M36541	docodont
M36558	*Amphitherium*
M45045	mammal indet.
m46001	*Borealestes*
M46037	mammal indet.
M46041	amphilestid
M46058	*Borealestes*
M46083	*Gobiconodon*
M46095	dryolestid
M46194	Morganucodontid
M46197	*Palaeoxonodon*
M46200	*Palaeoxonodon*
M46212	*Peraiocynodon*
M46213	*Palaeoxonodon*
M46220	*Palaeoxonodon*
M46222	*Krusatodon*
M46226	*Shuotherium*
M46234	multituberculate
M46242	*Palaeoxonodon*
m46253	"symmetrodonta"

M46289	*Kennetherium*
m46290	*Palaeoxonodon*
M46307	mammal indet.
M46321	mammal indet.
M46333	*Krusatodon*
M46350	*Palaeoxonodon*
M46388	*Palaeoxonodon*
M46392	*Palaeoxonodon*
M46399	*Borealestes*
M46404	*Borealestes*
M46417	mammal indet.
M46429	*Palaeoxonodon*
M46430	*Kennetherium*
M46434	*Cyrtlatherium*
M46436	*Palaeoxonodon*
M46437	*Krusatodon*
M46439	*Shuotherium*
M46441	mammal indet.
m46442	*Krusatodon*
M46444	mammal indet.
M46445	*Borealestes*
M46446	mammal indet.
M46448	*Borealestes*
M46454	docodont
M46456	*Krusatodon*
M46486	*Krusatodon*
M46488	mammal indet.
M46503	*Phascolotherium*
M46506	*Palaeoxonodon*
M46515	*Kennetherium*
M46517	*Kennetherium*
M46522	*Cyrtlatherium*
M46524	*Palaeoxonodon*
m46531	*Krusatodon*
M46542	mammal indet.
M46545	docodont
M46549	*Borealestes*
M46570	*Cyrtlatherium*
M46577	docodont
M46579	*Kirtlingtonia*
M46580	*Borealestes*
M46581	mammal indet.
M46584	docodont
M46597	gobiconodontid

M46605	eutriconodont
M46614	mammal indet.
M46614	mammal indet.
M46618	*Palaeoxonodon*
M46623	mammal indet.
M46631	mammal indet.
M46632	*Borealestes*
M46636	*Palaeoxonodon*
M46639	*Palaeoxonodon*
M46650A	mammal indet.
M46657	*Palaeoxonodon*
M46677	mammal indet.
M46684	*Kermackodon*
M46686	mammal indet.
M46688	*Cyrtlatherium*
M46698	*Palaeoxonodon*
M46701	*Palaeoxonodon*
M46702	*Palaeoxonodon*
M46704	mammal indet.
M46713	mammal indet.
M46728	*Borealestes*
M46741	mammal indet.
M46761	*Cyrtlatherium*
M46764	mammal indet.
M46768	*Shuotherium*
m46775	*Wareolestes*
M46778	*Cyrtlatherium*
M46781	*Phascolotherium*
M46784	docodont
M46785	*Cyrtlatherium*
M46786	*Palaeoxonodon*
M46792	*Palaeoxonodon*
M46798	*Cyrtlatherium*
M46809	*Borealestes*
M46821	*Eleutherodon*
M46832	multituberculate
m46841	*Borealestes*
M46864	mammal indet.
PG03	*Eleutherodon*
PG04	*Eleutherodon*
PG05	*Eleutherodon*
PG06	multituberculate
PG07	*Phascolotherium*
Pg10	*Phascolotherium*

PG12	*Eleutherodon*

Appendix 6. List of all Bathonian taxa imaged using synchrotron radiation-based micro-computed tomography.

Appendix 6.2. List of all fossil taxa used in body mass estimation

Higher order taxon	Taxon	Molar count	Min. molar count	Max. molar count	m1 Length (mm)	Dentary length (mm)
docodonta	*Agilodocodon*	4	4	4	1.27	20.5
Dryolestidae	*Amblotherium*	seven to nine	7	9	0.8	18.3
Amphidontidae	*Amphidon*	4	4	4	1.3	16.9
Eutriconodonta	*Amphilestes*	5	5	5	1.52	22
amphitheriida	*Amphitherium*	five to seven	5	7	1.17	24.7
Zhangeotheriidae	*Anebodon*	4	4	4	2.3	35
Eutriconodonta	*Aploconodon*	5	5	5	1	17.9
Dryolestoidea	*Araeodon*	5	5	5	0.9	17.4
Dryolestoidea	*Archaeotrigon*	4	4	4	1.2	21.7
australosphenida	*bishops*	3	3	3	1.7	18.42
Eutriconodonta	*Comodon*	5	5	5	1.5	25.6
Docodonta	*Docodon*	7	7	7	1.5	32.6
Eutriconodonta	*Repenomamus*	4	4	4		82
docodonta	*Docodon apoxys*	7	7	7	1.58	33.2
docodonta	*Docofossor*	4	4	4	1.3	17.3
Dryolestidae	*Dryolestes*	eight to nine	8	9	1.3	32.3
Dryolestoidea	*Foxraptor*	5	5	5	1.2	21.7
docodonta	*Fruitafossor*	3	3	3	0.5	12.5
Eutriconodonta	*Gobiconodon borissiaki*	5	5	5	2.6	35.8
Eutriconodonta	*Gobiconodon hoburensis*	5	5	5	1.4	20
docodonta	*Haldanodon*	5	5	5	1.58	22.7
amphidontidae	*Juchilestes*	6	6	6	1.8	29.1
Dryolestidae	*Krebsotherium*	8	8	8	1	24.3
Dryolestidae	*Laolestes*	8	8	8	1.1	27.3
Dryolestoidea	*Paurodon*	4	4	4	1.2	21.7
Eutriconodonta	*Phascolotherium*	5	5	5	2	30.8
Eutriconodonta	*Phascolotherium*	5	5	5	2	35.5
Eutriconodonta	*Priacodon*	3	3	3	2.3	28.5
Eutriconodonta	*Priacodon*	4	4	4	2.4	33
Multituberculate	*Psalodon*	?	?	?	2.1	26.6
metatheria	*Sinodelphys*	3	3	3	1.48	20.8
spalacotheriidae	*Spalacotherium*	6	6	6	1.72	32.7
Eutriconodonta	*Spinolestes*	4	4	4	1.8	30
Dryolestoidea	*Tathiodon*	four to five	4	5	1.2	21.7
tinodontidae	*Tinodon*	4	4	4	2.2	28.6
Eutriconodonta	*Triconolestes*	5	5	5	1.5	24
Eutriconodonta	*Trioracodon*	3	3	3	2.6	32
eutriconodonta	*Trioracodon*	3	3	3	3.75	45.3

Zhangeotheriidae	*Zhangeotherium*	6	6	6	1.6	32.2

Appendix 6.2. List of all fossil taxa used in body mass estimation.

Therian mammals experience an ecomorphological radiation during the Late Cretaceous and selective extinction at the K-Pg boundary

It is often postulated that mammalian diversity was suppressed during the Mesozoic Era and increased rapidly after the Cretaceous–Palaeogene (K–Pg) extinction event. We test this hypothesis by examining macroevolutionary patterns in early therian mammals, the group that gave rise to modern placentals and marsupials. We assess morphological disparity and dietary trends using morphometric analyses of lower molars, and we evaluate generic level taxonomic diversity patterns using techniques that account for sampling biases. In contrast with the suppression hypothesis, our results suggest that an ecomorphological diversification of therians began 10–20 Myr prior to the K–Pg extinction event, led by disparate metatherians and Eurasian faunas. This diversification is concurrent with ecomorphological radiations of multituberculate mammals and flowering plants, suggesting that mammals as a whole benefitted from the ecological rise of angiosperms. In further contrast with the suppression hypothesis, therian disparity decreased immediately after the K–Pg boundary, probably due to selective extinction against ecological specialists and metatherians. However, taxonomic diversity trends appear to have been decoupled from disparity patterns, remaining low in the Cretaceous and substantially increasing immediately after the K–Pg extinction event. The conflicting diversity and disparity patterns suggest that earliest Palaeocene extinction survivors, especially eutherian dietary generalists, underwent rapid taxonomic diversification without considerable morphological diversification.

Reference:

Grossnickle, D. M., & Newham, E. (2016). Therian mammals experience an ecomorphological radiation during the Late Cretaceous and selective extinction at the K-Pg boundary. *Proceedings of the Royal Society B. 283*(1832), 20160256.

Complex neuroanatomy in the rostrum of the Isle of Wight theropod *Neovenator salerii*

The discovery of large, complex, internal canals within the rostra of fossil reptiles has been linked with an enhanced tactile function utilised in an aquatic context, so far in pliosaurids, the Cretaceous theropod *Spinosaurus*, and the related spinosaurid *Baryonyx*. Here, we report the presence of a complex network of large, laterally situated, anastomosing channels, discovered via micro-focus computed tomography (μCT), in the premaxilla and maxilla of *Neovenator*, a mid-sized allosauroid theropod from the Early Cretaceous of the UK. We identify these channels as neurovascular canals, that include parts of the trigeminal nerve; many branches of this complex terminate on the external surfaces of the premaxilla and maxilla where they are associated with foramina. *Neovenator* is universally regarded as a 'typical' terrestrial, predatory theropod, and there are no indications that it was aquatic, amphibious, or unusual with respect to the ecology or behaviour predicted for allosauroids. Accordingly, we propose that enlarged neurovascular facial canals shouldn't be used to exclusively support a model of aquatic foraging in theropods and argue instead that an enhanced degree of facial sensitivity may have been linked with any number of alternative behavioural adaptations, among them defleshing behaviour, nest selection/maintenance or social interaction.

Reference:

Barker, C. T., Naish, D., Newham, E., Katsamenis, O. L., & Dyke, G. (2017). Complex neuroanatomy in the rostrum of the Isle of Wight theropod *Neovenator Salerii*. *Scientific Reports, 7*(1), 3749.

References

- Aboulfadl, H., & Hulliger, J. (2015). Absolute polarity determination of teeth cementum by phase sensitive second harmonic generation microscopy. *Journal of Structural Biology*, *192*(1), 67–75. https://doi.org/10.1016/j.jsb.2015.08.011
- Allan, G. H., Cassey, P., Snelling, E. P., Maloney, S. K., & Seymour, R. S. (2014). Blood flow for bone remodelling correlates with locomotion in living and extinct birds. *Journal of Experimental Biology*, *217*(16), 2956–2962. https://doi.org/10.1242/jeb.102889
- Ambekar, R., Chittenden, M., Jasiuk, I., & Toussaint, K. C. (2012). Quantitative second-harmonic generation microscopy for imaging porcine cortical bone: Comparison to SEM and its potential to investigate age-related changes. *Bone*, *50*(3), 643–650. https://doi.org/10.1016/j.bone.2011.11.013
- Andreasen, J. O. (1980). Analysis of pathogenesis and topography of replacement root resorption (ankylosis) after replantation of mature permanent incisors in monkeys. *Swedish Dental Journal*, *4*(6), 231–240.
- Andreasen, J. O. (1980). The effect of removal of the coagulum in the alveolus before replantation upon periodontal and pulpal healing of mature permanent incisors in monkeys. *International Journal of Oral Surgery*, *9*(6), 458–461. https://doi.org/10.1016/S0300-9785(80)80076-7
- Andreasen, J. O. (1980). A time-related study of periodontal healing and root resorption activity after replantation of mature permanent incisors in monkeys. *Swedish Dental Journal*, *4*(3), 101–110.
- Antón, S. C., & Snodgrass, J. J. (2012). Origins and Evolution of Genus Homo: New Perspectives. *Current Anthropology*, *53*(S6), S479–S496. https://doi.org/10.1086/667692
- Beamish, R. J., & Chilton, D. E. (1982). Preliminary evaluation of a method to determine the age of sablefish (Anoplopoma fimbria). *Canadian Journal of Fisheries and Aquatic Sciences*, *39*(2), 277–287.
- Beasley, M. J. (1987). On incremental banding as an indicator. *Proceedings of the University of Bristol Spelaeological Society*, *18*(1), 116–128.
- Beasley, M. J., Brown, W. A. B., & Legge, A. J. (1992). Incremental banding in dental cementum: mathods of preperation for teeth from archaeological sites and for modern comparative specimens. *Osteoarchaeology*, *2*(1), 37–50.

- Benjamini, Y., & Hochberg, Y. (1995). Controlling the false discovery rate: a practical and powerful approach to multiple testing. *Journal of the Royal Statistical Society. Series B (Methodological)*, 289–300.
- Benjamini, Y., & Yekutieli, D. (2001). The control of the false discovery rate in multiple testing under depenency. *Annals of Statistics*, 1165–1188.
- Bennett, A. F., & Ruben, J. A. (1979). Endothermy and activity in vertebrates. *Science*, *206*(4419), 649–654.
- Benoit, J., Manger, P. R., & Rubidge, B. S. (2016). Palaeoneurological clues to the evolution of defining mammalian soft tissue traits. *Scientific Reports*, *6*. https://doi.org/10.1038/srep25604
- Benoit, J., Fernandez, V., Manger, P. R., & Rubidge, B. S. (2017). Endocranial Casts of Pre-Mammalian Therapsids Reveal an Unexpected Neurological Diversity at the Deep Evolutionary Root of Mammals. *Brain, Behavior and Evolution*. https://doi.org/10.1159/000481525
- Bergdahl, M. (2000). Salivary flow and oral complaints in adult dental patients. *Community Dentistry and Oral Epidemiology*, *28*(1), 59–66. Retrieved from http://www.ncbi.nlm.nih.gov/pubmed/10634685
- Bernstein, L., Depue, R. H., Ross, R. K., Judd, H. L., Pike, M. C., & Henderson, B. E. (1986). Higher maternal levels of free estradiol in first compared to second pregnancy: Early gestational differences. *Journal of the National Cancer Institute*, *76*(6), 1035–1039. https://doi.org/10.1093/jnci/76.6.1035
- Bi, S., Wang, Y., Guan, J., Sheng, X., & Meng, J. (2014). Three new Jurassic euharamiyidan species reinforce early divergence of mammals. *Nature*, *514*(7524), 579–584. https://doi.org/10.1038/nature13718
- Birnbacher, L., Willner, M., Velroyen, A., Marschner, M., Hipp, A., Meiser, J., … Pfeiffer, F. (2016). Experimental Realisation of Grating-based Phase-contrast Computed Tomography. *Scientific Reports*, *6*, 24022. https://doi.org/10.1038/srep24022
- Bixler, D., Muhler, J. C., & Shafer, W. G. (1955). The effects of castration, sex hormones, and desalivation on dental caries in the rat. *Journal of Dental Research*, *34*(6), 889–894. https://doi.org/10.1177/00220345550340061301

- Blois, J. L., Zarnetske, P. L., Fitzpatrick, M. C., & Finnegan, S. (2013). Climate change and the past, present, and future of biotic interactions. *Science*. https://doi.org/10.1126/science.1237184
- Bodkin, J. L., Burdin, A. M., & Ryazanov, D. A. (2000). Age- and sex-specific mortality and population structure in sea otters. *Marine Mammal Science*, *16(1)*, 201–219. https://doi.org/DOI 10.1111/j.1748-7692.2000.tb00913.x
- Bodkin, J. L., Mulchahy, D., & Lensink, C. J. (1993). Age-specific reproduction in female sea otters (Enhydra lutris) from south-central Alaska: analysis of reproductive tracts. *Canadian Journal of Zoology*, *71*(9), 1811–1815.
- Boggess, K. A. (2008). Maternal oral health in pregnancy. *Obstetrics and Gynecology*. https://doi.org/10.1097/AOG.0b013e31816a49d3
- Bosshardt, D., Luder, H. U., & Schroeder, H. E. (1989). Rate and growth pattern of cementum apposition as compared to dentine and root formation in a fluorochrome-labelled monkey (Macaca fascicularis). *Journal de Biologie Buccale*, *17*(1), 3–13. Retrieved from http://www.ncbi.nlm.nih.gov/pubmed/2738051
- Bosshardt, D. D., & Schroeder, H. E. (1992). Initial formation of cellular intrinsic fiber cementum in developing human teeth. A light-and electron-microscopic study. *Cell Tissue Research*, *267*, 321–335.
- Bosshardt, D. D., & Schroeder, H. E. (1996). Cementogenesis reviewed: a comparison between human premolars and rodent molars. *The Anatomical Record*, *245*(2), 267–292.
- Bosshardt, D. D., & Selvig, K. A. (1997). Dental cementum: the dynamic tissue covering of the root. *Periodontology*, *13*(1), 41–75.
- Bosshardt, D., Selvig, K., Bilgin, E., Gürgan, C. A., Arpak, M. N., Bostanci, H. S., Levine, M. (1997). Dental cementum: the dynamic tissue covering of the root. *Periodontology 2000*, *13*(6), 41–75. https://doi.org/10.1902/jop.2008.070482
- Bosshardt, D. D. (2008). Biological mediators and periodontal regeneration: A review of enamel matrix proteins at the cellular and molecular levels. In *Journal of Clinical Periodontology* (Vol. 35, pp. 87–105). https://doi.org/10.1111/j.1600-051X.2008.01264.x
- Bosshardt, D. D., & Nanci, A. (2004). Hertwig's epithelial root sheath, enamel matrix proteins, and initiation of cementogenesis in porcine teeth. *Journal of Clinical Periodontology*, *31*(3), 184–192. https://doi.org/10.1111/j.0303-6979.2004.00473.x

- Bosshardt, D., & Schroeder, H. E. (1990). Evidence for rapid multipolar and slow unipolar production of human cellular and acellular cementum matrix with intrinsic fibers. *Journal of Clinical Periodontology*, *17*(9), 663–668. https://doi.org/10.1111/j.1600-051X.1990.tb01690.x

- Botha-Brink, J., & Angielczyk, K. D. (2010). Do extraordinarily high growth rates in Permo-Triassic dicynodonts (Therapsida, Anomodontia) explain their success before and after the end-Permian extinction? *Zoological Journal of the Linnean Society*, *160*(2), 341–365. https://doi.org/10.1111/j.1096-3642.2009.00601.x

- Botha-Brink, J., Codron, D., Huttenlocker, A. K., Angielczyk, K. D., & Ruta, M. (2016). Breeding young as a survival strategy during earth's greatest mass extinction. *Scientific Reports*, *6*. https://doi.org/10.1038/srep24053

- Bou, J., Casinos, A., & Ocaña, J. (1987). Allometry of the limb long bones of insectivores and rodents. *Journal of Morphology*, *192*(2), 113–123. https://doi.org/10.1002/jmor.1051920204

- Bouxsein, M. L., Boyd, S. K., Christiansen, B. A., Guldberg, R. E., Jepsen, K. J., & Müller, R. (2010). Guidelines for assessment of bone microstructure in rodents using micro-computed tomography. *Journal of Bone and Mineral Research*, *25*(7), 1468–1486.

- Bowen, W. H., & Koch, G. (1970). Determination of age in monkeys (Macaca irus) on the basis of dental development. *Laboratory Animals*, *4*(1), 113–123. https://doi.org/10.1258/002367770781036481

- Bowen, W. D., Sergeant, D. E., & Øritsland, T. (1983). Validation of age estimation in the harp seal, Phoca groenlandica, using dental annuli. *Canadian Journal of Fisheries and Aquatic Sciences*, *40*(9), 1430–1441.

- Boyde, A., & Jones, S. J. (1968). Scanning electron microscopy of cementum and Sahrpey fibre bone. *Zeitschrift Für Zellforschung Und Mikroskopische Anatomie*, *92*(4), 536–548.

- Brink, K. S., Chen, Y., Wu, Y., Liu, W., Shieh, D., Huang, T. D., … Brink, K. S. (2016). Dietary adaptions in the ultrastructure of dinosaur dentine. *Journal of The Royal Society Interface*, *13*(December), 20160626. https://doi.org/10.1098/rsif.2016.0626

- Brothwell, D. R. (1981). *Digging up Bones*. New York: Cornell University Press.

- Brown, E., McKee, T., DiTomaso, E., Pluen, A., Seed, B., Boucher, Y., & Jain, R. (2003). Dynamic imaging of collagen and its modulation in tumors in vivo using second-harmonic generation. *Nature Medicine*, *9*(6), 796–800. https://doi.org/10.1038/nm879

- Brown, J. R. M., Millard, A. C., & Campagnola, P. J. (2003). Macromolecular structure of cellulose studied by second-harmonic generation imaging microscopy. *Optics Letters*, *28*(22), 2207–2209. https://doi.org/10.1364/OL.28.002207

- Bucher, H. C., Guyatt, G. H., Cook, R. J., Hatala, R., Cook, D. J., Lang, J. D., & Hunt, D. (1996). Effect of calcium supplementation on pregnancy-induced hypertension and preeclampsia: a meta-analysis of randomized controlled trials. *Jama*, *275*(14), 1113–1117. Retrieved from http://jama.jamanetwork.com/article.aspx?articleid=400093

- Buckley, K., Matousek, P., Parker, A. W., & Goodship, A. E. (2012). Raman spectroscopy reveals differences in collagen secondary structure which relate to the levels of mineralisation in bones that have evolved for different functions. *Journal of Raman Spectroscopy*, *43*(9), 1237–1243. https://doi.org/10.1002/jrs.4038

- Buikstra, J. E., & Ubelaker, D. H. (1994). *Standards for data collection from human skeletal remains*. *Proceedings of a Seminar at the Field Museum of Natural History* (Vol. 68).

- Burghardt, A. J., Link, T. M., & Majumdar, S. (2011). High-resolution computed tomography for clinical imaging of bone microarchitecture. In *Clinical Orthopaedics and Related Research* (Vol. 469, pp. 2179–2193). https://doi.org/10.1007/s11999-010-1766-x

- Burke, A. (1992). *Prey movements and settlement patterns during the Upper palaeolithic in southwestern France*. New York University.

- Burke, A. (1994). The killing season: zooarchaeology and seasonality. *Canadian Zooarchaeology/Zooarchéologie Canadienne*, *6*, 2–6.

- Burke, A., & Castanet, J. (1995). Histological observations of cementum growth in horse teeth and their application to archaeology. *Journal of Archaeological Science*, *22*(4), 479–493.

- Butler, P., & Sigogneau-Russell, D. (2016). Diversity of triconodonts in the Middle Jurassic of Great Britain. *Palaeontologia Polonica*, *67*, 35–65. https://doi.org/10.4202/pp.2016.67_035

- Campagnola, P. J., & Loew, L. M. (2003). Second-harmonic imaging microscopy for visualizing biomolecular arrays in cells, tissues and organisms. *Nature Biotechnology*, *21*(11), 1356–60. https://doi.org/10.1038/nbt894
- Campana, S. E. (2001). Accuracy, precision and quality control in age determination, including a review of the use and abuse of age validation methods. *Journal of Fish Biology*, *59*(2), 197–242.
- Campana, S. E., Annand, M. C., & McMillan, J. I. (1995). Graphical and statistical methods for determining the consistency of age determinations. *Transactions of the American Fisheries Society*, *124*(1), 131–138.
- Campana, S. E., & Moksness, E. (1991). Accuracy and precision of age and hatch date estimates from otolith microstructure examination. *ICES Journal of Marine Science*, *48*(3), 303–316. https://doi.org/10.1093/icesjms/48.3.303
- Campione, N. E., & Evans, D. C. (2012). A universal scaling relationship between body mass and proximal limb bone dimensions in quadrupedal terrestrial tetrapods. *BMC Biology*, *10*. https://doi.org/10.1186/1741-7007-10-60
- Carrel, W. K. (1994). Reproductive history of female black bears from dental cementum. *International Conference on Bear Research and Management*, *9*(1994), 205–212.
- Carriero, A., Doube, M., Vogt, M., Busse, B., Zustin, J., Levchuk, A., Shefelbine, S. J. (2014). Altered lacunar and vascular porosity in osteogenesis imperfecta mouse bone as revealed by synchrotron tomography contributes to bone fragility. *Bone*, *61*, 116–124. https://doi.org/10.1016/j.bone.2013.12.020
- Castanet, J., Croci, S., Aujard, F., Perret, M., Cubo, J., & De Margerie, E. (2004). Lines of arrested growth in bone and age estimation in a small primate: Microcebus murinus. *Journal of Zoology*, *263*(1), 31–39. https://doi.org/10.1017/S0952836904004844
- Cedurlund, G., Kjellander, P., & Stålfelt, F. (1991). Age determination of roe deer by tooth wear and cementum layers-tests with known age material. In *Transactions of the 20th Congress of the International Union of Game Biologists, Gödöllö* (pp. 540–545).
- Chappard, C., Bensalah, S., Olivier, C., Gouttenoire, P. J., Marchadier, A., Benhamou, C., & Peyrin, F. (2013). 3D characterization of pores in the cortical bone of human femur in the elderly at different locations as determined by synchrotron micro-computed tomography images. *Osteoporosis International*, *24*(3), 1023–1033. https://doi.org/10.1007/s00198-012-2044-4

- Charles, D. K., Condon, K., Cheverud, J. M., & Buikstra, J. E. (1986). Cementum annulation and age determination in Homo sapiens. I. Tooth variability and observer error. *American Journal of Physical Anthropology*, *71*(3), 311–320. https://doi.org/10.1002/ajpa.1330710306
- Charnov, E. L. (2001). Evolution of mammal life histories. *Evolutionary Ecology Research*, *3*(5), 521–535. https://doi.org/10.1016/0047-2484(91)90077-9
- Chen, D., Blom, H., Sanchez, S., Tafforeau, P., & Ahlberg, P. E. (2016). The stem osteichthyan Andreolepis and the origin of tooth replacement. *Nature*, *539*(7628), 237–241. https://doi.org/10.1038/nature19812
- Chen, Y.-C., Lee, S.-Y., Wu, Y., Brink, K., Shieh, D.-B., Huang, T. D., Sun, C.-K. (2015). Third-harmonic generation microscopy reveals dental anatomy in ancient fossils. *Optics Letters*, *40*(7), 1354–7. https://doi.org/10.1364/OL.40.001354
- Chiu, B. (1999). Multiple infections in carotid atherosclerotic plaques. *Am Heart J*, *138*(5 Pt 2), S534-6. https://doi.org/a101755 [pii]
- Christensen-Dalsgaard, S. N., Aars, J., Andersen, M., Lockyer, C., & Yoccoz, N. G. (2010). Accuracy and precision in estimation of age of Norwegian Arctic polar bears. *Polar Biology*, *33*(5), 589–597.
- Cifelli, R. L., & Davis, B. M. (2013). Palaeontology: Jurassic fossils and mammalian antiquity. *Nature*. https://doi.org/10.1038/500160a
- Cipriano, A. (2002). Cold stress in captive great apes recorded in incremental lines of dental cementum. *Folia Primatologica*. https://doi.org/10.1159/000060416
- Clarke, A., & Pörtner, H. O. (2010). Temperature, metabolic power and the evolution of endothermy. *Biological Reviews*. https://doi.org/10.1111/j.1469-185X.2010.00122.x
- Close, R. A., Friedman, M., Lloyd, G. T., & Benson, R. B. J. (2015). Evidence for a mid-Jurassic adaptive radiation in mammals. *Current Biology*, *25*(16), 2137–2142. https://doi.org/10.1016/j.cub.2015.06.047
- Cohen, M. N., & Bennett, S. (1993). Skeletal Evidence for Sex Roles and Gender Hierarchies in prehistory. *Sex and Gender Hierarchies*, (1979), 273–296.
- Colard, T., Bertrand, B., Naji, S., Delannoy, Y., & Bécart, A. (2015). Toward the adoption of cementochronology in forensic context. *International Journal of Legal Medicine*. https://doi.org/10.1007/s00414-015-1172-8

- Colard, T., Falgayrac, G., Bertrand, B., Naji, S., Devos, O., Balsack, C., Penel, G. (2016). New insights on the composition and the structure of the acellular extrinsic fiber cementum by Raman analysis. *PLoS ONE*, *11*(12). https://doi.org/10.1371/journal.pone.0167316

- Condon, K., Charles, D. K., Cheverud, J. M., & Buikstra, J. E. (1986). Cementum annulation and age determination in Homo sapiens. II. Estimates and accuracy. *American Journal of Physical Anthropology*, *71*(3), 321–330.

- Coy, P. L., & Garshelis, D. L. (1992). Reconstructing reproductive histories of black bears from the incremental layering in dental cementum. *Canadian Journal of Zoology*, *70*(11), 2150–2160. https://doi.org/10.1139/z92-290

- Crompton, A. W., Owerkowicz, T., Bhullar, B. A. S., & Musinsky, C. (2017). Structure of the nasal region of non-mammalian cynodonts and mammaliaforms: Speculations on the evolution of mammalian endothermy. *Journal of Vertebrate Paleontology*, *37*(1). https://doi.org/10.1080/02724634.2017.1269116

- Crompton, A. W., Taylor, C. R., & Jagger, J. A. (1978). Evolution of homeothermy in mammals. *Nature*, *272*(5651), 333–336. https://doi.org/10.1038/272333a0

- Cunningham, J. A., Rucklin, M., Blom, H., Botella, H., & Donoghue, P. C. (2012). Testing models of dental development in the earliest bony vertebrates, Andreolepis and Lophosteus. *Biol Lett*, *8*(5), 833–837. https://doi.org/rsbl.2012.0357 [pii]\r10.1098/rsbl.2012.0357

- Czermak, A., Czermak, A., Ernst, H., & Grupe, G. (2006). A new method for the automated age-at-death evaluation by tooth-cementum annulation (TCA). *Anthropologischer Anzeiger*, 25–40.

- D'Incau, E., Couture, C., & Maureille, B. (2012). Human tooth wear in the past and the present: Tribological mechanisms, scoring systems, dental and skeletal compensations. *Archives of Oral Biology*. https://doi.org/10.1016/j.archoralbio.2011.08.021

- Dalzell, N., Kaptoge, S., Morris, N., Berthier, A., Koller, B., Braak, L., Reeve, J. (2009). Bone micro-architecture and determinants of strength in the radius and tibia: Age-related changes in a population-based study of normal adults measured with high-resolution pQCT. *Osteoporosis International*, *20*(10), 1683–1694. https://doi.org/10.1007/s00198-008-0833-6

- Dashzeveg, D., Novacek, M. J., Norell, M. A., Clark, J. M., Chiappe, L. M., Davidson, A., Altangerel, P. (1995). Extraordinary preservation in a new vertebrate assemblage from the Late Cretaceous of Mongolia. *Nature*, *374*(6521), 446–449. https://doi.org/10.1038/374446a0
- Dean, L. G., Kendal, R. L., Schapiro, S. J., Thierry, B., & Laland, K. N. (2012). Identification of the social and cognitive processes underlying human cumulative culture. *Science*, *335*(6072), 1114–1118. https://doi.org/10.1126/science.1213969
- DeGabriel, J. L., Moore, B. D., Foley, W. J., & Johnson, C. N. (2009). The effects of plant defensive chemistry on nutrient availability predict reproductive success in a mammal. *Ecology*, *90*(3), 711–719. https://doi.org/10.1890/08-0940.1
- Delman, L. A. (1955). Effect of gonadectomy on dental caries: review of the literature. *Journal of the American Dental Association (1939)*, *51*(2), 155–158. https://doi.org/10.14219/jada.archive.1955.0175
- DeMaster, D. P. (1984). Review of techniques used to estimate the average age at attainment of sexual maturity in marine mammals. *Reports of the International Whaling Comission, Special*, *6*, 175–179.
- DeSantis, L. R. G. (2016). Dental microwear textures: Reconstructing diets of fossil mammals. *Surface Topography: Metrology and Properties*. https://doi.org/10.1088/2051-672X/4/2/023002
- Dodds, M. W. J., Johnson, D. A., & Yeh, C. K. (2005). Health benefits of saliva: A review. *Journal of Dentistry*. https://doi.org/10.1016/j.jdent.2004.10.009
- Dong, W., Sullivan, P., & Stout, K. (1993). Comprehensive study of parameters for characterizing three-dimensional surface topography II: Statistical properties of parameter variation. *Wear*, *167*(1), 9–21. https://doi.org/10.1016/0043-1648(93)90050-V
- Dong, W. P., Sullivan, P. J., & Stout, K. J. (1992). Comprehensive study of parameters for characterizing three-dimensional surface topography I: Some inherent properties of parameter variation. *Wear*, *159*(2), 161–171. https://doi.org/10.1016/0043-1648(92)90299-N
- Douhard, M., Festa-Bianchet, M., Coltman, D. W., & Pelletier, F. (2016). Paternal reproductive success drives sex allocation in a wild mammal. *Evolution*, *70*(2), 358–368. https://doi.org/10.1111/evo.12860

- Dreyfuss, F., Frank, R. M., & Gutmann, B. (1964). LA sclérose dentinaire. *Bulletin Du Groupèment International Pour La Recherche Scientifique En Stomatologie & Odontologie*, *7*, 207–229.
- Driscoll, K. M., Jones, G. S., & Nichy, F. (1985). An efficient method by which to determine age of carnivores, suing dentine rings. *Journal of Zoology*, *205*(2), 309–313.
- Dudar, J. C., Pfeiffer, S., & Saunders, S. R. (1993). Evaluation of morphological and histological adult skeletal age-at-death estimation techniques using ribs. *Journal of Forensic Science*, *38*(3), 677–685.
- Dumont, M., Tafforeau, P., Bertin, T., Bhullar, B. A., Field, D., Schulp, A., … Louchart, A. (2016). Synchrotron imaging of dentition provides insights into the biology of Hesperornis and Ichthyornis, the "last" toothed birds. *BMC Evolutionary Biology*, *16*(1). https://doi.org/10.1186/s12862-016-0753-6
- Dunn, O. J. (1961). Multiple comparisons among means. *American Statistical Association*, *56*(293), 52–64.
- Dutta, S., & Sengupta, P. (2016). Men and mice: Relating their ages. *Life Sciences*. https://doi.org/10.1016/j.lfs.2015.10.025
- Enax, J., Fabritius, H. O., Rack, A., Prymak, O., Raabe, D., & Epple, M. (2013). Characterization of crocodile teeth: Correlation of composition, microstructure, and hardness. *Journal of Structural Biology*, *184*(2), 155–163. https://doi.org/10.1016/j.jsb.2013.09.018
- Erickson, G. M., Krick, B. A., Hamilton, M., Bourne, G. R., Norell, M. A., Lilleodden, E., & Sawyer, W. G. (2012). Complex dental structure and wear biomechanics in hadrosaurid dinosaurs. *Science*, *338*(6103), 98–101.
- Esfahani, M., Munir, K. S., Wen, C., Zhang, J., Durandet, Y., Wang, J., & Wong, Y. C. (2018). Mechanical properties of electrodeposited nanocrystalline and ultrafine-grained Zn-Sn coatings. *Surface and Coatings Technology*, *333*, 71–80. https://doi.org/10.1016/j.surfcoat.2017.10.059
- Evans, A. R. (2013). Shape descriptors as ecometrics in dental ecology. *Hystrix*. https://doi.org/10.4404/hystrix-24.1-6363
- Evans, S. E., Milner, A. R., Fraser, N. C., & Sues, H. D. (1994). Middle Jurassic microvertebrate assemblages from the British Isles. *In the Shadow of the Dinosaurs: Early Mesozoic Tetrapods*, 303–321.

- Fancy, S. G. (1980). Preparation of mammalian teeth for age determination by cementum layers: a review. *Wildlife Society Bulletin*, 242–248.
- Farmer, C. G. (2003). Reproduction: the adaptvie significance of endothermy. *The American Naturalist*, *162*(6), 826–840.
- Farmer, C. G. (2000). Parental Care: The Key to Understanding Endothermy and Other Convergent Features in Birds and Mammals. *The American Naturalist*, *155*(3), 326–334. https://doi.org/10.1086/303323
- Flessa, K. W., Cutler, A. H., & Meldahl, K. H. (1993). Time and taphonomy: Quantitative estimates of time-averaging and stratigraphic disorder in a shallow marine habitat. *Paleobiology*, *19*(2), 266–286. https://doi.org/10.1017/S0094837300015918
- Folarin, A. A., Konerding, M. A., Timonen, J., Nagl, S., & Pedley, R. B. (2010). Three-dimensional analysis of tumour vascular corrosion casts using stereoimaging and micro-computed tomography. *Microvascular Research*, *80*(1), 89–98. https://doi.org/10.1016/j.mvr.2010.03.007
- Foster, B. L. (2012). Methods for studying tooth root cementum by light microscopy. *International Journal of Oral Science*, *4*(3), 119.
- Foster, J. R. (2009). Preliminary body mass estimates for mammalian genera of the Morrison Formation (Upper Jurassic, North America). *PaleoBios*, *28*(3), 114–122.
- Fourmaux, S., Kieffer, J. C., & Krol, A. (2017). Ultrahigh resolution and briliance laser wakefield accelerator betatron X-ray source for rapid in vivo tomographic microvasculature imaging in small animal models. *SPIE Medical Imaging*, 1013715.
- Fourmax, S., Kieffer, J. C., & Krol, A. (2017). Ultrahigh resolution and brilliance laser wakefield accelerator betatron X-ray source for rapid in vivo tomographic microvasulature imaging in small animal models. *Medical Imaging 2017: Biomedical Applications in Molecular, Structural, and Functional Imaging*, *10137*, 1013715.
- Freeman, E. (1976). Mammal teeth from the Forest Marble (Middle Jurassic) of Oxfordshire, England. *Science*, *194*(4269), 1053–1055. https://doi.org/10.1126/science.194.4269.1053
- Freeman, E. F. (1979). A Middle Jurassic mammal bed from Oxfordshire. *Palaeontology*, *22*(1), 135–166.

- Freeman, W. T., & Adelson, E. H. (1991). The Design and Use of Steerable Filters. *IEEE Transactions on Pattern Analysis and Machine Intelligence*, *13*(9), 891–906. https://doi.org/10.1109/34.93808
- Freilich, M., Virapongse, C., Kier, E. L., Sarwar, M., & Bhimani, S. (1986). Foramen transversarium enlargement due to tortuosity of the vertebral artery: computed tomographic appearance. *Spine*, *11*(1), 95–98.
- Frie, A. K., Fagerheim, K. A., Hammill, M. O., Kapel, F. O., Lockyer, C., Stenson, G. B., Svetochev, V. (2011). Error in age estimation of harp seals (Pagophilus groenlandicus): results from a transatlantic, image-based, blind-reading experiment using known-age teeth. *ICES Journal of Marine Science*, *68*(9), 1942–1953.
- Frie, A. K., Hammill, M. O., Hauksson, E., Lind, Y., Lockyer, C., Stenman, O., & Svetocheva, O. (2013). Error patterns in age estimation and tooth readability assignment of grey seals (Halichoerus grypus): Results from a transatlantic, image-based, blind-reading study using known-age animals. *ICES Journal of Marine Science*, *70*(2), 418–430. https://doi.org/10.1093/icesjms/fss169
- Friedlander, A. H. (2002). The physiology, medical management and oral implications of menopause. *Journal of the American Dental Association*, *133*(1), 73–81. https://doi.org/10.14219/jada.archive.2002.0025
- Fuentes, A. (2016). The Extended Evolutionary Synthesis, Ethnography, and the Human Niche: Toward an Integrated Anthropology. *Current Anthropology*, *57*(S13), S13–S26. https://doi.org/10.1086/685684
- Fuentes, A., Wyczalkowski, M. A., & MacKinnon, K. C. (2010). Niche Construction through Cooperation: A Nonlinear Dynamics Contribution to Modeling Facets of the Evolutionary History in the Genus *Homo*. *Current Anthropology*, *51*(3), 435–444. https://doi.org/10.1086/651221
- Gadelmawla, E. S., Koura, M. M., Maksoud, T. M. A., Elewa, I. M., & Soliman, H. H. (2002). Roughness parameters. *Journal of Materials Processing Technology*, *123*(1), 133–145. https://doi.org/10.1016/S0924-0136(02)00060-2
- Gai, Z., Donoghue, P. C. J., Zhu, M., Janvier, P., & Stampanoni, M. (2011). Fossil jawless fish from China foreshadows early jawed vertebrate anatomy. *Nature*, *476*(7360), 324–327. https://doi.org/10.1038/nature10276

- Gajendra, S., & Kumar, J. V. (2004). Oral health and pregnancy: a review. *The New York State Dental Journal*, *70*(1), 40–44.
- García, R. A., & Zurriaguz, V. (2016). Histology of teeth and tooth attachment in titanosaurs (Dinosauria; Sauropoda). *Cretaceous Research*, *57*, 248–256. https://doi.org/10.1016/j.cretres.2015.09.006
- Gasaway, W. C., Harkness, D. B., & Rausch, R. A. (1978). Accuracy of moose age determinations from incisor cementum layers. *The Journal of Wildlife Management*, 558–563.
- Gauthier, J., & Schutkowski, H. (2013). Assessing the application of tooth cementum annulation relative to macroscopic aging techniques in an archeological sample. *HOMO-Journal of Comparative Human Biology*, *64*(1), 42–57. https://doi.org/10.1016/j.jchb.2012.11.001
- Geppert, E. G., & Muller, K. H. (1951). Apposition of the radicular cementum as a measurable manifestation of masticatory stress. *Deutsche Zahn, Mund, Und Kieferheilkunde Mit Zentralblatt Fur Die Gesamte Zahn, Mund, Und Kieferheilkunde*, *15*(1–2), 30.
- Gignac, P. M., Kley, N. J., Clarke, J. A., Colbert, M. W., Morhardt, A. C., Cerio, D., … Echols, M. S. (2016). Diffusable iodine-based contrast-enhanced computed tomography (diceCT): an emerging tool for rapid, high resolution, 3D imaging of metazoan soft tissues. *Journal of Anatomy*, *228*(6), 889–909.
- Gill, P. G., Purnell, M. A., Crumpton, N., Brown, K. R., Gostling, N. J., Stampanoni, M., & Rayfield, E. J. (2014). Dietary specializations and diversity in feeding ecology of the earliest stem mammals. *Nature*, *512*(7514), 303–305. https://doi.org/10.1038/nature13622
- Gingerich, P. D., & Smith, B. H. (1984). Allometric scaling in the dentition of primates and insectivores. In W. L. Jungers (Ed.), *Size and Scaling in Primate Biology* (pp. 257–272). New York: Plenum Press.
- Giroud, S., Blanc, S., Aujard, F., Bertrand, F., Gilbert, C., & Perret, M. (2008). Chronic food shortage and seasonal modulations of daily torpor and locomotor activity in the grey mouse lemur (*Microcebus murinus*). *American Journal of Physiology-Regulatory, Integrative and Comparative Physiology*, *294*(6), R1958–R1967. https://doi.org/10.1152/ajpregu.00794.2007

- Gittleman, J. L., & Stephens, P. R. (2012). Rates of metabolism and evolution. In R. M. Sibly, J. H. Brown, & A. Kodric-Brown (Eds.), *Metabolic Ecology: a Scaling Approach* (pp. 112–119). John Wiley & Sons.
- Goodwin, E. A., & Ballard, W. B. (1985). Use of tooth cementum for age determination of gray walves. *The Journal of Wildlife Management*, *49*(2), 313–316.
- Gourichon, L., & Parmigiani, V. (2016). Preliminary analysis of dental cementum of Lama guanicoe for the estimation of age and season at death: Studies of modern specimens and further archaeological applications. *Journal of Archaeological Science: Reports*, *6*, 856–861.
- Grady, J. M., Enquist, B. J., Dettweiler-Robinson, N. A., & Smith, F. A. (2014). Evidence for mesothermy in dinosaurs. *Science*, *344*(6189), 1268–1272.
- Grandfield, K., Chattah, N. L.-T., Djomehri, S., Eidelmann, N., Eichmiller, F. C., Webb, S., … Ho, S. P. (2014). The narwhal (Monodon monoceros) cementum-dentin junction: a functionally graded biointerphase. *Proceedings of the Institution of Mechanical Engineers. Part H, Journal of Engineering in Medicine*, *228*(8), 754–67. https://doi.org/10.1177/0954411914547553
- Grandfield, K., Herber, R. P., Chen, L., Djomehri, S., Tam, C., Lee, J. H., … Ho, S. P. (2015). Strain-guided mineralization in the bone-PDL-cementum complex of a rat periodontium. *Bone Reports*, *3*, 20–31. https://doi.org/10.1016/j.bonr.2015.04.002
- Grau, G. a, Sanderson, G. C., & Rogers, J. P. (1970). Age Determination of Raccoons. *The Journal of Wildlife Management*, *34*(2), 364–372. https://doi.org/10.2307/3799023
- Grigg, G. C., Beard, L. A., & Augee, M. L. (2004). The Evolution of Endothermy and Its Diversity in Mammals and Birds. *Physiological and Biochemical Zoology*, *77*(6), 982–997. https://doi.org/10.1086/425188
- Grine, F. E. (1991). Computed tomography and the measurement of enamel thickness in extant hominoids: implications for its palaeontological application. *Palaeontologica Africana*, *28*, 61–69.
- Gross, W. (1934). Die Typen des mikroskopischen Knochenbaues bei fossilen Stegoccphalen und Reptilien. *Anatomy and Embryology*, *103*(6), 731–764.
- Grossnickle, D. M., & Polly, P. D. (2013). Mammal disparity decreases during the Cretaceous angiosperm radiation. *Proceedings of the Royal Society B: Biological Sciences*, *280*(1771), 20132110–20132110. https://doi.org/10.1098/rspb.2013.2110

- Grossnickle, D. M., & Newham, E. (2016). Therian mammals experience an ecomorphological radiation during the Late Cretaceous and selective extinction at the K–Pg boundary. *Proceedings of the Royal Society B: Biological Sciences*, *283*(1832), 20160256. https://doi.org/10.1098/rspb.2016.0256
- Grue, H., & Jensen, B. (1979). Review of the formation of incremental lines in tooth cementum of terrestrial mammals [age determination, game animal, variation, sex, reproductive cycle, climate, region, condition of the animal]. *Danish Review of Game Biology*.

- Grue, H., & Jensen, B. (1979). Review of the formation of incremental lines in tooth cementum of terrestrial mammals [age determination, game animal, variation, sex, reproductive cycle, climate, region, condition of the animal]. *Danish Review of Game Biology*.

- Haigh, A., Kelly, M., Butler, F., & O'Riordan, R. M. (2014). Non-invasive methods of separating hedgehog (Erinaceus europaeus) age classes and an investigation into the age structure of road kill. *Acta Theriologica*, *59*(1), 165–171. https://doi.org/10.1007/s13364-013-0142-0
- Hames, W. (2003). Evolutionary Catastrophes: The Science of Mass Extinction. *Eos, Transactions American Geophysical Union*, *84*(21), 202. https://doi.org/10.1029/2003EO210009
- Hamlin, K. L., Pac, D. F., Sime, C. A., DeSimone, R. M., & Dusek, G. L. (2000). Evaluating the accuracy of ages obtained by two methods for Montana ungulates. *The Journal of Wildlife Management*, 441–449.
- Han, G., Mao, F., Bi, S., Wang, Y., & Meng, J. (2017). A Jurassic gliding euharamiyidan mammal with an ear of five auditory bones. *Nature*, *551*(7681), 451–456. https://doi.org/10.1038/nature24483
- Han, M., Giese, G., & Bille, J. (2005). Second harmonic generation imaging of collagen fibrils in cornea and sclera. *Optics Express*, *13*(15), 5791–5797. https://doi.org/10.1364/OPEX.13.005791
- Hara, T., Tanck, E., Homminga, J., & Huiskes, R. (2002). The influence of microcomputed tomography threshold variations on the assessment of structural and mechanical trabecular bone properties. *Bone*, *31*(1), 107–109. https://doi.org/10.1016/S8756-3282(02)00782-2

- Haugejorden, O. (1996). Using the DMF gender difference to assess the “major” role of fluoride toothpastes in the caries decline in industrialized countries: a meta-analysis. *Community Dent Oral Epidemiol*, *24*(6), 369–375. https://doi.org/10.1111/j.1600-0528.1996.tb00881.x
- Hedrick, M. S., & Hillman, S. S. (2016). What drove the evolution of endothermy? *Journal of Experimental Biology*, *219*(3), 300–301. https://doi.org/10.1242/jeb.128009
- Hiiemae, K. M., & Crompton, A. W. (1985). mastication, food transport, and swallowing. In M. Hildebrand, D. M. Bramble, K. F. Liem, & D. B. Wake (Eds.), *Functional Vertebrate Morphology* (pp. 262–290). Harvard University Press.
- Hiiemae, K. M., & Crompton, A. W. (1985). Mastication, food transport, and swallowing. In M. Hildebrand (Ed.), *Functional Vertebrate Morphology* (1st ed., pp. 262–290). Cambridge, Massachusetts: Harvard University Press.
- Hillenius, W. J. (1994). Turbinates in therapsids: Evidence for late Permian origins of mammalian endothermy. *Evolution*, *48*(2), 207–229. https://doi.org/10.2307/2410089
- Hillenius, W. J., & Ruben, J. A. (2004). The Evolution of Endothermy in Terrestrial Vertebrates: Who? When? Why? *Physiological and Biochemical Zoology*, *77*(6), 1019–1042. https://doi.org/10.1086/425185
- Hillson, S. (2001). Recording dental caries in archaeological human remains. *International Journal of Osteoarchaeology*, *11*(4), 249–289. https://doi.org/10.1002/oa.538
- Ho, S. P., Goodis, H., Balooch, M., Nonomura, G., Marshall, S. J., & Marshall, G. (2004). The effect of sample preparation technique on determination of structure and nanomechanical properties of human cementum hard tissue. *Biomaterials*, *25*(19), 4847–4857. https://doi.org/10.1016/j.biomaterials.2003.11.047
- Ho, S. P., Kurylo, M. P., Fong, T. K., Lee, S. S. J., Wagner, H. D., Ryder, M. I., & Marshall, G. W. (2010). The biomechanical characteristics of the bone-periodontal ligament-cementum complex. *Biomaterials*, *31*(25), 6635–6646. https://doi.org/10.1016/j.biomaterials.2010.05.024
- Ho, S. P., Marshall, S. J., Ryder, M. I., & Marshall, G. W. (2007). The tooth attachment mechanism defined by structure, chemical composition and mechanical properties of collagen fibers in the periodontium. *Biomaterials*, *28*(35), 5238–5245. https://doi.org/10.1016/j.biomaterials.2007.08.031

- Hoppa, R. D. (2000). Population variation in osteological aging criteria: An example from the pubic symphysis. *American Journal of Physical Anthropology*, *111*(2), 185–191. https://doi.org/10.1002/(SICI)1096-8644(200002)111:2<185::AID-AJPA5>3.0.CO;2-4

- Hopson, J. A. (2012). The Role of Foraging Mode in the Origin of Therapsids: Implications for the Origin of Mammalian Endothermy. *Fieldiana Life and Earth Sciences*, *5*, 126–148. https://doi.org/10.3158/2158-5520-5.1.126

- Hübscher, W., Barbakow, F., & Peters, O. A. (2003). Root-canal preparation with FlexMaster: Canal shapes analysed by micro-computed tomography. *International Endodontic Journal*, *36*(11), 740–747. https://doi.org/10.1046/j.1365-2591.2003.00723.x

- Hugoson, A. (1970). Gingivitis in pregnant women. A longitudinal clinical study. *Odontologisk Revy*, *21*(1), 1–20.

- Hulbert, A. J., Beard, L. A., & Grigg, G. C. (2008). The exceptional longevity of an egg-laying mammal, the short-beaked echidna (Tachyglossus aculeatus) is associated with peroxidation-resistant membrane composition. *Experimental Gerontology*, *43*(8), 729–733. https://doi.org/10.1016/j.exger.2008.05.015

- Hulbert, A. J., Pamplona, R., Buffenstein, R., & Buttemer, W. A. (2007). Life and Death: Metabolic Rate, Membrane Composition, and Life Span of Animals. *Physiological Reviews*, *87*(4), 1175–1213. https://doi.org/10.1152/physrev.00047.2006

- Hurng, J. M., Kurylo, M. P., Marshall, G. W., Webb, S. M., Ryder, M. I., & Ho, S. P. (2011). Discontinuities in the human bone-PDL-cementum complex. *Biomaterials*, *32*(29), 7106–7117. https://doi.org/10.1016/j.biomaterials.2011.06.021

- Huttenlocker, A. K., & Rega, E. (2012). The paleobiology and bone microstructure of pelycosaurian-grade synapsids. In A. Chinsamy-Turan (Ed.), *Forerunners of mammals: Radiation, histology biology* (pp. 90–119). Indiana: Indiana University Press.

- Huttenlocker, A. K., & Farmer, C. G. (2017). Bone Microvasculature Tracks Red Blood Cell Size Diminution in Triassic Mammal and Dinosaur Forerunners. *Current Biology*, *27*(1), 48–54. https://doi.org/10.1016/j.cub.2016.10.012

- Immel, A., Le Cabec, A., Bonazzi, M., Herbig, A., Temming, H., Schuenemann, V. J., Krause, J. (2016). Effect of X-ray irradiation on ancient DNA in sub-fossil bones - Guidelines for safe X-ray imaging. *Scientific Reports*, *6*. https://doi.org/10.1038/srep32969

- Inoue, T., Saito, M., Yamamoto, M., Fumio, N., & Miyazaki, T. (2013). Mineral density of coronal and radicular dentin. *Dental Medicine Research*, *33*(3), 248–251.
- Isoda, K., Ayukawa, Y., Tsukiyama, Y., Sogo, M., Matsushita, Y., & Koyano, K. (2012). Relationship between the bone density estimated by cone-beam computed tomography and the primary stability of dental implants. *Clinical Oral Implants Research*, *23*(7), 832–836. https://doi.org/10.1111/j.1600-0501.2011.02203.x
- Jang, A. T., Lin, J. D., Choi, R. M., Choi, E. M., Seto, M. L., Ryder, M. I., … Ho, S. P. (2014). Adaptive properties of human cementum and cementum dentin junction with age. *Journal of the Mechanical Behavior of Biomedical Materials*, *39*, 184–196. https://doi.org/10.1016/j.jmbbm.2014.07.015
- Jeffery, N. S., Stephenson, R. S., Gallagher, J. A., Jarvis, J. C., & Cox, P. G. (2011). Micro-computed tomography with iodine staining resolves the arrangement of muscle fibres. *Journal of Biomechanics*, *44*(1), 189–192. https://doi.org/10.1016/j.jbiomech.2010.08.027
- Ji, Q., Luo, Z. X., Yuan, C. X., & Tabrum, A. R. (2006). A swimming mammaliaform from the middle jurassic and ecomorphological diversification of early mammals. *Science*, *311*(5764), 1123–1127. https://doi.org/10.1126/science.1123026
- Jones, D. S. (1988). Sclerochronology and the size versus age problem. *Heterochrony in Evolution*, 93–108.
- Jordana, X., & Köhler, M. (2011). Enamel microstructure in the fossil bovid Myotragus balearicus (Majorca, Spain): implications for life-history evolution of dwarf mammals in insular ecosystems. *Palaeogeography, Palaeoclimatology, Palaeoecology*, *300*(1), 59–66.
- Umetani, K., & Fukushima, F. (2013). X-ray intravital microscopy for functional imaging in rat hearts using synchrotron radiation coronary microangiography. *The Review of Scientific Instruments*, *84*(3), 34302. https://doi.org/10.1063/1.4795830
- Kagerer, P., & Grupe, G. (2001). Age-at-death diagnosis and determination of life-history parameters by incremental lines in human dental cementum as an identification aid. *Forensic Science International*, *118*(1), 75–82.
- Kahn, J., & Mohead, M. (2010). *A protocol for use of Shortnose, Atlantic, Gulf, and Green sturgeons*. U.S. Department of Commerce, NOAA Tech. Memo. NMFS-OPR-45.

- Kaifu, Y., Kasai, K., Townsend, G. C., & Richards, L. C. (2003). Tooth Wear and the "Design" of the Human Dentition: A Perspective from Evolutionary Medicine. *American Journal of Physical Anthropology*. https://doi.org/10.1002/ajpa.10329
- Kaplan, H., Mueller, T., Gangestad, S., & Lancaster, J. (2003). Neural Capital and Life span Evolution among Primates and Humans. *Brain and Longevity*. Retrieved from http://scholar.google.com/scholar?hl=en&btnG=Search&q=intitle:Neural+Capital+and+Life+span+Evolution+among+Primates+and+Humans#0
- Kasetty, S., Rammanohar, M., & Raju Ragavendra, T. (2010). Dental cementum in age estimation: A polarized light and stereomicroscopic study. *Journal of Forensic Sciences*, *55*(3), 779–783. https://doi.org/10.1111/j.1556-4029.2010.01363.x
- Kay, R. F., & Cant, J. G. H. (1988). Age assessment using cementum annulus counts and tooth wear in a free-ranging population of Macaca mulatta. *American Journal of Primatology*, *15*(1), 1–15. https://doi.org/10.1002/ajp.1350150103
- Kemp, T. S. (2007). The origin of higher taxa: Macroevolutionary processes, and the case of the mammals. *Acta Zoologica*. https://doi.org/10.1111/j.1463-6395.2007.00248.x
- Kemp, T. S. (2006). The origin and early radiation of the therapsid mammal-like reptiles: A palaeobiological hypothesis. *Journal of Evolutionary Biology*. https://doi.org/10.1111/j.1420-9101.2005.01076.x
- Kendal, J., Tehrani, J. J., & Odling-Smee, J. (2011). Human niche construction in interdisciplinary focus. *Philosophical Transactions of the Royal Society B: Biological Sciences*, *366*(1566), 785–792. https://doi.org/10.1098/rstb.2010.0306
- Kermack, K. A., & Mussett, F. (1973). The lower jaw of Morganucodon. *Zoological Journal of the Linnean Society*, *53*(2), 87–175.
- Kielan-Jaworowska, Z., Cifelli, R. L., & Zhe-Xi Luo. (2006). Mammals from the Age of Dinosaurs Origins, Evolution, and Structure. *Journal of Mammalian Evolution*, *13*(2), 147–149. https://doi.org/10.1007/s10914-006-9010-x
- Kielan-Jaworowska, Z., & Hurum, J. H. (2006). Limb posture in early mammals : Sprawling or parasagittal. *Acta Palaeontologica Polonica*, *51*(3), 393–406.
- Kinnby, B., Matsson, L., & Åstedt, B. (1996). Aggravation of gingival inflammatory symptoms during pregnancy associated with the concentration of plasminogen activator

inhibitor type 2 (PAI-2) in gingival fluid. *Journal of Periodontal Research*, *31*(4), 271–277.

- Kitchen, M. J., Buckley, G. A., Gureyev, T. E., Wallace, M. J., Andres-Thio, N., Uesugi, K., … Hooper, S. B. (2017). CT dose reduction factors in the thousands using X-ray phase contrast. *Scientific Reports*, *7*(1). https://doi.org/10.1038/s41598-017-16264-x
- Klauenberg, K., & Lagona, F. (2007). Hidden Markov random field models for TCA image analysis. *Computational Statistics & Data Analysis*, *52*(2), 855–868.
- Klevezal, G. A. (1995). *Recording structures of mammals*. Routledge.
- Klevezal, G. A. (1975). On seasonal rhythms of growth in hibernating mammals. *Zoologicheskii Zhurnal*, *54*(1), 95–102.
- Klevezal, G. A., & Kleinenberg, S. E. (1967). *Age determination of mammals by layered structures in teeth and bone*. Sainte Anne de Bellevue, Quebec: Fisheries Research Board of Canada.
- Klevezal, G. A., & Kleinenberg, S. E. (1967). *Age determination of mammals from annual layers in teeth and bones*. USSR Acadamy of sciene Severtsov Institute of Animal Morphology.
- Klevezal, G. A., & Shishlina, N. I. (2001). Assessment of the season of death of ancient human from cementum annual layers. *Journal of Archaeological Science*, *28*(5), 481–486. https://doi.org/10.1006/jasc.2000.0585
- Klevezal, G. A., & Pucek, Z. (1987). Growth layers in tooth cement and dentine of European bison and its hybrids with domestic cattle. *Acta Theriologica*, *32*(9), 115–128. https://doi.org/10.4098/AT.arch.87-10
- Klevezal, G. A., & Stewart, B. S. (1994). Patterns and Calibration of Layering in Tooth Cementum of Female Northern Elephant Seals, Mirounga angustirostris. *Journal of Mammalogy*, *75*(2), 483–487. https://doi.org/10.2307/1382571
- Köhler, M., Marín-Moratalla, N., Jordana, X., & Aanes, R. (2012). Seasonal bone growth and physiology in endotherms shed light on dinosaur physiology. *Nature*, *487*(7407), 358–361. https://doi.org/10.1038/nature11264
- Kolb, C., Scheyer, T. M., Veitschegger, K., Forasiepi, A. M., Amson, E., Van der Geer, A. A. E., … Sánchez-Villagra, M. R. (2015). Mammalian bone palaeohistology: a survey

and new data with emphasis on island forms. *PeerJ*, *3*, e1358. https://doi.org/10.7717/peerj.1358

- Kolb, H. (1978). The formation of lines in the cementum of premolar teeth in foxes. *Journal of Zoology*, *185*(2), 259–263. https://doi.org/10.1111/j.1469-7998.1978.tb03326.x
- Koteja, P. (2000). Energy assimilation, parental care and the evolution of endothermy. *Proceedings of the Royal Society B: Biological Sciences*, *267*(1442), 479–484. https://doi.org/10.1098/rspb.2000.1025
- Kottek, M., Grieser, J., Beck, C., Rudolf, B., & Rubel, F. (2006). World map of the Köppen-Geiger climate classification updated. *Meteorologische Zeitschrift*, *15*(3), 259–263.
- Krause, D. W., Hoffmann, S., Wible, J. R., Kirk, E. C., Schultz, J. A., von Koenigswald, W., … Andriamialison, H. (2014). First cranial remains of a gondwanatherian mammal reveal remarkable mosaicism. *Nature*, *515*(7528), 512–517. https://doi.org/10.1038/nature13922
- Krenkel, M., Töpperwien, M., Dullin, C., Alves, F., & Salditt, T. (2016). Propagation-based phase-contrast tomography for high-resolution lung imaging with laboratory sources. *AIP Advances*, *6*(3). https://doi.org/10.1063/1.4943898
- Kryštufek, B., Pistotnik, M., & Časar, K. S. (2005). Age determination and age structure in the edible dormouse Glis glis based on incremental bone lines. *Mammal Review*, *35*(2), 210–214. https://doi.org/10.1111/j.1365-2907.2005.00056.x
- Kuhn, J. L., Goldstein, S. A., Feldkamp, L. A., Goulet, R. W., & Jesion, G. (1990). Evaluation of a microcomputed tomography system to study trabecular bone structure. *Journal of Orthopaedic Research*, *8*(6), 833–842.
- Kvaal, S. I., & Solheim, T. (1995). Incremental lines in human dental cementum in relation to age. *European Journal of Oral Sciences*, *103*(4), 225–230. https://doi.org/10.1111/j.1600-0722.1995.tb00164.x
- Kvaal, S. I., Solheim, T., & Bjerketvedt, D. (1996). Evaluation of preperation, staining and microscopic techniques for counting incremental lines in cementum of human teeth. *Biotechnic & Histochemistry*, *71*(4), 165–172.
- Kvam, T. (1984). Age determination in European lynx Lynx l. lynx by incremental lines in tooth cementum. *Acta Zoologica Fennica*, *171*, 221–223.

- Laine, M., Tenovuo, J., Lehtonen, O. P., Ojanotko-Harri, a, Vilja, P., & Tuohimaa, P. (1988). Pregnancy-related changes in human whole saliva. *Archives of Oral Biology*, *33*(12), 913–7. https://doi.org/10.1016/0003-9969(88)90022-2

- Laland, K. N., Kendall, J. K., & Brown, G. (2007). The niche construction perspective: implication for evolution and human behavior. *Evolutionary Psychology*, *5*, 51–66.

- Landon, D. B., Waite, C. A., Peterson, R. O., & Mech, L. D. (1998). Evaluation of Age Determination Techniques for Gray Wolves. *The Journal of Wildlife Management*, *62*(2), 674. https://doi.org/10.2307/3802343

- Larrue, A., Rattner, A., Peter, Z. A., Olivier, C., Laroche, N., Vico, L., & Peyrin, F. (2011). Synchrotron radiation micro-CT at the Micrometer scale for the analysis of the three-dimensional morphology of microcracks in human trabecular bone. *PLoS ONE*, *6*(7). https://doi.org/10.1371/journal.pone.0021297

- Le Cabec, A., Tang, N., & Tafforeau, P. (2015). Accessing developmental information of fossil hominin teeth using new synchrotron micortomography-based visualization techniques of dental surfaces and interfaces. *PloS One*, *10*(4), e0123019.

- LeBlanc, A. R., & Reisz, R. R. (2013). Periodontal ligament, cementum, and alveolar bone in the oldest herbivorous tetrapods, and their evolutionary significance. *PlosS One*, *8*(9), e74697.

- LeBlanc, A. R. H., Brink, K. S., Cullen, T. M., & Reisz, R. R. (2017). Evolutionary implications of tooth attachment versus tooth implantation: A case study using dinosaur, crocodilian, and mammal teeth. *Journal of Vertebrate Paleontology*, *37*(5). https://doi.org/10.1080/02724634.2017.1354006

- LeBlanc, A. R. H., Lamoureux, D. O., & Caldwell, M. W. (2017). Mosasaurs and snakes have a periodontal ligament: timing and extent of calcification, not tissue complexity, determines tooth attachment mode in reptiles. *Journal of Anatomy*, *231*(6), 869–885. https://doi.org/10.1111/joa.12686

- LeBlanc, A. R. H., & Reisz, R. R. (2013). Periodontal Ligament, Cementum, and Alveolar Bone in the Oldest Herbivorous Tetrapods, and Their Evolutionary Significance. *PLoS ONE*, *8*(9). https://doi.org/10.1371/journal.pone.0074697

- LeBlanc, A. R. H., Reisz, R. R., Brink, K. S., & Abdala, F. (2016). Mineralized periodontia in extinct relatives of mammals shed light on the evolutionary history of

mineral homeostasis in periodontal tissue maintenance. *Journal of Clinical Periodontology*. https://doi.org/10.1111/jcpe.12508

- Leider, A. S., & Garbarino, V. E. (1987). Generalized hypercementosis. *Oral Surgery, Oral Medicine, Oral Pathology*, *63*(3), 375–380.
- Leimola-Virtanen, R., Salo, T., Toikkanen, S., Pulkkinen, J., & Syrjänen, S. (2000). Expression of estrogen receptor (ER) in oral mucosa and salivary glands. *Maturitas*, *36*(2), 131–137. https://doi.org/S0378-5122(00)00138-9 [pii]
- Leimola-Virtanen, R., Helenius, H., & Laine, M. (1997). Hormone replacement therapy and some salivary antimicrobial factors in post- and perimenopausal women. *Maturitas*, *27*(2), 145–151. https://doi.org/10.1016/S0378-5122(97)00024-8
- Leiss-Holzinger, E., & Et, A. (2015). Imaging of the inner structure of cave bear teeth by novel non-destructive techniques. *Palaeontologia Electronica*, *18*(February), 1–15. Retrieved from http://palaeo-electronica.org
- Lenander-Lumikari, M., & Loimaranta, V. (2000). Saliva and Dental Caries. *Advances in Dental Research*, *14*(1), 40–47. https://doi.org/10.1177/08959374000140010601
- Leng, H., Wang, X., Ross, R. D., Niebur, G. L., & Roeder, R. K. (2008). Micro-computed tomography of fatigue microdamage in cortical bone using a barium sulfate contrast agent. *Journal of the Mechanical Behavior of Biomedical Materials*, *1*(1), 68–75. https://doi.org/10.1016/j.jmbbm.2007.06.002
- Levy, G. G., & Mailland, M. L. (1980). Histologic study of the effects of occlusal hypofunction following antagonist tooth extraction in the rat. *J Periodontol*, *51*(7), 393–399. https://doi.org/10.1902/jop.1980.51.7.393
- Lieberman, D. E. (1993). Life history variables preserved in dental cementum microstructure. *Science*, *261*(5125), 1162–64.
- Lieberman, D. E. (1994). The biological basis for seasonal increments in dental cementum and their application to archaeological research. *Journal of Archaeological Science*, *21*(4), 525–539.
- Lieberman, D. E., Deacon, T. W., & Meadow, R. H. (1990). Computer image enahncement and analysis of cementum increments as applied to teeth of Gazella gazella. *Journal of Archaeological Science*, *17*(5), 519–533.

- Lipsinic, F. E., Paunovich, E., Houston, G. D., & Robison, S. F. (1986). Correlation of age and incremental lines in the cementum of human teeth. *Journal of Forensic Sciences*, *31*(3), 982–9. Retrieved from http://www.ncbi.nlm.nih.gov/pubmed/2426387
- Listgarten, M. A., Lang, N. P., Schroeder, H. E., & Schroeder, A. (1991). Periodontal tissues and their counterparts around endosseous implants. *Clinical Oral Implants Research*. https://doi.org/10.1034/j.1600-0501.1991.020309.x
- Liu, F. T. Y., & Lin, H. S. (1973). Effect of the Contraceptive Steroids Norethynodrel and Mestranol on Dental Caries Activity in Young Adult Female Rats. *Journal of Dental Research*, *52*(4), 753–757. https://doi.org/10.1177/00220345730520041901
- Lohmann, U., Sausen, R., Bengtsson, L., Cubasch, U., Perlwitz, J., & Roeckner, E. (1993). The Köppen climate classification as a diagnostic tool for general circulation models. *Climate Research*, 177–193.
- Lovegrove, B. G. (2016). A phenology of the evolution of endothermy in birds and mammals. *Biological Reviews*. https://doi.org/10.1111/brv.12280
- Lovegrove, B. G. (2012). The evolution of endothermy in Cenozoic mammals: A plesiomorphic-apomorphic continuum. *Biological Reviews*. https://doi.org/10.1111/j.1469-185X.2011.00188.x
- Lovejoy, C. O., Meindl, R. S., Mensforth, R. P., & Barton, T. J. (1985). Multifactorial determination of skeletal age at death: A method and blind tests of its accuracy. *American Journal of Physical Anthropology*, *68*(1), 1–14. https://doi.org/10.1002/ajpa.1330680102
- Low, W. A., & McT, I. (1963). Age determination of deer by annular structure of dental cementum. *The Journal of Wildlife Management*, 466–471.
- Low, W., & Cowan, I. M. (1963). Age determination of deer by annular structure of dental cementum. *The Journal of Wildlife Management*, *27*(3), 466–471. https://doi.org/10.2307/3798521
- Lozano, M., Bermúdez de Castro, J. M., Carbonell, E., & Arsuaga, J. L. (2008). Non-masticatory uses of anterior teeth of Sima de los Huesos individuals (Sierra de Atapuerca, Spain). *Journal of Human Evolution*, *55*(4), 713–728. https://doi.org/10.1016/j.jhevol.2008.04.007
- Luan, X., Walker, C., Dangaria, S., Ito, Y., Druzinsky, R., Jarosius, K., … Rieppel, O. (2009). The mosasaur tooth attachment apparatus as paradigm for the evolution of the

gnathostome periodontium. *Evolution and Development*, *11*(3), 247–259. https://doi.org/10.1111/j.1525-142X.2009.00327.x

- Lukacs, J. R., & Largaespada, L. L. (2006). Explaining Sex Differences in Dental Caries Prevalence: Saliva, Hormones, and "Life-History" Etiologies. *American Journal of Human Biology*. https://doi.org/10.1002/ajhb
- Lukas, D., & Clutton-Brock, T. (2014). Costs of mating competition limit male lifetime breeding success in polygynous mammals. *Proceedings of the Royal Society B: Biological Sciences*, *281*(1786), 20140418–20140418. https://doi.org/10.1098/rspb.2014.0418
- Luo, Z. X., Crompton, A. W., & Sun, A. L. (2001). A new mammaliaform from the early Jurassic and evolution of mammalian characteristics. *Science*, *292*(5521), 1535–1540. https://doi.org/10.1126/science.1058476
- Luo, Z. X. (2007). Transformation and diversification in early mammal evolution. *Nature*. https://doi.org/10.1038/nature06277
- Luo, Z. X., Meng, Q. J., Grossnickle, D. M., Liu, D., Neander, A. I., Zhang, Y. G., & Ji, Q. (2017). New evidence for mammaliaform ear evolution and feeding adaptation in a Jurassic ecosystem. *Nature*, *548*(7667), 326–329. https://doi.org/10.1038/nature23483
- Luo, Z.-X., Gatesy, S. M., Jenkins, F. A., Amaral, W. W., & Shubin, N. H. (2015). Mandibular and dental characteristics of Late Triassic mammaliaform *Haramiyavia* and their ramifications for basal mammal evolution. *Proceedings of the National Academy of Sciences*, 201519387. https://doi.org/10.1073/pnas.1519387112
- Luo, Z.-X., Kielan-Jaworowska, Z., & Cifelli, R. L. (2004). Evolution of dental replacement in mammals. *Bulletin of Carnegie Museum of Natural History*, *36*, 159–175. https://doi.org/10.2992/0145-
- Machtei, E. E., Mahler, D., Sanduri, H., & Peled, M. (2004). The Effect of Menstrual Cycle on Periodontal Health. *Journal of Periodontology*, *75*(3), 408–412. https://doi.org/10.1902/jop.2004.75.3.408
- Magalhaes, J. P. d., Costa, J., & Church, G. M. (2007). An Analysis of the Relationship Between Metabolism, Developmental Schedules, and Longevity Using Phylogenetic Independent Contrasts. *The Journals of Gerontology Series A: Biological Sciences and Medical Sciences*, *62*(2), 149–160. https://doi.org/10.1093/gerona/62.2.149

- Mansbridge, J. N. (1959). Heredity and Dental Caries. *Journal of Dental Research*, *38*(2), 337–347. https://doi.org/10.1177/00220345590380021601
- Marenzana, M., Hagen, C. K., Borges, P. D. N., Endrizzi, M., Szafraniec, M. B., Vincent, T. L., … Olivo, A. (2014). Synchrotron- and laboratory-based X-ray phase-contrast imaging for imaging mouse articular cartilage in the absence of radiopaque contrast agents. *Philosophical Transactions. Series A, Mathematical, Physical, and Engineering Sciences*, *372*(2010), 20130127. https://doi.org/10.1098/rsta.2013.0127
- Marsh, P. D. (1999). Microbiologic aspects of dental plaque and dental caries. *Dental Clinics of North America*, *43*(4), 599–614, v–vi.
- Martin, A. P. (1995). Metabolic rate and directional nucleotide substitution in animal mitochondrial DNA. *Molecular Biology and Evolution*, *12*(6), 1124–1131. https://doi.org/10.1093/oxfordjournals.molbev.a040286
- Martin, E. G., & Palmer, C. (2014). Air Space Proportion in pterosaur limb bones using computed tomography and its implications for previous estimates of pneumaticity. *PLoS ONE*, *9*(5). https://doi.org/10.1371/journal.pone.0097159
- Martin, R. R., Naftal, S. J., Nelson, A. J., Feilen, A. B., & Naraez, A. (2004). Synchrotron X-ray flourescence and trace metals in the cementum rings of human teeth. *Journal of Environmental Monitoring*, *6*(10), 783–786.
- Martin, R. R., Naftel, S. J., Nelson, A. J., Feilen, A. B., & Narvaez, A. (2007). Metal distributions in the cementum rings of human teeth: possible depositional chronologies and diagenesis. *Journal of Archaeological Science*, *34*(6), 936–945. https://doi.org/10.1016/j.jas.2006.09.018
- Martin, T., Marugán-Lobón, J., Vullo, R., Martín-Abad, H., Luo, Z. X., & Buscalioni, A. D. (2015). A Cretaceous eutriconodont and integument evolution in early mammals. *Nature*, *526*(7573), 380–384. https://doi.org/10.1038/nature14905
- Martínez-Meyer, E., Peterson, A. T., & Hargrove, W. W. (2004). Ecological niches as stable distributional constraints on mammal species, with implications for Pleistocene extinctions and climate change projections for biodiversity. *Global Ecology and Biogeography*, *13*(4), 305–314. https://doi.org/10.1111/j.1466-822X.2004.00107.x
- Maxwell, E., Caldwell, M. W., & Lamoureux, D. O. (2011). Tooth histology in the Cretaceous ichthyosaur Platypterygius australis, and its significance for the conservation and divergence of mineralized tooth tissues. *Journal of Morphology*, *272*(2), 129–135.

- Mayo, S., Davis, T., Gureyev, T., Miller, P., Paganin, D., Pogany, a, … Wilkins, S. (2003). X-ray phase-contrast microscopy and microtomography. *Optics Express*, *11*(19), 2289–2302. https://doi.org/10.1364/OE.11.002289
- Mays, S. (1998). *The Archaeology of Human bones*. london: Routledge.
- Mays, S., de la Rua, C., & Molleson, T. (1995). Molar crown height as a means of evaluating existing dental wear scales for estimating age at death in human skeletal remains. *Journal of Archaeological Science*, *22*(5), 659–670. https://doi.org/10.1016/S0305-4403(95)80151-0
- McKee, J. K. (1995). Turnover patterns and species longevity of large mammals from the late pliocene and pleistocene of Southern Africa: A comparison of simulated and empirical data. *Journal of Theoretical Biology*, *172*(2), 141–147. https://doi.org/10.1006/jtbi.1995.0011
- McKerrow, W. S., Johnson, R. T., & Jakobson, M. E. (1969). Palaeoecological studies in the great Oolite at Kirtlington, Oxfordshire. *Palaeontology*, *12*, 56–83.
- McKillop, H., & Rogers, T. (1992). A test of several methods of skeletal age estimation using a documented archaeological sample. *Journal of the Canadian Society of Forensic Science*, *25*(2), 97–118. https://doi.org/10.1080/00085030.1992.10757005
- McLaughlin, C. R., Matula Jr, G. J., Cross, R. A., Halteman, W. H., Caron, M. A., & Morris, K. I. (1990). Precision and accuracy of estimating age of Maine black bears by cementum annuli. *Bears: Their Biology and Management*, 415–419.
- Mealey, B. L., & Moritz, A. J. (2003). Hormonal influences: Effects of diabetes mellitus and endogenous female sex steroid hormones on the periodontium. *Periodontology 2000*. https://doi.org/10.1046/j.0906-6713.2002.03206.x
- Medill, S., Derocher, A. E., Stirling, I., & Lunn, N. (2010). Reconstructing the reproductive history of female polar bears using cementum patterns of premolar teeth. *Polar Biology*, *33*(1), 115–124.
- Medill, S., Derocher, A. E., Stirling, I., Lunn, N., & Moses, R. A. (2009). Estimating cementum annuli width in polar bears: identifying sources of variation and error. *Journal of Mammology*, *90*(5), 1256–1264.
- Meng, J., Hu, Y., Wang, Y., Wang, X., & Li, C. (2006). A Mesozoic gliding mammal from northeastern China. *Nature*, *444*(7121), 889–893. https://doi.org/10.1038/nature05234

- Meng, Q. J., Ji, Q., Zhang, Y. G., Liu, D., Grossnickle, D. M., & Luo, Z. X. (2015). An arboreal docodont from the jurassic and mammaliaform ecological diversification. *Science*, *347*(6223), 764–768. https://doi.org/10.1126/science.1260879
- Metcalf, S. J., & Walker, R. J. (1994). A new Bathonian microvertebrate locality in the English Midlands. *Shadow of the Dinosaurs: Early Mesozoic Tetrapods*, 322–331.
- Metscher, B. D. (2009). MicroCT for comparative morphology: simple staining methods allow high-contrast 3D imaging of diverse non-mineralized animal tissues. *BMC Physiology*, *9*(1), 11. https://doi.org/10.1186/1472-6793-9-11
- Millien, V., & Bovy, H. (2010). When teeth and bones disagree: body mass estimation of a giant extinct rodent. *Journal of Mammalogy*, *91*(1), 11–18. https://doi.org/10.1644/08-MAMM-A-347R1.1
- Mitchell, B. (1967). Growth layers in dental cement for determining the age of red deer (Cervus Elaphus L.). *Journal of Animal Ecology Animal Ecology*, *36*(2), 279–293. https://doi.org/10.2307/2912
- Mitchell, B. (1967). Growth layers in dental cement for determining the age of red deer. *The Journal of Animal Ecology*, 279–293.
- Mohammadi, S., Larsson, E., Alves, F., Dal Monego, S., Biffi, S., Garravo, C., … Dullin, C. (2014). Quantitative evaluation of a single-distance phase-retrieval method applied on in-line phase-contrast images of a mouse lung. *Journal of Synchrotron Radiation*, *21*(4), 784–789.
- Mokso, R., Marone, F., Irvine, S., Nyvlt, M., Schwyn, D., Mader, K., … Stampanoni, M. (2013). Advantages of phase retrieval for fast x-ray tomographic microscopy. *Journal of Physics D: Applied Physics*, *46*(49). https://doi.org/10.1088/0022-3727/46/49/494004
- Mombelli, A., Gusberti, F. A., van Oosten, M. A. C., & Lang, N. P. (1989). Gingival health and gingivitis development during puberty: A 4-year longitudinal study. *Journal of Clinical Periodontology*, *16*(7), 451–456. https://doi.org/10.1111/j.1600-051X.1989.tb01674.x
- Moreaux, L., Sandre, O., & Mertz, J. (2000). Membrane imaging by second-harmonic generation microscopy. *Journal of the Optical Society of America B*, *17*(10), 1685. https://doi.org/10.1364/JOSAB.17.001685
- Morris, P. (1972). A review of mammalian age determination methods. *Mammal Review*, *2*(3), 69–104.

- Morrongiello, J. R., Thresher, R. E., & Smith, D. C. (2012). Aquatic biochronologies and climate change. *Nture Climate Change*, *2*(12), 849.
- Morse, A. (1945). Formic acid-sodium citrate decalcification and butyl alcohol dehydration of teeth and bones for sectioning in paraffin. *Journal of Dental Research*, *24*(3), 143–153. https://doi.org/10.1177/00220345450240030501
- Muhler, J. D., & Shafer, W. G. (1955). Experimental dental caries VII. *Journal of Dental Research*, *34*, 387–389.
- Murdock, D. J. E., Dong, X.-P., Repetski, J. E., Marone, F., Stampanoni, M., & Donoghue, P. C. J. (2013). The origin of conodonts and of vertebrate mineralized skeletons. *Nature*, *502*(7472), 546–9. https://doi.org/10.1038/nature12645
- Musey, V. C., Collins, D. C., Musey, P. I., Martino-Saltzman, D., & Preedy, J. R. K. (1987). Long-Term Effect of a First Pregnancy on the Secretion of Prolactin. *New England Journal of Medicine*, *316*(5), 229–234. https://doi.org/10.1056/NEJM198701293160501
- Naji, S., Colard, T., Blondiaux, J., Bertrand, B., D'Incau, E., & Bocquet-Appel, J. P. (2016). Cementochronology, to cut or not to cut? *International Journal of Paleopathology*.
- Newham, E., Benson, R., Upchurch, P., & Goswami, A. (2014). Mesozoic mammaliaform diversity: The effect of sampling corrections on reconstructions of evolutionary dynamics. *Palaeogeography, Palaeoclimatology, Palaeoecology*, *412*, 32–44. https://doi.org/10.1016/j.palaeo.2014.07.017
- Nixon, M., & Aguado, A. (2012). *Feature Extraction & Image Processing for Computer Vision, Third Edition*. *Feature Extraction & Image Processing for Computer Vision, Second Edition*. https://doi.org/10.1016/B978-0-12-396549-3.00003-3
- O'Brien, M. J., & Laland, K. N. (2012). Genes, Cuture and Agriculture: An example of human niche construction. *Current Anthropology*, *53*(4), 434–470. https://doi.org/10.1086/666585
- O'Meara, R. N., & Asher, R. J. (2016). The evolution of growth patterns in mammalian versus nonmammalian cynodonts. *Paleobiology*, *42*(3), 439–464. https://doi.org/10.1017/pab.2015.51

- Obertová, Z., & Francken, M. (2009). Tooth cementum annulation method: Accuracy and applicability. In *Frontiers of Oral Biology* (Vol. 13, pp. 184–189). https://doi.org/10.1159/000242415
- Olejniczak, A. J., Grine, F. E., & Martin, L. B. (2007). Micro-computed tomography of primate molars: Methodological aspects of three-dimensional data collection. *Dental Perspectives on Human Evolution: State of the Art Research in Dental Paleoanthropology*, 103–115. Retrieved from http://dx.doi.org/10.1007/978-1-4020-5845-5_7
- Olejniczak, A. J., & Grine, F. E. (2006). Assessment of the accuracy of dental enamel thickness measurements using microfocal X-ray computed tomography. *The Anatomical Record. Part A, Discoveries in Molecular, Cellular, and Evolutionary Biology*, *288*(3), 263–275. https://doi.org/10.1002/ar.a.20307
- Oli, M. K., & Dobson, F. S. (1999). Population cycles in small mammals: the role of age at sexual maturity. *Oikos*, *86*(3), 557–565. https://doi.org/10.2307/3546660
- Olivier, C., Houssaye, A., Jalil, N.-E., & Cubo, J. (2017). First palaeohistological inference of resting metabolic rate in an extinct synapsid, Moghreberia nmachouensis (Therapsida: Anomodontia). *Biological Journal of the Linnean Society*, *121*(2), 409–419. https://doi.org/10.1093/biolinnean/blw044
- Ostertag, A., Peyrin, F., Fernandez, S., Laredo, J. D., de Vernejoul, M. C., & Chappard, C. (2014). Cortical measurements of the tibia from high resolution peripheral quantitative computed tomography images: A comparison with synchrotron radiation micro-computed tomography. *Bone*, *63*, 7–14. https://doi.org/10.1016/j.bone.2014.02.009
- Owen, R. (1871). *Monograph of the fossil Mammalia of the Mesozoic formations*. Palaeontological Society.
- Owerkowicz, T., Musinsky, C., Middleton, K. M., & Crompton, A. W. (2015). Respiratory turbinates and the evolution of endothermy in mammals and birds. *Great Transformations in Vertebrate Evolution*, 143–165.
- Padian, K. (2013). *Bone histology of fossil tetrapods*. Berkely: University of California Press.
- Padian, K., & Lamm, E. T. (2013). *Bone histology of fossil tetrapods: advancing methods, analysis, and interpolation*. University of California Press.

- Paganin, D., Mayo, S. C., Gureyev, T. E., Miller, P. R., & Wilkins, S. W. (2002). Simultaneous phase and amplitude extraction from a single defocused image of a homogeneous object. *Journal of Microscopy*, *206*(1), 33–40. https://doi.org/10.1046/j.1365-2818.2002.01010.x

- Pasda, C. (2014). Regional variation in thule and colonial caribou hunting in West Greenland. *Arctic Anthropology*, *51*(4), 41–76. https://doi.org/10.3368/aa.51.1.41

- Pauwels, E., Van Loo, D., Cornillie, P., Brabant, L., & Van Hoorebeke, L. (2013). An exploratory study of contrast agents for soft tissue visualization by means of high resolution X-ray computed tomography imaging. *Journal of Microscopy*, *250*(1), 21–31. https://doi.org/10.1111/jmi.12013

- Pearson, D. A., Schaefer, T., Johnson, K. R., & Nichols, D. J. (2001). Palynologically calibrated vertebrate record from North Dakota consistent with abrupt dinosaur extinction at the Cretaceous-Tertiary boundary. *Geology*, *29*(1), 39–42. https://doi.org/10.1130/0091-7613(2001)?029<0039:PCVRFN>?2.0.CO

- Percival, R. S., Challacombe, S., & Marsh, P. D. (1994). Flow Rates of Resting Whole and Stimulated Parotid Saliva in Relation to Age and Gender. *Journal of Dental Research*, *73*(8), 1416–1420. https://doi.org/10.1177/00220345940730080401

- Pérez-Barbería, F. J., Duff, E. I., Brewer, M. J., & Guinness, F. E. (2014). Evaluation of methods to age Scottish red deer: The balance between accuracy and practicality. *Journal of Zoology*, *294*(3), 180–189. https://doi.org/10.1111/jzo.12166

- Persson, R. E. (1998). Oral health and medical status in dentate low-income older persons. *Special Care in Dentistry*, *18*(2), 70–77. https://doi.org/10.1111/j.1754-4505.1998.tb00907.x

- Peters, O. a, Laib, a, Göhring, T. N., & Barbakow, F. (2001). Changes in root canal geometry after preparation assessed by high-resolution computed tomography. *Journal of Endodontia*, *27*(1), 1–6. https://doi.org/10.1097/00004770-200101000-00001

- Pike-Tay, A. (1991). *Red deer hunting in the Upper Paleolithic of south-west France: a study in seasonality*. British Archaeological Reports Ltd.

- Pike-Tay, A., Cabrera Valdés, V., & De Quirós, F. B. (1999). Seasonal variations of the Middle-Upper Paleolithic transition at El Castillo, Cueva Morin and El Pendo (Cantabria, Spain). *Journal of Human Evolution*, *36*(3), 283–317. https://doi.org/10.1006/jhev.1998.0271

- Poggio, C., Ceci, M., Beltrami, R., Lombardini, M., & Colombo, M. (2014). Atomic force microscopy study of enamel remineralization. *Annali Di Stomatologia*, *5*(3), 98–102. Retrieved from http://www.pubmedcentral.nih.gov/articlerender.fcgi?artid=4252861&tool=pmcentrez&rendertype=abstract
- Pratt, I. V., Belev, G., Zhu, N., Chapman, L. D., & Cooper, D. M. L. (2015). In vivo imaging of rat cortical bone porosity by synchrotron phase contrast micro computed tomography. *Physics in Medicine and Biology*, *60*(1), 211–232. https://doi.org/10.1088/0031-9155/60/1/211
- Purnell, M. A., Crumpton, N., Gill, P. G., Jones, G., & Rayfield, E. J. (2013). Within-guild dietary discrimination from 3-D textural analysis of tooth microwear in insectivorous mammals. *Journal of Zoology*, *291*(4), 249–257. https://doi.org/10.1111/jzo.12068
- Purnell, M., Seehausen, O., & Galis, F. (2012). Quantitative three-dimensional microtextural analyses of tooth wear as a tool for dietary discrimination in fishes. *Journal of The Royal Society Interface*, *9*(74), 2225–2233. https://doi.org/10.1098/rsif.2012.0140
- Quental, T. B., & Marshall, C. R. (2013). How the red queen drives terrestrial mammals to extinction. *Science*, *341*(6143), 290–292. https://doi.org/10.1126/science.1239431
- Rand, D. M. (1994). Thermal habit, metabolic rate and the evolution of mitochondrial DNA. *Trends in Ecology & Evolution*, *9*(4), 125–31. https://doi.org/10.1016/0169-5347(94)90176-7
- Ray, S., Botha, J., & Chinsamy, A. (2004). Bone histology and growth patterns of some nonmammalian therapsids. *Journal of Vertebrate Paleontology*, *24*(3), 634–648. https://doi.org/10.1671/0272-4634(2004)024[0634:BHAGPO]2.0.CO;2
- Réale, D., Martin, J., Coltman, D. W., Poissant, J., & Festa-Bianchet, M. (2009). Male personality, life-history strategies and reproductive success in a promiscuous mammal. *Journal of Evolutionary Biology*, *22*(8), 1599–1607. https://doi.org/10.1111/j.1420-9101.2009.01781.x
- Renz, H., & Radlanski, R. J. (2006). Incremental lines in root cementum of human teeth - A reliable age marker? *HOMO- Journal of Comparative Human Biology*, *57*(1), 29–50. https://doi.org/10.1016/j.jchb.2005.09.002

- Rey, K., Amiot, R., Fourel, F., Abdala, F., Fluteau, F., Jalil, N. E., Lécuyer, C. (2017). Oxygen isotopes suggest elevated thermometabolism within multiple permo-triassic therapsid clades. *ELife*, *6*. https://doi.org/10.7554/eLife.28589

- Rincon, J. C., Young, W. G., & Bartold, P. M. (2006). The epithelial cell rests of Malassez--a role in periodontal regeneration? *Journal of Periodontal Research*, *41*(4), 245–52. https://doi.org/10.1111/j.1600-0765.2006.00880.x

- Ritz-Timme, S., Cattaneo, C., Collins, M. J., Waite, E. R., Schütz, H. W., Kaatsch, H. J., & Borrman, H. I. M. (2000). Age estimation: The state of the art in relation to the specific demands of forensic practise. *International Journal of Legal Medicine*. https://doi.org/10.1007/s004140050283

- Rökert, H. (1956). Variations in calcification of cementum and dentin as seen by the use of microradiographic technique. *Experientia*, *12*(16).

- Roksandic, M., Vlak, D., Schillaci, M. A., & Voicu, D. (2009). Applicability of tooth cementum annulation to an archaeological population. *American Journal of Physical Anthropology*, *140*(3), 583–588.

- Rolandsen, C. M., Solberg, E. J., Heim, M., Holmstrøm, F., Solem, M. I., & Sæther, B. E. (2008). Accuracy and repeatability of moose (Alces alces) age estimated from dental cement layers. *European Journal of Wildlife Research*, *54*(1), 6–14.

- Rosing-Asvid, A., Born, E. W., & Kingsley, M. C. S. (2002). Age at sexual maturity of males and timing of the mating season of polar bears (Ursus maritimus) in Greenland. *Polar Biology*, *25*, 878–883. https://doi.org/DOI 10.1007/s00300-002-0430-7

- Ross, R. D., & Roeder, R. K. (2011). Binding affinity of surface functionalized gold nanoparticles to hydroxyapatite. *Journal of Biomedical Materials Research - Part A*, *99 A*(1), 58–66. https://doi.org/10.1002/jbm.a.33165

- Rowe, T. (1988). Definition, diagnosis, and origin of Mammalia. *Journal of Vertebrate Palaeontology*, *8*(3), 241–264.

- Rowe, T., & frank, L. R. (2011). The disappearing third dimension. *Science, 331*(6018), 712-714.

- Rowe, T. B., Macrini, T. E., & Luo, Z.-X. (2011). Fossil Evidence on Origin of the Mammalian Brain. *Science*, *332*(6032), 955–957. https://doi.org/10.1126/science.1203117

- Rücklin, M., Donoghue, P. C. J., Johanson, Z., Trinajstic, K. M., Marone, F., & Stampanoni, M. (2012). Development of teeth and jaws in the earliest jawed vertebrates. *Nature*, *491*(V), 748–752. https://doi.org/10.1038/nature11555

- Ruf, I., Luo, Z. X., Wible, J. R., & Martin, T. (2009). Petrosal anatomy and inner ear structures of the Late Jurassic Henkelotherium (Mammalia, Cladotheria, Dryolestoidea): Insight into the early evolution of the ear region in cladotherian mammals. *Journal of Anatomy*, *214*(5), 679–693. https://doi.org/10.1111/j.1469-7580.2009.01059.x

- Ruf, I., Maier, W., Rodrigues, P. G., & Schultz, C. L. (2014). Nasal Anatomy of the Non-mammaliaform Cynodont Brasilitherium riograndensis (Eucynodontia, Therapsida) Reveals New Insight into Mammalian Evolution. *Anatomical Record*, *297*(11), 2018–2030. https://doi.org/10.1002/ar.23022

- Russell, S. L., & Mayberry, L. J. (2008). Pregnancy and oral health: A review and recommendations to reduce gaps in practice and research. *MCN The American Journal of Maternal/Child Nursing*, *33*(1), 32–37. https://doi.org/10.1097/01.NMC.0000305655.86495.39

- Sacher, G. A. (1975). Maturation and longevity in relation to cranial capacity in hominid evolution. *Primate Functional Morphology and Evolution*, 417–441.

- Sacher, G. A. (1959). Relation of lifespan to brain weight and body weight in mammals. In *CIBA Foundation Colloquia on Aging* (pp. 115–141). https://doi.org/10.1002/9780470715253.ch9

- Salehi, H., Terrer, E., Panayotov, I., Levallois, B., Jacquot, B., Tassery, H., & Cuisinier, F. (2013). Functional mapping of human sound and carious enamel and dentin with Raman spectroscopy. *Journal of Biophotonics*, *6*(10), 765–774. https://doi.org/10.1002/jbio.201200095

- Sanchez, S., Ahlberg, P. E., Trinajstic, K. M., Mirone, A., & Tafforeau, P. (2012). Three-dimensional synchrotron virtual paleohistology: a new insight into the world of fossil bone microstructures. *Microscopy and Microanalysis*, *18*, 1095–1105. https://doi.org/10.1017/S1431927612001079

- Sanchez, S., Tafforeau, P., Clack, J. A., & Ahlberg, P. E. (2016). Life history of the stem tetrapod Acanthostega revealed by synchrotron microtomography. *Nature*, *537*(7620), 1–12. https://doi.org/10.1038/nature19354

- Saunders, S. R., Fitzgerald, C., Rogers, T., Dudar, C., & McKillop, H. (1992). A test of several methods of skeletal age estimation using a documented archaeological sample. *Canadian Society of Forensic Science Journal*, *25*(2), 97–118.
- Schaff, F., Bech, M., Zaslansky, P., Jud, C., Liebi, M., Guizar-Sicairos, M., & Pfeiffer, F. (2015). Six-dimensional real and reciprocal space small-angle X-ray scattering tomography. *Nature*, *527*(7578), 353–356. https://doi.org/10.1038/nature16060
- Schneider, C. A., Rasband, W. S., & Eliceiri, K. W. (2012). NIH Image to ImageJ: 25 years of image analysis. *Nature Methods*. https://doi.org/10.1038/nmeth.2089
- Schneider, P., Krucker, T., Meyer, E., Ulmann-Schuler, A., Weber, B., Stampanoni, M., & Müller, R. (2009). Simultaneous 3D visualization and quantification of murine bone and bone vasculature using micro-computed tomography and vascular replica. *Microscopy Research and Technique*, *72*(9), 690–701. https://doi.org/10.1002/jemt.20720
- Schroeder, H. E. (1993). Human cellular mixed stratified cementum: a tissue with alternating layers of acellular extrinsic-and cellular intrinsic fiber cementum. *Schweizer Monatsschrift Fur Zahnmedizin=Revue Mensuelle Suisse d'Odonto-Stomatologie= Rivista Mensile Svizzera Di Odontologia e Stomatologia*, *103*(5), 550–560.
- Schroeder, H. E. (1986). *The periodontium. Handbook of microscopic anatomy* (V). Berlin: Springer Verlag.
- Schulze, K. A., Balooch, M., Balooch, G., Marshall, G. W., & Marshall, S. J. (20045). Micro-Raman spectroscopic investigation of dental calcified tissues. *Journal of Biomedical Materials Research Part A*, *69*(4), 286–293.
- Schwartz, G. T., Thackeray, J. F., Reid, C., & van Reenan, J. F. (1998). Enamel thickness and the topography of the enamel-dentine junction in South African Plio-Pleistocene hominids with special reference to the Carabelli trait. *Journal of Human Evolution*, *35*(4–5), 523–542. https://doi.org/10.1006/jhev.1998.0239
- Schwartz, G. T., & Dean, C. (2000). Interpreting the hominid dentition:ontogenetic and phylogenetic aspects. *Linnean Society Symposium Series*, *20*.
- Schwartz, J. H. (1995). *Skeleton Keys: An introduction to human skeletal morphology, development and analysis*. Oxford: Oxford University Press.
- Scrivner, J. H., Johnson, C. A., & Sego, C. A. (2014). Use of cementum annuli and eye-lens weight for aging coyotes. *Wildlife Society Bulletin*, *38*(4), 874–877.

- Scrivner, J. H., Johnson, C. A., & Sego, C. A. (2014). Use of cementum annuli and eye-lens weight for aging coyotes. *Wildlife Society Bulletin*, *38*(4), 874–877. https://doi.org/10.1002/wsb.455
- Seymour, R. S., Smith, S. L., White, C. R., Henderson, D. M., & Schwarz-Wings, D. (2012). Blood flow to long bones indicates activity metabolism in mammals, reptiles and dinosaurs. *Proceedings of the Royal Society B: Biological Sciences*, *279*(1728), 451–456. https://doi.org/10.1098/rspb.2011.0968
- Shafer, W. G. (1954). Experimental dental caries III. *Journal of Dental Research*, *33*, 842–848.
- Shattuck, M. R., & Williams, S. A. (2010). Arboreality has allowed for the evolution of increased longevity in mammals. *Proceedings of the National Academy of Sciences*, *107*(10), 4635–4639. https://doi.org/10.1073/pnas.0911439107
- Shelton, C. D., & Sander, P. M. (2017). Long bone histology of Ophiacodon reveals the geologically earliest occurrence of fibrolamellar bone in the mammalian stem lineage. *Comptes Rendus Palevol*, *16*(4), 397–424.
- Sibly, R. M., & Brown, J. H. (2007). Effects of body size and lifestyle on evolution of mammal life histories. *Proceedings of the National Academy of Sciences*, *104*(45), 17707–17712. https://doi.org/10.1073/pnas.0707725104
- Silk, H., Douglass, A. B., Douglass, J. M., & Silk, L. (2008). Oral health during pregnancy. *American Family Physician*. https://doi.org/10.3109/14767050902926954
- Smith, D. W. (1989). Is greater female longevity a general finding among animals? *Biological Reviews of the Cambridge Philosophical Society*, *64*(1), 1–12. https://doi.org/10.1111/j.1469-185X.1989.tb00635.x
- Smith, K. G., Strother, K. A., Rose, J. C., & Savelle, J. M. (1994). Chemical Ultrastructure of Cementum Growth-Layers of Teeth of Black Bears. *Journal of Mammalogy*, *75*(2), 406–409. https://doi.org/10.2307/1382560
- Smith, T. M., & Tafforeau, P. (2008). New visions of dental tissue research: tooth development, chemisty, and structure. *Evolutionary Anthropology: Issues, News and Reviews*, *17*(5), 213–226.
- Smith, T. M., Tafforeau, P., Le Cabec, A., Bonnin, A., Houssaye, A., Pouech, J., … Mentor, C. G. (2015). Dental ontogeny in pliocene and early pleistocene hominins. *PloS One*, *10*(2), e0118118.

- Smith, T. M. (2008). Incremental dental development: Methods and applications in hominoid evolutionary studies. *Journal of Human Evolution*, *54*(2), 205–224. https://doi.org/10.1016/j.jhevol.2007.09.020
- Smith, T. M., Tafforeau, P., Reid, D. J., Pouech, J., Lazzari, V., Zermeno, J. P., Hublin, J.-J. (2010). Dental evidence for ontogenetic differences between modern humans and Neanderthals. *PNAS*, *107*(49), 20923–20928. https://doi.org/10.1073/pnas.1010906107
- Souza, L. N., Lima, S. M., Pimenta, F. J. G. S., Souza, A. C. R. A., & Gomez, R. S. (2004). Atypical hypercementosis versus cementoblastoma. *Dentomaxillofacial Radiology*, *33*(4), 267–270. https://doi.org/10.1259/dmfr/30077628
- Spencer Larsen, C. (1995). Biological Changes in Human Populations with Agriculture. *Annual Review of Anthropology*, *24*(1), 185–213. https://doi.org/10.1146/annurev.anthro.24.1.185
- Spinage, C. A. (1973). A review of age determination of mammals by means of teeth, with especial reference to Africa. *African Journal of Ecology*, *11*(2), 165–187.
- Stewart, R. E. A., Stewart, B. E., Stirling, I., & Street, E. (1996). Counts of Growth Layer Groups in Cementum and Dentine in Ringed Seals (phoca Hispida). *Marine Mammal Science*, *12*(3), 383–401. https://doi.org/10.1111/j.1748-7692.1996.tb00591.x
- Stock, S. R., Finney, L. A., Telser, A., Maxey, E., Vogt, S., & Okasinski, J. S. (2017). Cementum structure in Beluga whale teeth. *Acta Biomaterialia*, *48*, 289–299. https://doi.org/10.1016/j.actbio.2016.11.015
- Stout, K. (2000). Three Dimensional Surface Topography. *Three Dimensional Surface Topography*, 19–94. https://doi.org/10.1016/B978-185718026-8/50117-X
- Stout, S. D., & Paine, R. R. (1992). Histological age estimation using rib and clavicle. *American Journal of Physical Anthropology*, *87*(1), 111–115.
- Stout, S. D., & Paine, R. R. (1992). Histological age estimation using rib and clavicle. *American Journal of Physical Anthropology*, *87*(1), 111–115. https://doi.org/10.1002/ajpa.1330870110
- Strandberg, S., Wretling, M.-L., Wredmark, T., & Shalabi, A. (2010). Reliability of computed tomography measurements in assessment of thigh muscle cross-sectional area and attenuation. *BMC Medical Imaging*, *10*, 18. https://doi.org/10.1186/1471-2342-10-18

- Stutz, A. J. (2002). Polarizing microscopy identification of chemical diagenesis in archaeological cementum. *Journal of Archaeological Science*, *29*(11), 1327–1347. https://doi.org/10.1006/jasc.2001.0805
- Surarit, R., Krishnamra, N., & Seriwatanachai, D. (2016). Prolactin receptor and osteogenic induction of prolactin in human periodontal ligament fibroblasts. *Cell Biology International*, *40*(4), 419–427. https://doi.org/10.1002/cbin.10580
- Tafforeau, P., Bentaleb, I., Jaeger, J. J., & Martin, C. (2007). Nature of laminations and mineralization in rhinoceros enamel using histology and X-ray microtomography: potential implications for palaeoenvironmental isotopic studies. *Palaeogeography, Palaeoclimatology, Palaeoecology*, *246*(2), 206–227.
- Tafforeau, P., & Smith, T. M. (2008). Nondestructive imaging of hominid dental microstructure using phase contrast X-ray synchrotron microtomography. *Journal of Human Evolution*, *54*(2), 272–278.
- Tsuda, H., Ruben, J., & Arends, J. (1996). Raman spectra of human dentin mineral. *European Journal of Oral Sciences*, *104*(2 (Pt 1)), 123–131. https://doi.org/10.1111/j.1600-0722.1996.tb00056.x
- Tumarkin-Deratzian, A. R. (2007). Fibrolamellar Bone in Wild Adult Alligator Mississippiensis. *Journal of Herpetology*, *41*(2), 341–345. https://doi.org/10.1670/0022-1511(2007)41[341:FBIWAA]2.0.CO;2
- Twitchett, R. J. (2007). The Lilliput effect in the aftermath of the end-Permian extinction event. *Palaeogeography, Palaeoclimatology, Palaeoecology*, *252*(1–2), 132–144. https://doi.org/10.1016/j.palaeo.2006.11.038
- Umetani, K., & Fukushima, K. (2013). X-ray intravital microscopy for functional imaging in rat hearts using synchrotron radiation coronary microangiography. *Rev Sci Instrum*, *84*(3), 34302. https://doi.org/10.1063/1.4795830
- van den Broek, W. L. F. (1983). *Ageing deepwater fish species: report of a visit to the Uniter Kingdom September-November 1982*. Wellington, NZ.
- Veiberg, V., Loe, L. E., Mysterud, A., Solberg, E. J., Langvatn, R., & Stenseth, N. C. (2007). The ecology and evolution of tooth wear in red deer and moose. *Oikos*, *116*(11), 1805–1818. https://doi.org/10.1111/j.2007.0030-1299.16159.x

- von Biela, V. R., Testa, J. W., Gill, V. A., & Burns, J. M. (2008). Evaluating Cementum to Determine Past Reproduction in Northern Sea Otters. *Journal of Wildlife Management*, *72*(3), 618–624. https://doi.org/10.2193/2007-218
- von Cramon-Taubadel, N. (2011). Global human mandibular variation reflects differences in agricultural and hunter-gatherer subsistence strategies. *Proceedings of the National Academy of Sciences*, *108*(49), 19546–19551. https://doi.org/10.1073/pnas.1113050108
- von Koenigswald, W., & Mörs, T. (2001). The enamel microstructure of Anchitheriomys (Rodentia, Mammalia) in comparison with that of other beavers and of porcupines. *Paläontologische Zeitschrift*, *74*(4), 601–612.
- Vullo, R., Girard, V., Azar, D., & Néraudeau, D. (2010). Mammalian hairs in early cretaceous amber. *Naturwissenschaften*, *97*(7), 683–687. https://doi.org/10.1007/s00114-010-0677-8
- Waldman, M., & Savage, R. J. G. (1972). The first Jurassic mammal from Scotland. *Journal of the Geological Society*, *128*(2), 119–125.
- Walker, P., & Hewlett, B. (1990). Dental health diet and social status among Central African foragers and farmers. *American Anthropologist*, *92*(2), 383–398. https://doi.org/10.1525/aa.1990.92.2.02a00080
- Wall-Scheffler, C. M., & Foley, R. A. (2008). Digital cementum luminance analysis (DCLA): a tool for the analysis of climatic and seasonal signals in dental cementum. *International Journal of Osteoarchaeology*, *18*(1), 11–27.
- Wall, C. M., & Wall, Z. R. (2006). Research design in digital luminance analysis. *Journal of Archaeological Science*, *33*, 1152–1156.
- Wallace, J. M. (2012). Applications of atomic force microscopy for the assessment of nanoscale morphological and mechanical properties of bone. *Bone*. https://doi.org/10.1016/j.bone.2011.11.008
- Wedel, V. L., Found, G., & Nusse, G. (2015). A 37-year-old cold case identification using novel and collaborative methods. *Journal of Forensic Identification*, *65*(4), 733.
- Wedel, V. L., & Wescott, D. J. (2016). Using dental cementum increment analysis to estimate age and season of death in African Americans from an historical cemetery in Missouri. *International Journal of Paleopathology*, *15*, 134–139. https://doi.org/10.1016/j.ijpp.2015.10.003

- Wellington, S. L., & Vinegar, H. J. (1987). X-ray computerized tomography. *Journal of Petroleum Technology*, *39*(8), 885–898. https://doi.org/10.2118/16983-PA
- Werner, J., Sfakianakis, N., Rendall, A. D., & Griebeler, E. M. (2018). Energy intake functions and energy budgets of ectotherms and endotherms derived from their ontogenetic growth in body mass and timing of sexual maturation. *Journal of Theoretical Biology*, *444*, 83–92. https://doi.org/10.1016/j.jtbi.2018.02.007
- Wilson, G. P., Evans, A. R., Corfe, I. J., Smits, P. D., Fortelius, M., & Jernvall, J. (2012). Adaptive radiation of multituberculate mammals before the extinction of dinosaurs. *Nature*, *483*(7390), 457–460. https://doi.org/10.1038/nature10880
- Wittwer-Backofen, U., Gampe, J., & Vaupel, J. W. (2004). Tooth cementum annulation for age estimation: Results from a large known-age validation study. *American Journal of Physical Anthropology*, *123*(2), 119–129.
- Xiong, J., Gronthos, S., & Bartold, P. M. (2013). Role Of The Epithelial Cell Rests Of Malassez In The Development, Maintenance And Regeneration Of Periodontal Ligament Tissues. *Periodontology 2000*, *63*(1), 217–233. https://doi.org/10.1111/prd.12023
- Zander, H. A., & Hürzeler, B. (1958). Continuous cementum apposition. *Journal of Dental Research*, *37*(6), 1035–1044.
- Zander, H. A., & Hürzeler, B. (1958). Continuous Cementum Apposition. *Journal of Dental Research*, *37*(6), 1035–1044. https://doi.org/10.1177/00220345580370060301
- Zeller-Plumhoff, B., Mead, J. L., Tan, D., Roose, T., Clough, G. F., Boardman, R. P., & Schneider, P. (2017). Soft tissue 3D imaging in the lab through optimised propagation-based phase contrast computed tomography. *Optics Express*, *25*(26), 33451. https://doi.org/10.1364/OE.25.033451
- Zhang, Z., Ross, R. D., & Roeder, R. K. (2010). Preparation of functionalized gold nanoparticles as a targeted X-ray contrast agent for damaged bone tissue. *Nanoscale*, *2*, 582–586. https://doi.org/10.1039/b9nr00317g
- Zheng, X., Bi, S., Wang, X., & Meng, J. (2013). A new arboreal haramiyid shows the diversity of crown mammals in the Jurassic period. *Nature*, *500*(7461), 199–202. https://doi.org/10.1038/nature12353
- Zhivotovsky, L. A. (1982). Indicators of population variability in polymorphic features. *Fenetika Populjacij [Population Phenetics]*, 38–44.

- Zhou, C. F., Wu, S., Martin, T., & Luo, Z. X. (2013). A Jurassic mammaliaform and the earliest mammalian evolutionary adaptations. *Nature*, *500*(7461), 163–167. https://doi.org/10.1038/nature12429
- Zug, G. R., & Stanley Rand, A. (1987). Estimation of Age in Nesting Female Iguana iguana: Testing Skeletochronology in a Tropical Lizard. *Amphibia Reptilia*, *8*(3), 237–249. https://doi.org/10.1163/156853887X00289
- Zullinger, E. M., Ricklefs, R. E., Redford, K. H., & Mace, G. M. (1984). Fitting Sigmoidal Equations to Mammalian Growth Curves. *Journal of Mammalogy*, *65*(4), 607–636. https://doi.org/10.2307/1380844